



IntechOpen

Advances in Microfluidics
New Applications in Biology, Energy, and
Materials Sciences

Edited by Xiao-Ying Yu



WEB OF SCIENCE™

ADVANCES IN MICROFLUIDICS - NEW APPLICATIONS IN BIOLOGY, ENERGY, AND MATERIALS SCIENCES

Edited by **Xiao-Ying Yu**

Advances in Microfluidics - New Applications in Biology, Energy, and Materials Sciences

<http://dx.doi.org/10.5772/60788>

Edited by Xiao-Ying Yu

Contributors

Yaakov Nahmias, Elishai Ezra Tsur, Danny Bavli, Babak Taghavi, Jiantong Li, Mikael Östling, Shi Cheng, Natalia Bakhtina, Neil MacKinnon, Jan Korvink, Daniel Nieto, Gerard O'Connor, John Yan, Adrien Chauvet, Anne-Marie Haghiri-Gosnet, Janet Ledesma-García, Noe Arjona, Jesus A. Díaz-Real, Francisco M. Cuevas-Muñiz, Minerva Guerra-Balcázar, Luis Gerardo Arriaga, Marianne Fillet, Kai Seng Koh, Yong Ren, Yaping Zhang, Meng Gao, Lin Gui, Chin-Tai Chen, Taotao Fu, Jason Fleischer, Nicolas C Pegard, Marton Toth, Monica Driscoll, Chien-Hung Lu, Victor Sebastian, Kiyoshi Ohnuma, Shinji Sugiura, Kohji Nakazawa, Toshiyuki Kanamori

© The Editor(s) and the Author(s) 2016

The moral rights of the and the author(s) have been asserted.

All rights to the book as a whole are reserved by INTECH. The book as a whole (compilation) cannot be reproduced, distributed or used for commercial or non-commercial purposes without INTECH's written permission.

Enquiries concerning the use of the book should be directed to INTECH rights and permissions department (permissions@intechopen.com).

Violations are liable to prosecution under the governing Copyright Law.



Individual chapters of this publication are distributed under the terms of the Creative Commons Attribution 3.0 Unported License which permits commercial use, distribution and reproduction of the individual chapters, provided the original author(s) and source publication are appropriately acknowledged. If so indicated, certain images may not be included under the Creative Commons license. In such cases users will need to obtain permission from the license holder to reproduce the material. More details and guidelines concerning content reuse and adaptation can be found at <http://www.intechopen.com/copyright-policy.html>.

Notice

Statements and opinions expressed in the chapters are these of the individual contributors and not necessarily those of the editors or publisher. No responsibility is accepted for the accuracy of information contained in the published chapters. The publisher assumes no responsibility for any damage or injury to persons or property arising out of the use of any materials, instructions, methods or ideas contained in the book.

First published in Croatia, 2016 by INTECH d.o.o.

eBook (PDF) Published by IN TECH d.o.o.

Place and year of publication of eBook (PDF): Rijeka, 2019.

IntechOpen is the global imprint of IN TECH d.o.o.

Printed in Croatia

Legal deposit, Croatia: National and University Library in Zagreb

Additional hard and PDF copies can be obtained from orders@intechopen.com

Advances in Microfluidics - New Applications in Biology, Energy, and Materials Sciences

Edited by Xiao-Ying Yu

p. cm.

Print ISBN 978-953-51-2785-7

Online ISBN 978-953-51-2786-4

eBook (PDF) ISBN 978-953-51-4147-1

We are IntechOpen, the world's leading publisher of Open Access books Built by scientists, for scientists

3,800+

Open access books available

116,000+

International authors and editors

120M+

Downloads

151

Countries delivered to

Our authors are among the
Top 1%

most cited scientists

12.2%

Contributors from top 500 universities



WEB OF SCIENCE™

Selection of our books indexed in the Book Citation Index
in Web of Science™ Core Collection (BKCI)

Interested in publishing with us?
Contact book.department@intechopen.com

Numbers displayed above are based on latest data collected.
For more information visit www.intechopen.com



Meet the editor



Dr. Yu was trained as a physical chemist and kineticist at the University of Michigan, Ann Arbor, Michigan, USA. She did her postdoctoral research at Brookhaven National Laboratory and Colorado State University, USA. She has been a senior scientist at Pacific Northwest National Laboratory since 2006. She has led the development of a novel meso-scale imaging tool based on microfluidics at PNNL since 2009, which has resulted in two issued patents, a prestigious R&D 100 Awards, and a Federal Laboratory Consortium Technology Transfer Excellence Award. Dr. Yu has developed new concepts in aerosol sampling and led and participated in many field studies for in situ measurements of aerosols. Dr. Yu is the chair of the Department of Energy chemical exposure working group and a member of the TEEL Advisory Group for consequence assessment.

Contents

Preface XIII

Section 1 Biological Applications 1

Chapter 1 **Advances in Low Volume Sample Analysis Using Microfluidic Separation Techniques 3**

Virginie Houbart and Marianne Fillet

Chapter 2 **Molecular Microfluidic Bioanalysis: Recent Progress in Preconcentration, Separation, and Detection 31**

Emmanuel Roy, Antoine Pallandre, Bacem Zribi, Marie-Charlotte Horny, François-Damien Delapierre, Andrea Cattoni, Jean Gamby and Anne-Marie Haghiri-Gosnet

Chapter 3 **Application of Microfluidics in Stem Cell Culture 67**

Shinji Sugiura, Kohji Nakazawa, Toshiyuki Kanamori and Kiyoshi Ohnuma

Chapter 4 **Advanced Microfluidic Assays for *Caenorhabditis elegans* 91**

Natalia A. Bakhtina, Neil MacKinnon and Jan G. Korvink

Section 2 Imaging and Spectroscopy 115

Chapter 5 **Microfluidics for Ultrafast Spectroscopy 117**

Adrien A. P. Chauvet

Chapter 6 **Flow-Scanning Microfluidic Imaging 135**

Nicolas Pégard, Chien-Hung Lu, Marton Toth, Monica Driscoll and Jason Fleischer

Section 3 Microfluidics and Electronics 163

Chapter 7 **Integrated Control of Microfluidics – Application in Fluid Routing, Sensor Synchronization, and Real-Time Feedback Control 165**

Elishai Ezra, Danny Bavli and Yaakov Nahmias

Chapter 8 **Microfluidics for Soft Electronics 189**

Babak Taghavi, Jiantong Li, Mikael Östling and Shi Cheng

Chapter 9 **Microfluidic Sensors and Circuits for Internet of Things Applications 213**

John Yan

Chapter 10 **Electroosmotic Flow Pump 237**

Meng Gao and Lin Gui

Section 4 Fabrications and Applications in Energy Research 255

Chapter 11 **Laser-Based Fabrication for Microfluidics Devices on Glass for Medical Applications 257**

Daniel Nieto García and Gerard O'Connor

Chapter 12 **Microfluidics in Membraneless Fuel Cells 273**

Jesus A. Diaz-Real, Minerva Guerra-Balcázar, Noe Arjona, Francisco Cuevas-Muñiz, Luis Gerardo Arriaga and Janet Ledesma-García

Chapter 13 **Microfluidics in CO₂ Capture, Sequestration, and Applications 293**

Taotao Fu

Chapter 14 **Generation and Evaporation of Microsprays 315**

Chin-Tai Chen

Chapter 15 **Overview of Materials for Microfluidic Applications 335**

Emmanuel Roy, Antoine Pallandre, Bacem Zribi, Marie-Charlotte Horny, François Damien Delapierre, Andrea Cattoni, Jean Gamby and Anne-Marie Haghiri-Gosnet

Section 5 Microfluidics and Material Synthesis 357

Chapter 16 **Synthesis of Functional Materials by Non-Newtonian
Microfluidic Multiphase System 359**

Yong Ren, Kai Seng Koh and Yaping Zhang

Chapter 17 **High and Efficient Production of Nanomaterials by Microfluidic
Reactor Approaches 385**

Victor Sebastian Cabeza

Preface

Microfluidics has seen a rapid development in the last decade as a result of the seminal work pioneered by Dr. Whitesides group and many others since the 1990s. Integrating science and technology, microfluidics has grown steadily as a new industry and scientific field. This is a field filled with imagination, ingenuity, and enthusiasm from many researchers across disciplines.

The InTech Open Access Publisher kindly asked me to edit a new book presenting recent advances and applications in microfluidics. This book is a timely report from many researchers who are actively practicing in the field. Each chapter represents the perspective of their views of the past, present, and future of microfluidics and its unique associations with their diverse research. The content of the book is easy to follow. It can be used by a researcher or student who is eager to learn more about microfluidics. Moreover, it can serve those who are experts and want to get a quick update from peers.

This book consists of five sections including the following: (1) Biological Applications, (2) Imaging and Spectroscopy, (3) Microfluidics and Electronics; (4) Fabrications and Applications in Energy Research, and (5) Microfluidics and Material Synthesis. Each section presents review articles with a particular focus in that area. While some space is given to more general overview of the fabrication techniques and materials used in microfluidics, most chapters are dedicated to new concepts, results, and applications. Specifically, the more widely known biological applications are listed in Section 1. Readers may find intriguing applications of microfluidics in imaging and spectroscopy besides conventional optical microscopy and spectroscopy in Section 2. Section 3 showcases examples of the integration of electronics and microfluidics as more researchers are exploring the marriage between MEMS and microfluidics. Section 4 provides some familiar backgrounds of microfluidic fabrication. However, the majority of the content in this part is geared at microfluidic applications in energy-related research such as fuel cells and carbon dioxide sequestration. Section 5 contains new results of material synthesis using microfluidics.

This book covers a wide range of new topics. The intent is to provide readers with a fresh view of the future directions of microfluidics based on the current research. It is a pleasure to acknowledge the InTech editors who helped to get everything in a timely manner, especially Ms. Iva Simcic for her persistence.

Xiao-Ying Yu
Pacific Northwest National Laboratory,
Richland, WA, USA

Biological Applications

Advances in Low Volume Sample Analysis Using Microfluidic Separation Techniques

Virginie Houbart and Marianne Fillet

Additional information is available at the end of the chapter

<http://dx.doi.org/10.5772/64952>

Abstract

During the last decades, a great interest has been shown for miniaturised separation techniques. The use of microfluidic techniques fulfills the constant needs for increasing sample throughput and analysis sensitivity, while reducing costs and sample volume consumption. In this chapter, three microfluidic separation techniques will be addressed: capillary electrophoresis, gas chromatography and liquid chromatography. A special attention will be paid to miniaturised liquid chromatography, with a deep investigation of its advantages compared with classical liquid chromatography. Sample preparation adapted to low volumes (a few μl) will also be discussed.

Keywords: Separation, miniaturisation, microfluidics, sensitivity

1. Introduction

Separation techniques are widely used for the analysis of biomolecules as well as small molecules in various fields, as genomics, proteomics or pharmaceutical sciences. Due to the wide range of separation techniques, numerous studies have been conducted aiming to improve performances in terms of sample preparation, sensitivity, cost or analysis throughput.

Liquid chromatography (LC) is the most employed separation technique, but alternative techniques such as capillary electrophoresis (CE) and gas chromatography (GC) are nevertheless helpful to provide orthogonal separation capabilities. Ultraviolet, electrochemical and fluorescence detection are used to detect the target compounds, but mass spectrometry (MS) detection offers enhanced sensitivity and additional structural information since co-eluting compounds are differentially detected according to their mass-to-charge ratio.

Miniaturisation is a general trend common to many areas in sciences and technology. Down-scaling the separation techniques has been initiated in the 1970s, but miniaturisation has mainly experienced an exponential growth since the 1990s. Reducing the size of the separation supports brings valuable advantages as analysis time reduction, increased sensitivity and low sample and reagent consumption. However, the limited loading capacity of microfluidic devices is a drawback. Adequate sample preparation, pre-concentration and appropriate device can circumvent these inherent limitations.

2. Microfluidic separation techniques

2.1. Capillary electrophoresis

2.1.1. Instrumentation

Capillary electrophoresis (CE) is a microscale analytical technique based on the separation of compounds according to their charge-to-size ratio. The first CE device was described by Hjertén in 1967 that performed the electrophoretic separations in narrow bore tubes of 300 μm inner diameter (i.d.) for the analysis of various analytes (inorganic ions, nucleotides, proteins) [1]. In 1981, Jorgenson and Lukacs demonstrated for the first time that capillaries with a smaller i.d. (75 μm) could provide high separation efficiency using high voltages (30 kV), due to the small capillary dimensions that allowed good dissipation of Joule heat produced by such a high voltage [2].

Most modern CE instruments are very simple: a high voltage power supply, an autosampler with injection system, a capillary (25–100 μm i.d. and more often 50–75 μm , 20–100 cm length) and a detector coupled to a computer for data acquisition (Figure 1A).

Briefly, a capillary made of fused silica coated with a layer of polyimide is filled with a background electrolyte solution. When an optical detection (commonly UV or fluorescence) is employed, two electrodes are placed in buffer reservoirs to provide the necessary electrical contact between the high voltage supply and the capillary. To perform an analysis, the sample is loaded into the capillary by applying either a pressure difference (hydrodynamic injection) or an electric field (electrokinetic injection) between both extremities of the capillary. Optical detection is performed through a detection window directly on the capillary.

The hyphenation of CE to MS was first presented in 1987 by Olivares et al. that proposed an interface between CE and MS with an electrospray ionisation source (ESI) [3]. Alternative ionisation method has been described for CE-MS [4], as continuous flow-fast atom bombardment ionisation (CF-FAB) [5], atmospheric pressure chemical ionisation (APCI) [6] or atmospheric pressure photochemical ionisation (APPI) [7]. The CE-MS coupling provides structural information, enhanced sensitivity and selectivity compared with an optical detection. The CE-MS instrument configuration is modified to allow the direct entrance of the analytes into the mass spectrometer (Figure 1B).

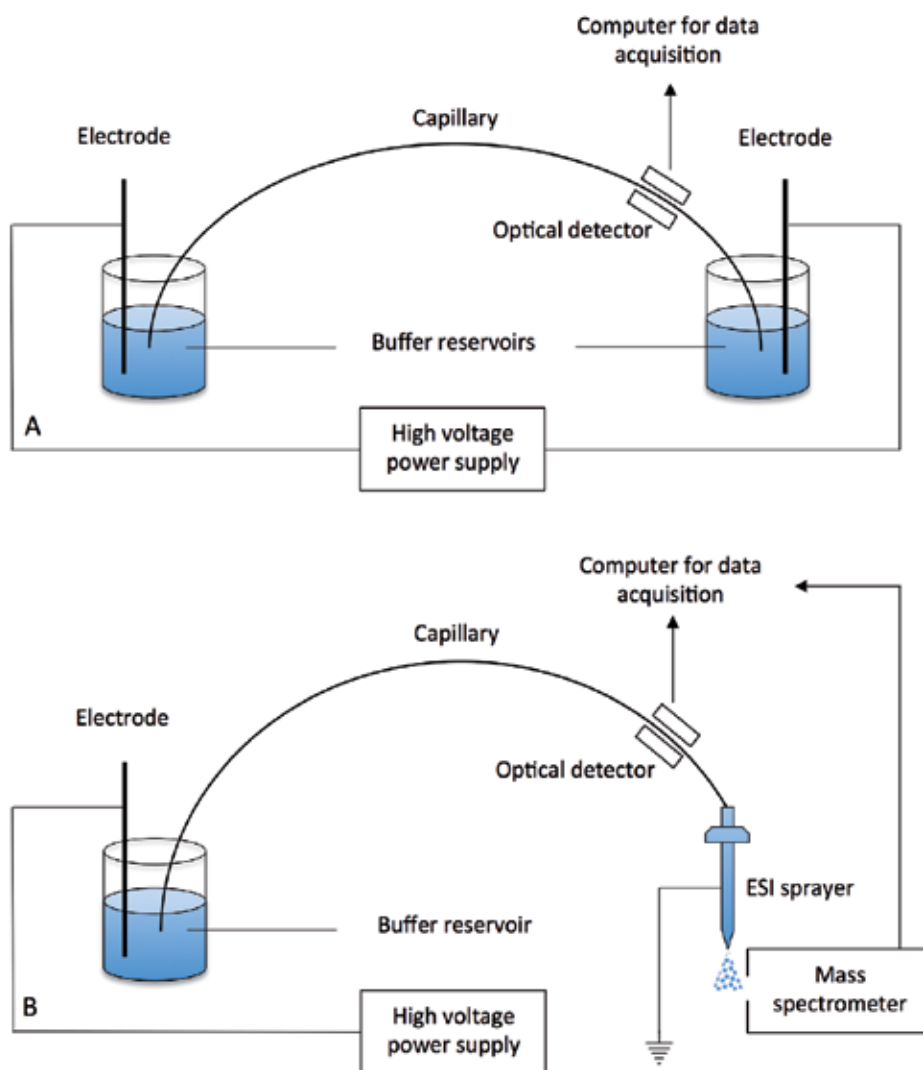


Figure 1. Schematic representation of a classical capillary electrophoresis system with an optical detection (A) and the coupling to a mass spectrometer (B).

The coupling of CE to MS can be achieved using a sheath liquid interface or a sheathless interface. The use of an additional liquid, the sheath liquid, to the electrophoretic effluent allows the formation of an electrical contact at the capillary MS output that is necessary for the electrophoretic separation, and enables the electrospray formation. In addition, the background electrolyte composition can be modified by dilution with the sheath liquid to ensure the compatibility with MS detection. However, the dilution process decreases the sensitivity in proportion with the sheath liquid flow rate.

Sheathless interfaces overcome the dilution-related sensitivity limitations encountered when using a sheath liquid interface. In this configuration, the electrical contact cannot be established through a liquid junction; the electrical contact may be established by many different techniques, e.g. by the insertion of the separation capillary into a conductive sprayer or the coating of the outlet end of the capillary by a conductive material.

2.1.2. Capillary electrophoresis on chip

In the light of the small dimensions of the separation capillary, classical CE is naturally classified into the category of miniaturised separation techniques. During the past few years, a new trend in CE instrumentation has emerged: the miniaturisation of CE into an integrated chip device for hyphenation to MS [12]. Since the introduction of the first chip-based electrophoresis device by Manz et al. [13], chip design has undergone continuous evolution from a single-channel design to more complex layouts integrating all the analytical steps on a single component. The actual classical chip design is made of two crossed microchannels, solution reservoirs for the sample and the waste, and reservoirs at the cathode and the anode for the buffer (Figure 2A) [14].

Interfacing a CE chip to an ESI-MS detector can be realised by spraying directly from the chip [15] or from a capillary sprayer attached to the chip [16] (Figure 2B).

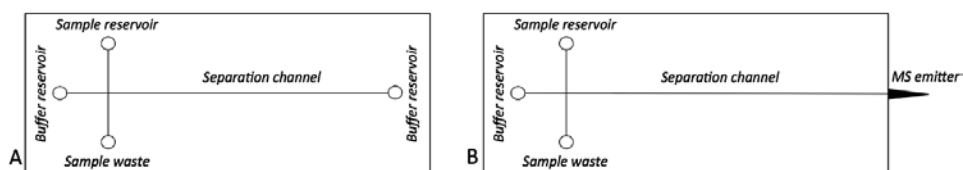


Figure 2. CE chip (A) and CE-MS (B) chip basic configuration.

In 1999 Agilent launched the Bioanalyser 2100, the first commercial microfluidics-based platform for DNA, RNA, protein and cell analysis. Separation is performed by capillary electrophoresis in channels containing a gel matrix. This device is the miniaturised counterpart of gel electrophoresis analysis (e.g. SDS-PAGE for proteins and agarose gel electrophoresis for nucleic acids) [17, 18]. In this device, sample with a volume between 1 and 6 μl moves through the loading channels, and a fraction of this volume is injected into the separation channel filled with a gel matrix. Fluorescence detection is performed on the chip itself. Total analysis time (including sample loading, separation, staining and destaining) is 30–40 min on the Bioanalyser chip, what is much shorter than the few hours (up to 1 day) required for the classical gel electrophoresis process.

Advantages of CE downscaling are reduced analysis times (minutes to seconds), low sample volume requirements (to the picolitre range), low solvent consumption and high throughput capabilities through the possibility of performing simultaneous separations in parallel channels [12].

Many applications using CE on chip have been developed for the analysis of a wide range of matrices and analytes: food analysis (including small molecules, organic acids, heavy metals, toxins, microorganisms or allergens) [19], amino acid analysis [20] or even intact protein characterisation [21].

2.2. Gas chromatography

Gas chromatography (GC) was first described by James and Martin in 1952. They presented a separation of volatile fatty acids on diatomaceous earth impregnated with a mixture of silicone oil and stearic acid as stationary phase, and a flow of nitrogen as the mobile phase [22]. GC underwent an explosive progression during the next decade, with applications for the petroleum industry [23], followed by biochemical applications [24, 25].

First GC separations were performed on packed columns of 1–5 mm i.d. Column length limitations due to backpressure drop led to the introduction of capillary GC columns [26, 27]. In such columns, the stationary phase is coated on the inner walls of the capillary to form a thin film (wall-coated open tubular, WCOT), or impregnated into a porous layer (porous layer open tubular, PLOT) [28]. Since capillary GC columns have less than 1 mm i.d. (typically 0.05–0.53 mm), this technique could already be considered as miniaturised.

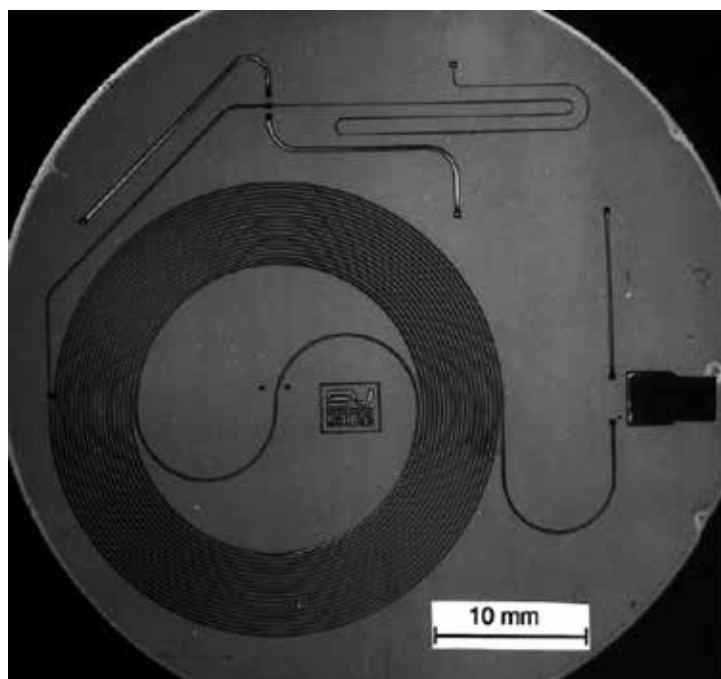


Figure 3. Angell's GC chip integrating sample injection valve, separation column and detector [29].

However, since the 1970s researchers have been trying to integrate all the components of a gas chromatographer including the detector on a single piece, or chip. In 1979, Angell proposed a

silicon wafer chip including a sample injection valve, a 1.5 m column and a detector [29] (Figure 3). In the next decades, other homemade chips were proposed, but to our knowledge no commercial version of a small and portable GC chip has been proposed so far.

A few applications have been developed on microbore GC systems, but research is still more dedicated to reliable miniaturised system development rather than method development [32].

2.3. Liquid chromatography

Liquid chromatography is the most commonly used separation technique with a wide range of applications. The precursor of liquid chromatography was the Russian scientific Mikhail Semenovich Tswett. He discovered that plant leave extracts poured on a column packed with particles could be separated into distinct coloured bands. In 1956, Van Deemter published his famous work about the fundamental equation of the relationship between mobile phase linear velocity and height equivalent to a theoretical plate (Figure 4) [33]. The modern appellation high pressure (now interchangeable with performance) liquid chromatography was first introduced by Horvath in 1970 to designate liquid chromatography performed on reduced ($<10\ \mu\text{m}$) porous particles. Since the 1970s, LC underwent an explosive popularity to become a standard separation technique with continuous progress in stationary phase variety and performances, hardware features and fields of applications.

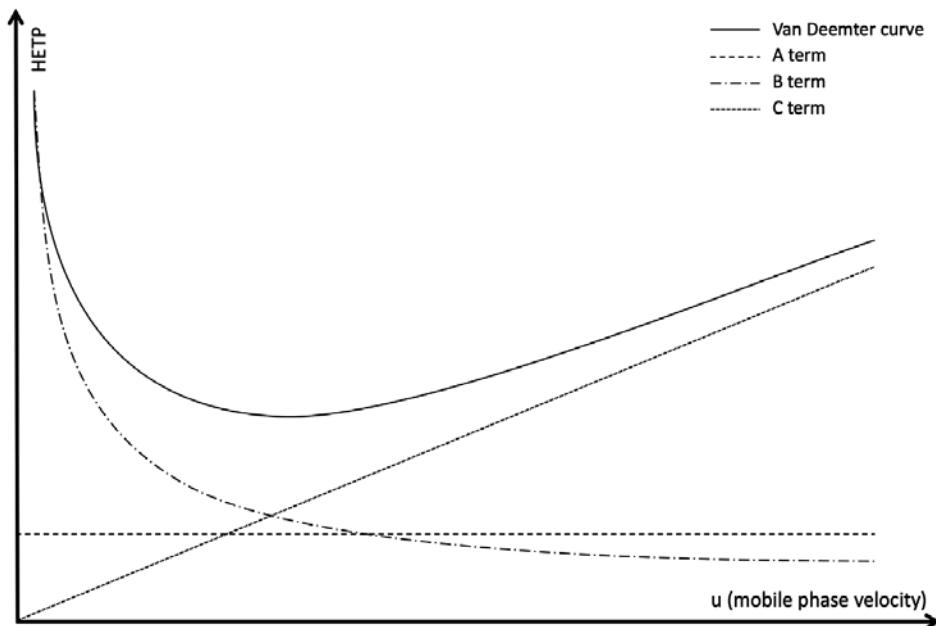


Figure 4. Van Deemter plot deconvolution: (A) Eddy diffusion term; (B) longitudinal diffusion term; (C) resistance to mass transfer term.

Two major research axes of LC have been developed (Figure 5) to comply with the growing needs in increasing the analysis throughput, enhancing sensitivity and reducing analysis cost and environmental footprint through a decrease in solvent consumption [35].

2.3.1. Stationary phase particle size reduction

Considerable gains in terms of sensitivity and analysis time (or chromatographic resolution) could be obtained by reducing the stationary phase particle size to less than 2 μm , giving rise to ultra-high performance liquid chromatography (UHPLC). The use of smaller particles can significantly reduce the height equivalent of a theoretical plate (HETP) generated in a separation.

$$HETP = A + \frac{B}{u} + Cu \quad (1)$$

where u is the mobile phase velocity, A is the Eddy diffusion term, B is the longitudinal diffusion term and C is the resistance to mass transfer term.

The C term mobile phase component C_m can be expanded to the following relationship, showing its dependency on the square of particle size:

$$C_m = \omega \frac{d_p^2}{D_m} \quad (2)$$

where k is the retention factor, d_p is the particle diameter, D_m is the diffusion coefficient of the solute in the mobile phase and ω is the pore size distribution, shape and particle size distribution coefficient.

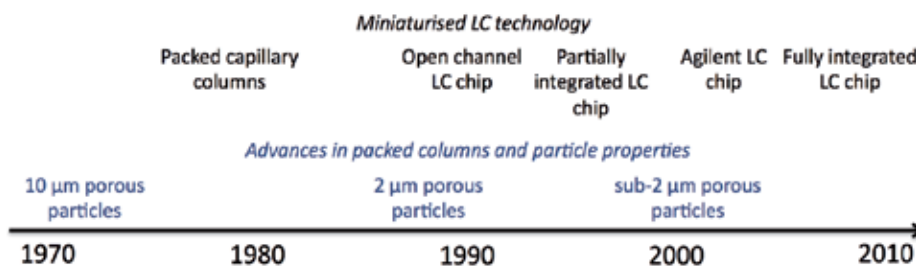


Figure 5. Historical trends in development of HPLC and on-chip LC (adapted from Lavrik et al.'s review [34]).

Particle size reduction has been initiated since the beginning of the spreading of HPLC as a separation technique, but technical limitations related to the pressure drop caused by particle size reduction delayed the commercialisation of sub-2 μm particle columns with classical

dimensions [36]. The first pumps able to face ultra-high pressure were presented by Jorgenson [37] shortly followed by Lee et al. in the late 1990s. In 2004, Waters commercialised the first UHPLC system that was design to deliver pressure up to 1000 bar [41].

2.3.2. Column inner diameter reduction

In parallel with the reduction of particle size, the miniaturisation of LC columns in terms of inner diameter encounters a growing interest since the late 1970s [42].

As previously developed, downscaling the inner diameter of the separation support increases sensitivity with up to 3–4 orders of magnitude in a reduced analysis time. In addition to the advantages of UHPLC, LC miniaturisation reduces drastically the requirements in terms of sample and mobile phase volume.

Miniaturised columns operated on classical LC systems have been described, but void volumes that are very large compared with flow rates and column volumes are responsible for peak dispersion. For that reason, the integration of chromatographic components on a chip (separation channels and electrospray emitters for MS detection, but also additional channels, connections and microvalves) has rapidly been the major strategy to minimise void volumes and efficiency drop [43].

In 1978, Tsuda and Novotny experienced with the performances of packed glass capillaries with 50–200 μm inner diameters.

During the next years, research on chip technology was mainly focused on electroosmosis- or electrophoretic-driven separations due to the technical challenge represented by the connection between LC pumps and chips.

2.3.2.1. Open-channel chromatography

The simplest way to perform miniaturised liquid chromatography on chip is to coat the inner walls of the channels with chemical groups that may interact with the compounds of interest, i.e. to perform open-channel chromatography. In 1990, Manz et al. proposed the first chip prototype for open-tubular liquid chromatography made of silicon and coupled to a miniaturised conductometric detector connected to a classical LC pump [46]. Jacobson et al. proposed the first open-channel separation application on a glass chip coated with octadecylsilane chains in 1994, with low theoretical plate heights (4.1–5 μm) [47]. Due to the small specific surface of such systems, researchers conceived coating modifications to increase the phase ratio (ratio between the volume of stationary phase and the volume of mobile phase): porous layer open-tubular (PLOT) columns, functionalised particles embedded in a porous layer [50] or immobilisation of nanoparticles onto the walls [51].

Open-channel chromatography (with an ideal i.d. of 10–20 μm) provides high efficiency since the molecular diffusion is the only contributor to band broadening. However, due to its limited specific surface, column capacity stays low even with stationary phase modifications.

2.3.2.2. Micropillars, collocated monolith support structures and nanotubes

Micropillars, collocated monolith support structures (COMOSS) or nanotubes may combine small channel dimensions and large specific surfaces. COMOSS were introduced in 1998 by He and Regnier in response to the difficulty to produce chromatographic columns from wafers [52]. They proposed an approach where the stationary phase is not created by polymerisation *in situ*, but by etching the chip material (e.g. quartz, polydimethylsiloxane (PDMS) or cyclic olefin copolymer (COC)) that may be further functionalised. The result is a highly well-ordered structure (Figure 6) obtained as separation support. Eddy diffusion term in the Van Deemter equation is consequently much reduced, leading to high separation efficiency.

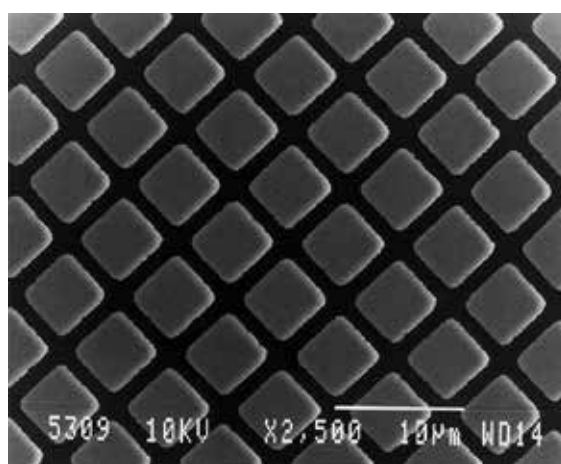


Figure 6. SEM image of a COMOSS organised structure [52].

PDMS can be considered as a C_1 phase, but its hydrophobicity is too low to perform adequate separation; PDMS monolithic pillars could therefore be functionalised by octasilane, octadecylsilane or other groups to improve analyte separation (Figure 7).

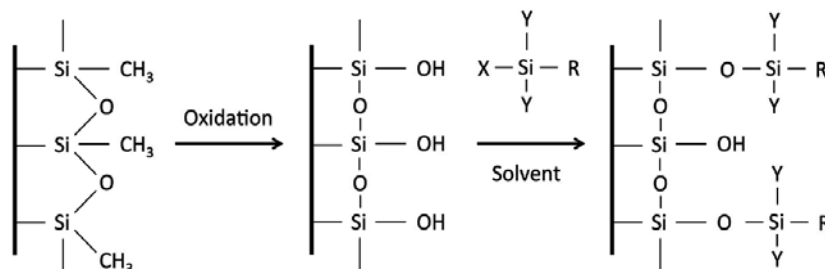


Figure 7. PDMS functionalisation.

COC stationary phase has been presented for the first time by Gustafsson et al. in 2008 [55]. This material presents interesting features in terms of chemical inertness and stability in hydro-organic solvents. The hydrophobic character of COC allows it to be used as chip substrate and stationary phase. COMOSS chips made of on-porous materials as PDMS and COC have high separation efficiency, but low sample capacity due to the low interaction surface.

In addition to non-porous materials as PDMS or COC, superficially porous pillars have been proposed to circumvent the low sample capacity. Two orders of magnitude could be gained in terms of specific surface, increasing the chip sample capacity [56]. Another approach is the *in situ* growth of nanotubes on a COMOSS structure. Increased sample loading capacity and better retention than with C₁₈-functionalised pillars could be obtained [43].

2.3.2.3. Miniaturised monolithic columns

Monoliths are continuous stationary phase beds generated by *in situ* polymerisation of monomers in the presence of porogen agents, resulting in a bimodal structure that exhibits macropores (>50–100 nm) that allow the mobile phase to pass through the column, and mesopores (<20 nm) that offers a high interaction surface for analyte retention [57]. Monolith retention properties can be defined before the polymerisation process by adjusting reagent nature and proportion, or by functionalising the polymer bed. Monoliths present undeniable chromatographic features and deserve to be more thoroughly understood in terms of synthesis parameters and their impact on chromatographic properties [43].

2.3.2.4. Packed particles

Besides the above-mentioned novel LC-chip stationary phases, silica particles can also be employed with the advantage of being well-known due to their broad utilisation for decades in classical LC; a wide range of particle functionalisation types and specifications have been commercialised for a long time. However, special attention has to be paid to particle packing homogeneity and immobilisation of the particles inside the microchannel.

Different column packing procedures have been developed to find the best way to obtain homogenous particle beds. Particles could be brought into chromatographic channels and trapped between weirs or frits that prevent further particle movements. Micromachined frits demonstrate better efficiency than sintered frits that generate more band dispersion [61]. Another procedure was developed for the first time in 2002 by Ceriotti et al. [62]. They proposed a fritless configuration where the particulate bed is retained in the chromatographic channel by a tapered profile at the end of the column. Improvements to this concept were proposed by Gomez et al. that presented a packing process with increased particulate bed stability.

2.3.3. The Agilent HPLC-chip

In 2005, Agilent developed and commercialised a miniaturised HPLC-chip system designed for direct coupling to a mass spectrometer [60]. Polyimide was chosen as chip substrate material due to its chemical and physical inertness, and the low MS background generated.

The fabrication process consists in laser ablation of polyimide film to form the microfluidic channels, ports, chambers and columns followed by deposition of electrical contacts for the electrospray. The last step is the packing of the sample enrichment column and LC column with the stationary phase [65]. This latter operation is performed by introducing isopropanol particle slurries into both channels under a pressure of 120 bar. A wide range of particle chemistries, dimensions and porosities are available in classical Agilent LC columns that can be packed into the chip device.

Chromatographic separations on the Agilent HPLC chip are performed using pressure-driven mobile phase flow. Interfacing macrodimension pumps to nanodimension channels is made through a Chip-Cube interface in which the chip device is sandwiched between the rotor and stator (Figure 8) of a valve. Transfer capillaries from pumps, injector and to waste are connected to the valve stator, ensuring a tight and zero void-volume connection.

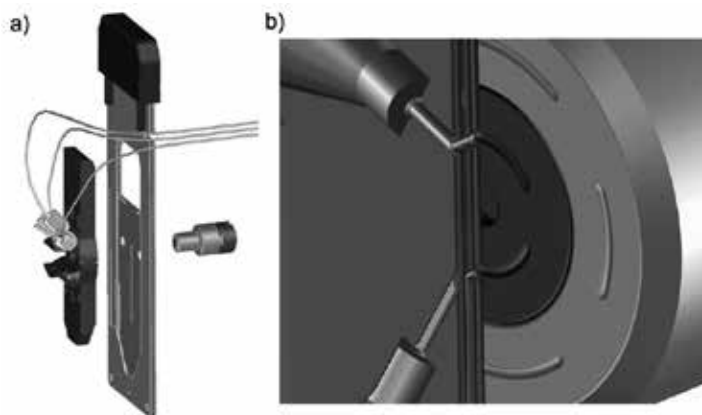


Figure 8. Valve rotor (right) and stator (left) connected with transfer capillaries (A); cut-out view of fluidic connections (left), chip (middle) and valve rotor (right) [65].

Analysis on HPLC-chip consists of sample loading on an enrichment column pushed by a first pump equipped with a split flow device and working at capillary flow rate. After microvalve switching, a second pump delivering a split nanoflow rate is employed to perform chromatographic separation, passing through the enrichment column and the separation channel.

HPLC-chip hyphenation to MS is ensured by an electrospray emitter incorporated in the chip device. The electrospray tip is formed of a prolongation of the polyimide laminated films that constitute the chip substrate. The latter is laser ablated to the appropriate shape (45 μm diameter and 2 mm long) and coated with a conductive metal.

The integrated design of this miniaturised device reduces drastically void volumes and leakage possibilities. Moreover, HPLC-chip is easy to use and compatible with classical LC modules (pumps, autosampler/injector), which opened a wide field of applications.

Since its commercialisation in 2005, HPLC-chip has been used in qualitative analysis of tryptic peptides and proteins, and quantitative analysis of small molecules and peptides [72].

3. Interests of miniaturised LC

3.1. Injection volume

As in classical HPLC, the maximal volume that can be injected without causing a chromatographic band distortion is expressed by the following equation :

$$V_{max} = \frac{\theta \cdot D \cdot \pi \cdot L \cdot d_c^2 \cdot \epsilon_c \cdot (1+k)}{\sqrt{N}} \quad (3)$$

where θ is the fractional loss of the column plate number caused by the injection, D is the constant describing the injection profile, L is the column length, d_c is the column i.d., ϵ_c the is column porosity, k the is retention factor and N the is column efficiency expressed by the theoretical plate number.

As shown in this equation, V_{max} is the proportional to the square of d_c , and the following relationship can be established:

$$\frac{V_{max}^{miniaturised}}{V_{max}^{classical}} = \frac{d_c^2^{miniaturised}}{d_c^2^{classical}} \quad (4)$$

For two columns that have the same length, efficiency and porosity but differ by their inner diameter (4.6 mm for classical dimensions and 75 μm for the miniaturised version), a theoretical injection volume reduction factor of 3762 should be observed (e.g. 10 μl onto a conventional system to approximately 2.5 nl on a nano-LC column) while keeping the same chromatographic performances. Such a reduction of the required injection volume represents an undeniable advantage of miniaturised LC systems, since a growing interest is brought, for instance, to the analysis of biological matrices that are often available in limited volumes.

In practice, a great sensitivity gain can be obtained by injecting higher volumes onto the miniaturised chromatographic system, without causing peak distortion due to an overload. In the case of micro-LC, different peak compression techniques have been studied, such as on-column concentration or sample plug bracketing. In nano-LC, a trapping column is often connected to the analytical column by a valve, allowing large sample volumes to be loaded onto the system and the sample to be pre-concentrated.

3.2. Peak concentration

A reduction of the inner diameter of a chromatographic column results in a higher peak concentration at the detector (C_{max}), as shown in the following equation:

$$C_{max} = \sqrt{\frac{N}{2\pi}} \times \frac{4m}{\pi \cdot L \cdot V_o \cdot \epsilon_c \cdot (1+k)} \quad (5)$$

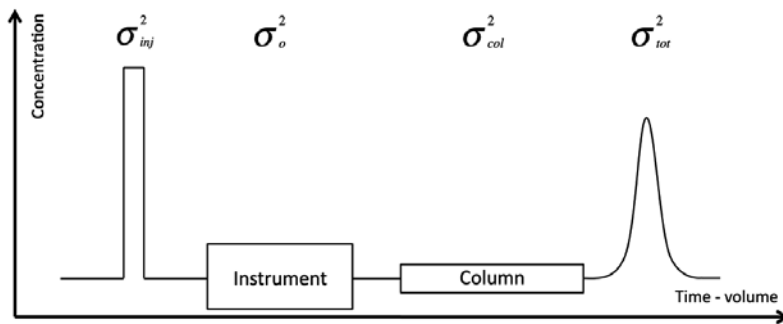


Figure 9. Schematic representation of band broadening components in a chromatographic system (adapted from Lauer [79]).

where m is the total amount of sample loaded on the column and V_0 is the column volume.

C_{\max} is proportional to m and to N , and inversely proportional to V_0 . Since V_0 is directly related to d_c , C_{\max} is inversely proportional to the square of column diameter. In other words, Eq. (6) can be used to illustrate the sensitivity gain that can be expected with miniaturised columns.

$$\frac{C_{\max}^{\text{miniaturised}}}{C_{\max}^{\text{classical}}} = \frac{V_0^{\text{classical}}}{V_0^{\text{miniaturised}}} = \frac{d_c^2 \text{ classical}}{d_c^2 \text{ miniaturised}} \quad (6)$$

Downscaling the size from classical dimensions (4.6 mm) to miniaturised dimensions (75 μm) would theoretically result in a gain factor of C_{\max} of 3762.

3.3. Void volume reduction

Void volumes are detrimental to the chromatographic performances in all LC configurations. However, when working with miniaturised systems, the smallest void volume can act as a mixing chamber and result in an important loss in sensitivity and separation efficiency. The total band dispersion occurring in a chromatographic system (Figure 9) can be expressed by the total variance σ_{tot}^2 that sums the variances due to the column (σ_{col}^2) and to the rest of the chromatographic system (σ_{ext}^2).

$$\sigma_{\text{tot}}^2 = \sigma_{\text{ext}}^2 + \sigma_{\text{col}}^2 \quad (7)$$

Band dispersion due to the column, σ_{col}^2 , is in particular a function of column volume (and consequently to d_c^2) and efficiency, which are physical properties that cannot be changed for a given column in order to decrease peak broadening:

$$\sigma_{col}^2 = \frac{\pi.L.d_c^2.\epsilon_c.(1+k)}{4\sqrt{N}} \quad (8)$$

However, other factors having an influence on band broadening through σ_{ext}^2 can be expressed as:

$$\sigma_{ext}^2 = \frac{V_{inj}^2}{d_c^2} + \sigma_0^2 \quad (9)$$

where V_{inj}^2 is the injection volume, σ_0^2 is the instrument variance and σ_{ext}^2 is the extra-column variance.

As shown in this equation, V_{inj}^2 and σ_0^2 are directly related to σ_{ext}^2 [79]. In other words, the minimisation of extra-column void volumes by using the smallest connection capillaries and fittings possible is clearly beneficial to avoid chromatographic band dispersion.

In the light of these considerations, systems with very low extra-column void volumes have been developed including integrated systems (see Section 2.3.3).

3.4. Low flow rate

Mobile phase flow rate F is a value that is also related to the internal column diameter as seen in Eq. (10):

$$F = \frac{\pi.d_c^2.\epsilon_c.u}{4} \quad (10)$$

where u is the mobile phase velocity.

The following relationship can be written in Eq. (11):

$$\frac{F_{classical}}{F_{miniaturised}} = \frac{d_{classical}^2}{d_{miniaturised}^2} \quad (11)$$

This drastic flow rate reduction has evident economical and ecological advantages, especially when working with pumping systems that directly deliver the right mobile phase flow rate without involving the use of a split flow system.

3.5. Retention volume

The retention volume V_R is defined as the mobile phase volume that is required to elute a compound of a given retention time t_R :

$$V_R = t_R \cdot F = t_R \cdot \frac{\pi \cdot d_c^2}{4} \cdot \epsilon_c \cdot u \quad (12)$$

In the light of the reduced column dimensions in miniaturised LC systems compared with classical systems, the mobile phase volume that is needed to elute a compound with a specified k value is reduced proportionally to the square of the internal column diameter, as shown in Eq. (13).

$$\frac{V_{R^{classical}}}{V_{R^{miniaturised}}} = \frac{d_{classical}^2}{d_{miniaturised}^2} \quad (13)$$

3.6. Hyphenation to MS

When using mass spectrometry, compounds of interest have to carry a net positive or negative charge, depending on the mode that is employed. Analyte electrospray ionisation occurs in three major steps: first, charged droplets are formed from the chromatographic eluent under the action of a strong electric field. The eluent takes the shape of a cone (the Taylor cone) when a critical electric field threshold is reached. A pneumatic assistance is required to provide stable droplet formation in the classical LC [80]. Then, charged droplets undergo Coulomb fission into smaller daughter droplets: eluent solvent progressively evaporates in the heated source until reaching the Rayleigh limit where the electrostatic repulsion forces are exactly equal to the surface tension of the solvent [81]. Beyond the Rayleigh limit, droplets become unstable and divide into smaller droplets. Eq. (14) presents the relationship between droplet charge and Rayleigh radius.

$$Q^2 = 64\pi^2 \epsilon_0 \gamma R_R^3 \quad (14)$$

where Q is the droplet charge, ϵ_0 is the vacuum permittivity and R_R is the Rayleigh radius.

The ion transfer from small droplets to the gas phase can happen following two mechanisms. The ion evaporation model described by Iribarne and Thomson is commonly admitted to describe the small ion formation [81]. According to this model, the electric field at the droplet surface becomes strong enough at an intermediate state and before reaching the Rayleigh limit to directly desorb ions from the droplet (Figure 10) [82].

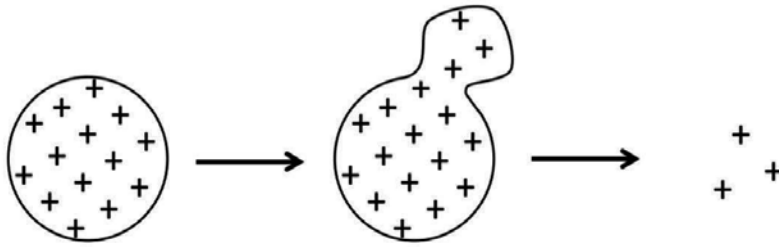


Figure 10. Ion evaporation model.

A second model proposed by Dole, or the charged residue model, could be appropriate to describe protein ionisation. This model suggests that successive Coulomb fissions occurring when the Rayleigh limit is reached, finally yielding droplets containing one single charge (Figure 11) [83].

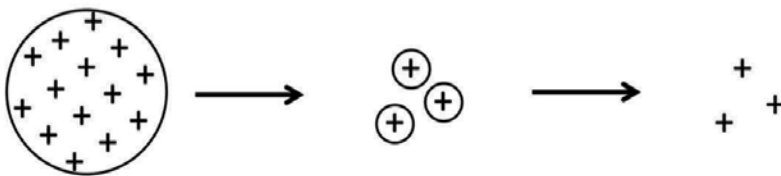


Figure 11. Charge residue model.

Nanoelectrospray (nano-ESI) source was first introduced in 1994 as a response to the development of low flow separation devices. Typical flow rates in nano-ESI are 200–1000 nl/min and the i.d. of spray emitter is about 10–20 μm . The interest of such a miniaturised ionisation source is the improvement of the overall ionisation efficiency (the number of ions recorded at the detector divided by the number of analyte molecule sprayed) [86]. Since signal intensity with ESI sources is concentration sensitive rather than mass sensitive, low analyte amount are advantageously detected at lower flow rates with higher peak concentrations thanks to the miniaturised technique, as previously explained. Lower flow rates as well as narrower emitter tip orifice produce smaller droplets (2–3 orders of magnitude reduction), and desolvation efficiency is increased: smaller initial droplet size requires less Coulomb fission and solvent evaporation to release charged compounds into gas phase, making a larger portion of ions available to detection.

4. Sample preparation

In the light of the previously described features of miniaturised separation techniques, having low volume samples with the highest concentration possible is a clear objective. On the other

hand, analysis of complex media (e.g. environmental, forensic, food, pharmaceutical or biological samples) requires preliminary purification to isolate analyte from contaminants and interferences, and to avoid column or capillary blockage, reduced separation phase lifetime and MS ion suppression. In addition, sample preparation may allow analyte concentration and analyte matrix simplification to make the sample fully compatible with separation technique and detection.

The combination of miniaturised sample preparation and separation techniques offers the main advantages of high throughput, high sensitivity and low costs. The most employed miniaturised sample preparation techniques are briefly described below.

Liquid-liquid extraction (LLE) is a sample preparation technique that relies on the partition of analytes between two immiscible liquid phases. The best results are obtained for compounds showing a clear preference for one liquid over the other one. Factors that influence compound partition include liquid phase polarity, pH, analyte pK_a and polarity, and mixing and contact duration. Micro liquid-liquid extraction (MLLE) is a simple downscaling of classical LLE procedure. The use of lower sample volumes has economical and ecological advantages since the apolar liquid phase is often constituted of alkanes (e.g. pentane, hexane and cyclohexane) or chlorinated solvents; moreover, reduced solvent volumes may lead to the increased analyte concentration.

Solid-phase microextraction (SPME) is a miniaturised sample preparation process involving a fused-silica rod coated with a polymeric layer employed as extraction medium. This technique is applied for the extraction of trace compounds from liquid or gas samples [94] (Figure 12). Analyte desorption is performed by heating the SPME fibre in a classical GC injector for volatile and thermally stable compounds, or by a special desorption device for non-volatile or thermally unstable compounds for subsequent LC [95, 96] or CE [97] analysis.

Dried spots are an expanding way of microsampling and purifying biological samples as blood (dried blood spots, DBS), serum (dried serum spots, DSS) or plasma (dried plasma spots, DPS). A few microliters of a biological fluid are collected on a filter paper and allowed to dry. The dried spot is then punched out and desorbed in an appropriate mixture of solvent chosen to enable maximal analyte extraction while minimising interference desorption (Figure 13). In addition to analytical advantages as small sample volume requirements and low cost, dried spots are very convenient from a sampling point of view: the collection technique is not invasive and can be performed without pain, e.g. for pharmacokinetic studies on laboratory animals or for systematic disease screening on newborns.

Finally, solid-phase extraction (SPE) follows the miniaturisation trend by reducing cartridge and solid phase bed volume (Figure 14A and B). In this technique, sample is loaded in a tube containing a few mg to a few tens mg particles maintained in the bottom of the cartridge by two frits. Sample loading solvent has to be carefully chosen to ensure analyte retention on the particles. Washing steps are then performed to remove a maximal amount of contaminants and interferences that are co-retained on the solid phase, while maintaining analyte-particle interactions. Elution is the final step of SPE to collect a sample containing the analyte for further analysis. Downscaling SPE support allows preparing sample volumes as low as 10 μ l, and

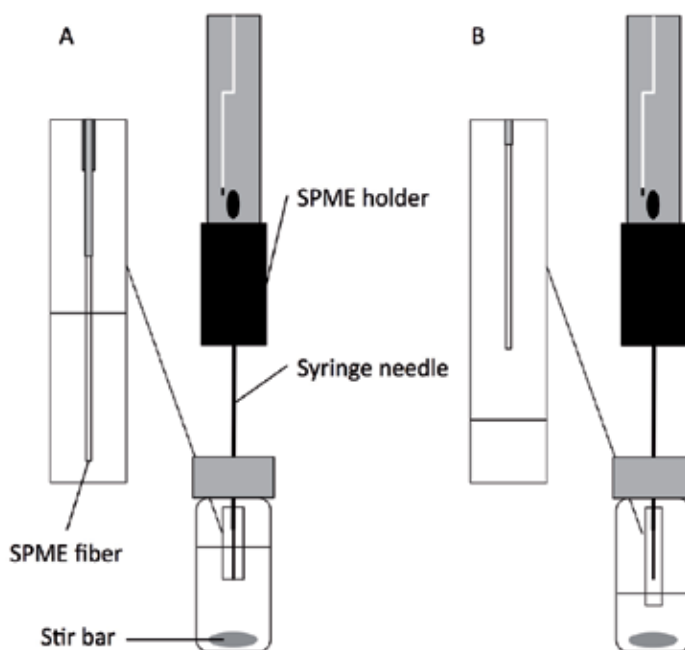


Figure 12. Extraction from aqueous sample solution by conventional SPME device. (A) Liquid phase sampling and (B) headspace sampling [99].

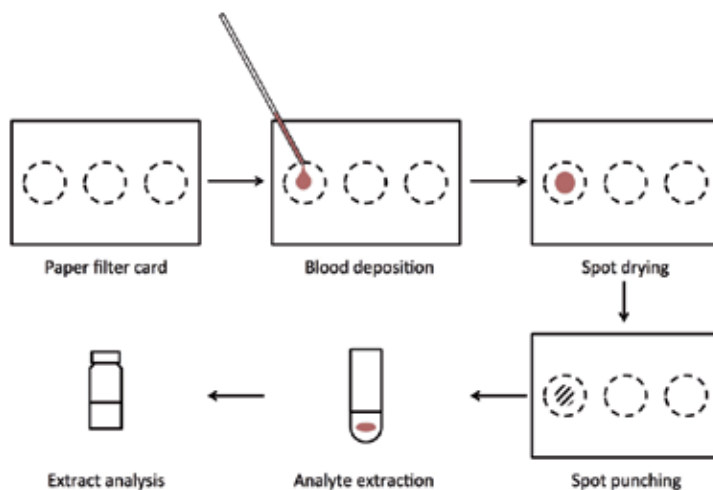


Figure 13. DBS sampling and extraction procedure.

analyte elution by similar volumes. Moreover, SPE or micro-SPE supports are increasingly available in 96-well format (Figure 14C) to provide high extraction throughput by the use of multichannel pipettes or extraction automation.

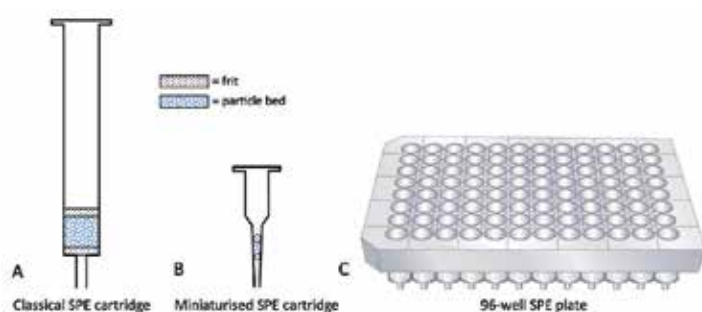


Figure 14. (A) Classical SPE cartridge. (B) Miniaturised SPE cartridge. (C) 96-well SPE plate.

5. Conclusions and perspectives

To summarise, the advantages of microfluidic devices include their small size, improved sensitivity, low sample volume requirements, rapid analysis, potential disposability, and importantly their ease of use that eliminates the need for skilled personnel to perform the assays. In the same time, ethical, analytical and sample availability considerations are a challenge faced by many (bio)analytical laboratories and have resulted in a drive to limit sample volume.

Integration of various nanotechniques through microfabrication processes and advances in detection devices and informatics drive new types of analysis facilitating on-site multicomponent analysis resulting in rapid diagnostic tools and rapid screening methods in various application fields (clinical, pharmaceutical and biopharmaceutical, environmental, food analysis, etc.).

Acknowledgements

The authors thank the Fund for Scientific Research (F.R.S.-FNRS, Belgium), the Walloon Region (WR), the Leon Fredericq Fund and University of Liege for financial support.

Author details

Virginie Houbart and Marianne Fillet*

*Address all correspondence to: marianne.fillet@ulg.ac.be

Laboratory for the Analysis of Medicines (LAM), Department of Pharmacy, CIRM, University of Liege, Liege, Belgium

References

- [1] Hjertén S. Free zone electrophoresis. *Chromatographic Reviews*. 1967;9:122–219. doi:10.1016/0009-5907(67)80003-6.
- [2] Jorgenson JW, Lukacs KD. Zone electrophoresis in open-tubular glass capillaries. *Analytical Chemistry*. 1981;53:1298–302. doi:10.1021/ac00231a037.
- [3] Olivares JA, Nguyen NT, Yonker CR, Smith RD. On-line mass spectrometric detection for capillary zone electrophoresis. *Analytical Chemistry*. 1987;59:1230–2. doi:10.1021/ac00135a034.
- [4] Hommerson P, Khan AM, de Jong GJ, Somsen GW. Ionization techniques in capillary electrophoresis-mass spectrometry: principles, design, and application. *Mass Spectrometry Reviews*. 2011;30:1096–120. doi:10.1002/mas.20313.
- [5] Moseley MA, Deterding LJ, Tomer KB, Jorgenson JW. Capillary-zone electrophoresis/fast-atom bombardment mass spectrometry: design of an on-line coaxial continuous-flow interface. *Rapid Communications in Mass Spectrometry*. 1989;3:87–93. doi:10.1002/rcm.1290030310
- [6] Takada Y, Sakairi M, Koizumi H. Atmospheric pressure chemical ionization interface for capillary electrophoresis/mass spectrometry. *Analytical Chemistry*. 1995;67:1474–6. doi:10.1021/ac00104a027.
- [7] Nilsson SL, Andersson C, Sjöberg PJR, Bylund D, Petersson P, Jörntén-Karlsson M, et al. Phosphate buffers in capillary electrophoresis/mass spectrometry using atmospheric pressure photoionization and electrospray ionization. *Rapid Communications in Mass Spectrometry*. 2003;17:2267–72. doi:10.1002/rcm.1182.
- [8] Chang YZ, Her GR. Sheathless capillary electrophoresis/electrospray mass spectrometry using a carbon-coated fused-silica capillary. *Analytical Chemistry*. 1999;72:626–30. doi:10.1021/ac990535e.
- [9] Nilsson S, Klett O, Svedberg M, Amirkhani A, Nyholm L. Gold-coated fused-silica sheathless electrospray emitters based on vapor-deposited titanium adhesion layers. *Rapid Communications in Mass Spectrometry*. 2003;17:1535–40. doi:10.1002/rcm.1082.
- [10] Wahl JH, Gale DC, Smith RD. Sheathless capillary electrophoresis-electrospray ionization mass spectrometry using 10 μm I.D. capillaries: analyses of tryptic digests of cytochrome *c*. *Journal of Chromatography A*. 1994;659:217–22. doi:10.1016/0021-9673(94)85026-7.
- [11] Barnidge DR, Nilsson S, Markides KE. A design for low-flow sheathless electrospray emitters. *Analytical Chemistry*. 1999;71:4115–8.

- [12] Schappler J, Veuthey J-L, Rudaz S. 18 Coupling CE and microchip-based devices with mass spectrometry. In: Satinder A, Jimidar MI, editors. *Separation Science and Technology*. Volume 9. Academic Press; 2008. p. 477–521.
- [13] Manz A, Graber N, Widmer HM. Miniaturized total chemical analysis systems: a novel concept for chemical sensing. *Sensors and Actuators B: Chemical*. 1990;1:244–8.
- [14] Kitagawa F, Otsuka K. Recent progress in microchip electrophoresis-mass spectrometry. *Journal of Pharmaceutical and Biomedical Analysis*. 2011;55:668–78. doi:10.1016/j.jpba.2010.11.013.
- [15] Zhang B, Liu H, Karger BL, Foret F. Microfabricated devices for capillary electrophoresis-electrospray mass spectrometry. *Analytical Chemistry*. 1999;71:3258–64.
- [16] Lazar IM, Ramsey RS, Sundberg S, Michael Ramsey J. Subattomole-sensitivity microchip nanoelectrospray source with time-of-flight mass spectrometry detection. *Analytical Chemistry*. 1999;71:3627–31.
- [17] Panaro NJ, Yuen PK, Sakazume T, Fortina P, Kricka LJ, Wilding P. Evaluation of DNA fragment sizing and quantification by the Agilent 2100 Bioanalyzer. *Clinical Chemistry*. 2000;46:1851–3.
- [18] Kuschel M, Neumann T, Barthmaier P, Kratzmeier M. Use of lab-on-a-chip technology for protein sizing and quantitation. *Journal of Biomolecular Techniques: JBT*. 2002;13:172.
- [19] Martín A, Vilela D, Escarpa A. Food analysis on microchip electrophoresis: an updated review. *Electrophoresis*. 2012;33:2212–27. doi:10.1002/elps.201200049.
- [20] Poinot V, Carpéné M-A, Bouajila J, Gavard P, Feurer B, Couderc F. Recent advances in amino acid analysis by capillary electrophoresis. *Electrophoresis*. 2012;33:14–35. doi:10.1002/elps.201100360.
- [21] Haselberg R, de Jong GJ, Somsen GW. Capillary electrophoresis–mass spectrometry for the analysis of intact proteins 2007–2010. *Electrophoresis*. 2011;32:66–82. doi:10.1002/elps.201000364.
- [22] James AT, Martin AJ. Gas-liquid partition chromatography; the separation and micro-estimation of volatile fatty acids from formic acid to dodecanoic acid. *The Biochemical Journal*. 1952;50:679–90.
- [23] Smolková-Keulemansová E. A few milestones on the journey of chromatography. *HRC Journal of High Resolution Chromatography*. 2000;23:497–501.
- [24] Lipsky SR, Landowne RA. Gas chromatography–biochemical applications. *Annual Review of Biochemistry*. 1960;29:649–68.
- [25] Zlatkis A, Oró JF, Kimball AP. Direct amino acid analysis by gas chromatography. *Analytical Chemistry*. 1960;32:162–4.

- [26] Martin A, Desty D. Vapour Phase Chromatography. Butterworths, London; 1957. p. 1.
- [27] Golay M. Gas chromatography. Academic Press. New York; 1958.
- [28] Bartle KD, Myers P. History of gas chromatography. *TrAC Trends in Analytical Chemistry*. 2002;21:547–57. doi:10.1016/S0165-9936(02)00806-3.
- [29] Terry SC, Jerman JH, Angell JB. A gas chromatographic air analyzer fabricated on a silicon wafer. *IEEE Transactions on Electron Devices*. 1979;26:1880–6.
- [30] Gross GM, Grate JW, Synovec RE. Monolayer-protected gold nanoparticles as an efficient stationary phase for open tubular gas chromatography using a square capillary. *Journal of Chromatography A*. 2004;1029:185–92. doi:10.1016/j.chroma.2003.12.058.
- [31] Narayanan S, Alfeeli B, Agah M. A micro gas chromatography chip with an embedded non-cascaded thermal conductivity detector. *Procedia Engineering*. 2010;5:29–32. doi:10.1016/j.proeng.2010.09.040.
- [32] Tranchida PQ, Mondello L. Current-day employment of the micro-bore open-tubular capillary column in the gas chromatography field. *Journal of Chromatography A*. 2012;1261:23–36. doi:10.1016/j.chroma.2012.05.074.
- [33] van Deemter JJ, Zuiderweg FJ, Klinkenberg A. Longitudinal diffusion and resistance to mass transfer as causes of nonideality in chromatography. *Chemical Engineering Science*. 1995;50:3869–82. doi:10.1016/0009-2509(96)81813-6.
- [34] Lavrik NV, Taylor LT, Sepaniak MJ. Nanotechnology and chip level systems for pressure driven liquid chromatography and emerging analytical separation techniques: a review. *Analytica Chimica Acta*. 2011;694:6–20. doi:10.1016/j.aca.2011.03.059.
- [35] Lin S-L, Bai H-Y, Lin T-Y, Fuh M-R. Microfluidic chip-based liquid chromatography coupled to mass spectrometry for determination of small molecules in bioanalytical applications. *Electrophoresis*. 2012;33:635–43. doi:10.1002/elps.201100380.
- [36] Snyder LR. Peer reviewed: HPLC: past and present. *Analytical Chemistry*. 2000;72:412 A–20 A. doi:10.1021/ac002846r.
- [37] MacNair JE, Lewis KC, Jorgenson JW. Ultrahigh-pressure reversed-phase liquid chromatography in packed capillary columns. *Analytical Chemistry*. 1997;69:983–9. doi:10.1021/ac961094r.
- [38] Lippert JA, Xin B, Wu N, Lee ML. Fast ultrahigh-pressure liquid chromatography: on-column UV and time-of-flight mass spectrometric detection. *Journal of Microcolumn Separations*. 1999;11:631–43. doi:10.1002/(SICI)1520-667X(199911)11:9<631::AID-MCS1>3.0.CO;2-I.
- [39] Wu N, Clausen AM. Fundamental and practical aspects of ultrahigh pressure liquid chromatography for fast separations. *Journal of Separation Science*. 2007;30:1167–82. doi:10.1002/jssc.200700026.

- [40] Wu N, Collins DC, Lippert JA, Xiang Y, Lee ML. Ultrahigh pressure liquid chromatography/time-of-flight mass spectrometry for fast separations. *Journal of Microcolumn Separations*. 2000;12:462–9. doi:10.1002/1520-667X(2000)12:8<462::AID-MCS5>3.0.CO;2-F.
- [41] Mazzeo JR, D. Neue U, Kele M, Plumb RS. Advancing LC Performance with smaller particles and higher pressure. *Analytical Chemistry*. 2005;77:460 A–7 A. doi:10.1021/ac053516f.
- [42] Oosterkamp AJ, Gelpi E, Abian J. Quantitative peptide bioanalysis using column-switching nano liquid chromatography/mass spectrometry. *Journal of Mass Spectrometry*. 1998;33:976–83. doi:10.1002/(SICI)1096-9888(1998100)33:10<976::AID-JMS710>3.0.CO;2-7.
- [43] Faure K. Liquid chromatography on chip. *Electrophoresis*. 2010;31:2499–511. doi:10.1002/elps.201000051.
- [44] Tsuda T, Novotny M. Packed microcapillary columns in high performance liquid chromatography. *Analytical Chemistry*. 1978;50:271–5. doi:10.1021/ac50024a026.
- [45] Novotny M. Recent advances in microcolumn liquid chromatography. *Analytical Chemistry*. 1988;60:500A–10A. doi:10.1021/ac00159a718.
- [46] Manz A, Miyahara Y, Miura J, Watanabe Y, Miyagi H, Sato K. Design of an open-tubular column liquid chromatograph using silicon chip technology. *Sensors and Actuators B: Chemical*. 1990;1:249–55. doi:10.1016/0925-4005(90)80210-q.
- [47] Jacobson SC, Hergenroeder R, Koutny LB, Ramsey JM. Open channel electrochromatography on a microchip. *Analytical Chemistry*. 1994;66:2369–73. doi:10.1021/ac00086a024.
- [48] Eeltink SS, Frechet, M. Open-tubular capillary columns with a porous layer of monolithic polymer for highly efficient and fast separations in electrochromatography. *Electrophoresis*. 2006;27:4249–56.
- [49] Rogeberg M, Wilson SR, Greibrokk T, Lundanes E. Separation of intact proteins on porous layer open tubular (PLOT) columns. *Journal of Chromatography A*. 2010;1217:2782–6. doi:10.1016/j.chroma.2010.02.025.
- [50] Yang X, Jenkins G, Franzke J, Manz A. Shear-driven pumping and Fourier transform detection for on chip circular chromatography applications. *Lab on a Chip*. 2005;5:764–71. doi:10.1039/B502121A.
- [51] Li H-F, Zeng H, Chen Z, Lin J-M. Chip-based enantioselective open-tubular capillary electrochromatography using bovine serum albumin-gold nanoparticle conjugates as the stationary phase. *Electrophoresis*. 2009;30:1022–9. doi:10.1002/elps.200800359.

- [52] He B, Regnier F. Microfabricated liquid chromatography columns based on collocated monolith support structures. *Journal of Pharmaceutical and Biomedical Analysis*. 1998;17:925–32. doi:10.1016/S0731-7085(98)00060-0.
- [53] Slentz BE, Penner NA, Lugowska E, Regnier F. Nanoliter capillary electrochromatography columns based on collocated monolithic support structures molded in poly(dimethyl siloxane). *Electrophoresis*. 2001;22:3736–43. doi:10.1002/1522-2683(200109)22:17<3736::AID-ELPS3736>3.0.CO;2-Y.
- [54] Pumera M. Microchip-based electrochromatography: designs and applications. *Talanta*. 2005;66:1048–62. doi:10.1016/j.talanta.2005.01.006.
- [55] Gustafsson O, Mogensen KB, Kutter JP. Underivatized cyclic olefin copolymer as substrate material and stationary phase for capillary and microchip electrochromatography. *Electrophoresis*. 2008;29:3145–52. doi:10.1002/elps.200800131.
- [56] De Malsche W, Clicq D, Verdoold V, Gzil P, Desmet G, Gardeniers H. Integration of porous layers in ordered pillar arrays for liquid chromatography. *Lab on a Chip*. 2007;7:1705–11. doi:10.1039/B710507J.
- [57] Cabrera K. Applications of silica-based monolithic HPLC columns. *Journal of Separation Science*. 2004;27:843–52. doi:10.1002/jssc.200401827.
- [58] Smith NW, Evans MB. The analysis of pharmaceutical compounds using electrochromatography. *Chromatographia*. 1994;38:649–57. doi:10.1007/BF02277170.
- [59] Oleschuk RD, Shultz-Lockyear LL, Ning Y, Harrison DJ. Trapping of bead-based reagents within microfluidic systems: on-chip solid-phase extraction and electrochromatography. *Analytical Chemistry*. 1999;72:585–90. doi:10.1021/ac990751n.
- [60] Yin H, Killeen K, Brennen R, Sobek D, Werlich M, van de Goor T. Microfluidic chip for peptide analysis with an integrated HPLC column, sample enrichment column, and nanoelectrospray tip. *Analytical Chemistry*. 2005;77:527–33. doi:10.1021/ac049068d.
- [61] Ehlert S, Kraiczek K, Mora J-A, Dittmann M, Rozing GP, Tallarek U. Separation efficiency of particle-packed HPLC microchips. *Analytical Chemistry*. 2008;80:5945–50. doi:10.1021/ac800576v.
- [62] Ceriotti L, de Rooij NF, Verpoorte E. An integrated fritless column for on-chip capillary electrochromatography with conventional stationary phases. *Analytical Chemistry*. 2002;74:639–47. doi:10.1021/ac0109467.
- [63] Gaspar A, Piyasena ME, Gomez FA. Fabrication of fritless chromatographic microchips packed with conventional reversed-phase silica particles. *Analytical Chemistry*. 2007;79:7906–9. doi:10.1021/ac071106g.

- [64] Gaspar A, Hernandez L, Stevens S, Gomez FA. Electrochromatography in microchips packed with conventional reversed-phase silica particles. *Electrophoresis*. 2008;29:1638–42. doi:10.1002/elps.200700489.
- [65] Yin H, Killeen K. The fundamental aspects and applications of Agilent HPLC-chip. *Journal of Separation Science*. 2007;30:1427–34. doi:10.1002/jssc.200600454.
- [66] Zhang Y, Yang H, Pöschl U. Analysis of nitrated proteins and tryptic peptides by HPLC-chip-MS/MS: site-specific quantification, nitration degree, and reactivity of tyrosine residues. *Analytical and Bioanalytical Chemistry*. 2011;399:459–71. doi:10.1007/s00216-010-4280-9.
- [67] Vollmer M, Goor T. HPLC-Chip/MS Technology in proteomic profiling. In: Foote RS, Lee JW, editors. *Micro and Nano Technologies in Bioanalysis. Methods in Molecular Biology™*. Volume 544. Totowa: Humana Press; 2009. p. 3–15.
- [68] Hardouin J, Joubert-Caron R, Caron M. HPLC-chip-mass spectrometry for protein signature identifications. *Journal of Separation Science*. 2007;30:1482–7. doi:10.1002/jssc.200600444.
- [69] Horvatovich P, Govorukhina NI, Reijmers TH, van der Zee AG, Suits F, Bischoff R. Chip-LC-MS for label-free profiling of human serum. *Electrophoresis*. 2007;28:4493–505. doi:10.1002/elps.200600719.
- [70] Flamini R, De Rosso M, Smaniotto A, Panighel A, Vedova AD, Seraglia R, et al. Fast analysis of isobaric grape anthocyanins by Chip-liquid chromatography/mass spectrometry. *Rapid Communication in Mass Spectrometry*. 2009;23:2891–6. doi:10.1002/rcm.4199.
- [71] Houbart V, Servais AC, Charlier TD, Pawluski JL, Abts F, Fillet M. A validated microfluidics-based LC-chip-MS/MS method for the quantitation of fluoxetine and norfluoxetine in rat serum. *Electrophoresis*. 2012;33:3370–9. doi:10.1002/elps.201200168.
- [72] Houbart V, Cobraiville G, Lecomte F, Debrus B, Hubert P, Fillet M. Development of a nano-liquid chromatography on chip tandem mass spectrometry method for high-sensitivity hepcidin quantitation. *Journal of Chromatography A*. 2011;1218:9046–54. doi:10.1016/j.chroma.2011.10.030.
- [73] Chervet JP, Ursem M, Salzmann JP. Instrumental requirements for nanoscale liquid chromatography. *Analytical Chemistry*. 1996;68:1507–12. doi:10.1021/ac9508964.
- [74] Claessens HA, Kuyken MAJ. A comparative study of large volume injection techniques for microbore columns in HPLC. *Chromatographia*. 1987;23:331–6. doi:10.1007/BF02316178.
- [75] Vissers JPC, de Ru AH, Ursem M, Chervet J-P. Optimised injection techniques for micro and capillary liquid chromatography. *Journal of Chromatography A*. 1996;746:1–7. doi:10.1016/0021-9673(96)00322-6.

- [76] Leon-Gonzalez ME, Rosales-Conrado N, Perez-Arribas LV, Polo-Diez LM. Large injection volumes in capillary liquid chromatography: Study of the effect of focusing on chromatographic performance. *Journal of Chromatography A*. 2010;1217:7507–13. doi:10.1016/j.chroma.2010.09.076.
- [77] Tao D, Zhang L, Shan Y, Liang Z, Zhang Y. Recent advances in micro-scale and nano-scale high-performance liquid-phase chromatography for proteome research. *Analytical and Bioanalytical Chemistry*. 2011;399:229–41. doi:10.1007/s00216-010-3946-7.
- [78] Lauer HH, Rozing GP. The selection of optimal conditions in HPLC II. The influence of column dimensions and sample size on solute detection. *Chromatographia*. 1982;15:409–13. doi:10.1007/BF02261599.
- [79] Lauer HH, Rozing GP. The selection of optimum conditions in HPLC I. The determination of external band spreading in LC instruments. *Chromatographia*. 1981;14:641–7. doi:10.1007/BF02291104.
- [80] Ikonomou MG, Blades AT, Kebarle P. Electrospray-ion spray: a comparison of mechanisms and performance. *Analytical Chemistry*. 1991;63:1989–98. doi:10.1021/ac00018a017.
- [81] Kebarle P. A brief overview of the present status of the mechanisms involved in electrospray mass spectrometry. *Journal of Mass Spectrometry*. 2000;35:804–17. doi:10.1002/1096-9888(200007)35:7<804::AID-JMS22>3.0.CO;2-Q.
- [82] Iribarne JV, Thomson BA. On the evaporation of small ions from charged droplets. *The Journal of Chemical Physics*. 1976;64:2287–94.
- [83] Dole M, Mack LL, Hines RL, Mobley RC, Ferguson LD, Alice MB. Molecular beams of macroions. *The Journal of Chemical Physics*. 1968;49:2240–9.
- [84] Wilm MS, Mann M. Electrospray and Taylor-Cone theory, Dole's beam of macromolecules at last? *International Journal of Mass Spectrometry and Ion Processes*. 1994;136:167–80.
- [85] Emmett MR, Caprioli RM. Micro-electrospray mass spectrometry: ultra-high-sensitivity analysis of peptides and proteins. *Journal of the American Society for Mass Spectrometry*. 1994;5:605–13. doi:10.1016/1044-0305(94)85001-1.
- [86] Wilm M, Mann M. Analytical properties of the nanoelectrospray ion source. *Analytical Chemistry*. 1996;68:1–8.
- [87] El-Faramawy A, Siu KW, Thomson BA. Efficiency of nano-electrospray ionization. *Journal of the American Society for Mass Spectrometry*. 2005;16:1702–7. doi:10.1016/j.jasms.2005.06.011.
- [88] Abian J, Oosterkamp AJ, Gelpí E. Comparison of conventional, narrow-bore and capillary liquid chromatography/mass spectrometry for electrospray ionization mass

- spectrometry: practical considerations. *Journal of Mass Spectrometry*. 1999;34:244–54. doi:10.1002/(SICI)1096-9888(199904)34:4<244::AID-JMS775>3.0.CO;2-0.
- [89] Juraschek R, Dülcks T, Karas M. Nanoelectrospray—more than just a minimized-flow electrospray ionization source. *Journal of the American Society for Mass Spectrometry*. 1999;10:300–8. doi:10.1016/S1044-0305(98)00157-3.
- [90] Karas M, Bahr U, Dülcks T. Nano-electrospray ionization mass spectrometry: addressing analytical problems beyond routine. *Fresenius' Journal of Analytical Chemistry*. 2000;366:669–76.
- [91] Schmidt A, Karas M, Dülcks T. Effect of different solution flow rates on analyte ion signals in nano-ESI MS, or: when does ESI turn into nano-ESI? *Journal of the American Society for Mass Spectrometry*. 2003;14:492–500.
- [92] Zapf A, Heyer R, Stan H-J. Rapid micro liquid-liquid extraction method for trace analysis of organic contaminants in drinking water. *Journal of Chromatography A*. 1995;694:453–61. doi:10.1016/0021-9673(94)01199-O.
- [93] Montesinos I, Gallego M. Solvent-minimized extraction for determining halonitromethanes and trihalomethanes in water. *Journal of Chromatography A*. 2012;1248:1–8. doi:10.1016/j.chroma.2012.05.067.
- [94] Louch D, Motlagh S, Pawliszyn J. Dynamics of organic compound extraction from water using liquid-coated fused silica fibers. *Analytical Chemistry*. 1992;64:1187–99.
- [95] Salleh SH, Saito Y, Jinno K. An approach to solventless sample preparation procedure for pesticides analysis using solid phase microextraction/supercritical fluid extraction technique. *Analytica Chimica Acta*. 2000;418:69–77.
- [96] Jinno K, Kawazoe M, Hayashida M. Solid-phase microextraction coupled with microcolumn liquid chromatography for the analysis of amitriptyline in human urine. *Chromatographia*. 2000;52:309–13.
- [97] Whang CW, Pawliszyn J. Solid phase microextraction coupled to capillary electrophoresis. *Analytical Communications*. 1998;35:353–6.
- [98] Saito Y, Kawazoe M, Imaizumi M, Morishima Y, Nakao Y, Hatano K, et al. Miniaturized sample preparation and separation methods for environmental and drug analyses. *Analytical Sciences*. 2002;18:7–17.
- [99] Saito Y, Jinno K. Miniaturized sample preparation combined with liquid phase separations. *Journal of Chromatography A*. 2003;1000:53–67. doi:10.1016/S0021-9673(03)00307-8.
- [100] Deglon J, Thomas A, Daali Y, Lauer E, Samer C, Desmeules J, et al. Automated system for on-line desorption of dried blood spots applied to LC/MS/MS pharmacokinetic study of flurbiprofen and its metabolite. *Journal of Pharmaceutical and Biomedical Analysis*. 2011;54:359–67. doi:10.1016/J.jpba.2010.08.032.

- [101] Abu-Rabie P, Spooner N. Dried matrix spot direct analysis: evaluating the robustness of a direct elution technique for use in quantitative bioanalysis. *Bioanalysis*. 2011;3:2769–81. doi:10.4155/bio.11.270.
- [102] McDade TWS, Snodgrass J. What a drop can do: dried blood spots as a minimally invasive method for integrating biomarkers into population-based research. *Demography*. 2007;44:899-925.
- [103] Li W-T. Dried blood spot sampling in combination with LC-MS/MS for quantitative analysis of small molecules. *Biomed Chromatogr*. 2010;24:49-65.
- [104] Britz-McKibbin P. Expanded newborn screening of inborn errors of metabolism by capillary electrophoresis-electrospray ionization-mass spectrometry (CE-ESI-MS). *Methods Mol Biol*. 2013;919:43-56.
- [105] Gilar M, Bouvier ES, Compton BJ. Advances in sample preparation in electromigration, chromatographic and mass spectrometric separation methods. *Journal of Chromatography A*. 2001;909:111–35. doi:10.1016/S0021-9673(00)01108-0.
- [106] Ekström S, Wallman L, Hök D, Marko-Varga G, Laurell T. Miniaturized solid-phase extraction and sample preparation for MALDI MS using a microfabricated integrated selective enrichment target. *Journal of Proteome Research*. 2006;5:1071-81. doi: 10.1021/pr050434z.

Molecular Microfluidic Bioanalysis: Recent Progress in Preconcentration, Separation, and Detection

Emmanuel Roy, Antoine Pallandre, Bacem Zribi, Marie-Charlotte Horny, François-Damien Delapierre, Andrea Cattoni, Jean Gamby and Anne-Marie Haghiri-Gosnet

Additional information is available at the end of the chapter

<http://dx.doi.org/10.5772/65772>

Abstract

This chapter reviews the state-of-art of microfluidic devices for molecular bioanalysis with a focus on the key functionalities that have to be successfully integrated, such as preconcentration, separation, signal amplification, and detection. The first part focuses on both passive and electrophoretic separation/sorting methods, whereas the second part is devoted to miniaturized biosensors that are integrated in the last stage of the fluidic device.

Keywords: microfluidic bioanalysis, separation, concentration, on-a-chip optical detection, electrochemical sensors

1. Introduction

Advances in biochemistry and technology for enhancing sensitivity and selectivity of bioanalysis play a central role in clinical chemistry and medical diagnostics. The latter are performed much earlier to prevent disease or in a repetitive manner to define more specific and personal therapies. However, such analytical protocols are often implemented at the macro-scale level where large volumes of samples are needed. The development of microfluidic bioanalysis thus becomes important, since these platforms can offer short analysis time to result in volume smaller than 1 μl , low cost, multiplexed analysis of several analytes, and portability. Therefore, the development of extremely sensitive, highly selective, simple, robust and yet inexpensive miniaturized platforms has become essential for a wide range of applications, including clinical diagnostics, environmental monitoring, and food safety testing. This chapter reviews the state-of-art of microfluidic devices for molecular bioanalysis with a focus

on the key functionalities that have been successfully integrated in the chip, such as preconcentration, separation, and detection.

Impressive innovations have been demonstrated allowing selectively sorting, concentrating, and amplifying analytes of interest [1–3]. Therefore, the first section of this chapter mainly targets passive and electrical-based strategies for biomolecular and cellular purification, and concentration toward genomic, proteomic, and metabolite applications. The second part focuses on sensitive and selective detection techniques. Two routes are described: (i) on-chip detection based on nanostructured biophotonic sensors and (ii) electrochemical detection. These sensors are integrated in small microchannels or microchambers where specific enhanced sensing properties are generated. The correlation between the biosensor interface and its microfluidic environment for optimal detection of analytes is reviewed. Fundamental kinetics and mass-transport versus the microfluidic properties in terms of fluidic characteristics is introduced for highly operative and sensitive microfluidic applications.

2. Microfluidic filtration, concentration, and sorting

Molecular extraction and purification from a biofluid for diagnostic and therapeutic purposes using microfluidics are sensitive issues. Such objectives are challenging regarding the manipulation of the complex biofluid system such as blood or sputum. Moreover, the extraction and purification steps are also important for the quality and the pertinence of the analyte identification and quantification. Each progress and advance will definitively help the clinicians for proper medication. The advantages of such a microfluidic device for genomic pathogenic recognition are also of tremendous importance, because such a platform can shorten the sample analysis time compared to classical methods. Conventional processing methods for preconcentration and separation of analytes entail numerous manual and time-consuming steps. Consequently, it requires most often highly skilled operators, who do not always guarantee the absence of mishandling and contaminants. As a unique example of the needs for rapid molecular extraction from blood, sepsis and blood stream infections that are a major cause of death [4] impose daily patient follow-up to doctors in virology and bacteriology. Antimicrobial therapy should thus be curtailed as early as practicable, ideally just after the identification of the causative pathogen. Indeed, delay in effective treatment reduces the survival rate on average of 8% for the each following 6-hour period [5–7]. However, extraction of pathogen agents in the range of 1–5 units per ml with clinical relevance is a critical issue. Meanwhile, the gold standard blood culture (BC) approach for pathogenic and antibiotic susceptibility identification remains yet a major limitation with turnaround time of 2–5 days [8, 9]. Moreover, less than 10% of blood samples processed from hospitalized patients with blood infections are positive [10, 11]. Decreasing the sample analysis time compared to classical methods with microfluidics thus appears very challenging for diagnosis. In this section, main sorting, extraction, and purification methods are introduced.

2.1. Passive approaches

2.1.1. Surface binding technique

Solid-phase extraction technique (SPE) is the most widely used preconcentration and purification technique. Capture is performed through a hydrophobic interaction between the analyte and a confined monolith element. Subsequently, a washing step to eliminate interference components is achieved. Finally, the elution step releases the trapped components. From cardiac biomarkers, nucleic acids to proteins, monolith materials with or without functionalization are used as the preferred on-chip approach for purification and concentration. Indeed, monoliths are intensely used, because of ease of preparation, wide ranges of formulation, and adjustable surface area and porosity. Monoliths are commonly prepared via photo-polymerization or sol-gel approaches. Recently, in a PCO microfluidic chip based on an octyl-methacrylate-based polymer monolith, Yang et al. [12] have shown that the ratio of monomer to pyrogen can be adjusted to change the porosity of the column. In addition, the system features a fluorescence labeling capability where model HSP90 proteins were labeled on-column, prior to their elution. Extending the range of suitable materials for SPE integration in an all polymer approach, Lounsbury et al. [13] developed an original PMMA-based column extraction method within a fully integrated device for the sample-to-PCR products collection. From buccal swabs to whole blood samples, they showed a ~5-fold reduction in processing time for complete amplicon purification and extraction. Beyond continuous and static monolith approaches, bead materials alternatively might be used for capture and extraction. Indeed, using silica beads, and others chitosan-coated beads among others methods, many systems have been implemented. However, some limitations may occur due to packing difficulties in such complicated designs. Using a dual-weir filtration strategy for bead immobilization, Zhong et al. [14] were able to extract and purify λ DNA in a glass chip system, finally eluted in a small volume of ~8 μ L. In order to circumvent the relative difficulties of bead packing, static silicon micropillars have been fabricated directly inside the microchannel. Repeatedly separated micropillars promote recombined multiple flow streams favoring DNA contact with the silica surface areas. Since extreme high flow rates can be operated (10 ml min⁻¹), this strategy appears of great interest for medical applications. Finally, the system featured a binding capacity of 57 ± 5 ng cm⁻² [15]. For medical applications, the direct molecular concentration from a real biofluid remains a difficult issue; therefore, it might be preferred to extract a cellular group instead of a molecular species. Indeed, super-macroporous cryogels, with interlinking pores ranging from 10 to 100 μ m, with added targeted ligands inside the gel trapped cells of interests [16]. In addition to blood cells, bacteria such as *Escherichia coli* have been shown to absorb over the gel.

The definitive easiness and reported performance of SPE strategy position this approach at the leading position for on-chip purification and concentration. Additionally, since two decades, numerous similar off-chip SPE and bead technologies have been developed and even been commercialized, their integration inside lab-on-a-chip (LOC) system should, therefore, benefit from those achievements. Agilent (Santa Clara, CA, USA) and Bio-Rad (Hercules, CA, USA) companies developed their 2100 Bioanalyzer and Experion™ automated electrophoresis

systems, respectively, for nucleic acids and protein analysis. These systems perform all of the steps of gel-based electrophoresis synthesis, molecular staining and final imaging.

2.1.2. Solvent extraction

As solid phase extraction, solvent phase extraction is an off-chip mature technique for separation and preconcentration of analytes. Liquid-liquid extraction (LLE) in the LOC system benefits from short molecular diffusion, low consumption and high extraction efficiency due to large specific interfacial areas. Chen et al. [17] reported a concentration factor of over 1000 for butyl-Rhodamine B using only few hundreds picoliters of organic solvents. Kitamor's group developed several glass chip extraction systems with channels ranging from 20 to 200 μm for successive extraction of Nickel and Cobalt complexes [18, 19], drugs of abuse species concentrated from urine (amphetamine, mephentermine) [20] and finally carbamate pesticides for agronomics purposes [21]. Especially for molecular microbiology, LLE is a conventional method for nucleic acid purification and extraction from lysate of various clinical isolates. Indeed, the cellular membrane components and proteins move toward the organic/aqueous interface while the DNA stays in the aqueous phase, which is then subsequently removed. Based on phenol-aqueous extraction system, Reddy and Zahn [22] performed either genomic or plasmid DNA extraction and concentration in a 30 μm deep and 80 μm wide microchannel glass chip. Several optimization strategies based on flow velocities and their profile properties for enhanced interface stability and surface modification have been proposed. Concerning microstructures and surfactants that are the most concerned parameters for extraction performance improvements, the readers could further read to the following complete review [23].

To sum up this section, regarding materials, one could clearly observe that all reported systems have been realized using either glass, silicon, or quartz interface. Straightforwardly understood, it should be noticed that with the involved organic solvent, polymer approach lack of intrinsic chemical resistance, avoiding their use in the field. But on the other side, glass bonding, typically achieved in between 350 and 650°C for several tens of minutes, induced major drawbacks (i.e., bioreagents integration and biochemical surface functionalization), heavy cost issues and limited throughputs. Dedicated efforts to implement highly chemically resistance polymers such as a Teflon-like (e.g., PFA, PEFE) or polyimide interface should be a way for significant advances of liquid-liquid extraction methodology for cost-effective LOC platforms, where additional downstream amplification and detection means with on-board reagents would be, therefore, possible to be integrated.

2.1.3. Microscale filters

Compared to SPE or liquid-liquid phase extraction methods, microscale filtration is performed in a single buffer system. Typical filtration approaches involve two large mechanisms. First, the filtering effects those permit sorting through their pores by steric exclusion. Second, electric fields that will induce transport of the analyte inside or at the vicinity of the pores sites. Only representative works based on the first steric aspect, considered as "passive approach," are addressed in this section. Exclusion/enrichment effects based on electrical fields are presented later in (Section 3.2).

Mainly four types of filtering approaches are commonly used: membrane, weir, pillars, and cross-flow. First, integration of optically clear polycarbonate track-etched membrane is one of the preferred options for membrane based filtration approach. At low cost, an impressive range of membrane features are available with thicknesses ranging from 5 to 50 μm , pores sizes from 10 nm to 10 μm , and pores density from 10 + 5 to 10 + 9 pores cm^{-2} . Additionally, such membranes can be easily integrated in a multilayered microfluidic system. In order to reduce their clogging and fouling issues specific microfluidic protocols have been investigated. Using the periodic reverse flow strategy, Redkar and Davis [24] have shown that the final average flux obtained with backflushing is still 20–30 times higher than filtration without the reserve flow strategy. Recently, in order to separate diverse multicomponents from a sample, Lo and Zahn [25] have integrated three membranes with pore size of 0.4, 2, and 5 μm in a microfluidic chip. Therefore, from one side to the other, they demonstrated the separation of sheep blood into its components. Conventional membrane filtration has been also optimized through the cross-flow approach. Recently, Aran et al. [26, 27] reported a cross-flow filtration using the track etched membrane integrated in a microchannel for the continuous bacteria extraction from whole blood for sepsis interest and also plasma protein extraction during cardiac surgery. Compared to isoporous planar membrane integration, the weir and pillar-based filtration approaches benefit of added advantages such as the flexibility of microfluidic design and microfabrication since pore size, filter orientation, and geometry can be modified on demand in order to improve microscale interaction in between filters structures and filtrate. Recently, using a weir-type filter, Chung et al. [28], developed a microfluidic cell sorter for circulating tumor cell (CTC) concentration and analysis. Moreover, the continuously separation is achieved at a high flow rate of up to 20 ml/h (see Figure 1a). Micropillar arrays for CTC isolation, fetal red blood cell enrichment and removal of pathogens have been also intensively used in microfluidic environments [29, 30, 31]. For further interest, we refer the readers to the following reviews [32, 33].

2.1.4. Hydrodynamic sorting and concentration techniques

Hydrodynamic methods that are passive approaches represent the most widely used strategies for sorting and concentrating micron-sized objects. Hydrodynamic methods rely on any external field other than the forces developed by the fluid on the analyte. These techniques not only ease the overall concerns of integration, but also feature promising potential for high-throughput and enhanced parallel purposes. Additionally, hydrodynamic techniques are label-free. Relying mainly on microscale microfluidic effects based on deterministic lateral displacement (DLD) [34], hydrodynamic focusing [35], and inertial migration mechanism [36, 37], various demonstrations have been already reported. In this section, we only report for few significant examples for each approach, for in-depth review and exhaustive hydrodynamic understanding, we refer the readers to aforementioned publications [38].

Last refinement for DLD systems focused on the optimization of the geometrical boundary of micropillar components which drive the separation performance of the system. In that sense, Inglis [39] has proposed fluidic aberrant corrections for enhanced separation characteristics. In order to reduce clogging and fluidic resistance for high DLD performance, Louterback et

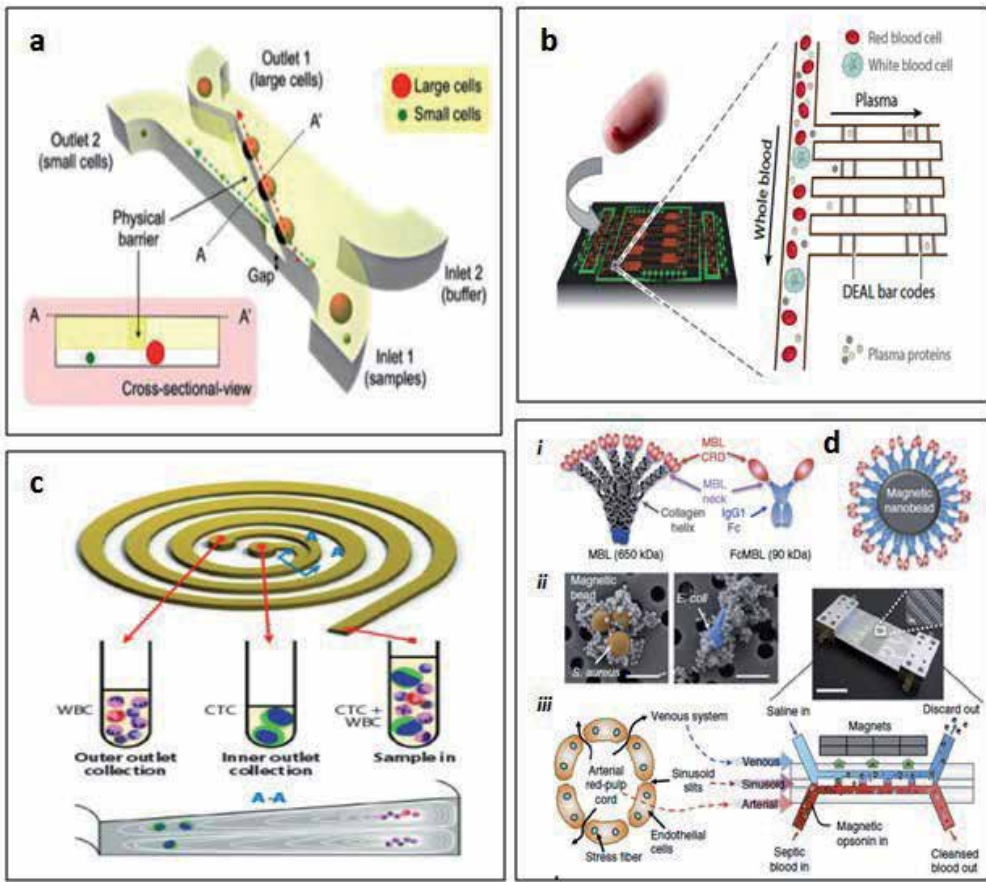


Figure 1. (a) Schematic illustration of a cross-flow microfluidic cell sorter used to separate circulating tumor cells from normal blood cells. Large cancer cells move along the weir-type barrier and are collected at one outlet while smaller hematological cells pass through a gap underneath the barrier, and are directed to a separate outlet. (b) An integrated blood barcode chip for a protein assay. Plasma is separated from blood collected from a fingerprick by harnessing the Zweifach-Fung effect. Proteins in plasma are skimmed and analyzed *in situ* within the antibody barcode arrays. (c) Schematic of particle separation using a spiral microchannel with a trapezoidal cross-section. At the outlet of the spiral microchannel (the A-A cross-section), CTCs are focused near the inner wall due to the combination of inertial lift force and Dean drag force at the outlet; white blood cells (WBCs) and platelets are trapped inside the core of the Dean vortex, which is formed closer to the outer wall. (d) (i) Magnetic opsonin and biospleen device. Design scheme of native mannose-binding lectin (MBL) to produce the generic opsonin FcMBL and its coating on magnetic nanobeads to ensure stable and to facilitate protein purification. (ii) Pseudocolored scanning electron micrographs showing magnetic beads (128 nm) bound to the bacteria *S. aureus* (orange/brown; left) and *E. coli* (blue; right). Scale bars, 1 μm ; arrows indicate pathogen with bound beads. (iii) Schematics of a venous sinus in the red pulp of the spleen (left) and a longitudinal view of the biospleen (right), with a photograph of an engineered device (right).

al. [40] have integrated several pillar structures (circular vs. triangular) and their gaps. Finally, combining those two corrections, 85% of CTC recovery was achieved operating at an impressive flow rate of 10 ml/min [41]. *E. coli* and trypanosomes pathogenic cell extraction by DLD have been reported using circular posts of 6 and 20 μm , respectively [42, 43].

Hydrodynamic focusing refers to the use of flow streams to achieve cell or bead concentration and isolation. It is a size-based approach controlled by the flow rates, channel geometry and downstream channel configurations. For continuous plasma extraction, Vermesh et al. [44], developed an integrated blood bar code system displaying two units. First acted for plasma microfluidic skimming, when the size of the cells are comparable to a main central channel width the cells at a bifurcation point migrate toward this high flow rate channel while plasma penetrates adjacent perpendicular channels. The harvested proteins can then react on probes deposited inside the adjacent channels as illustrated in Figure 1(b).

Finally, due to its improved performance when operating at high flows, inertial focusing in recent years has gained tremendous interest for diagnostics, therapeutics and cell applications. Related to the combined effects of the two size-dependent forces, the inertial lift force ($FL \propto a^4$), and when operating in a curved channel, the additional Dean drag force ($FD \propto a$), diverse lateral positions across the channel section will be favored for specific particle geometry for sorting and concentration purposes [45]. In a recent study, using optimized spiral devices with trapezoidal cross-section, a recovery of 80% of CTC from 7.5 ml of whole blood have been reported in 8 min (Figure 1c) [46]. Using a combination of hydrodynamics and inertial focusing methods, Clime et al. [47] recently, devised a system for the concentration, and the cleaning of a wide range of pathogenic agents from a ground beef sample. The enrichment strategies and numerous alternatives related to the use of both microfilter and hydrodynamic methods close the loop for the concentration and sorting of micron-sized objects (cells, coupling microparticles to nucleic acids, proteins, etc.). Therefore, it is subsequently possible to reach molecular extraction and eventual higher concentration with the help of aforementioned SPE and LLE means.

In a natural manner too, those considerations might be extended to the use of magnetic labeled approaches where nanoparticles and microbeads can be implemented for enhanced sorting and concentration in combination with the aforementioned tools. However, such topics are not covered in this section. But as a unique example, we wish to report a microfluidic extracorporeal blood-cleansing device recently published in the Nature Medicine Journal [48], where therapy has been used for large spectrum of pathogen and toxin removal from blood. The capture was performed with magnetic nanobeads coated with human mannose-binding lectin under the application of an external magnet through a micron-sized nanoporous membrane, which pull the opsonin-bound pathogens and toxins out from the blood. The system was operated at a tremendous throughput up to 1.25 l/h in an *in vitro* approach and the extraction performance cleared more than 90% of bacteria out stream (Figure 1d).

2.2. Electrophoretic separation and preconcentration on-a-microchip

The first experimental examples of μ TAS have been published in the 1990s. Whereas the conventional separation systems are based on chromatographic methods, the separation on-a-chip most often relies on electromigration methods and particularly with free zone electrophoresis [49–51]. The conventional chromatographic systems are generally considered to be more robust and reliable for quality control or medical purposes. However, the miniaturization of analytical systems has shown that electrophoresis on a chip is a versatile analytical separa-

tion technique that may provide high separation efficiency. Manz et al. [52] have pioneered the electrophoretic separation of sample mixtures in glass microchips. Their work that is one of the most cited papers has demonstrated the ability of a simple chip with optical detection to separate several amino acids in 15 s. The electrophoretic and electroosmotic mobility are the two contributions of transport in electrophoresis:

$$v = (\mu_e + \mu_{eof}) \quad (1)$$

where v is the migration velocity of the analyte, μ_{eof} is the electroosmotic mobility and E is the electric field.

Compared to the parabolic profile with Poiseuille flow obtained for chromatographic techniques, electrophoresis in a microchannel produces a plug-like flow with more homogenous distribution of the velocity vectors. Thus, the electrophoretic profile presents sharp peak and it helps to improve the analytical resolution. The surface to volume ratio is rather high in microfluidics and the electroosmotic mobility expression renders electrophoresis very sensitive to the surface state of the inner wall of the microfluidic channels. From this assessment, we could think that the modulation of surface charge is one way to improve the robustness of analytical performances of electrophoresis-based separation on-a-chip. The resolution in this kind of separation is also directly linked to the electroosmotic mobility by the following equation [53]:

$$R = \frac{1}{4(2)^{\frac{1}{2}}} (\mu_{e1} - \mu_{e2}) \left[\frac{E}{D(\mu_e + \mu_{eof})} \right]^{1/2} \quad (2)$$

where μ_{e1} and μ_{e2} are, respectively, the electrophoretic mobilities of two different analytes and upper lined μ_e is the mean electrophoretic mobility, and D is the diffusion coefficient.

By considering Eq. (2), if the mean electrophoretic mobility and the electroosmotic mobility have opposite sign and similar absolute values the resolution parameter R is maximized. Various strategies have been published in the literature to adjust the surface charge and thus the electroosmotic mobility. The simplest way to tune this parameter is to perform surface treatment with polymers, self-assembled monolayers by adding organic solvents in the buffer [54].

Another strategy consists of integrating a fluidic transistor in the separation channel. The gate voltage of the fluidic transistor will modify the surface state in a more versatile manner. Van den Berg et al. [55] pioneered the introduction of insulated electrodes in the separation microchannel. The electrode and the upper insulating layer interact with the ionic species of the liquid/solid interface to adjust the surface charge. This first microfluidic transistor has shown its ability to drastically change the zeta potential. This microfluidic device is capable of adjusting the electroosmotic mobility and even choosing the direction of its vector. This

dynamic control of electroosmotic flow (EOF) requires a calibration of the gate voltage versus the electroosmotic mobility in the chosen buffer.

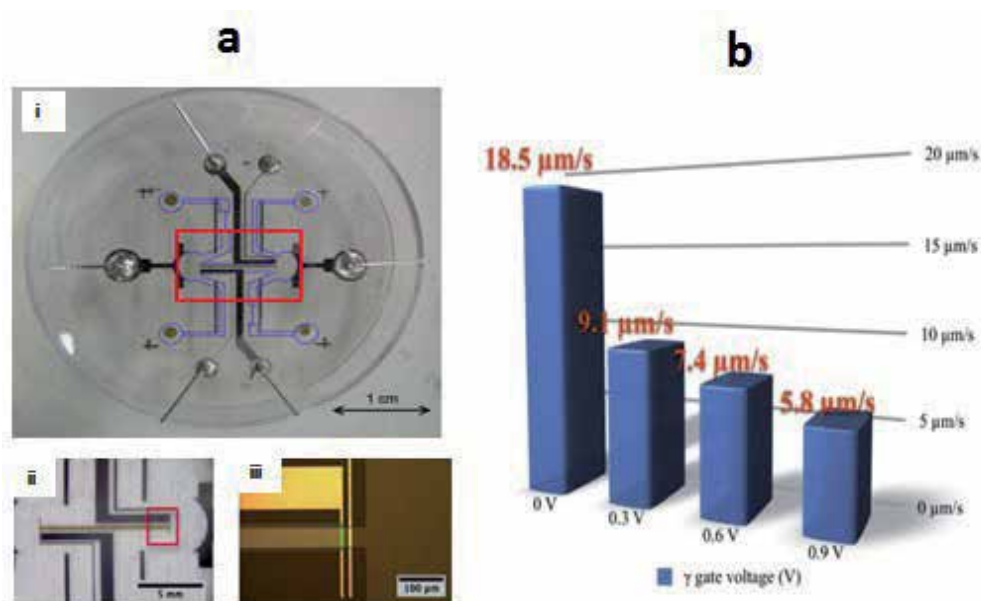


Figure 2. (a) Photography of the Wheatstone fluidic bridge bearing a fluidic transistor in the middle. The blue dashed lines are showing the fluidic network of the device. A zoom of the red box of the (i) photography is given in (ii). This optical microscopy image shows the three pairs of electrodes in the central microchannel. The brown scheme of the central channel bearing a fluidic field effect transistor. Again a zoom of the red window of the B image is proposed in (iii). In this latest image we distinguish the reference electrode of the right part of the fluidic transistor. The gate electrode (green) is placed between the ITO adhesion layer and the SiC polarizable layer. (b) Velocities of the fluorescent microbeads measured from the PIV image analysis as function of the gate voltage of the fluidic transistor. Electrophoresis in the central channel is still 3.33 V/cm.

In Haghiri's group, a new generation of fluidic field effect transistor (FFET) with a direct contact between a polarizable electrode and the buffer has been proposed and studied since 2007 [56]. This fluidic component requires less voltage to adjust the surface charge and avoids the problem of current leakage from the insulating layer that is observed during ageing with the Van den Berg's transistor. On the other side, the polarizable interface will be more sensitive to unspecific adsorption or any surface contaminations. Our first attempt to adjust the surface charge with such polarizable interface was already published and we partially succeeded to control the zeta potential with three different materials. With the first generation of FFETs, some electrochemical reactions have been observed, leading to the partial destruction of the transistor. Moreover, the linear variation of the electroosmotic mobility versus the gate voltage could be surprising since the equivalent electrical model includes a capacitance. For the second generation of FFETs to avoid these parasitic electrochemical reactions, the gate voltage of the polarizable interface should be adjusted from a reference electrode close to the transistor. In

addition, voltage followers have been integrated in the electric system of the transistor. The electric potential of two reference electrodes at both side of the transistor could thus be connected to these voltage followers to precisely adjust the gate voltage. Moreover, the SiC polarizable interface does not directly adhere onto the glass surface since a layer of ITO (indium titanium oxide) between the substrate and the polarizable layer allows to electrically isolate the SiC polarizable interface. This configuration of flow field effect transistor was integrated in the Wheatstone fluidic bridge to measure the EOF mobility as a function of time. Compared to the first generation FFET transistor without reference electrodes a drastic decrease of the electrochemical reaction was observed. A microfabrication process including WL-5150 photosensitive resist and metal deposition onto glass substrates was optimized. The inlets and outlets of the device are opened by gently sandblasting the upper glass substrate. The total thickness of the double ITO/SiC layer is 200 nm. Pictures of the Wheatstone fluidic bridge with a transistor are given in Figure 2(a). The fluidic flow in the central channel is controlled by the modulation of the EOF flow and thus can be adjusted by the value of the gate voltage. A 5 V transverse electric field was applied with the extreme electrodes for electrophoresis. The gate voltage values were less than 1 V in the polarizable window of the SiC. Particle image velocimetry (PIV) was used to characterize the fluidic flow as a function of the gate voltage. Indeed, 1 μm diameter fluorescent bead was injected in an aqueous 10^{-3} mol/l KCl solution. Finally, the modulation of the fluidic flow as function of the gate voltage is shown in Figure 2(b). It should be noticeable that the amplitude of the velocity is decreased by more than a factor three between a gate voltage of 0.9 and 0 V. The gate voltages used in these experiments are very low compared to values used in the MIE (metal-insulator-electrolyte) configuration (few hundreds Volts).

The development of electrophoresis on-a-chip has led to high-throughput microfabrication methods to produce cost-effective miniaturized fluidic devices. Recently, Liedert et al. [57] reported a foil-based PMMA chips fabricated by high-throughput roll-to-roll (R2R) process for the identification of the antibiotic resistance gene *mecA* in *Staphylococcus epidermidis*.

Pu et al. [58] pioneered molecular enrichment using nanofluidic devices. Electropreconcentration with nanoslit is used to rapidly and locally increase the concentration of low abundant species. The group of Santiago [59], leader in the field, performed most efficient and innovative ways to preconcentrate several analytes and address the most significant theoretical concerns. However, the influence of several parameters such as ionic strength, chemical nature of the buffer or the surface charge of the inner walls of the device is not yet fully understood and there is still a need for pertinent preconcentration diagrams. The micro-nano-microstructure and real pictures of the electropreconcentration chip are presented in Figure 3(a) [60]. Moreover, we add in this figure the velocity profiles by considering the electrophoretic and the electroosmotic contributions and the influence of an additional hydrodynamic pressure. This additional pressure permits modification of the position of the preconcentration plug and even stabilizes some propagating regimes. Moreover, such hydrodynamic pressure stabilizes the concentration polarization effect and controls the selective preconcentration of analytes in terms of preconcentration rate and localization as compared to pure electrical preconcentration (see Figure 3b).

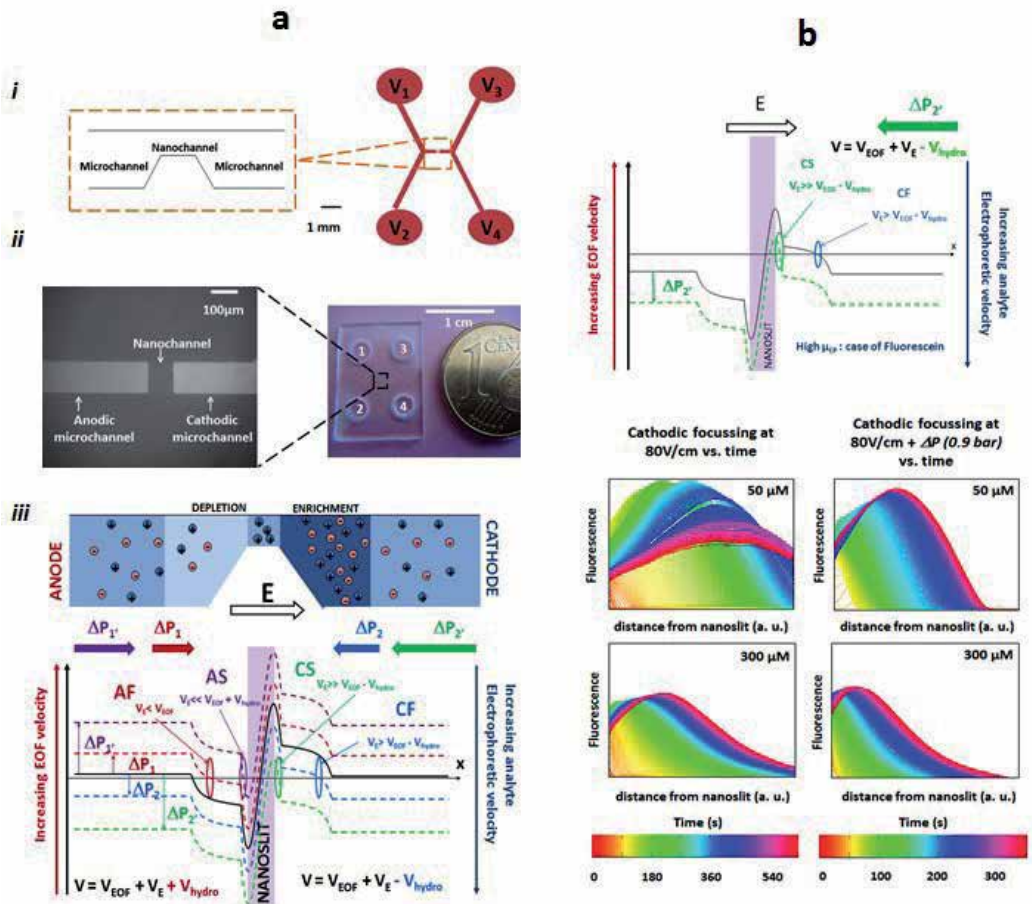


Figure 3. (a) (i) Scheme of the central channel of the preconcentration device. The nanoslit is connected by two microchannels to obtain the microchannel/nanoslit/microchannel structure (MNM). (ii) Microscopy picture of the MNM structure during an electropreconcentration experiment. The fluorescent analytes are injected at both sides of the device. On the right we show a photograph of the whole preconcentration device. (iii) The mechanism of pressure-assisted preconcentration and separation. The local transport rate profile is represented in the MNM structure (velocity of the molecule vs. distance in the structure). The black curve gives the classical preconcentration global velocity of BSA when an electric field is applied as a function of the distance. Four other cases are depicted: two cases with the application of a positive pressure (from the anode to the cathode), which has the effect of moving up the curve in the diagram and obtaining the two anodic regimes depending on the value of the pressure (anodic stacking in purple and anodic focusing in red), two cases with the application of a negative pressure (from the cathode to the anode), which has the effect of moving down the curve and obtaining the two cathodic regimes (cathodic stacking in green and cathodic focusing in blue). (b) Experiments with fluorescein show the role of the ionic strength and the addition of a hydrodynamic pressure over the evolution of the preconcentration profiles (left) a conventional electropreconcentration compared to (right) a cathodic-pressure-assisted electropreconcentration [60].

3. Detection components and microfluidic strategy

3.1. Introduction to MEMS detection

This section focuses on miniaturized sensors designed for getting, which are integrated in the last stage of the fluidic lab-on-a-chip (LOC) device after preconcentration and separation previously discussed. Integrated microfluidic biosensors can be classified into two main categories: (1) bulk detection, more often named labeled detection allowing identification of analytes flowing inside the fluidic channel with prelabeling of the target with a marker (fluorescent or electroactive marker) and (2) “label-free” detection, where physical effects during biochemical recognition are directly measured after binding of the target analyte on the chemical probe. More often this detection mode occurs on a surface, which has been functionalized with the bioreceptor (probe) [61]. Figure 4(a) illustrates these two routes for a classical “Primary antibody/Antigen” couple. The biochemical recognition is mainly governed by the choice of the appropriate biochemical receptor that will specifically bind to the target of interest. Receptors are thus integrated in architectures specifically designed to be well adapted for both analyte and transduction method. Figure 4(b) presents the different existing architectures [2]. In brief, transducers have been paired with antibodies (or antibody fragments, i.e., proteins that are produced by the immune system) [62, 63] see Figure 4(b) (i), with aptamers [64] (see Figure 4b(ii)) and other receptors as recognition elements (Figures 4b(iii)–(v)). For surface detection, if the affinity of the biomolecular recognition is high ($K_a = k_{on}/k_{off}$ ranging from 10^9 up to 10^{13} for the case of biotin and streptavidin), the identification of the target can be highly selective during its capture by the bioreceptor. If the specificity of the biochemical recognition is fully determined by the nature of bioreceptor, the sensitivity, also called “Limit-of-Detection” (LoD) and the dynamic range of the sensor are strongly related to the intrinsic properties of the transducer.

It is thus of interest to review different intrinsic properties of the transduction, which can be mechanical, magnetic, optical, or electrical (Figure 5) [65–71]. They are very few comparative studies on intrinsic sensitivity in the literature. However, the reader could refer to the excellent review paper of Arlett et al. [73] published in Nature in 2011, which summarizes and compares the performance of mechanical, optical, and electrical transduction methods. Mechanical sensors are based on cantilever assays where the specific binding of analytes induces lateral stress, resulting in bending of the free-end of the cantilever. One major limitation of surface cantilever detection (Figure 5b) concerns nonspecific binding occurring at the bottom cantilever surface that can negate the bending and thus alter the detection. Recently, Ndieyira et al. [66] have shown that it is possible to overcome competing stresses from opposing cantilever surfaces allowing direct capture of HIV molecules at 500 fM within 15 min. Magnetic sensors have been mainly used to manipulate magnetic beads in fluidic channels that are used as magnetic label for cell sorting or bead detection [67]. We do not detail such sensors in this chapter since extensive reviews exist. The reader can refer to the excellent reviews from Pamme and Gijs that give a general overview of magnetic integrated sensors [74, 67]. The last part of this chapter is devoted to intrinsic performances of both optical and electrochemical biosensors

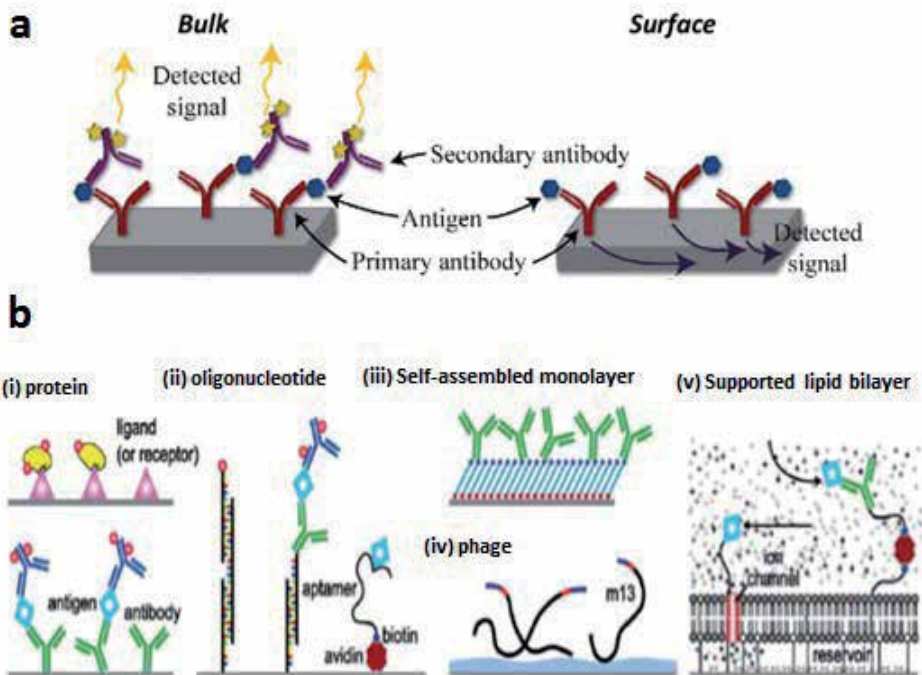


Figure 4. Comparison between (a) labeled and (b) label-free detection methods, reprinted from [61], examples of the different architectures for surface functionalization, reprinted from [2].

and, finally, we conclude with recommendations for optimizing fluidic parameters in order to enhance the capture of biomolecules.

3.2. Optical and photonic detection

In general optical biosensors are divided in fluorescence-based and label-free detection. In fluorescent-based detection (bulk), the evanescent field is used to enhance the excitation (or the emission) of the fluorescent dye used to tag the analyte of interest. In contrast, in label-free detection, the target molecules are not labeled and are detected in their natural forms. Optical sensing remains an important route for which record sensitivities were demonstrated through the considerable progress of photonic nanostructures. We focus in this section on integrated photonics nanosensors that are based on direct coupling between light and fluid since the strength of this interaction determines the intrinsic sensitivity [75]. Before, discussing the specific properties of the different photonic sensors, it is of interest to illustrate how such photonic nanostructures could be integrated inside the microfluidic chip.

The optofluidics device thus integrating source and detector exhibits new optical properties related to the nature of liquids. This concept of optofluidics multilevel platform has been introduced by Psaltis at the University of Caltech in the United States [76]. In such platform three levels are stacked: (1) the base of the device (bottom layer) that contains the optical

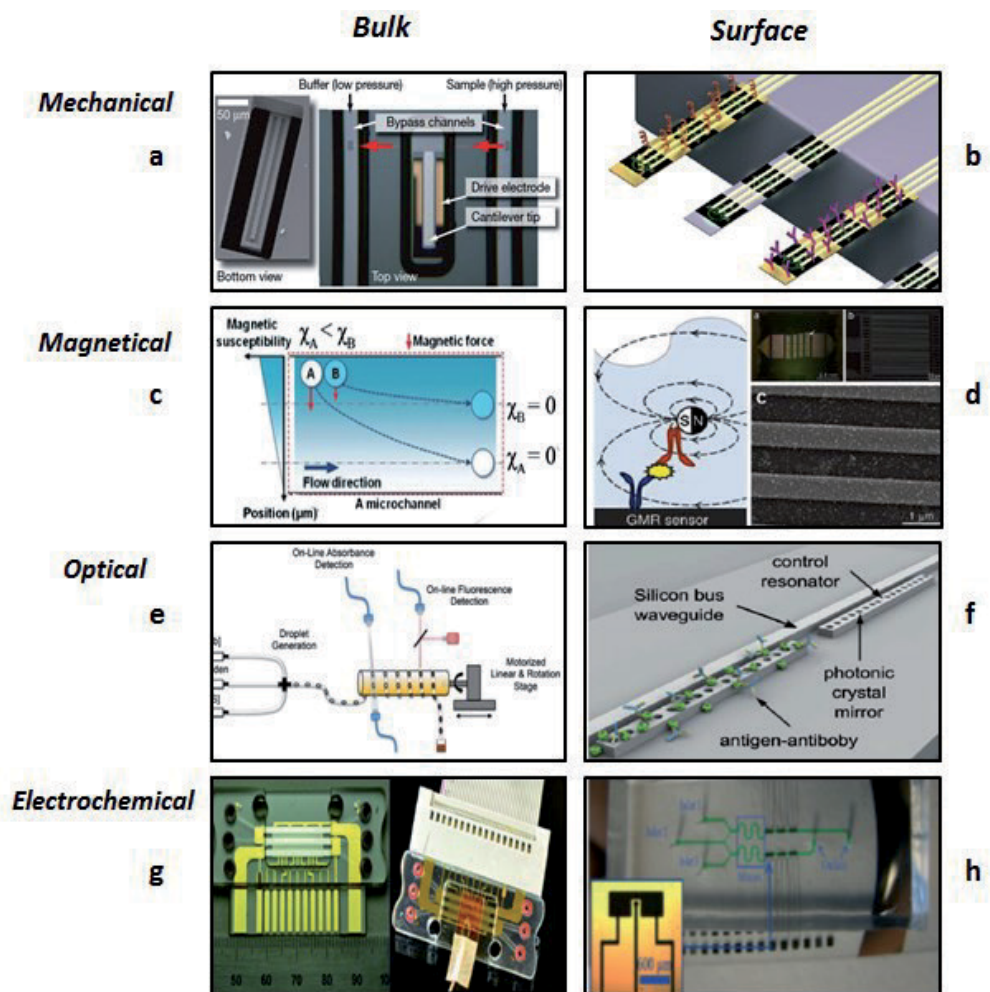


Figure 5. Examples of integrated biosensors presented as function of the nature of the transduction for both bulk and surface routes, reprinted from (a) [65] and (b) [66], (c) [67] and (d) [68]; (e) [69] and (f) [70]; (g) [71], and (h) [72].

elements, namely, the springs, the waveguides and the optical sensors (photonic-crystal or plasmonic nanostructures), (2) the intermediate layer that includes the fluidic microchannels for the circulation of biological fluid, and (3) the top layer that contains the actuators for liquid handling, i.e., valves and pumps. Figure 6 presents the hypothetical architecture of such ideal optofluidic platform based on photonic nanostructure as sensor [75, 77]. If the optical sensors are structured in the bottom layer to dimensions smaller than the wavelength of the order of 100 nm, the fluidic channels have, in turn, typical widths of hundreds of micrometers and lengths of several millimeters. There are still very few complete demonstration platforms, which integrates all the optical components (source, waveguides, and detectors) and fluid control tools. All current researches converge toward this ultimate goal of integration, hoping to increase the portability of the chip and the sensitivity of optical detectors.

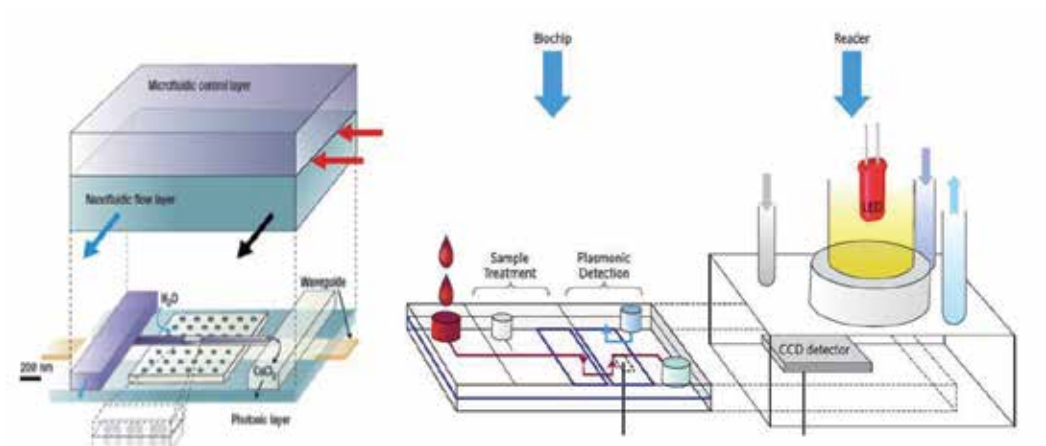


Figure 6. Hypothetical architectures for integration of photonic nanostructures with a cross-section of the fluidic chamber containing the sensor (left) and a global view of both chip and reader (right), from references [75, 77].

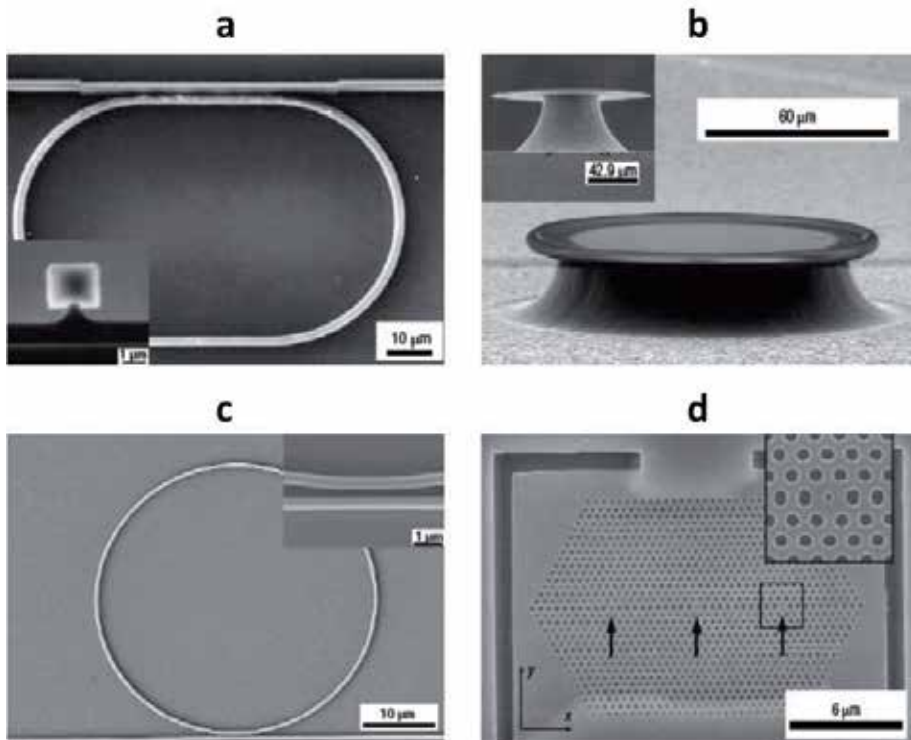


Figure 7. Scanning electron micrograph of various microcavities that can be used for biosensing with (a) suspended polymer microring from [79], (b) silica suspended microdisk (inset) and silica microtoroid from [81], (c) silicon microring from [82], and (d) planar photonic crystal in an InGaAsP membrane from [83].

In an optical biosensor the strength of light-matter interaction is enhanced by the presence of a guided or a localized optical mode with an evanescent field with subwavelength spatial extension [84, 85]. Guided mode can be excited in dielectric or metallic waveguide. A typical example is the case of the surface plasmon resonances (SPR) [80], an electromagnetic guided mode excited at the interface between a noble metal and a dielectric. Localized modes can be excited in dielectric structures like photonic crystals [86, 87] (Figure 7d) or ring resonators [79, 82] (Figure 7a and c) and in metallic nanoantenna resulting in the so-called localized surface plasmon resonance (LSPR) (Figure 7d) [83].

The light confinement can be used to increase the scattering (or the absorption) cross-section of the analyte molecules or to measure the refractive index (RI) change induced by molecular interactions. The most studied example of the first category is surface-enhanced Raman spectroscopy (SERS). SERS is a spectroscopic technique in which the inelastic scattering of monochromatic light provides information about vibrational, rotational, and other low frequency transitions in molecules of the analyte. Here, we limit the scope of this section to the so-called RI-based label-free detection. The presence of the analyte immobilized on the sensor surface through a specific biochemical reaction results in a RI change in the near field region of the optical mode. The RI change induces a modification of the dispersion relation of the guided mode or a shift in the position of the localized resonance that is monitored in real time. The performance of an RI-based optical sensor is most commonly characterized through the bulk sensitivity $S = \Delta\lambda/\Delta n$ [nm/RIU (Refractive Index Unit)] in which λ is the resonance wavelength of the optical mode and n is the refractive index of the medium probed by the near-field of the optical mode. Since it is easier to detect a given resonance shift for narrow lines, the figure of merit $FOM = S/FWHM$ (where FWHM is the full width at half-maximum of the resonance) is a more meaningful measure of the performance of the sensor. An important parameter that is difficult to quantify is the extension of the evanescent field of the optical mode. In an optical biosensor, the analyte (with RI ~ 1.5) is specifically immobilized at the sensor surface, where the intensity of the evanescent field is higher. The rest of the evanescent field probes the RI of the buffer solution (RI ~ 1.33). The effective RI change probed by the whole near field of the optical mode depends on the overlap between the evanescent electromagnetic field and the analyte. Highly confined modes are therefore more sensitive to small analytes. This explains why, despite their relative high sensitivity and FOM (typically 3300 nm/RIU and 50), SPR-based biosensors fail to detect small molecules like biotin because of the relatively large extension of their evanescent field that exponentially decays over 200–300 nm away from the surface. On the other side, LSPR-based biosensors have relatively smaller sensitivity and FOM (typically 400 nm/RIU and 2), but their evanescent field exponentially decays over a distance 10 times smaller than that of a SPR mode [88, 89].

To our knowledge the highest FOM and field confinement achieved to date for a localized optical mode was reported by Cattoni et al. [90] in arrays of plasmonic nanocavities fabricated by soft UV nanoimprint lithography (Figure 8). The plasmonic nanocavity is designed and ensures total absorption of light at the plasmonic resonance. Sensitivity, FOM, and optical field confinement are parameters that strictly depend on the physics behind the nanophotonic element used as a sensor. These parameters alone cannot be related to the biosensor perform-

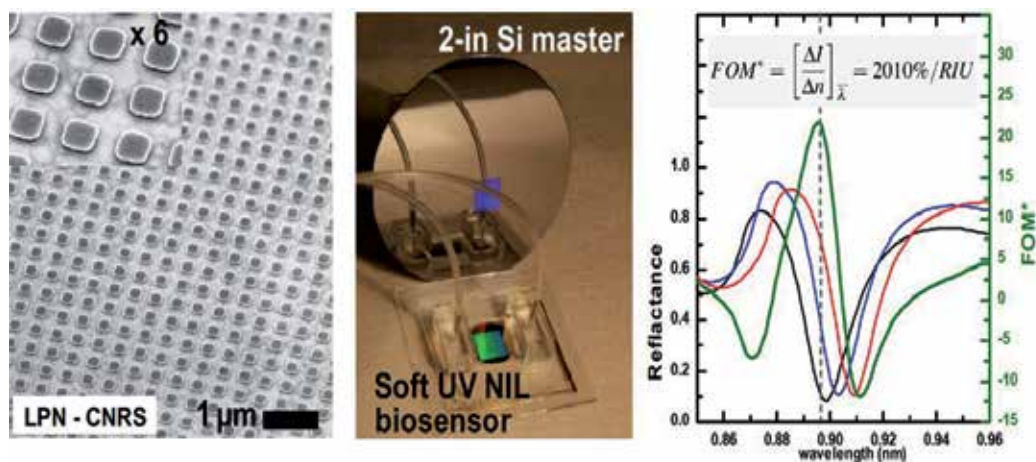


Figure 8. Left: SEM image of the 2D metal-insulator-metal nanocavities fabricated by Soft UV NIL using a hard-PDMS/PDMS stamp. Center: picture of the biosensor integrated in a microfluidic chamber and silicon master mold used to fabricate the hard-PDMS/PDMS stamp. Right: Spectral shift of the second-order mode for different RI solutions: water (black line), ethanol-water solution (blue line), and pure ethanol (red line). The green line corresponds to the FOM calculated as function of the wavelength using the equation in the inset, from [90].

ance, since it is only an indication of signal strength. The parameter typically used to characterize the performance of a biosensor is the LOD. The LOD can be deduced by taking into account the noise in the transduction signal, σ , i.e., the minimum resolvable signal: $LOD = \sigma/S$, where S is the sensitivity. The LOD can therefore be improved by increasing the sensitivity (and the light confinement) and by reducing the noise level. For an optical RI-based label-free sensor, there are typically three ways to specify LOD: in units of refractive index units (RIU), in surface mass density of the analyte (pg/mm) or in analyte concentration (ng/mL or molarity). The LOD specified in terms of RIU is easy to measure and useful to roughly compare the sensing performances of different optical sensor.

As previously mentioned, it does not take into account the extension of the field confinement because the measure is made varying the RI over the whole extension of the probing near field. Reported values for SPR-based sensor have LOD up to 10^{-8} RIU, dielectric waveguide and ring resonator LOD up to 10^{-7} RIU and photonic crystals LOD up to 10^{-5} RIU [87, 89]. The extension of the field confinement is taken into account when the detection limit is specified in terms of surface mass density, which is what a biosensor actually measures. LOD in terms of surface mass density is difficult to determine accurately, but it can be used to compare more precisely the performance of different optical sensors. Finally, LOD defined in terms of sample concentration is easy to determine and it can be used to compare more precisely the sensor performance. Of course it depends on the specific analyte and its affinity to the biorecognition molecule grafted to the biosensor surface. For this reason, LOD, chemical affinity between a specific analyte and the relative bioreceptors and microfluidic parameters must be considered all together in the optimization of the overall performances of the sensor. Acímovic et al. [91] demonstrated state-of-the-art paralleled LSPR-based lab-on-a-chip composed with 32 sensing

sites distributed across eight independent microfluidic channels with very high reproducibility/repeatability (Figure 9). In particular they demonstrated the fast detection of relevant cancer biomarkers (human alpha-feto-protein and prostate specific antigen) down to concentrations of 500 pg/ml in a complex matrix consisting of 50% human serum.

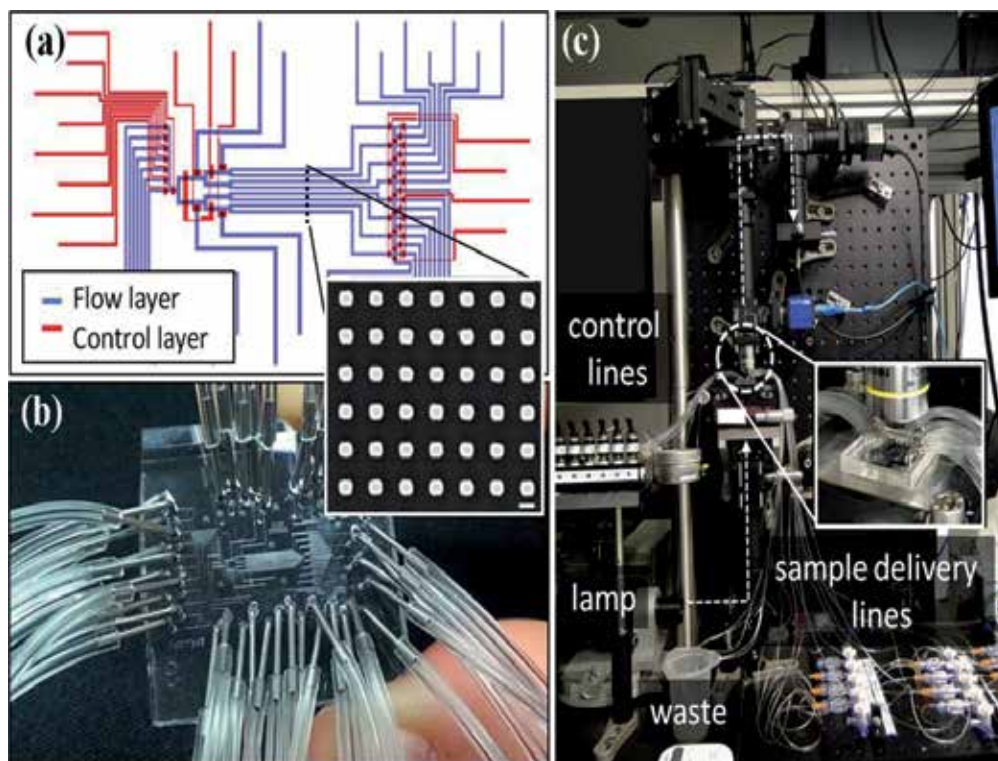


Figure 9. Description of the sensing platform: schematic of the flow and control layers (a) and final connected chip. (b) The inset shows a standard SEM image of the plasmonic gold sensors. Scale bar = 200 nm. (c) Overview of the optical setup. From [91].

3.3. Electrochemical detection

3.3.1. Introduction to microfluidic detection

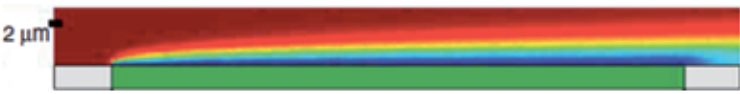
Initially sensing research focused mainly on the performances of the transducer and the biomolecular recognition, without discussing the role of microfluidic parameters. To obtain a well performing analytical device these components have to be considered all together in the optimization of the overall performances of the sensor. Achieving fast time less than one minute, specific and sensitive detection at concentration on the femtomolar level or even less appear thus an actual challenge for the microfluidic community. If the main advantage of microfluidic devices is to reduce the volume and to efficiently deliver target molecules to the sensor surface, working with such extremely reduced size and concentration raises funda-

mental questions about physical and chemical limits. Independent of the intrinsic sensibility of the sensor (optical or electrochemical), all the fluidic conditions have to be chosen in order to favor binding mechanisms. For most of applications, if the fluidic system works under “extreme fast” flow at a high Péclet number (Pe_H), the number of captured molecules per unit of time is largely enhanced (see Box 1 that resumes the pertinent fluidic parameters). The geometry of the fluidic channel (the height H and the width W_c), the size of the sensor (the width W_s and the length L) and the volumetric flow rate Q have thus to be precisely defined to fix if the system will work in a reaction-limited or diffusion-limited regime.

Box 1 - Kinetics and mass-transport in microfluidics devices

To determine in microfluidic devices whether analytes are depleted in the vicinity of the sensor surface and which limiting factor governs kinetics, several parameters have to be considered.

First, the two Péclet numbers, $Pe_H = Q/D \times W_c$ with subscript H to specify the channel height as the relevant parameter and $Pe_s = 6(L/H)^2 Pe_H$, where D is the diffusion rate, Q is the volumetric flow rate, W_c is the channel width and L is the sensor length. Let us consider the case of a microscale sensor with $L = 50 \mu\text{m}$ and $W_s = 50 \mu\text{m}$ integrated in a microfluidic channel with $H = W_c = 100 \mu\text{m}$, through which a target solution with diffusivity $D = 10 \mu\text{m}^2/\text{s}$ flows at a flow rate $Q = 10 \mu\text{l}/\text{min}$. Such microfluidic system exhibits large values of both Péclet numbers: $Pe_H = 1.7 \times 10^5$ and $Pe_s = 2.5 \times 10^7$ which means that the depletion zone is thinner than the channel and the sensor:



$$\delta_s \sim L_s / (Pe_s)^{1/3} = 800 \text{ nm} \ll L < H$$

The total flux or collection rate of target molecules can also be deduced from $J_D = Dc_0W_sF$ where c_0 is the initial concentration of the target and $F \approx 0.81 Pe_s^{1/3}$ the dimensionless mass transport flux: $J_D = 0.15$ molecules per second or one binding event every 7 s. In other words, a high number of targets can be trapped in the thin depletion layer where they can reach rapidly the sensor surface to fast stick on the probe and react. Working under high flow with microscale integrated sensors allows trapping sufficient molecules even in extremely diluted solutions. See ref. 92 for more details.

In 2008, Squires, Messinger and Manalis proposed a theoretical approach to estimate the interplay between diffusion, convection, and reaction [92]. Their complete analysis gives some guidelines to estimate some fundamental quantities, such as fluxes, collection rates, and equilibration times. Based on dimensionless parameters that are straightforward to compute, their simple approach is very useful in characterizing and designing systems. Two Péclet numbers, Pe_H and Pe_s , characterize the nature of the mass-transport depletion zone around the sensor. At low values of Pe_H ($Pe_H \ll 1$ at extremely slow flow), the system is in a diffusive regime, with a depletion zone that extends far upstream in the whole thickness of the channel. Even if all molecules are collected, the time of capture is so high (hours or days) that such diffusive regime appears very limited for real applications. At high Pe_H ($Pe_H \gg 1$ at extremely fast flow), a depletion zone thinner than the channel (δ_s) exists and a second pertinent Péclet number Pe_s can be used to calculate whether this depletion is thicker or thinner than the sensor itself. Box 1 gives the more important equations useful for optimizing integrated microfluidic devices that involve very small volumes of sample. One should ensure that the sensor exhibits enough

sites to bind target molecules maximally. It appears that the sensor should be preferably microstructured with dimensions ranging from 100 μm to several hundreds of microns instead of tens of nanometers as for nanowires.

3.3.2. Current status and state-of-the-art of electrochemical detection

The need for a miniaturized sensor, portable, with fewer components has allowed the development of electric sensors (chemical or biochemical) [93]. Successful integration of microelectrodes opens the way for the development of electrical and electrochemical detection in microsystems. Indeed, the development of microfabrication techniques to produce microelectrodes was decisive for bioelectroanalysis. The advantage of making electrical transducer sensors is to have portable electrical and electrochemical sensors with easy operation, a great performance in the detection and a low power consumption (applied and measured signals require only a voltage generator). In addition, it contains few components on the very small dimension reducing drastically the size of the final microsystem [94]. In general, electrical sensors operate an electrical signal (current or potential) by amperometry, voltammetry [95, 96], or electrochemical impedance spectroscopy [97]. Electrochemical strategy has been used over a wide range of biochemical identification and analysis purposes from traditional genomics and proteomics areas but it find through cellomics and gases detection increasing interests. For traditional, micro-array DNA electrochemical detection, many works have been reported, and even additional on-board components such as cellular lysis, and genomic preamplification been also incorporated. Indeed, Ferguson et al. [98] have demonstrated the integration of loop-mediated isothermal amplification (LAMP) means coupled with a sequence-specific electrochemical detection in a disposable, monolithic chip. Using this platform, the authors have demonstrated detection of genomic DNA from *Salmonella enterica serovar Typhimurium* LT2 with a limit of detection of 10 aM. On the proteomics side, a recent paper from O. Kelley et al. [99], demonstrated clinical relevance for an electrochemical enzyme-linked immunosorbent assay for HIV antibodies identification. The current method derived from the oxidation increased linearly over a wide antibody concentration range (0.001–1 $\mu\text{g. ml}^{-1}$), with a detection limit of 1 ng. ml^{-1} (6.7 pM). For cellomics purposes, Zór et al. [100] recently, demonstrated a powerful electrochemical based integrated platform for real-time monitoring of cellular dynamics. Their system performed, the complete cell based assays comprising on-line electrode cleaning, sterilization, surface functionalization, cell seeding, cultivation, and electrochemical real-time monitoring of cellular dynamics. To demonstrate the versatility and the multifunctionality of the platform, additionally the authors reported for the amperometric monitoring of intracellular redox activity in yeast (*Saccharomyces cerevisiae*), and detection of exocytotically released dopamine from rat pheochromocytoma cells. As mentioned previously, the electrical sensors seem to be more appropriate for easy integration on μTAS development. We shall consider in the following sections the most widely used techniques such as potentiometry, amperometry or voltammetry, and impedance spectroscopy. Concerning the latter, the advantages of contactless microelectrodes integration on-a-chip for impedance measurement and recent applications are discussed.

3.3.3. Potentiometry

We only discuss some potentiometric microsystems, i.e., the systems that have been manufactured at least partly using photolithography or other micromachining techniques and incorporate electrical or electrochemical measurement. This definition excludes a large group of potentiometric electrochemical sensors using microelectrodes. The reason for this exclusion is that the microelectrodes are a smaller version of their macroscopic analogue and their function is similar to larger electrode [101]. From the practical point of view, a potentiometric transducer within microsystem should include a conductive contact, a reference electrode and a microchannel for the fluid flow over the sensing surfaces [102].

Microfabrication of potentiometric sensors has several advantages over conventional electrodes, in particular by the dimensions of the measuring system, which is less expensive [103]. Indeed, emergence of lab-on-a-chip applications have benefited from the development of potentiometric sensors on small surfaces in contact with fluidic. Microfluidic systems with potentiometric detection have been developed and characterized. Among them, it can be mentioned the microanalyzer prototypes based on potentiometric measurements for various applications in analytical chemistry and biochemistry, such as ions detection [104], proteins [105], and Ph [106, 107]. The achievement of receptors based on low temperature co-fired ceramic or LTCC for potentiometric microsystems (called μ POT) offers good electrical and mechanical properties, as well as reliability and stability measures. Schöning et al. [108] developed potentiometric microsensor porous silicon, where microporous layer is formed by electrochemical etching. Thus, the microstructured surface allows the enlargement of the active area of the microsensor, which increases the measured capacitance. For instance Lakard et al. [107] developed potentiometric pH microsensors based on films of electrosynthesized polypyrrole, whose electrodes are fabricated by photolithography. The study showed that thin polypyrrole films present the best potentiometric linear responses in pH in the range of 2–11.

3.3.4. Amperometry and voltammetry

Amperometry and voltammetry techniques use the measurement of the electric current response of a working electrode against the applied potential in the electrochemical cell. The amperometric transductions within microdevices have wide applications in biosensing [109, 110]. Research in biosensors domain using amperometric sensors were initiated by Clark in 1956 by studying the oxygen electrodes [111]. In amperometric microsystems, the current measured with high sensitivity is linearly dependent on the concentration to be detected. This sensitivity is highlighted in the work of Pijanowska et al. [95] about the detection of glucose. These biosensors also have the advantage of being faster, cheaper, and more available than conductimetric and potentiometric biosensors [109]. Other studies have focused on the measurement of enzyme activity measured within miniaturized amperometric and voltammetric cells, using grafted proteins on the surface of the microelectrodes. These microdevices have the characteristic to give fast response [110]. The results showed a high linearity between the measured responses of the biosensor and the concentrations of the sample. Furthermore, microsystems in amperometric and voltammetric transduction have been successfully adapted

in capillary electrophoresis, conducted in a chip for toxicity detection of phenolic compounds [112] and synthetic food colorants [113].

The integration of a reference microelectrode in a microfluidic chip is often a hard step. Recently, Faure et al. [72] have proposed an alternative strategy requiring less microfabrication steps according to a configuration with two microelectrodes for electrochemical detection in glass/PDMS microfluidic chips. As displayed in Figure 10(b), it consists of using two micro-band electrodes of the same material with a surface ratio of 22 for the counter-electrode ($S = 0.31 \text{ mm}^2$) with respect to the working microelectrode area ($S = 0.014 \text{ mm}^2$). Therefore, the counter-electrode can be considered as a pseudo-reference since the current density flowing through it is much smaller than that flowing in the working electrode, thus, limiting possible variations on the rest of potentials. To this end, the redox couple $[\text{Fe(III)}(\text{CN})_6]^{3-}/[\text{Fe(II)}(\text{CN})_6]^{4-}$ is used to impose a 0 V as reference potential (see Figure 10). The chip performance using this geometry has been characterized using cyclic voltammetry according to the hydrodynamic conditions in chip, while differential pulse voltammetry (DPV) as it appears in Figure 10, with regard to its analytical performance was preferred for the LOD of transthyretin (TTR). The quantification of transthyretin peptide is a major interest for the diagnosis of familial amyloid polyneuropathy at transthyretin (ATTR) [114]. The obtained LOD for the TTR was determined at 25 nM, a value of 100-fold lower than that reported in conventional capillary electrophoresis coupled to the laser-induced fluorescence (LIF) under the same experimental conditions [115].

3.3.5. Electrical impedance spectroscopy

The electrochemical impedance spectroscopy is a well-established technique. Thus, the need to access to more sensitive and more precise measurements within microdevices opened novel strategies for sensor development that enable integration of electrical or electrochemical impedance spectroscopy. Among the areas where the impedance measurements are the most used, its noninvasive characteristic is crucial for many applications such as for counting, identification, and detection of particles or cells in biology and biochemistry [116]. In the last years, impedance measurements in microsystems have been mainly pursued to measure the electrical conductivity of liquid [117], the dielectric properties of the particles in suspension or in flow [116, 118], the properties of the cell membranes [119], the kinetics of enzymatic reactions [120], and the adsorption of red bloods on the sensor surfaces [121]. For instance, Park et al. [122] have improved a microfluidic device developed earlier by Ferrier et al. [123]. The microdevice was used for the detection of polystyrene microbeads and cancerous cells. In brief, the device comprised a microfluidic channel and two parallel planar electrodes for particles (microbeads and cells) actuation using dielectrophoresis (DEP), and a trap reservoir containing the electrodes for the impedance measurements. The study showed that measured impedance variations were in relation to the trapping and release of the microbeads and the cell in the reservoir. Ayliffe et al. [124] have also demonstrated the ability to detect the presence of a single particle using flow cytometry combined with the impedance measurement in a microfluidic device. The principle consists in measuring the electric impedance at the passage of a particle or a cell through a microchannel with electrodes disposed on its surface in order to detect each

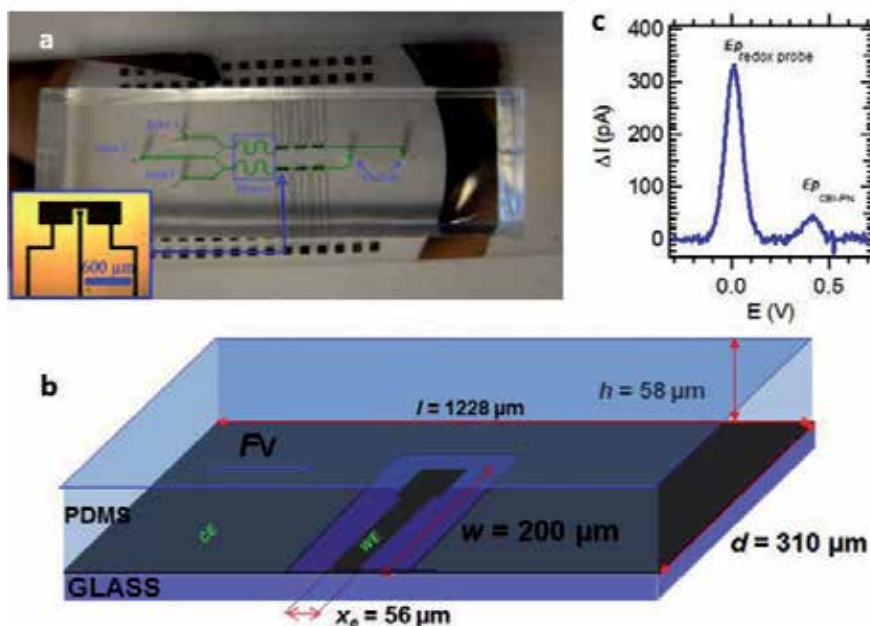


Figure 10. (a) Picture of several pairs of two microelectrodes networks located on the microchannel junction for multi-detection possibility. The fluidic microchannels allowing the sample injection with several configurations (inlet 1, 2, 3). (b) Schematic view of the detection area with a pair of microelectrodes (CE, counter electrode, WE, working electrode). The fluidic channel, WE, and CE microband electrodes characteristic dimensions: h , d , w , x_e , and l are indicated and the B scheme is not to the scale. (c) Differential pulse voltammetry of 25 μM Transferrin peptide (CBI-PN) in the presence of 1 mM $[\text{Fe(III)(CN)}_6]^{3-}/\text{Fe(II)(CN)}_6]^{4-}$ redox couple as potential reference in buffer 100 mM borate pH 9/MeOH (50/50, v/v). Scan rate 25 mV s^{-1} modulation time 100 ms modulation amplitude 7.5 mV under a flow rate of 0.05 $\mu\text{L s}^{-1}$ from [72].

particle flowing [125]. Hediger et al. [126] have investigated on microfluidic devices for detection using impedance spectroscopy in the medical domain. The microdevice was achieved by plasma etching on a silicon substrate with platinum electrodes for detection. The preliminary test in case of device filled with sodium chloride at various concentrations underlined that the measured impedance module plateaus recorded between 10 kHz and 100 Hz decreased with an increase of NaCl concentration. As they expected, the resistance of the microchannel was found as being conversely proportional to solution conductivity.

In the last decades, other kinds of microdevices were developed with electrodes in contactless configuration with the electrolyte [128, 129]. The latter have emerged to overcome some limitations due to microelectrodes contamination, corrosion, or degradation [130]. In the next part, we focus on this original electrode configuration for which the start-of-art and the advantages are discussed for sensing and biosensing development.

Microfluidic chips with a detection module in noncontact mode have the particularity of having galvanically isolated microelectrodes embedded in a dielectric layer. The configuration in noncontact mode has several advantages in comparison with the traditional mode in contact. The encountered inconvenience for solution with microelectrode in contact is

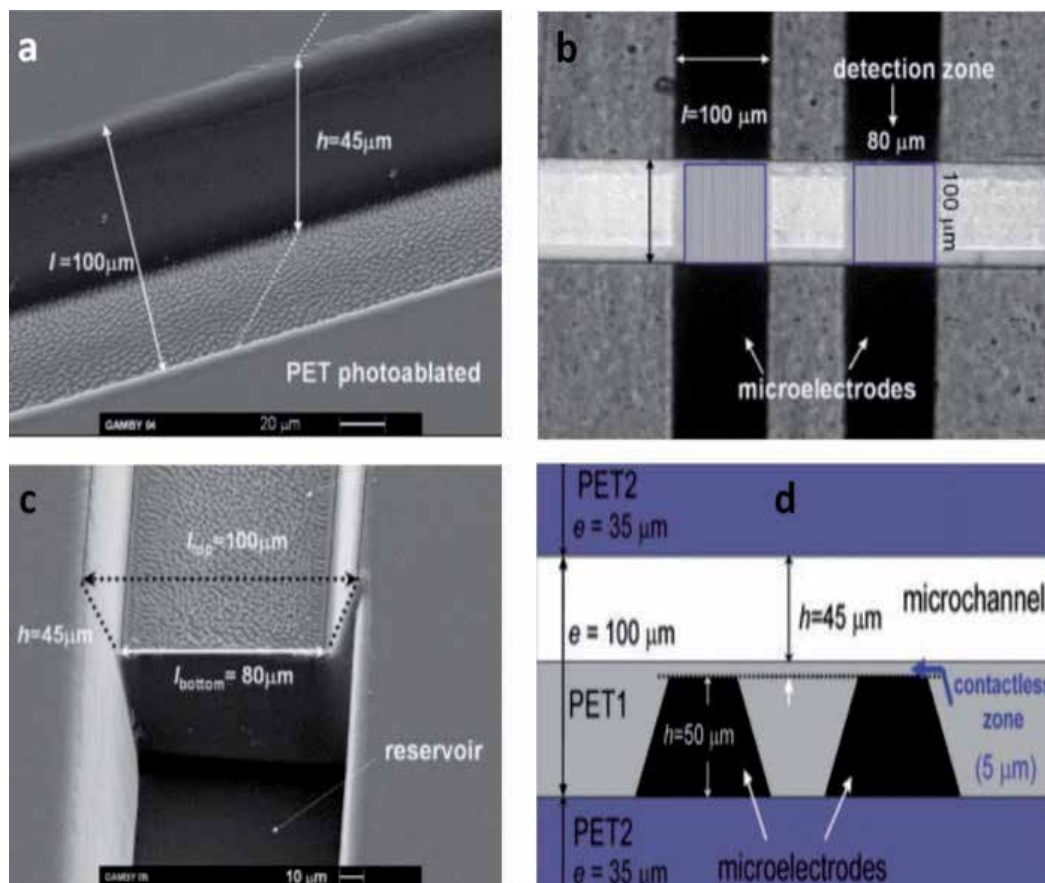


Figure 11. (a) Scanning electron microscopy (SEM) images of the PET photoablated microchannel with a cross-section of $45 \times 100 \mu\text{m}$ and a length of 1.4 cm. (b) Optical image of the detection zone global view including the planar microelectrodes (inverted optical microscope), vertically, the two band electrodes beneath the horizontal flow channel. The detection zone represents the area where capacitive coupling takes place. (c) The SEM image of the trapezoidal section of the microchannel. (b) Side view of the contactless zone, which is about $5 \mu\text{m}$ and represents the thickness separation between the flow microchannel and the planar microelectrodes [127].

avoided, for instance, the microelectrode passivation or corrosion, the bubble generation due to uncontrolled faradic reactions on electrodes [132]. The first configuration of photoablated polyethylene terephthalate PET as flexible microchips with microelectrodes galvanically isolated into the PET was patented in 2004 [133], and then published by Gamby et al. [127]. Indeed, this system was called "SuperCapacitive Admittance Tomoscopy" (SCAT), based on the observation of a thin solvent layer on a dielectric thin film through two embedded microband electrodes (Figure 12). Indeed, the PET dielectric layer coating the two parallel microelectrodes contains a microchannel with chemically modified surface for adsorption of biomolecules [134].

The study is carried out by applying an alternating voltage of 0.1–3 V in the high frequencies (1 kHz–10 MHz) between the two microelectrodes. Indeed, a capacitive coupling effect appears

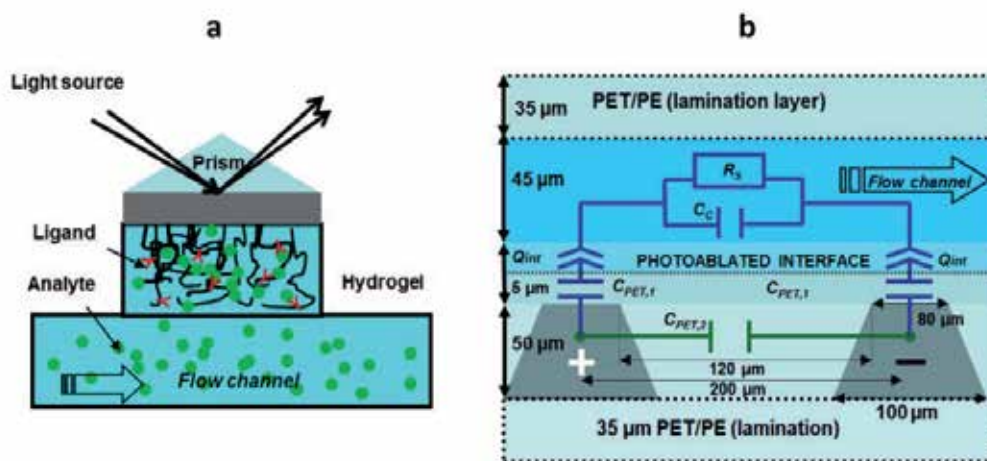


Figure 12. (a) Schematic representation of the BIACORE optical biosensor. The hydrogel is 100 nm high approximately. The ligand is immobilized in the hydrogel the analyte flows in the channel and diffuses in the gel where it binds to the ligand. (b) Cross-section of the dielectric interface microelectrode/ PET/ microchannel and the corresponding electrical equivalent circuit: $C_{PET,2}$ for the 120 μm -PET layer impedance (distance separation), $C_{PET,1}$ for the 5 μm -PET layer impedance (noncontact layer thickness), the element CPE, Q_{int} for the interfacial impedance (photoablated surface) [134].

through the dielectric layer, on the microelectrodes hand with electronic charges and on the other hand with microchannel filled with ionic charges. This enables the admittance measurement, which is itself related to the surface state of the PET chemically modified. The SCAT is suitable for the real-time study of electrostatic interactions analyte/substrate on any dielectric having a modified surface. Gamby et al. [127] have investigated the microchannel internal surface modification in the noncontact microdevice and they have showed that the surface charge can be turned and provides an opportunity to enhance the polymer-protein interactions. For instance, adsorption of β -Lactoglobulin in PET microchannel modified (poly(L-lysine) (PLL) adsorbed on gold nanoparticles bearing thiol-carboxylate functions) has been studied in the range of high-frequencies from 1 MHz to 1 kHz with an amplitude of 0.5 V, and finally, an LOD of 4.5×10^{-16} M was reported. The proof of concept of affinity biosensor development by using dielectric impedance detection on insulating PET was investigated and compared to an optical transduction such as surface plasmon resonance (SPR) illustrated on Figure 12 [131]. Proteins are not labeled, as in optical biosensor, even if they need to be attached to the polymer surface coupled with the microelectrodes when a biomolecular interaction occurs. As displayed in Figure 12, modeling the microchip interface using an appropriate equivalent circuit permits to extract the value of the interfacial capacitance for ultra-low protein concentration. The promising results obtained with this methodology make it a competing method in comparison with other transductions for bioanalytical developments. The equilibrium association constant was calculated for the affinity between the probe and the target and was estimated equal to 5×10^7 M^{-1} in agreement with the one determined with SPR technique [78]. The promising results obtained with this strategy make it a competitive biosensor in comparison with SPR.

4. Conclusion

The development of a microfluidic system involves a myriad of issues and the proper selection of pertinent strategies regarding the overall feasibility, fabrication processes and targeted detection goals. At a starting point, due to its sensitivity and unfortunately, due to the fact that many materials platform and their related fabrication and conditioning means are yet be clearly identified and developed as a protocol, the coupled materials and fabrication relationship should be one of the top priorities. Undoubtedly, the most significant concern should be oriented toward the adaptation of the bioassay protocol in the specific microfluidic format, at this stage the robustness and the stability of the microfluidic operability should be taken into account in order to efficiently contribute to novel successful collaborations between different biologists, clinicians and the microfluidic communities.

Author details

Emmanuel Roy, Antoine Pallandre, Bacem Zribi, Marie-Charlotte Horny, François-Damien Delapierre, Andrea Cattoni, Jean Gamby and Anne-Marie Haghiri-Gosnet*

*Address all correspondence to: anne-marie.haghiri-gosnet@lpn.cnrs.fr

Centre for Nanoscience and Nanotechnology, CNRS, University Paris Sud, University Paris Saclay, Marcoussis, France

References

- [1] A. Arora, G. Simone, G. B. Salieb-Beugelaar, J. Tae Kim and A. Manz, Latest developments in micro total analysis systems, *Anal. Chem.*, 82, 4830–47, 2010.
- [2] L. Gervais, N. de Rooij and E. Delamarche, Microfluidic chips for point-of-care immunodiagnosics, *Adv. Mater.*, 23, H151–76, 2011.
- [3] N. T. Tran, I. Ayed, A. Pallandre and M. Taverna, Recent innovations in protein separation by electrophoretic methods: An update, *Electrophoresis*, 31, 147–73, 2010.
- [4] M. Goto and M. N. Al-Hasan, Overall burden of bloodstream infection and nosocomial bloodstream infection in North America and Europe, *Clin. Microbiol. Infect.*, 19(6), 501–9, 2013.
- [5] A. Kumar, D. Roberts, K. E. Wood, B. Light, J. E. Parrillo and S. S. Sharma, Duration of hypotension before initiation of effective antimicrobial therapy is the critical determinant of survival in human septic shock, *Crit. Care Med.*, 34(6), 1589–96, 2006.

- [6] R. P. Dellinger, M. N. Levy, A. Rhodes, D. Annane, H. Gerlach and S. M. Opal, Surviving sepsis campaign: International guidelines for management of severe sepsis and septic shock, *Intensive Care Med.*, 39(2), 165–228, 2013.
- [7] M. E. de Kraker, V. Jarlier, J. C. Monen, O. E. Heuer, N. van de Sande and H. Grundmann, The changing epidemiology of bacteraemias in Europe: trends from the European Antimicrobial Resistance Surveillance System, *Clin. Microbiol. Infect.*, 19(9), 860–8, 2013.
- [8] E. J. Baron, M. P. Weinstein, W. M. Dunne, P. Yagupsky, D. F. Welch, D. M. Wilson and C. Cumitech, *Blood Cultures IV*. ASM Press, 2005, Washington, DC. 3.
- [9] C. Pautas, E. Sbidian, Y. Hicheri, S. Bastuji-Garin, S. Bretagne and C. Corbel, A new workflow for the microbiological diagnosis of febrile neutropenia in patients with a central venous catheter, *J. Antimicrob. Chemother.*, 68(4), 943–6, 2012.
- [10] C. Brun-Buisson, P. Meshaka, P. Pinton, B. Vallet, EPISEPSIS: A reappraisal of the epidemiology and outcome of severe sepsis in French intensive care units, *Intensive Care Med.*, 30(4), 580–8, 2004.
- [11] K. Reinhart, M. Bauer, N. C. Riedemann and C. S. Hartog, New approaches to sepsis: molecular diagnostics and biomarkers, *Clin. Microbiol. Rev.*, 25(4), 609–34, 2012.
- [12] R. Yang, J. V. Pagaduan, M. Yu and A. T. Woolley, On chip preconcentration and fluorescence labeling of model proteins by use of monolith columns: Device fabrication, optimization and automation, *Anal. Bioanal. Chem.*, 407, 737–747, 2015.
- [13] J. A. Lounsbury, A. Karlsson, D. C. Miranian, S. M. Cronk, D. A. Nelson, J. Li, D. M. Haverstick, P. Kinnon, D. J. Saul and J. P. Landers, From sample to PCR product in under 45 minutes: A polymeric integrated microdevice for clinical and forensic DNA analysis, *Lab Chip*, 13, 1384–93, 2013.
- [14] R. Zhong, D. Liu, L. Yu, N. Ye, Z. Dai, J. Qin and B. Lin, Fabrication of two-weir structure-based packed columns for on-chip solid-phase extraction of DNA, *Electrophoresis*, 28(16), 2920–26, 2007.
- [15] J. West, M. Boerlin, A. D. Jadhav and E. Clancy, Silicon microstructure arrays for DNA extraction by solid phase sample contacting at high flow rates, *Sens. Actuators B*, 126, 664–71, 2007.
- [16] M. B. Dainiak, I. Y. Galaev, A. Kumar, F. M. Plieva and B. Mattiasson, Chromatography of living cells using supermacroporous cryogels, *Adv. Biochem. Eng. Biotechnol.*, 106, 101–27, 2007.
- [17] H. Chen, Q. Fang, X. F. Yin and Z. L. Fang, Microfluidic chip-based liquid-liquid extraction and preconcentration using a subnanoliter-droplet trapping technique, *Lab Chip*, 5(7), 719–25, 2005.

- [18] A. Aota, M. Nonaka, A. Hibara and T. Kitamori, Countercurrent laminar microflow for highly efficient solvent extraction, *Angew. Chem. Int. Ed.*, 46, 878–80, 2007.
- [19] T. Minagawa, M. Tokeshi and T. Kitamori, Integration of a wet analysis system on a glass chip: Determination of Co(II) as 2-nitroso-1-naphthol chelates by solvent extraction and thermal lens microscopy, *Lab Chip*, 1, 72–5, 2001.
- [20] H. Miyaguchi, M. Tokeshi, Y. Kikutani, A. Hibara, H. Inoue and T. Kitamori, Microchip-based liquid-liquid extraction for gas-chromatography analysis of amphetamine-type stimulants in urine, *J. Chromatogr. A*, 1129, 105–10, 2006.
- [21] A. Smirnova, K. Shimura, A. Hibara, M. A. Proskurnin and T. Kitamori, Pesticide analysis by MEKC on a microchip with hydrodynamic injection from organic extract, *J. Sep. Sci.*, 31, 904–8, 2008 (Special Issue: *Micellar Electrokinetic Chromatography*).
- [22] V. Reddy and J. D. Zahn, Interfacial stabilization of organic-aqueous two-phase microflows for a miniaturized DNA extraction module, *J. Colloid Interface Sci.*, 286, 158–65, 2005.
- [23] N. Assmann, A. Ladosz and P. R. von Rohr, Continuous micro liquid-liquid extraction (Review), *Chem. Eng. Technol.*, 36(6), 921–36, 2013.
- [24] S. G. Redkar and R. H. Davis, Cross-flow microfiltration with high-frequency reverse filtration, *AIChE J.*, 41, 501–8, 1995.
- [25] M.-C. Lo and J. D. Zahn, Development of a multi-compartment microfiltration device for particle fractionation, 16th international conference on miniaturized systems for chemistry and life sciences, Okinawa, Japan, 2012.
- [26] K. Aran, A. Fok, L. A. Sasso, N. Kamdar, Y. Guan, Q. Sun, A. Üндar and J. D. Zahn, Microfiltration platform for continuous blood plasma protein extraction from whole blood during cardiac surgery, *Lab Chip*, 11, 2858–68, 2011.
- [27] K. Aran, M. Morales, L. A. Sasso, J. Lo, J. Zheng, I. Johnson and J. D. Zahn, Microfiltration device for continuous label-free bacteria separation from whole blood for sepsis, the 15th international conference on miniaturized systems for chemistry and life sciences, MicroTAS, 2011.
- [28] J. Chung, H. Shao, T. Reiner, D. Issadore, R. Weissleder and H. Lee, Microfluidic cell sorter (μ FCS) for on-chip capture and analysis of single cells, *Adv. Healthc. Mater.*, 1(4), 432–6, 2012.
- [29] H. Mohamed, M. Murray, J. N. Turner and M. Caggana, Isolation of tumor cells using size and deformation, *J. Chromatogr. A*, 1216, 8289–95, 2009.
- [30] D. Lee, P. Sukuma, A. Mahyuddin, M. Choolani and G. Xu, Separation of model mixtures of ϵ -globin positive fetal nucleated red blood cells and a nucleated erythrocytes using a microfluidic device, *J. Chromatogr. A*, 1217(11), 1862–66, 2010.

- [31] S. K. Murthy, P. Sethu, G. Vunjak-Novakovic, M. Toner and M. Radisic, Size-based microfluidic enrichment of neonatal rat cardiac cell populations, *Biomed. Microdevices.*, 8(3), 231–37, 2006.
- [32] S. Tripathi, Y. V. Bala Varun Kumar, A. Prabhakar, S. S. Joshi and A. Agrawal, Passive blood plasma separation at the microscale: A review of design principles and microdevices, *J. Micromech. MicroEng.*, 25, 083001, 2015.
- [33] P. Sajeesh and A. Kumar Sen, Particle separation and sorting in microfluidic devices: A review, *Microfluid. Nanofluid.*, 17, 1–52, 2014.
- [34] L. R. Huang, E. C. Cox, R. H. Austin and J. C. Sturm, Continuous particle separation through deterministic lateral displacement, *Science*, 304, 987–90, 2004.
- [35] J. Zhou and I. Papautsky, Fundamentals of inertial focusing in microchannels, *Lab Chip*, 13(6), 1121–32, 2013.
- [36] D. Di Carlo, Inertial microfluidics, *Lab Chip*, 9, 3038–46, 2009.
- [37] D. Di Carlo, D. Irimia, R. G. Tompkins and M. Toner, Continuous inertial focusing, ordering, and separation of particles in microchannels. *PNAS*, 104(48), 18892–97, 2007.
- [38] J. McGrath, M. Jimenez and H. Bridle, Deterministic lateral displacement for particle separation: A review, *Lab Chip*, 14, 4139–58, 2014.
- [39] D. W. Inglis, Efficient microfluidic particle separation arrays, *Appl. Phys. Lett.*, 94(1), 013510, 2009.
- [40] K. Loutharback, K. S. Chou, J. Newman, J. Puchalla and R. H. Austin, Improved performance of deterministic lateral displacement arrays with triangular posts, *Microfluid. Nanofluid.*, 9(6), 1143–49, 2010.
- [41] K. Loutharback, J. D’Silva, L. Liu, A. Wu, R. H. Austin and J. C. Sturm, Deterministic separation of cancer cells from blood at 10 mL/min, *AIP Adv.*, 2(4), 042107, 2012.
- [42] K. K. Zeming, S. Ranjan and Y. Zhang, Rotational separation of non-spherical bioparticles using I-shaped pillar arrays in a microfluidic device, *Nat. Commun.*, 4, 1625, 2013.
- [43] M. Al-Fandi, M. Al-Rousan, M. A. Jaradat and L. Al-Ebbini, New design for the separation of microorganisms using microfluidic deterministic lateral displacement, *Robot. Comput. Integr. Manuf.*, 27, 237–44, 2011.
- [44] R. Fan, O. Vermesh, A. Srivastava, B. K. H. Yen and L. Qin L, Integrated barcode chips for rapid, multiplexed analysis of proteins in microliter quantities of blood, *Nat. Biotechnol.*, 26(12), 1373–78, 2008.
- [45] J. M. Martel and M. Toner, Inertial focusing in microfluidics, *Annu. Rev. Biomed. Eng.*, 16(1), 371–96, 2014.

- [46] M. E. Warkiani, G. Guan, K. B. Luan and A. A. S. Bhagat, Slanted spiral microfluidics for the ultra-fast, label-free isolation of circulating tumor cells, *Lab Chip*, 14, 128–37, 2014.
- [47] L. Clime, X. D. Hoa, N. Corneau, K. J. Morton, C. Luebbert, M. Mounier, D. Brassard, M. Geissler, S. Bidawid, Jeff Farber and T. Veres, Microfluidic filtration and extraction of pathogens from food samples by hydrodynamic focusing and inertial lateral migration, *Biomed. Microdevices*, 17, 17, 2015.
- [48] J. H. Kang, M. Super, C. Wing Yung, R. M. Cooper, K. Domansky, A. R. Graveline, T. Mammoto, J. B. Berthet, H. Tobin, M. J. Cartwright, A. L. Watters, M. Rottman, A. Waterhouse, A. Mammoto, N. Gamini, M. J. Rodas, A. Kole, A. Jiang, T. M. Valentin, A. Diaz, K. Takahashi and Donald E Ingber, An extracorporeal blood-cleansing device for sepsis therapy, *Nat. Med.*, 20(10), 1211–21, 2014.
- [49] H. J. Hjertén, Free zone electrophoresis, *Chromatogr. Rev.*, 9, 122–219, 1967.
- [50] "Capillary Electrophoresis Methods and Protocols" Editors: Schmitt-Kopplin, Philippe (Ed.) 2008 Springer ISBN 978-1-59745-376-9, Humana Press Inc, Totowa, NJ.
- [51] "Capillary Electrophoresis and Microchip Capillary Electrophoresis: Principles, Applications, and Limitations", Carlos D. Garcia, Karin Y. Chumbimuni-Torres, Emanuel Carrilho 2013 Wiley, San Antonio, TX, USA, ISBN: 978-0-470-57217-7
- [52] A. Manz, N. Graber and H. M. Widmer, Miniaturized total chemical analysis systems: A novel concept for chemical sensing, *Sens. Actuators B Chem.*, 1(1), 244–48, 1990.
- [53] J. W. Jorgenson and K. D. Lukacs, Capillary zone electrophoresis, *Science*, 222, 266–72, 1983.
- [54] A. Pallandre, B. de Lambert, R. Attia, A. M. Jonas, J.-L. Viovy, Surface treatment and characterization: Perspectives to electrophoresis and Lab-on-Chips, *Electrophoresis*, 27, 584–610, 2006.
- [55] R. B. M. Schasfoort, S. Schlautmann, L. Hendrikse and A. van den Berg, Field-effect flow control for microfabricated fluidic networks, *Science*, 286, 942–45, 1999.
- [56] A. Plecis, J. Tazid, A. Pallandre, P. Martinhon, C. Deslouis, Y. Chen and A. M. Haghir-Gosnet, Flow field effect transistors with polarisable interface for EOF tunable microfluidic separation devices, *Lab Chip*, 10, 1245–53, 2010.
- [57] R. Liedert, L. K. Amundsen, A. Hokkanen, M. Mäki, A. Aittakorpi, M. Pakanen, J. R. Scherer, R. A. Mathies, M. Kurkinen, S. Uusitalo, L. Hakalahti, T. K. Nevanen, H. Siitari and H. Söderlund, Disposable roll-to-roll hot embossed electrophoresis chip for detection of antibiotic resistance gene *mecA* in bacteria, *Lab Chip*, 12, 333–39, 2012.
- [58] Q. Pu, J. Yun, H. Temkin and S. Liu, Ion-enrichment and ion-depletion effect of nano-channel structures, *Nano Lett.*, 4, 1099–1103, 2004.

- [59] T. A. Zangle, A. Mani and J. G. Santiago, Theory and experiments of concentration polarization and ion focusing at microchannel and nanochannel interfaces, *Chem. Soc. Rev.*, 39, 1014–35, 2010.
- [60] A. C. Louer, A. Plecis, A. Pallandre, J. C. Galas, A. Estevez-Torres and A. M. Haghiri-Gosnet, Pressure-assisted selective preconcentration in a straight nanochannel, *Anal. Chem.*, 85, 7948, 2013.
- [61] S. Mehrabani, A. J. Maker and A. M. Armani, Hybrid integrated label-free chemical and biological sensor, *Sensors*, 14, 5890–928, 2014.
- [62] K. V. Gobi, H. Iwasaka and N. Miura, Self-assembled PEG monolayer based SPR immunosensor for label-free detection of insulin, *Biosens. Bioelectron.*, 22, 1382–89, 2007.
- [63] K. V. Gobi, S. J. Kim, H. Tanaka, Y. Shoyama and N. Miura, Novel surface plasmon resonance (SPR) immunosensor based on monomolecular layer of physically-adsorbed ovalbumin conjugate for detection of 2,4-dichlorophenoxyacetic acid and atomic force microscopy study, *Sens. Actuators B*, 123, 583–93, 2007.
- [64] K. S. Kim, H.-S. Lee, J.-A. Yang, M.-H. Jo and S. K. Hahn, The fabrication, characterization and application of aptamer-functionalized Si-nanowire FET biosensors, *Nanotechnology*, 20, 235501, 2009.
- [65] T. P. Burg, M. Godin, S. M. Knudsen, W. Shen, G. Carlson, J. S. Foster, K. Babcock and S. R. Manalis, Weighing of biomolecules, single cells and single nanoparticles in fluid, *Nature*, 446, 1066–69, 2007.
- [66] S. B. Patil, M. Vöggtli, B. Webb, G. Mazza, M. Pinzani, Y.-A. Soh, R. A. McKendry and J. W. Ndieyira, Decoupling competing surface binding kinetics and reconfiguration of receptor footprint for ultrasensitive stress assays, *Nat. Nanotechnol.*, 10, 899–907, 2015.
- [67] H. C. Tekin and M. A. M. Gijs, Ultrasensitive protein detection: A case for microfluidic magnetic bead-based assays, *Lab Chip*, 13, 4711–39, 2013.
- [68] R. S. Gaster, D. A. Hall, C. H. Nielsen, S. J. Osterfeld, H. Yu, K. E. Mach, R. J. Wilson, B. Murmann, J. C. Liao, S. S. Gambhir and S. X. Wang, Matrix-insensitive protein assays push the limits of biosensors in medicine, *Nat. Med.*, 15, 1327–32, 2009.
- [69] I. Lignos, S. Stavrakis, A. Kilaj and A. J. deMello, Millisecond-timescale monitoring of PbS nanoparticle nucleation and growth using droplet-based microfluidics, *Small*, 11(32), 4009–17, 2015.
- [70] S. Mandal, J. M. Goddard and D. Erickson, A multiplexed optofluidic biomolecular sensor for low mass detection, *Lab Chip*, 9, 2924–32, 2009.
- [71] T. L. Edwards, J. C. Harper, R. Polsky, D. M. Lopez, D. R. Wheeler, A. C. Allen and S. M. Brozik, A parallel microfluidic channel fixture fabricated using laser ablated plas-

- tic laminates for electrochemical and chemiluminescent biodetection of DNA, *Biomicrofluidics*, 5,044115,2011.
- [72] M. Faure, A. Pallandre, S. Chebil, I. Le Potier, M. Taverna, B. Tribollet, C. Deslouis, A.-M. Haghiri-Gosnet and J. Gamby, Improved electrochemical detection of a transthyretin synthetic peptide in the nanomolar range with a two-electrode system integrated in a glass/PDMS microchip, *Lab Chip*, 14, 2800–05, 2014.
- [73] J. L. Arlett, E. B. Myers and M. L. Roukes, Comparative advantages of mechanical biosensors, *Nat. Nanotechnol.*, 6, 203–15, 2011.
- [74] N. Pamme, Magnetism and microfluidics, *Lab Chip*, 6, 24–38, 2006.
- [75] C. Monat, P. Domachuk and B. J. Eggleton, Integrated optofluidics: A new river of light, *Nat. Photon.*, 1, 106–114, 2007.
- [76] D. Psaltis, S. R. Quake and C. Yang, Developing optofluidic technology through the fusion of microfluidics and optics, *Nature*, 442, 381–86, 2006.
- [77] A. G. Brolo, Plasmonics for future biosensors, *Nat. Photon.*, 6, 709–13, 2012.
- [78] A. Kausaite, M. van Dijk, J. Castrop, A. Ramanaviciene, J. P. Baltrus, J. Acaite and A. Ramanavicius, Surface plasmon resonance label-free monitoring of antibody antigen interactions in real time, *Biochem. Mol. Biol. Educ.*, 35, 57–63, 2007.
- [79] C. Y. Chao, L. J. Guo, Biochemical sensors based on polymer microrings with sharp asymmetrical resonance, *Appl. Phys. Lett.*, 83, 1527–29, 2003.
- [80] D. K. Armani, T. J. Kippenberg, S. M. Spillane and K. J. Vahala, Ultra-high-Q toroid microcavity on a chip, *Nature*, 421, 925–28, 2003.
- [81] T. J. Kippenberg, S. M. Spillane, D. K. Armani and K. J. Vahala, Fabrication and coupling to planar high-Q silica disk microcavities, *Appl. Phys. Lett.*, 83, 797–99, 2003.
- [82] J. Niehusmann, A. Vörckel, P. H. Bolivar, T. Wahlbrink, W. Henschel and H. Kurz, Ultrahigh-quality-factor silicon-on-insulator microring resonator, *Opt. Lett.*, 29, 2861–63, 2004.
- [83] M. Loncar, A. Scherer and Y. Qiu, Photonic crystal laser sources for chemical detection, *Appl. Phys. Lett.*, 82, 4648–4650, 2003.
- [84] X. Fan, I. M. White, S. I. Shopova, H. Zhu, J. D. Suter and Y. Sun, Sensitive optical biosensors for unlabeled targets: A review, *Anal. Chim. Acta*, 620, 8–26, 2008.
- [85] S. M. Borisov and O. S. Wolfbeis, Optical Biosensors, *Chem. Rev.*, 108, 423–61, 2008.
- [86] J. D. Joannopoulos and S. G. Johnson, Photonic crystals: Molding the flow of light, Princeton University Press, 2008, Princeton, New Jersey.
- [87] C. Fenzl, T. Hirsch and O. S. Wolfbeis, Photonic crystals for chemical sensing and biosensing, *Angew. Chem. Int. Ed.*, 53, 3318–35, 2014.

- [88] D. Stuart, A. Haes, C. Yonzon, E. Hicks and R. P. Van Duyne, Biological applications of localised surface plasmonic phenomena, *IEEE Proc. Nanobiotechnol.*, 152, 13–32, 2005.
- [89] M. Svedendahl, S. Chen, A. Dmitriev and M. Käll, Refractometric sensing using propagating versus localized surface plasmons: A direct comparison, *Nano Lett.*, 9, 4428–33, 2009.
- [90] A. Cattoni, P. Ghenuche, A.-M. Haghiri-Gosnet, D. Decanini, J. Chen, J.-L. Pelouard and S. Collin, $\lambda^3/1000$ plasmonic nanocavities for biosensing fabricated by soft UV nanoimprint Lithography, *Nano Lett.*, 11, 3557–63, 2011.
- [91] S. S. Acímovic, M. A. Ortega, V. Sanz, J. Berthelot, J. L. Garcia-Cordero, J. Renger, S. J. Maerkl, M. P. Kreuzer and R. Quidant, LSPR chip for parallel, rapid, and sensitive detection of cancer markers in serum, *Nano Lett.*, 14, 2636–41, 2014.
- [92] T. M Squires, R. J Messinger and S. R. Manalis, Making it stick: Convection, reaction and diffusion in surface-based biosensors, *Nat. Biotechnol.*, 26, 417–26, 2008.
- [93] J. S. Rossier, M. A. Roberts, R. Ferrigno and H. H. Girault, Electrochemical detection in polymer microchannels, *Anal. Chem.*, 71, 4294–99, 1999.
- [94] V. Tsouti, C. Boutopoulos, I. Zergioti and S. Chatzandroulis, Capacitive microsystems for biological sensing, *Biosens. Bioelectron.*, 27, 1–11, 2011.
- [95] D. G. Pijanowska, A. J. Sprenkels, W. Olthuis and P. Bergveld, A flow-through amperometric sensor for micro-analytical systems, *Sens. Actuators B: Chem.*, 91, 98–102, 2003.
- [96] S. E. Rosenwald, N. Dontha and W. G. Kuhr, A laser ablation method for the spatial segregation of enzyme and redox sites on carbon fiber microelectrodes, *Anal. Chem.*, 70, 1133–40, 1998.
- [97] J. S. Daniels and N. Pourmand, Label-free impedance biosensors: Opportunities and challenges, *Electroanalysis*, 19, 1239–57, 2007.
- [98] B. S. Ferguson, S. F. Buchsbaum, J. S. Swensen, K. Hsieh, X. Lou and H. T. Soh, Integrated microfluidic electrochemical DNA sensor, *Anal. Chem.*, 81, 6503–08, 2009.
- [99] A. Bhimji, A. A. Zaragoza, L. S. Live and S. O. Kelley, Electrochemical enzyme-linked immunosorbent assay featuring proximal reagent generation: Detection of human immunodeficiency virus antibodies in clinical samples, *Anal. Chem.*, 85(14), 6813–19, 2013.
- [100] K. Zór, A. Heiskanen, C. Caviglia, M. Vergani, E. Landini, F. Shah, M. Carminati, A. Martínez-Serrano, T. Ramos Moreno, M. Kokaia, D. Benayahu, Z. Keresztes, D. Papkovsky, U. Wollenberger, W. E. Svendsen, M. Dimaki, G. Ferrari, R. Raiteri, M. Sampietro, M. Dufva and J. Emnéus, A compact multifunctional microfluidic platform for

- exploring cellular dynamics in real-time using electrochemical detection, *RSC Adv.*, 4, 63761–71, 2014.
- [101] J. Janata, Potentiometric microsensors, *Chem. Rev.*, 90, 691–3, 1990.
- [102] S. A. Almeida, E. Arasa, M. Puyol, C. S. Martinez-Cisneros, J. Alonso-Chamarro, M. C. Montenegro and M. G. Sales, Novel LTCC-potentiometric microfluidic device for biparametric analysis of organic compounds carrying plastic antibodies as ionophores: Application to sulfamethoxazole and trimethoprim, *Biosens. Bioelectron.*, 30, 197–203, 2011.
- [103] S. S. Hassan, H. E. Sayour and S. S. Al-Mehrezi, A novel planar miniaturized potentiometric sensor for flow injection analysis of nitrates in wastewaters, fertilizers and pharmaceuticals, *Anal. Chim. Acta*, 581, 13–18, 2007.
- [104] N. Ibáñez-García, M. Baeza, M. Puyol, R. Gómez, M. Batlle and J. Alonso-Chamarro, Biparametric potentiometric analytical microsystem based on the green tape technology, *Electroanalysis*, 22, 2376–82, 2010.
- [105] T. Ahuja, I. A. Mir and D. Kumar, Potentiometric urea biosensor based on BSA embedded surface modified polypyrrole film, *Sens. Actuators B: Chem.*, 134, 140–45, 2008.
- [106] M. J. Natan, D. Belanger, M. K. Carpenter and M. S. Wrighton, pH-sensitive nickel(II) hydroxide-based microelectrochemical transistors, *J. Phys. Chem.*, 91, 1834–42, 1987.
- [107] B. Lakard, O. Segut, S. Lakard, G. Herljem and T. Gharbi, Potentiometric miniaturized pH sensors based on polypyrrole films, *Sens. Actuators B: Chem.*, 122, 101–8, 2007
- [108] M. J. Schöning, F. Ronkel, M. Crott, M. Thust, J. W. Schultze, P. Kordos and H. Lüth, Miniaturization of potentiometric sensors using porous silicon microtechnology, *Electrochim. Acta*, 42, 3185–93, 1997.
- [109] S. V. Dzyadevych, V. N. Arkhypova, A. P. Soldatkin, A. V. El'skaya, C. Martelet and N. Jaffrezic-Renault, Amperometric enzyme biosensors: Past, present and future, *IRBM*, 29, 171–80, 2008.
- [110] Y. Chao, H. Yue, B. L. Hassler, R. M. Worden and A. J. Mason, Amperometric electrochemical microsystem for a miniaturized protein biosensor array, biomedical circuits and systems, *IEEE Transactions on*, 3, 160–68, 2009.
- [111] L. C. Clark, Monitor and control of blood and tissue oxygen tensions, *Trans. Am. Soc. Artif. Intern. Organs*, 2, 41, 1956.
- [112] J. Wang, M. P. Chatrathi and B. Tian, Capillary electrophoresis microchips with thick-film amperometric detectors: separation and detection of phenolic compounds, *Anal. Chim. Acta*, 416, 9–14, 2000.
- [113] N. Dossi, R. Toniolo, A. Pizzariello, S. Susmel, F. Perennes and G. Bontempelli, A capillary electrophoresis microsystem for the rapid in-channel amperometric detection of synthetic dyes in food, *J. Electroanal. Chem.*, 601, 1–7, 2007.

- [114] M. Faure, S. Korchane, I. Le Potier, A. Pallandre, C. Deslouis, A.-M. Haghiri-Gosnet and J. Gamby, Investigating of labeling and detection of transthyretin synthetic peptide derivatized with naphthalene-2,3-dicarboxaldehyde, *Talanta*, 116, 8–13, 2013.
- [115] S. Korchane, A. Pallandre, C. Przybylski, C. Poas, F. Gonnet, M. Taverna, R. Daniel and I. Le Potier, Derivatization strategies for CE-LIF analysis of biomarkers: toward a clinical diagnostic of familial transthyretin amyloidosis, *Electrophoresis*, 35, 1050–59, 2014.
- [116] T. Sun and H. Morgan, Single-cell microfluidic impedance cytometry: a review, *Microfluid Nanofluid*, 8, 423–43, 2010.
- [117] F. Opekar, P. Tůma and K. Štulík, Contactless impedance sensors and their application to flow measurements, *Sensors*, 13, 2786–01, 2013.
- [118] G. M. Dittami, H. E. Ayliffe, C. S. King and R. D. Rabbitt, A multilayer MEMS platform for single-cell electric impedance spectroscopy and electrochemical analysis, microactuators, microsensors, and microsystems : a joint IEEE and ASME publication on microstructures, *J. microelectromech.*, 17, 850–62, 2008.
- [119] J. L. Hong, K. C. Lan, L. S. Jang, Electrical characteristics analysis of various cancer cells using a microfluidic device based on single-cell impedance measurement, *Sens. Actuators B: Chem.*, 173, 927–934, 2012.
- [120] M. Faure, M. Kechadi, B. Sotta, J. Gamby and B. Tribollet, Contact free impedance methodology for investigating enzymatic reactions into dielectric polymer microchip, *Electroanalysis*, 25, 1151–58, 2013.
- [121] T. Sun, E. J. Swindle, J. E. Collins, J. A. Holloway, D. E. Davies and H. Morgan, On-chip epithelial barrier function assays using electrical impedance spectroscopy, *Lab Chip*, 10, 1611–17, 2010.
- [122] H. Park, D. Kim and K. S. Yun, Single-cell manipulation on microfluidic chip by dielectrophoretic actuation and impedance detection, *Sens. Actuators B: Chem.*, 150, 167–73, 2010.
- [123] G. A. Ferrier, A. N. Hladio, D. J. Thomson, G. E. Bridges, M. Hedayatipoor, S. Olson and M. R. Freeman, Microfluidic electromanipulation with capacitive detection for the mechanical analysis of cells, *Biomicrofluidics*, 2, 044102–13, 2008.
- [124] H. E. Ayliffe, A. Bruno Frazier and R. D. Rabbitt, Electric impedance spectroscopy using microchannels with integrated metal electrodes, *J. Microelectromech. Syst.*, 8, 50–57, 1999.
- [125] M. Evander, A. J. Ricco, J. Morser, G. T. Kovacs, L. L. Leung and L. Giovangrandi, Microfluidic impedance cytometer for platelet analysis, *Lab Chip*, 13, 722–729, 2013.
- [126] S. Hediger, A. Sayah and M. A. Gijs, Fabrication of a novel microsystem for the electrical characterisation of cell arrays, *Sens. Actuators B: Chem.*, 56, 175–80, 1999.

- [127] J. Gamby, J. P. Abid, B. Tribollet and H. H. Girault, Nanomosaic network for the detection of proteins without direct electrical contact, *Small*, 4, 802–9, 2008.
- [128] A. J. Zemmann, E. Schnell, D. Volgger and G. K. Bonn, Contactless conductivity detection for capillary electrophoresis, *Anal. Chem.*, 70, 563–67, 1998.
- [129] M. Pumera, Contactless conductivity detection for microfluidics: Designs and applications, *Talanta*, 74, 358–64, 2007.
- [130] B. Gaš, M. Demjaněnko and J. Vacík, High-frequency contactless conductivity detection in isotachopheresis, *J. Chromatogr. A*, 192, 253–57, 1980.
- [131] J. Gamby, J.-P. Abid and H. H. Girault, Supercapacitive admittance tomography, *J. Am. Chem. Soc.*, 127, 13300–04, 2005.
- [132] J. Gamby, J. P. Abid, M. Abid, J. P. Ansermet and H. H. Girault, Nanowires network for biomolecular detection using contactless impedance tomography technique, *Anal. Chem.*, 78, 5289–95, 2006.
- [133] J.-P. Abid, J. O. Gamby and H. H. Girault, Adsorption monitoring device for contactless testing of sensors using capacitive admittance, in, *Ecole Polytechnique Federale de Lausanne, Switzerland*, p. 33, 2006.
- [134] M. Kechadi, B. Sotta, L. Chaal, B. Tribollet and J. Gamby, A real time affinity biosensor on an insulated polymer using electric impedance spectroscopy in dielectric microchips, *Analyst*, 139, 3115–21, 2014.

Application of Microfluidics in Stem Cell Culture

Shinji Sugiura, Kohji Nakazawa, Toshiyuki Kanamori and Kiyoshi Ohnuma

Additional information is available at the end of the chapter

<http://dx.doi.org/10.5772/64714>

Abstract

In this chapter, we review the recent developments, including our studies on the micro-fabricated devices applicable to stem cell culture. We will focus on the application of pluripotent stem cells including embryonic stem cells and induced pluripotent stem cells. In the first section, we provide a background on microfluidic devices, including their fabrication technology, characteristics, and the advantages of their application in stem cell culture. The second section outlines the use of micropatterning technology in stem cell culture. The use of microwell array technology in stem cell culture is explored in the third section. In the fourth section, we discuss the use of the microfluidic perfusion culture system for stem cell culture, and the last section is a summary of the current state of the art and perspectives of microfluidic technologies in stem cell culture.

Keywords: Embryonic stem (ES) cells, induced pluripotent stem (iPS) cells, microfluidic perfusion culture, micropatterning, microwell array

1. Introduction

This section provides a general background on microfluidic devices and explains the general microfabrication technologies applicable to stem cell culture including embryonic stem (ES) cells and induced pluripotent stem (iPS) cells. We will discuss the importance of small-scale patterning, three-dimensional structure, and medium flow in terms of microenvironment control and the importance of small volumes, in terms of research cost, for industrial application.

1.1. Microfabrication technology available for stem cell culture

Microfabrication technology progressed rapidly with the development of semiconductor industry in the 20th century. By the end of the 20th century, the application of microfabrication

technology started to grow in different research areas including biotechnology. In biotechnology, microfabrication technology was initially used for molecular analyses of DNA and proteins and gradually its application diversified to cell culture. This technology enabled precise fabrication of structures with sizes as small as submicrometer, replication of the fabricated structure, liquid manipulation in very small volumes, portability of the devices, and usage of small amounts of expensive reagents. Owing to these advantages, microfabrication technology is expected to create new applications in the cell culture including stem cells.

Many types of materials, including inorganic materials, metals, polymers, and plastics, are applicable to microfabrication. Silicon and glass have been used to fabricate microstructures and semiconductor devices [1, 2]. Polydimethylsiloxane (PDMS), a silicone elastomer, is the most popular material used for the fabrication of microfluidic cell culture devices due to the ease of fabrication, optical transparency, gas permeability, low chemical reactivity, and inexpensiveness. In addition, microstructure of PDMS is generally fabricated by soft lithography in a few days [3]. This easy and quick process broadens the use of microfluidic devices in cell culture applications. In soft lithography process, replica of microstructure in PDMS can be repeatedly fabricated from a microstructure of photoresist that is originally made using photolithography [4, 5]. A multilayered microstructure of PDMS can also be fabricated by using multilayered photoresist pattern [6, 7]. Details of the fabrication method used for soft lithography have been described in previous studies [3, 8]. Many biologists are currently using this convenient microfabrication technology.

Soft lithography is a convenient method for fabricating microstructures on a laboratory scale. Scientists can fabricate dozens of microfluidic devices by themselves for their research. However, for industrial applications, hundreds or thousands of microfluidic devices are required. In addition, it is known that PDMS absorb small hydrophobic molecules [9]. Therefore, other materials applicable to mass production and capable of avoiding molecular adsorption are desired for the industrial application of microfluidic devices. Low-cost fabrication technologies such as injection molding [10, 11] and rapid prototyping [12, 13] are promising fabrication technologies that can address the above-mentioned issues.

In addition, cell culture often requires extracellular matrixes (ECMs). Therefore, microfabrication of biomaterials, such as hydrogel, is of interest to biologists and engineers. Photofabricated hydrogels have been studied extensively to create microstructure in the hydrogels [14]. These microfabricated hydrogels have been used for tissue engineering.

1.2. Characteristics of microfabricated cell culture device

Significant features that affect a microfluidic device are flow viscosity, interfacial tension, laminar flow, fast diffusion, etc. [15]. The characteristic flow profile enabled the formation of special microenvironment including chemical [16] and temperature gradients [17]. Also, a microfluidic perfusion culture continuously supplies nutrient and removes waste, and therefore keeps the culture condition more stable and constant compared with a static cell culture [18]. Furthermore, a microfluidic perfusion culture potentially provides new opportunities for cell culture applications because of the precise control of the microscale environment [19–22]. For example, some cell types, such as endothelial cells, are sensitive to shear

stress caused by the flow of the medium [23]. Another example, in 3D culture condition, such as spheroid culture, molecular transport in the microchannels can be controlled by convection flow and the controlled molecular transport affects the state of inner cells in the spheroids [24]. Therefore, microfluidic perfusion culture can be used for both fundamental research and drug development.

Another feature of cell culture in microfluidic device is its small volume. The miniaturized assays are expected to increase experimental throughput and reliability for drug discovery applications [25–27]. This is an important aspect for the application of microfluidic technology to stem cell culture because culturing stem cells, especially human iPSCs, is cost-prohibitive [28]. Microfluidic systems are cost-effective because these systems need small quantity of culture medium and reagents.

In addition, microfluidic device can generate many cell culture conditions using microfluidic network. For example, we have developed a microfluidic network to generate step-wise serial dilutions [29]. We also reported the method to fabricate combinatorial microenvironment array on a microfluidic device [30]. Titmarsh et al. reported a microfluidic network to generate combinatorial array of culture conditions composed of multiple soluble factors at different concentrations [31], and applied this device for the analysis of human embryonic stem cell culture conditions. We think these examples are just the beginning of the application of microfabrication technology in stem cell culture. Possibly, there are additional scopes for applications because many unknown phenomena regarding stem cell culture are yet to be understood.

1.3. Control of cell culture microenvironment

Conventionally, cell culture has been carried out in Petri dishes as static culture. In Petri dishes, the actively growing cells form monolayer sheet and culture media is placed on the cells. In this static monolayer culture, cells grow at randomly arranged positions and medium is exchanged regularly in batches. The stem cells are cultured in a similar manner. In contrast, cells in our bodies form highly ordered 3D microstructures and respond to their surrounding microenvironments including soluble factors, ECMs, contact-dependent intercellular signals, and mechanical signals. Therefore, the 3D nature of native, complex microenvironments is not accurately recapitulated in traditional cell culture on Petri dishes[32]. Microfabrication technology has the potential to control the parameters to simulate these complex 3D microenvironments.

2. Micropatterning technology in stem cell culture

Monolayer cultures of stem cells garnered considerable attention after human ES/iPS cells were established, because these cells are cultured as a monolayer colony and cannot survive without adhering to the surface of the culture dish. In addition, the differentiation of these cells is sensitive to cell density because cell-cell interactions affect stem cell differentiation. Thus, regulation of cell adhesion and control of shape and size of the stem cell monolayer colony are

very important for maintaining stem cell potential and for inducing these stem cells to differentiate into specific cells types. In this section, we reviewed the micropatterning technology and its application in human iPS cell culture.

2.1. Micropatterning for human ES/iPS cells: difference between human and mouse ES/iPS cells

Human ES/iPS cells can differentiate all kinds of human body cells [33, 34]. Human ES cells generated by somatic cell nuclear transfer and human iPS cells contain the donor's genetic information. Therefore, ES/iPS cells can be a good source of cells for rejection-free transplantation of tissues and disease-specific drug screening [34, 35].

Although ES and iPS cells share most of the properties, there are clear differences between mouse and human ES/iPS cells (Figure 1). Mouse ES/iPS cells can survive after single-cell dissociation, but human ES/iPS cells undergo apoptosis¹ [36] following their single-cell dissociation. Thus, the culture conditions and adhesion of human ES/iPS cells need to be carefully controlled to ensure their survival and growth.

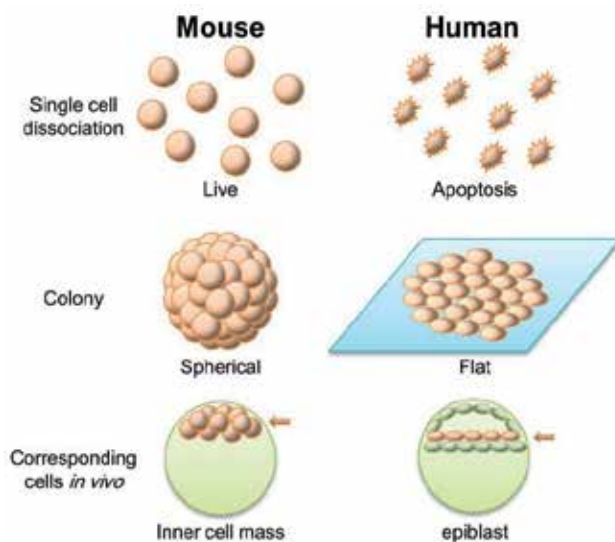


Figure 1. Difference between mouse and human ES/iPS cells.

Moreover, there are morphological differences between mouse and human ES/iPS cell colonies. Mouse ES/iPS cells form spherical aggregates [37–39] and human ES/iPS cells form flat monolayer colonies [33, 34]. Because the colony size is important for maintaining pluripotency and controlling cell differentiation in ES/iPS cells (see section 3), two-dimensional cell

¹ Apoptosis caused by single cell dissociation is partially rescued by adding Y-27632, a selective inhibitor of p160-Rho-associated coiled-coil kinase (ROCK).

patterning is especially important for human ES/iPS cells. Warmflash et al. [40] showed that the differentiation pattern of human ES/iPS cells depended on the size of monolayer colonies.

In addition, although both mouse and human ES cells are derived from inner cell mass of the blastocysts, the properties of mouse ES/iPS cells are closer to that of the inner cell mass, while the properties of human ES/iPS cells are closer to that of epiblast, which is a monolayer of cells arising from the inner cell mass [41]. The epiblast is functionally and molecularly distinct from inner cell mass, and is also pluripotent. Thus, micropatterning technology is important, especially for human ES/iPS cells.

2.2. Micropatterning technology

Although there are many cell micropatterning techniques available [42–47], two important features need to be considered while applying this technique to human ES/iPS cells. The human ES/iPS cell differentiation protocols take a few days to few months, and the cell pattern needs to be long lasting. Although there have been reports of successful patterning of ES/iPS cells, the cells have been found to escape from the pattern within a few days [43, 46]. The other feature is ease of pattern preparation. Many micropatterning methods require some special equipment and techniques that are not easy to perform routinely in cell biology laboratory.

2.3. Micropatterning technology in human ES/iPS cells

We succeeded in forming human iPS cells pattern on the PDMS surface by a simple technique using plasma² oxidation with perforated mask and defined culture conditions [48, 49]. As described above, PDMS is one of the most popular biocompatible materials for research and development of cell culture microdevices. Plasma treatment on PDMS oxidized $\equiv\text{Si}-\text{CH}_3$ groups to generate $\equiv\text{Si}-\text{O}-\text{Si}\equiv$ groups suggests that hydrophilic and siliceous layers were formed on the surface [5, 49].

We first studied the effects of vitronectin and γ -globulin on hiPSC adhesion to plasma-treated and untreated PDMS surfaces under defined culture conditions [49]. We chose vitronectin and γ -globulin because they have contrasting properties. Vitronectin as well as fibronectin and laminin mediate hiPSC attachment, because vitronectin and fibronectin are ligands of integrin $\alpha 5\beta 1$ and $\alpha v\beta 1$, and laminin is a ligand of integrin $\alpha 6\beta 1$ and $\alpha v\beta 5$, all of which are known to be expressed on ES/iPS cells surface [50–53]. Moreover, vitronectin is especially suitable for coating on glass ($\equiv\text{Si}-\text{O}-\text{Si}\equiv$) [54]. On the other hand, γ -globulin is adsorbed by hydrophobic surfaces and does not mediate cell adhesion [55]. Immunostaining showed that vitronectin and γ -globulin were adsorbed on both plasma-treated and plasma-untreated PDMS surfaces when these proteins were applied separately. However, vitronectin was preferentially adsorbed on plasma-treated surfaces whereas γ -globulin was adsorbed on untreated surfaces when the mixture of vitronectin and γ -globulin was applied. Human iPSCs adhered to the vitronectin-rich plasma-treated surfaces but not to the γ -globulin-rich untreated surfaces.

² In this chapter, plasma refers to low-pressure plasma, not blood plasma, unless otherwise stated.

Based on the results, we succeeded in making a monolayer pattern of human iPS cells by using perforated masks to prepare plasma-patterned PDMS substrates [49]. The patterned human iPS cells expressed undifferentiated-cell markers and did not escape from the patterned area for at least 7 days. The patterned PDMS could be stored for up to 6 days before hiPSCs were plated. Furthermore, we demonstrate that not only γ -globulin but also bovine serum albumin (BSA) could be used to block human iPS cell adhesion on plasma-untreated PDMS surfaces (Figure 2) [48]. The hiPSCs proliferated without escaping from the patterned area and finally detached spontaneously from the discs to form spheroids.

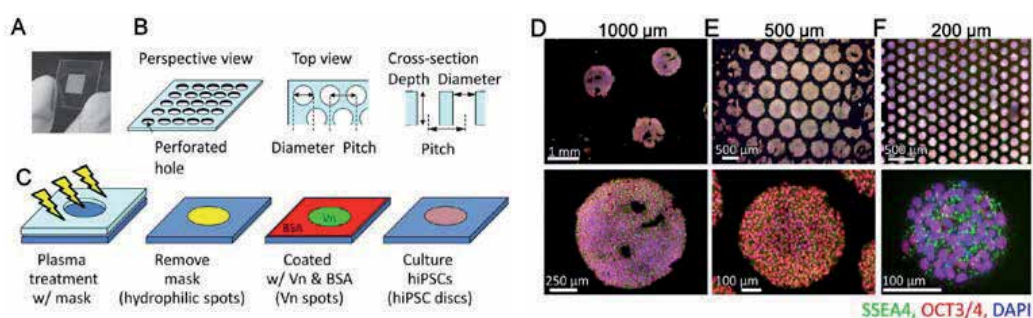


Figure 2. Micropatterned human iPS cells created by plasma patterning of PDMS surfaces and single-step coating of vitronectin and BSA. (A, B) Perforated PMMA masks. (C) Schematic of the micro patterning procedure. (D–F) Immunostaining of patterned cells with undifferentiated cells marker anti-SSEA4 (green) and anti-OCT3/4 (red). Nuclei were stained with DAPI (blue). Lower panels show high magnification images. Reproduced from Yamada et al. [48] with permission from Begell House.

Our micropatterning method presents four advantages over previously reported methods [42, 56]. (1) The plasma treatment through perforated masks enables equal patterning on a wide area, therefore a large number of homogeneously patterned cells can be created reproducibly. (2) Single-step coating of a mixture of proteins is quite simple and easy. Similar methods of producing cell patterning required additional steps, including multistep protein coatings of BSA followed by ECM [56]. (3) The cost-effectiveness and availability of γ -globulin, especially BSA is high. (4) Although there are many types of micro-fabrication tools to make equally sized spheroids, most of them are expensive and difficult to use in cell culture labs [42]. Our method is an easy and cost-effective way to fabricate hiPSC discs and spheroids.

2.4. Harvesting micropatterned human ES/iPS cells by controlling divalent cation

Cell sheets such as retinal pigment epithelium and cardiomyocytes derived from human iPS cells have been developed for applications in regenerative medicine [57, 58]. We tried to harvest micropatterned human ES/iPS cells without their splitting off. Conventionally, cell sheets are harvested using special equipments, such as a temperature-responsive surface

and magnet [59, 60]. In contrast, we focused on integrin and cadherin, which are adhesion molecules on the cell surface. Cadherins mediate cell-cell adhesion at physiological concentration of Ca^{2+} [61]. On the other hand, integrins mediate cell-ECM adhesion and depend largely on Mg^{2+} [62]. Thus, a solution containing physiological concentration of Ca^{2+} , but no Mg^{2+} , could be used to harvest cells as large cell clumps under serum-free culture condition. As expected, simple incubation in PBS with Ca^{2+} without Mg^{2+} followed by gentle pipetting enabled us to harvest the cells as sheets without cells splitting off (Figure 3) [63]. Similar results were obtained for early-differentiated cells and for hepatic progenitors derived from human iPS cells. These results suggest that the cells can be routinely and simply harvested as a large sheet by using a solution with Ca^{2+} and without Mg^{2+} .

Our methods introduced here can be also used practically to mimic epiblast (Figure 1) in early human embryonic development. We believe that our cell patterning method will be useful for the development of new bioengineering tools to search for effective cell differentiation methods and to test drug safety for early human embryonic development.

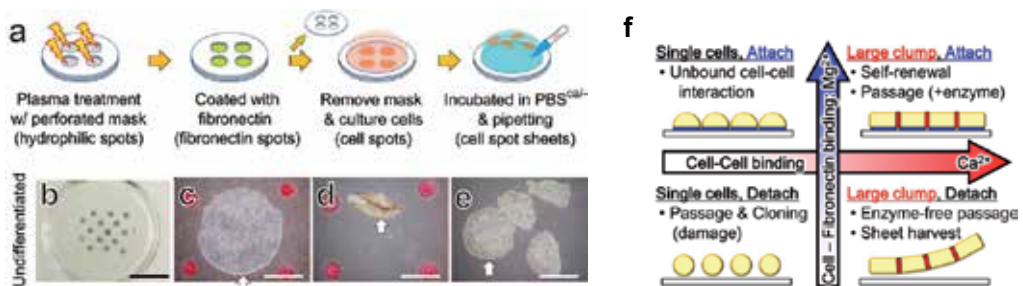


Figure 3. Human iPS cells sheet harvesting. (A) Schematics of spot sheet formation and harvest. (B) ALP staining of the hiPSCs plated on 2-mm-diameter fibronectin spots. Phase-contrast micrographs before (C) and after (D, E) 15 min in PBS with Ca^{2+} followed by pipetting. The white arrows indicate the same cellspot sheet (C–E). The red spots in (C, D) are position makers. Scale bars are 1 cm (B), 1 mm (C–E). (F) Schematics of the effects of Mg^{2+} and Ca^{2+} on hPSCs culture. Cell-cell and cell-ECM adhesion depend largely on Ca^{2+} (abscissa) and Mg^{2+} (ordinate), respectively. Large cell clumps and sheets can then be harvested by dissociating in low Mg^{2+} and high Ca^{2+} solution (lower right). Reproduced from Ohnuma et al. [63] under a Creative Commons Attribution 3.0 Unported License.

3. Microwell array technology in stem cell culture

The formation of three-dimensional cell aggregates called embryoid bodies (EBs) that resemble the embryo structure is the principle behind in vitro differentiation of stem cells. Microwell array is a promising platform for generating EBs, in which microwells of several hundred micrometers size are regularly fabricated on a culture substratum. It controls EB size and produces large number of homogenous EBs. An added advantage of microwell array culture is that it can influence the fate of differentiating cells in EBs. In this section, we review the architectures of microwell arrays, microwell array culture of ES/iPS cells, and the relationships between microwell conditions and EB properties.

3.1. Embryoid body (EB) culture

For *in vitro* differentiation of stem cells, one of the superior strategies is to imitate *in vivo* development processes. Three-dimensional aggregate of stem cells called embryoid body resembles early embryo. The multicellular interactions generated with the EB formation trigger cell differentiation. Thus, the EB culture has been used as a principal method for *in vitro* early differentiation of stem cells.

The EB is formed by the rearrangement and compaction of stem cell aggregates. Therefore, the differences in EB sizes affect the diffusion of soluble molecules, the extent of cell-ECM and cell-cell interactions, and the generation of mechanical forces (Figure 4A). Consequently, it affects the differentiation and fate of stem cells [64–66]. Thus, the culture technique capable of modulating EB size is important to regulate stem cell differentiation.

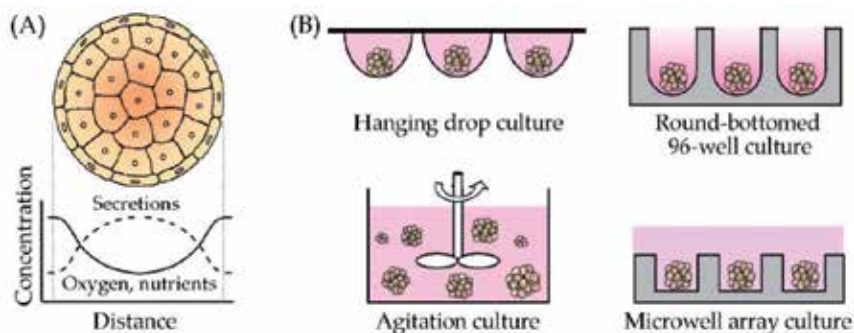


Figure 4. (A) EB characteristics and (B) methods for EB formation.

3.2. Methods for EB formation

The EB formation occurs if cell-cell adhesion is stronger than cell-surface material adhesion. Therefore, we can lead the EB formation by designing a culture environment, which promotes cell-cell adhesion. Typical methods for EB formation are hanging drop culture, round-bottomed 96-well culture, and agitation or rotational culture (Figure 4B) [67, 68]. The agitation culture can achieve mass production of EBs; however, it is difficult to control the EB size. In contrast, the hanging drop and round-bottomed 96-well cultures can control the EB size, but their scale-up is difficult. Furthermore, these methods pose difficulties in handling of the formed EBs.

Recently, microwell array has been advocated as a promising technique over the current methods. It is a culture platform in which microwells of several hundred micrometers size are regularly fabricated on a culture plate (Figure 4B). Recently, various microwell arrays have been developed by researchers [69]. Generally, the number of microwells is from tens to thousands per culture plate, and these microwells are laid as triangular or square arrangements on the plate. The microwells having various shapes such as column, square, and pyramid have been fabricated by photolithography, soft lithography mold, micromachining, etc. [70–72].

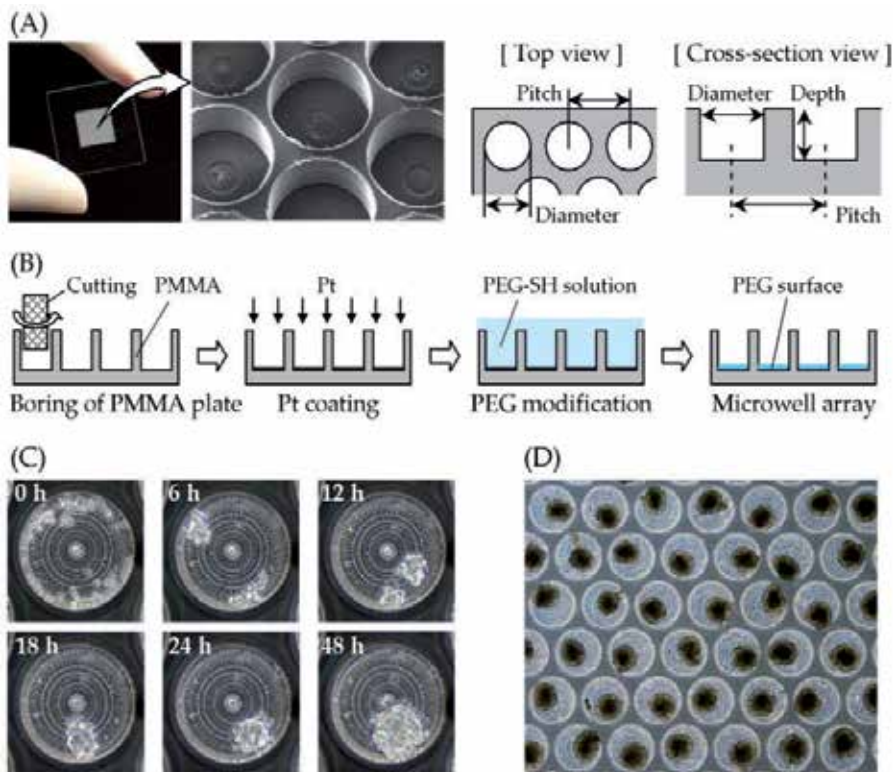


Figure 5. (A) Microwell array, (B) manufacturing processes, (C) EB formation, and (D) culture in the microwell array.

Furthermore, most microwell arrays are designed with cell nonadhesion surfaces to promote the EB formation. Such microwell arrays can generate a large number of homogenous EBs, with controlled size, and allow easy EB handling.

3.3. Our microwell array

We developed a microwell array comprising columnar microwells in triangular arrangement on a poly-methylmethacrylate (PMMA) plate with the surface modified by polyethylene glycol (PEG) to render cell nonadhesion (Figure 5A) [73, 74]. This was fabricated as follows (Figure 2B). The microwell structure of array was fabricated using a programmable micromilling system. Subsequently, the array surface was coated with thin layer of platinum using an ion sputter unit, and immersed in a PEG-SH solution. The PEG molecule formed covalent attachment via its thiol group to the platinum layer, thus modifying the surface. The microwell array manufactured via this process was used for the stem cell culture.

Figure 5C shows the changes in cell morphologies of mouse ES cells within the microwell. The cells that were seeded on the array began to aggregate within several hours of inoculation, and they spontaneously formed a single EB in each microwell of array within 1 day of culturing. Although none of the EBs adhered on the microwell surface, all EBs were held within the

microwells throughout the culture period. Consequently, the mass production of homogenous EBs was achieved in the single array (Figure 5D).

3.4. EB properties in the microwell array culture

The microwell array could arbitrarily vary the microwell conditions such as well number, diameter and depth of well, distance of wells, and cell density. To clarify the characteristics of microwell array culture, we evaluated the effects of microwell diameter and cell density on the EB properties of mouse ES cells [75, 76].

Four similar arrays comprising 195 microwells were fabricated with microwell diameters of 400, 600, 800, and 1000 μm to evaluate the relationship between the microwell diameter and EB property. The hanging drop (HD) culture was used as a control method. In this experiment, the inoculated cell density was at 1000 cells/well or 1000 cells/drop, and the cells were cultured in a medium without LIF and inducers.

Figure 6A shows the changes in EB sizes. The EB sizes at the initial stage were almost same (approximately 150 μm) under all culture conditions. Although the EB in the HD culture grew drastically with increasing culture time, the growth in the microwell culture was repressed compared with that in HD culture. Furthermore, the changes in EB sizes depended on the scale of microwell, and the EB growth in larger microwells was higher than that in smaller microwells. Figure 6B shows the gene expression levels of hepatic (AFP), cardiac (αMHC), and vascular (Flk1) differentiation markers. The differentiation fates of EBs were nearly the same under all conditions, but the gene expression levels varied with culture conditions. The expressions of differentiation markers were highest in HD culture, and gradually decreased in 1000, 800, 600, 400 μm arrays in that order. These results indicate that the EB growth and differentiation rate can be controlled by diameters of microwell, and that they are promoted in larger microwell conditions. These differences may be attributed to special culture environments provided by the microwell culture. The existence of micro spaces (microwell) might have facilitated accumulation of various soluble factors which were secreted from the cells. Additionally, interference effects caused by the neighboring EBs could occur because of extensive EBs on an array. Consequently, the accumulation of paracrine/autocrine factors and/or the concentrations of oxygen and nutrients in the culture medium vary by the array conditions, and the balances of these factors may regulate the EB properties.

To evaluate the relationship between the inoculated cell density and EB property, the cells at densities of 100, 1000, or 10000 cells/well were inoculated to the array that comprised 195 microwells with 600 μm diameter. Figures 7A and B show the changes in EB sizes and the gene expression levels of differentiation markers, respectively. The change in the EB size of array at 100 cells/well was higher than that of array at 1000 cells/well. In contrast, the cells of array at 10000 cells/well hardly proliferated, and the EB size that formed at the initial stage was maintained throughout the culture period. The expression levels of differentiation markers were the smallest in the array at 10000 cells/well. The expression of vascular (Flk1) differentiation was highest in the array at 100 cells/well, but the array at 1000 cells/well promoted hepatic (AFP) and cardiac (αMHC) differentiations rather than vascular differentiation, indicating that the inoculated cell density affects the differentiation fate of EBs. These differ-

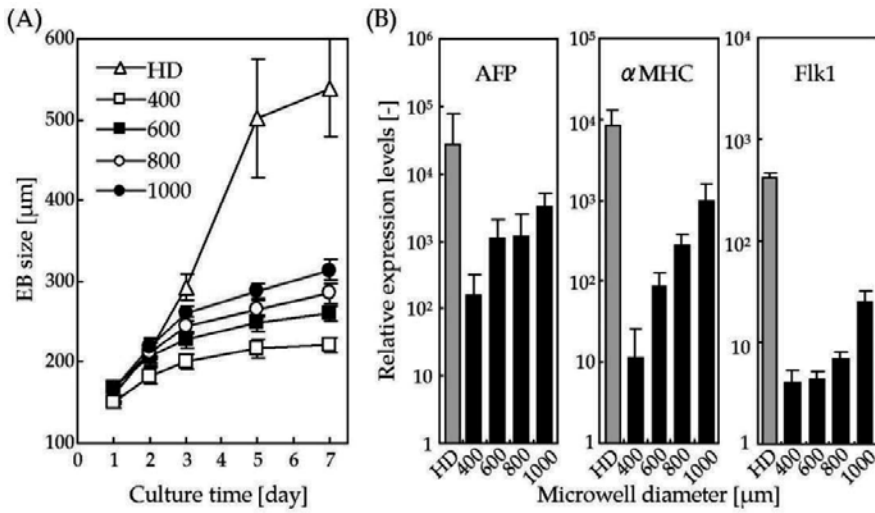


Figure 6. (A) Changes in the EB sizes and (B) the gene expression levels of differentiation markers after 7 days of culture.

ences may be caused mainly by the differences in size of EB formed at the initial stage, because the EB size affects the generation of intercellular interactions which trigger the cell differentiation. This explanation is also supported by the facts that similar results were also observed in the HD culture.

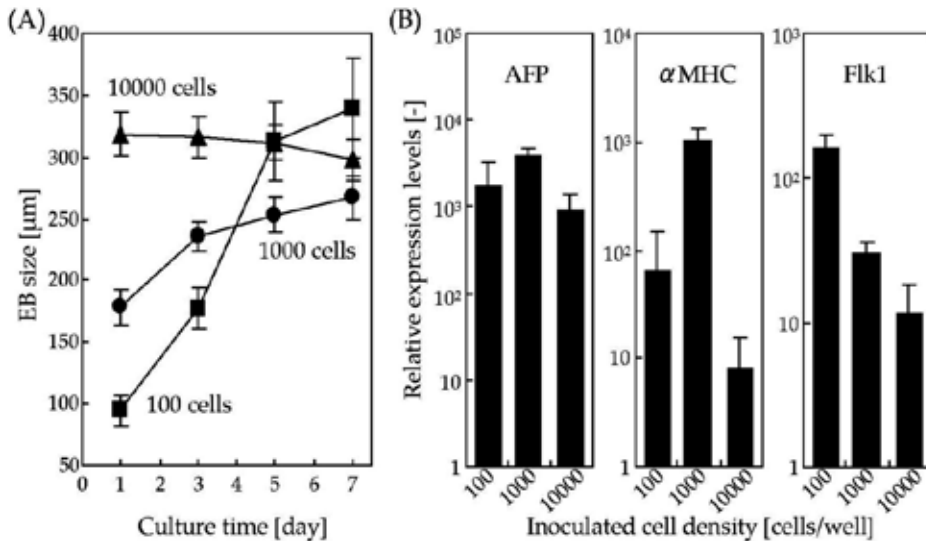


Figure 7. (A) Changes in the EB size and (B) the gene expression levels of differentiation markers after 7 days of culture.

In conclusion, the microwell array culture could control EB size and allow mass production of homogenous EBs. Furthermore, we demonstrated that differentiation fates of stem cells in the microwell array culture were similar to previous HD culture, and that the architectures of microwell array could control the EB growth and differentiation rates. These characteristics offer advantages over previous methods. Thus, the microwell array may be applicable as a cellular platform that can control the *in vitro* properties of EB.

4. Microfluidic perfusion system in stem cell culture

The control over microenvironment is important for controlling the stem cell fate, which is affected by various soluble factors supplied by the culture medium and by autocrine and paracrine mechanisms. Microfluidic perfusion enables the control of spatial and temporal profiles of the concentration of soluble factors. In this section, we review the use of the microfluidic perfusion culture system, and recent applications of the microfluidic perfusion culture system in the culture of human ES/iPS cells.

4.1. Microfluidic perfusion culture

Generally, microfluidic perfusion culture in a microfluidic device is carried out using syringe pumps [77, 78]. However, liquid handling using syringe pumps is cumbersome because it requires connection of many tubes from syringe pumps to the microfluidic device. To address this issue, we developed a pressure-driven perfusion culture system, in which multiple liquids could be handled by simply applying pressure in the liquid reservoir. This is a convenient system to create different culture conditions in a single microfluidic device [79]. We also developed a microfluidic network to generate serial dilution concentration profiles using this pressure-driven perfusion culture system [80]. We applied this pressure-driven perfusion culture system to determine IC_{50} by using the serial dilution microfluidic network [29]. In these studies, we developed the perfusion culture microchamber array chip equipped with 12 perfusion culture microchambers. The culture microchambers were connected to a serial dilution microfluidic network that could generate 12 different stepwise concentration profiles (Figure 8A). We have successfully applied this pressure-driven microfluidic perfusion culture system to a dose-response assay of model anticancer drug, paclitaxel. The obtained IC_{50} of paclitaxel was similar to that obtained by using traditional microplate assay (Figure 8B).

We have also developed an integrated microfluidic device that contains 384 microchambers in a single device. (Figure 9) [81]. In this device, 12 different drugs were diluted stepwise in the serial dilution microfluidic network into eight different concentrations. Each microchannel for each concentration is connected to four cell culture microchambers (Figure 9B). In total, 384 assays (12 drugs \times 8 concentrations \times 4 microchambers) could be carried out simultaneously. The culture media with 12 different drugs, the culture media without drug, and cell suspension were loaded in the liquid reservoir using a micropipette (Figure 9A). By applying appropriate pressure, serial dilution concentration profiles spanning 3 orders of magnitude were generated in six dilution steps. Theoretically, IC_{50} of 12 drugs could be determined in the single-experiment setup.

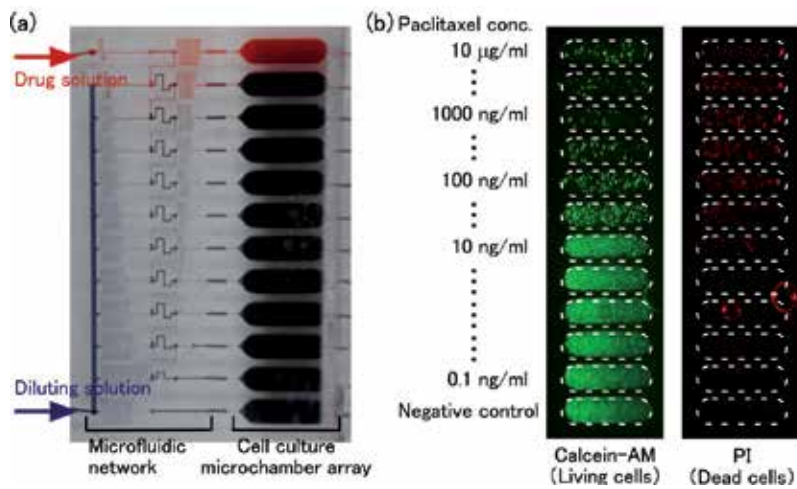


Figure 8. Photographs of the perfusion culture microchamber array chip equipped with a serial dilution microfluidic network. (A) Serial dilution microfluidic network and the cell culture microchambers. (B) Fluorometric cell growth measurement for drug cytotoxicity assay. Reprinted with permission from Sugiura et al. [29]. Copyright (2010) American Chemical Society.

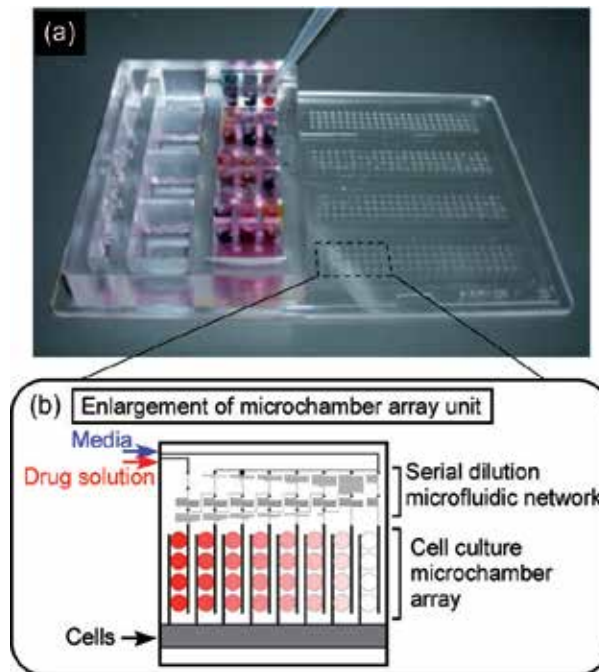


Figure 9. Microplate-sized integrated perfusion culture microchamber array chip. (A) Photographs of the integrated perfusion culture microchamber array chip. (B) Enlarged view of a microchamber array unit. Reproduced from Hattori et al. [81] with permission from CBMS.

4.2. Microfluidic perfusion system for human iPS cells under defined culture conditions

We tried to control the state of human ES/iPS cell cultures by using microfluidics perfusion system and defined the culture conditions [82]. Microfluidics perfusion system enables us to control spatial and temporal application of the soluble factors to the cells. On the other hand, defined culture conditions enable us to control the kinds of factors that are applied to the cells. Thus, the combination of microfluidic perfusion system and defined culture conditions enable us to control microenvironment and replicate stem cells niche in vitro.

Conventional culture methods for human ES/iPS cells use many undefined supplements including liquid additives such as knockout serum replacement (KSR; Life technologies, Grand island, NY, USA) and coating matrix such as Matrigel (BD Biosciences, Mississauga, Canada) [83]. These undefined supplements contain unknown quantity of growth factors, hormones, and integrin receptors, all of which affect human ES/iPS cells states. Thus, they are not suitable for being used to control state of human ES/iPS cells. Therefore, culture systems, which consist of defined supplements including hormones and cytokines and a defined coating matrix such as fibronectin or laminin, have been developed [84–86]. These defined culture systems enabled us to assess the direct responses of added factors without masking by undefined factors and to control differentiation of human ES/iPS cells.

We designed a perfusion culture microchamber array chip that was suitable for ECM coating, cell loading, and human iPS cells perfusion culture based on our previous reports [30, 79]. In this system [82], ECM-coating solution and cell suspensions were loaded in all microchambers through a cell-inlet port (Figure 10A, right) via cell-inlet main channels (Figures 10B and C). The culture media are supplied from a medium-inlet port (Figure 10A, left) via medium-inlet main channels (Figures 10B and C). By applying air pressure to these channels, four different culture conditions can be generated (Figure 10B).

To coat microchambers with purified ECM-coating matrix, we applied two modifications to our system. First modification was the reduction of medium flow resistance at the medium-inlet channel³ and the second was intermittent pressure application for medium perfusion. ECM-coating solution was compulsorily loaded in dried microchambers prior to cell suspension loading. Because the flow resistance of the liquid was much higher than that of the air, this extracoating step decreased the cell loading flow-rate at the same pressure compared with our previous system, in which the cells were loaded into dried microchambers without an ECM-coating solution.⁴ Thus, the medium-inlet channels were modified to be thick to increase the flow rate of cell suspension, resulting in an increase in the medium perfusion flow rate at the same pressure. As a result, intermittent pressure was applied during perfusion culture to keep the average flow rate almost the same as in previous systems. Based on the coating experiment, we chose fibronectin as ECM for coating microchambers.

³ The medium-inlet branch channel is much more shallow than other microchannels; therefore, the flow rate in each microchamber is determined by the maximum fluidic resistance of the medium-inlet branch channel.

⁴ The microchambers were coated unintentionally because serum contains ECM such as fibronectin, laminin, and vitronectin.

We found that the growth rate of human iPS cells under pressure-driven perfusion culture conditions was higher than under static culture conditions in the microchamber array. We also applied our new system to self-renewal and differentiation cultures of human iPS cells. Immunocytochemical analysis showed that the state of the human iPS cells was successfully controlled (Figure 9). Moreover, the effects of three antitumor drugs on human iPS cells were comparable between microchamber array and 96-well plates.

We believe that our system will be a platform technology in future for large-scale screening of fully defined conditions for differentiation cultures on integrated microfluidic devices.

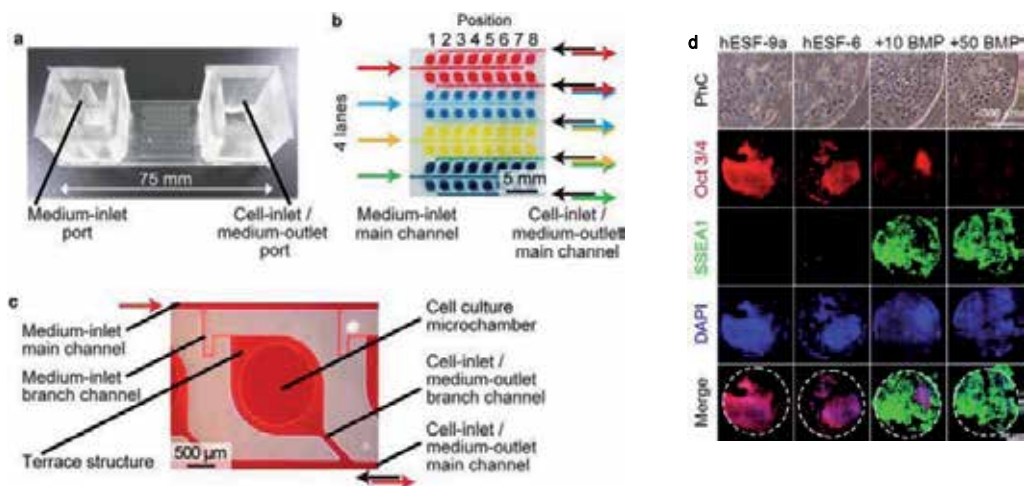


Figure 10. Structure of the perfusion culture microchamber array chip. (A) Overview of the perfusion culture microchamber array chip. (B) Enlarged view of the array with four dye solutions. (C) Enlarged view of the microchamber. (D) Undifferentiated and differentiated human iPS cells in the microchamber array chip. The four lanes of the array were perfused with four types of defined culture medium: hESF-9a (including a growth factor to keep the cells in undifferentiated state), hESF-6 medium (without growth factor), and hESF-6 medium supplemented with 10 ng/mL BMP4 (+10 BMP) or 50 ng/mL BMP4 (+50 BMP). BMP4 induces early differentiation. Microphotographs were taken at day 3. PhC: the top panels show phase-contrast micrographs. The lower panels show immunocytochemistry of the self-renewal marker, Oct 3/4 (red), the early differentiation marker, SSEA1 (green), nuclear staining with DAPI (blue), and the merged image. The white dotted lines represent the edges of cell culture microchamber. Reproduced from Yamada et al. [82] with permission from John Wiley and Sons.

5. Summary and perspectives

In this chapter, we introduced the current state of the art of microfabrication technologies used in stem cell culture. As described above, this technology has already been applied to micro-patterning, EB formation, and microfluidic perfusion culture. The microenvironment controlled by these microfabrication technologies provided sophisticated culture conditions compared to that of conventional static monolayer culture. As a result, stem cell cultures could be carried out in a controlled manner. So far, some obvious advantages of the use of micro-

fabrication technology in stem cell culture include control of stem cell fate, easy cultivation method, and reduction in culture volume.

Although methods discussed achieved certain success to control the culture microenvironment, the use of microfluidics in human ES/iPS cell studies is still limited [77, 87–91]. For example, the induction of fully functional organs and the fabrication of complicated 3D structure mimicking an intact organ is still difficult. Moreover, culture conditions available in current microfluidic technology are basically limited to conventional 2D cultures. Even cultivation of cellular aggregate in microfluidic device is still challenging. We believe that these challenges will be addressed gradually in the future by interdisciplinary approaches including mechanical engineering, material science, device design, and cell biology.

Acknowledgements

This work was supported in part by funding to KO from the Japan Agency for Medical Research and Development. The funding bodies had no role in the study design, data collection or analysis, decision to publish, or preparation of the manuscript.

Author details

Shinji Sugiura¹, Kohji Nakazawa², Toshiyuki Kanamori¹ and Kiyoshi Ohnuma^{3*}

*Address all correspondence to: kohnuma@vos.nagaokaut.ac.jp

1 Biotechnology Research Institute for Drug Discovery, National Institute of Advanced Industrial Science and Technology (AIST), Tsukuba, Ibaraki, Japan

2 Faculty of Environmental Engineering, The University of Kitakyushu, Kitakyushu, Fukuoka, Japan

3 Department of Bioengineering, Nagaoka University of Technology, Nagaoka, Niigata, Japan

References

- [1] Manz A, Harrison DJ, Verpoorte EMJ, Fettinger JC, Paulus A, Ludi H, et al. Planar chips technology for miniaturization and integration of separation techniques into monitoring systems—Capillary electrophoresis on a chip. *Journal of Chromatography*. 1992 Feb 28;593(1–2):253–8. PubMed PMID: ISI:A1992HJ35500037.

- [2] Harrison DJ, Fluri K, Seiler K, Fan ZH, Effenhauser CS, Manz A. Micromachining a miniaturized capillary electrophoresis-based chemical-analysis system on a chip. *Science*. 1993 Aug 13;261(5123):895–7. PubMed PMID: ISI:A1993LR89700032.
- [3] Xia YN, Whitesides GM. Soft lithography. *Angewandte Chemie-International Edition*. 1998 Mar 16;37(5):551–75. PubMed PMID: ISI:000072649300001.
- [4] Deng T, Wu HK, Brittain ST, Whitesides GM. Prototyping of masks, masters, and stamps/molds for soft lithography using an office printer and photographic reduction. *Analytical Chemistry*. 2000 Jul 15;72(14):3176–80. PubMed PMID: ISI:000088347100025.
- [5] Duffy DC, McDonald JC, Schueller OJA, Whitesides GM. Rapid prototyping of microfluidic systems in poly(dimethylsiloxane). *Analytical Chemistry*. 1998 Dec 01;70(23):4974–84.
- [6] Hung PJ, Lee PJ, Sabounchi P, Aghdam N, Lin R, Lee LP. A novel high aspect ratio microfluidic design to provide a stable and uniform microenvironment for cell growth in a high throughput mammalian cell culture array. *Lab on a Chip*. 2005;5(1):44–8. PubMed PMID: ISI:000225889000007.
- [7] Leclerc E, Sakai Y, Fujii T. Cell culture in 3-dimensional microfluidic structure of PDMS (polydimethylsiloxane). *Biomedical Microdevices*. 2003 Jun;5(2):109–14. PubMed PMID: ISI:000183903900003.
- [8] Hattori K, Sugiura S, Kanamori T. *Microfluidic perfusion culture. Animal cell biotechnology—methods and protocols*. 3 edn: Springer Heidelberg, Germany; 2013. p. 251–63.
- [9] Toepke MW, Beebe DJ. PDMS absorption of small molecules and consequences in microfluidic applications. *Lab on a Chip*. 2006 Dec;6(12):1484–6. PubMed PMID: ISI:000243212600009.
- [10] Sollier E, Murray C, Maoddi P, Di Carlo D. Rapid prototyping polymers for microfluidic devices and high pressure injections. *Lab on a Chip*. 2011;11(22): 3752-65.
- [11] Schutte J, Freudigmann C, Benz K, Bottger J, Gebhardt R, Stelzle M. A method for patterned in situ biofunctionalization in injection-molded microfluidic devices. *Lab on a Chip*. 2010;10(19):2551–8.
- [12] O'Neill PF, Ben Azouz A, Vazquez M, Liu J, Marczak S, Slouka Z, et al. Advances in three-dimensional rapid prototyping of microfluidic devices for biological applications. *Biomicrofluidics*. 2014 Sep;8(5):052112. PubMed PMID: WOS:000344226200024. English.
- [13] Au AK, Bhattacharjee N, Horowitz LF, Chang TC, Folch A. 3D-printed microfluidic automation. *Lab on a chip*. 2015 Mar;15(8):1294–301. PubMed PMID: MEDLINE:25738695. English.

- [14] Zorlutuna P, Annabi N, Camci-Unal G, Nikkhah M, Cha JM, Nichol JW, et al. Microfabricated biomaterials for engineering 3D tissues. *Advanced Materials*. 2012;24(14):1782–804.
- [15] Jensen KF. Microchemical systems: status, challenges, and opportunities. *Aiche Journal*. 1999 Oct;45(10):2051–4. PubMed PMID: ISI:000083057000002.
- [16] Jeon NL, Baskaran H, Dertinger SKW, Whitesides GM, Van de Water L, Toner M. Neutrophil chemotaxis in linear and complex gradients of interleukin-8 formed in a microfabricated device. *Nature Biotechnology*. 2002 Aug;20(8):826–30. PubMed PMID: ISI:000177182500035.
- [17] Lucchetta EM, Lee JH, Fu LA, Patel NH, Ismagilov RF. Dynamics of *Drosophila* embryonic patterning network perturbed in space and time using microfluidics. *Nature*. 2005 Apr 28;434(7037):1134–8. PubMed PMID: ISI:000228693300044. English.
- [18] Wu MH, Huang SB, Lee GB. Microfluidic cell culture systems for drug research. *Lab on a Chip*. 2010;10(8):939–56. PubMed PMID: ISI:000276218900001.
- [19] Inamdar NK, Borenstein JT. Microfluidic cell culture models for tissue engineering. *Current Opinion in Biotechnology*. 2011 Oct;22(5):681–9. PubMed PMID: WOS:000296114600012. English.
- [20] Neuzil P, Giselbrecht S, Lange K, Huang TJ, Manz A. Revisiting lab-on-a-chip technology for drug discovery. *Nature Reviews Drug Discovery*. 2012 Aug;11(8):620–32. PubMed PMID: WOS:000307101100020. English.
- [21] van Midwoud PM, Verpoorte E, Groothuis GMM. Microfluidic devices for in vitro studies on liver drug metabolism and toxicity. *Integrative Biology*. 2012;3(5):509–21. PubMed PMID: WOS:000290170600001. English.
- [22] van der Meer AD, van den Berg A. Organs-on-chips: breaking the in vitro impasse. *Integrative Biology*. 2012;4(5):461–70. PubMed PMID: WOS:000303321100001. English.
- [23] Hattori K, Munehira Y, Kobayashi H, Satoh T, Sugiura S, Kanamori T. Microfluidic perfusion culture chip providing different strengths of shear stress for analysis of vascular endothelial function. *Journal of Bioscience and Bioengineering*. 2014 ;118(3): 327–32.
- [24] Sakai Y, Hattori K, Yanagawa F, Sugiura S, Kanamori T, Nakazawa K. Detachably assembled microfluidic device for perfusion culture and post-culture analysis of a spheroid array. *Biotechnology Journal*. 2014;9(7):971–9.
- [25] El-Ali J, Sorger PK, Jensen KF. Cells on chips. *Nature*. 2006 07/27/print;442(7101):403–11.
- [26] Hong J, Edel JB, deMello AJ. Micro- and nanofluidic systems for high-throughput biological screening. *Drug Discovery Today*. 2009 Feb;14(3–4):134–46. PubMed PMID: ISI:000263638400004.

- [27] Kang LF, Chung BG, Langer R, Khademhosseini A. Microfluidics for drug discovery and development: from target selection to product lifecycle management. *Drug Discovery Today*. 2008 Jan;13(1–2):1–13. PubMed PMID: WOS:000252883000001.
- [28] Hattori K, Sugiura S, Kanamori T, Ohnuma K. Is microfluidic perfusion culture the future for large-scale screening of human-induced pluripotent stem cells? *Pharmaceutical Bioprocessing*. 2014;2(4):303–5.
- [29] Sugiura S, Hattori K, Kanamori T. Microfluidic serial dilution cell-based assay for analyzing drug dose response over a wide concentration range. *Analytical Chemistry*. 2010 Oct;82(19):8278–82. PubMed PMID: WOS:000282257400056.
- [30] Hattori K, Sugiura S, Kanamori T. Microenvironment array chip for cell culture environment screening. *Lab on a Chip*. 2011;11(2):212–4. PubMed PMID: WOS:000285514700003.
- [31] Drew T, Justin C-W. Microbioreactor array for full-factorial analysis of provision of multiple soluble factors in cellular microenvironments. *Biotechnology and Bioengineering*. 2009;104(6):1240–4.
- [32] Pampaloni F, Reynaud EG, Stelzer EHK. The third dimension bridges the gap between cell culture and live tissue. *Nature Reviews Molecular Cell Biology*. 2007 Oct;8(10):839–45. PubMed PMID: ISI:000249642900016.
- [33] Thomson JA, Itskovitz-Eldor J, Shapiro SS, Waknitz MA, Swiergiel JJ, Marshall VS, et al. Embryonic stem cell lines derived from human blastocysts. *Science*. 1998 Nov 6;282(5391):1145–7. PubMed PMID: 9804556. Epub 1998/11/06.eng.
- [34] Takahashi K, Tanabe K, Ohnuki M, Narita M, Ichisaka T, Tomoda K, et al. Induction of pluripotent stem cells from adult human fibroblasts by defined factors. *Cell*. 2007 Nov 30;131(5):861–72. PubMed PMID: 18035408. Epub 2007/11/24.eng.
- [35] Tachibana M, Amato P, Sparman M, Gutierrez NM, Tippner-Hedges R, Ma H, et al. Human embryonic stem cells derived by somatic cell nuclear transfer. *Cell*. 2013 Jun 6;153(6):1228–38. PubMed PMID: 23683578. Epub 2013/05/21.eng.
- [36] Watanabe K, Ueno M, Kamiya D, Nishiyama A, Matsumura M, Wataya T, et al. A ROCK inhibitor permits survival of dissociated human embryonic stem cells. *Nature Biotechnology*. 2007 Jun;25(6):681–6. PubMed PMID: 17529971. Epub 2007/05/29.eng.
- [37] Evans MJ, Kaufman MH. Establishment in culture of pluripotential cells from mouse embryos. *Nature*. 1981;292(5819):154–6.
- [38] Martin GR. Isolation of a pluripotent cell line from early mouse embryos cultured in medium conditioned by teratocarcinoma stem cells. *Proceedings of the National Academy of Sciences*. 1981;78(12):7634–8.

- [39] Takahashi K, Yamanaka S. Induction of pluripotent stem cells from mouse embryonic and adult fibroblast cultures by defined factors. *Cell*. 2006 Aug 25;126(4):663–76. PubMed PMID: 16904174. Epub 2006/08/15.eng.
- [40] Warmflash A, Sorre B, Etoc F, Siggia ED, Brivanlou AH. A method to recapitulate early embryonic spatial patterning in human embryonic stem cells. *Nature Methods*. 2014; 11(8): 847–54.
- [41] Nichols J, Smith A. Naive and primed pluripotent states. *Cell stem cell*. 2009;4(6): 487–92.
- [42] Mrksich M, Whitesides GM. Patterning self-assembled monolayers using microcontact printing: a new technology for biosensors? *Trends Biotech*. 1995;13(6):228–35.
- [43] Park J, Cho CH, Parashurama N, Li Y, Berthiaume F, Toner M, et al. Microfabrication-based modulation of embryonic stem cell differentiation. *Lab on a Chip*. 2007;7(8):1018–28.
- [44] Gupta K, Kim DH, Ellison D, Smith C, Kundu A, Tuan J, et al. Lab-on-a-chip devices as an emerging platform for stem cell biology. *Lab on a Chip*. 2010;10(16):2019–31. PubMed PMID: WOS:000280394800001.
- [45] Saha K, Mei Y, Reisterer CM, Pyzocha NK, Yang J, Muffat J, et al. Surface-engineered substrates for improved human pluripotent stem cell culture under fully defined conditions. *Proceedings of the National Academy of Sciences*. 2011;108(46):18714–9.
- [46] Paik I, Scurr DJ, Morris B, Hall G, Denning C, Alexander MR, et al. Rapid micropatterning of cell lines and human pluripotent stem cells on elastomeric membranes. *Biotechnology and Bioengineering*. 2012;109(10):2630–41.
- [47] Hattori K, Yoshimitsu R, Sugiura S, Maruyama A, Ohnuma K, Kanamori T. Masked plasma oxidation: simple micropatterning of extracellular matrix in a closed microchamber array. *Rsc Advances*. 2013;3(39):17749–54. PubMed PMID: WOS: 000325275300022.
- [48] Yamada R, Hattori K, Tagaya M, Sasaki T, Miyamoto D, Nakazawa K, et al. Plasma-patterned polydimethylsiloxane surface with single-step coating of a mixture of vitronectin and albumin enables the formation of small discs and spheroids of human iPS. *Plasma Medicine*. 2014;4(1–4):165–76.
- [49] Yamada R, Hattori K, Tachikawa S, Tagaya M, Sasaki T, Sugiura S, et al. Control of adhesion of human induced pluripotent stem cells to plasma-patterned polydimethylsiloxane coated with vitronectin and γ -globulin. *Journal of Bioscience and Bioengineering*. 2014;118(3):315–22.
- [50] Barczyk M, Carracedo S, Gullberg D. Integrins. *Cell and tissue research*. 2010;339(1): 269–80.
- [51] Miyazaki T, Futaki S, Hasegawa K, Kawasaki M, Sanzen N, Hayashi M, et al. Recombinant human laminin isoforms can support the undifferentiated growth of hu-

- man embryonic stem cells. *Biochemical and Biophysical Research Communications*. 2008 Oct 10;375(1):27–32. PubMed PMID: 18675790. Epub 2008/08/05.eng.
- [52] Rowland TJ, Miller LM, Blaschke AJ, Doss EL, Bonham AJ, Hikita ST, et al. Roles of integrins in human induced pluripotent stem cell growth on matrigel and vitronectin. *Stem Cells and Development*. 2009 Oct 7. PubMed PMID: 19811096. Epub 2009/10/09.eng.
- [53] Hayashi Y, Furue MK, Okamoto T, Ohnuma K, Myoishi Y, Fukuhara Y, et al. Integrins regulate mouse embryonic stem cell self-renewal. *Stem Cells*. 2007 Dec;25(12):3005–15. PubMed PMID: 17717067. Epub 2007/08/25.eng.
- [54] Hayman EG, Pierschbacher MD, Ohgren Y, Ruoslahti E. Serum spreading factor (vitronectin) is present at the cell surface and in tissues. *Proceedings of the National Academy of Sciences*. 1983;80(13):4003–7.
- [55] Parker CW, Osterland CK. Hydrophobic binding sites on immunoglobulins. *Biochemistry*. 1970;9(5):1074–82.
- [56] Tourovskaja A, Barber T, Wickes BT, Hirdes D, Grin B, Castner DG, et al. Micropatterns of chemisorbed cell adhesion-repellent films using oxygen plasma etching and elastomeric masks. *Langmuir*. 2003;19(11):4754–64.
- [57] Kamao H, Mandai M, Okamoto S, Sakai N, Suga A, Sugita S, et al. Characterization of human induced pluripotent stem cell-derived retinal pigment epithelium cell sheets aiming for clinical application. *Stem Cell Reports*. 2014; 2(2): 205-218.
- [58] Matsuura K, Wada M, Shimizu T, Haraguchi Y, Konishi K, Shiba Y, et al. Creation of human cardiac cell sheets using pluripotent stem cells. *Biochemical and Biophysical Research Communications*. 2012;425:321–7.
- [59] Yang J, Yamato M, Shimizu T, Sekine H, Ohashi K, Kanzaki M, et al. Reconstruction of functional tissues with cell sheet engineering. *Biomaterials*. 2007;28(34):5033–43.
- [60] Kito T, Shibata R, Ishii M, Suzuki H, Himeno T, Kataoka Y, et al. iPS cell sheets created by a novel magnetite tissue engineering method for reparative angiogenesis. *Scientific Reports*. 2013;3:1418.
- [61] Shirayoshi Y, Okada TS, Takeichi M. The calcium-dependent cell-cell adhesion system regulates inner cell mass formation and cell surface polarization in early mouse development. *Cell*. 1983;35(3 Pt 2):631.
- [62] Mould AP, Akiyama SK, Humphries MJ. Regulation of integrin $\alpha 5 \beta 1$ -fibronectin interactions by divalent cations. Evidence for distinct classes of binding sites for Mn^{2+} , Mg^{2+} , and Ca^{2+} . *Journal of Biol Chem*. 1995 Nov 3;270(44):26270–7. PubMed PMID: 7592835. Epub 1995/11/03.eng.
- [63] Ohnuma K, Fujiki A, Yanagihara K, Tachikawa S, Hayashi Y, Ito Y, et al. Enzyme-free passage of human pluripotent stem cells by controlling divalent cations. *Scientific Reports*. 2014;4:4646. Epub 2014/04/11.

- [64] Bratt-Leal AM, Carpenedo RL, McDevitt TC. Engineering the embryoid body micro-environment to direct embryonic stem cell differentiation. *Biotechnology Progress*. 2009;25(1):43–51.
- [65] Ng ES, Davis RP, Azzola L, Stanley EG, Elefanty AG. Forced aggregation of defined numbers of human embryonic stem cells into embryoid bodies fosters robust, reproducible hematopoietic differentiation. *Blood*. 2005;106(5):1601–3.
- [66] Burrige PW, Anderson D, Priddle H, Barbadillo Munoz MD, Chamberlain S, Allegrucci C, et al. Improved human embryonic stem cell embryoid body homogeneity and cardiomyocyte differentiation from a novel V-96 plate aggregation system highlights interline variability. *Stem Cells*. 2007;25(4):929–38.
- [67] Kinney MA, Sargent CY, McDevitt TC. The multiparametric effects of hydrodynamic environments on stem cell culture. *Tissue Engineering Part B: Reviews*. 2011;17(4):249–62.
- [68] Kurosawa H. Methods for inducing embryoid body formation: in vitro differentiation system of embryonic stem cells. *Journal of Bioscience and Bioengineering*. 2007;103(5):389–98.
- [69] Hsiao C, Palecek SP. Microwell regulation of pluripotent stem cell self-renewal and differentiation. *Bionanoscience*. 2012;2(4):266–76.
- [70] Kinney MA, Saeed R, McDevitt TC. Systematic analysis of embryonic stem cell differentiation in hydrodynamic environments with controlled embryoid body size. *Integrative Biology*. 2012;4(6):641–50.
- [71] Azarin SM, Lian X, Larson EA, Popelka HM, de Pablo JJ, Palecek SP. Modulation of Wnt/ β -catenin signaling in human embryonic stem cells using a 3-D microwell array. *Biomaterials*. 2012;33(7):2041–9.
- [72] Schukur L, Zorlutuna P, Cha JM, Bae H, Khademhosseini A. Directed differentiation of sizecontrolled embryoid bodies towards endothelial and cardiac lineages in RGD-modified poly (ethylene glycol) hydrogels. *Advanced Healthcare Materials*. 2013;2(1):195–205.
- [73] Sakai Y, Yoshida S, Yoshiura Y, Mori R, Tamura T, Yahiro K, et al. Effect of microwell chip structure on cell microsphere production of various animal cells. *Journal of Bioscience and Bioengineering*. 2010;110(2):223–9.
- [74] Sakai Y, Nakazawa K. Technique for the control of spheroid diameter using micro-fabricated chips. *Acta Biomaterialia*. 2007;3(6):1033–40.
- [75] Nakazawa K, Yoshiura Y, Koga H, Sakai Y. Characterization of mouse embryoid bodies cultured on microwell chips with different well sizes. *Journal of Bioscience and Bioengineering*. 2013;116(5):628–33.

- [76] Sakai Y, Yoshiura Y, Nakazawa K. Embryoid body culture of mouse embryonic stem cells using microwell and micropatterned chips. *Journal of Bioscience and Bioengineering*. 2011;111(1):85–91.
- [77] Kim L, Vahey MD, Lee H-Y, Voldman J. Microfluidic arrays for logarithmically perfused embryonic stem cell culture. *Lab on a Chip*. 2006;6(3):394–406.
- [78] Lee PJ, Hung PJ, Rao VM, Lee LP. Nanoliter scale microreactor array for quantitative cell biology. *Biotechnology and Bioengineering*. 2006;94(1):5–14.
- [79] Sugiura S, Edahiro J-i, Kikuchi K, Sumaru K, Kanamori T. Pressure-driven perfusion culture microchamber array for a parallel drug cytotoxicity assay. *Biotechnology and Bioengineering*. 2008;100(6):1156–65.
- [80] Hattori K, Sugiura S, Kanamori T. Generation of arbitrary monotonic concentration profiles by a serial dilution microfluidic network composed of microchannels with a high fluidic-resistance ratio. *Lab on a Chip*. 2009;9(12):1763–72. PubMed PMID: WOS:000266616000017.
- [81] Hattori K, Sugiura S, Kanamori T, editors. Integrated perfusion culture micro-chamber array chip for high-throughput drug dose response assay. *The Proceedings of Conference MicroTAS 2010*; 1559-61. 2010 ; Groningen.
- [82] Yoshimitsu R, Hattori K, Sugiura S, Kondo Y, Yamada R, Tachikawa S, et al. Microfluidic perfusion culture of human induced pluripotent stem cells under fully defined culture conditions. *Biotechnology and Bioengineering*. 2014;111(5):937–47.
- [83] Hughes CS, Postovit LM, Lajoie GA. Matrigel: a complex protein mixture required for optimal growth of cell culture. *Proteomics*. 2010;10(9):1886–90.
- [84] Furue MK, Na J, Jackson JP, Okamoto T, Jones M, Baker D, et al. Heparin promotes the growth of human embryonic stem cells in a defined serum-free medium. *Proceedings of the National Academy of Sciences United States of America*. 2008 Sep 9;105(36):13409–14. PubMed PMID: 18725626. Epub 2008/08/30.eng.
- [85] Braam SR, Zeinstra L, Litjens S, Ward-van Oostwaard D, van den Brink S, van Laake L, et al. Recombinant vitronectin is a functionally defined substrate that supports human embryonic stem cell self-renewal via $\alpha V\beta 5$ integrin. *Stem Cells*. 2008;26(9):2257–65.
- [86] Hayashi Y, Chan T, Warashina M, Fukuda M, Ariizumi T, Okabayashi K, et al. Reduction of N-glycolylneuraminic acid in human induced pluripotent stem cells generated or cultured under feeder- and serum-free defined conditions. *PLoS ONE*. 2010;5(11):e14099. PubMed PMID: 21124894. Epub 2010/12/03.eng.
- [87] Titmarsh D, Hidalgo A, Turner J, Wolvetang E, Cooper-white J. Optimization of flowrate for expansion of human embryonic stem cells in perfusion microreactors. *Biotechnology and Bioengineering*. 2011;108(12):2894–904.

- [88] Titmarsh DM, Hudson JE, Hidalgo A, Elefanty AG, Stanley EG, Wolvetang EJ, et al. Microbioreactor arrays for full factorial screening of exogenous and paracrine factors in human embryonic stem cell differentiation. *PLoS ONE*. 2012;7(12):e52405.
- [89] Khoury M, Bransky A, Korin N, Konak LC, Enikolopov G, Tzchori I, et al. A microfluidic traps system supporting prolonged culture of human embryonic stem cells aggregates. *Biomedical Microdevices*. 2010;12(6):1001–8.
- [90] Villa-Diaz LG, Torisawa YS, Uchida T, Ding J, Nogueira-de-Souza NC, O'Shea KS, et al. Microfluidic culture of single human embryonic stem cell colonies. *Lab on a Chip*. 2009 Jun 21;9(12):1749–55. PubMed PMID: 19495459. Epub 2009/06/06.eng.
- [91] Kamei K, Guo S, Yu ZT, Takahashi H, Gschweng E, Suh C, et al. An integrated microfluidic culture device for quantitative analysis of human embryonic stem cells. *Lab on a Chip*. 2009 Feb 21;9(4):555–63. PubMed PMID: 19190791. Epub 2009/02/05.eng.

Advanced Microfluidic Assays for *Caenorhabditis elegans*

Natalia A. Bakhtina, Neil MacKinnon and Jan G. Korvink

Additional information is available at the end of the chapter

<http://dx.doi.org/10.5772/64283>

Abstract

The *in vivo* analysis of a model organism, such as the nematode *Caenorhabditis elegans*, enables fundamental biomedical studies, including development, genetics, and neurobiology. In recent years, microfluidics technology has emerged as an attractive and enabling tool for the study of the multicellular organism. Advances in the application of microfluidics to *C. elegans* assays facilitate the manipulation of nematodes in high-throughput format and allow for the precise spatial and temporal control of their environment. In this chapter, we aim to illustrate the current microfluidic approaches for the investigation of behavior and neurobiology in *C. elegans* and discuss the trends of future development.

Keywords: *C. elegans*, chip-based, manipulation, microfluidics, model organism

1. Introduction

The invertebrate *Caenorhabditis elegans*, *Drosophila melanogaster*, and the vertebrate zebrafish (*Danio rerio*) are the most widely studied multicellular organisms. The *in vivo* analysis of these model organisms allows the understanding of many complex physiological processes, addressing many of the questions relevant to human biology. The choice of model organism depends on the biological question under investigation. For example, *C. elegans* is simple enough to be experimentally tractable. It has a short life cycle (3 days at 25 °C) and lifespan (15–17 days at 25 °C), passes through four larva (L1–L4) stages and an adult stage [1]. Its small size (1–1.2 mm long and 80 µm wide), transparent body at all life stages, and preferred food source (*Escherichia coli*) simplify its maintenance on agar plates or liquid cultures allowing visualization of individual cells and organs in intact animals. *C. elegans* possesses one of the simplest central nervous systems (the adult hermaphrodite has 302 neurons). Because it is so well studied, rapid identification of signaling pathways, for instance, in studies of aging, has

become possible. About 40 % of human disease genes have an orthologue in the genome of *C. elegans*, including those genes associated with Alzheimer disease, Parkinson's disease, Huntington's disease (HD), and many other neurodegenerative disorders [1–3]. This astonishing degree of correspondence permits the modeling of human ailments in a simple invertebrate without involving actual human subjects and provides a meaningful insight into the pathogenesis of a complex disease phenotype.

Traditionally, behavioral genetics is employed as a prime method for neurobiological studies in *C. elegans*. It is based on manual worm manipulation on a Petri dish or a multiwell plate, and monitoring the effects on various biological processes, such as growth and fertility, by visual inspection. Refreshment of old buffer solutions by a fresh solution is invasive and causes stress both to the larvae and adults. For drug screening, the concentration of the active compounds in the exposing solution might not be precisely controlled because of evaporation and non-selective adsorption effects on the wall of the wells. Permanent immobilization of the worm for further neuronal analysis is performed by means of glue or anesthetics. These methods are time consuming, expensive, tedious, prone to human flaws, and frequently result in failure. To address these problems, novel technologies for the manipulation of multicellular organisms are needed.

Microfluidics has recently been adopted as an instrument both to expand and accelerate progress related to the treatment of human diseases and injuries. Due to precise and automated manipulation of fluids and samples (e.g., single cell, multicellular organism, etc.) in a system of channels (10–150 μm), a microfluidic-based approach is able to open up aspects that would remain hidden from traditional laboratory techniques. The technology provides a junction between engineering and pure sciences with an immense potential for offering simple and practical solutions. The unique properties of this technology are highlighted by several aspects. First, the dimensions of microfluidic channels perfectly match to the size of samples, allowing precise manipulation. With moving parts, flowing fluids, or other passive mechanisms, microsystems can be used to align samples with a particular orientation with ease as compared to hand-manipulations. Second, the ability to manipulate small amounts of liquid makes it suitable for the precise delivery of small amounts of reagent. Due to the laminar nature of the flow at the micro scale, efficient mass and energy transfer can be controlled in a completely predictable manner (e.g., diffusion of dissolved gases across tens of microns through fluids or polymer membrane materials). Third, based on relatively inexpensive polymer-based fabrication techniques, such as polydimethylsiloxane (PDMS) replica molding, it has become feasible to realize disposable, economic, and biocompatible systems [4]. Complex structures, adapted to different applications, can be easily fabricated in a short time. Finally, the capability to realize large-scale integration makes it possible to handle a large population of samples in parallel or in series for high-throughput assays. For example, COPAS BIOSORT high-throughput analysis system from Union Biometrica, Inc. (USA), enables the performing of high-speed imaging and offers the possibility of studying a large quantity of individual worms, thereby providing detailed statistical information on the biological variance within the same population.

Substantial advances in microfluidic techniques and particular research interest in *C. elegans* have driven the development of numerous microchip-based systems. They have been reviewed a number of times focusing on various aspects of miniaturized systems, their advantages, application challenges, and scientific potential [5–19]. A summary of microfluidic-based systems with respect to the organism, organ, or tissue studies was presented by Sivagnanam et al. [5]. All available on-chip approaches for *C. elegans* investigations were systemized by the authors [6]. A classification diagram for structuring of approximately 100 references that simplifies their search according to five evaluated aspects (measured output data, and method for sorting, immobilization, stimulation, and detection of *C. elegans*) is included. In addition, we listed the relevant sorting, immobilization, and imaging methods that have been reported in recent literature, and indicated the main qualitative and quantitative characteristics for each.

This chapter provides a comprehensive overview of recent microfluidic-based approaches for investigations of worm behavior and neurobiology (Figure 1). This includes a discussion on tools and approaches needed to ensure high-throughput manipulation (culturing, sorting, and immobilization) and assaying for behavioral and neuronal studies. In addition, a perspective of novel methods for studies of metabolic activity facilitated by microfluidics is presented.

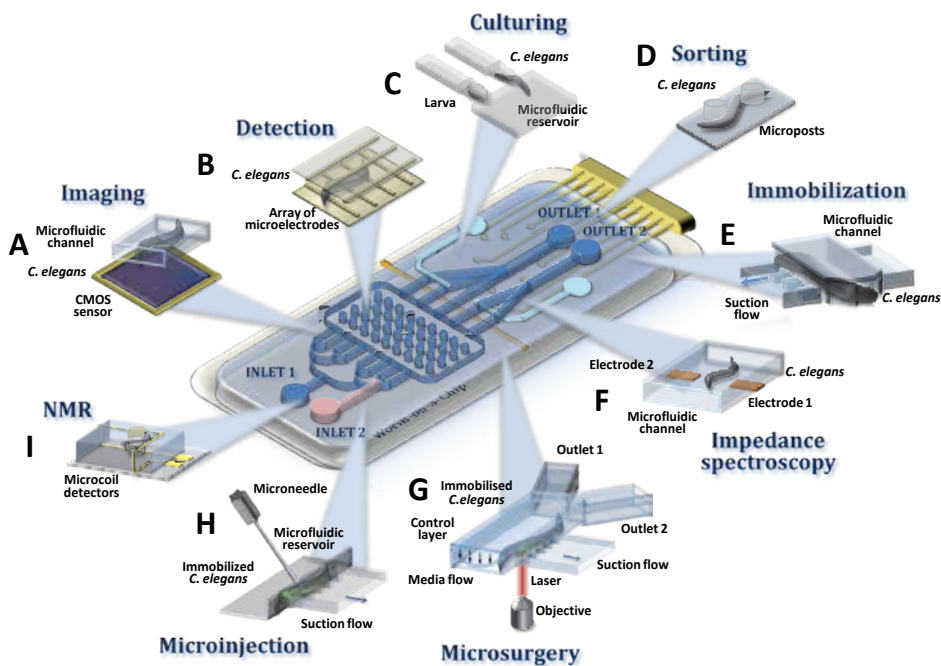


Figure 1. Schematic illustration of a microfluidic platform for *C. elegans* assaying. The structure of this chapter is as follows: in Section 2 we summarize the most frequently utilized imaging (A) and detection (B) methods; in Section 3 we concentrate our attention on different techniques for worm-on-a-chip manipulation, such as culturing, sorting, and immobilization (C, D, and E); Section 4 provides an overview of behavioral and neuronal phenotypes of *C. elegans* facilitated by different analysis techniques, including electrochemical impedance spectroscopy (F), microsurgery (G), and microinjection (H); additionally, Section 5 presents the methods utilized for metabolic activity studies (I).

2. Microfluidic approaches for *C. elegans* detection

Conventional optical imaging is an established detection technique for the observation of biological samples (e.g., cells, microorganisms, etc.). Microscopy-based (fluorescent, nonfluorescent, or their various combinations) systems can be used to extract valuable and unique data (e.g., image the activity of specific neurons) from biological samples. Combined with microfluidics, these systems offer several important advantages required for high-throughput screening [7–10]. Fully automated components, software control, and image processing tools make commercial confocal microscopes extremely versatile for real-time and high-resolution diagnosis. However, conventional optical imaging systems are quite expensive, bulky, and limit the miniaturization of chip-based systems. An overview of different optical imaging approaches in microfluidics (e.g., conventional optical imaging, lensless imaging, etc.) and their applications was recently presented by several research groups [20–22].

To overcome limitations mentioned above, researchers utilize on-chip or lensless imaging technologies. On-chip imaging systems for *C. elegans*, including contact optofluidic imaging [23, 24], direct shadow imaging [25], holographic imaging [26–28], in combination with automated data processing have enabled the observation and characterization of key behavioral parameters *in vivo* at micrometer and nanometer resolution (Figure 1A and B). Lensless imaging has the advantage of cointegration of microfluidics, microelectronics, and optical components into one platform. This has guaranteed an increase of the image quality, and has provided an ultimate spatial resolution of approximately 0.9 μm and a throughput approaching 40 worms per minute [23]. The combination with fluorescence imaging holds a great potential for screening of cellular processes [28].

Another promising approach is a lensless and sensor-less monitoring of the nematodes' movement in various microenvironments [29]. In a micro-electro-fluidic (MEF) grid, a moving nematode is detected by change in the electrical impedance at the intersection regions of the microelectrode grid, formed by two identical orthogonally arranged arrays of metal lines (Figure 1B). The approach ensured the real-time readout of the crawling nematode with a spatial resolution of 30 μm (the distance between grid lines) of the reconstructed images at the frequency of 174 Hz per readout.

Usually, the use of fluorescence-based techniques, such as calcium imaging or green fluorescent protein (GFP) expression, and microfluidics to image the activity of specific neurons requires chemically or genetically labeled animals to be immobilized for imaging at a cellular level [30–32]. An “immobilization-free” approach detection is achieved via two pairs of integrated optical fibers. Through the measurements of optical density and fluorescence, the fibers can detect and differentiate wild-type and green fluorescent protein (GFP)-type *C. elegans* even when they flow at high speeds (switching time of 1 s per worm) [33]. This has proven to be a well-controlled method for automated handling of worms in a high-throughput manner with a sorting accuracy of more than 96 %.

3. Microfluidic techniques for *C. elegans* manipulation

Environmental control and manipulation of whole animal poses significant challenges (e.g., animal's body orientation, precise delivery of chemicals, etc.). Transferring traditional neurobiology and behavioral investigation techniques to the microfluidic platform has the potential to overcome these challenges. This is driven by substantial progress in integration of functional components (e.g., valves, detectors, etc.) that allow the monitoring of various steps, such as administration, distribution, metabolism, and toxicity during drug screening. The advanced microfluidic approach offers both qualitative and quantitative data from a single organism by automatic high-throughput manipulation. For example, the worms can be oriented at regular positions on a substrate due to hydrodynamic forces in a microfluidic chip for the determination of gene function in a high-throughput manner [34]. In this section, we discuss general manipulation techniques, such as culturing, sorting, and immobilization.

Culturing. To interpret the underlying metabolic changes and specific developmental processes during nematode ageing, longitudinal experiments over the entire lifespan are necessary. Imaging and monitoring of the embryogenesis require specific techniques, which include single embryo isolation and mounting. Worm culturing can be dramatically improved using an automated microfluidic platform for culturing, phenotyping, and long-term live imaging of *C. elegans* embryo and larvae using microfluidic chambers (Figure 2A) and droplet encapsulation (Figure 2B) [35–47]. In combination with image recognition algorithms these “worm-chips” have successfully demonstrated their high potential at enhancing worm handling (e.g., automatic nutrient and waste exchange), accurate imaging, and automated analysis of embryonic morphogenesis during embryonic development [48]. Requiring the loading of only a few adult worms into the chip, the ensuing *C. elegans* embryo population could be processed at the same time.

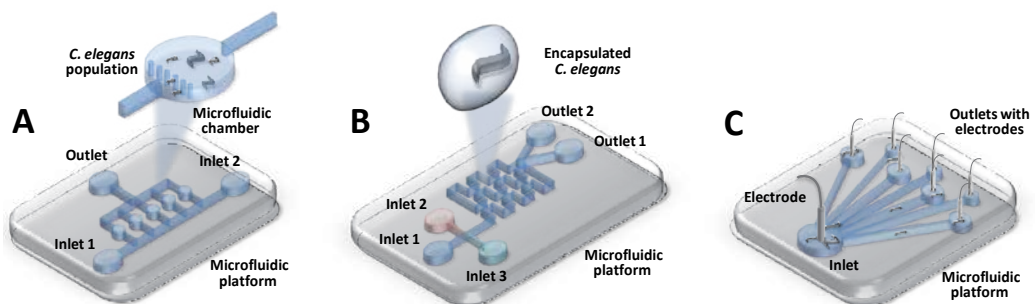


Figure 2. Schematic illustration of the microfluidic platforms for *C. elegans* culturing (A) [35] and sorting based on droplet encapsulation (B) [42–44] or electro taxis (C) [49].

Sorting. *C. elegans* exhibits age-dependent specific neuron and behavioral responses. For instance, usage of both the early-stage and adult worms may increase the physiological relevance of drug candidates during the identification process and reveals potential toxic effects. Therefore, sorting (age or size synchronization) of worm populations or individuals is

often required for further diagnostics. For example, a passive sorting method is based on self-regulated worm distribution and loading into an array of narrowing channels [36, 50, 51] or microchambers [36, 37, 40, 52–55] with an average loading effectiveness rate of approximately 65 %. Once the worm enters the microchannel, the hydrodynamic resistance increases dramatically, thereby locking a single worm inside the chamber.

When considering high-throughput manipulation, automatic classification of worms (e.g., wild-type from mutants) becomes of high relevance. Typically, sorting involves individual *C. elegans* loading and separation, for instance, according to genetic phenotype for downstream analysis [31, 32, 34, 36, 56–60]. Together with real-time rapid image extraction and data processing, media flow in the microfluidic channel is driven by a syringe and is controlled by on-chip functional components, such as PDMS valves. Automatic sample positioning can guarantee rapid classification based on synaptic characteristics with sorting throughput at a rate of 900 worms per hour and an overall sorting accuracy of 96.5 % [32]. Depending on the extracted data, the worm could be flushed to either a waste or a sorting outlet by valve actuation.

Several other techniques have been successfully implemented in high-throughput studies [61–63]. In these systems, sorting is accomplished based on size difference in a passive, but extremely high throughput (up to 1200 worms per min) and selective manner (94 % of adults with 0.2 % larva contamination) [62]. The device body contains an array of microstructured post (or filters) and a network of microfluidic channels allowing a large population of adult worms and larvae to be oriented in the desired direction.

Immobilization. Because of the high mobility, *C. elegans* immobilization is required for further developmental studies (e.g., neurosurgery). Manual handling and immobilization (e.g., by gluing or anesthesia) suffer from low throughput and is limited in long-term monitoring [1]. Immobilization in a microfluidic channel provides a simple well-controlled mechanism for automated handling of worms in a high-throughput manner. One of the widely used techniques is based on mechanical force. Several immobilization techniques are used to lock an individual worm against a microchannel wall in a robust and reversible manner. The first method involves microarrays of fixed-geometry clamps for *C. elegans* immobilization, which is a simple way to restrict the motion employing a single PDMS layer [36, 51, 64–67]. Using a constant pressure difference between the inlet and outlet of the device to drive fluid flow, an array of up to 128 wedge-shaped microchannels can be filled by nematodes with up to 90 % efficiency [68]. The second method includes a flexible PDMS membrane for squeezing the worm into the side of microfluidic channel under an external pressure through a control layer above the main chamber [51, 57–59, 67, 69, 70]. A third method is to trap of *C. elegans* by suction flow (Figure 1E), which is based on a vacuum-assisted restraint that aligns the worm along its axis [31, 71]. To highlight the utility of both immobilization techniques several research groups have combined suction posts with either flexible membranes [56, 65, 72, 73] or microchannel narrowing [30, 74–77] for extremely stable immobilization during microsurgery (Figure 1G).

Microfluidic devices offer advantages for both spatial and temporal control of the animal's position and microenvironment at the microscale. Based on acoustic wave in a single-layer microfluidic chip, on-chip manipulation technique permitted trapping and rotational manip-

ulation *C. elegans* regardless of shape and physical properties in the x- or y-directions for extended periods of time without inducing physiological damage [78, 79]. By implementation of a cooling liquid supply through a control layer to lower a worm's temperature down to 4 °C, *C. elegans* can be immobilized with a throughput up to 400 worms per hour for short-term cooling (~2 s) [32, 52]. Alternatively, light-induced sublethal heat can be used to increase the worm temperature (up to 31–37 °C) for its immobilization [80].

Gases, including carbon dioxide (CO₂) and nitrogen (N₂), are sensed by *C. elegans* and serve as a partial and complete method to eliminate worm mobility [67, 69, 76]. By passing pure gas from a control layer into a flow layer microenvironment, *C. elegans* can be immobilized in a channel with improved sensitivity and increased resolution.

4. Microfluidic approach for *C. elegans* sensing function and behavior

In this section, we review the use of microfluidic chips for *C. elegans* investigations under controlled physical and chemical conditions that have been advantageously used, for example, as integrated biosensors for toxicological experiments and drug screening. The two major methods of assaying are behavioral and molecular (or neuronal) studies. In behavioral studies, discussed in Section 4.1, the movement is generally analyzed by observation the animal's behavior in response to stimulation (e.g., touch, drugs, odorants, food, temperature, gases, osmolytes, or light). The key issues in neuronal studies, covered by Section 4.2, are the intracellular processes and neuronal signaling.

4.1. Behavioral studies of *C. elegans*'s responses to different stimuli

C. elegans explores its surrounding environment and moves according to environmental stimuli, including temperature, chemical, electric field, and light, which are detected by 24 sensilla organs and various isolated sensor neurons [1]. Obtaining meaningful data about the mechanism of environmental sensing requires strict control over the experimental conditions. Moreover, when a high number of identical biological samples are needed to be screened, a common need and challenge of the experimental procedure is the precise manipulation of worms with an emphasis on high throughput. Microfluidics offers a straightforward solution for automation and parallelization of screening in a rapid, sensitive, and accurate manner.

The environmental cues can be applied by devices, embedded in a chip-based microfluidic system, to analyze the behavioral response of the microorganism. For example, active and automated local manipulation and chemical stimulation of the individual worms can be achieved by implementation of multilayer PDMS layers. Because of *C. elegans*' small size and its ability to grow in liquid, on-chip imaging systems and automated data processing facilitate the observation and characterization of key behavioral parameters *in vivo* with micrometer and nanometer resolution.

Locomotion. Owing to the precision achievable by microlithographic techniques, researchers have been able to investigate in-depth different locomotion patterns (by varying the size and

spacing of posts), applied muscular forces (by measuring the deflection of posts) (Figure 1D) and motility quantification (time-averaged kinetic power over the swimming cycle) [81–90]. In contrast to traditional experimental techniques, these systems permitted straightforward dynamic force detection of moving nematodes. Whereas the motion of the animals in the artificial soil device exhibited the same principal characteristics of the motion of crawling on agar, the constraints on motion caused by the posts better mimicked the complexity of *C. elegans*' natural environment [91]. To further study crawling behavior, a number of PDMS microfluidic devices were presented that consisted of sinusoidal channels of varying wavelengths [84, 86, 87].

These devices allow researchers to manipulate the oscillating body motion of the crawling animals and investigate the biophysical and neuronal mechanisms of locomotion and proprioception. Microfluidics facilitates precise environmental control that was demonstrated by modifying the chemicals' concentration of the main chamber rapidly or and immediately observing the effect on locomotion [83]. Obviously, tracking animals through such a rapid media exchange would not be possible in a larger environment.

Electrotaxis. *C. elegans* exhibits responsive behavior to electric fields, mediated by certain amphid sensory neurons. These neurons are sensitive to both the direction and strength of the electrical signal, and forced the animal to move toward a negatively charged pole [1]. Analysis of the nematode's electrotaxis provides a detailed model of how neurons function together to generate a behavioral response to electric fields. When microfluidic chambers are combined with electrodes to deliver electrical stimuli, both behavioral and neuronal screening can be performed, providing the chance to elucidate potential treatment for human muscular disorders. Many microfluidic systems were proposed for fully automated control of electro-taxis, which overcame many of the inherent problems of manual operation [49, 92–98].

Normally, worms are exposed to a uniform electric field generated by two electrodes (e.g., platinum wires) embedded in inlet and outlet reservoirs and connected to external electrical drive circuitry (Figure 2C). Exposure to direct (DC), alternating (AC), and pulsed DC electric fields in a specified range of strengths has been employed as a means of guiding nematodes in a binary manner (e.g., start and stop), for sorting, and for immobilization, aiming to provide a close look at the mechanism of neuronal signaling transduced into behavioral responses [86, 92, 93, 98–100]. Such movement-based microfluidic devices permit the differentiation of worms according to locomotive abilities and similar physiological states, for instance, to distinguish adults from larva, or healthy worms from uncoordinated, and to locate individuals defective in electric field sensing. This guiding technique allows high throughput (up to 60 worms per min) and method selectivity of 70–90 %.

The progress achieved in microfabrication technologies has made monolithic integration of electrodes into microfluidic platform possible (Figure 1F). Micropatterned electrodes on the sidewalls of microfluidic channels (i.e., without blocking optical visibility) provides a simple means of creating electrofluidic glass chips to flexibly control the movement of *C. elegans* in a sensitive and reproducible manner [101]. Placing the microelectrodes inside the microfluidic environment as close to the animal as possible allows one to create transient pores in the cell membrane, which permits the diffusion of extracellular compounds that are present in the

vicinity of the pore into the interior of the cell [102]. All of these results demonstrate the potential of using active microfluidic devices as an alternative to Petri dishes for *C. elegans* assays.

Chemicals. Microfluidics is particularly attractive for many applications where *C. elegans* are used as integrated biosensors for toxicological experiments and drug screening. Behavioral investigations in response to chemical stimuli include real-time locomotion diagnostics of *C. elegans*. The effect on worm physiology to a variety of anesthetics, such as tricaine, muscimol, sodium azide, and levamisole [29, 55, 69, 93], odors, such as hermaphrodite-conditioned media and nicotine, and odors produced by pathogenic bacteria [55, 103–108], chemicals, such as zinc ion (Zn^{2+}) and glucose [109], different osmolarity levels [66, 71], was successfully examined by precise chemical control in a time- and dose-dependent manner. In most cases, pre- and postexposure locomotion phenotypes are compared by a variety of parameters (e.g., average velocity, individual head swing orientations, etc.).

Other stimuli. The ability of integration and individual worm manipulation makes microfluidic devices attractive platforms for understanding the correlation between *C. elegans*' neuronal and behavioral responses. Based on the properties of a microfluidic device, temperature stimuli could be delivered to individual worms accurately by flexible chip design and fluidic manipulation. Behavioral mechanisms in response to temperature change is quantified in terms of an average head angle of a semi-restrained animal [74] or swimming movements of the individuals heated in a microdroplet array [107].

Although the *C. elegans* has no light-sensing organs, it modulates a response to light known as phototaxis [50, 92, 109]. To analyze *C. elegans*' sensitivity to light, wild-type and mutant nematodes are illuminated with light and their behavioral response are examined. It was experimentally demonstrated that illumination to green light is preferable for animals, while blue light triggers muscle depolarization and further body contraction.

4.2. Neuronal studies

Behavioral studies, such as physiological responses, in a whole organism population include not only movement-based analyses but also monitoring of the *C. elegans*' neuronal activity in a confined space. Coupled with microfluidic-based systems, existing neuronal recording techniques (e.g., by calcium imaging or green fluorescent protein (GFP) expression) examine neuronal responses to sensory inputs of a single animal at a time under precise environmental control. For example, it was found that immobilizing a portion of the worm can directly override rhythmic activity and may cause changes in transport parameters of the touch neuron [69, 110]. In order to explore locomotive behavior and the underlying molecular mechanism, Wang et al. monitored a subcellular distribution of the DAF-16 gene that regulates different stress responses [91]. The experiments showed an increase of DAF-16 nuclear localization, attributed to crowding stress, in a microcolumn array with intervals from 40 to 200 μm between microposts (Figure 1D). As a result, a system-level understanding of the worm's motor circuit can be obtained.

One application where microfluidics and fluorescent-based imaging open up aspects that would remain hidden from traditional laboratory techniques is drug screening. *C. elegans* can be an effective test-bed for a wide range of water-soluble chemical compounds (e.g., glycerol [30, 66, 74, 75], anticancer drugs [48], heavy metals [54], sodium chloride NaCl [58, 65, 71, 83, 111, 112], copper(II) chloride CuCl₂ [66, 74], levamisole [70], manganese [102], antibiotics [104], isoamyl alcohol [113], cyanide [114], etc.). Microfluidic network manipulation allows the automation in a high-throughput manner and under reproducible experimental conditions while analysis of the nematode's chemosensitivity provides a detailed model of how neurons function together to generate behavioral response. For example, neurotransmitters and hormones, such as 1-methyl-4-phenylpyridinium (MPP+), 6-hydroxy dopamine (6-OHDA), and rotenone, have widespread effects as chemical regulators for coordinating physiological activity throughout the body of both nematodes and humans [1]. The microfluidic-based experiments proved that MPP +, 6-OHDA, and rotenone induce mobility defects in the animal (i.e., significant reduction in speed) after treatment and was potentially neurotoxic for dopaminergic neurons [43, 51, 112].

Due to PDMS microfluidic devices, much progress has been made to overcome the limitations of precise chemical control. The effect of ageing on physiological properties of the ASH chemosensory neuron can be characterized and quantified by the direct delivery of a chemical odor to the nose of *C. elegans* [30]. To emphasize the influence of different anesthetics on subcellular activity, a microfluidic platform was used for studying the contribution of vesicle transport to synaptic growth [70]. As a result, imaging of subcellular processes, such as pre-synaptic vesicle transport, intraflagellar transport (IFT), dendritic transport, and migration of neuroblasts during early developmental stages of the nematode, has become feasible. Monitoring of neuron activity (e.g., ASH neurons) with respect to osmotic gradient, can access the pattern-generating activity (e.g., individual head swing orientations) of the chemosensory circuit [66].

Another field where polymer-based fabrication techniques have already demonstrated themselves, is in investigations of gas sensing in nematodes [69, 76, 115–117]. In order to understand how oxygen level variation causes behavioral and physiological changes, freely moving adult animals were subjected to a gas-phase oxygen gradient. Experiments showed that specific soluble guanylate cyclase homologues (GCY-31, GCY-33, GCY-35, and GCY-36), located in URX, AQR, and PQR sensory neurons, activate hypoxia or hyperoxia avoidance [115, 116].

For many applications, such as characterizing stochastic neural responses, it should be beneficial to increase experimental throughput at the expense of image resolution. Microfluidics promotes simultaneous recording of calcium transients in individual neurons from multiple animals (up to 20), and increases experimental throughput [82, 118]. Thus, a systematic characterization of chemosensory neuron responses to multiple odors, odor concentrations, and temporal patterns, as well as responses to pharmacological manipulation can be performed.

The described experiments benefit enormously from the use of microfluidic technologies. The precise handling and chemical mixing of chemicals and neurotoxins in nanoliter volume droplets tremendously decreases reagent consumption and reaction time. The combination of brightfield imaging, fluorescent imaging, and microfluidics allows *in vivo* observation of biomolecules and automated analysis of protein aggregation phenomena in *C. elegans* for amyotrophic lateral sclerosis (ALS) at unprecedented resolution [119]. The level of precision that researchers have already achieved demonstrates the potential for the dissection of neuronal function and toxin-induced neurodegeneration *in vivo*.

4.2.1. Intracellular studying techniques

Several other techniques for studying and characterization of intracellular processes, including dielectrophoresis and electrochemical impedance spectroscopy, have been adopted by researchers for whole-animal drug screening (Figure 1F) [77, 92, 120, 121]. These methods use a noninvasive electrophysiological readout of neuromuscular function and can provide high-quality neurogenetic and neuropharmacological data on nematodes. Automatic real-time monitoring and parallelization (up to 8 worms simultaneously) with throughput of up to 12 worms per hour facilitate the rapid neuroactive drug screening, e.g., effects of drugs on neurons, as well as on muscles [77, 121].

4.2.2. Microsurgery and microinjection

In combination with microfluidics and optical image analysis systems, microsurgery and microinjection are employed for *in vivo* neuronal regeneration and cell-to-cell communication studies [52, 73, 80, 122–127]. Because the nervous system is described in great detail, the role of an individual neuron can be directly studied with laser ablation experiments (Figure 1G). Using a laser nanobeam in the UV wavelength region, fluorescent-labeled whole cell ablation is possible and a single synapse removal can be achieved [124–127]. Afterward, the resulting phenotypes (e.g., degeneration and regeneration) can be examined *in vivo*. Advances in optical imaging and microfluidic methods support this procedure. The capabilities of current chip-based systems are sufficient to perform precise animal manipulations, required for high immobilization stability of the worm, and complex image-based assaying with high throughput (up to 200 animals per hour with a success rate of 89 %) [52, 122]. This provides approximately one order of magnitude improvement over manually performed axotomies (when considering study of a single population) and gives an opportunity to perform genetic screening in a reasonable timeframe to identify the molecular mechanisms involved in nerve regeneration and degeneration.

The *in vivo* injection of chemical materials that have significant implications in genetics, drug discovery, and other biological applications is another way to study the mechanisms underlying intercellular communication in *C. elegans* (Figure 1H). Using a single needle tip of the micromanipulator, localized chemical stimulation can be delivered to a single intestinal cell of the immobilized worms [123, 128].

5. Conclusions and perspectives

The advances in microfabrication technologies have demonstrated the potential of using active lab-on-a-chip (LoC) devices as an alternative to microwell plates for worm-based assays. LoC technology offers a straightforward solution to all of the problems during manual manipulation. Complex three-dimensional (3D) microenvironments have been created, where a whole population of worms is cultured and analyzed in a reproducible way. Currently available microfluidic-based systems are capable of recording from sensory neurons in animals *in vivo*, whose neuronal responses could be correlated with behavior. Microsurgery and microinjection allow the investigation of many processes, including the role of individual neurons in neuronal networks and in cell-to-cell interaction. Obviously, this is pushing forward fundamental studies in biology and biochemistry.

The use of fluorescence-based techniques and microfluidics to image the activity of specific neurons requires that animals be labeled either chemically or genetically. However, for monitoring certain biological processes, fluorescent labeling might be inconvenient or may interfere with normal behavior. Moreover, many dynamic phenomena of motile samples might be missed during impedance spectroscopy, microsurgery, and microinjection because of the long-term immobilization required for subcellular-level stabilization of *C. elegans*. This makes monitoring of actual metabolic activity impossible.

Several other approaches can be used to study the neuronal and metabolic activity of a biological system. For example, nuclear magnetic resonance imaging (MRI) and nuclear magnetic resonance spectroscopy (NMR) are two of the most information-rich methods that provide a unique opportunity to link morphological, functional, and chemically specific spectroscopic information from small volume (e.g., μl) samples (Figure 1I). MRI and NMR uses strong time-varying radio frequency (RF) fields to generate a weak specific RF response from a certain tissue type [129]. Because the technology is noninvasive and only nonionizing radiation is absorbed and emitted, it might be especially suitable for the study of *C. elegans* in the identification and quantification of metabolites (intermediate products of metabolism) within the metabolic pathway *in vivo* [130–136].

In many of the reviewed research articles, the easy integration of microfluidic control and detection modules was a key factor in helping to link *in vitro* and *ex vivo* experimental investigations. The ability of *C. elegans* tracking in real time (i.e., with minimal latency) for further diagnostic applications could provide a close look at the cellular, molecular, and genetic levels. Consequently, an understanding of the underlying molecular mechanisms in multicellular model organisms would provide a unique opportunity to unthread analogous and complex biological processes in humans. This certainly will promote more automated and higher throughput applications in the future.

Acknowledgements

We gratefully acknowledge financial support from the European Research Council (ERC) (contract number 290586 from 1.07.2012), which funded this work.

Author details

Natalia A. Bakhtina^{1,2*}, Neil MacKinnon² and Jan G. Korvink²

*Address all correspondence to: natalia.bakhtina@kit.edu

1 Laboratory for Simulation, IMTEK – Department of Microsystems Engineering, University of Freiburg, Freiburg, Germany

2 Korvink's Group, Institute of Microstructure Technology (IMT), Karlsruhe Institute of Technology (KIT), Germany

References

- [1] Riddle DL, Blumenthal T, Meyer BJ, Priess JR. *C. elegans* II, 1997.
- [2] Markaki M, Tavernarakis N. Modeling human diseases in *Caenorhabditis elegans*. *Biotechnol. J.* 2010, 5: 1261–1276. DOI: 10.1002/biot.201000183.
- [3] Alexander AG, Marfil V, Li C. Use of *Caenorhabditis elegans* as a model to study Alzheimer's disease and other neurodegenerative diseases. *Front Genet.* 2014, 5: 1–21. DOI: 10.3389/fgene.2014.00279.
- [4] Duffy DC, McDonald JC, Schueller OJA, Whitesides G. Rapid prototyping of microfluidic systems in poly(dimethylsiloxane). *Anal. Chem.* 1998, 70: 4974–4984. DOI: 10.1021/ac980656z.
- [5] Sivagnanam V, Gijs MAM. Exploring living multicellular organisms, organs, and tissues using microfluidic systems. *Chem. Rev.* 2013, 113: 3214–3247. DOI: 10.1021/cr200432q.
- [6] Bakhtina NA, Korvink JG. Microfluidic laboratories for *C. elegans* enhance fundamental studies in biology. *RSC Adv.* 2014, 4: 4691–4709. DOI: 10.1039/c3ra43758b.
- [7] Ben-Yakar A, Chronis N, Lu H. Microfluidics for the analysis of behavior, nerve regeneration, and neural cell biology in *C. elegans*. *Curr. Opin. Neurobiol.* 2009, 19: 561–567. DOI: 10.1016/j.conb.2009.10.010.
- [8] Chronis N. Worm chips: microtools for *C. elegans* biology. *Lab Chip* 2010, 10: 432–437. DOI: 10.1039/b919983g.
- [9] Taylor AM, Jeon NL. Micro-scale and microfluidic devices for neurobiology. *Curr. Opin. Neurobiol.* 2010, 20: 640–647. DOI: 10.1016/j.conb.2010.07.011.
- [10] Crane MM, Chung K, Stirman J, Lu H. Microfluidics-enabled phenotyping, imaging, and screening of multicellular organisms. *Lab Chip* 2010, 10: 1509–1517. DOI: 10.1039/b927258e.

- [11] Jian-Ping J, Fan Y, Xin-Chun L, Yan-Yan Y, Zuan-Guang C. Advances on biomedical research in *Caenorhabditis elegans* based on microfluidic device. *Prog. Biochem. Biophys.* 2011, 38: 877–883. DOI: 10.3724/SP.J.1206.2011.00079.
- [12] Shi W, Wen H, Lin B, Qin J. Microfluidic platform for the study of *Caenorhabditis elegans*. *Top. Curr. Chem.* 2011, 304: 323–338. DOI: 10.1007/128_2011_145.
- [13] Yanik MF, Rohde CB, Pardo-Martin C. Technologies for micromanipulating, imaging, and phenotyping small invertebrates and vertebrates. *Annu. Rev. Biomed. Eng.* 2011, 13: 185–217. DOI: 10.1146/annurev-bioeng-071910-124703.
- [14] Xu X, Kim SK. The early bird catches the worm: new technologies for the *Caenorhabditis elegans* toolkit. *Nat. Rev. Genet.* 2011, 12: 793–801. DOI: 10.1038/nrg3050.
- [15] Wlodkowic D, Khoshmanesh K, Akagi J, Williamsand DE, Cooper JM. Wormometry-on-a-chip: innovative technologies for in situ analysis of small multicellular organisms. *Cytometry Part A* 2011, 79: 799–813. DOI: 10.1002/cyto.a.21070.
- [16] San-Miguel A, Lu H. Microfluidics as a tool for *C. elegans* research, in *WormBook*, ed. The *C. elegans* Research Community, 2013. DOI: 10.1895/wormbook.1.162.1.
- [17] Rezai P, Salam S, Selvaganapathy PR, Gupta BP. Microfluidic systems to study the biology of human diseases and identify potential therapeutic targets in *C. elegans*, in *Integrated Microsystems*, ed. Iniewski K, CRC Press, 581–608; 2011.
- [18] Hui W, JianHua Q. Analysis of *Caenorhabditis elegans* in microfluidic devices. *Sci. China: Chem.* 2012, 55: 484–493. DOI: 10.1007/s11426-012-4541-x.
- [19] Wlodkowic D, Khoshmanesh K, Akagi J, Williams DE, Cooper JM. Wormometry-on-a-chip: innovative technologies for in-situ analysis of small multicellular organisms. *Cytometry, Part A* 2011, 79: 799–813. DOI: 10.1002/cyto.a.21070.
- [20] Gurkan UA, Moon S, Geckil H, Xu F, Wang S, Lu TJ, Demirci U. Miniaturized lensless imaging systems for cell and microorganism visualization in point-of-care testing. *Biotechnol. J.* 2011, 6: 138–149. DOI: 10.1002/biot.201000427.
- [21] Zhu H, Isikman SO, Mudanyali O, Greenbaum A, Ozcan A. Optical imaging techniques for point-of-care diagnostics. *Lab Chip* 2013, 13: 51–67. DOI: 10.1039/c2lc40864c.
- [22] Wu J, Zheng G, Lee LM. Optical imaging techniques in microfluidics and their applications. *Lab Chip* 2012, 12: 3566–3575. DOI: 10.1039/c2lc40517b.
- [23] Heng X, Erickson D, Baugh LR, Yaqoob Z, Sternberg PW, Psaltis D, Yang C. Optofluidic microscopy — a method for implementing a high resolution optical microscope on a chip. *Lab Chip* 2006, 6: 1274–1276. DOI: 10.1039/B604676B.
- [24] Cui X, Lee LM, Heng X, Zhong W, Sternberg PW, Psaltis D, Yang C. Lensless high-resolution on-chip optofluidic microscopes for *Caenorhabditis elegans* and cell imaging. *Proc. Natl. Acad. Sci. U. S. A.* 2008, 105: 10670–10675. DOI: 10.1073/pnas.0804612105.

- [25] Lange D, Storment CW, Conley CA, Kovacs GTA. A microfluidic shadow imaging system for the study of the nematode *Caenorhabditis elegans* in space. *Sens. Actuat. B* 2005, 107: 904–914. DOI: 10.1016/j.snb.2004.12.039.
- [26] Isikman SO, Sencan I, Mudanyali O, Bishara W, Oztoprak C, Ozcan A. Lens-free optical tomographic microscope with a large imaging volume on a chip. *Lab Chip*, 2010, 10: 1109–1112. DOI: 10.1073/pnas.1015638108.
- [27] Bishara W, Zhu H, Ozcan A. Holographic opto-fluidic microscopy. *Opt. Express* 2010, 18: 27499–27510. DOI: 10.1364/OE.18.027499.
- [28] Coskun AF, Sencan I, Su T, Ozcan A. Lensfree fluorescent on-chip imaging of transgenic *Caenorhabditis elegans* over an ultra-wide field-of-view. *PLoS One* 2011, 6: e15955. DOI: 10.1371/journal.pone.0015955.
- [29] Liu P, Martin RJ, Dong L. Micro-electro-fluidic grids for nematodes: A lens-less, image-sensor-less approach for on-chip tracking of nematode locomotion. *Lab Chip* 2013, 13: 650–661. DOI: 10.1039/c2lc41174a.
- [30] Chokshi TV, Bazopoulou D, Chronis N. An automated microfluidic platform for calcium imaging of chemosensory neurons in *Caenorhabditis elegans*. *Lab Chip* 2010, 10: 2758–2763. DOI: 10.1039/c004658b.
- [31] Rohde CB, Zeng F, Gonzalez-Rubio R, Angel M, Yanik MF. Microfluidic system for on-chip high-throughput whole-animal sorting and screening at subcellular resolution. *Proc. Natl. Acad. Sci. U. S. A.* 2007, 104: 13891–13895. DOI: 10.1073/pnas.0706513104.
- [32] Chung K, Crane MM, Lu H. Automated on-chip rapid microscopy, phenotyping and sorting of *C. elegans*. *Nat. Methods* 2008, 5: 637–643. DOI: 10.1038/nmeth.1227.
- [33] Yan Y, Ng LF, Ng LT, Choi KB, Gruber J, Bettiol AA, Thakor NV. A continuous-flow *C. elegans* sorting system with integrated optical fiber detection and laminar flow switching. *Lab Chip* 2014, 14: 4000–4006. DOI: 10.1039/c4lc00494a.
- [34] Caceres IC, Valmas N, Hilliard MA, Lu H. Laterally orienting *C. elegans* using geometry at microscale for high-throughput visual screens in neurodegeneration and neuronal development studies. *PLoS One* 2012, 7: e35037. DOI: 10.1371/journal.pone.0035037.
- [35] Li S, Stone HA, Murphy CT. A microfluidic device and automatic counting system for the study of *C. elegans* reproductive aging. *Lab Chip* 2015, 15: 524–531. DOI: 10.1039/c4lc01028k.
- [36] Hulme SE, Shevkopylas SS, McGuigan AP, Apfeld J, Fontana W, Whitesides GM. Lifespan-on-a-chip: microfluidic chambers for performing lifelong observation of *C. elegans*. *Lab Chip* 2010, 10: 589–597. DOI: 10.1039/b919265d.

- [37] Krajniak J, Lu H. Long-term high-resolution imaging and culture of *C. elegans* in chip-gel hybrid microfluidic device for developmental studies. *Lab Chip* 2010, 10: 1862–1868. DOI: 10.1039/c001986k.
- [38] Kim N, Dempsey CM, Zoval JV, Sze J, Madou MJ. Automated microfluidic compact disc (CD) cultivation system of *Caenorhabditis elegans*. *Sens. Actuat. B* 2007, 122: 511–518. DOI: 10.1016/j.snb.2006.06.026.
- [39] Bringmann H. Agarose hydrogel microcompartments for imaging sleep- and wake-like behavior and nervous system development in *Caenorhabditis elegans* larvae. *J. Neurosci. Methods* 2011, 201: 78–88. DOI: 10.1016/j.jneumeth.2011.07.013.
- [40] Xian B, Shen J, Chen W, Sun N, Qiao N, Jiang D, Yu T, Men Y, Pang Z, Kaeberlein M, Huang Y, Han JD. WormFarm: a quantitative control and measurement device toward automated *Caenorhabditis elegans* aging analysis. *Aging Cell* 2013, 12: 398–409. DOI: 10.1111/accel.12063.
- [41] Jung J, Nakajima M, Tajima H, Huang Q, Fukuda T J. A microfluidic device for the continuous culture and analysis of *Caenorhabditis elegans* in a toxic aqueous environment. *Micromech. Microeng.* 2013, 23: 085008. DOI: 10.1088/0960-1317/23/8/085008.
- [42] Aubry G, Zhan M, Lu H. Hydrogel-droplet microfluidic platform for high-resolution imaging and sorting of early larval *Caenorhabditis elegans*. *Lab Chip* 2015, 15: 1424–1431. DOI: 10.1039/c4lc01384k.
- [43] Shi W, Qin J, Ye N, Lin B. Droplet-based microfluidic system for individual *Caenorhabditis elegans* assay. *Lab Chip* 2008, 8: 1432–1435. DOI: 10.1039/b808753a.
- [44] Clausell-Tormos J, Lieber D, Baret J, El-Harrak A, Miller OJ, Frenz L, Blouwolff J, Humphry KJ, Koester S, Duan H, Holtze C, Weitz DA, Griffiths AD, Merten CA. Droplet-based microfluidic platforms for the encapsulation and screening of mammalian cells and multicellular organisms. *Chem. Biol.* 2008, 15: 427–437. DOI: 10.1016/j.chembiol.2008.04.004.
- [45] Uppaluri S, Brangwynne CP. A size threshold governs *Caenorhabditis elegans* developmental progression. *Proc. R. Soc. B* 282: 20151283. DOI:10.1098/rspb.2015.1283.
- [46] Turek M, Besseling J, Bringmann H. Agarose microchambers for long-term calcium imaging of *Caenorhabditis elegans*. *J. Vis. Exp.* 2015, 100: e52742 (8 pp.), DOI: 10.3791/52742.
- [47] Turek M, Besseling J, Spies J, Koenig S, Bringmann H. Sleep-active neuron specification and sleep induction require FLP-11 neuropeptides to systemically induce sleep. *eLife* 2016, 5: e12499 (18 pp.). DOI: 10.7554/eLife.12499.
- [48] Cornaglia M, Mouchiroud L, Marette A, Narasimhan S, Lehnert T, Jovaisaite V, Auwerx J, Gijs MAM. An automated microfluidic platform for *C. elegans* embryo arraying, phenotyping, and long-term live imaging. *Scientific Reports* 2015, 5:10192 (13 pp.). DOI: 10.1038/srep10192.

- [49] Wang X, Hu R, Ge A, Hu L, Wang S, Feng X, Du W, Liu B. Highly efficient microfluidic sorting device for synchronizing developmental stages of *C. elegans* based on deflecting electrotaxis. *Lab Chip* 2015, 15: 2513–2521. DOI: 10.1039/c5lc00354g.
- [50] Allen PB, Sgro AE, Chao DL, Doepker BE, Edgar JS, Shen K, Chiu DT. Single-synapse ablation and long-term imaging in live *C. elegans*. *J. Neurosci. Methods* 2008, 173: 20–26. DOI: 10.1016/j.jneumeth.2008.05.007.
- [51] Ma H, Jiang L, Shi W, Qin J, Lin B. A programmable microvalve-based microfluidic array for characterization of neurotoxin-induced responses of individual *C. elegans*. *Biomicrofluidics* 2009, 3: 044114. DOI: 10.1063/1.3274313.
- [52] Chung K, Lu H. Automated high-throughput cell microsurgery on-chip. *Lab Chip* 2009, 9: 2764–2766. DOI: 10.1039/b910703g.
- [53] Yang J, Chen Z, Ching P, Shi Q, Li X. An integrated microfluidic platform for evaluating *in vivo* antimicrobial activity of natural compounds using a whole-animal infection model. *Lab Chip* 2013, 13: 3373–3382. DOI: 10.1039/c3lc50264c.
- [54] Wen H, Shi W, Qin J. Multiparameter evaluation of the longevity in *C. elegans* under stress using an integrated microfluidic device. *Biomed. Microdevices* 2012, 14: 721–728. DOI: 10.1007/s10544-012-9652-9.
- [55] Chung K, Zhan M, Srinivasan J, Sternberg PW, Gong E, Schroeder FC, Lu H. Microfluidic chamber arrays for whole-organism high-throughput chemical screening. *Lab Chip* 2011, 11: 3689–3697. DOI: 10.1039/c1lc20400a.
- [56] Zeng F, Rohde CB, Yanik MF. Sub-cellular precision on-chip small-animal immobilization, multi-photon imaging and femtosecond-laser manipulation. *Lab Chip* 2008, 8: 653–656. DOI: 10.1039/b804808h.
- [57] Guo SX, Bourgeois F, Chokshi T, Durr NJ, Hilliard MA, Chronis N, Ben-Yakar A. Femtosecond laser nanoaxotomy lab-on-a-chip for *in vivo* nerve regeneration studies. *Nat. Methods* 2008, 5: 531–533. DOI: 10.1038/NMETH.1203.
- [58] Yang J, Chen Z, Yang F, Wang S, Hou F. A microfluidic device for rapid screening of chemotaxis-defective *Caenorhabditis elegans* mutants. *Biomed. Microdevices* 2013, 15: 211–220. DOI: 10.1007/s10544-012-9719-7.
- [59] Crane MM, Chung K, Lu H. Computer-enhanced high-throughput genetic screens of *C. elegans* in a microfluidic system. *Lab Chip* 2009, 9: 38–40. DOI: 10.1039/b813730g.
- [60] Crane MM, Stirman JN, Ou CY, Kurshan PT, Rehg JM, Shen K, Lu H. Autonomous screening of *C. elegans* identifies genes implicated in synaptogenesis. *Nat. Methods* 2012, 9: 977–980. DOI: 10.1038/nmeth.2141.
- [61] Ai X, Zhuo W, Liang Q, McGrath PT, Lu H. A high-throughput device for size based separation of *C. elegans* developmental stages. *Lab Chip* 2014, 14: 1746–1752. DOI: 10.1039/c3lc51334c.

- [62] Solvas XC, Geier FM, Leori AM, Bundy JG, Edela JB, Mello AJ. High-throughput age synchronisation of *Caenorhabditis elegans*. Chem. Commun. 2011, 47: 9801–9803. DOI: 10.1039/c1cc14076k.
- [63] Dong L, Cornaglia M, Lehnert T, Gijs MAM. Versatile size-dependent sorting of *C. elegans* nematodes and embryos using a tunable microfluidic filter structure. Lab Chip 2016, 16: 574–585. DOI: 10.1039/C5LC01328C.
- [64] Lee H, Kim SA, Coakley S, Mugno P, Hammarlund M, Hilliard MA, Lu H. A multi-channel device for high-density targetselective stimulation and long-term monitoring of cells and subcellular features in *C. elegans*. Lab Chip 2014, 14: 4513–4522. DOI: 10.1039/c4lc00789a.
- [65] Wang Y, Wang J, Du W, Feng XJ, Liu B. Identification of the neuronal effects of ethanol on *C. elegans* by *in vivo* fluorescence imaging on a microfluidic chip. Anal. Bioanal. Chem. 2011, 399: 3475–3481. DOI: 10.1007/s00216-010-4148-z.
- [66] Chronis N, Zimmer M, Bargmann C. Microfluidics for *in vivo* imaging of neuronal and behavioral activity in *Caenorhabditis elegans*. Nat. Methods 2007, 4: 727–731. DOI: 10.1038/nmeth1075.
- [67] Chokshi TV, Ben-Yakar A, Chronis N. CO₂ and compressive immobilization of *C. elegans* on-chip. Lab Chip 2009, 9: 151–157. DOI: 10.1039/b807345g.
- [68] Hulme SE, Shevkopyas SS, Apfeld J, Fontana W, Whitesides GM. A microfabricated array of clamps for immobilizing and imaging *C. elegans*. Lab Chip 2007, 7: 1515–1523. DOI: 10.1039/b707861g.
- [69] Mondal S, Ahlawat S, Rau K, Venkataraman V, Koushika SP. Imaging *in vivo* neuronal transport in genetic model organisms using microfluidic devices. Traffic 2011, 12: 372–385. DOI: 10.1111/j.1600-0854.2010.01157.x.
- [70] Mondal S, Ahlawat S, Rau K, Venkataraman V, Koushika SP. Imaging *in vivo* neuronal transport in genetic model organisms using microfluidic devices. Traffic 2011, 12: 372–385. DOI: 10.1111/j.1600-0854.2010.01157.x.
- [71] McCormick KE, Gaertner BE, Sottile M, Phillips PC, Lockery SR. Microfluidic Devices for analysis of spatial orientation behaviors in semi-restrained *Caenorhabditis elegans*. PLoS One 2011, 6: e25710. DOI: 10.1371/journal.pone.0025710.
- [72] Gilleland CL, Rohde CB, Zeng F, Yanik MF. Microfluidic immobilization of physiologically active *Caenorhabditis elegans*. Nat. Protoc. 2010, 5: 1888–1902. DOI: 10.1038/nprot.2010.143.
- [73] Rohde CB, Gilleland C, Samara C, Norton S, Haggarty S, Yanik MF. Microfluidic *in vivo* screen identifies compounds enhancing neuronal regeneration. Conf. Proc. IEEE Eng. Med. Biol. Soc. 2009, 5950–5952. DOI: 10.1109/IEMBS.2009.5334771.

- [74] Wang J, Feng X, Du W, Liu B. Microfluidic worm-chip for *in vivo* analysis of neuronal activity upon dynamic chemical stimulations. *Anal. Chim. Acta.* 2011, 701: 23–28. DOI: 10.1016/j.aca.2011.06.007.
- [75] Wang J, Li Z, Xu Z, Hu L, Feng X, Chen M, Du W, Wu Z, Luo Q, Xu T, Liu B. Development of an integrated microfluidic device for evaluating of *in vivo* chemo-sensing of intact *Caenorhabditis elegans*. *Sens. Actuat. B* 2013, 178: 343–349. DOI: 10.1016/j.snb.2012.12.102.
- [76] Hu L, Wang J, Feng X, Du W, Liu B. Microfluidic device for analysis of gas-evoked neuronal sensing in *C. elegans*. *Sens. Actuat. B: Chem* 2015, 209: 109–115. DOI: 10.1016/j.snb.2014.11.081.
- [77] Lockery SR, Hulme SE, Roberts WM, Robinson KJ, Laromaine A, Lindsay TH, Whitesides GM, Weeks JC. A microfluidic device for whole-animal drug screening using electrophysiological measures in the nematode *C. elegans*. *Lab Chip* 2012, 12: 2211–2220. DOI: 10.1039/c2lc00001f.
- [78] Ding X, Lin SS, Kiraly B, Yue H, Li S, Chiang I, Shi J, Benkovic SJ, Huang TJ. On-chip manipulation of single microparticles, cells, and organisms using surface acoustic waves. *Proc. Natl. Acad. Sci. U.S.A.* 2012, 1–5. DOI: 10.1073/pnas.1209288109.
- [79] Ahmed D, Ozcelik A, Bojanala N, Nama N, Upadhyay A, Chen Y, Hanna-Rose W, Huang TJ. Rotational manipulation of single cells and organisms using acoustic waves. *Nat. Commun.* 2016, 7: 11085 (11 pp.). DOI: 10.1038/ncomms11085.
- [80] Chuang H, Chen H, Chen C, Chiu W. Immobilization of the nematode *Caenorhabditis elegans* with addressable light-Induced heat knockdown (ALINK). *Lab Chip* 2013, 13: 2980–2989. DOI: 10.1039/c3lc50454a.
- [81] Qiu Z, Tu L, Huang L, Zhu T, Nock V, Yu E, Liu X, Wang W. An integrated platform enabling optogenetic illumination of *Caenorhabditis elegans* neurons and muscular force measurement in microstructured environments. *Biomicrofluidics* 2015, 9: 014123. DOI: 10.1063/1.4908595.
- [82] Larsch J, Ventimiglia D, Bargmann CI, Albrecht DR. High-throughput imaging of neuronal activity in *Caenorhabditis elegans*. *PNAS* 2013, 110: e4266 (7 pp.). DOI: 10.1073/pnas.1318325110.
- [83] Lockery SR, Lawton KJ, Doll JC, Faumont S, Coulthard SM, Thiele TR, Chronis N, McCormick KE, Goodman MB, Pruitt BL. Artificial dirt: microfluidic substrates for nematode neurobiology and behavior. *J. Neurophysiol.* 2008, 99: 3136–3143. DOI: 10.1152/jn.91327.2007.
- [84] Park S, Hwang H, Nam S, Martinez F, Austin RH, Ryu WS. Enhanced *Caenorhabditis elegans* locomotion in a structured microfluidic environment. *PLoS One* 2008, 3: e2550. DOI: 10.1371/journal.pone.0002550.

- [85] Johari S, Nock V, Alkaisi MM, Wang W. On-chip analysis of *C. elegans* muscular forces and locomotion patterns in microstructured environments. *Lab Chip* 2013, 13: 1699–1707. DOI: 10.1039/c3lc41403e.
- [86] Han B, Kim D, Ko UH, Shin JH. A sorting strategy for *C. elegans* based on size-dependent motility and electrotaxis in a micro-structured channel. *Lab Chip* 2012, 12: 4128–4134. DOI: 10.1039/C2LC40209B.
- [87] Parashar A, Lycke R, Carr JA, Pandey S. Amplitude-modulated sinusoidal microchannels for observing adaptability in *C. elegans* locomotion. *Biomicrofluidics* 2011, 5: 024112–024119. DOI: 10.1063/1.3604391.
- [88] Doll JC, Harjee N, Klejwa N, Kwon R, Coulthard SM, Petzold B, Goodman MB, Pruitt BL. SU-8 force sensing pillar arrays for biological measurements. *Lab Chip* 2009, 9: 1449–1454. DOI: 10.1039/b818622g.
- [89] Oliver CR, Gourgou E, Bazopoulou D, Chronis N, Hart AJ. On-demand isolation and manipulation of *C. elegans* by In Vitro maskless photopatterning. *PLoS One* 2016, 11: e0145935 (16 pp.). DOI:10.1371/journal.pone.0145935.
- [90] Kuo WJ, Sie YS, Chuang HS. Characterizations of kinetic power and propulsion of the nematode *Caenorhabditis elegans* based on a micro-particle image velocimetry system. *Biomicrofluidics* 2014, 8: 024116. DOI: 10.1063/1.4872061.
- [91] Wang X, Tang L, Xia Y, Hu L, Feng X, Du W, Liu B. Stress response of *Caenorhabditis elegans* induced by space crowding in a micro-column array chip. *Integr. Biol.* 2013, 5: 728–737. DOI: 10.1039/C3IB20289E.
- [92] Chuang H, Raizen D, Lamb A, Dabbish N, Bau H. Dielectrophoresis of *Caenorhabditis elegans*. *Lab Chip* 2011, 11: 599–604. DOI: 10.1039/C0LC00532K.
- [93] Carr JA, Parashar A, Gibson R, Robertson AP, Martin RJ, Pandey S. A microfluidic platform for high-sensitivity, real-time drug screening on *C. elegans* and parasitic nematodes. *Lab Chip* 2011, 11: 2385–2396. DOI: 10.1039/C1LC20170K.
- [94] Rezai P, Salam S, Selvaganapathy PR, Gupta BP. Effect of pulse direct current signals on electrotactic movement of nematodes *Caenorhabditis elegans* and *Caenorhabditis briggsae*. *Biomicrofluidics* 2011, 5: 044116. DOI: 10.1063/1.3665224.
- [95] Rezai P, Siddiqui A, Salam S, Selvaganapathy PR, Gupta BP. Behavior of *Caenorhabditis elegans* in alternating electric field and its application to their localization and control. *Appl. Phys. Lett.* 2010, 96: 153702 (3 pp.). DOI: 10.1063/1.3383223.
- [96] Rezai P, Siddiqui A, Selvaganapathy PR, Gupta BP. Electrical sorting of *Caenorhabditis elegans*. *Lab Chip* 2012, 12: 1831–1840. DOI: 10.1039/c2lc20967e.
- [97] Rezai P, Siddiqui A, Selvaganapathy PR, Gupta BP. Electrotaxis of *Caenorhabditis elegans* in a microfluidic environment. *Lab Chip* 2010, 10: 220–226. DOI: 10.1039/B917486A.

- [98] Tong J, Rezai P, Salam S, Selvaganapathy PR, Gupta BP. Microfluidic-based electro-taxis for on-demand quantitative analysis of *Caenorhabditis elegans*' locomotion. *J. Vis. Exp.* 2013, 75: e50226. DOI: 10.3791/50226.
- [99] Maniere X, Lebois F, Matic I, Ladoux B, Meglio JD, Hersen P. Running worms: *C. elegans* self-sorting by electro-taxis. *PLoS One* 2011, 6: e16637. DOI: 10.1371/journal.pone.0016637.
- [100] Jung J, Nakajima M, Takeuchi M, Najdovski Z, Huang Q, Fukuda T. Microfluidic device to measure the speed of *C. elegans* using the resistance change of the flexible electrode. *Micromachines* 2016, 7: 50 (12 pp.). DOI: 10.3390/mi7030050.
- [101] Xu J, Wu D, Ip JY, Midorikawaa K, Sugioka K. Vertical sidewall electrodes monolithically integrated into 3D glass microfluidic chips using water-assisted femtosecond-laser fabrication for *in situ* control of electro-taxis. *RSC Adv.* 2015, 5: 24072–24080. DOI: 10.1039/c5ra00256g.
- [102] Zhang B, Li Y, He Q, Qin J, Yu Y, Li X, Zhang L, Yao M, Liu J, Chen Z. Microfluidic platform integrated with worm-counting setup for assessing manganese toxicity. *Bio-microfluidics* 2014, 8: 054110. DOI: 10.1063/1.4896663.
- [103] Zhang Y, Lu H, Bargmann CI. Pathogenic bacteria induce aversive olfactory learning in *Caenorhabditis elegans*. *Nature* 2005, 438: 179–184. DOI: 10.1038/nature04216.
- [104] Chalasani SH, Chronis N, Tsunozaki M, Gray JM, Ramot D, Goodman MB, Bargmann CI. Dissecting a circuit for olfactory behaviour in *Caenorhabditis elegans*. *Nature* 2007, 450: 63–70. DOI: 10.1038/nature06292.
- [105] Zhang Y, Lu H, Bargmann CI. Pathogenic bacteria induce aversive olfactory learning in *Caenorhabditis elegans*. *Nature* 2005, 438: 179–184. DOI: 10.1038/nature04216.
- [106] Albrecht DR, Bargmann CI. High-content behavioral analysis of *Caenorhabditis elegans* in precise spatiotemporal chemical environments. *Nat. Methods* 2011, 8: 599–605. DOI: 10.1038/nmeth.1630.
- [107] Luo L, Gabel CV, Ha H, Zhang Y, Samuel ADT. Olfactory behavior of swimming *C. elegans* analyzed by measuring motile responses to temporal variations of odorants. *J. Neurophysiol.* 2008, 99: 2617–2625. DOI: 10.1152/jn.00053.2008.
- [108] Stirman JN, Brauner M, Gottschalk A, Lu H. High-throughput study of synaptic transmission at the neuromuscular junction enabled by optogenetics and microfluidics. *J. Neurosci. Methods* 2010, 191: 90–93. DOI: 10.1016/j.jneumeth.2010.05.019.
- [109] Song P1, Zhang W, Sobolevski A, Bernard K, Hekimi S, Liu X. A microfluidic device for efficient chemical testing using *Caenorhabditis elegans*. *Biomed. Microdevices.* 2015, 17: 38–48. DOI: 10.1007/s10544-015-9939-8.
- [110] Wen Q, Po MD, Hulme E, Chen S, Liu X, Kwok SW, Gershow M, Leifer AM, Butler V, C Fang-Yen, Kawano T, Schafer WR, Whitesides G, Wyart M, Chklovskii DB, Zhen M, Samuel ADT. Proprioceptive coupling within motor neurons drives *C. ele-*

- gans* forward locomotion. *Neuron* 2012, 76: 750–761. DOI: 10.1016/j.neuron.2012.08.039.
- [111] Hwang H, Kim E, Kim SH, Park S. A sensitive *C. elegans* chemotaxis assay using microfluidic device generating a linear gradient of chemoeffectors. *Bull. Korean Chem. Soc.* 2015, 36: 1096–1099. DOI: 10.1002/bkcs.10201.
- [112] Salam S, Ansari A, Amon S, Rezai P, Selvaganapathy PR, Mishra RK, Gupta BP. A microfluidic phenotype analysis system reveals function of sensory and dopaminergic neuron signaling in *C. elegans* electrostatic swimming behavior. *Worm* 2013, 2: e24558. DOI: 10.4161/worm.24558.
- [113] Chalasani SH, Chronis N, Tsunozaki M, Gray JM, Ramot D, Goodman MB, Bargmann CI. Dissecting a circuit for olfactory behaviour in *Caenorhabditis elegans*. *Nature* 2007, 450: 63–70. DOI: 10.1038/nature06292.
- [114] Saldanha JN, Parashar A, Pandey S, Powell-Coffman JA. Multiparameter behavioral analyses provide insights to mechanisms of cyanide resistance in *Caenorhabditis elegans*. *Toxicol. Sci.* 2013, 135: 156–168. DOI: 10.1093/toxsci/kft138.
- [115] Gray JM, Karow DS, Lu H, Chang AJ, Chang JS, Ellis RE, Marletta MA, Bargmann CI. Oxygen sensation and social feeding mediated by a *C. elegans* guanylate cyclase homologue. *Nature* 2004, 430: 317–322. DOI: 10.1038/nature02714.
- [116] Zimmer M, Gray JM, Pokala N, Chang AJ, Karow DS, Marletta MA, Hudson ML, Morton DB, Chronis N, Bargmann CI. Neurons detect increases and decreases in oxygen levels using distinct guanylate cyclases. *Neuron* 2009, 61: 865–879. DOI: 10.1016/j.neuron.2009.02.013.
- [117] Santos SI, Mathew M, Loza-Alvarez P. Real time imaging of femtosecond laser induced nano-neurosurgery dynamics in *C. elegans*. *Opt. Express* 2010, 18: 364–377. DOI: 10.1364/OE.18.000364.
- [118] Buonanno M, Garty G, Grad M, Gendrel M, Hobert O, Brenner DJ. Microbeam irradiation of *C. elegans nematode* in microfluidic channels. *Radiat. Environ. Biophys.* 2013, 52: 531–537. DOI 10.1007/s00411-013-0485-6.
- [119] Cornaglia M, Krishnamani G, Mouchiroud L, Sorrentino V, Lehnert T, Auwerx J, Gijs MAM. Automated longitudinal monitoring of in vivo protein aggregation in neurodegenerative disease *C. elegans* models. *Mol. Neurodegener* 2016, 11: 1–13. DOI: 10.1186/s13024-016-0083-6.
- [120] Hu C, O'Connor V, Holden-Dye L, Morgan H. *Conf. Proc. MicroTAS 2013*, pp. 1441–1443. DOI: 10.13140/2.1.1565.0244.
- [121] Hu C, Dillon J, Kearn J, Murray C, O'Connor V, Holden-Dye L, Morgan H. Neuro-Chip: a microfluidic electrophysiological device for genetic and chemical biology screening of *Caenorhabditis elegans* adult and larvae. *PLoS One* 2013, 8: e64297. DOI: 10.1371/journal.pone.0064297.

- [122] Gokce SK, Guo SX, Ghorashian N, Everett WN, Jarrell T, et al. (2014) A fully automated microfluidic femtosecond laser axotomy platform for nerve regeneration studies in *C. elegans*. PLoS One 2014, 9: e113917 (28 pp.). DOI: 10.1371/journal.pone.0113917.
- [123] Zhao X, Xu F, Tang L, Du W, Feng X, Liu BF. Microfluidic chip-based *C. elegans* microinjection system for investigating cell-cell communication *in vivo*. Biosens. Bioelectron. 2013, 50: 28–34. DOI: 10.1016/j.bios.2013.06.024.
- [124] Gilleland CL, Rohde CB, Zeng F, Yanik MF. Microfluidic immobilization of physiologically active *Caenorhabditis elegans*. Nat. Protoc. 2010, 5: 1888–1902. DOI: 10.1038/nprot.2010.143.
- [125] Ben-Yakar A, Bourgeois F. Ultrafast laser nanosurgery in microfluidics for genome-wide screenings. Curr. Opin. Biotechnol. 2009, 20: 100–105. DOI: 10.1016/j.copbio.2009.01.008.
- [126] Samara C, Rohde CB, Gilleland CL, Norton S, Haggarty SJ, Yanik MF. Large-scale *in vivo* femtosecond laser neurosurgery screen reveals small-molecule enhancer of regeneration. Proc. Natl. Acad. Sci. U. S. A. 2010, 107: 18342–18347. DOI: 10.1073/pnas.1005372107.
- [127] Fang-Yen C, Gabel CV, Samuel ADT, Bargmann CI, Avery LS. Laser microsurgery in *Caenorhabditis elegans*. Methods Cell Biol. 2012, 107: 177–206. DOI: 10.1016/B978-0-12-394620-1.00006-0.
- [128] Song P, Dong X, Liu X. A microfluidic device for automated, high-speed microinjection of *Caenorhabditis elegans*. Biomicrofluidics 2016, 10: 011912 (12 pp.). DOI: 10.1063/1.4941984.
- [129] Callaghan P. Principles of nuclear magnetic resonance microscopy, UK: Oxford Science Publications, Corby; 1991.
- [130] Trautwein C, Spengler N, MacKinnon N, Wallrabe U, Eimer S, Korvink JG. Quantitative metabolomics of the nematode *C. elegans* in a microfluidic chip device with NMR spectroscopy. Conf. Proc. Euromar 2014, 29 June– 3 July, Zurich, Switzerland.
- [131] Spengler N, Moazenzadeh A, Meier RC, Badilita V, Korvink JG, Wallrabe U. Microfabricated Helmholtz coil featuring disposable microfluidic sample inserts for applications in nuclear magnetic resonance. J. Micromech. Microeng. 2014, 24: 034004 (10 pp.). DOI: 10.1088/0960-1317/24/3/034004.
- [132] Gruschke OG, Baxan N, Clad L, Kratt K, von Elverfeldt D, Peter A, Hennig J, Badilita V, Wallrabe U, Korvink JG. Lab on a chip phased-array MR multi-platform analysis system. Lab Chip 2012, 12: 495–502. DOI: 10.1039/C2LC20585H.
- [133] Aguayo JB, Blackband SJ, Schoeniger J, Mattingly M, Hintermann M. Nuclear magnetic resonance imaging of a single cell. Nature 1986, 322: 190–191. DOI: 10.1038/322190a0.

- [134] Kalfe A, Telfah A, Lambert J, Hergenröder R. Looking into living cell systems: planar waveguide microfluidic NMR detector for in vitro metabolomics of tumor spheroids. *Anal. Chem.* 2015, 87: 7402–7410. DOI: 10.1021/acs.analchem.5b01603.
- [135] Meier RC, Höfflin J, Badilita V, Wallrabe U, Korvink JG. Microfluidic integration of wirebonded microcoils for on-chip applications in nuclear magnetic resonance. *J. Microelectromech. Syst.* 2014, 24: 045021 (12 pp.). DOI: 10.1088/0960-1317/24/4/045021.
- [136] Wong A, Li X, Molin L, Solari F, Elena-Herrmann B, Sakellariou D. μ high resolution-magic-angle spinning NMR spectroscopy for metabolic phenotyping of *Caenorhabditis elegans*. *Anal. Chem.* 2014, 86: 6064–6070. DOI: 10.1021/ac501208z.

Imaging and Spectroscopy

Microfluidics for Ultrafast Spectroscopy

Adrien A. P. Chauvet

Additional information is available at the end of the chapter

<http://dx.doi.org/10.5772/64428>

Abstract

Ultrafast laser technologies became one of the essential tool in the characterization of molecular compounds. Being comprised of spectroscopists, laser scientists, chemists and biologists, the “ultrafast community” is often disconnected and consequently unaware of the developments in microfluidic systems. The challenges of studying limited amount of precious liquid sample by means of ultrafast spectroscopy remains silent and, while no commercial systems are available, each research group is developing its own “home-made” options. This chapter will therefore contribute in filling up the gap that exist between the two communities, that of the ultrafast spectroscopy and that of microfluidics by revealing the importance of this analytical tool as well as the advantages of applying microfluidic technics to it. In this goal, the chapter will focus of the recently developed microfluidic flow-cell. With a minimal volume of about 250 μL , the flow-cell enables the study of precious protein complexes that are simply not available in larger quantities. The multiple advantages of the microfluidic flow-cell will be illustrated by the analysis of the cytochrome *bc₁*. In particular, the study will describe how the capabilities of the microfluidic flow-cell enabled the resolution of the ultrafast electronic and nuclear dynamics of specific embedded chromophores.

Keywords: Microfluidics, Ultrafast Spectroscopy, Liquid Sample

1. Introduction

The aim of this chapter is to address the gap that exists between two research communities: ultrafast spectroscopy and microfluidics. Indeed, the development of pulsed laser systems in the last few decades has ushered in new techniques in ultrafast spectroscopy. These techniques have opened new doors for the study of fundamental photo-chemical and photo-physical behavior of a variety of photosynthetic protein complexes.[1] For methodological reasons, i.e. samples being rare and the use of highly specialized equipment, there existed a pressing need to apply microfluidics systems in ultrafast spectroscopy, two fields that unfortunately

developed separately and whose researchers are rarely knowledgeable in both areas. For the microfluidic readers who may be unfamiliar with this literature, I introduce, in the first part of this chapter, the basic concepts of ultrafast pump-probe spectroscopy. In so doing, I highlight the relevance of this technique in gaining understanding protein dynamics and therefore biological properties and functions. It is in fact due to the laborious procedures that are involved in the purification processes of these proteins complexes that most biological samples are only available in sub-milliliters quantities. In the second part of this chapter, I will therefore expose some of the most common solutions that are in use in order to manipulate liquid samples in ultrafast spectroscopy. Finally, in the third part of this chapter, I describe one of the latest applications to the field of ultrafast spectroscopy—what is now called microfluidics—as it handles micro-liters volumes of a given sample. I illustrate the benefits of the application of such a microfluidic system through an analysis the of the cytochrome bc_1 . I conclude with a discussion on the areas of the present microfluidic flow-cell in need of further research and investigation.

2. The need for microfluidics in ultrafast spectroscopy

In this section I will introduce the field of ultrafast spectroscopy to which the microfluidics systems will be applied. I describe the basics of the technique and its relevance to the current fundamental research efforts in biochemistry and biophysics. In the last section of this chapter, I cover the practical challenges that emerge from such studies, which justify the need for microfluidics.

2.1. Ultrafast transient absorption spectroscopy

Transient absorption is a spectroscopic technique whose aim is to resolve the relaxation dynamics of an excited molecule “simply” by looking at its spectral modifications. The technique involves two principal light beam: a pump and a probe. While the role of the pump is to promote the molecule to a particular excited state, the probe is used to “look” at the state in which this molecule is in. The fact that these light beams are not continuous but are strains of pulses allows one to excite the molecule for a brief instant (the duration of the pulse) and to probe its state at a later time. The light pulses are first produced in a cavity (oscillator) that is built around a doped crystal such as titanium doped sapphire crystals (Ti:S) as shown in Figure 1.[2]

The crystal, when excited, serves as a photon tank that will amplify any pulses passing through, via stimulated emission. The cavity then enters into a “mode locked” state as soon as the enclosed pulse strains are in resonance with the dimension of the cavity itself. The energy trapped within the cavity builds up until the pulses are intense enough to leak through one of the cavity end-mirror. Typical Ti:S cavity produces strains of ~ 30 fs pulses centered around ~ 800 nm at 80 MHz repetition rate; each pulse being about tenth of nano-Joules. The extracted pulses are then amplified in a similar fashion by passing in a second cavity comprised of a second Ti:S crystal.[2] The frequency is however decreased to few kHz in order to reach few

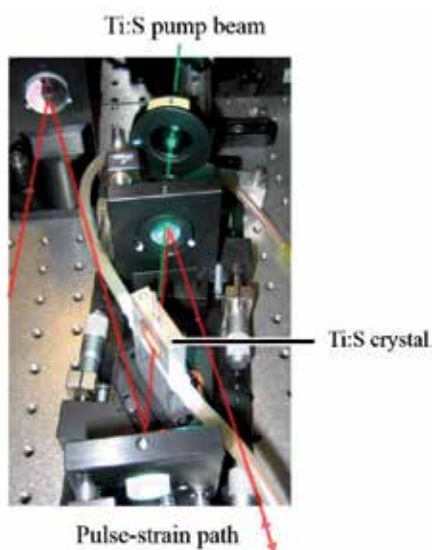


Figure 1. Ti:S crystal cavity.

milli-Joules per pulses. It is these amplified pulses that are then split into pump and probe pulses.

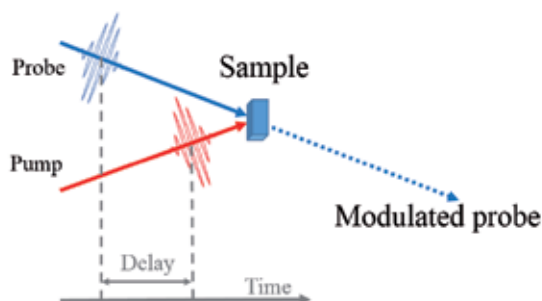


Figure 2. Pump-probe experimental scheme.

As illustrated in Figure 2, varying the time delay that separate both pump and probe enables to follow the evolution of the transient excited states over time. This delay is introduced by physically increasing the path of one of the pump or probe arm of the setup via a precision stage. In a typical configuration, a 30 cm stage provides with a temporal window of about 4 ns (round-trip). The time resolution with which we can follow the molecular dynamics is then given by the duration of the light pulses themselves. A regular transient absorption setup is today capable of producing amplified strains of ~40 fs pulse with a kHz repetition rate. Such femto-to-nano-second time window corresponds to the dynamics of energy and electron transfer within and between molecules as well as local structural modifications.[3] Further-

more, the high repetition rate and the development in matters of laser stability and detection system gives the ability to monitor the absorption changes of a single molecule out of a thousand (corresponding to changes of $\sim 10^{-4}$ OD) in less than a second of accumulation time. [4] With such setups, it is for example possible to trigger the charge separation in the Photosystem I protein complex and to follow the liberated electron as it progresses from one side of the protein to the other. [4] Another example is the monitoring of the heme-ligand dissociation and rebinding dynamics that results from the absorption of a photon such as it is the case of various types of cytochromes. [5, 6]

The use of non-linear optics, such as in the famous and various kind of optical parametric amplifiers (OPA, Non-collinear OPA and multi-pass OPA) [7] as well as the different pulse shaping devices (in either transmission or reflection), [8] gives the ability to tune both the pump and the probe to the desire wavelength, therefore enabling to excite and to follow a particular molecular transition. For example, in the study of the bacterial reaction centers complexes, being comprise of multiple types of pigments that are spectrally distinct, careful tuning of the pump allows to preferably excite one pigment while living the others in their fundamental state. [9]

It is therefore out of the development in laser technology and specifically in tunable table-top pulsed lasers that the field of ultrafast spectroscopy came to know the success it knows today.

2.2. Studying biological samples

As implied in the previous section, transient spectroscopy is best suited for the study of compounds that have distinct spectral feature. Fortunately, most organic compounds are made of either aromatic amino acids or incorporates chromophores within their protein structure, each having distinct spectral features. The technics consequently became in the past decade a common analytical tool for biologists and chemists. Ultrafast transient spectroscopy is indeed used for a broad range of investigations: being sensitive to changes in absorption spectrum of the proteins, it is possible to collect data on local conformational deformations, electronic transitions and (low) vibrational modes of oscillation within molecules, intra and inter molecular energy and electron transfers, etc. [10] In the field of solar energy conversion for example, which is one of today's essential topic in our energy savvy societies, this technique allowed to better understand the conversion processes from light to consumable energy. In particular, the study of photosynthesis showed how the specific arrangement of pigment within larger protein structure either favor the absorption and passing of the photon energy, as it takes place in antennae systems, or favors the generation of a charge separated state, as it happens in photosynthetic reaction centers, [4, 9] which results in the liberation of a high energy, and therefore usable, electron. Other chromophores can also serve as electron docking sites and electron carriers. [6] The knowledge gained from such studies is then applied for medical and industrial purposes and used to optimize specific molecular reactions. From these examples, it is possible to understand why the study of biological samples by means of ultrafast transient spectroscopy, among other spectroscopic techniques, became and remains one of the standard analytical tool for the fundamental understanding of a broad range of molecular dynamics.

2.3. The challenges of the application

As discussed above, ultrafast transient spectroscopy is suitable for the study of biological samples. These samples are usually made of purified and solvated proteins. Once a particular molecule is excited, the deposited energy ultimately dissipates into the solvent (so long as the changes are not permanent). It is to remember that the typical repetition rate of the pulses are in the order of the kHz and at this rate the sample is excited about every milliseconds. The risk is that the photo-induced molecular modifications live for a time that is comparable, which will then results in a rapid saturation of the sample. In other words, the excited molecule might not have sufficient time to relax to its fundamental state before the coming of the next light pulse. Saturation thus takes place and as the molecules gets overexcited: they are unable to release the deposited energy quickly enough and end up by "burning". In order to avoid such consequences, the sample is usually flown in front of the laser beams. The condition is that the flux is high enough so that the sample is refreshed for each laser pulse.

The second major constraint is related to the quantity of the sample available. The sample being made of purified proteins, it is then concentrated in order to reach an optical density that is suitable for spectroscopic analysis. Ideally, transient absorption spectroscopy requires an optical density of about 0.6 for the transition of interest, which in the case of heme protein corresponds to a concentration of hundreds of micro molar. The samples are consequently limited in terms of volumes and sub-milliliters quantities already requires months-long of successive growth of the organisms and protein purification cycles.[11, 12]

The third constraint concerns the susceptibility of the sample in respect to its solvent and atmosphere in which it is enclosed. Indeed some biological samples are hydrophobic and require to be dissolved in various chemicals in order to avoid aggregation and the subsequent scattering of the light pulses, such as it is the case for solvated porphyrins. Many samples are also sensitive to oxygen and therefore require the atmosphere to be controlled. For example, myoglobin is able to effectively bind a variety of diatomic molecule. It however has a high affinity for oxygen, so much that it is not possible to study its deoxygenated state unless in anaerobic conditions.[13]

In conclusion, ultrafast transient spectroscopy is today one of the standard analytical tool for whoever desire to study the local structural, electronic and vibrational photo-induced dynamics. In particular, solvated chromophores and chromophore-containing proteins are well suited for the techniques as they can be specifically targeted via their absorption band. However, these liquid samples are often limited in quantities and have to be flown in order to avoid any photo-damages. From these challenges arise the need for microfluidics so as to flow the limited sample volumes. Furthermore, in order to perform ultrafast spectroscopic measurement, the probe pulses must pass through the sample, therefore through the flow-cell in which it is enclosed. The cell consequently requires adequate windows that do not alter the signal-to-noise ratio nor the temporal and spectral resolution of the apparatus. Additionally, due to the properties and high sensitivity of certain samples, the cell must be resistant to the solvent while providing control of the atmosphere. In such cases, the sample must be hermetically confined within the microfluidic system which therefore has to also play the role of an anaerobic chamber.

3. Most common solutions available

In this section I will review different techniques that are commonly employed to flow the sample in front of the laser beam. I will discuss the advantages and inconveniences of each in terms of their compatibilities with the requirements of ultrafast spectroscopic laser systems.

3.1. Flow cell

The main idea is to flow the sample in between two transparent plates. These windows are usually made of quartz so as to permit the broadband (near UV-Visible-near IR) beams to pass through. This type of cell allows for small path lengths and thin windows, down to 0.02 mm such as the one shown in Figure 3, therefore reducing scattering of the excitation beam through the quartz. The thin windows also have the advantage to minimally alter the pulse duration (limited group velocity dispersion), therefore allowing for an optimal time resolution. Furthermore, the cell is steady and its stability allows for optimal signal to noise levels.

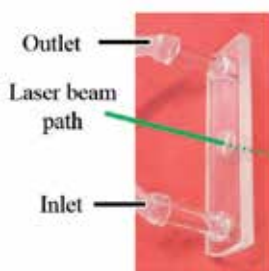


Figure 3. Flow cell from Starna Cell [14]

The quartz cells, by themselves, are commercially available.[14] However, due to their size, these cells already enclose about one milliliter of sample. Furthermore they must be connected to a pump, typically a peristaltic or flow-through pump, in order to generate the flow. Altogether, the flow cell system requires few tenths of milliliters and is consequently not adequate for precious samples that are simply not available in such quantities.

3.2. Liquid micro-jet

The term micro here comes from the diameter of the jet itself, which produces a couple of centimeters-long of regular flow. The advantage of expelling the sample as a jet is to remove the constraints of having it to pass through windows, i.e. avoiding any additional absorption, scattering and group velocity dispersion. It therefore allows pump probe experiment in all spectral region including UV and X-ray region. Associated with an adequate sample collector, as shown in Figure 4, it is also applicable in vacuum chambers and becomes suitable for photoelectron spectroscopy.[15]



Figure 4. Micro-jet implemented for photo-electron spectroscopy. Courtesy of José Ojeda, EPFL.

The inconvenience of having to produce a constant flow rate is that the sample must pass through a sophisticated HPLC pump,[15-17] which consequently requires sample volumes that are larger than our targeted sub-milliliter. Note also that while passing in either the air or in vacuum, the sample's solvent is subjected to evaporation. In such conditions, recycling of the sample results in a change of the sample's concentration and temperature over the course of the experiment.[16] Furthermore, the high speed at which the sample go through the nozzle induces charging of the liquid and or of the nozzle, which might alter the measurement.[17]

3.3. Spinning /moving cell

The idea behind the spinning-cell is similar to that of the flow cell as the sample is housed between two circular glass plates that are spaced by the desirable optical path-length.[18] While rotating, the sample either creates a rim at the edge of the cell, or at lower speed, the solution remains at the bottom of the cell and is constantly mixed due to friction with the glass as shown in Figure 5. The advantage is that it typically requires minimal amounts of sample (~0.3 mL) as well as to provide control over the initial atmosphere in which the sample is enclosed since the sample is hermetically confined.

However, because the rotation of the glass plate causes the excitation beam to sweep a large surface, the cleanness of the plates is directly related to the noise. It is consequently burdensome to clean. Furthermore, the fact of having a moving piece of glass in which the beam is focused renders the alignment of the cell crucial, and any slight asymmetry of the glass plates has consequences on the transmitted probe beam. Also, since the glass plates are typically few cm in diameter, the required minimal thickness of the glass lowers the time resolution. Another inconvenience is that once the cell is set it does not allow access to the enclosed sample and each experiments therefore requires its own sample preparation.

In conclusion, the proposed solutions used to flow the sample in front of the laser beam have each distinct advantages and inconveniences, and none ideally respond to all the requirement, i.e. is suitable for sub-milliliter sample volumes; provides a close atmosphere; grant access to the sample once closed; affecting minimally the signal-to-noise ratio and resolution of the

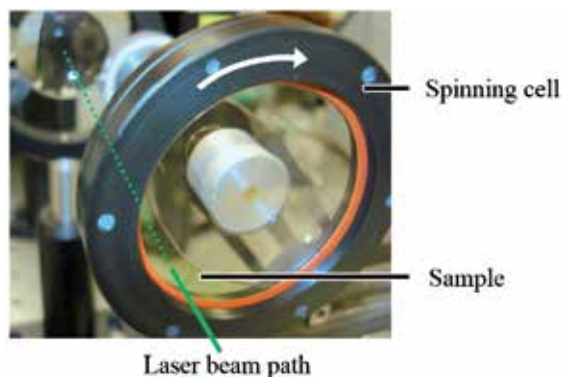


Figure 5. Spinning cell used in few-kHz spectroscopy setups.

apparatus. Through these few examples I hope to have convinced the reader of the need for a development in the application of microfluidic system to the field of ultrafast spectroscopy.

4. Recent improvement and application: the microfluidic flow cell

In this section I will describe the recently developed microfluidic flow-cell in order to illustrate the importance and advantages of applying microfluidic systems to the field of ultrafast spectroscopy. I will show that recent improvements in the field of microfluidics have the capabilities to solve the previously mentioned constraint all at once. I will thus discuss the advantages of the system in light of the other technics. Following the technical properties I will illustrate the flow-cell's effectiveness through a study done on rare *bc*-cytochrome and conclude with an appeal for further development.

4.1. The microfluidic flow-cell

The microfluidic flow-cell, [19] as illustrated in Figure 6, is composed of three main elements that are connected via flexible tubing of 1-mm diameter:

The decantation chamber is a home-made polymer cylindrical chamber as shown in Figure 6. The 0.5-mm diameter inlet and outlet are at the bottom of the chamber in order to minimize turbulences that are created at high flow rates. The chamber requires a minimal amount of ~50 μL of liquid sample in order to have a continuous flow between the inlet and outlet. Any excess of sample fills up the chamber and allows the bubbles that might be enclosed in the closed circuit to rise to the surface. The bubbles are naturally trapped by the chamber while passing through at low flow-speed. At high flow-speed however, larger sample volume are required in order to avoid the suction of air due to the liquid's turbulences. The top of the chamber is threaded to fit a standard septum screw cap. This allows for the addition of chemicals to the enclosed solution while keeping the confined atmosphere protected and avoiding evaporation of the solvents.

The *capillary window* is made of a square quartz silica capillary bought from Composite Metal Services Ltd (CMS). It has a path-length of 0.5 mm with 0.1-mm thin walls. Knowing that the focus of the laser beam is about 100 μm in diameter, the window can easily be set within the beam path. The capillary is fixed at the center of a xyz-rotation mount that allows for fine adjustment of the angle between the incident beam and the window.

The *turbisc pump* is a design from CSEM.[20] In short, the flow is created by direct friction between a grooved barrel and the liquid. The inner volume that the pump contains is about 100 μL only. Because the housing and the seal are respectively made out of Polyetherimide and of Polyetheretherketone, the pump is relatively resistant to chemicals.

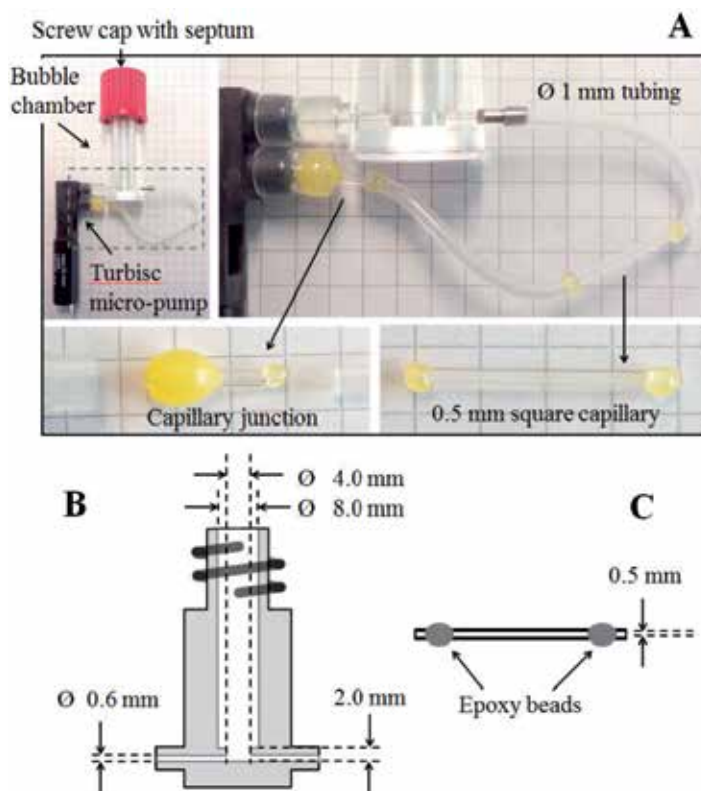


Figure 6. (A) Overall view of the assembled system, with zoom on the capillary junctions. (B) Side view of the bubble chamber and (C) of the capillary window. Reproduced from Ref. [19].

When the pump, the chamber and the capillary are connected, the minimal volume of sample needed for good working conditions is about 250 μL only. This configuration includes a total tubing (1-mm inner diameter) length of ~ 6 cm and a sufficient amount of sample in the cuvette to avoid the suction of bubbles due to turbulences with a minimal flow of ~ 0.1 ml/sec. The flow is proportional to the voltage applied to the pump and under the same configuration the maximum flow rate was measured to be ~ 0.36 mL/sec, as shown in Figure 7.

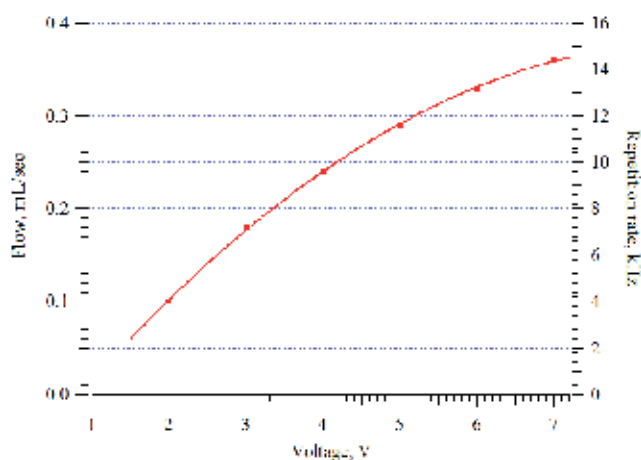


Figure 7. Measured flow-rate (dots) and its best fit (line, 2nd order polynomial) while the pump is connected to ~6 cm of 1-mm diameter tubing and ~1-cm long 0.5x0.5 mm² square capillary. In order to ensure fresh sample at each laser shot, while assuming a typical laser focus size of 100 μ m, the expected maximum repetition rate of excitation is indicated as a reference only (right axis).

While assuming a typical laser focus diameter of 100 μ m within the 0.5x0.5 mm² square capillary, the flow, when assumed to be uniform, is expected to effectively refresh the sample within the laser focus for each laser shot at an excitation rate of up to ~14 kHz. In practice, it is to remember that the flow is impeded on the edges of the capillary and consequently the value of 14 kHz has to be taken as an upper limit only. Taking into account that the inner volume of the pump is only about 100 μ L, it represents one of the best (if not the actual best) compromise between flow-rate and required volume. The assembled microfluidic flow cell, in working conditions is shown in Figure 8.

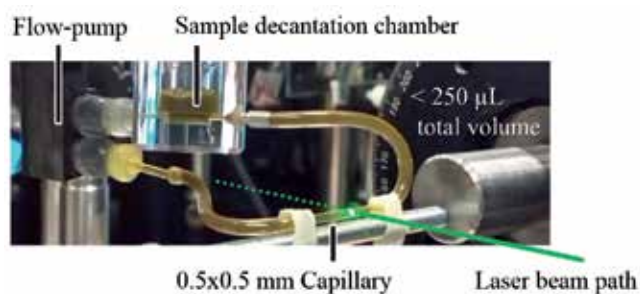


Figure 8. Microfluidic flow-cell in action

4.2. Example of application: the study of cytochrome *bc*₁ complexes

In order to illustrate the applicability of the microfluidic flow-cell as well as some of its advantages I present here a unique analysis, that of the Cytochrome (cyt) *bc*₁ complex. [6] The

cyt bc_1 complex is a key player in mitochondrial and bacterial respiratory chains.[21] It is the main actor in the protonmotive Q cycle and results in the formation of a proton gradient across the membrane via a series of embedded hemes as shown in Figure 9.[22-24] The generated potential gradient serves as the driving force for the synthesis of ATP, the universal energy transporter in living organisms. The understanding of the protein complex is therefore of primary importance. However the sample is rare and mainly because of the limited quantity available after each purification process, the heme dynamics were until then never studied by means of ultrafast spectroscopy.

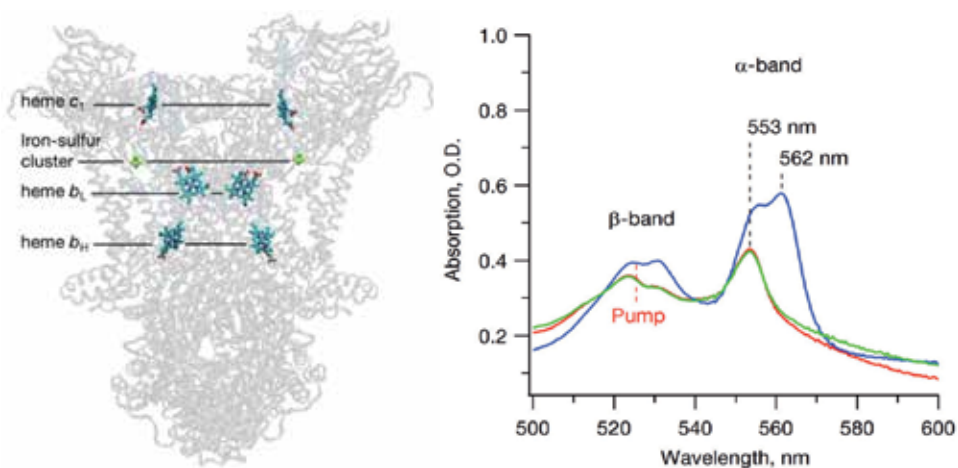


Figure 9. (Left) Structure of the bc_1 complex[25] with the protein backbone being shaded for clear visualization of the key actors in the proton-coupled-electron mechanisms. (Right) Static absorption spectrum of the sequential reduction and oxidation of the cyt bc_1 dimer complex: after pre-reduction by ubiquinol and before (red, c_1 -hemes reduced) and right after (blue, b - and c_1 -hemes reduced) the addition of dithionite, and at the end, after oxidation of the complexes by oxygen (green, c_1 -hemes reduced). The 523-nm excitation pump is indicated as reference. Reproduced from Ref. [6] with permission from the Royal Society of Chemistry.

Thanks to the microfluidic flow-cell, and more particularly to the access it provides to the sample via the septum, the reduction and oxidation of the hemes of interests could be controlled chemically. All data were therefore taken from the same sample preparation within the same experiment, in the same experimental conditions. The different signals that emerge from the reduced states of the hemes could then be directly compared: either the c_1 -hemes can be exclusively reduced, or both c_1 - and b -hemes can be reduced together. Direct subtraction of the two data set enabled the extraction of the sole signal from the b -hemes, as shown in Figure 10.

The dynamics of each heme type could be analysed separately by means of singular value decomposition and global fitting as described in detail elsewhere.[6] The resulting decay associated spectra, shown in Figure 11, revealed the clear differences between the b - and c_1 -hemes behaviours within the bc_1 protein complex: while the c_1 -hemes undergo photo-dissociation of their axial ligand as a result of ultrafast laser excitation, the b -hemes were shown to undergo photo-oxidation with a high (> 0.4) quantum yield that is beyond all expectations.

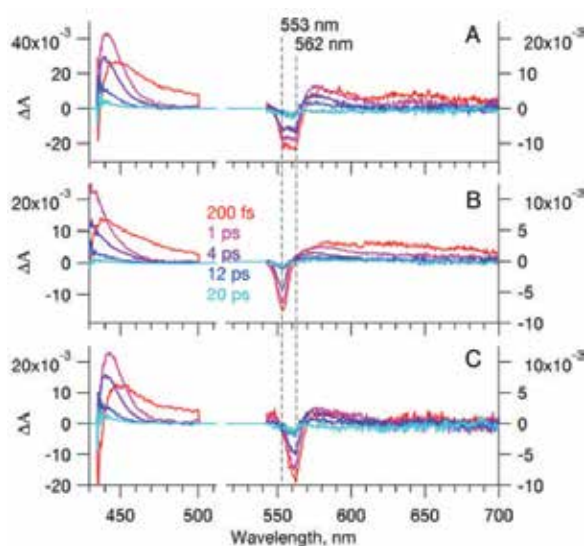


Figure 10. (A) Spectra at selected time delays while both *b*- and *c*₁-hemes are reduced. (B) Spectra at selected time delays while only the *c*₁-hemes are left reduced. (C) Difference (A-B) corresponding solely to the signal of the ferrous *b*-heme, as discussed in the text. Note that the vertical scales below and above 515 nm differs by a factor of two. Reproduced from Ref. [6] with permission from the Royal Society of Chemistry.

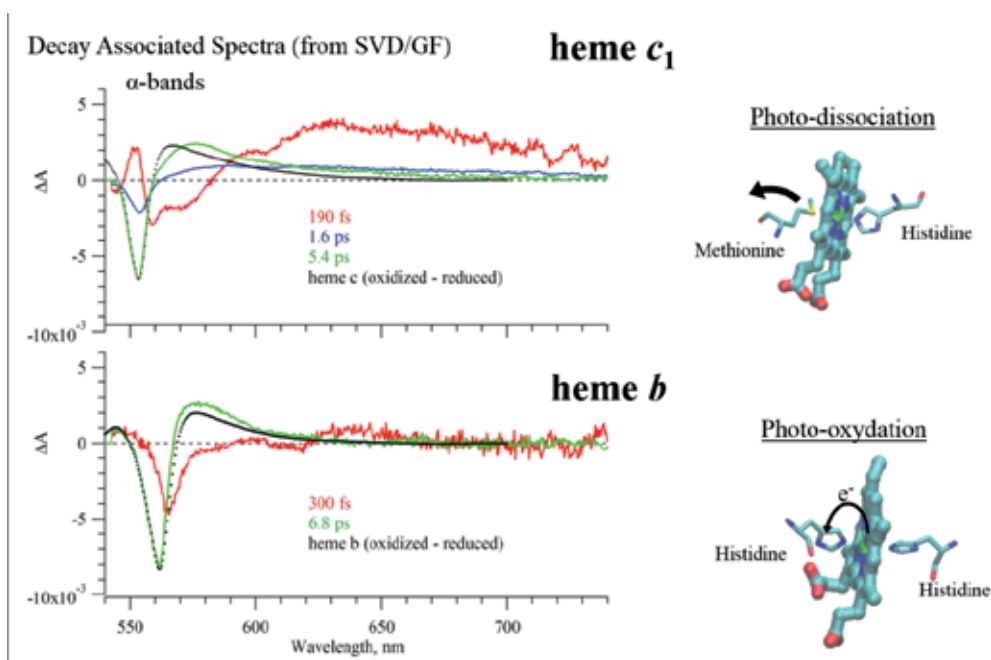


Figure 11. Photo-dissociation of the *c*₁-heme (left) and photo-oxidation of the *b*-heme (right) upon light excitation of the *cyt bc*₁ complex. Reproduced from Ref. [6] with permission from the Royal Society of Chemistry.

The *b*-heme's high electronic reactivity makes sense in the light of *cyt bc₁* having to efficiently fulfil its role in the Q-cycle: it favours the reduction and oxidation of the ubiquinone and ubiquinol, respectively.[22] The *b*-hemes have to efficiently "process" the electrons, which demand them to easily loose or gain electron. Similar electronic-reactivity would in fact be counterproductive in soluble cytochromes as they would less efficiently keep their electrons from being scavenged by other solutes. The hydrophilic environment of the *bc₁* core on the other hand preserves the *b*-hemes from unwanted solvated electron carrier and their high electronic reactivity is then an advantage. In contrast to the high electronic reactivity of the *b*-hemes, the high photo-dissociation quantum yield of the *c₁*-hemes can be understood as being an efficient "heat sink" that protects the reduced state of the heme against light excitations.

Overall, this study illustrate that, even though the *b*-hemes in *cyt bc₁* and in other *cyt b* have similar ligation to their protein backbone; specific structural constraints and amino-acid arrangements result in clearly different responses, and therefore functions. While cytochromes were known to serve only as electron carriers, this study demonstrates that with the appropriate environment, light-induced charge separation can readily be initiated within single heme structures. The use of the microfluidic flow-cell therefore not only enabled the study of this rare protein complex, but allowed to shine light on the relevance of local heme-bonding and structural environment in initiating larger chemical reactions. This particular case study is only one example of how the field of ultrafast spectroscopy can benefit from the application of microfluidics technologies.

4.3. Call for development

As I mentioned, the described microfluidic flow-cell, beside the numerous advantages it provides in respect to the other systems commonly employed, is certainly not perfect, which leaves room for improvement.

For example, in terms of sample volumes, most of the liquid is contained in the pump that is used to generate the flow and in the tubing. Miniaturization of both would allow to use even smaller sample volumes. Already the small turbisc pump that is employed uses a newly developed friction based technologies[20] that is able to flow even viscous samples. The samples studied in ultrafast spectroscopy are however water-like and, not being in need of the actual viscous sample capabilities of the pump. I can therefore imagine that a simplified version of the pump would be sufficient and require even smaller volumes. Concerning the actual 1 mm diameter tubing, that links the pump with the capillary, it could be replaced by other microfluidics technologies that uses micro-channels that are specifically designed for spectroscopy.[26] The goal through these proposed improvements is to reduce the amount of liquid used, keeping in mind that reducing further the diameter of the channels might impede the overall flow rate.

Another field of improvement that I see is that of the control over the inner atmosphere of the cell in which the sample is enclosed. As I mentioned, the actual pumping is done by friction between a grooved barrel and the sample. The spinning motion is however done via a shaft and under high pressure difference between the inner and outer part of the cell, either the sample can leak through or air can be sucked in via the shaft's joints. In order to palliate to this

issue, I can imagine that the shaft would be replaced, not by another mechanical interaction, but remote electromagnetical interaction so as to preserve the inner atmosphere of the sample. Such systems are already implemented for applications in biomedical for example.[27] Furthermore, the microfluidic flow-cell uses epoxy beads in order to hermetically fit the square capillary in the cylindrical tubing. Better seal could be achieved if the capillary themselves were to be made with initial beads on each sides such as it is the case for the larger commercially available flow-cells.[14]

At last, I would like to precise that, due to friction between the sample and the capillary, the capillary does not provide with a flow that is homogeneous. Sample that is the closest to the window has consequently lower flow rate and might not be refreshed for each laser pulse, being therefore subjected to photo-damage. One solution would be to employ the newly developed Electro-Osmotic flow systems that are used to generate homogeneous flows.[28]

In conclusion, the microfluidic flow-cell that I propose is specifically designed to fits the requirement imposed by the ultrafast spectroscopy of quantity-limited and sensitive sample, while it remains cost effective and easy to use. As an illustration of the flow-cell's effectiveness, I showed how its implementation enabled the study of the cytochrome bc_1 . More precisely, I was able to resolve the ultrafast electronic and nuclear motions that precedes some of the larger physiological function of the protein. The microfluidic flow-cell not only facilitates but also opens the door to the study of a whole range of samples that cannot be purified in large quantities such as it is the case for most organic compound that are extracted from living organisms.

The advantages of this microfluidic flow-cell over other pre-existing solutions are clear; as clear as there is room for development.

5. General conclusion

The implementation of the microfluidic flow-cell to the field of ultrafast spectroscopy can be considered as one of the first attempts to bridge two communities, i.e. that of microfluidics and that of ultrafast spectroscopy. In this chapter I have first described the technique of ultrafast spectroscopy in order to show its requirements in terms of sample as well as the importance of such analytical tool when applied to the study of biological protein complexes. In particular, ultrafast transient spectroscopy became one of the essential approach for whoever desires to understand the local electronic and nuclear modifications that are at the origin of the larger physiological functions of proteins. I then exposed the advantages and inconveniences of the different techniques that are commonly used in order to flow liquid samples in front of the laser beams. The aim of this discussion is to better appreciate how the application of microfluidics technologies is able to responds to the challenges raised by the technique. In this aim, the recently developed microfluidic flow-cell is adequate as it requires only about 250 μL while generating flow rate that are suitable for high repetition rate laser systems. Its steady window and decantation chamber allow for an optimal time and spectral resolution. By providing direct access to the sample while running a single experiment and

monitoring chemical changes in “real time”, the microfluidic system enables studies that were otherwise not possible. The advantages of microfluidics over other usual systems are numerous but as it represents only one of the first attempt, there is ample room for improvement. In this regard, one of the goal of this chapter is to serve as an initial step in an effort to bridge the microfluidics community with that of ultrafast spectroscopy in order to foster new ideas, new applications and new perspectives.

Acknowledgements

Thanks to Professor S. Savikhin (Purdue University, USA) as well as to Professor M. Chergui (EPFL, Switzerland) from whose laboratory of Ultrafast Spectroscopy the different pictures are taken. The described microfluidic flow cell as well as the *cyt bc₁*'s study have been funded by the Swiss NSF via the NCCR:MUST, by the FP7 Marie Curie COFUND, by the Excellence Initiative of the German Federal and State Governments (EXC 294, BIOSS) and by the Deutsche Forschungsgemeinschaft (RTG 1976).

Author details

Adrien A. P. Chauvet*

Address all correspondence to: adrien.chauvet@unige.ch

GAP-Biophotonics, Geneva University, Geneva, Switzerland

References

- [1] Berera R, van Grondelle R, Kennis JTM. Ultrafast transient absorption spectroscopy: principles and application to photosynthetic systems. *Photosynth Res.* 2009;101:105-18.
- [2] Koechner W. *Solid-State Laser Engineering*. 6th ed: Springer; 2006.
- [3] Rosspeintner A, Lang B, Vauthey E. Ultrafast Photochemistry in Liquids. *Annu Rev Phys Chem.* 2013;64:247-71.
- [4] Chauvet A, Dashdorj N, Golbeck JH, Johnson TW, Savikhin S. Spectral Resolution of the Primary Electron Acceptor A0 in Photosystem I. *J Phys Chem B.* 2012;116(10):3380-6.
- [5] Vos MH, Battistoni A, Lechavue C, Marden MC, Kiger L, Desbois A, et al. Ultrafast Heme-Residue Bond Formation in Six-Coordinate Heme Proteins: Implications for Functional Ligand Exchange. *Biochemistry.* 2008;47:5718-23.

- [6] Chauvet AAP, Al Haddad A, Kao W-C, van Mourik F, Hunte C, Chergui M. Photo-induced dynamics of the heme centers in cytochrome *bc₁*. *Phys Chem Chem Phys*. 2014.
- [7] Cerullo G, De Silvestri S. Ultrafast Optical Parametric Amplifiers. *Rev Sci Instrum*. 2003;74(1).
- [8] Weiner AM. Femtosecond Pulse Shaping Using Spatial Light Modulators. *Rev Sci Instrum*. 2000;71(1929).
- [9] Chauvet A, Sarrou J, Lin S, Romberger SP, Golbeck JH, Savikhin S, et al. Temporal and Spectral Characterization of the Photosynthetic Reaction Center from *Heliobacterium modesticaldum*. *Photosynth Res*. 2013;116:1-9.
- [10] Rosspeintner A, Bernhard Lang B, Vauthey E. Ultrafast Photochemistry in Liquids. *Annu Rev Phys Chem*. 2013;64:247-71.
- [11] Mitra S. Sample Preparation Techniques in Analytical Chemistry. Winefordner JD, editor: John Wiley & sons, INC.; 2003.
- [12] Berg JM, Tymoczko JL, Stryer L. The Purification of Proteins is an Essential First Step in Understanding their Function. In: Moran S, Hadler GL, Zimmerman P, editors. *Biochemistry*. 5th edition ed: W H Freeman; 2002.
- [13] Monni R, Al Haddad A, van Mourik F, Auböck G, Chergui M. Tryptophan-to-Heme Electron Transfer in Ferrous Myoglobins. *PNAS*. 2015;112(18):5602-06.
- [14] Starna Cells. Linear Flow Cells, Type 48 series http://www.starnacells.com/d_cells_s/flow/linear/T048.html2015.
- [15] Arrell CA, Ojeda J, Sabbar M, Okell WA, Witting T, Siegel T, et al. A Simple Electron Time-of-Flight Spectrometer for Ultrafast Vacuum Ultraviolet Photoelectron Spectroscopy of Liquid Solutions. *Rev Sci Instrum*. 2014;85(103117).
- [16] A. K. Charge Transfer to Solvent Dynamics in Iodide Aqueous Solution Studied at Ionization Threshold: Freie Universität Berlin; 2015.
- [17] Duffin AM, Saykally RJ. Electrokinetic Power Generation from Liquid Water Microjets. *J Phys Chem*. 2008;112:17018-22.
- [18] Savikhin S, Wells T, Song P-S, Struve WS. Ultrafast Pump-Probe Spectroscopy of Native Etiolated Oat Phytochrome. *Biochemistry*. 1993;32:7512-8.
- [19] Chauvet A, Tibiletti T, Caffarri S, Chergui M. A microfluidic flow-cell for the study of the ultrafast dynamics of biological systems. *Rev Sci Instrum*. 2014;85: 103118.
- [20] Lisibach A, Casartelli E, Schmid N, editors. Flow Investigation in a Disk Micropump. ASME 2010 3rd Joint US-European Fluids Engineering Summer Meeting and 8th International Conference on Nanochannels, Microchannels, and Minichannels; 2010; Montreal, Quebec, Canada.

- [21] Berry EA, Guergova-Kuras M, Huang L, Crofts AR. Structure and Function of Cytochrome bc Complexes. *Annu Rev Biochem.* 2000;69:1005-75.
- [22] Crofts AR. Proton-coupled electron transfer at the Qo-site of the bc₁ complex controls the rate of ubihydroquinone oxidation. *Biochem Biophys Acta.* 2004;1655:77-92.
- [23] Hunte C, Solmaz SRN, Palsdóttir H, Wenz T. A Structural Perspective on Mechanism and Function of the Cytochrome bc₁ Complex. *Results Probl Cell Differ.* 2007;45:253-78.
- [24] Trumpower BL. Cytochrome bc₁ Complexes of Microorganisms. *Microbiol Rev.* 1990;54(2):101-29.
- [25] Solmaz SRN, Hunte C. Structure of Complex III with Bound Cytochrome c in Reduced State and Definition of a Minimal Core Interface for Electron Transfer. *J Biol Chem.* 2008;283(25):17542-49.
- [26] Horrocks HM, Tosatto L, Dear AJ, Garcia GA, Iljina M, Cremades N, et al. Fast Flow Microfluidics and Single-Molecule Fluorescence for the Rapid Characterization of α -Synuclein Oligomers. *Anal Chem.* 2015;87(17):8818-26.
- [27] Al-Halhouli AT, Kilani MI, Büttgenbach S. Development of a novel electromagnetic pump for biomedical applications. *Sensor Actuat A-Phys.* 2010;162:172-6.
- [28] Stone HA, Stroock AD, Ajdari A. Engineering Flows in Small Devices: Microfluidics Toward a Lab-on-a-Chip. *Annu Rev Fluid Mech.* 2004;36:381-411.

Flow-Scanning Microfluidic Imaging

Nicolas Pégard, Chien-Hung Lu, Marton Toth, Monica Driscoll and Jason Fleischer

Additional information is available at the end of the chapter

<http://dx.doi.org/10.5772/64707>

Abstract

The advantages of microfluidics for fast analysis of microscopic suspensions have led to the commercial development of flow cytometers. In this chapter, we propose new microscopy methods that combine controlled motion of micro-organisms in a laminar microfluidic flow, optics, and computation. We propose three new imaging modalities. We first introduce a flow-based version of structured illumination microscopy, where the necessary phase shifts are no longer obtained by controlled displacement of the illumination pattern but by flowing the sample itself. Then, we propose a three-dimensional (3D) deconvolution microscopy method with a microfluidic device for continuous acquisition of gradually defocused images. Finally, we introduce a microfluidic device for phase-space image acquisition, and computational methods for the reconstruction of either phase of intensity, in 3D. The imaging modalities we introduce all retain the benefits of fluid systems for noninvasive bioimaging. The proposed devices can easily be integrated on existing microscopes as a modified microscope slide, or on flow cytometers, and aquatic imagers with minor adjustments. Alternative on-chip implementations are also possible, with lens-free devices, and near-field optical and microfluidic elements directly assembled on the surface of a CCD (Charge-Coupled Device) or CMOS (Complementary metal-oxide-semiconductor) chip.

Keywords: lab on-a-chip, microscopy, computational imaging, optofluidics, cytometry, structured illumination, deconvolution, light field, tomography

1. Introduction

1.1. Microfluidic structured illumination microscopy

The resolution of an optical imaging system is subject to the diffraction limit, which for a fixed wavelength is governed by the numerical aperture (NA) of the system. A popular technique

to go beyond these limits is structured illumination (SI) [1–7], in which a known illumination pattern (usually periodic) is projected onto a sample. Spectral beating of this pattern with the object modes folds high-resolution information into lower spatial frequencies (Moiré patterns) that can be detected by the imaging device. Deconvolving this photonic aliasing can improve resolution by a factor of two [1–6]. Greater improvements are possible using nonlinearity [7] or with successive applications of structured illumination with higher spatial frequency patterns. Alternatively, structured illumination may be viewed as a type of diffraction, in which the signal is shifted in the spectral frequency domain by an amount equal to the applied grating period (see Figure 1). This imaging technique, however, requires the acquisition of several raw images (at least three) with a series of precise displacements of the illumination pattern in order to remove phase ambiguity. Previous SI systems relied on mechanical moving parts (e.g., piezoelectric actuators) [4] or on a spatial light modulator (SLM) [8] to perform the shift. These methods add complexity to the imaging system and can significantly reduce the image acquisition speed. Further, mechanical movement is subject to vibration error and artifacts, while SLMs are limited by their pixel size.

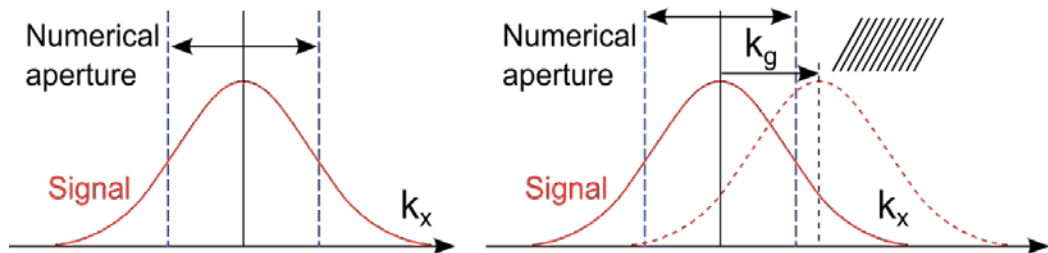


Figure 1. The principle of structured illumination microscopy is to increase imaging resolution beyond the limit of a microscope objective. An optical signal carries a given distribution of spatial frequencies (red curve), but the range of frequencies that can be collected is limited by the numerical aperture (NA) of the optical system (dashed blue line). Illuminating the sample with structured light that is patterned with a spatial frequency k_g shifts the distribution and brings higher spatial frequencies back into the NA-limited imaging domain.

Separate from the structured illumination approach, fluidic imaging systems for improved resolution have been developed. In microfluidic microscopes and aquatic imagers, these systems have received renewed attention with the development of integrated optofluidic devices, which are lensless imagers that place flowing samples directly over a detector [9–11]. Among their advantages is simple and low-cost object manipulation, with little or no sample preparation. In most devices, the flow is used only to provide object throughput (e.g., to measure gas kinetics [12], live cells [13], or two-phase flow [14]). However, the flow can be used as an additional degree of freedom for imaging. For example, recent work has used fluid transport as a scanning mechanism to enhance resolution, either by using small holes before the detector [9] or by taking multiple frames with subpixel displacements [10]. In the former method, the small apertures limit the amount of light captured and greatly reduce the effective recording area. In the latter method, resolution is limited by the camera frame rate (vs. flow speed) and edge effects from pixels. In all cases, the illumination was kept as uniform as possible.

Here, we combine a steady illumination pattern and use the fluid flow to provide the necessary scanning that shifts the phase of the illumination pattern with respect to the object. From a flow perspective, the instant wavenumber (k -space) shift gives improved spatial resolution at greater speeds than subpixel methods, with better use of the camera's dynamic range. The combined scheme thus retains all the benefits of fluidics, including high sample throughput and object sorting [15], while enabling easy integration with existing microscopes, flow cytometers, and aquatic imaging systems.

1.2. Reconstruction algorithm for flow-based structured illumination

In standard applications of SI, the illumination is simply a periodic pattern which is displaced (phase-shifted) by a convenient amount, such as a quarter wavelength ($\pi/2$ in phase). In a fluidic system, however, the phase shift between frames will depend on the flow velocity and the camera frame rate. For that reason, we first consider the problem of an arbitrary phase shift of the illumination pattern between two consecutive frames. Let A be the object to be imaged and P be the point-spread function. The p^{th} recorded image is given by

$$I_p(x) = \int P(u)A(x+u)M(x+u-p\delta)du \tag{1}$$

where we allow for a non-ideal displacement, δ , due to fluid flow, and where M is the structured illumination pattern. To generate a fixed illumination pattern, we consider the 0th and $\pm 1^{\text{st}}$ order mode of a diffraction grating so that the structured illumination pattern $M(x) = \left| g + \frac{1}{2}e^{i\beta \cdot x} + \frac{1}{2}e^{-i\beta \cdot x} \right|^2 = \left(g^2 + \frac{1}{2} \right) + 2g\cos(\beta \cdot x) + \frac{1}{2}\cos(2\beta \cdot x)$, where g is the ratio of the grating efficiency between the 0th and $\pm 1^{\text{st}}$ -order diffraction. Here, we neglect the last term, assuming that the resolving power of the imaging system is not enough to detect the Moiré patterns caused by the double frequency 2β . In the following derivation, we use the form $M(x) = U + 2\cos(\beta \cdot x)$, where $U = g + \frac{1}{2g}$.

Fourier transforming the convolution product in Eq. (1) gives

$$\tilde{X}_p(k) = \tilde{P}(k) \left[U\tilde{A}(k) + \gamma^p \tilde{A}_\beta(k) + \gamma^{-p} \tilde{A}_{-\beta}(k) \right] \tag{2}$$

where $\tilde{X}_p(k) = e^{ip\delta \cdot k} \tilde{I}_p(k)$, $\gamma = e^{ip\delta \cdot \beta}$, and $\tilde{A}_{\pm\beta}(k) = \tilde{A}(k \mp \beta)$. For simplicity, we use the optical transfer function $\tilde{P}(k) = 1$ for $\|k\| < k_0$ and $\tilde{P}(k) = 0$ elsewhere, where k_0 is the maximum spatial frequency that can be resolved. Using three consecutive frames, we deduce

$$\begin{bmatrix} \tilde{X}_{p+1} - \tilde{X}_p \\ \tilde{X}_p - \tilde{X}_{p-1} \end{bmatrix} = \tilde{P}(k) \cdot (\gamma - 1) \begin{bmatrix} \gamma^p & \gamma^{-p-1} \\ \gamma^{p-1} & \gamma^{-p} \end{bmatrix} \begin{bmatrix} \tilde{A}_\beta(k) \\ \tilde{A}_{-\beta}(k) \end{bmatrix} \tag{3}$$

which can be inverted to reconstruct the object field with extended resolution A_E :

$$A_E(x) = \mathcal{R} \begin{bmatrix} I_{p+1}(x + \delta) \\ I_p(x) \\ I_{p-1}(x - \delta) \end{bmatrix} \tag{4}$$

where

$$\mathcal{R} = \frac{\gamma}{(\gamma - 1)^2} \begin{bmatrix} \frac{\gamma^{1-p}}{\gamma + 1} e^{-i\beta \cdot x} + \frac{\gamma^p}{\gamma + 1} e^{i\beta \cdot x} - \frac{1}{U} \\ -\gamma^{-p} e^{-i\beta \cdot x} - \gamma^p e^{i\beta \cdot x} + \frac{\gamma^2 + 1}{\gamma U} \\ \frac{\gamma^{-p}}{\gamma + 1} e^{-i\beta \cdot x} + \frac{\gamma^{1+p}}{\gamma + 1} e^{i\beta \cdot x} - \frac{1}{U} \end{bmatrix}^t \tag{5}$$

In Section 4, we provide a detailed derivation of this result.

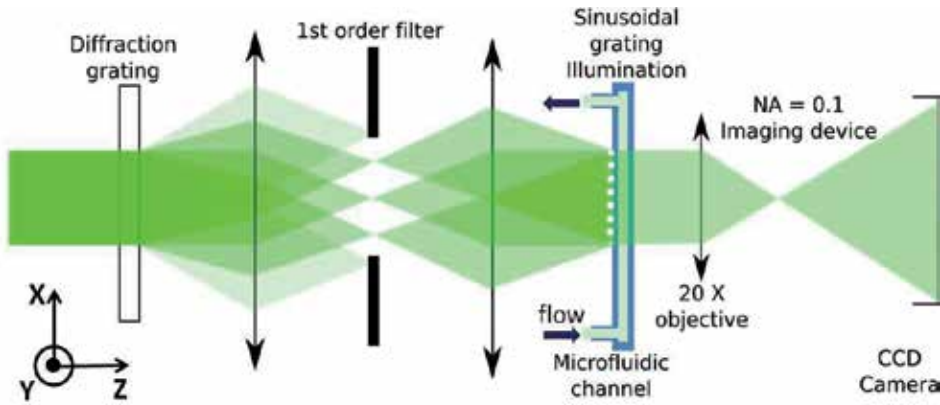


Figure 2. A 500 μm wide, 50 μm deep fluidic channel is at the focal plane of a 20 \times objective lens. The imaging system has low numerical aperture (NA = 0.1). The structured illumination source is a steady sinusoidal profile (2.78 μm stripes) orthogonal to the flow direction. Images are recorded on a CCD camera at a frame rate of 15 frames/s (fps).

1.3. Experimental setup

The experimental setup is shown in Figure 2. The microfluidic channel is a 500 μm wide, 50 μm deep groove etched on a glass slide. To generate the structured light, a 532 nm continuous laser is patterned using a transmission grating and then demagnified to reduce the fringe spacing. This light then illuminates the channel with a steady sinusoidal pattern: 2.78 μm

stripes oriented orthogonal to the fluid flow direction. While the SI technique will work for any imaging system, including lensless ones, we place the channel at the focal plane of an optical microscope. As a compromise between magnification and field of view, e.g. for water analysis, we use a 20× optical objective. The objective is part of a 4*f* imaging configuration with an aperture located at the confocal plane. The resulting value of the numerical aperture (NA = 0.1) corresponds to a resolution limit of approximately 4 μm.

As a proof of principle, we flow a suspension of yeast particles in glycerol through the microfluidic channel. Multiple images are recorded by a CCD camera (pixel size 9.9 μm) at a constant frame rate (15 fps). Figure 3(a)-(c) shows three consecutive frames. It is clear that different features of the object are revealed as it flows past the stationary illumination pattern.

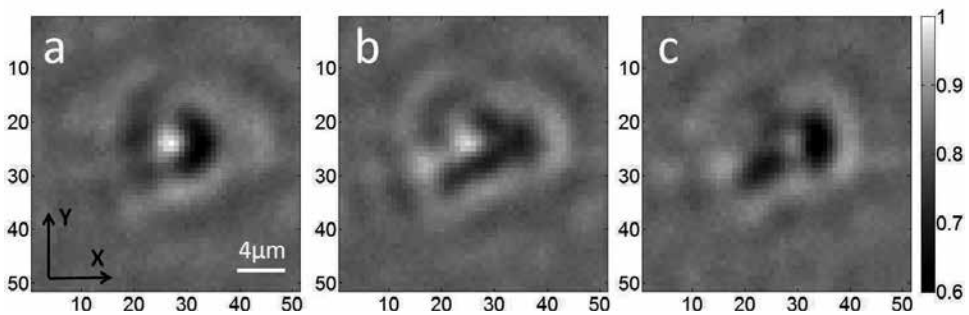


Figure 3. Three consecutive frames of two yeast particles under structured illumination. The constant phase shift ($\delta\phi = 0.28\pi$) of the illumination pattern between consecutive frames shows the evolution of the recorded Moiré pattern.

For numerical reconstruction, we first assume that particles flowing along the center of the microfluidic channel undergo a negligible amount of rotation during three consecutive frames time (Poiseuille-type laminar flow with negligible on-axis velocity shear). The displacement of the object between two consecutive frames, δ , is then determined by the maximization of the cross-correlation function:

$$C(u) = -\int (I_1(x) - I_2(x - u))^2 dx \quad (6)$$

For the conditions here, we obtain $\delta = 0.8 \mu\text{m}$, which corresponds to a flow velocity of 12 μm/s, and a phase shift of $\delta\phi = 0.28\pi$ between consecutive frames. We note that when the spatial frequency of the illumination pattern $|\beta| < 2k_0$, it is necessary to consider the overlap among the modes $\tilde{A}(k)$, $\tilde{A}_\beta(k + \beta)$ and $\tilde{A}_{-\beta}(k - \beta)$. We conduct an average reconstruction among all overlaps to evaluate the corresponding spatial frequencies.

Experimental results are shown in Figure 4. The yeast image without structured illumination is shown in Figure 4(a), and numerical reconstruction of the yeast particles using Eq. (4) is shown in Figure 4(c). It is clear that SI provides greater visibility and reveals more details than the uniform illumination image, even for a 1D illumination pattern. The amount of improve-

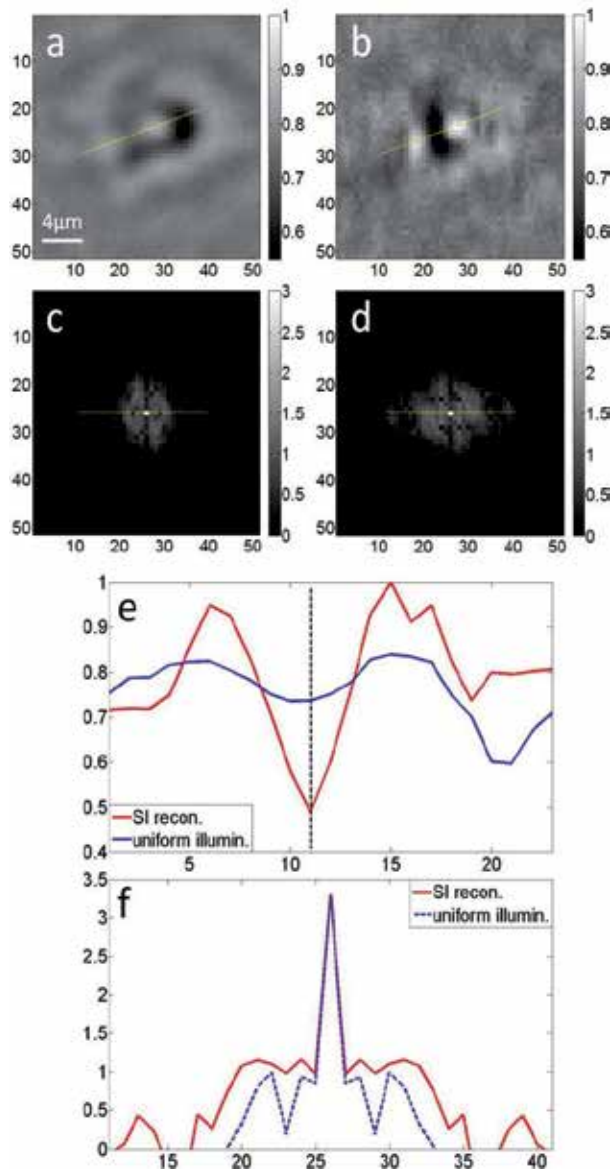


Figure 4. Flow-scanning structured illumination reconstruction of yeast cells. (a) Reference image with uniform illumination (without SI). (b) Reconstructed yeast particles using SI, calculated with the three consecutive images of Figure 3(a)–(c) and Eq. (4). (c) Fourier spectrum of (a), log scale (d) Fourier spectrum of (b), log scale. (e and f) Line profiles of the cross-sections shown in (a and b) and (c and d), respectively.

ment can be quantified using the visibility $V = (I_{\max} - I_{\min}) / (I_{\max} + I_{\min})$, where $V = 0.15$ corresponds to the Rayleigh resolution criterion. Figure 4(e) shows cross-sections of the intensity along the line connecting the two particles. For uniform illumination, the image of the left yeast particle is well below the Rayleigh limit ($V_{\text{left}} = 0.07$) while the right particle is barely visible ($V_{\text{right}} = 0.18$).

In contrast, the respective visibilities increase to 0.48 and 0.50 with structured illumination. The results shown in Figure 4(e) indicate that the left and right yeast particles are approximately 2 and 3 μm in diameter, respectively, with a center-of-mass separation of 4 μm . These measurements would not be possible using only uniform illumination, which is limited to the bare system resolution (4 μm). This ability to discriminate using a single criterion, such as Rayleigh criterion, is necessary for many applications, e.g., automated identification and classification.

Another metric of improvement follows from a measurement of the spatial frequency spectrum. Figure 4(b) and (d) shows the magnitude of Fourier transform of Figure 4(a) and (c), respectively (in log scale). Compared to the uniform illumination case of Figure 4(b), Figure 4(d) displays many more spatial frequencies along the flow direction. According to the line profiles in Figure 4(f), structured illumination provides twice as many spatial frequencies along the illumination pattern direction, k_x , in agreement with linear theory [1–5] and the x -space observations. In terms of k -space area, we measure a coverage ratio of 2.3, corresponding to an equivalent radius ratio ($=k_{\text{extended}}/k_0$) of 1.5. This is a significant improvement considering that only a 1D illumination pattern was used.

1.4. Structured illumination with non-ideal phase shifts

Structured illumination for super-resolution microscopy has been extensively developed. To date, all techniques have however relied on precisely controlled phase shifts of the illumination grating. Here, we consider the case of microfluidic structured illumination, where the illumination pattern remains steady, and where the phase shifts are induced by displacing the object at constant speed in a microfluidic channel above a fixed illumination grating. This approach does not allow precise control of the inter frame phase shifts and requires a more complex reconstruction technique. For this, we derive this solution and show simulation results for proof of concept. We define the following notations.

- $\mathcal{A}(x)$ is the object absorption density. This is the unknown distribution which we want to measure with extended resolution.
- $m(x)$ is the structural mask—a known illumination pattern in the object plane. Here, we use $m(x) = U + 2\cos(\beta \cdot x)$.
- $\text{PSP}(x)$ is the point-spread function of the image detector (CCD) in the object plane—it represents the resolution limit of the imaging system (CCD and lens system.). Its Fourier Transform $\mathcal{F}[\mathcal{P}]$ represents the optical transfer function, $\text{OTF}(k)$.
- “ \otimes ” is the convolution product $(f \otimes g)(x) = \int f(x-x')g(x')dx'$.
- “ \cdot ” is the scalar multiplication.
- “ \mathcal{F} ” is the Fourier Transform operator, e.g., $\mathcal{F}[f \otimes g] = \mathcal{F}[f] \cdot \mathcal{F}[g]$.
- “ x ” represents a vector in real space.

- “ k ” represents a wavevector in the spatial frequency space (Fourier space).

Structured Illumination enables the reconstruction of extended resolution beyond the numerical aperture of a given imaging device. By illuminating the sample with a known high definition pattern, it is possible to wrap high spatial frequencies into visible large-scale Moiré patterns. Structured illumination is a well-known imaging technique [16, 17]. Current algorithms rely on pattern phase shifting by displacement of the illumination source. Here, instead, OFM microscopy leads us to displace the sample. Furthermore, because flow measurement is extremely difficult in a fluid channel, the phase shift between frames is not well controlled. In this paragraph, we solve the problem of extended resolution reconstruction for an arbitrary object displacement δ between frames.

Let v be the speed of the flow, and T be the time between frames, so that $\delta = vT$ is the displacement of the sample between two frames (assumed to be constant). Let β be the wavevector of the illumination pattern. Assuming constant flow speed, and constant image rate, we may write that the p^{th} recorded signal is given by

$$I_p(x) = PSP(x) \otimes \mathcal{A}(x - p\delta) \mathcal{M}(x) \quad (7)$$

where

$$\mathcal{M}(x) = U + e^{i\beta \cdot x} + e^{-i\beta \cdot x} \quad (8)$$

In k space, this corresponds to

$$\tilde{I}_p(k) = \text{OTF}(k) \cdot \left(\mathcal{F}[\mathcal{A}(x - p\delta)] \otimes \mathcal{F}[\mathcal{M}(x)] \right) \quad (9)$$

where

$$\mathcal{F}[\mathcal{M}(x)] = U\delta(k) + \delta(k - \beta) + \delta(k + \beta) \quad (10)$$

and

$$\mathcal{F}[\mathcal{A}(x - p\delta)] = e^{-ip\delta \cdot k} \tilde{\mathcal{A}}(k) \quad (11)$$

Defining $\tilde{X}_p(k) = \tilde{I}_p(k) e^{ip\delta \cdot k}$ and $\gamma = e^{i\delta \cdot \beta}$ Eq. (9) becomes

$$\tilde{X}_p(k) = \text{OTF}(k) \cdot \left(U\tilde{\mathcal{A}}(k) + \gamma^p \tilde{\mathcal{A}}(k - \beta) + \gamma^{-p} \tilde{\mathcal{A}}(k + \beta) \right) \quad (12)$$

$$\tilde{X}_{p+1}(k) - \tilde{X}_p(k) = \text{OTF}(k) \cdot \left(\gamma^p (\gamma - 1) \tilde{A}(k - \beta) + \gamma^{-p} \left(\frac{1}{\gamma} - 1 \right) \tilde{A}(k + \beta) \right)$$

Assuming $\forall k, |k| < k_0$, so that $\text{OTF}(k) = 1$, we deduce that $\forall p \in \mathbb{Z}$, and $\forall |k| < k_0$

$$\begin{aligned} \tilde{A}(k - \beta) &= \frac{\gamma^{1-p}}{(\gamma - 1)^2 (\gamma + 1)} \left[\gamma (\tilde{X}_{p+1}(k) - \tilde{X}_p(k)) - (\tilde{X}_p(k) - \tilde{X}_{p-1}(k)) \right] \\ \tilde{A}(k + \beta) &= \frac{\gamma^{1+p}}{(\gamma - 1)^2 (\gamma + 1)} \left[-\gamma (\tilde{X}_p(k) - \tilde{X}_{p-1}(k)) + (\tilde{X}_{p+1}(k) - \tilde{X}_p(k)) \right] \end{aligned}$$

Writing $J_p(x) = I_p(x + p\delta)$, this becomes

$$\tilde{A}(k + \beta) = \frac{\gamma^{1-p}}{(\gamma - 1)^2 (\gamma + 1)} \mathcal{F} \left[\gamma J_{p+1}(x) - (\gamma + 1) J_p(x) + J_{p-1}(x) \right] \quad (13)$$

$$\tilde{A}(k - \beta) = \frac{\gamma^{1+p}}{(\gamma - 1)^2 (\gamma + 1)} \mathcal{F} \left[J_{p+1}(x) - (\gamma + 1) J_p(x) + \gamma J_{p-1}(x) \right] \quad (14)$$

$$\tilde{A}(k) = \frac{\gamma}{U(\gamma - 1)^2} \mathcal{F} \left[-J_{p+1}(x) + \frac{\gamma^2 + 1}{\gamma} J_p(x) - J_{p-1}(x) \right] \quad (15)$$

where δ and β are experimental parameters that are either known or derived from the measurements. The time lapse between recorded frames, as well as the speed of the fluid, should be identical. By recording a series of images $I_p, p \in [1, N]$, we may use Eqs. (13)–(15) in order to reconstruct the extended k -space.

Accordingly, the extended resolution \mathcal{A}_{EXT} becomes

$$\widetilde{\mathcal{A}}_{\text{EXT}}(k) = \tilde{A}(k + \beta) + \tilde{A}(k) + \tilde{A}(k - \beta) \quad (16)$$

$$\begin{aligned} \widetilde{\mathcal{A}}_{\text{EXT}}(k) &= \frac{\gamma}{(\gamma - 1)^2} \mathcal{F} \left[\left(\frac{\gamma}{\gamma + 1} \alpha_+ + \frac{1}{\gamma + 1} \alpha_- - \frac{1}{U} \right) J_{p+1}(x) \right. \\ &\quad \left. - \left(\alpha_+ + \alpha_- - \frac{\gamma^2 + 1}{\gamma} \frac{1}{U} \right) J_p(x) \right. \\ &\quad \left. + \left(\frac{1}{\gamma + 1} \alpha_+ + \frac{\gamma}{\gamma + 1} \alpha_- - \frac{1}{U} \right) J_{p-1}(x) \right] \end{aligned} \quad (17)$$

where $\alpha_+ = \gamma^{-p} e^{\beta x}$, and $\alpha_- = \gamma^p e^{-\beta x}$. Inverting the Fourier transform gives the result in Eqs. (4) and (5).

2. 3D microfluidic microscopy

In this section, we present two applications of microfluidic flow for 3D microscopy. The first method uses a microfluidic channel that is tilted along the optical axis. We record several progressively defocused images of the flowing sample as it passes across the focal plane. The resulting focal stack is then processed using a Wiener deconvolution algorithm to generate three-dimensional images. Experimental results are shown on flowing yeast cells and reveal precise surface profile information. The second method is a 3D tomography device that combines a light source providing patterned illumination through a slit aperture, a microfluidic channel, and a Fourier lens for simultaneous acquisition of multiple perspective angles in the phase-space domain. 3D absorption is retrieved using standard back-projection algorithms, here a limited-domain inverse Radon transform. Simultaneously, 3D differential phase contrast images are obtained by computational refocusing and asymmetric comparison of complementary illumination angles. We have implemented the technique on a compact glass slide. We demonstrate non invasive 3D phase contrast and absorption imaging capabilities on live, freely swimming *C. elegans*.

The microfluidic channel eliminates the need for a precise translation stage to control the extra degree of freedom required to acquire 3D images on a 2D sensor. Here, either with defocusing or flow scanning. In addition, high sample throughput in an insulated, nontoxic, liquid environment perfectly fits the usual requirements for bio-compatibility.

2.1. 3D microfluidic microscopy using a tilted channel

In the simplest description of an imaging system, with a fixed lens, the imaging condition ensures sharp images when an object is located at a particular depth called focal plane. Here, by tilting the channel [18], samples can descend through this plane, so that different cross-sections will sequentially come into focus.

2.1.1. Experimental setup

The experimental device is presented in Figure 5. The microfluidic channel (500 μm width, 50 μm depth) is etched on a glass slide and placed under a standard wide-field microscope. The slide is tilted by a 15° angle with respect to the optical axis of the microscope objective. The tilt angle, α , is chosen to represent a good compromise between magnification and axial defocusing range. The channel is illuminated with incoherent white light, and the CMOS camera records a $25\times$ magnified image at a constant frame rate, here: 30 fps. We demonstrate the principle with a suspension of yeast cells in glycerol flowing through the microfluidic channel.

The frame rate and the flow speed are selected to allow the acquisition of 100 consecutive frames as each sample passes from one end of the observation window to the other. A constant

flow is maintained using a fixed pressure difference (a 50 cm hydrostatic water column) between the channel input and output. Exposure is adjusted to minimize the flow-induced blur, here below the resolution limit of the imaging device. With shallow channel depth, high kinematic fluid viscosity yields a Hagen–Poiseuille-type laminar flow [19]. Also, the concentration of particles is lower than $250 \mu\text{l}^{-1}$ allowing for easy separation and minimal interactions between flowing particles.

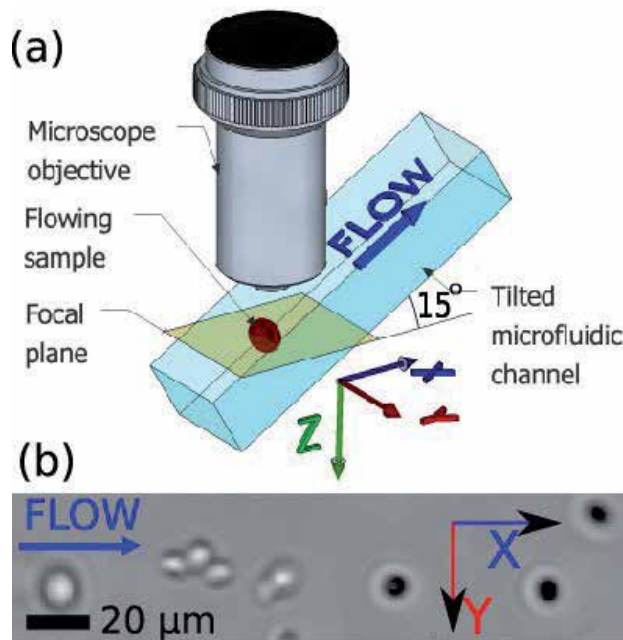


Figure 5. (a) The experimental device is a microfluidic channel placed under the objective of a wide field microscope with a tilt angle of 15° along the optical axis. The sample is carried by the laminar flow along the channel at constant velocity with a static pressure difference. We record video data with a CMOS camera operating at a constant frame rate. (b) Samples, seen as they flow along the channel axis and pass across the focal plane.

2.1.2. Controlled motion and rotation in a laminar liquid flow

The velocity distribution of the flow (see Figure 6) is parabolic. Particles in suspension flow at a constant velocity along the channel axis. However, except for the central axis of the channel, they also experience shear-induced rotation. Here, the acquisition of accurate focal stacks relies on the absence of rotation (or its compensation), and our setup has been designed to minimize the effects of shear in all directions. Along the channel axis u , $\nabla v \cdot u = 0$, and the absence of rotation is a property of the laminar flow. Along the y -axis, we choose to only observe samples flowing in the middle part of a wide channel. Similarly, along the z -axis rotating objects are excluded by considering only particles flowing at the highest velocity in the middle of the channel, where the shear effects cancel. In practice, rotation can be minimized by injecting particles in the center of the channel with microfluidic injection on a separate channel. We note,

however, that object rotation may be useful in other contexts, e.g., for multiple viewpoints, and is easily accessible by changing the injection point or imaging different parts of the flow.

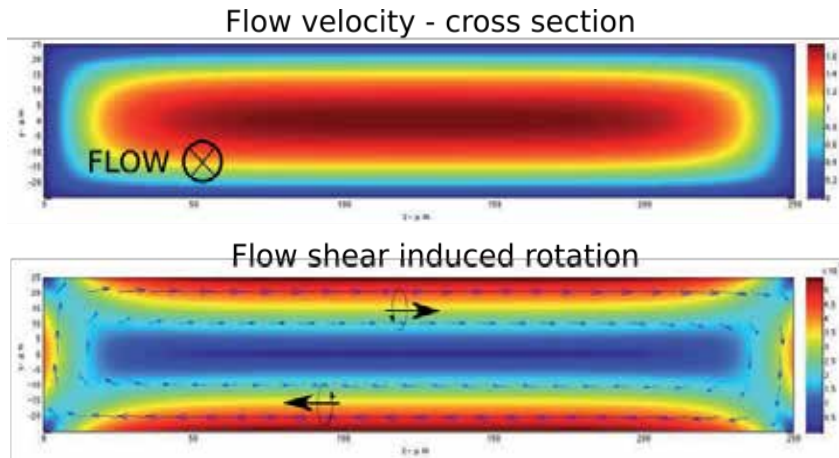


Figure 6. Flow velocity and shear in a laminar flow for a rectangular channel section. Small particles propagate along the streamlines of the flow, and shear effects resulting from the liquid-channel edge interface induce rotations for samples propagating away from the central axis.

2.1.3. Extraction of gradually defocused images

Focal stacks are generated by tracking samples flowing into the channel, as shown in Figure 7. The background noise is subtracted from the signal, and the zero value of the signal (in gray) corresponds to the nominal transparency of the free-running fluid. Letting $I_n(x,y)$ be the intensity of the n th recorded frame. The focal stack, S , is given by

$$S(x, y, z_0 + n|\delta|\sin(\alpha)) = I_n(x + n|\delta|, y) \quad (18)$$

where v is the flow velocity, T , is the frame recording period, and $\delta = Tv$, is the object displacement along the channel axis between two frames.

2.1.4. Focal stack alignment using a defocusing invariant

The extraction of accurate focal stacks is based on aligning successive views of the moving sample as it passes across the focal plane. We experimentally estimate this displacement using the fluid flow velocity and the frame rate, but we also correct for possible position errors using a simple method of particle tracking detailed based on an optical property of defocused images. We compute the center of mass of an image and show that in the case of defocused images of 3D objects with symmetric point-spread functions, the center of mass does not depend on the amount of defocusing [20] (see Figure 8).

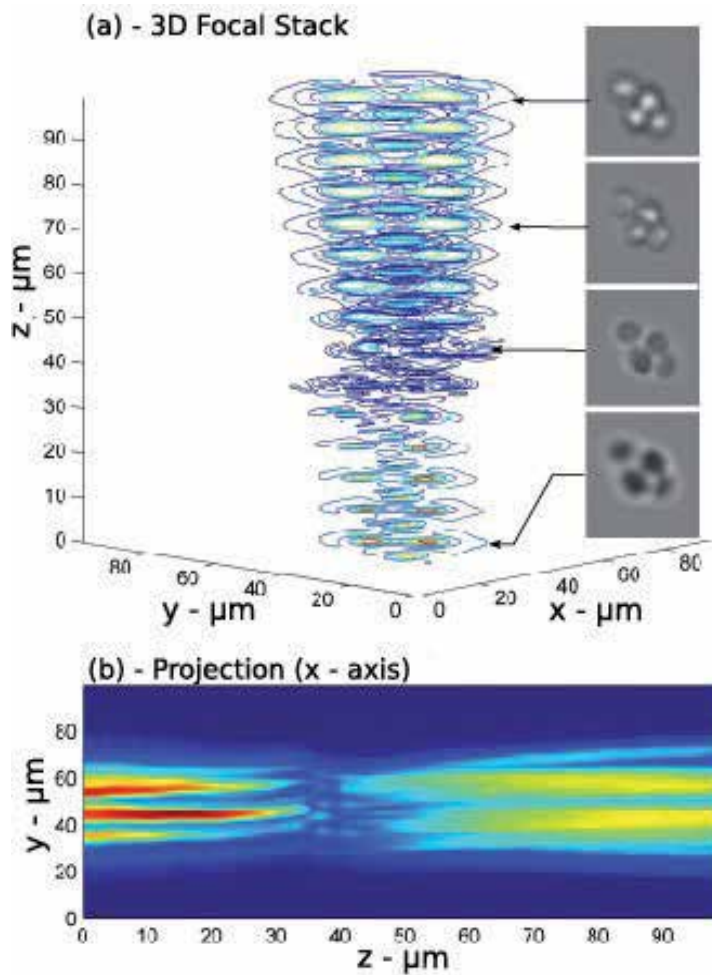


Figure 7. We record focal stacks by observing samples in-motion passing through the tilted microfluidic channel and across the focal plane. With constant flow velocity and frame rate, we record ≈ 100 progressively defocused frames along the z -axis. We digitally track the object with an algorithm based on defocusing invariant properties of the center of gravity of the image. This allows perfect vertical alignment of the focal stack. (a) We measure iso-intensity contours of yeast cells through focus ($\approx 36 \mu\text{m}$). Insets show images of cells at selected levels. (b) Normalized intensity display of the focal stack with background subtracted.

2.1.5. Wiener deconvolution

The reconstruction of the volume absorption distribution of the object, O , relies on solving the well-known deconvolution problem using the experimentally measured focal stack, S , and point-spread function, P in 3D space. O satisfies the volume integral

$$S(r) = [O \otimes P](r) = \int O(r+r')P(r')dr' \quad (19)$$

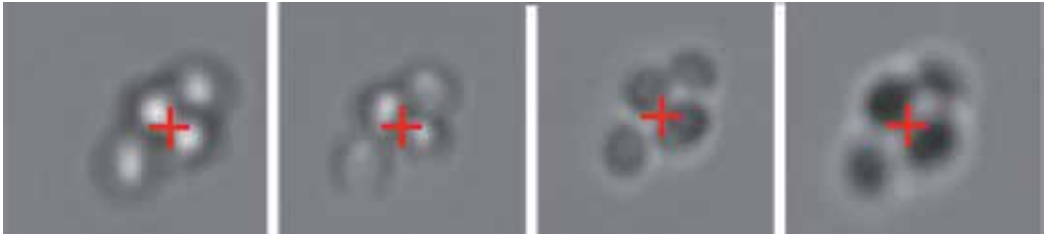


Figure 8. Samples are observed as they flow along the u_x axis and pass across the focal plane. For each acquired image, we compute the center of mass, or first moment, of the image data (red cross). This quantity is a defocusing invariant and can be used to correct for motion correction and imperfections of the laminar flow.

where $r = x.x + y.y + z.z$. Ideally, the optical transfer function, $\mathcal{F}[P]$, is positive and the solution for Eq. (8) is given by

$$O \approx \mathcal{F}^{-1} \left[\frac{\mathcal{F}[S]}{\mathcal{F}[P]} \right] \quad (20)$$

Unfortunately, this solution is known to be extremely sensitive to experimental noise [21]. Several noise-reducing techniques exist to facilitate object recovery when the point-spread function is not known, e.g., maximum likelihood estimation [22] and blind deconvolution [23]. In these methods, which in general are computationally complex, the point-spread function is guessed instead of measured. Adaptive measures [24] are particularly suited to flowing objects, and engineered point-spread functions [25], can be used as well. In this experiment, we choose to measure the point-spread function of the microscope directly by applying the same focal stack acquisition procedure introduced above to a suspension of submicron-sized reference particles. For this calibration, we use a sparse suspension of 800 nm dyed polystyrene beads in glycerol. Flow velocity, frame rate, and exposure conditions are identical as those selected for imaging the samples. We record a focal stack and track one of the flowing reference particles, align the defocused images using the defocusing invariant G_{μ} , and check that the field of observation is clear of other flowing objects. The resulting stack, centered in the window of computation and normalized to a unitary absorption, represents the point-spread function of the microfluidic microscope for this particular tilt angle. While not done here, these reference particles can be embedded in the flow with the samples, as real-time reference points for changing conditions and/or shear compensation. Even with a known, precisely measured point-spread function, the inversion (Eq. (20)) is sensitive to zeros and noise in the measurement. To compensate for this, we use a Wiener deconvolution filter [26]. In this approach, we return to Eq. (19) and consider explicitly an additive noise term, N , which we assume to be independent from the signal.

Eq. (19) becomes

$$S(r) = [O \otimes P](r) + N(r) \quad (21)$$

The Wiener filter finds the best deconvolution operator, D , so that the retrieved object O_R :

$$O_R(r) = [D \otimes S](r) \quad (22)$$

minimizes the RMS reconstruction error, E , given by

$$E = |O - O_R|^2 \quad (23)$$

Here, the Wiener solution, representing an optimal compromise between noise and resolution, is therefore given by

$$O_R \approx \mathcal{F}^{-1} \left[\frac{\mathcal{F}[S]}{\mathcal{F}[P] + \epsilon} \right] \quad (24)$$

where $\epsilon = \frac{\langle |N|^2 \rangle}{\langle |S|^2 \rangle} = 1.2 \cdot 10^{-3}$, is a regularization constant corresponding to the inverse value of the signal-to-noise ratio. Here, the signal intensity is normalized to 1 and the root-mean-square value of the noise (background intensity) is measured and time-averaged in an empty area near the flowing object.

2.1.6. Results

Experimental results on flowing yeast cells are shown in Figure 9. The focal stack, S , and the point-spread function, P , are each processed using Eq. (24). We compute iso-level surface contours from the retrieved three-dimensional data. Figure 9(a) shows a these contours and their projection view along the optical axis, revealing small-scale surface features ($\approx 1-2 \mu\text{m}$), which are clearly resolved (though smoothed somewhat by the regularization process). These features most likely represent early-stage budding of the yeast cells, though other factors can also contribute to their specific morphology [27]. In Figure 9(b), we show contours from the side. All the cells lie in the same vertical plane (a result of the controlled injection), and each cell has flat side walls. This deformation is common in flowing cells [28] and is often used as a diagnostic tool [29]. Many details that are hidden in standard imaging using 2D projections, such as cell orientation, 3D shape, and surface roughness, are readily apparent in the volume images here.

2.2. Microfluidic flow-scanning tomography

In the previous section, we demonstrated 3D surface topology of flowing objects. In this section, we present methods for full-volume tomography [30]. Depending on the respective size of the microfluidic channel and the flowing objects, two methods for the acquisition of tomographic optical projections are shown in Figure 10.

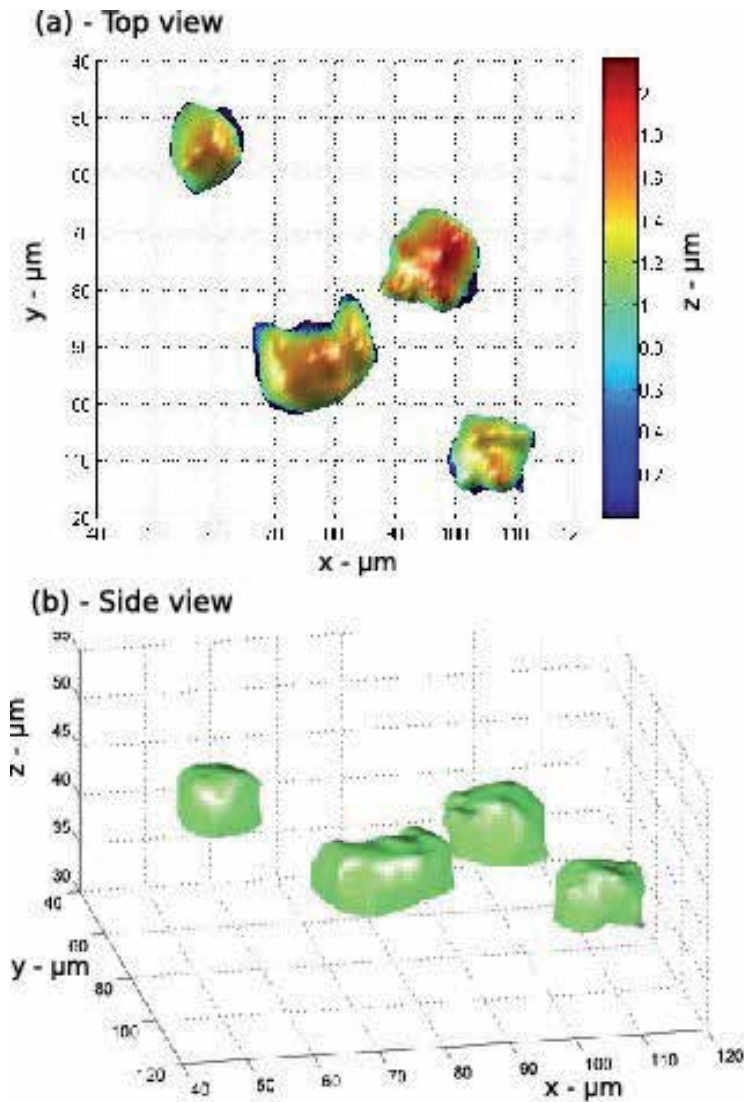


Figure 9. The 3D structure of the object is digitally reconstructed using Eq. (24). (a) An iso-level surface shows subcellular structures at the surface of the cellular membrane. (b) A 3D view of the aggregated yeast cells flowing along the channel axis (z).

The method proposed in Figure 10(a) can be implemented by placing a channel in the optical path of an optical microscope. Here, we will present in greater details the lens-based, flow-scanning tomography technique shown in Figure 10(b).

The phase-space distribution is a 4D space that describes an entire light field, with spatial position $\{x,y\}$ and phase information $\{k_x,k_y\}$ (wave/ray propagation direction). 4D light-field acquisition requires more advanced recording methods than traditional imaging, such as

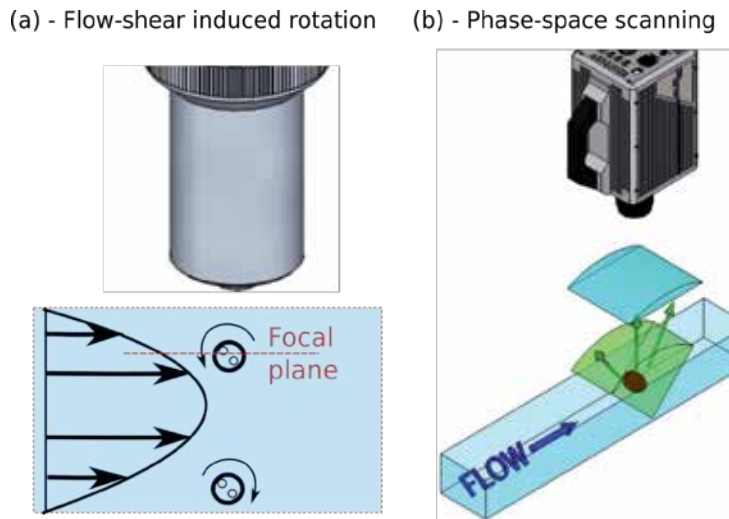


Figure 10. There are two methods for 3D microfluidic tomography. (a) By observing objects flowing at a focal plane located near the upper (or lower) face of the channel, laminar flow-shear effects induce rotation of the objects suspended in the flowing fluid. (b) For larger samples, we introduce a phase-space flow-scanning methods that simultaneously records multiple optical projections along a broad range of angles, slice by slice, as the samples flow across an optical slit.

scanning Fourier windows [31], wave front sensors [32], or light-field cameras [33]. Here, we demonstrate a technique that enables the acquisition of a 3D subspace $\{x, y, k_x\}$ of the 4D light field. We then extract 3D images showing phase and intensity information in two separate tomograms using computational imaging methods. We propose a microfluidic device that combines an illumination source, patterned with a slit aperture along the (y) axis, and a cylindrical lens to collect the light passing through the sample. When placed into an optical microscope, the device enables the simultaneous acquisition of multiple views of the slit aperture for a broad range of perspective angles. This $\{y, k_x\}$ image is recorded by the video camera while the object flows through the microfluidic channel past the slit aperture. Motion therefore provides line-by-line scanning along the (x) axis.

This new approach has several advantages. Each frame records data that are relative to a specific slice through the object. Consequently, there is very little redundancy between the information contained in two distinctive frames. This means that sampling of the optical signal is very effective. In addition, as we show in the experimental results, line-by-line acquisition is very robust to sample motion. This is a great advantage for in-vivo imaging applications.

2.2.1. Experimental setup

The experimental setup is shown in Figure 11. A white light-emitting diode (LED) light source provides a uniform illumination given by $I(x, y, \theta_x, \theta_y) = I_0$, which is restricted with a slit aperture $I(|x| > 0.5 \mu\text{m}) = 0$. The stage is positioned at the focal plane of an optical microscope, in this case a $f = 2$ mm objective with a 6 mm working distance and numerical aperture

(NA=0.70). In between, we place a cylindrical lens at a focal distance ($f'=2\text{ mm}$) from the aperture. With this 1D optical Fourier transform, we record the angular spectrum k_x for each point y illuminated along the slit axis (y). The result is a continuous range of perspective angles for projection tomography, given by $\theta_{\text{MAX}}=2\arcsin\left(\frac{\text{NA}}{n}\right)$, where n is the refractive index of the flowing fluid. In the experiments below, we use a buffer solution for *in vivo* experiments with *C. elegans*, with ($n\approx 1.33$).

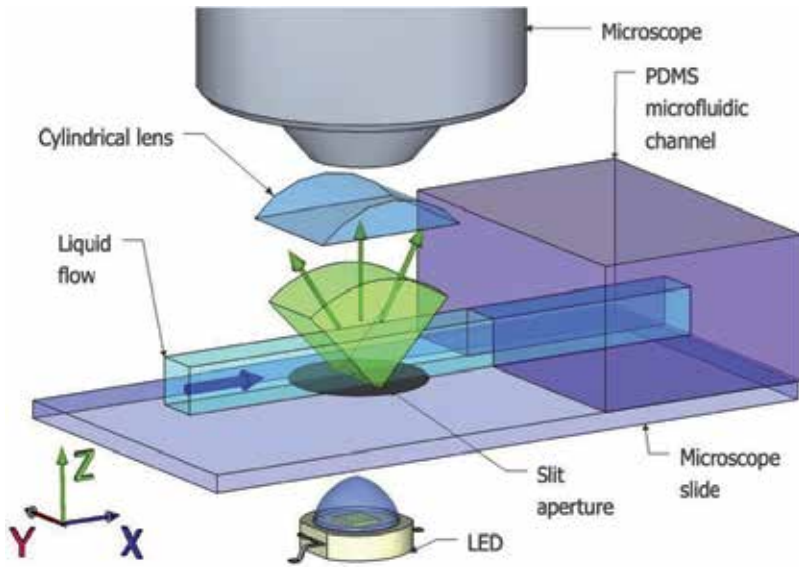


Figure 11. Experimental device. A microfluidic channel is fitted with a $1\ \mu\text{m}$ wide slit aperture along the y -axis that provides a static, cylindrical illumination pattern (in green). A cylindrical lens in a Fourier imaging configuration converts the transmitted light beam into a phase-space image $\{y, k_x\}$. All components are assembled onto a standard microscope slide to be used directly in a microscope.

We adjust the flow speed and frame rate so that $|\delta_x| \approx 2\ \mu\text{m}$.

In Figure 12, we show the optical path from source to detector. In the (y, z) plane, the objective creates an image of the $100\ \mu\text{m}$ wide microfluidic channel cross-section (with a $50\times$ magnification) onto the camera. The optical resolution is limited by the numerical aperture of the microscope objective and given by

$$R_y = \frac{\lambda}{2\text{NA}} \approx 0.4\ \mu\text{m} \quad (25)$$

where λ is the imaging wavelength (here, we use $\lambda=500\text{ nm}$ at the center of the led spectrum). In the (x, z) plane, the Fourier lens separates the continuous range of perspective views of the slit along the other axis of the camera. With an adjustable slit aperture, we reduce the numerical aperture to $\text{NA}_x=0.15$. The optical resolution limit along the slit axis is given by

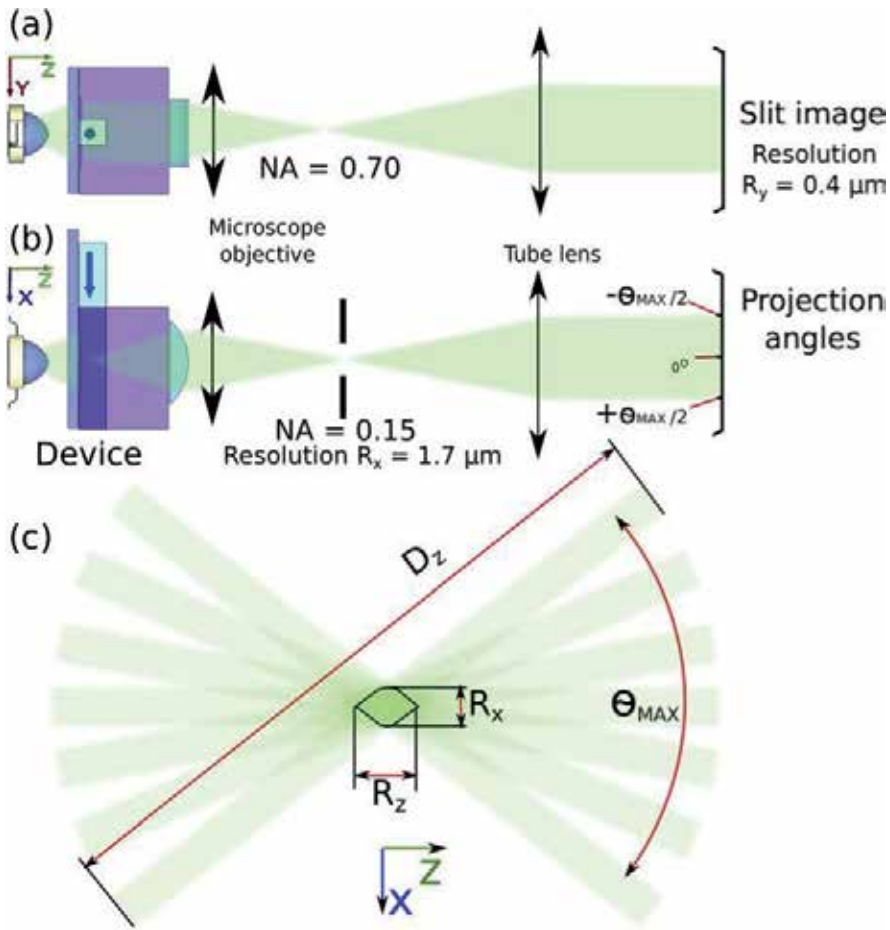


Figure 12. (a) The microfluidic slide is placed at the focal plane of an optical microscope, with a video camera for data acquisition. (b) A secondary slit aperture is used to adjust the depth of field of the acquired optical projections by reducing the effective numerical aperture to $NA_x = 0.15$ along the slit axis. This is a required tradeoff between focal depth and resolution. (c) Each acquired frame contains a continuous range of optical projections of the slit aperture. The depth of field is given by D_z . The resolution R_z along the z -axis corresponds to the size of the domain intersecting all optical projections in the angular range given by θ_{MAX} .

$$R_x = \frac{\lambda}{2NA_x} \approx 1.7 \mu\text{m} \quad (26)$$

The resolution along the z -axis corresponds to the geometrical limitations of the projection area shown in Figure 12 (c) and is given by

$$R_z = \frac{\delta x}{\tan(\theta_{MAX} / 2)} \approx 3.2 \mu\text{m} \quad (27)$$

The associated depth of field, required to acquire 3D information for stack reconstruction, is given by $D_z = \frac{2\lambda}{NA_x^2} \approx 50 \mu\text{m}$. In the simplest case demonstrated here, the limitation of the NA along this axis is a required tradeoff between depth of field and resolution:

$$D_z = \frac{8}{\lambda} R_x^2 \quad (28)$$

We note, however, that additional computational methods are possible to overcome this relation [34].

2.2.2. 3D absorption tomography

The first imaging modality of the device is 3D absorption tomography. As the sample flows in the channel, we record N consecutive frames:

$$I_n(k_x, y), n = 1, \dots, N \quad (29)$$

The raw data are then reassembled into the angular projection domain P_θ , given by

$$P_\theta(x, y) = I_n\left(\frac{2\pi}{\lambda} \sin \theta, y\right) \quad (30)$$

where

$$n = \left\lfloor \frac{x \cos \theta}{VT} \right\rfloor \quad (31)$$

P_θ contains $(x-y)$ views of the flowing sample for different values of the projection angle $|\theta_x| < \theta_{\text{MAX}}/2$. Because each frame contains simultaneous perspective views of the slit aperture, all projected views are already aligned and therefore marginally affected by long-range sample motion. Reconstruction of the 3D structure $S(x, y, z)$ is directly derived from data with tomographic back-projection algorithms, here an inverse Radon transform, by applying the Fourier Slice Theorem to $\widehat{P}_\theta = \mathcal{F}_x[P_\theta]$:

$$\widehat{P}_\theta(k, y) = \widehat{S}(k \cos(\theta), y, k \sin(\theta)) \quad (32)$$

Finally, we retrieve the 3D structure:

$$S(x, y, z) = \mathcal{F}_{x,z}^{-1}[\widehat{S}] \quad (33)$$

A proof-of-principle experiment is shown in Figure 13. We used a translation stage to displace the microscopic sample at a constant speed along the x -axis, and a prepared microscope slide

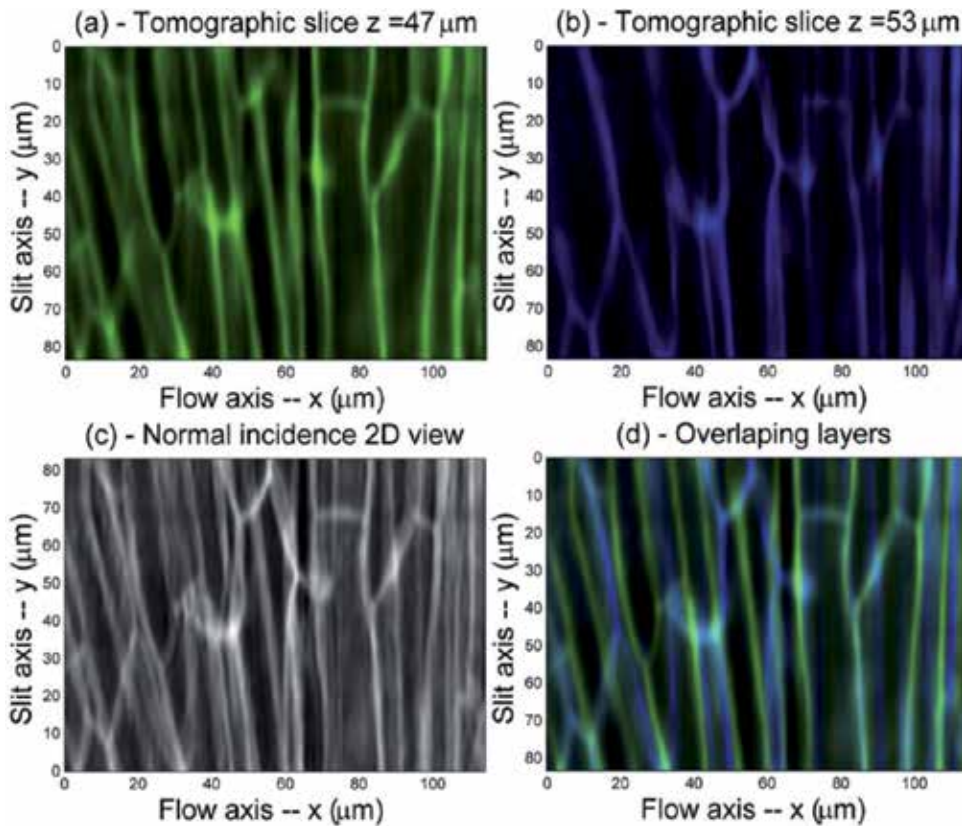


Figure 13. Experimental proof of principle showing the 3D imaging capabilities of the tomographic microscopy device on a prepared microscope slide. A translation stage provides the constant speed displacement along the x -axis during data acquisition. Tomographic views are shown at two different levels (a) in green and (b) in blue color maps. (c) The image as it would have been observed in a white light microscope is compared to (d), an overlapping image of (a) and (b) showing layer separation capability with a $6 \mu\text{m}$ depth difference.

with well-known biomaterial (Elodea leaf slice) to calibrate the phase-space microscopy setup. The 3D structure of cell walls was retrieved and depth information was obtained with enough spatial resolution to distinguish two cellular layers with a $6 \mu\text{m}$ depth difference (Figure 13(a) and (b)). Such separation is not possible with conventional 2D microscopy (Figure 13(c) and (d)).

2.2.3. 3D differential phase contrast tomography

The second imaging modality of the device is 3D differential phase-contrast (DPC) tomography. We consider the angular projection domain P_θ defined previously, and first digitally refocus our data by gradually shifting all perspective views as if the intersection of all projection directions was displaced along the optical axis by a depth z from the center of the channel [35]. The virtually defocused views at depth, z , are given by

$$P_{\theta}^z(x, y) = P_{\theta}(x + z \tan \theta, y) \quad (34)$$

An individual DPC image [36] at focal depth z is then given by

$$\Delta\phi_z^z(x, y) = \frac{I_L^z(x, y) - I_R^z(x, y)}{I_L^z(x, y) + I_R^z(x, y)} \quad (35)$$

where

$$I_L^z(x, y) = \int_{\theta=-\theta_{\text{MAX}}}^0 P_{\theta}^z(x, y) \quad (36)$$

and

$$I_R^z(x, y) = \int_{\theta=0}^{\theta_{\text{MAX}}} P_{\theta}^z(x, y) \quad (37)$$

The resulting DPC tomogram is given by

$$\Delta\phi(x, y, z) = \Delta\phi_z^z(x, y) \quad (38)$$

Because DPC ($\Delta\phi$) and intensity S are simply different methods of processing the raw data (I_n), the two imaging modalities are perfectly registered. This alignment also provides a strong foundation for other methods of phase retrieval, e.g., for ambiguities in reconstruction [37], and does not suffer from possible artifacts present in coherent methods, e.g., speckle and sensitivity to interference jitter. In addition, phase measurement can also be made quantitative with suitable calibration, and it is possible to combine phase and intensity reconstructions to compute the full (complex) refractive index profile [38].

2.2.4. Results on *C. elegans*

Now we demonstrate 3D imaging of a live *C. elegans* nematode freely swimming in the microfluidic channel. An XX-hermaphrodite is raised at room temperature to the adult stage of development, using standard techniques [39], and placed into a water-based liquid environment with balanced electrolytes (M9 buffer solution). The motion of the nematode along the (y, z) directions is limited by the boundaries of the microfluidic channel but can also be accounted for by preprocessing data, and cancelled with digital frame alignment techniques.

The phase-space scanning microscope setup used in Figure 13 was modified to integrate a 100 μm deep, 100 μm wide microfluidic channel for *C. elegans* 3D tomography. A low flow speed, 10 $\text{nL}\cdot\text{s}^{-1}$, was chosen to provide the best compromise between the available frame rate of the camera and desired resolution.

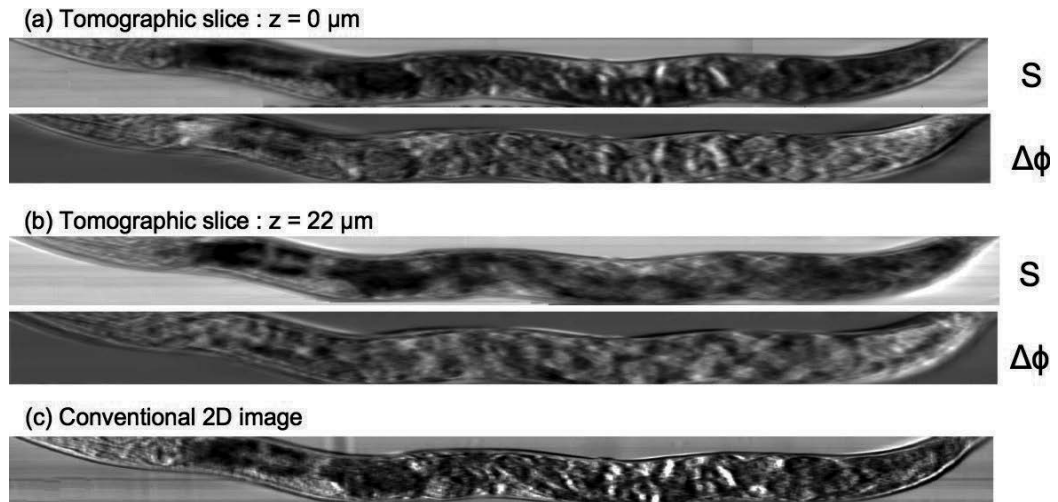


Figure 14. Experimental results on live, adult, awake, wild type *C. elegans* nematodes. We display absorption (S) and differential phase contrast ($\Delta\phi$) tomographic images for two different depths ((a) $z = 0 \mu\text{m}$, and (b) $z = 22 \mu\text{m}$). Tomographic data show the precise 3D location of the reproductive system with eggs (a), and of the digestive system (intestine), the cuticle and oblique somatic muscle fibers 22 μm above (b). In a conventional white light microscopy device (c), these internal features overlap on the same image and it is nearly impossible to identify and locate them.

Experimental results for 3D amplitude and phase contrast tomography are shown in Figure 14. Figure 14(a) and (b) shows digital slices of the retrieved 3D tomogram at two z -levels of interest ($z = 0 \mu\text{m}$ and $z = 22 \mu\text{m}$). At each depth level, two images on the nematode show absorption, from optical projection tomography (S), and difference phase-contrast (DPC) tomography ($\Delta\phi$). In the reference frame at $z = 0 \mu\text{m}$, absorption tomographic slices (S) show the pharynx and its two bulbs on the left side (head), and the reproductive system, with a view of the eggs in the center part of the body. At a different depth ($z = 22 \mu\text{m}$), the digestive system, with distal gonad and the intestine, is clearly apparent.

Differential phase contrast is well suited for the observation of interfaces between tissue layers with different refractive indices. With nearly transparent live roundworms, the DPC tomographic slices ($\Delta\phi$) enable the observation and localization of a few eggs at a time at each depth level. Eggs that could not be observed clearly with absorption images only at the level of the digestive system ($z = 22 \mu\text{m}$).

We show a conventional optical microscopy image of the worm in Figure 14(c) to compare our technology with more conventional imaging methods. Here, because all the structures previously identified now overlap in a single image, it is much harder to identify them from

only one perspective view. In addition, it is also impossible to find their respective positions along the optical axis.

3. Conclusion

In conclusion, we have presented several microfluidic microscopy methods that combine a liquid channel, optical instrumentation, and computational imaging.

These technologies inherit the advantages of microfluidic channels. Samples move with the flow in a biocompatible fluid and are guided precisely to the observation window for optical imaging. High sample throughput allows both large data sets for population studies as well as repeated imaging of the same sample for longitudinal studies (e.g., to track development/aging or to evaluate drug delivery and response). Microfluidics also provides a pathway for object sorting and fully automated imaging with little to no sample preparation.

By using the flow as a degree of freedom for imaging, we allow the imaging sensor to capture a more diverse data set than is possible with static samples. Beyond simple multiplicity of images, multiple illumination orientations, shifts, and perspectives are possible. Computational analysis then leverages the image diversity into improvements in resolution, quantitative measurement of surface structure, and even 3D tomographic imaging of phase and absorption. Remarkably, the flow also allows for a certain amount of self-error correction, as integrating the known properties of cell transport in a laminar flow enables computational adjustment for imperfections of the microfluidic channel, such as pinching and fabrication defects, as well as variations in the flow velocity.

These microfluidic microscopy methods can be either scaled down in size for individual cells or scaled up for larger animals. They can operate on their own or be integrated easily with existing devices, such as flow cytometers, microscopes, and imaging systems, e.g., with a modified microscope slide. Likewise, they can be implemented with or without lenses, enabling a variety of miniaturized, on-chip forms. And finally, they can coexist with other modalities of imaging, such as spectroscopy and (photo-) acoustic sampling, for the acquisition of higher-dimensional data cubes.

Author details

Nicolas Pégard¹, Chien-Hung Lu¹, Marton Toth¹, Monica Driscoll¹ and Jason Fleischer^{2*}

*Address all correspondence to: jasonf@princeton.edu

¹ Department of Electrical Engineering, Princeton University, Olden Street, Princeton, USA

² Department of Molecular Biology and Biochemistry Nelson Biological Labs, Rutgers University, Piscataway, USA

References

- [1] Lukosz W, Marchand M. Optischen abbildung unter ueberschreitung der beugungsbedingten aufloesungsgrenze. *Journal of Modern Optics*, 1963; 10(3):241–255.
- [2] Neil M, Squire A, Jusikaitis A, Bastiaens P, Wilson T. Wide-field optically sectioning fluorescence microscopy with laser illumination. *Journal of microscopy*, 2000;197(1):1–4.
- [3] Heintzmann R, Cremer CG. Laterally modulated excitation microscopy: improvement of resolution by using a diffraction grating. In *BiOS Europe'98*. International Society for Optics and Photonics; 1999. pp. 185–196.
- [4] Gustafsson MGL, Agard DA, Sedat JW. Doubling the lateral resolution of wide-field fluorescence microscopy using structured illumination. In *BiOS 2000. The International Symposium on Biomedical Optics*. International Society for Optics and Photonics; 2000. pp. 141–150.
- [5] Lu CH, Pégard NC, Fleischer JW. Flow-based structured illumination. *Applied Physics Letters*, 2013;102:161115.
- [6] Frohn JT, Knapp HF, Stemmer A. True optical resolution beyond the Rayleigh limit achieved by standing wave illumination. *Proceedings of the National Academy of Sciences of the United States of America*, 2000;97(13):7232–7236.
- [7] Gustafsson MGL. Nonlinear structured-illumination microscopy: wide-field fluorescence imaging with theoretically unlimited resolution. *Proceedings of the National Academy of Sciences of the United States of America*, 2005;102(37):13081–13086.
- [8] Kner P, Chhun BB, Griffis ER, Winoto L, Gustafsson MGL. Super-resolution video microscopy of live cells by structured illumination. *Nature Methods*, 2009;6(5):339–342.
- [9] Yang S, Zheng G, Lee SAH, Yang C. Stereoscopic optofluidic on-chip microscope. In *Winter Topicals (WTM), 2011 IEEE*. IEEE; 2011. pp. 91–92
- [10] Heng X, Erickson D, Ryan Baugh L, Yaqoob Z, Sternberg PW, Psaltis D, Yang C. Optofluidic microscopy, a method for implementing a high resolution optical microscope on a chip. *Lab on a Chip*, 2006;6(10):1274–1276.
- [11] Isikman SO, Bishara W, Mavandadi S, Yu Frank W, Feng S, Lau R, Ozcan A. Lens-free optical tomographic microscope with a large imaging volume on a chip. *Proceedings of the National Academy of Sciences of the United States of America*, 2011;108(18): 7296–7301.
- [12] Kristensson E, Richter M, Pettersson S-G, Ald'en M, Andersson-Engels S. Spatially resolved, single-ended two-dimensional visualization of gas flow phenomena using structured illumination. *Applied Optics*, 2008;47(21):3927–3931.

- [13] Fiolka R, Shao L, Hesper Rego E, Davidson MW, Gustafsson MGL. Time-lapse two-color 3d imaging of live cells with doubled resolution using structured illumination. *Proceedings of the National Academy of Sciences of the United States of America*, 2012;109(14):5311–5315.
- [14] Kristensson E, Berrocal E, Richter M, Pettersson S-G, Ald'en M. High-speed structured planar laser illumination for contrast improvement of two-phase flow images. *Optics Letters*, 2008;33(23):2752–2754.
- [15] Kim P, Abkarian M, Stone HA. Hierarchical folding of elastic membranes under biaxial compressive stress. *Nature Materials*, 2011;10(12):952–957.
- [16] Gustafsson MGL. Surpassing the lateral resolution limit by a factor of two using structured illumination microscopy. *Journal of Microscopy*, 2000;198(2):82–87.
- [17] Gustafsson MGL. Nonlinear structured-illumination microscopy: wide-field fluorescence imaging with theoretically unlimited resolution. *Proceedings of the National Academy of Sciences of the United States of America*, 2005;102(37):13081–13086.
- [18] Pégard NC, Fleischer JW. 3D deconvolution microfluidic microscopy using a tilted channel, *Journal of Biomedical Optics*, 2013;18:040503.
- [19] Stone HA, Kim S. Microfluidics: basic issues, applications, and challenges. *AIChE Journal*, 2004;47(6):1250–1254.
- [20] Reed Teague M. Deterministic phase retrieval: a green's function solution. *JOSA*, 1983;73(11):1434–1441.
- [21] Tikhonov AN, Goncharky AV, Stepanov VV, Yagola AG. *Numerical methods for the solution of ill-posed problems*, vol. 328. Springer; 1995.
- [22] Richardson WH. Bayesian-based iterative method of image restoration. *JOSA*, 1972;62(1):55–59.
- [23] Chan TF, Wong C-K. Total variation blind deconvolution. *IEEE Transactions on Image Processing*, 1998;7(3):370–375.
- [24] Dong W, Zhang L, Shi G, Wu X. Image deburring and super-resolution by adaptive sparse domain selection and adaptive regularization. *IEEE Transactions on Image Processing*, 2011;20(7):1838–1857.
- [25] Quirin S, Prasanna Pavani SR, Piestun R. Optimal 3D single molecule localization for super resolution microscopy with aberrations and engineered point spread functions. *Proceedings of the National Academy of Sciences of the United States of America*, 2012;109(3):675– 679.
- [26] Chatwin CR, Wang RK. *Frequency domain filtering strategies for hybrid optical information processing*. Research Studies Press Ltd.; 1996.
- [27] Ohya Y, Sese J, Yukawa M, Sano F, Nakatani Y, Saito TL, Saka A, Fukuda T, Ishihara S, Oka S, et al. High-dimensional and large-scale phenotyping of yeast mutants. *Pro-*

- ceedings of the National Academy of Sciences of the United States of America*, 2005;102(52): 19015–19020.
- [28] Abkarian M, Faivre M, Horton R, Smistrup K, Best-Popescu CA, Stone HA. Cellular-scale hydrodynamics. *Biomedical Materials*, 2008;3(3):034011.
- [29] Westendorf C, Bae AJ, Erlenkamper C, Galland E, Franck C, Bodenschatz E, Beta C. Live cell flattening – traditional and novel approaches. *BMC Biophysics*, 2010;3(1):9.
- [30] Pégard NC, Toth ML, Driscoll M, Fleischer JW. Flow-scanning optical tomography. *Lab on a Chip*, 2014;(14):4447–4450.
- [31] Waller L, Situ G, Fleischer JW. Phase-space measurement and coherence synthesis of optical beams. *Nature Photonics*, 2012;6(7):474–479.
- [32] Hartmann J. Bemerkungen über den bau und die justirung von spektrographen. *Z. Instrumentenk., 1900;20(47):2.*
- [33] Ng R, Levoy M, Brédif M, Duval G, Horowitz M, Hanrahan P. Light field photography with a hand-held plenoptic camera. *Computer Science Technical Report CSTR*, 2005;2(11).
- [34] Forster B, Van De Ville D, Berent J, Sage D, Unser M. Complex wavelets for extended depth-of-field: a new method for the fusion of multichannel microscopy images. *Microscopy Research and Technique*, 2004;65(1–2):33–42.
- [35] Tian L, Wang J, Waller L. 3D differential phase-contrast microscopy with computational illumination using an led array. *Optical Letters*, 2014;39(5):1326–1329.
- [36] Hamilton DK, Sheppard CJR. Differential phase contrast in scanning optical microscopy. *Journal of Microscopy*, 1984;133(1):27–39.
- [37] Seldin JH, Fienup JR. Numerical investigation of the uniqueness of phase retrieval. *Journal of Optical Society of America A*, 1990;7(3):412–427.
- [38] Arnison MR, Larkin KG, Sheppard KJR, Smith NI, Cogswell CJ. Linear phase imaging using differential interference contrast microscopy. *Journal of Microscopy*, 2004;214(1):7–12.
- [39] Stiernagle T. Maintenance of *C. elegans*. *C. elegans: a practical approach*; 1999. pp. 51–67.

Microfluidics and Electronics

Integrated Control of Microfluidics – Application in Fluid Routing, Sensor Synchronization, and Real-Time Feedback Control

Elishai Ezra, Danny Bavli and Yaakov Nahmias

Additional information is available at the end of the chapter

<http://dx.doi.org/10.5772/64429>

Abstract

Microfluidic applications range from combinatorial chemical synthesis to high-throughput screening, with platforms integrating analog perfusion components, digitally controlled microvalves, and a range of sensors that demand a variety of communication protocols. A comprehensive solution for microfluidic control has to support an arbitrary combination of microfluidic components and to meet the demand for easy-to-operate system as it arises from the growing community of unspecialized microfluidics users. It should also be an easy to modify and extendable platform, which offer an adequate computational resources, preferably without a need for a local computer terminal for increased mobility. Here we will describe several implementation of microfluidics control technologies and propose a microprocessor-based unit that unifies them. Integrated control can streamline the generation process of complex perfusion sequences required for sensor-integrated microfluidic platforms that demand iterative operation procedures such as calibration, sensing, data acquisition, and decision making. It also enables the implementation of intricate optimization protocols, which often require significant computational resources. System integration is an imperative developmental milestone for the field of microfluidics, both in terms of the scalability of increasingly complex platforms that still lack standardization, and the incorporation and adoption of emerging technologies in biomedical research. Here we describe a modular integration and synchronization of a complex multicomponent microfluidic platform.

Keywords: Gadgeteer, integrated control, microprocessor, optimization

1. Introduction

First, we will provide a general review of microfluidics control paradigms and applications, focusing on embedded control.

1.1. Microfluidics: Applications to control

Microfluidic technology delivers the potential for high-throughput and high-content studies in a wide spectrum of experimental sciences, from biology to chemistry and physics. It provides the ability to precisely control experiments at the microscale [1–4], and enables easy and fast automation using computer-controlled micromechanical valves [5, 6]. Indeed, the ever-increasing desire to delve into biology at single entity level has made microfluidics remarkably relevant for the biological domain. By virtue of microfluidic's compatible length scale, compliant surface chemistry and the minuscule reagent volume usually required, microfluidics has opened up new research opportunities in the field of biological science, which even a decade ago looked utterly unattainable [7]. For example, Bhatia and colleagues used microfabricated stamps to generate a micropattern for coculturing hepatocytes and 3T3 fibroblasts in the study of cell-cell interactions [2]; Ho and colleagues used an enhanced field-induced dielectrophoresis trap to pattern hepatocytes and endothelial cells in a radial pattern to mimic the lobular morphology of liver tissue [8]; and Quake and colleagues developed a microfluidic device consisting of thousands of microfabricated switches for a genomic analysis at single-cell resolution [9].

Major microfluidics platforms include capillary, centrifugal, electrokinetic, and pressure-driven platforms [10]. In laboratory settings, pressure-driven platforms are dominant. Microfluidics handling in pressure-driven platforms often includes the control of three main aspects: fluid perfusion, valves control, and sensors monitoring. Fluid perfusion is mostly implemented using linear actuated devices such as syringe pumps and pressure sources. Syringe pumps are commercially available and can be usually controlled manually or via a computer using standard data protocols such as USB, RS-485, RS-232, or GPBI (IEEE-488). For example, the syringe pump PHD ULTRA by Harvard Apparatus can be controlled manually using a touch screen and embedded software that features sequence templates and method wizards, using standard data protocols. Pressure sources are often found in standard laboratory settings and are also commercially available. Pressure sources can be controlled with a pressure regulator, which can be configured either manually usually by turning a knob that compresses a fine-pitched spring or by a computer. A dominant subclass of computer-controlled regulators is based on proportional converters, where a current or a voltage proportionally sets the level of the output pressure. For example, FESTO's lines of products: VPPE™ feature regulators that proportionally match the regulator output pressure to a range of voltage. The level of voltage can be controlled via a computer-connected control unit (FESTO's setpoint value module). Other companies commercialize more expensive integrated products. For example, Elveflow (powered by National Instruments™) commercializes a line of products called AF-1™ that integrates a pressure source and a computer-controlled regulator. While several companies commercialize integrated control products, they are usually configured using closed-source software, which is often limited to a specific line of products.

Since its original development in the laboratory of Prof. Stephen Quake, the microfluidic valve became the basic unit of fluid handling in pressure-driven microfluidic-based platforms and it plays a role analogous to that of the transistor in semiconductor electronics [11]. Today's

conventional biological automation paradigm is being replaced by the integration of microfluidic devices with mechanical valves [12]. This technology enables the automation of experiments and has been used in applications such as protein crystallography [13], genetic analysis [14], amino acid analysis [15], high-throughput screening [12], bioreactors [16], chemical synthesis [17], and single-cell analysis [18]. The current design of a microfluidic valve uses air pressure or thermal actuation [19] to control microstructured switches fabricated from two-layered polydimethylsiloxane (PDMS) [11]. During the fabrication process, a membrane is formed where the control channel and flow channel intersect orthogonally, constructing a valve. Current state-of-the-art microfluidic devices integrate numerous microvalves (microfluidics large-scale integration (LSI)) that need to be independently or jointly controlled using individual pressure lines. The main control method of microfluidic valves is based on a branched pressure source implemented with pressure manifolds. Each manifold outlet can be digitally controlled with specialized hardware/software, which is commercially available. For example, FESTO commercialized a modular pressure manifold called MH-1 that can be configured to integrate an arbitrary number of pressure lines. Each pressure line requires a controllable digital line. The Microfluidics Foundry at Stanford University established one popular method of controlling manifolds' digital lines. They distributed a microcontroller and an integrated circuit that can use a computer to configure each of the manifold's pressure lines independently via MATLAB® or LabVIEW (<https://goo.gl/dnWFKX>). Other companies have commercialized specialized systems for controlling multiple pressure lines. For example, Elveflow® commercializes a line of products called OB-1™ that enable independent control of four pressure lines and Fluigent™ commercializes OEM, a line of products that enable the control of up to eight pressure lines.

Digital microfluidic is emerging technology for precise control and manipulation of discrete liquid droplets, and it is based on an array of self-addressable electrodes that control the drops' surface tension. Control of such system is readily integrated since conventional pumps, valves, or channels are not involved [20]. In the past decade, digital microfluidics has been applied to a range of problems in biology, chemistry, and medicine. For example, Walker and colleagues used digital microfluidics for electrophoretic separations [21], Schmalzing and colleagues used it for DNA analysis [22], and Figeye and colleagues used it for protein/enzyme analysis [23]. Control of such microfluidics platforms is based on activate/deactivate electrodes patterned in the device.

1.2. Embedded control

An embedded system is a microprocessor-based control platform, built to manage and regulate a definite range of functions with a limited user interface and a self-contained on-chip memory [24]. In virtually every control-embedded system, the goal is to control an aspect of an electromechanical system—from laser microscopy to digital cameras. Microprocessors are deeply ingrained into modern day life with over 6 billion new microprocessors used each year [25]. Modern cars, for example, may have tens of microprocessors controlling different functions. One of them, the engine management system, controls the fuel mixture and ignition, alters the parameters and timing based on independent sensor-derived real-time data analysis,

and sends indication status to the driver [24]. An embedded system consists of a processor, which provides the computational resources; a nonvolatile memory that contains initialization routines and software; peripherals that include sensors and input/output interfaces; software which constitutes the initialization and configuration procedures, the operating system, and the application; and algorithms, which are key constituents of the software and can range from mathematical processing to models of the external environment which are used to interpret information from external sensors. A typical architecture of an embedded control system is shown in Figure 1.

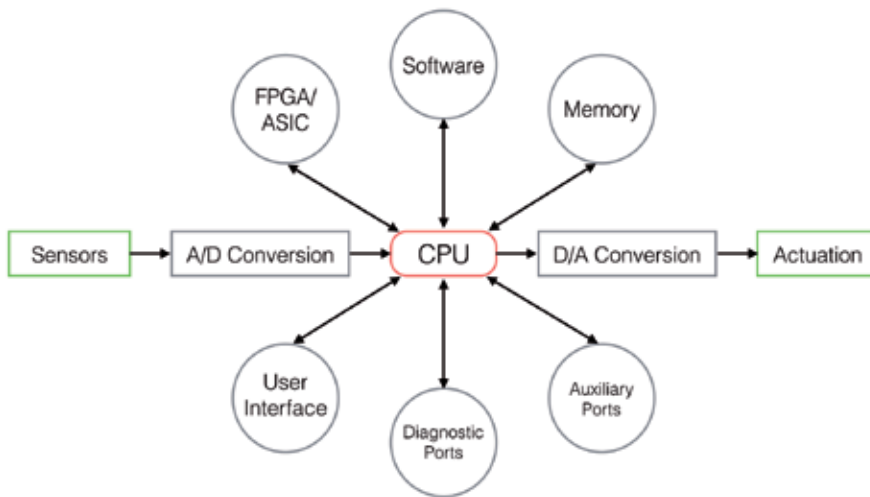


Figure 1. A typical architecture of an embedded control system.

The two most important complimentary technologies in embedded systems design are Application-Specific Integrated Circuits (ASICs) [26] and System on a Chip (SoC) [27]. ASIC is a customized integrated circuit, which was designed for a particular use. It can be designed to efficiently implement combinatorial logic circuits in very high density of up to 100 million gates/chip using hardware description languages. ASICs can be found in a wide spectrum of electronic devices, from custom real-time image processing [28, 29] to speech synthesis [30] and acoustic features extraction [31]. Because ASICs are custom-made, they are only available to the company, which designed them and are considered proprietary technology. Modern ASICs, include a CPU, memory controller, main memory, I/O control, and the various buses and interconnects. For example, ASIC of SoC architecture for speech recognition and speech compression may contain a microprocessor, a DSP (Digital Signal Processor, which was optimized for digital signal processing), two codecs (coder/decoder—capable of encoding or decoding a digital data streams), and input/output analog channels [32].

Another important design strategy in embedded design is the Field Programmable Gate Array (FPGA) [33]. The user configures FPGA after manufacturing (in contrary to ASICs, which are built according to a specific design layout). FPGAs contain arrays of programmable logic

blocks and a hierarchy of reconfigurable interconnects that allow blocks to be combinatorially wired [34].

The development of such systems requires extensive expertise across electronic circuit design (logic, circuit, and physical), PCB layout, and system programming. A schematic of a typical design process for ASIC-based board is shown in Figure 2. While the design of ASICs and FPGAs can potentially produce extremely efficient designs, their impact is very limited because they cannot be utilized for the exploration or validation of new product concepts [35].

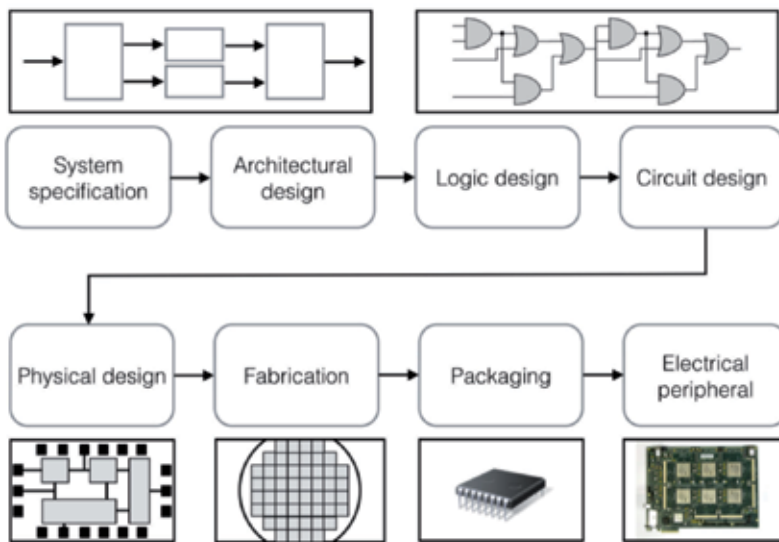


Figure 2. A typical design process of ASIC-based microprocessor.

2. Open-source microcontrollers

Throughout the last decade, engineers have been exploiting the notion of hardware and software abstraction (component-based architectures) to speed the development of increasingly complex control systems [36]. For example, the European Disappearing Computer Initiative explored different options for creating a modular system for prototyping and proposed a common processing and communications circuit board with a variety of ways to connect sensors and actuators [37]. Similar to hardware, software was also based on a modular approach, containing core libraries for control and communication. Simultaneously, “Wiring” was developed (<http://wiring.org.co>)—a microcontroller coupled with an accessible programming language (which was built upon “Processing” [38]) that targeted artists and designers. The Arduino system has taken the notion of low-cost and accessible components and tools much further. Arduino has arguably become the standard open-source platform for physical prototyping, with a vibrant developers’ community and a tremendous range of supported

hardware. Arduino is an open-source hardware board, designed around an 8-bit Atmel AVR microcontroller, which can be programmed with C or C++, and it was used numerous times in laboratory settings (Figure 3). For example, the Arduino Geiger was designed to implement a radiation detector, pHduino was designed to implement a pH meter, Xoscillo was designed to implement an oscilloscope, and OpenPCR was designed to perform DNA analysis [39]. Over the past few years, several additional platforms have been developed that complement the Arduino world in various ways. One example is the Raspberry Pi, which is manufactured by Newark Corporation (Figure 3). Raspberry Pi functions as a computer, commonly operated with Linux, and includes most of the components found on a regular computer: CPU, GPU, memory, USB ports, and video/audio inputs and outputs. Another example is the Gadgeteer, open-source microcontroller commercialized by Microsoft and built upon the .NET microframework (Figure 3). The Gadgeteer FEZ Spider Mainboard features a 72 MHz 32-bit ARM7 Processor, 16 MB RAM, LCD controller, and a full support of TCP/IP Stack with SSL, HTTP, TCP, UDP, and DHCP. The Gadgeteer can be connected to Ethernet, a WIFI driver and 3D modems. It supports standard data protocols such as USB, SPI, and I²C, and include UART (enabling communication via EIA, RS-232, RS-422, RS-485). By using expansion modules, the Gadgeteer can be used for wireless communication with Bluetooth, radio, GPS, Xbee WIFI, IR, and RFID. Importantly, the FEZ spider mainboard features 76 GPIOs (general purpose inputs/outputs) digital lines, which can be individually addressed and configured. Another important aspect is the wide range of sensor modules, which were especially designed for the Gadgeteer.



Figure 3. Open-source microcontrollers.

3. Microfluidic control system

Here will review several integrated control platforms for digital and pressure-driven microfluidics.

3.1. Dropbot: Integrated control for digital microfluidics platforms

As was described above, a control of a digital-microfluidic device is based on activate/deactivate electrodes, which were patterned on the device for the direct manipulation of

droplets with no need of actuating mechanical valves nor pressure sources and pumps. In 2013, Fobel and colleagues introduced the design of an open-source control and automation system termed DropBot, which enables manipulation of drop's position and velocity by driving up to 320 independent electrodes [40]. The DropBot is based on an Arduino microcontroller board and is consists of a high-voltage amplifier, high-voltage driver boards, a webcam, and a PC. The system continuously monitors the amplifier output and device impedance to maintain a stable actuation voltage and to track the position and velocity of drops. A schematic of the DropBot control system is shown in Figure 4.

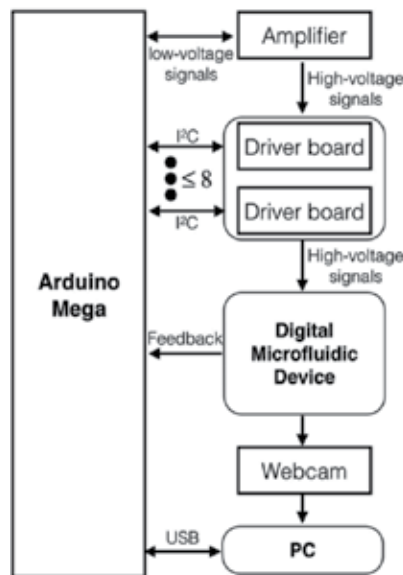


Figure 4. Schematic of the DropBot control system.

3.2. Control of microfluidic routing

Fabrication and characterization of a microfluidic valve

Microfabrication techniques have been developed in the microelectronics industry to create complex electronic circuits with minimum feature sizes currently as small as 7 nm [41]. Techniques for creating the insulating or conducting features include physical vapor deposition, chemical vapor deposition, sputter coating, molecular beam epitaxy, and chemical beam epitaxy [42]. Integrated circuits are created using deposition of conductive areas in a process known as photolithography [43]. Photolithography allows the creation of complex geometric patterns with small feature sizes and it is widely utilized for microfluidics and lab-on-a-chip fabrication. Photolithography is commonly performed using a light sensitive material (photoresist) and a photomask. A positive photoresist becomes soluble where it has been exposed to light, while a negative photoresist becomes insoluble where it has been exposed to light. Following exposure, devices are typically heated and treated with solvents to remove the

soluble photoresist and develop a cured device. Using conventional optical techniques, the minimum feature size that can be created is limited by the diffraction limit of light. For ultraviolet (UV) light (248 nm) features as small as 70 nm can be defined. For microfluidic applications, a variation known as soft photolithography is often used. The hardened product of standard photolithography is used as a master and elastomeric PDMS is poured and cured over it. The channels' width is determined by the photomask and the channels' height is determined by the thickness of the patterned photoresist. PDMS is often chosen for chemical and biological experiments due to its low cost, high oxygen permeability, fast curing time, hydrophobicity, and low toxicity. PDMS forms an irreversible bond to glass using plasma activation, allowing its use with high magnification inverted microscope objectives. Since three-dimensional (3D) control of features is generally limited to time-consuming layer-by-layer alignment [44], most microfluidic designs are limited to two-dimensional (2D) geometries. However, recent fabrication techniques such as 3D printing aim to change that [45, 46]. For example, Bhargava and colleagues showed that 3D printing could be used to rapidly fabricate discrete microfluidic elements that can be assembled into complex 3D circuits [47].

The monolithic micromechanical valve is constructed from two PDMS replica moldings, which are bonded together using plasma activation and curing agent diffusion. One layer defines the control channels, and the other defines the flow channels. Membranes are formed at the intersection of the two layers, allowing valves actuation [11]. A micromechanical valve can be configured in two formations: "push-down" and "push-up". While in a "push-down" formation, the flow layer is aligned below the control layer, in a "push-up" formation the flow layer is aligned above the control layer (Figure 5, left). A "push-down" formation exposes the flow layer to the glass, facilitating prebonding surface modification. Actuation pressure depends on valve dimensions and membrane thickness. However, typically, "push-down" formation requires higher actuation pressure for proper switching relatively to a "push-up" formation—a fact that significantly limits the flow channel height. Performance of both valve formations is highly dependent on the flow channel cross-sectional profile [1]. Valves with square flow channel profiles leave pockets of fluid flow, causing leakage (Figure 5, left). Perfectly sealed valves require rounded flow channels, which are typically fabricated using a thermal reflow of photoresist (Figure 5, right). Generally, all resists which do not crosslink have a certain softening point and thus can be used for reflow. While most negative resists cross-link, all common positive resists do not cross-link and start to soften at approximately 100–130°C.

Here, microfluidic valves were fabricated, actuated, and visualized using a color dye (Figure 6A). Valves were characterized by leakage and response time, which were analyzed repeatedly after 100, 7500, and 15,000 switching cycles to ensure mechanical endurance. Briefly, leakage was calculated with negatively pressurized channels, each withdraws different color dye. Response time was calculated from high frame rate recordings of the valve actuation process. Switching pressure (0% leakage) was measured as 4.5 PSI. No significant changes were noticed after 15,000 switching cycles (Figure 6B). Switches were utilized to create flow cycles of red and blue color dyes in a microfluidic channel for evaluation. The measured total response time is 28 ms, and a mechanical response time of 20 ms.

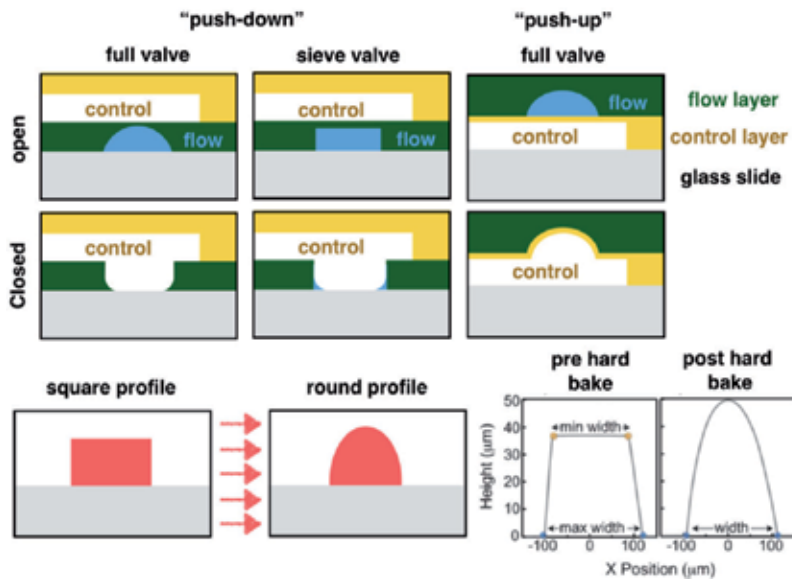


Figure 5. "push-up" and "push-down" valves formations [1].

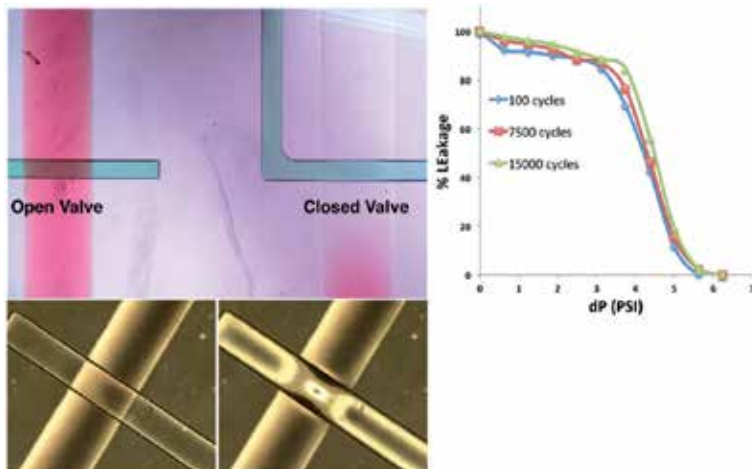


Figure 6. Valves evaluation and characterization. Valves were visualized using color dyes and inspected with a microscope inspection. Leakage was quantified after 100, 7500, and 15,000 switching cycles.

4. Microfluidic large-scale integration

The incorporation of microfluidic valves in a fluidic circuits has enabled the creation of a variety of functional fluidic modules such as micromixers [48, 49], gradient generators [49],

multiplexers [50, 51] and peristaltic pumps [51]. For example, Gomez and colleagues developed a cell culture system, which enables automated culture of 96 cell chambers in parallel that feeds from 16 different inlets through an integrated mixer, a pump, and a multiplexer [52]. The 16 fluid inlets were connected in a binary tree manifold that features an equal fluidic resistance in all branches. The root of the tree was connected to a mixer, which delivers the fluid to a multiplexer for distribution to the chambers. System schematic is shown in Figure 7. Medium injection into the chambers was perfused with an on-chip peristaltic pump, which was implemented using a series of three valves. In this setup, the microfluidic valves were USB controlled with custom electronic units via pneumatic solenoid valves. A different control module, which was connected to a microscope, controlled the temperature and gas composition. Independently, cells were imaged in two-hour intervals. A pressure-driven perfusion system was used to seed the cells and to drive reagents. A custom MATLAB application was written for automatic operation of the actuation sequences based on the user-supplied schedule.

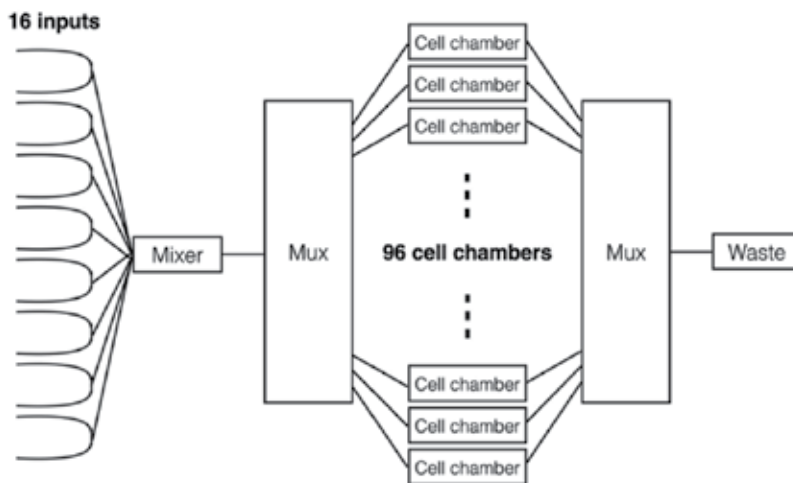


Figure 7. Schematic of an automated culture of 96 cell chambers.

5. Integrated control of pressure-driven microfluidic-based platforms

5.1. Design and specifications

Pressure-driven microfluidic-based platforms are composed of discrete analog and digital perfusion components and sensors that have separate communication protocols, power requirements, and control interfaces limiting system integration. To address this, we designed a control unit based on Gadgeteer FEZ Spider mainboard containing 32-bit ARM7 microprocessor and 11 MB of user available RAM, extended with the Hub AP5 board for a total of 23 control sockets [53]. To bridge between the control unit and the perfusion components, we designed a microfluidic shield that bridges variable power consumption, modulates power

distribution from a standard AC source, and implements control of analog lines. Specifically, analog signal modulation was carried out using passive linear voltage dividers, featuring an output range of 0–10 V and a 7-bit SPI controlled potentiometer with volatile memory. The shield permits a rapid replacement of through-holes resistors in each voltage-dividing module, to modulate the system dynamic range. In addition, as solenoid valve actuation requires 1 W (5/10 V), we implemented a series of high current Darlington transistor arrays supporting 24 units of 1 W (5/10 V) digital lines, each line connected to two Darlington channels supplying up to 0.5 A each. Our Darlington transistors have an operating delay time of 0.15 μ s and a turn-off delay of 1.8 μ s enabling 0.5 MHz of switching capabilities, significantly faster than solenoid response time of 30–50 ms. System schematics is shown in Figure 8. Importantly, our system provides the user with hardware plug and play interface embedded within the Microsoft.Net microenvironment that enables rapid prototyping utilizing programs such as MATLAB for user interface design.

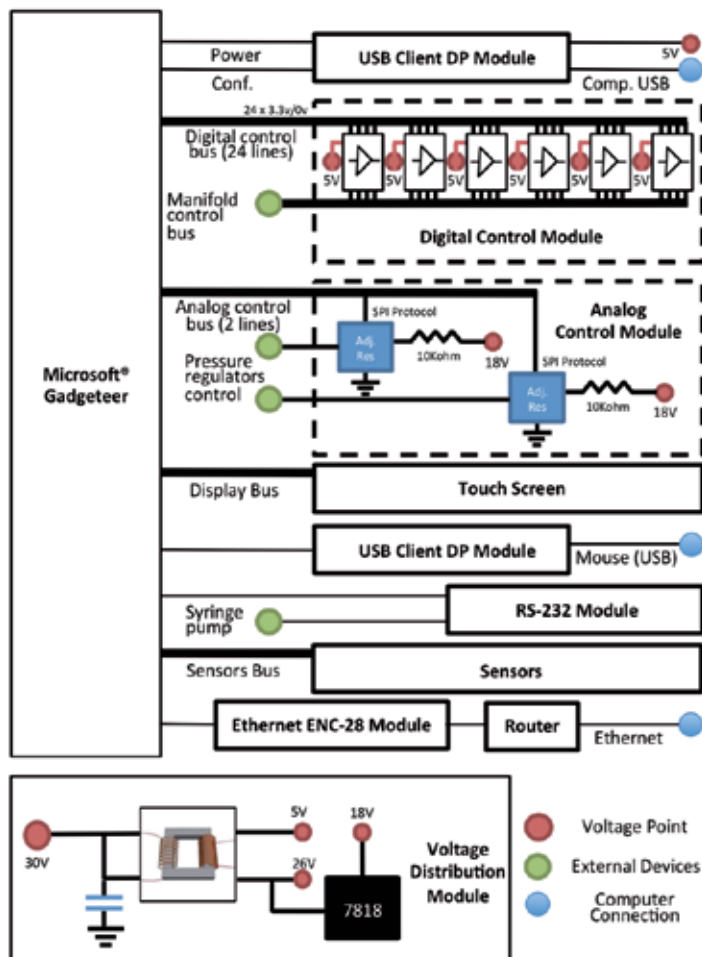


Figure 8. Schematic of the microprocessor-based control unit for pressure-driven microfluidic-based platforms.

5.2. Gadgeteer microcontroller

The.NET Gadgeteer is a rapid open-source development platform that utilizes mainboards and plug-and-play modules that maintained standard connections by Microsoft. The.NET Micro Framework combines the advantages of object-oriented programming, solderless assembly of electronics, and support for customizable physical design [54]. A.NET Gadgeteer system is composed of a mainboard containing an embedded processor and a variety of modules, which connect to the mainboard through a simple plug-and-play interface. There is a great variety of.NET Gadgeteer modules, which are currently available, including: display, camera, networking, storage, and a variety of sensors and input controls. New modules are constantly developed. The.NET Gadgeteer mainboard's sockets are numbered, and each is also labeled with one or more letters, which indicate which modules, can be plugged into it (Figure 9). The.NET Gadgeteer devices are programmed in C Sharp using the.NET Micro Framework via Visual Studio in a desktop, web or phone IDE. An intuitive visual designer and advanced auto code generation capabilities are also provided.

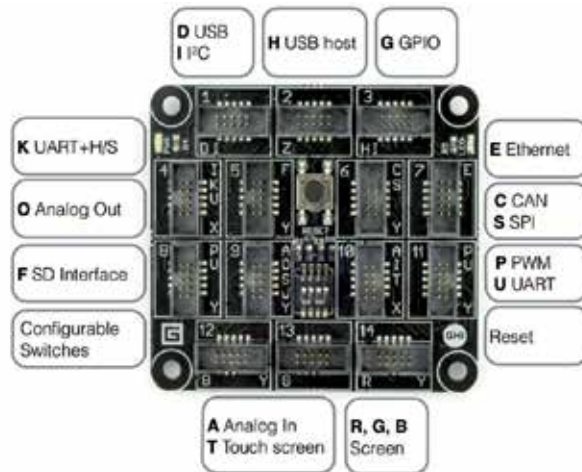


Figure 9. FEZ Spider Gadgeteer mainboard layout.

Gadgeteer mainboards expose their I/O interface through sockets. Each socket is a 10-way connector, with pins labeled 1 through 10. Mainboard sockets support one or more different types. A letter represents each socket type. When a mainboard socket is labeled with a socket type letter, it guarantees a particular set of electrical connections and interfaces on the sockets pins [55]. The full hardware layout of the integrated control system (from the IDE perspective) is presented in Figure 10. Gadgeteer mainboard and extension modules were purchased from GHI electronics (Madison Heights, MI). The control unit was composed of a 32-bit ARM7 microprocessor mounted on the Microsoft FEZ Spider Gadgeteer mainboard. Mainboard functionality was extended with Hub AP5 module that adds 9 additional sockets, a USB client Dual Power module to enable microprocessor programming, a TE35 LCA 3.5" touchscreen display module, USB and RS-232 modules that allows the control of sensors and peripherals.

A serial camera L1 module was added directly for optical inspection. Finally, Ethernet ENC28 module provided a TCP/IP operation mode.

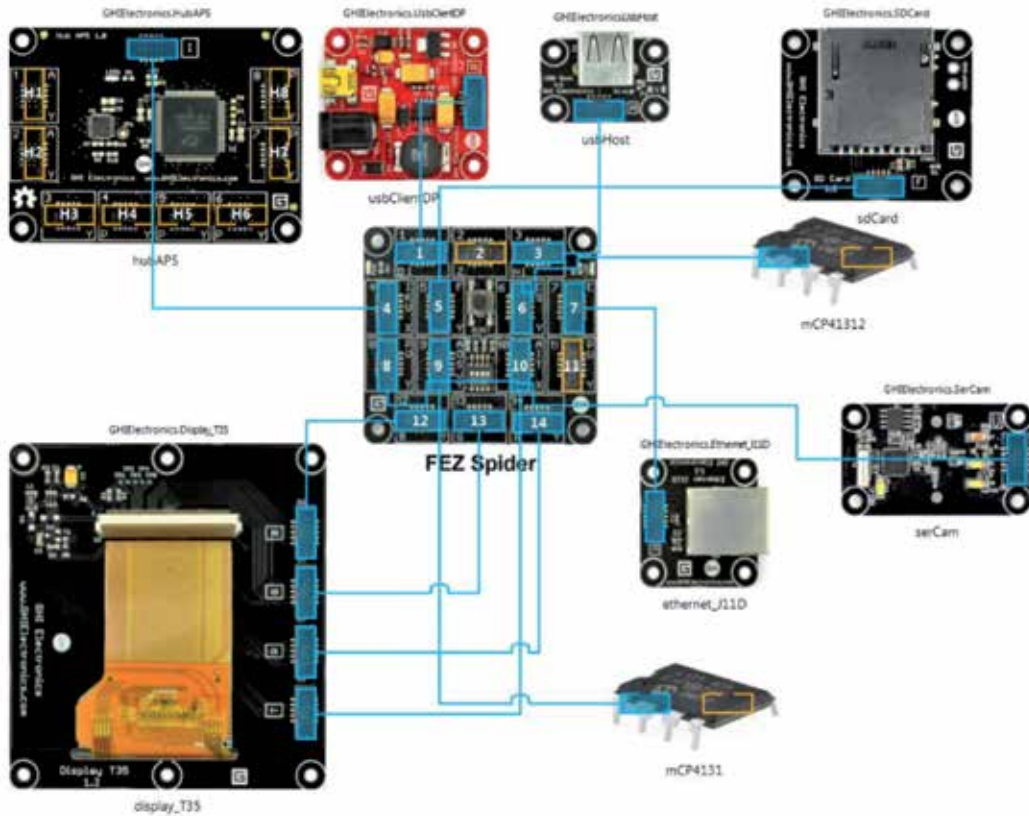


Figure 10. Hardware layout of the integrated control system from the IDE perspective.

5.3. High-current interface circuit

The high-current interface circuit was designed using DipTrace software and printed in a two-layer layout at Beta LAYOUT (Aarbergen, Germany). Controller unit case was designed and fabricated in the Hebrew University workshop. Our control system required a branched voltage module that integrates numerous voltage stabilization circuits and an array of capacitors that filter high-frequency ripple voltages and spikes. The control unit is connected to a standard 220 V, 50 Hz AC power outlet, which was electromagnetically inducted to 5 V using Mean Well NES-35-5 transformer (New Taipei City, Taiwan) that powers the micro-processor and the digital control unit and to 26 V using Mean Well NES-2-24 transformer that powers the pressure regulators and the analog voltage module via an 18 V linear voltage regulator purchased from Toshiba (Tokyo, Japan). The 24 controllable high current digital lines were controlled by the general-purpose input output (GPIO) sockets via a series of high current

TD62783 Darlington transistor arrays purchased from Toshiba. Each driver supports 3.3 V logic operation and a 5 V driving voltage. The analog control module was composed of passive linear voltage dividers, which were implemented using a passive resistor and a 7-bit SPI-controlled MCP4131 potentiometer with volatile memory purchased from Microchip (Chandler, AZ). Gadgeteer driver library was expanded to support the SPI data protocol controlling the potentiometer.

6. Integrated control for combinatorial mixing and real-time sensors monitoring

Microfluidic integrated control provides a straightforward way to automate complex procedures such as mixing, sensors monitoring, and implementation of feedback loops for execution of optimization protocols. In a recent work, we described a utilization of a microfluidic-based system, illustrated in Figure 11, to combinatorially mix samples for the creation of a target color, which was specified by the user, using an implementation of different optimization algorithms such as genetic algorithm, simulated annealing, multiple hill climbing, and random walk. Briefly, the control unit was connected to analog pressure regulators driving two 12-valve pressure manifolds that control a microfluidic switchboard and positive-pressure perfusion. The switchboard fed into an equipressure combinatorial mixer containing an inspection chamber monitored by a UART-controlled optical CCD sensor connected back to the FEZ Spider mainboard, completing the circuit. Flow is driven by positive pressure provided by a second, independently controlled pressure manifold. Pressure across the manifold is held constant by an analog regulator, resulting in an equal pressure distribution on all open ports, and a constant fluid velocity irrespective of the number and combination of inputs. The generated mixture of colors is inspected optically in the inspection chamber. Acquired data is communicated to the control unit that makes the decision regarding the next mixing stage according to the specified optimization protocol.

The growing field of interest in the integration of microfluidics further complicates integrated control with sensors [56]. A growing focus is given to microphysiometers devices that are able to noninvasively measure a metabolic parameter of living cells on a chip [57]. Most commonly, those parameters include cellular acidification, cellular adhesion, oxygen consumption, and energy metabolites such as glucose uptake and lactate production. Sensor monitoring is accomplished by specialized hardware/software via different measures, most commonly being changes in impedance, current, and electric potential. For example, Molecular Devices® commercialized Cytosensor® to measure extracellular acidification [58], as well as lactate and glucose levels [59]. Bionas® commercialized the Discovery 2500 System™ that continuously provides measurements of oxygen consumption and cell impedance [60]. Sensor monitoring is accomplished by specialized hardware/software via different measures, most commonly being changes in impedance, current, and electric potential [61]. Others are based on light emission, ion selective field effect transistors, and resonant frequency [62, 63]. Each of the sensing unit requires a unique hardware/software module, which is able to capture measure, record, analyze, and display it to the user. For example, Molecular Devices® offers variety of

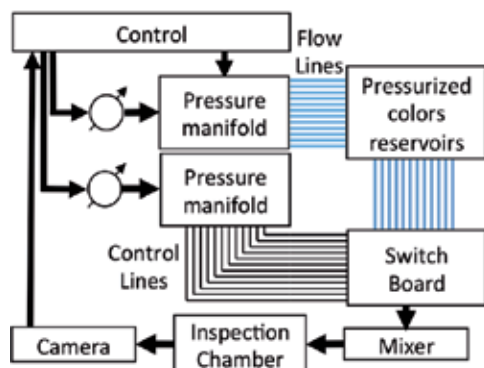


Figure 11. Schematic of the integrated control circuit for combinatorial mixing and real-time sensors monitoring.

data acquisition and analysis software packages, such as the SoftMax®, which serves as the user interface to their popular sensing modules.

Recently, we utilized the switchboard and the control unit for real time monitoring of environmental toxicity requires evaluating the presence of unknown toxins in drinking water and soil samples. The system schematic is illustrated in Figure 12. Briefly, human Huh7 cells were seeded in a microfluidic chamber at a density of 10^6 cells/ml producing a confluence monolayer. Cells were exposed to $100 \mu\text{M}$ of the pesticide rotenone, a mitochondrial complex I inhibitor. Perfusate was connected to a high-resistance waste syringe and a single inlet of the microfluidic switchboard for automated sampling (Figure 12A). We used the microfluidic switchboard to perfuse a sequence of buffer, air, sample, and air over an enzymatic-amperometric lactate sensor every two hours. Introduction of air acts as a diffusion barrier preventing sample contamination and providing zero-point calibration. The electrochemical sensor was connected to an embedded potentiostat that can communicate with the Gadgeteer using a UART protocol. A fully automated 16.5 hours experiment was programed allowing the derivation of a time-of-death of 5.5 hours.

7. Emerging control paradigms

An important movement in the development of integrated control circuits for microfluidics lies within the development of field-deployable and autonomous microfluidic-based systems. For example, Chen and colleagues developed an enzyme-linked immunosorbent assay (ELISA) that can be conducted in field-deployable microfluidic device with smartphone-based imaging [64]. This point-of-care diagnostic device utilizes electrodes that can convert electric current into a microfluidic pump via gas bubble expansion during electrolytic reactions. The micropump receives power from the mobile phone and transports the analytes through the microfluidic device for ELISA. Cleary and colleagues developed a field deployable microfluidic

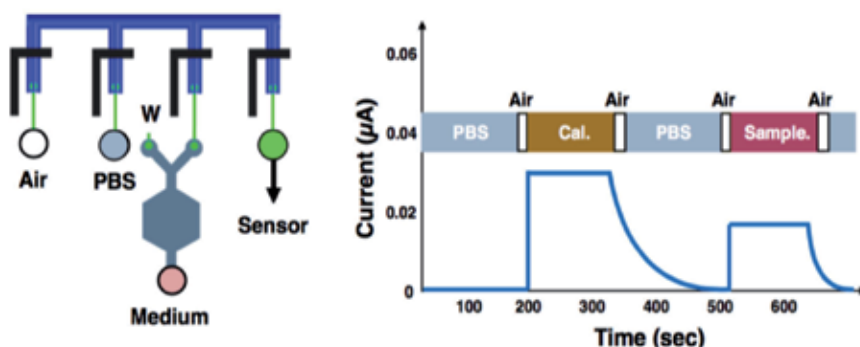


Figure 12. Flow system schematics automated perfusion sequences for sensor monitoring.

dic system for water quality monitoring. The system is composed of the microfluidic device where the mixing, reaction, and detection takes place, a phosphate chemical sensor, an optical detection system that composed of a light source and a photodiode detector and a microcontroller (MSP430F449 by Texas Instruments). The microcontroller controls the analytical components, fluid handling, data acquisition and storage, and wireless communication. This movement of integration is highly specialized and specifically developed for particular applications.

Another important movement aim to replace the need of external support equipment such as mechanical pumps and pressure-actuated valves. A recent development aims to make the control and the functionality of a pump redundant by designing a light operated micropumps. Sze et al. developed this pump by utilizing light energy to activate bacteriorhodopsin and sugar transporter proteins, which create an osmotic pressure gradient and drive fluid flow [65]. Zimmermann and colleagues developed an autonomous capillary system, in which wettable capillary valves were implemented by employing an abruptly changing geometry of the flow path, and are able to delay or stop a moving liquid [66]. Kojima and colleagues also proposed a new concept for autonomous switching of valves and pumps by employing electrowetting principles [67]. While nonmechanical pumps were utilized for different applications they currently offer limited pressure generation capabilities compared to mechanical pumps.

Currently, control logic is implemented in a computer or a microprocessor, where its interface with the fluidic circulatory is via sensors or pneumatic solenoid valves. However, one emerging control paradigm aim to integrate the control logic on-chip. It is claimed that as the development of electronic logic gates simplified the construction and operation of electronic devices, pneumatic logic gates could reduce the number of external controllers [68]. A variety of different approaches were suggested in the past few years. Microfluidic logic gates were used to route fluids in complex networks and to perform simple on-chip calculations. For example, Cheow et al. developed droplet-based logic gates where the absence of a dispersed phase liquid in a continuous phase liquid represent 1 and 0, respectively. They were able to demonstrate various logic gates such as *and*, *or* and *not* [69]. Prakash et al. were able to utilize

this principle to implement flip-flops, ring oscillators, ripple counters, and synchronizers, which provides an on-chip synchronized flow control mechanism [70]. Toepke et al. forward implemented programmable autonomous timers and rheostats [71]. Zaho et al. used digital microfluidics to implement logical gates with simple droplets manipulation techniques such as transporting, merging, and splitting [72]. They used their platform to compress multiple test-outcome droplets into a single droplet. A more recent development is the development of logical gates with microfluidic valves. Rhee and colleagues developed a pneumatic microprocessor, which was constructed from various combinations of microfluidic logic gates [68]. They developed an 8-bit pneumatic microprocessor that decodes a temporal command sequence, apply logic calculations, stores information for signal transportation and maintenance, and execute commands in target devices. Despite the great interest in such on-chip computing and control logic, their utilization is still anecdotal and not widely spread. This is probably due to the fabrication and operational complexity of such control circuits and their limited application that they are currently support.

8. Conclusions

System integration is an imperative developmental milestone for the field of microfluidics, both in terms of the scalability of increasingly complex platforms that still lack standardization, as well as the incorporation and adoption of emerging technologies in biomedical research. This work describes a modular integration and synchronization of a complex microfluidic platform permitting implementation of user-independent optimization algorithms. The versatility and modularity of our open-system unit can be rapidly adopted by leading groups in the field for automation and optimization of droplet generation, inertial focusing purification, single-cell analysis, and large-scale integration. We also described a series of emerging control paradigms including on-chip control logic, autonomous valves and micropumps, and application-specific control integration.

Author details

Elishai Ezra^{1,2}, Danny Bavli¹ and Yaakov Nahmias^{1,3*}

*Address all correspondence to: yahmias@cs.huji.ac.il

1 Center for Bioengineering, The Hebrew University, Jerusalem, Israel

2 Faculty of Engineering and Computer Science, Jerusalem College of Technology, Jerusalem, Israel

3 Department of Cell and Developmental Biology, The Hebrew University, Jerusalem, Israel

References

- [1] Fordyce, P. M., Diaz-Botia, C. A., DeRisi, J. L., and Gomez-Sjoberg, R., 2012, "Systematic characterization of feature dimensions and closing pressures for microfluidic valves produced via photoresist reflow," *Lab on a chip*, 12(21), pp. 4287–4295.
- [2] Bhatia, S. N., Yarmush, M. L., and Toner, M., 1997, "Controlling cell interactions by micropatterning in co-cultures: hepatocytes and 3T3 fibroblasts," *Journal of biomedical materials research*, 34(2), pp. 189–199.
- [3] Cheung, Y. K., Gillette, B. M., Zhong, M., Ramcharan, S., and Sia, S. K., 2007, "Direct patterning of composite biocompatible microstructures using microfluidics," *Lab on a chip*, 7(5), pp. 574–579.
- [4] Mu, X., Zheng, W., Sun, J., Zhang, W., and Jiang, X., 2013, "Microfluidics for manipulating cells," *Small*, 9(1), pp. 9–21.
- [5] Kartalov, E. P., Zhong, J. F., Scherer, A., Quake, S. R., Taylor, C. R., and Anderson, W. F., 2006, "High-throughput multi-antigen microfluidic fluorescence immunoassays," *BioTechniques*, 40(1), pp. 85–90.
- [6] Sanchez-Freire, V., Ebert, A. D., Kalisky, T., Quake, S. R., and Wu, J. C., 2012, "Microfluidic single-cell real-time PCR for comparative analysis of gene expression patterns," *Nature protocols*, 7(5), pp. 829–838.
- [7] Das, T., and Chakraborty, S., 2009, "Biomicrofluidics: Recent trends and future challenges," *Sadhana*, 34(4), pp. 573–590.
- [8] Ho, C. T., Lin, R. Z., Chang, W. Y., Chang, H. Y., and Liu, C. H., 2006, "Rapid heterogeneous liver-cell on-chip patterning via the enhanced field-induced dielectrophoresis trap," *Lab on a chip*, 6(6), pp. 724–734.
- [9] Kalisky, T., Blainey, P., and Quake, S. R., 2011, "Genomic analysis at the single-cell level," *Annual review of genetics*, 45.
- [10] Mark, D., Haeberle, S., Roth, G., von Stetten, F., and Zengerle, R., 2010, "Microfluidic lab-on-a-chip platforms: requirements, characteristics and applications," *Chemical Society reviews*, 39(3), pp. 1153–1182.
- [11] Melin, J., and Quake, S. R., 2007, "Microfluidic large-scale integration: the evolution of design rules for biological automation," *Annual review of biophysics and biomolecular structure*, 36, pp. 213–231.
- [12] Thorsen, T., Maerkl, S. J., and Quake, S. R., 2002, "Microfluidic large-scale integration," *Science*, 298(5593), pp. 580–584.
- [13] Hansen, C. L., Classen, S., Berger, J. M., and Quake, S. R., 2006, "A microfluidic device for kinetic optimization of protein crystallization and in situ structure determination," *Journal of the American Chemical Society*, 128(10), pp. 3142–3143.

- [14] Liu, J., Hansen, C., and Quake, S. R., 2003, "Solving the "world-to-chip" interface problem with a microfluidic matrix," *Analytical chemistry*, 75(18), pp. 4718–4723.
- [15] Skelley, A. M., Scherer, J. R., Aubrey, A. D., Grover, W. H., Ivester, R. H., Ehrenfreund, P., Grunthaler, F. J., Bada, J. L., and Mathies, R. A., 2005, "Development and evaluation of a microdevice for amino acid biomarker detection and analysis on Mars," *Proceedings of the National Academy of Sciences of the United States of America*, 102(4), pp. 1041–1046.
- [16] Gu, W., Zhu, X., Futai, N., Cho, B. S., and Takayama, S., 2004, "Computerized microfluidic cell culture using elastomeric channels and Braille displays," *Proceedings of the National Academy of Sciences of the United States of America*, 101(45), pp. 15861–15866.
- [17] Lee, C.-C., Sui, G., Elizarov, A., Shu, C. J., Shin, Y.-S., Dooley, A. N., Huang, J., Daridon, A., Wyatt, P., and Stout, D., 2005, "Multistep synthesis of a radiolabeled imaging probe using integrated microfluidics," *Science*, 310(5755), pp. 1793–1796.
- [18] Marcus, J. S., Anderson, W. F., and Quake, S. R., 2006, "Microfluidic single-cell mRNA isolation and analysis," *Analytical chemistry*, 78(9), pp. 3084–3089.
- [19] Gu, P., Liu, K., Chen, H., Nishida, T., and Fan, Z. H., 2011, "Chemical-assisted bonding of thermoplastics/elastomer for fabricating microfluidic valves," *Analytical chemistry*, 83(1), pp. 446–452.
- [20] Pollack, M. G., Shenderov, A. D., and Fair, R. B., 2002, "Electrowetting-based actuation of droplets for integrated microfluidics," *Lab on a chip*, 2(2), pp. 96–101.
- [21] Walker, P. A., 3rd, Morris, M. D., Burns, M. A., and Johnson, B. N., 1998, "Isotachophoretic separations on a microchip. Normal Raman spectroscopy detection," *Analytical chemistry*, 70(18), pp. 3766–3769.
- [22] Schmalzing, D., Koutny, L., Adourian, A., Belgrader, P., Matsudaira, P., and Ehrlich, D., 1997, "DNA typing in thirty seconds with a microfabricated device," *Proceedings of the National Academy of Sciences of the United States of America*, 94(19), pp. 10273–10278.
- [23] Figeys, D., Gygi, S. P., McKinnon, G., and Aebersold, R., 1998, "An integrated microfluidics-tandem mass spectrometry system for automated protein analysis," *Analytical chemistry*, 70(18), pp. 3728–3734.
- [24] Heath, S., 2002, *Embedded systems design*, Newnes.
- [25] Barr, M., and Massa, A., 2006, *Programming embedded systems: with C and GNU development tools*, "O'Reilly Media, Inc."
- [26] Sutlieff, C., 1991, "Testing time for ASICs," *IEE Review*, 37(1), pp. 27–31.
- [27] Henkel, J., Wolf, W., and Chakradhar, S., "On-chip networks: A scalable, communication-centric embedded system design paradigm," *Proc. VLSI Design, 2004. Proceedings. 17th International Conference on, IEEE*, pp. 845–851.
- [28] Maeder, A., Rauscher, R., and Lohse, J., "An ASIC for image processing applications based on internal and external parallelism," *Proc. CompEuro'91. Advanced Comput-*

- er Technology, Reliable Systems and Applications. 5th Annual European Computer Conference. Proceedings., IEEE, pp. 608–612.
- [29] Valle, M., Nateri, G., Caviglia, D. D., Bisio, G. M., and Briozzo, L., "An ASIC design for real-time image processing in industrial applications," Proc. European Design and Test Conference, 1995. ED&TC 1995, Proceedings., IEEE, pp. 385–390.
- [30] Yu, C., Hu, H.-T., and Lin, C.-Y., 2003, "Design and implantation of an ASIC architecture for 1.6 kbps speech synthesis," *Consumer Electronics, IEEE Transactions on*, 49(3), pp. 731–736.
- [31] Schmadecke, I., and Blume, H., "Hardware-accelerator design for energy-efficient acoustic feature extraction," Proc. Consumer Electronics (GCCE), 2013 IEEE 2nd Global Conference on, IEEE, pp. 135–139.
- [32] Dong, M., Liu, J., and Liu, R., "Speech interface ASIC of SOC architecture for embedded application," Proc. Signal Processing, 2002 6th International Conference on, IEEE, pp. 402–405.
- [33] Weikun, X., Huibin, Z., and Qiuli, Z., "Testing FPGA devices on an Automatic Test Equipment," Proc. Information and Automation (ICIA), 2013 IEEE International Conference on, IEEE, pp. 65–70.
- [34] Monmasson, E., and Cirstea, M. N., 2007, "FPGA design methodology for industrial control systems—A review," *Industrial Electronics, IEEE Transactions on*, 54(4), pp. 1824–1842.
- [35] Hodges, S., Villar, N., Scott, J., and Schmidt, A., 2012, "A new era for ubicomp development," *Pervasive Computing, IEEE*, 11(1), pp. 5–9.
- [36] Kubitzka, T., Pohl, N., Dingler, T., Schneegass, S., Weichel, C., and Schmidt, A., 2013, "Ingredients for a new wave of ubicomp products," *IEEE Pervasive Computing*(3), pp. 5–8.
- [37] Gellersen, H., Kortuem, G., Schmidt, A., and Beigl, M., 2004, "Physical prototyping with smart-its," *Pervasive Computing, IEEE*, 3(3), pp. 74–82.
- [38] Reas, C., and Fry, B., 2007, *Processing: a programming handbook for visual designers and artists*, Mit Press.
- [39] Pearce, J. M., 2012, "Materials science. Building research equipment with free, open-source hardware," *Science*, 337(6100), pp. 1303–1304.
- [40] Fobel, R., Fobel, C., and Wheeler, A. R., 2013, "DropBot: An open-source digital microfluidic control system with precise control of electrostatic driving force and instantaneous drop velocity measurement," *Applied Physics Letters*, 102(19), p. 193513.
- [41] Chaudhari, A., Ghoshal, T., Shaw, M. T., Cummins, C., Borah, D., Holmes, J. D., and Morris, M. A., "Formation of sub-7 nm feature size PS-b-P4VP block copolymer struc-

- tures by solvent vapour process," *Proc. SPIE Advanced Lithography, International Society for Optics and Photonics*, p. 905110.
- [42] Jackson, M. J., 2005, *Microfabrication and nanomanufacturing*, CRC Press, Boca Raton, Florida.
- [43] Kim, P., Kwon, K. W., Park, M. C., Lee, S. H., Kim, S. M., and Suh, K. Y., 2008, "Soft lithography for microfluidics: a review," *Biochip J.* 2, 1-11, 2008
- [44] Yao, P., Schneider, G., Prather, D., Wetzel, E., and O'Brien, D., 2005, "Fabrication of three-dimensional photonic crystals with multilayer photolithography," *Optics express*, 13(7), pp. 2370–2376.
- [45] Kitson, P. J., Rosnes, M. H., Sans, V., Dragone, V., and Cronin, L., 2012, "Configurable 3D-Printed millifluidic and microfluidic 'lab on a chip' reactionware devices," *Lab on a chip*, 12(18), pp. 3267–3271.
- [46] Gross, B. C., Erkal, J. L., Lockwood, S. Y., Chen, C., and Spence, D. M., 2014, "Evaluation of 3D printing and its potential impact on biotechnology and the chemical sciences," *Analytical chemistry*, 86(7), pp. 3240–3253.
- [47] Bhargava, K. C., Thompson, B., and Malmstadt, N., 2014, "Discrete elements for 3D microfluidics," *Proceedings of the National Academy of Sciences of the United States of America*, 111(42), pp. 15013–15018.
- [48] Lee, C. Y., Chang, C. L., Wang, Y. N., and Fu, L. M., 2011, "Microfluidic mixing: a review," *International journal of molecular sciences*, 12(5), pp. 3263–3287.
- [49] Chen, C. F., Liu, J., Chang, C. C., and DeVoe, D. L., 2009, "High-pressure on-chip mechanical valves for thermoplastic microfluidic devices," *Lab on a chip*, 9(24), pp. 3511–3516.
- [50] Cooksey, G. A., Sip, C. G., and Folch, A., 2009, "A multi-purpose microfluidic perfusion system with combinatorial choice of inputs, mixtures, gradient patterns, and flow rates," *Lab on a chip*, 9(3), pp. 417–426.
- [51] Araci, I. E., and Quake, S. R., 2012, "Microfluidic very large scale integration (mVLSI) with integrated micromechanical valves," *Lab on a chip*, 12(16), pp. 2803–2806.
- [52] Gomez-Sjoberg, R., Leyrat, A. A., Pirone, D. M., Chen, C. S., and Quake, S. R., 2007, "Versatile, fully automated, microfluidic cell culture system," *Analytical chemistry*, 79(22), pp. 8557–8563.
- [53] Ezra, E., Maor, I., Bavli, D., Shalom, I., Levy, G., Prill, S., Jaeger, M. S., and Nahmias, Y., 2015, "Microprocessor-based integration of microfluidic control for the implementation of automated sensor monitoring and multithreaded optimization algorithms," *Biomedical microdevices*, 17(4), p. 82.
- [54] Villar, N., Scott, J., and Hodges, S., "Prototyping with microsoft. net gadgeteer," *Proc. Proceedings of the fifth international conference on Tangible, embedded, and embodied interaction*, ACM, pp. 377–380.

- [55] Monk, S., 2012, Getting started with. NET Gadgeteer, " O'Reilly Media, Inc."
- [56] Wu, J., and Gu, M., 2011, "Microfluidic sensing: state of the art fabrication and detection techniques," *Journal of biomedical optics*, 16(8), p. 080901.
- [57] Weltin, A., Slotwinski, K., Kieninger, J., Moser, I., Jobst, G., Wego, M., Ehret, R., and Urban, G. A., 2014, "Cell culture monitoring for drug screening and cancer research: a transparent, microfluidic, multi-sensor microsystem," *Lab on a chip*, 14(1), pp. 138–146.
- [58] Dean G. Hafeman, W. P., Harden McConnell, 1988, "Light-addressable potentiometric sensor for biochemical systems.," *Science*, 240(4856), pp. 1182–1185.
- [59] Eklund Sven, T. R., Snider, Rachel, Carney Clare, Wright David, Wikswo John, Cliffel David, 2009, "Metabolic Discrimination of Select List Agents by Monitoring Cellular Responses in a Multianalyte Microphysiometer," *Sensors*, 9(3), pp. 2117–2133.
- [60] Alborzinia, H., Can, S., Holenya, P., Scholl, C., Lederer, E., Kitanovic, I., and Wödl, S., 2011, "Real-Time Monitoring of Cisplatin-Induced Cell Death," *PLoS ONE*, 6(5), p. e19714.
- [61] Weltin, A., Slotwinski, K., Kieninger, J., Moser, I., Jobst, G., Wego, M., Ehret, R., and Urban, G. A., 2014, "Cell culture monitoring for drug screening and cancer research: a transparent, microfluidic, multi-sensor microsystem," *Lab on a Chip*, 14(1), pp. 138–146.
- [62] Lehmann, M., Baumann, W., Brischwein, M., Gahle, H., Freund, I., Ehret, R., Drechsler, S., Palzer, H., Kleintges, M., Sieben, U., and Wolf, B., 2001, "Simultaneous measurement of cellular respiration and acidification with a single CMOS ISFET," *Biosensors & bioelectronics*, 16(3), pp. 195–203.
- [63] Eklund, S. E., Thompson, R. G., Snider, R. M., Carney, C. K., Wright, D. W., Wikswo, J., and Cliffel, D. E., 2009, "Metabolic discrimination of select list agents by monitoring cellular responses in a multianalyte microphysiometer," *Sensors*, 9(3), pp. 2117–2133.
- [64] Chen, A., Wang, R., Bever, C. R., Xing, S., Hammock, B. D., and Pan, T., 2014, "Smart-phone-interfaced lab-on-a-chip devices for field-deployable enzyme-linked immunosorbent assay," *Biomicrofluidics*, 8(6), p. 064101.
- [65] Tsun-kay Jackie, S., Jin, L., and Prashanta, D., 2015, "Design and modeling of a light powered biomimicry micropump," *Journal of Micromechanics and Microengineering*, 25(6), p. 065009.
- [66] Zimmermann, M., Hunziker, P., and Delamarche, E., 2008, "Valves for autonomous capillary systems," *Microfluid Nanofluid*, 5(3), pp. 395–402.
- [67] Kojima, K., and Suzuki, H., "Programmed autonomous microfluidics using microvalves and micropumps," *Proc. Micro Electro Mechanical Systems (MEMS)*, 2011 IEEE 24th International Conference on, pp. 1173–1176.

- [68] Rhee, M., and Burns, M. A., 2009, "Microfluidic pneumatic logic circuits and digital pneumatic microprocessors for integrated microfluidic systems," *Lab on a chip*, 9(21), pp. 3131–3143.
- [69] Cheow, L. F., Yobas, L., and Kwong, D.-L., 2007, "Digital microfluidics: Droplet based logic gates," *Applied Physics Letters*, 90(5), p. 054107.
- [70] Prakash, M., and Gershenfeld, N., 2007, "Microfluidic bubble logic," *Science*, 315(5813), pp. 832–835.
- [71] Toepke, M. W., Abhyankar, V. V., and Beebe, D. J., 2007, "Microfluidic logic gates and timers," *Lab on a chip*, 7(11), pp. 1449–1453.
- [72] Zhao, Y., and Chakrabarty, K., 2014, "Microfluidic Logic Gates," *Encyclopedia of Microfluidics and Nanofluidics*, D. Li, ed., Springer US, pp. 1–18.

Microfluidics for Soft Electronics

Babak Taghavi, Jiantong Li, Mikael Östling and Shi Cheng

Additional information is available at the end of the chapter

<http://dx.doi.org/10.5772/63376>

Abstract

Microfluidics-based soft electronic systems have the potential to assist conventional rigid devices and circuits to achieve extreme levels of elasticity in wearable electronics and other applications. The goal of employing microfluidics-based approach among other existing methods is to enhance users comfort through fulfillment of wearable's mechanical performance requirements such as flexibility, twistability, and stretchability. This chapter presents a brief survey of different solutions for developing elastic electronics and a thorough review of the progress in microfluidics-based approaches. This chapter mainly focuses on the description of the fabrication process, design, and measurement steps of different antennas and complex systems realized using microfluidic interconnects.

Keywords: Elastic antennas, liquid metal, microfluidics, stretchable electronics, wearable technology

1. Introduction

In recent years, wearable electronics have received increasing attention in both academic research and industrial development. Wearable electronics are being utilized in various applications, including healthcare and medical electronic devices [1] as well as consumer electronics and robotics [2]. Human body surfaces are huge compared to the sizes of electronic components. Large-area coverage is sometimes a must-have feature, where tiny wearable gadgets are certainly not a good fit. Consider an electronic system equipped with multiple sensors, each placed at a fingertip for pressure sensing, and a radio frequency (RF) transmitter associated with an antenna to wirelessly send out the sensing data. Each sensor is connected to the core transmitter circuit by long, in the order of 10 cm, interconnects. Additionally, an antenna with a size of few centimeters is needed for RF communication. Therefore, the overall size of such an integrated electronic device can be as large as 50–100 cm². Using conventional rigid printed circuit board (PCB) techniques to develop this kind of systems would inevitably

lead to a clumsy gadget that will most likely give an uncomfortable experience to the wearer. As wearable devices intimately interact with users' body and skin, their physical shapes and impact on haptic feelings of wearers are very important design considerations. Human body is soft and our skin is stretchable, especially on joints, thus any external gadget that comes into seamless contact with our body should feature certain degree of flexibility and stretchability in order to facilitate natural motions [3]. Researchers have been experimenting different materials and assembly methods to create more human-friendly wearable systems. Flexibility can be achieved by implementing electronics on thin flexible substrates, ranging from polyimide-based Kapton films such as circuit boards to thin film transistors (TFTs) on device level. Such flexible electronic devices and systems can withstand moderate folding and twisting, but not stressing. Excessive straining often results in non-reversible mechanical deformation and permanent electrical failure. Achieving stretchability with maintained electronic functions is significantly more challenging. Radically new fabrication techniques and design strategies are required to realize soft electronics, capable of reaching extreme levels of reversible bendability, twistability, and stretchability.

Significant advances have been made in the emerging field of soft electronics in the past two decades. Great potential has been shown in numerous new appealing applications, e.g., body-worn healthcare/medical sensing systems, ergonomic units, and tissue engineering constructs, where conventional rigid, bulky electronics are facing insurmountable obstacles to fulfill the demands. One of the most promising concepts is soft, rubbery electronic devices, implemented in the form of elastic structures, materials, or a combination of both [4]. Wavy silicon ribbons to realize stretchable silicon integrated circuits (ICs) have been reported [5]. Also, integration of TFTs on prestressed substrates has been proposed [6].

Unlike complex, miniaturized semiconductor-based active circuits, many passive components such as interconnects, sensors, and antennas, which occupy the major areas in large-area electronic devices and systems, can only be shrunk at the expense of efficiency, sensitivity, and functionalities. Elasticity of such large passive devices, thereby, dominates the overall flexibility and stretchability of integrated electronics. Various approaches to implement stretchable interconnects have been presented [7,8]. One typical example is meandered metallic interconnects built on flex foils, operating at different frequency ranges [9]. Flexible and stretchable interconnects, realized by incorporating low melting temperature solder alloy into microstructured channels in polydimethylsiloxane (PDMS), were first proposed by Siegel, et al. [10]. Various properties of different solder metals and alloys, including melting temperature, electrical conductivity, Brinell hardness, and material costs, were also investigated. Later, room temperature liquid metal alloy-, eutectic gallium and indium (EGaIn), filled microfluidic channels acting as elastic direct current (DC) interconnects have been demonstrated [11]. Additional appealing characteristics of EGaIn, such as good rheological properties, excellent wetting on almost any surfaces, and low toxicity, make it well suited for microfluidics-based soft electronics that might be in proximity contact with human body in practical use [12]. The first stretchable electronic devices, operating at radio frequencies, are a liquid metal unbalanced loop antenna and a fluidic ultra-wideband planar inverted cone antenna (PICA). Both antennas were implemented by utilizing liquid metal alloy, galinstan,

incorporated into microstructured, elastomeric channel matrices [13,14]. Similar concept was also proposed to demonstrate a stretchable dipole antenna. Modified inhomogeneous elastomer substrate was subsequently used to significantly improve elasticity of stretchable antennas [15]. A hybrid integration approach for combining active circuits on flexible PCBs and large-area stretchable passive electronics for RF radiation sensing was later reported by Cheng and Wu [16]. This integration strategy was afterwards expanded to create multi-layer, self-contained, large-area, elastic wireless strain sensor [17]. Standalone patch antenna using serpentine channels filled with EGaIN was also published [18]. More recently, a reconfigurable fluidic serpentine antenna with varying resonant frequency in response to strain was presented [19]. Moreover, successful development of new fabrication techniques for microfluidics-based soft electronics has been demonstrated [20].

The following sections present and discuss recent advances in the emerging field of microfluidics-based soft electronics. This chapter focuses on ultracompliant, elastic electronic devices and systems, with the capability of wireless communications and remote sensing. Following sections start with an elaborate description of the fabrication process, followed by presentation of several application examples of microfluidics-based RF elastic electronics. Measurement results on foldable, twistable, stretchable antennas and integrated devices under different mechanical deformations are also shown. This chapter ends with a glimpse of some ongoing research activities at the Department of Integrated Devices and Circuits, KTH Royal Institute of Technology, Sweden, among which new advanced processing techniques and nanomaterials, e.g., inkjet-printed, high precision, graphene resistors and conductors, are being investigated to enable novel sensing functions. Furthermore, feasibilities of utilizing elastic, microfluidic RF energy harvesters for wireless charging of soft energy storage units or remote powering active stretchable electronics are discussed.

2. Fabrication process

Microfluidic channel design procedure can be concisely described in three major steps, which are soft lithography, reverse molding, and liquid metal injection. Similar to PCB routings, depending on the complexity and architecture of circuits and antennas, a single or a multi-layer configuration can be selected to develop an electronic system. First, fabrication processes of single-layer liquid metal-filled channel matrices embedded in PDMS elastomers are presented in this section. Subsequently, processing steps for implementing multi-layer microfluidics-based soft electronic devices are described in detail. Finally, heterogeneous integration method for connecting active circuits assembled on flexible PCBs to microstructured fluidic channels encased in elastomeric substrates is discussed.

2.1. Single-layer microfluidic, elastic channels

Single-layer microfluidic channels are developed on bare silicon wafers, which are used as the substrate for molding and formation of elastic layers. SU8 photoresist is employed as a reverse mold for fluidic channels, and its thickness determines the height of microfluidic

channels. SU8 photoresist is spin coated on a silicon wafer as shown in Figure 1(a). As discussed in the Introduction, microfluidic channels act the same as conductor traces on conventional PCBs; therefore, their patterns are designed in the similar way as routing the traces on PCBs. The designed patterns are then used to build the corresponding lithography mask. After transferring the pattern to the photoresist and removing unexposed parts, the mold is ready for casting the channels. Cross-sectional view of the developed mold on silicon is displayed in Figure 1(b). The prepared mold is then thermally stabilized at 150 °C for 30 minutes to enhance the adhesion between silicon and the remaining SU8 layer. PDMS is used as the soft substrate because of its stretchability, transparency, and relatively easy preparation process. PDMS is widely used in bioelectronics and microfluidic applications such as lab-on-a-chip. It is prepared by mixing PDMS prepolymer and cross linker (Elastosil RT601A and B, Wacker Chemie, Munich, Germany) with 9:1 mass ratio. As shown in Figure 1(c), PDMS should be poured on top of the silicon to form the substrate. In addition to the patterned structures, a thin layer of PDMS is prepared on the blank silicon wafer to form a cover layer for the reversely molded PDMS. After degassing, both patterned and blank PDMS layers are cured at 70 °C for 30 minutes to solidify the PDMS layers. Once the PDMS layers are ready, it is time to peel them off from the silicon carriers as illustrated in Figure 1(e). Before proceeding to the next step, numerous openings should be punched on the patterned structure so that the channels can be accessed for liquid metal injection through those openings. The PDMS layers are bonded together using corona discharging (ETP, Chicago, IL, USA) activation afterwards. At this stage, fabrication of the microfluidic channels is completed and the subsequent step is to inject galinstan into the channels as seen in Figure 1(g). Galinstan is a liquid metal alloy, consisting of 68.5% Ga; 21.5% In; and 10%, Sn. It is in liquid state from -19 to 1300 °C, and it also features a good electrical conductivity of 3.46×10^6 S/m and non-toxicity in comparison with mercury. Its excellent wettability on almost any surface simplifies the channel filling process and ensures good electrical continuity despite of mechanical deformation. After filling the channels, a visual inspection or a simple electrical conductivity check should be performed to ensure that all electrical connections are established as expected. All openings except feeding points for electrical measurement and interconnections with active circuits are sealed with uncured PDMS droplets to prevent any liquid metal leakage. Cross-sectional and top view of the resulting single-layer microfluidic channels filled with liquid metal in a PDMS substrate are shown in Figure 1(h) and (i).

2.2. Multi-layer microfluidic, elastic channels

Some applications necessitate multi-layer structures. Additional channel layers make it possible to implement more sophisticated structures that are not feasible to build in a single-layer configuration. As depicted in Figure 2, fabrication steps resemble the previously presented processes for constructing a single-layer structure. Extra channel layers, however, require more lithography and bonding steps. In most applications, as shown in Section 2.3, feeding points on the same side of an elastomer substrate are often needed to facilitate circuit assembly or characterizations. For assessing the bottom liquid metal filled channels from the top surface of the PDMS substrate, an additional inlet is punched through the top and middle layers after bonding. In the liquid metal injection phase, top layer channels are filled and then

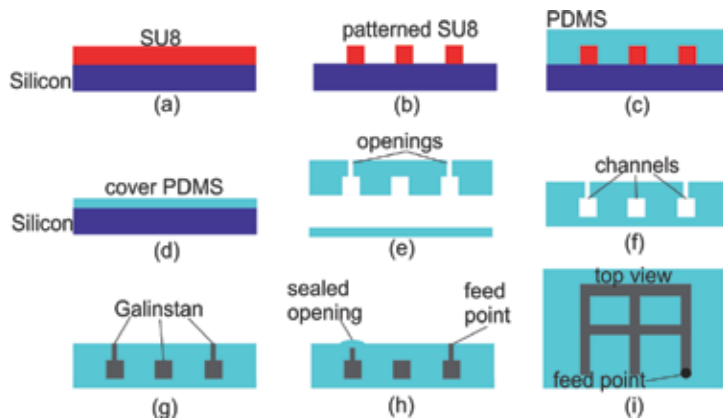


Figure 1. Single-layer microfluidic soft electronics fabrication process.

openings 2 and 5 are temporarily sealed by small pieces of Scotch tapes and opening 1 is encapsulated with uncured PDMS. Afterwards, the structure is flipped to the other side and galinstan is injected into the channel and both openings 3 and 4 are permanently sealed with uncured PDMS droplets. Later, the bonded substrate is flipped over and the temporary sealants are removed. After verifying all connections, the sample is cured at 85 °C for about 30 minutes.

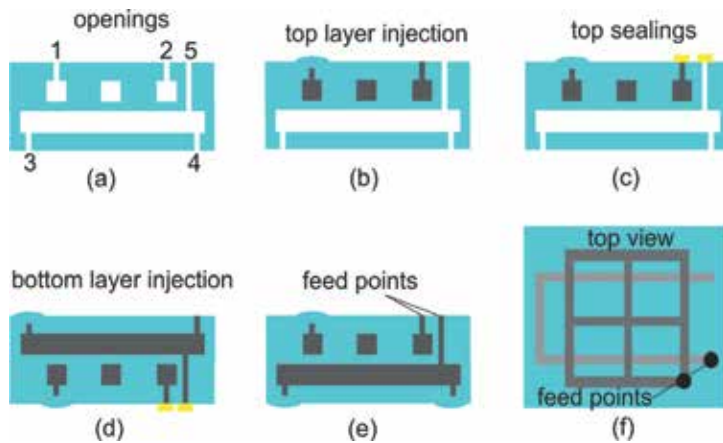


Figure 2. Processing steps of multi-layer microfluidic soft electronics.

2.3. Strain isolation cells

Active circuits play an essential role in modern electronic systems. Purely passive microfluidic soft electronics without any active components can only be used in very limited application scenarios in practice. A pressing issue is how to realize active electronics in bendable, flexible,

and stretchable manners. Implementing active circuits using microfluidic technologies would be ideal, but to our best knowledge, none of the existing microfluidic techniques support fabrication of high performance, basic active components, such as diodes and transistors, operating at gigahertz frequency range. A compromising solution is to heterogeneously integrate off-the-shelf packaged IC chipsets with passive microfluidic electronics. Here the biggest challenge lies in how to create reliable interconnections between rigid IC chips associated with discrete components and liquid metal filled elastic channels. Figure 3 illustrates a hybrid integration strategy, where IC chipsets as well as external lumped components are first assembled on a small piece of flexible PCB. Such a quasi-flexible circuit contains complex routing and most connections with high reliability. The subsequent step is to implement interconnects between flexible circuits and microfluidic elastic channels via solid metallic pins. Since much fewer connections are needed at this step, the overall reliability of such interconnects are dramatically improved. In order to address the issue of mechanical mismatch between elastomers and rigid components, strain isolation cells, the so-called local stiffening cells (LSCs), are introduced to encapsulate PCBs and metal pins with locally thickened PDMS. Although such cells are a bit more rigid than any other areas on the PDMS elastomer and inevitably degrade the overall elasticity of integrated devices to some extent, they can effectively minimize mechanical deformation around active circuits and interconnect pins when the entire devices are being folded, twisted, or stressed. Reliable galvanic contacts between metal pins and liquid metal alloy are crucial. Soldering tin plating on metallic pins is employed to ensure good electrical connections between solid and liquid metals, thanks to superior wetting properties of galinstan on tin. As depicted in Figure 3, a semi-spherical solder ball is also mounted on the bottom surface of each tin plated pin at one end to further improve the reliability of the connection to fluid metal.

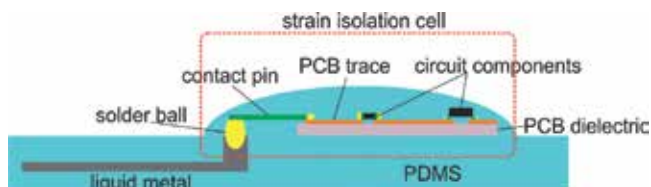


Figure 3. Hybrid integration of flexible active circuits and fluidic, elastic passive electronics.

3. Microfluidics-based elastic antennas and heterogeneously integrated RF electronics

Fabrication methods introduced in Section 2 are applied to realize different elastic RF-integrated electronic devices and systems. This section presents the design, fabrication, and measured results on standalone single-layer foldable, twistable, stretchable antennas; a fluidic soft RF radiation sensor; and a multi-layer, microfluidic, reversibly stretchable, large-area wireless strain sensor.

3.1. Liquid metal stretchable unbalanced loop antenna

An unbalanced loop antenna, operating at 2.4 GHz Industrial, Scientific, and Medical (ISM) band, is designed, fabricated, and characterized, using single-layer microfluidic channels filled with liquid metal. Schematic of the resulting loop antenna prototype as well as a cross-sectional view of microfluidic channels are shown in Figure 4. The antenna consists of a loop radiating element and a semi-circular, meshed ground plane. The loop is grounded at one end and isolated from the ground plane at the other end for coaxial cable feeding.

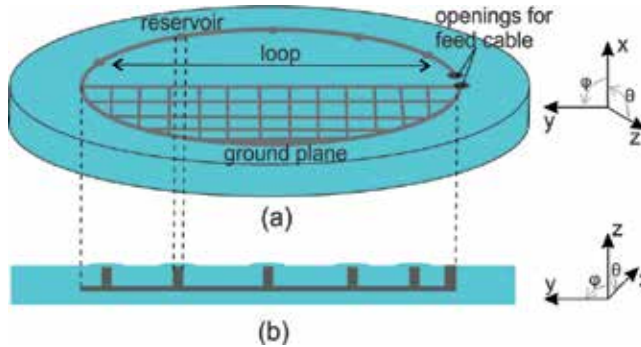


Figure 4. Schematic of liquid metal stretchable unbalanced loop antenna: (a) overlook view, (b) cross-sectional view.

The resonant frequency (f_{res}) of a loop antenna is a function of the loop length and can be approximated by the following Equation 1:

$$f_{res} \approx \frac{c}{2L_{loop}\sqrt{\epsilon_{eff}}}, \quad (1)$$

where c is the velocity of light in free space, L_{loop} is the loop length, and ϵ_{eff} is the effective permittivity, which is about 1 for very thin PDMS layers. According to the equation, to obtain $f_{res} = 2.4$ GHz, the loop should be 5.6 cm in length. Numerical simulations are performed in Ansoft HFSS to verify antenna port impedance and radiation characteristics. As seen in Figure 4, numerous small cylinders are aligned along the loop-shaped channel, in which extra liquid metal alloy can be stored and released to guarantee reliable galvanic connections while the antenna is mechanically deformed. It should be noted that the presence of such liquid metal reservoirs results in slightly increased electrical length of the loop antenna so that a minor decrease in resonant frequency compared with the value calculated from the equation can be observed both in simulations and measurements. For example, if the loop length, L_{loop} , equals 56.4 mm, the resonant frequency, f_{res} , derived according to the equation should be 2.7 GHz. However, considering the effect of reservoirs, $f_{res} = 2.4$ GHz is obtained in numerical simulations. Once the simulation results meet the requirements, the antenna layout is exported to print a mask on transparency for subsequent soft lithography process. The printed plastic mask is then used to transfer the antenna patterns to the SU8 photoresist and to fabricate the antenna

following the fabrication steps described in Section 2.1. The resulting unbalanced loop antenna prototype is illustrated in Figure 5.

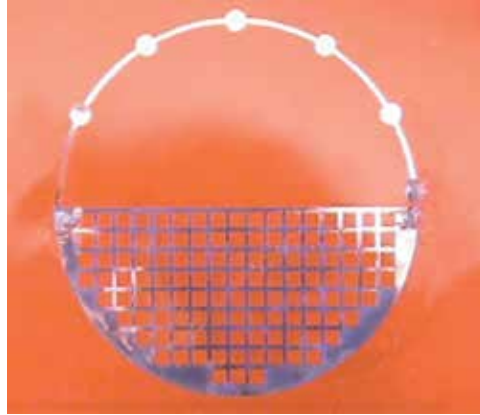


Figure 5. Photograph of the fabricated fluidic stretchable loop antenna.

In order to verify simulated results, the port impedance and radiation characteristics are measured using a vector network analyzer in an anechoic chamber. All experiments are first carried out with the antenna in its relaxed state. Measurement results along with the corresponding simulations are shown in Figure 6.

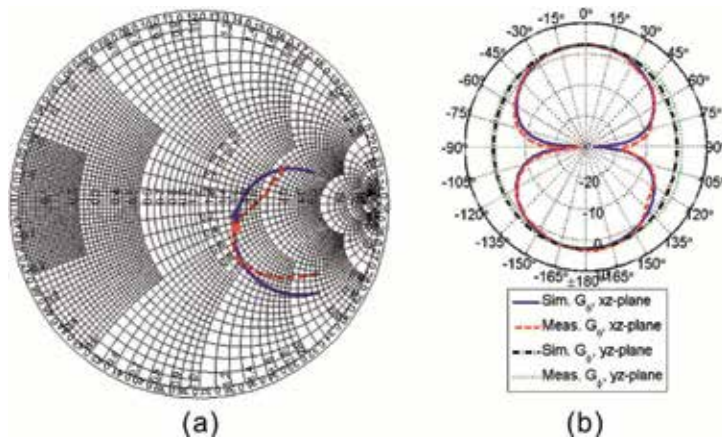


Figure 6. (a) Simulated (solid line) and measured (dotted line) reflection coefficient (S_{11}) and (b) radiation patterns of the liquid metal-based stretchable unbalanced loop antenna. The coordinate system is depicted in Figure 4.

Mechanical performance of the microfluidic elastic antenna is tested under various deformations as shown in Figure 7. It is observed that the unbalanced loop antenna prototype can withstand omnidirectional straining, as well as severe folding and twisting, and return to its original shape after the removal of external forces.

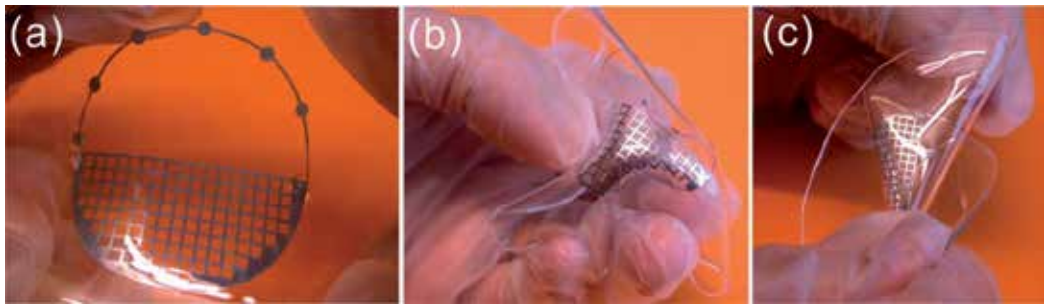


Figure 7. Photographs of the unbalanced loop antenna in (a) omnidirectionally strained, (b) twisted, and (c) folded states.

Electrical properties of the fluidic soft antenna in response to varying strains applied along its x - and y -axis are also characterized. Photographs of the elastic antenna in its relaxed and stressed states are displayed in Figure 8.

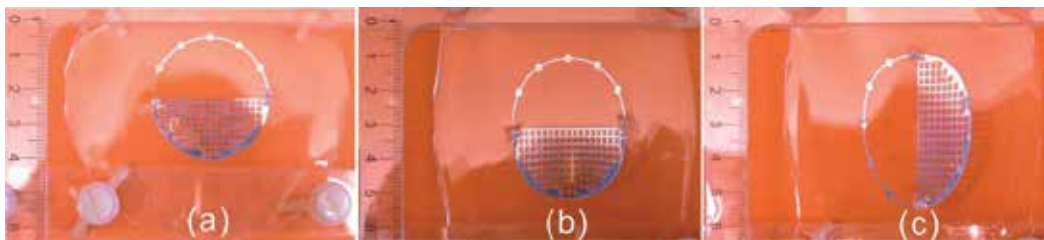


Figure 8. Photograph of the resulting elastic loop antenna in its (a) relaxed state, and with 40% strain along (b) x - and (c) y -axes. The corresponding coordinate system is shown in Figure 4.

Figure 9 presents measured port impedance and radiation patterns of the loop antenna in different states. The decrease in the antenna resonant frequency can be explained by an increased antenna size as a result of stretching. Antennas often exhibit wider radiation bandwidth than impedance bandwidth. This is why, measured radiation efficiency remains relatively stable despite being strained. No dramatic electrical performance degradation is detected in the experiments. It implies that no interruption in electrical connections occurs during antenna deformation. This is mainly because of the superior wettability of galinstan on the inner surfaces of elastomeric channels as well as its good electrical conductivity.

3.2. Elastic electromagnetic radiation sensor

Our daily life has been greatly benefiting from revolutionary mobile communication technologies rapidly developed in the past decades. Billions of portable devices, equipped with wireless links, are new parts of our everyday life. People and electronic equipment and systems are connected anywhere at any time. Rising concerns on potential health issues caused by the exposure to RF radiation has been expressed by both scientists and the public. It is, thereby, worth monitoring the level of ambient electromagnetic (EM) wave radiation to assess possible

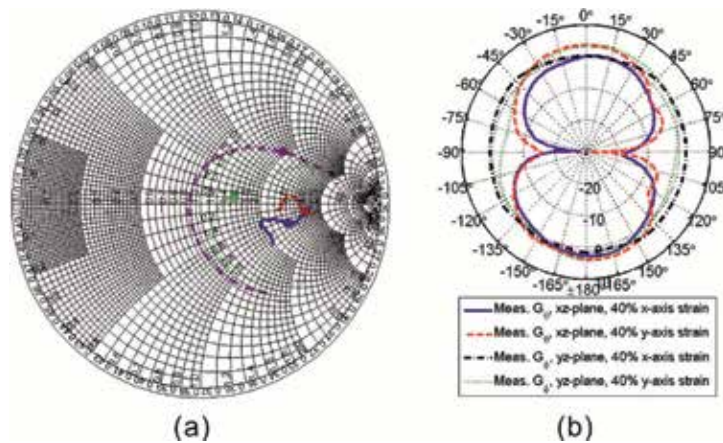


Figure 9. Measured (a) port impedance and (b) radiation patterns of the stretchable unbalanced loop antenna. The coordinate system is seen in Figure 4.

hazards and improve signal coverage quality in real life. In order to make it more portable, an EM radiation sensor can be developed as a wearable device. As discussed in the Introduction Section 1, better user experience can be achieved by constructing such a radiation sensor in ultracompliant, soft, and elastic manners. An RF power detector circuit assembled on a flex foil and encapsulated in an LSC is designed and interconnected to a microfluidics-based stretchable antenna to form a hybrid device, *cf.* Figure 10. Target operating frequency of the proposed radiation sensor is 900 MHz. A uniplanar rectangular unbalanced loop antenna is chosen for its ease of fabrication. The overall dimensions of the loop obtained from full wave simulations conducted in Ansoft HFSS are 86.9 mm × 88.0 mm × 1.0 mm. Ambient RF radiation is picked up from free space and directed to the input of the RF power sensing module via an elastic, fluidic antenna. The injected RF energy is then proportionally converted to DC voltages at the RF power detector IC output. The upper and lower sensing range of RF radiation energy is determined by the dynamic range of the power detection IC chipset. The chosen IC chip features a dynamic range from approximately -60 dBm to 0 dBm that is sufficient in most application scenarios. Apart from the core IC, three coupling and decoupling surface mounted device (SMD) capacitors along with an input matching inductor are needed. The entire power sensing active circuit mounted on a flexible PCB is powered externally, using a pack of four AA batteries connected serially. A light emitting diode (LED) is soldered at the voltage output of the power detector for visualization, which will be switched on when the received RF energy exceeds the pre-defined threshold. More details about the integrated RF radiation sensor can be found in Figure 10.

Prior to connecting the microfluidic antenna to the active circuit, electrical performance of both the antenna and the detector circuit is evaluated separately. Figure 11 shows measured reflection coefficient of the loop antenna in different stretched modes.

The output DC voltage of the standalone active circuit in response to varying RF input power is characterized. In this experiment, continuous wave (CW) signal with incremental power

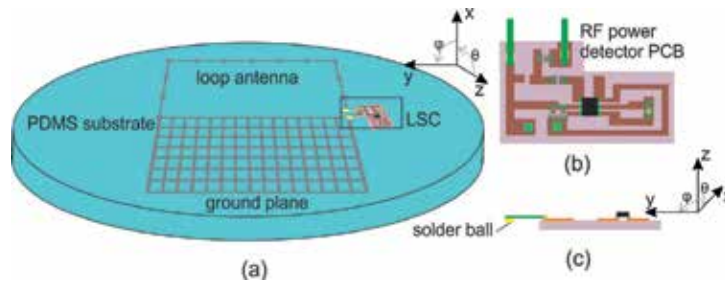


Figure 10. Schematic view of the elastic EM sensor: (a) overlook view of the integrated sensor, (b) top view, and (c) cross view of the flexible active circuit.

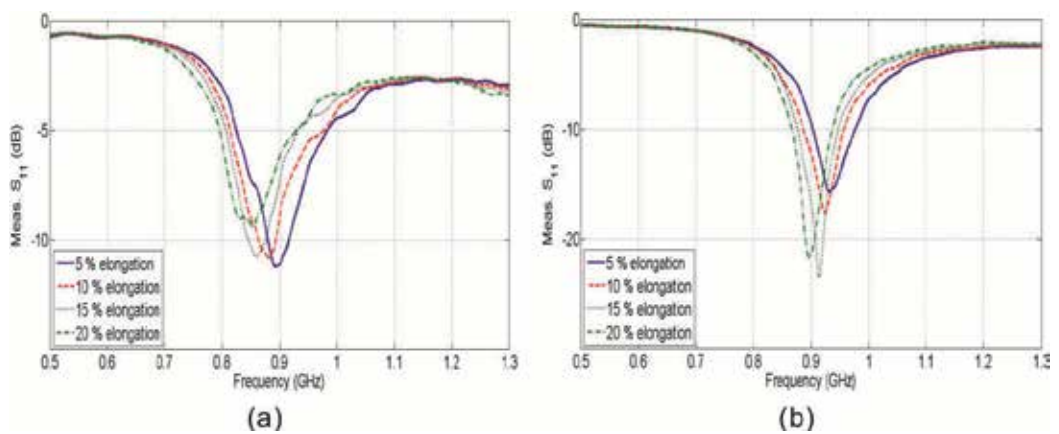


Figure 11. Measured reflection coefficient of the microfluidic elastic rectangular loop antenna in response to varying strain applied along its (a) x - and (b) y -axis. The coordinate system is presented in Figure 10.

level generated from a signal synthesizer is fed into the RF power detector input through an RF coaxial cable, and the LED indicator at the DC voltage output is temporally disconnected. The output voltage of the RF power detector as a function of input power is shown in Figure 12, in which fairly linear behavior is achieved over the entire dynamic range.

Subsequently, the PCB is assembled on the PDMS substrate using the proposed hybrid integration method. The fabricated elastic EM radiation sensor is shown in Figure 13.

The measurement setup illustrated in Figure 14 is utilized to demonstrate RF radiation sensing capability of the integrated sensor device in ordinary office environment. The distance from the dedicated radiation source comprising a standard horn antenna and a signal generator to the elastic RF radiation sensor is approximately 5 m.

The transmitter sends out a CW signal at 900 MHz with variable power levels into the free space. The LED indicator on the integrated stretchable sensor device is on when being exposed to high levels of radiation. The ON/OFF state of the LED indicator only depends on the level of the RF power received by the microfluidic stretchable loop antenna. Increased distance

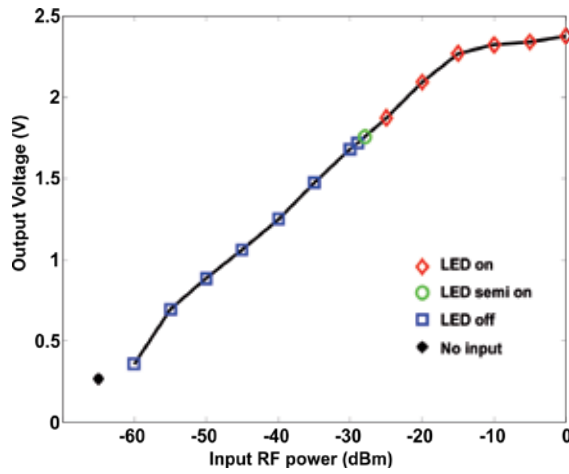


Figure 12. RF power module output voltage and LED status versus input RF power.

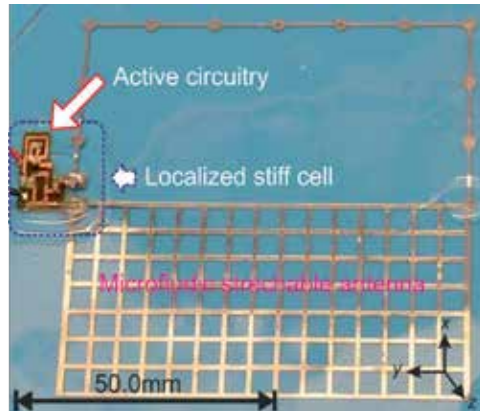


Figure 13. Photograph of the resulting elastic EM radiation sensor prototype.

between the radiation source and the sensor would result in greater free space loss. Higher power is, therefore, required from the RF signal generator to turn on the LED in this case. In addition to measurements in its relaxed state, the stretchable EM radiation detector is also tested in its folded, twisted, and strained modes. Figure 15 shows that the implemented microfluidics- based soft radiation sensor prototype remains functioning regardless of deformation.

3.3. Fluidic, elastic ultra-wideband antenna

Antennas with broad operational frequency bands are sometimes required. In ultra-wideband (UWB) systems, an extremely broad frequency range from 3.1 GHz to 10.6 GHz needs to be covered using a single antenna. Implementing a UWB antenna in highly flexible, bendable,

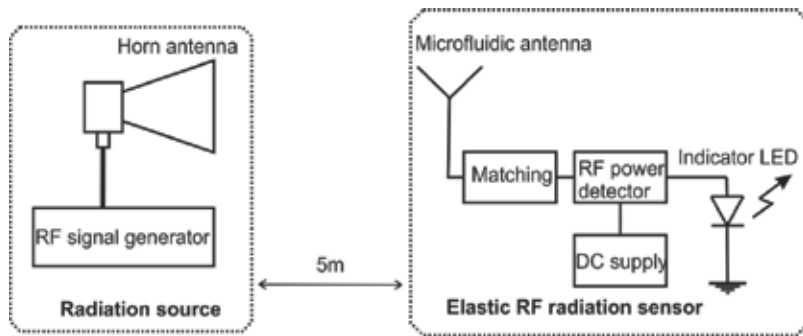


Figure 14. Schematic of the demonstration setup for the implemented elastic RF radiation sensor.

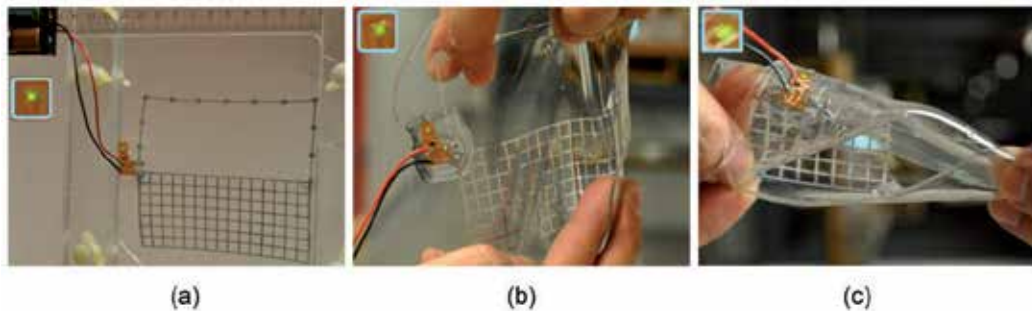


Figure 15. Photographs of the elastic EM radiation sensor operating under deformation: with 15% elongation along its (a) x - and (b) y -axis, (c) omnidirectional stressing, and (d) severe twisting. The corresponding coordinate system can be found in Figure 10.

and stretchable formats would be of great interest. Such an antenna can also be deployed in other applications that only require a fractional bandwidth of UWB, as it is expected to feature robust electrical characteristics in some narrower frequency ranges under deformation. A non-resonant antenna, PICA, is chosen because of its uniplanar configuration and ease of fabrication. The lower and upper operational frequencies of a PICA are determined by the height of the inverted cone and the size of the gap between the radiator and the ground, respectively. Its tapered shape gradually transforms the free space impedance of 377Ω to 50Ω over a wide frequency range. Full wave simulations performed in Ansoft HFSS suggest a radius of 10 mm (R) and a gap size of $300 \mu\text{m}$ (G) for covering the operational frequency range of 3–11 GHz. Schematic views of the liquid metal elastic PICA are seen in Figure 16. Similar to the previously presented microfluidic antennas, its ground and radiating element are realized in meshed configurations to separate the top and bottom PDMS membranes.

Mechanical properties of the fabricated antenna are first evaluated. Figure 17 shows that the resulting PICA prototype is reversibly stretchable, foldable, and twistable. After removing external forces, the antenna always returns to its original shape without any visible mechanical damages.

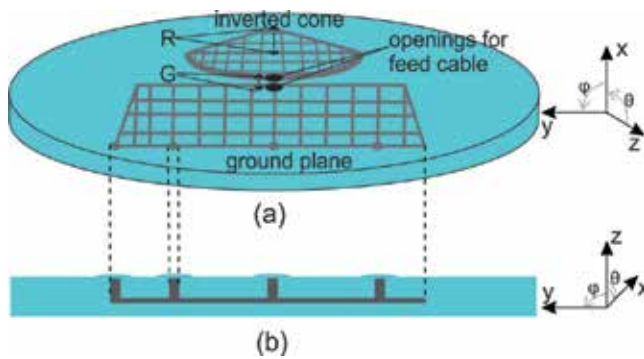


Figure 16. Schematic of the microfluidics- based stretchable ultra-wide band antenna: (a) overlook view and (b) cross view of microfluidic channels in a PDMS elastomer.

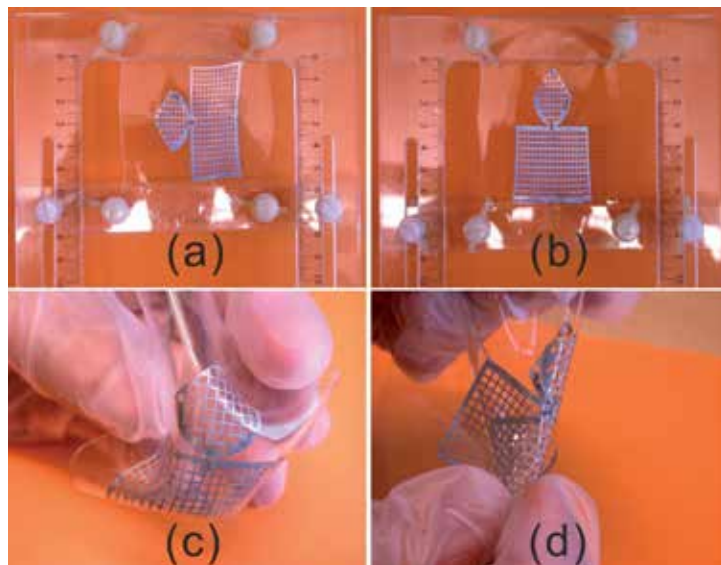


Figure 17. Photographs of the elastic PICA under deformation: (a) 40% strain along (a) x - and (b) y -axes, (c) and (d) severe folding and twisting. The coordinate system is shown in Figure 16.

Relative stretchability as high as 100% should be within reach according the data sheet of the PDMS elastomer in use. Openings in the top PDMS membrane as well as the rigid feed cable set an upper limit of approximately 50% on stretchability. Low temperature test is also performed, using a household freezer with a lowest temperature of $-24\text{ }^{\circ}\text{C}$. No mechanical failure can be found after cooling the antenna prototype at $-24\text{ }^{\circ}\text{C}$ for 2 hours.

Port impedance and radiation characteristics of the microfluidics- based stretchable PICA are all measured at room temperature. Measured reflection coefficient, S_{11} , of the relaxed antenna is in line with the corresponding simulated result and good impedance matching ($S_{11} < -10\text{ dB}$) is achieved between 3 GHz and 11 GHz, as seen in Figure 18.

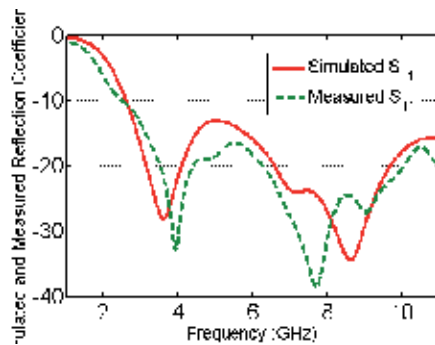


Figure 18. Simulated and measured S_{11} of the stretchable ultra-wide band PICA in its original state.

Reflection coefficients of the stretchable fluidic PICA are also characterized in various flexed states. Experimental data presented in Figure 19 indicate that robust impedance matching is achieved even if the microfluidic PICA is strained.

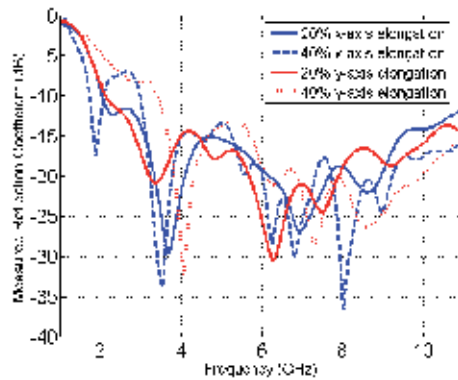


Figure 19. Measured S_{11} of the flexed PICA. The coordinate system can be found in Figure 16.

Stretching the antenna along its x -axis leads to increased height of the inverted cone and lowered first resonant frequency. Port impedance at higher frequencies remains stable in spite of stressing, as it is mainly governed by the impedance transformer formed by the tapered shape and the small gap between the antenna radiating element and the ground plane. Excessive strains along the x -axis might deteriorate impedance matching performance to some extent because of significantly increased gap size and severe deformation of the impedance transformer. Elongation along the y -axis only slightly impacts measured reflection coefficients because of relatively small changes in the tapered shape and the gap size. Radiation patterns of the relaxed and flexed elastic PICA are measured at 2.5 GHz and 5 GHz. Figure 20 illustrates the measured data at 2.5 GHz.

In comparison with antenna gain, variations on measured radiation patterns as a result of stressing are greater. Broad beam coverage similar to an ordinary monopole antenna is

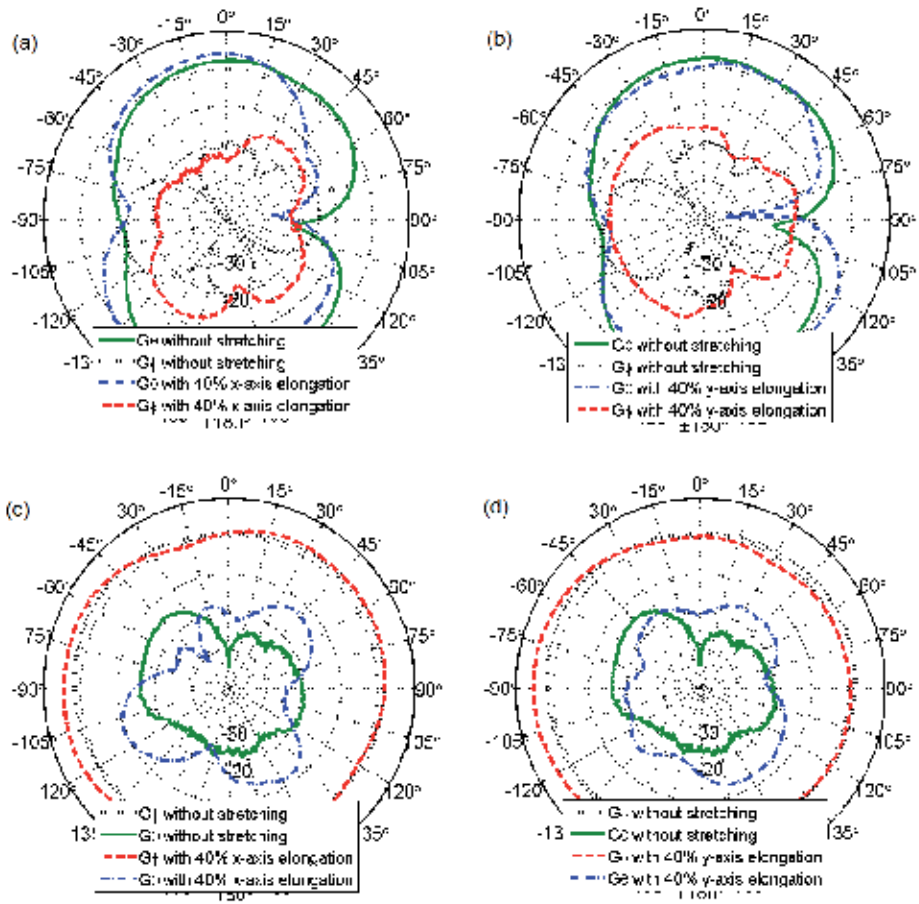


Figure 20. Measured radiation patterns of the relaxed and stressed PICA in the (a), (b) xz-, and (c), (d) yz-plane. The corresponding coordinate system is depicted in Figure 16.

achieved in both relaxed and flexed cases. Maximum gain of approximately 2.2 dBi is measured at 2.5 GHz. Detailed results on radiation characteristics of the resulting elastic PICA can be found in Cheng et al. [14]. Strong ripples are seen in measured radiation patterns at 5 GHz. The major cause for these fast ripples is frequency- dependent disturbance introduced by the feed cable in the experiments.

Radiation efficiency is another important figure of merit for terminal antennas featuring omnidirectional radiation patterns. A custom-designed reverberation chamber is employed for rapid radiation efficiency measurements. Experimental results at different frequencies are plotted in Figure 21.

Although measured radiation efficiency decreases a bit at 3 GHz during stretching, it still remains above 70%, an acceptable figure, better than many commercially available antennas. No significant efficiency drop is detected over the entire frequency range. This further verifies

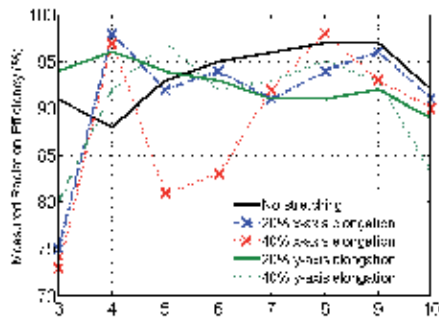


Figure 21. Measured radiation efficiency of the PICA in its relaxed and stretched states. The coordinate system is presented in Figure 16.

the robustness of electrical connections in the implemented PICA under different forms of deformation.

3.4. Multifunctional, microfluidics- based patch antenna and reversibly stretchable, self-contained, wireless strain sensor

A natural further step in the development of the emerging field of microfluidic soft electronics is to create more sophisticated multi-layered electronic devices and systems that can potentially open up a full spectrum of new applications. This, however, poses new challenges in device design, fabrication, and integration. The fabrication process of multi-layer microfluidic, elastomeric channels proposed in Section 2.2 is utilized to implement a reversibly stretchable, large-area, wireless strain sensor. This section details the design, fabrication, assembly, and characterizations of the sensor device.

The integrated wireless strain sensor contains an RF transmitter on a flexible PCB and a multifunctional, microfluidic, stretchable patch antenna for both wireless communication and strain sensing. The fluidic patch antenna is constructed in a double-layer configuration, *cf.* Figure 22. The principle for using an elastic antenna for strain sensing is simple. Because the resonant frequency of the patch antenna in use is largely determined by its electrical length along the x -axis, elongation along this direction would result in greater electrical length so that it decreases its resonant frequency. In the case of a patch antenna with narrow bandwidth (or high quality factor, Q), considerable impedance mismatch will occur at its original resonant frequency as a result of strain along its x -axis. When feeding such an antenna with a 50Ω source at a constant power level, significantly decreased radiation will be measured in the far-field. Higher strain sensing sensitivity can be attained by reducing antenna bandwidth. But decreasing bandwidth would put high demands on fabrication precision. A tradeoff between sensitivity and fabrication yield has to be made. In addition to the multifunctional antenna, the integrated sensor also contains a simplified RF transmitter, which can be externally powered by a stack of two AA batteries connected serially. Details of this integrated electronic sensor device can be found in the schematic views presented in Figure 22.

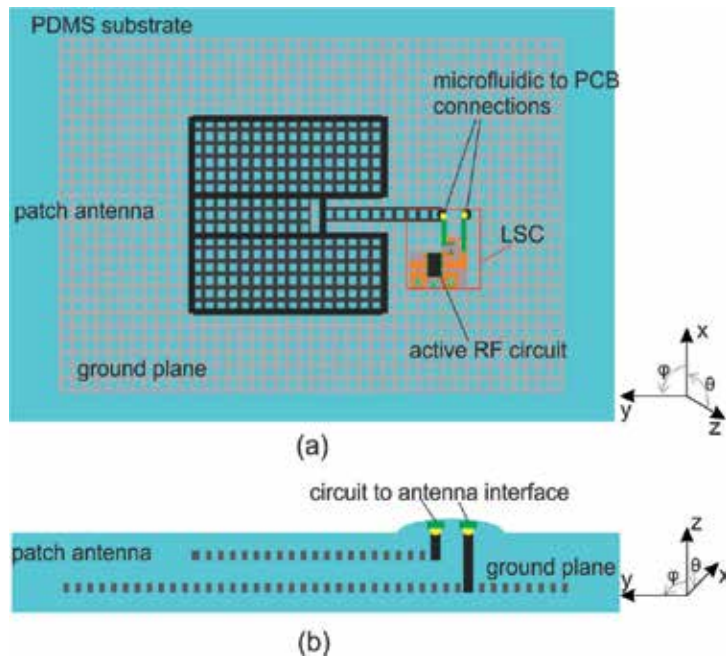


Figure 22. Schematic view of the proposed elastic wireless strain sensor: (a) top view and (b) cross view of microfluidic channels.

The designed patch antenna is fed by a short piece of microstrip. The spacing between the patch and the ground plane determines the bandwidth of the antenna. The greater the spacing is, the wider bandwidth the antenna features. Impedance bandwidth is also affected by dielectric losses of the substrate. Lossy dielectric materials would increase antenna bandwidth at the expense of radiation efficiency. Poor radiation efficiency should be definitely avoided, as it significantly shortens remote sensing range. Resembling microfluidic antennas reported in the previous sections, both the antenna patch and ground plane are realized in the meshed configuration. The active circuit assembled on a flex foil comprises a 1.5 GHz voltage controlled oscillator (VCO) associated with a few discrete components. The effective strain sensing area is as large as the overall size of the integrated sensor, approximately $110.0 \text{ mm} \times 80.0 \text{ mm}$. It makes the resulting wireless sensor well suited for remote, large-area strain sensing.

Mechanical properties should be taken into account in the design as well. Thinner PDMS substrates are preferred because of higher elasticity. A very thin substrate would, however, constrain the spacing between the patch and the ground plane, and lead to too narrow antenna bandwidth. Parametric analysis in numerical simulations shows that good compromise values for the overall thickness, and the spacing are 2.5 mm and 1.5 mm. A microfluidic, flexible, stretchable wireless strain sensor is implemented, following the fabrication and integration process described previously. Two openings on the top surface of the PDMS elastomer are utilized for hybrid integration with RF transmitter. A photograph of the fabricated sensor device is presented in Figure 23.

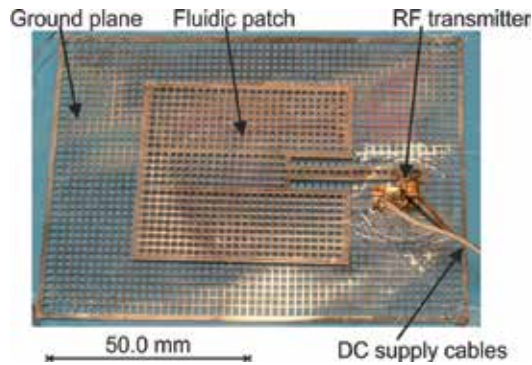


Figure 23. Photograph of the resulting microfluidics- based stretchable wireless strain sensor.

Prior to the final integration, the standalone patch antenna and RF transmitter circuit are tested individually. Reflection coefficients of the fluidic soft patch in response to varying strains are seen in Figure 24.

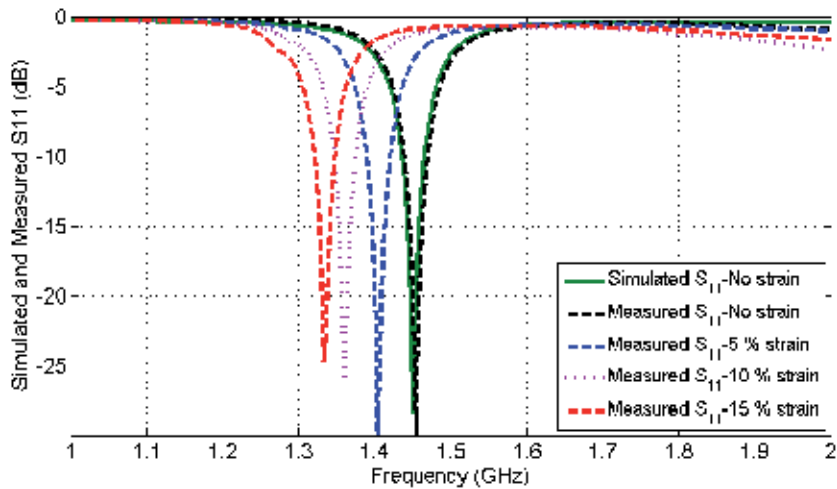


Figure 24. Simulated and measured S11 of the standalone fluidic patch antenna in its original state, and with varying strain along x -axis. The coordinate system is seen in Figure 22.

Experimental results indicate a dramatic resonant frequency decrease in response to incremental strain along the x -axis. Significant mismatch losses are observed at the oscillation frequency, 1.46 GHz, of the VCO during stretching. Measured radiation patterns (including mismatch losses) depicted in Figure 25 show greater than 10 dB realized antenna gain drop when the patch antenna is stressed from its original state to 15% elongation along the x -axis. Front-to-back ratio of radiation patterns is better than 10 dB. It should be noted that the meshed ground plane acts as an effective radiation shield and excellent front-to-back ratio of higher than 10 dB implies good forward radiation.

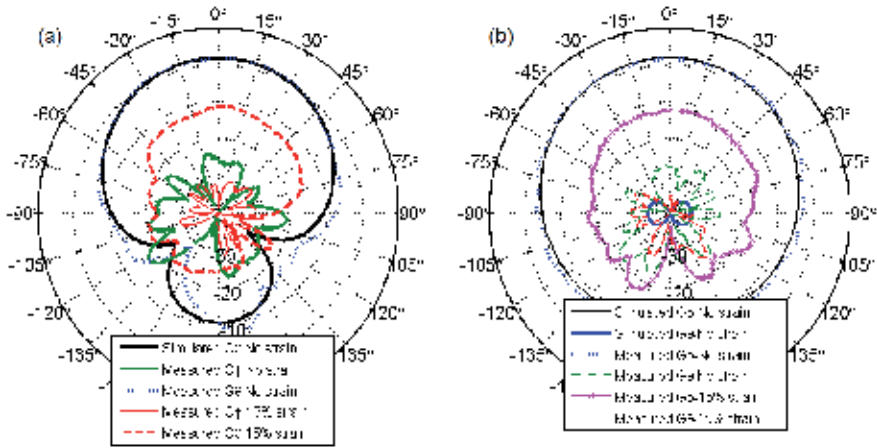


Figure 25. Simulated and measured radiation patterns (including mismatch losses) of the relaxed and flexed microfluidic patch antenna in the (a) xz- and (b) yz-plane. The coordinate system is shown in Figure 22.

After antenna measurements, the active circuit and the elastic antenna are heterogeneously integrated. On the other end of the wireless strain sensing system, a custom-designed receiver is developed to receive and interpret sensing data. The system diagram of the entire test setup for the elastic wireless strain sensor is illustrated in Figure 26.

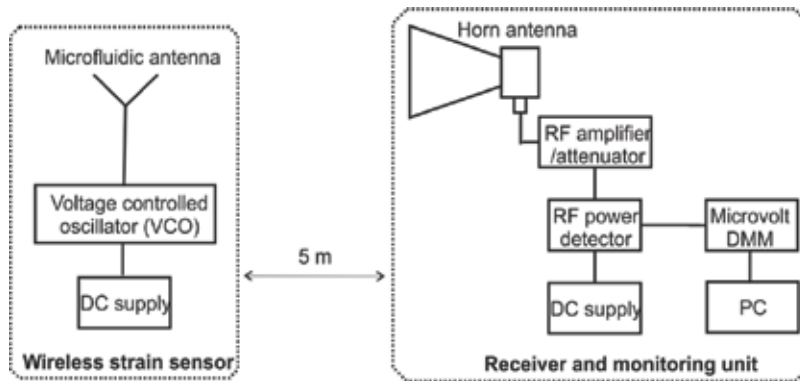


Figure 26. Illustration of the setup for demonstrating the microfluidic, reversibly stretchable, large-area wireless strain sensor.

As shown in Figure 26, the receiver consists of numerous sub-modules for RF power detection and is assisted by a personal computer (PC) for data readout and plotting. The output of the RF power detector is a DC voltage, proportional to the input RF power level. This voltage is measured by a high resolution digital multi-meter (DMM) controlled by the PC. The receiver unit is calibrated with varying RF power around 1.5 GHz, using a high precision synthesizer prior to the actual measurements.

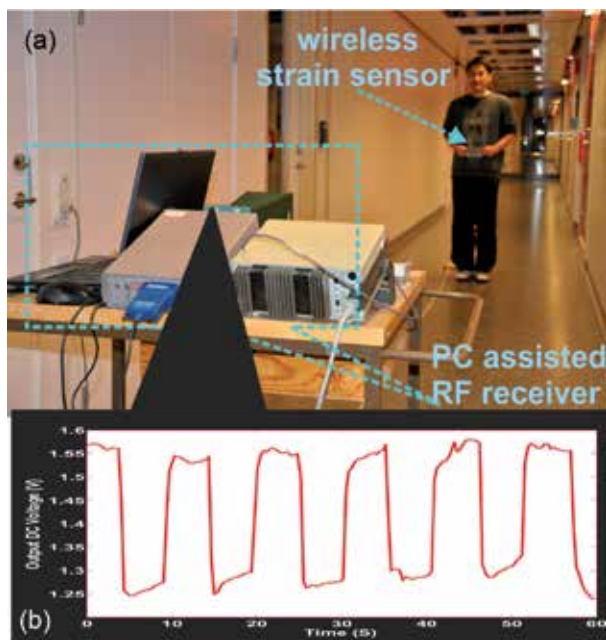


Figure 27. (a) Photograph of the demonstration of the elastic, wireless strain sensor. (b) Voltage readouts at a custom-designed PC-aided receiver.

The microfluidic, reversibly stretchable wireless strain sensor is tested in an ordinary office environment, *cf.* Figure 27. The distance between the integrated sensor and the receiver station is roughly 5 m. Repeated strain with a period of approximately 10 seconds is manually applied along the x -axis of the sensor. The plot in Figure 27 displays the data readout at the PC, which is in line with the manual stretch. Reversibility can also be clearly seen in the plot, as the measured voltage always returns to the original level after the removal of external strain. Such an integrated sensor can be deployed as a comfortable wearable electronic device for real-time monitoring of body motion.

4. Conclusion

An overview in the emerging field of ultracompliant, soft electronics that can be twisted, compressed, and stressed into almost any arbitrary shapes has been presented. Different strategies for realizing bendable, flexible, stretchable electronic devices and systems have been briefly discussed. Microfluidics-based soft electronics, one of the most promising approaches for implemented elastomeric electronics, has been addressed in detail. Fabrication techniques, hybrid integration concepts, as well as various electronic devices built in microfluidic, elastic formats are the focus of this chapter. Appealing application examples, ranging from single-layer standalone fluidic stretchable antennas to multi-layer, self-contained, large-area, wireless sensors, have been demonstrated.

Research efforts in incorporating new materials and novel technologies into soft electronics are ongoing. Figure 28 shows an example of a hand-shaped, soft, rubbery sensor for multi-point, remote pressure sensing. Emerging nanomaterials and fabrication processes, e.g., pressure-activated conductive rubber and inkjet-printed graphene-based flexible circuits, are introduced to create novel pressure sensors and active RF electronics. Feasibilities of implementing microfluidic, elastic EM energy harvesting devices are also being explored. Successful outcomes will pave the way for realizing batteryless, ultracompliant, wearable and implanted electronics that can be powered by ambient EM energy generated from billions of wireless devices around us.



Figure 28. Photograph of the stretchable multi-point, wireless pressure sensor prototype.

Microfluidic flexible, compressible, stretchable electronics together with other members in the new category of soft electronics are reshaping the world of electronics so as to the future of our daily life. The number of cell phones already outpaced the world population in 2014. It is anticipated that the total number of connected devices will grow to approximately seven times of the entire population in the coming 5 years, among which billions of soft electronic devices will be found in many new applications, including healthcare/medical monitoring, tissue engineering, bio-inspired robotics, and so on.

Acknowledgements

Dr. Shi Cheng currently holds a Young Research Fellow position financed by the Swedish Research Council (VR) under the contract (Avtals-ID: C0486501). Also Dr. Jiantong Li acknowledges Göran Gustafsson Foundation for the financial support through the Young Researcher Prize (No. 1415 B).

Author details

Babak Taghavi¹, Jiantong Li¹, Mikael Östling¹ and Shi Cheng^{1,2}

1 KTH, Royal Institute of Technology, Sweden

2 Ericsson AB, Sweden

References

- [1] Rutherford J.J. Wearable Technology. *Engineering in Medicine and Biology Magazine, IEEE*. 2010;29(3):19-24. DOI: 10.1109/MEMB.2010.936550
- [2] Verthey R., Accoto D. Wearable Robotics. *Robotics & Automation Magazine, IEEE*. 2014;21(4):19-110. DOI: 10.1109/MRA.2014.2364732
- [3] Honda W., Harada S., Arie T., Akita S., Takei K. Flexible Electronics: Wearable, Human-Interactive, Health-Monitoring, Wireless Devices Fabricated by Macroscale Printing Techniques. *Advanced Functional Materials*. 2014;24(22):3298. DOI: 10.1002/adfm.201470144
- [4] Rogers J.A., Someya T., Huang Y. Materials and Mechanics for Stretchable Electronics. *Science*. 2010;327:1603. DOI: 10.1126/science.1182383
- [5] Kim D.H., Ahn J.H., Choi W. M., Kim H.S., Kim T.H., Song J. Z., et al.. Stretchable and Foldable Silicon Integrated Circuits. *Science*. 2008;320(5875):507-511. DOI: 10.1126/science.1154367
- [6] Lacour S.P., Wagner S., Huang Z.Y., Suo Z. Stretchable Gold Conductors on Elastic Substrates. *Applied Physics Letters*. 2003;82(15):2404-2406. DOI: 10.1063/1.1565683
- [7] Lacour S. P., Jones J., Wagner S., Li T., Suo Z. Stretchable Interconnects for Elastic Electronic Surfaces. *Proceedings of the IEEE*. 2005;93(8):1459 -1467. DOI: 10.1109/JPROC.2005.851502

- [8] Haopeng W., Debao Z., Jianguo C. Development of a Stretchable Conductor Array with Embedded Metal Nanowires. *IEEE Transactions on Nanotechnology*. 2013;12(4):561-565. DOI: 10.1109/TNANO.2013.2258172
- [9] Brosteaux D., Axisa F., Gonzalez M., Vanfleteren J. Design and Fabrication of Elastic Interconnections for Stretchable Electronic Circuits. *Electron Device Letters, IEEE*. 2007;28(7):552 - 554. DOI: 10.1109/LED.2007.897887
- [10] Siegel A. C., Bruzewicz D. A., Weibel D. B., Whitesides G. M. Microsolidics: Fabrication of Three-Dimensional Metallic Microstructures in Poly(dimethylsiloxane). *Advanced Materials*. 2007;19:727-733. DOI: 10.1002/adma.200601787
- [11] Kim H., Son C., Ziaie B. A Multiaxial Stretchable Interconnect Using Liquid-Alloy-Filled Elastomeric Microchannels. *Applied Physics Letters*. 2008;92(011904):1-3. DOI: 10.1063/1.2829595
- [12] Dickey M. D., Chiechi R. C., Larsen R. J., Weiss E. A., Weitz D. A., Whitesides G. M. Eutectic Gallium-Indium (EGaIn): A Liquid Metal Alloy for the Formation of Stable Structures in Microchannels at Room Temperature. *Advanced Functional Materials*. 2008;18:1097-1104. DOI: 10.1002/adfm.200701216
- [13] Cheng S., Rydberg A., Hjort K., Wu Z. Liquid Metal Stretchable Unbalanced Loop Antenna. *Applied Physics Letters*. 2009; 94:144103. DOI: 10.1063/1.3114381
- [14] Cheng S., Wu Z., Hallbjörner P., Hjort K., Rydberg A. Foldable and Stretchable Liquid Metal Planar Inverted Cone Antenna. *IEEE Transactions on Antennas and Propagation*. 2009;57(12):3765-3771. DOI: 10.1109/TAP.2009.2024560
- [15] Kubo M., Li X., Kim C., Hashimoto M., Wiley B. J., Whitesides G.M. Stretchable Microfluidic Radiofrequency Antennas. *Advanced Materials*. 2010;22:2749-2752. DOI: 10.1002/adma.200904201
- [16] Cheng S., Wu Z. Microfluidic Stretchable RF Electronics. *Lab on a Chip*. 2010;10:3227-3234. DOI: 10.1039/c005159d
- [17] Cheng S., Wu Z. A Microfluidic, Reversibly Stretchable, Large-Area Wireless Strain Sensor. *Advanced Functional Materials*. 2011;21:2282-2290. DOI: 10.1002/adfm.201002508
- [18] Hayes G. J., So J. H., Qusba A., Dickey M. D., Lazzi G. Flexible Liquid Metal Alloy (EGaIn) Microstrip Patch Antenna. *IEEE Transactions on Antennas and Propagation*. 2012;60(5):2151-2156. DOI: 10.1109/TAP.2012.2189698
- [19] Huang Y., Wang Y., Xiao L., Liu H., Dong W., Yin Z. Microfluidic Serpentine Antennas with Designed Mechanical Tunability. *Lab on a Chip*. 2014;14:4205-4212. DOI: 10.1039/c4lc00762j
- [20] Jeong S. H., Hagman A., Hjort K., Jobs M., Sundqvist J., Wu Z. Liquid Alloy Printing of Microfluidic Stretchable Electronics. *Lab on a Chip*. 2012;12:4657-4664. DOI: 10.1039/c2lc40628d

Microfluidic Sensors and Circuits for Internet of Things Applications

John Yan

Additional information is available at the end of the chapter

<http://dx.doi.org/10.5772/64346>

Abstract

As we move into the Internet of Things (IoT) and cloud computing era, the number of sensors deployed which seamlessly integrate themselves into environment is growing rapidly. These sensors should be minimally intrusive, both optically and mechanically, while providing high temporal and spatial contextual awareness of its environment. In this chapter, microfluidic sensors and circuits are presented to better bridge the physical and digital world for healthcare applications. Specifically, a discussion of cardiovascular sensing, glaucoma diagnosis and flexible tactile sensor arrays for smart skin application is presented.

Keywords: Circuits, digital health, internet of things, microfluidics, pervasive computing, sensors

1. Introduction

As we move into the Internet of Things (IoT) and cloud computing era, the number of sensors deployed that seamlessly integrate themselves into environment is growing rapidly [1–3]. The research and development challenges to create a smart and interconnected world necessitate a new paradigm in Internet architecture. This architecture requires the consideration of security, software platforms, ethical implications, standardization, smart sensors, and pragmatic business models. This chapter has honed down this broad vision to specifically focus on a few contributions from microfluidic sensors and circuits to better bridge the physical and digital world for healthcare applications.

1.1. Overview of Internet of Things for healthcare

As we move into the IoT and cloud computing era, the number of sensors deployed that seamlessly integrate themselves into environment is growing rapidly. This concept is descri-

bed a totally interconnected world where devices of every shape and size are manufactured with “smart” capabilities that allow them to communicate and interact with other devices, exchange data, make autonomous decisions, and perform useful tasks based on preset conditions. Figure 1 shows an ecosystem of IoT’s relationship with people and the home within the modern cloud computing environment. Wearable devices and sensors would be ubiquitously employed to continuously monitor health and infrastructure that would subsequently be uploaded to data centers and archived as datasets. These datasets then provide the training necessary for data scientists and physicians to make intelligent predictions based on the behavior of its clients.

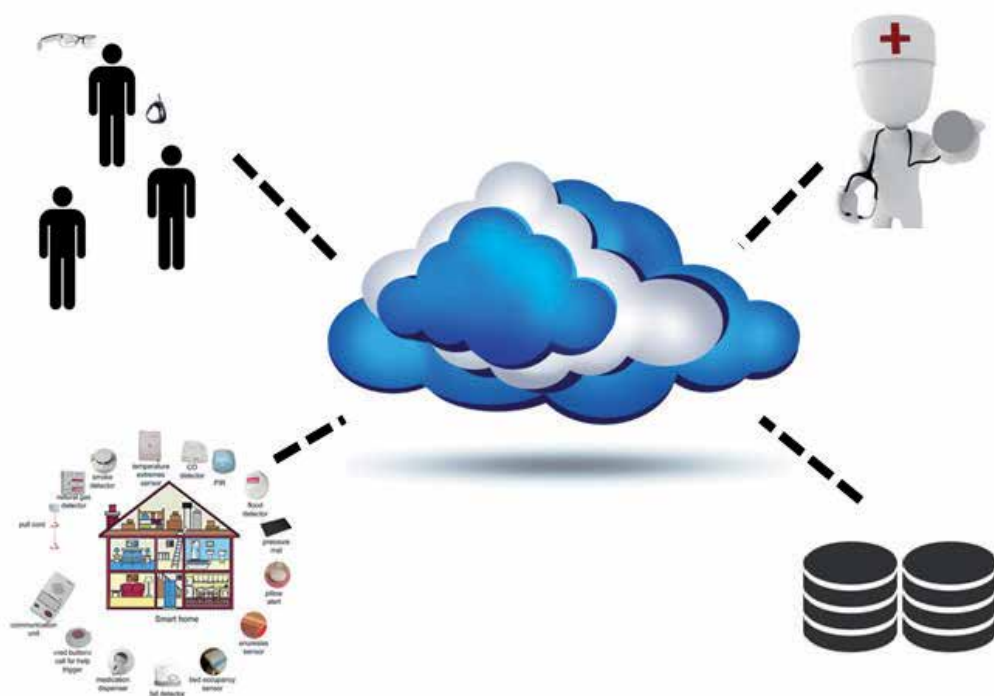


Figure 1. Data flow of Internet of Things devices for healthcare applications.

1.2. Microfluidics for IoT

Microfluidics is a multidisciplinary field intersecting engineering, nanotechnology, physics, and chemistry with practical applications to design systems in which small volumes of fluids will be handled [4–6]. In this chapter, we touch on the various facets of this multidisciplinary field and present applications on how microfluidic circuits and sensors can be utilized in an IoT environment. Figure 2 shows the variety of sensors and circuits for IoT healthcare applications ranging from cardiovascular sensing (to be integrated with smart-watch applications [7]) to unpowered microfluidic pressure sensors for glaucoma diagnosis [8] to flexible

tactile sensor arrays for smart skin applications [9]. Each of these devices will be addressed in more detail throughout this chapter.

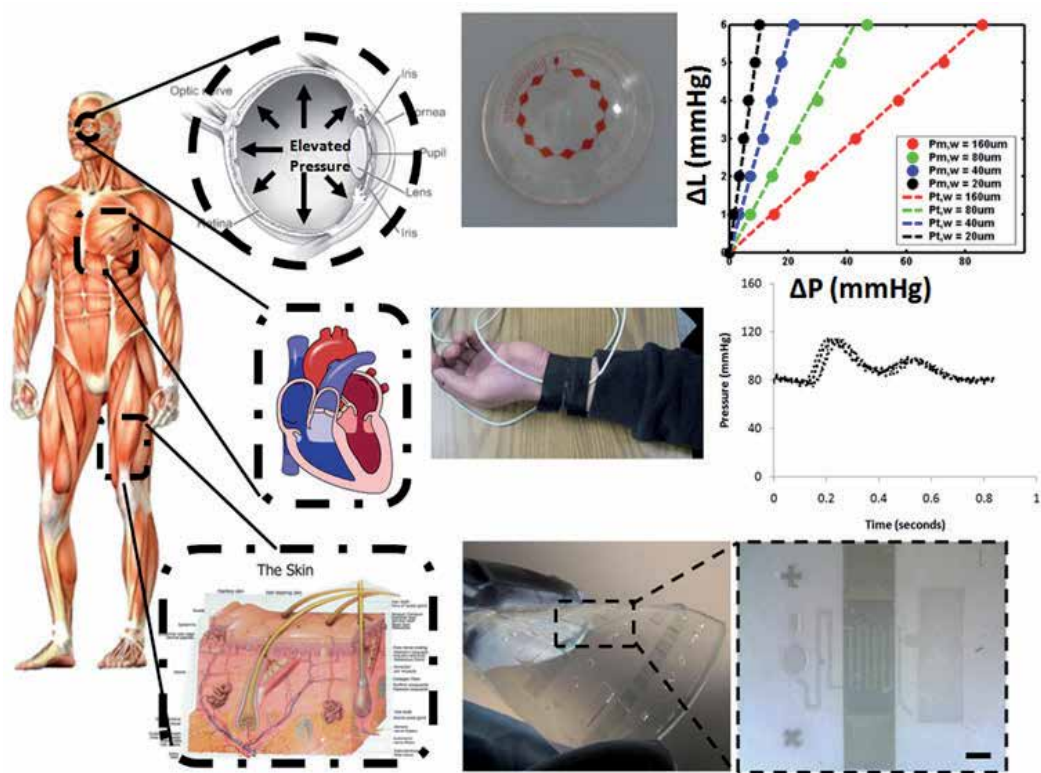


Figure 2. Example of IoT sensors for healthcare applications.

2. Coupled optomechanical pressure and flow measurements

Cardiovascular disease (CVD) is estimated to affect 81 million Americans adults [10]. An important determinant of these diseases is the arterial wall stiffness [11]. This section describes the development of a simple, non-invasive, real-time detection system that utilizes pulse wave velocity and pressure pulsation measurements to estimate vascular resistance and compliance in the radial artery that can provide the physician important diagnostic information. This system is realized by utilizing a 780 nm laser Doppler velocimeter to obtain the local flow rates and a piezoelectric pressure sensor to measure the pressure pulsation at the radial artery. Here, the sensor measurement results at the proximal and distal radial arteries are presented in both the time and frequency domain. While the presented results are demonstrated utilizing tabletop instrument, ultimately this system can be completely integrated for a light-weight,

portable, real-time monitoring system that can potentially be embedded into textiles for seamless monitoring of important cardiovascular signals.

Figure 3 shows an overview of the IoT device that is used to monitor the vascular impedance through coupled optomechanical pressure (P) and flow (Q) measurements whose form factor should be small enough to be integrated with a wrist watch. On top of the biomaterial (bone, skin, blood, etc.) lies an optically transparent pressure sensor with integrated optics and electronics for digital signal processing and wireless communication to the cloud. Such a device facilitates the monitoring of signatures of cardiovascular disease using personalized datasets for real-time, continuous monitoring.

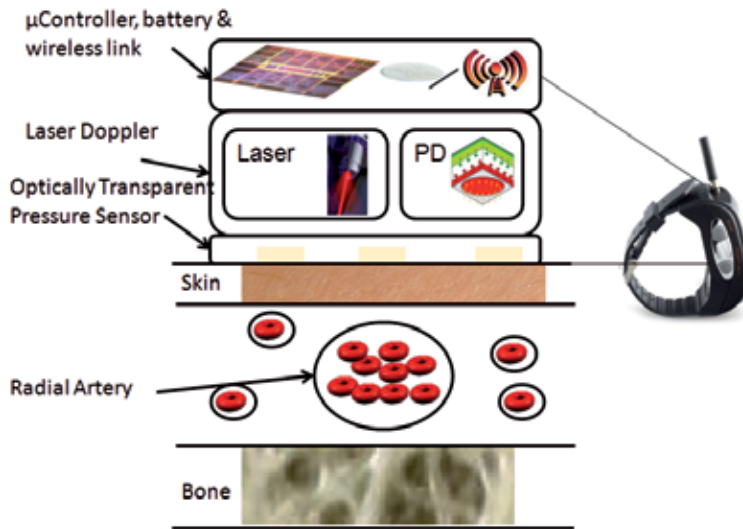


Figure 3. IoT vascular impedance assessment through coupled optomechanical pressure and flow measurements.

To measure the arterial flow, the laser Doppler principle, consisting of a laser light source shone on the radial artery and collection of the backscattered light collected by the photodiode, can be used. The total backscattered light consists of a component from the static tissue and a component with frequency shifted light, whose shifted amount is dependent on the speed of moving blood. These two components are collected and mixed on a photodetector whose corresponding photocurrent can then be post processed to indicate the velocity of moving red blood cells. This optical detection system should utilize $\lambda_0 = 780$ nm light with a typical output power of less than 1 mW of power. Therefore, the flow is:

$$Q = v_{s,r} \pi r^2 = - \frac{\Delta f}{n_{\text{bio,tissue}}} \lambda_0 \pi r^2 \quad (1)$$

where $n_{\text{bio,tissue}}(780 \text{ nm}) \sim 2.6$.

The pressure sensor utilizes the concept tonometry to apply tension to the radial artery. The pressure sensor should be sufficiently flexible to conform to the skin and be optically transparent to the laser Doppler velocimeter system. Furthermore, it should have a sensitivity of 2 mmHg with a dynamic pressure range of 200 mmHg and an electromechanical bandwidth of 10 Hz. A detailed description of the construction and operation of such a pressure sensor built on microfluidic concepts will be described later on in this chapter.

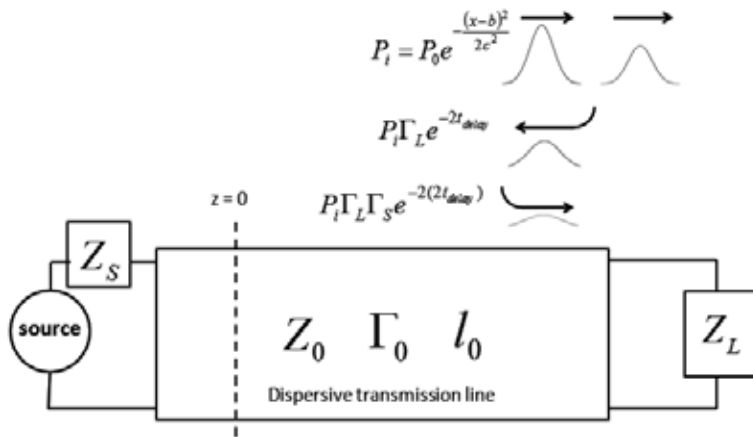


Figure 4. Model of cardiovascular system.

To describe the cardiovascular system, one can use transmission line analog between hydraulic transmission system of compliant tubes and an electrical transmission lines as shown Figure 4. Here, the blood flow and pressure waveforms are used to provide a baseline model to validate our measurement results where the signal source represents the heart. Based on the coupled Navier-Stokes equations [12]:

$$-\frac{\partial P}{\partial x} = QR + L \frac{\partial Q}{\partial t} \tag{2}$$

$$-\frac{\partial Q}{\partial x} = PG + C \frac{\partial P}{\partial t} \tag{3}$$

where arterial flow can be modeled as a dispersive transmission lines that broadens and distortions as it travels downward the hydraulic line. The different frequency components of propagation are then described by the standard impedance (Z_0) and reflection (Γ) relationships:

$$Z_0 = \sqrt{\frac{R + j\omega L}{G + j\omega C}} \tag{4}$$

$$\Gamma_L = \frac{Z_L - Z_0}{Z_L + Z_0} \quad (5)$$

$$\Gamma_S = \frac{Z_S - Z_0}{Z_S + Z_0} \quad (6)$$

where Γ_L is the reflection coefficient at the load and Γ_S is the reflection coefficient at the source. The mechanical resistance (R), compliance (C), and inductance (L) are governed by the following equations:

$$R = \frac{P}{Q} \quad (7)$$

$$C = \frac{\partial V}{\partial P} \quad (8)$$

$$L = \frac{P}{dQ/dt} \quad (9)$$

where resistance is the ratio of pressure over flow, compliance is the change of volume of fluid (∂V) over the change of pressure (∂P) and the inductance is pressure over the change of flow with respect to time (dQ/dt).

When the pressure and flow can be modeled as a Gaussian pulse with reflected waves that occur during discontinuities of impedances:

$$P(z=0) = P_i + P_r = P_i(1 + \Gamma e^{-2t_{\text{delay}}} + \Gamma^2 e^{-2(2t_{\text{delay}})} \dots) \quad (10)$$

$$t_{\text{delay}} = \frac{1}{\text{length}} \frac{\omega}{\beta} \quad (11)$$

A sample of the measured results is shown in Figure 5 where the vascular impedance values of compliance, inductance and resistance can be obtained. Using reflection amplitudes, we can obtain the source and load impedance values. From the waveform, we not only know the vascular impedance at the point of optomechanical measurement but we can also estimate the vascular impedance at the source and load. The discontinuities along the arterial hydraulic line are a result of bifurcations that leads to reflected waves along the dispersive line. Time

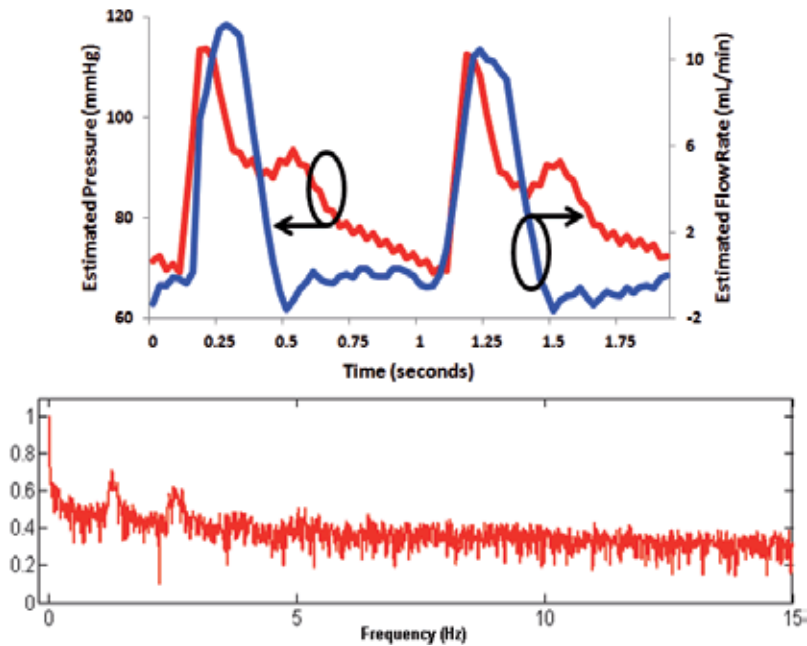


Figure 5. Sample of measured results from vascular impedance assessment of coupled optomechanical pressure and flow: (a) time domain; (b) frequency domain.

domain information can also be discrete Fourier transformed, whose signal can be improved with windowing functions due to the discrete sampling nature, to find spectral information.

3. Microfluidic sensor for point-of-care glaucoma diagnosis

An important microfluidic sensor developed for IoT applications is for the continuous monitoring of glaucoma that an estimated 67 million people are believed to suffer worldwide [13]. Patients with glaucoma are considered “well controlled” if their mean intraocular pressure (IOP) is lower than 21 mmHg. Owing to a rapidly aging population, it is estimated that the number of open angle glaucoma cases will increase to 3.4 million in 2020, making it the second leading cause of blindness and the first leading cause of irreversible blindness in the United States. Since unregulated IOP can lead to irreversible blindness by pinching the optic nerve, as seen in Figure 6, it is of paramount importance to monitor this pressure and make low-cost, point-of-care diagnostic tools available. Various wireless techniques have been conceived to continuously monitor intraocular pressure [16–19], which require radio frequency (RF) power transfer to power the device. However, a slew of potential health issues can arise from long term exposure to the high RF power transfer needed to power the device. Microfluidic solutions provides an unique solution due to its low-cost and biocompatible material construct that is additionally amendible to large-scale manufacturing.

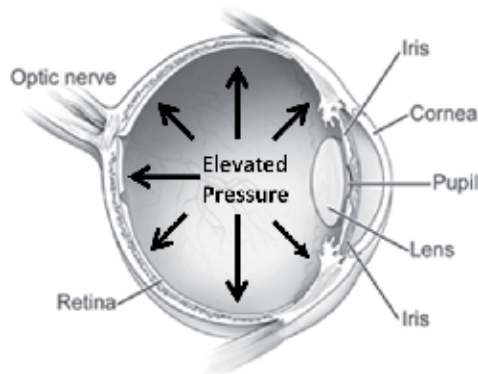


Figure 6. Glaucoma is a result of build up of intraocular pressure; figure adopted from [20].

The dynamical IOP measure is based on Laplace's principle where the pressure inside the hydraulic chamber (P_t) is dynamically determined by loading pressure and measured by the built-in microfluidic pressure sensor. The sensing membrane deflects and measures the pressure difference (P_s) at each contact point through the individual surface sensing element(s). Polydimethylsiloxane (PDMS) is used as the structural material to create the flexible, polymeric membrane and surface sensing for its elasticity and flexibility as well as excellent physical properties with a Young's modulus (E) of approximately 500 kPa [21].

The device to test the sensing principle is illustrated in Figure 7. It consists of a large, circular sensing chamber network with height H and radius r . This is followed by sensing channels of width w and height h , which act as the sensing elements. When local pressure is applied to the sensing chamber network, an internal strain is induced on the elastomer structure. This generates a pressure gradient internally within the microfluidic network. As a result, the compression of the sensing chamber leads to an outward fluid displacement onto the sensing channel. As stress is released from the sensing chamber, the elastomer recovery properties of PDMS create a negative pressure to withdraw fluid from the sensing channel.

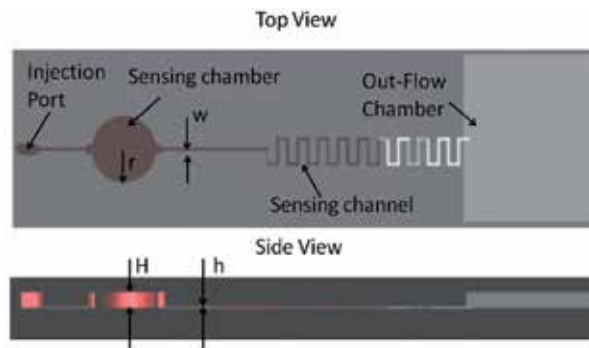


Figure 7. Schematic illustration of calibration device.

The microfluidic network is carefully designed to prevent air bubble formation at the sensing chamber during the injection process. This is done by installing an injection port before the sensing chamber network. Laplace valves at the entrance and exit of the sensing chamber are designed to prevent bubble cavitation as the fluid flows from the fluidic interconnects to the sensing chamber. To minimize compressive effects of displacement of air in the sensing channel during fluidic displacement, a large out-flow chamber is designed to have a volume a thousand times larger than the sensing channel, acting as a pressure relief conduit. A long, rectangular straight sensing channel is used to characterize the sensing principle of the device since its laminar flow profile characteristics are well understood. By optically observing the magnitude of fluidic displaced, the resulting pressure on the sensing chamber can be determined.

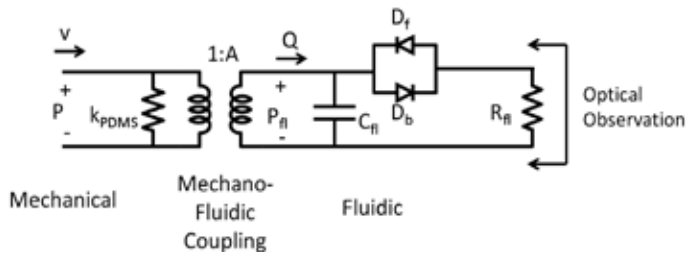


Figure 8. Equivalent circuit model of transducer.

The mechano-fluidic transduction can be modeled as a circuit network as shown in Figure 8. Pressure applied to the sensing chamber with a set velocity results in a corresponding flow of fluid due to the change in the internal pressure displacement. A transformer is used to model the conversion from solid mechanical displacement of the elastomer to the fluidic displacement in the microfluidic network. The displacement amplification A is set by the geometry of the sensing chamber and sensing channel. The stiffness of the sensing chamber is:

$$k_{PDMS} = \frac{\text{stress}}{\text{strain}} \quad (12)$$

According to the strain-stress relationship, the change of the micro-chamber height can be expressed as, $\Delta H/H = \sigma/E$, where E is Young's Modulus of PDMS elastomer, and σ is the loading pressure. The displaced fluidic volume enters the incompressible microchannel, where the geometry (i.e., the cross-section area) determines the wetted length (Δl) of the colored fluid. Herein, the sensitivity (S) can be calculated as

$$S = \frac{P}{\Delta l} = \frac{whE}{\pi r^2 H} \quad (13)$$

To assess the frequency response of the sensor, the microfluidic sensing system can be modeled as a first-order linear circuit, in which the micro-chamber membrane compliance C and the microchannel resistance R are:

$$C = \frac{\pi r^2 H}{E} \quad (14)$$

$$R = \frac{12 \mu \Delta l}{wh^3} \quad (15)$$

where μ is the viscosity of the sensing fluid. D_i and D_b represent the effect of surface tension and the resulting difference in internal pressure that needs to be overcome before the fluid can displace in the sensing channel. This surface tension is set by the surface properties of the material.

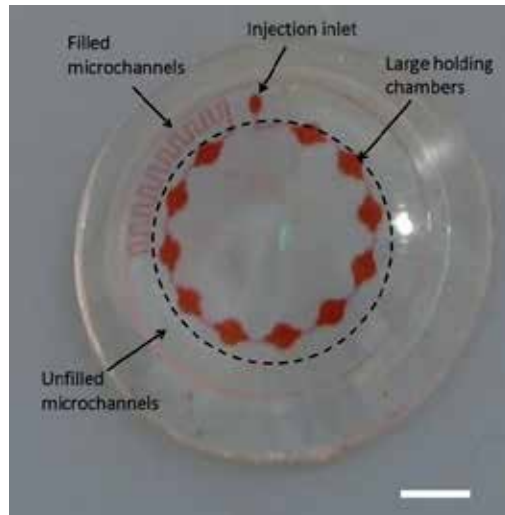


Figure 9. Optical photograph of the microfabricated device; scale bar is 5 mm.

To analyze the fluidic response, it is assumed that flow is dominated by pressure driven flow in the laminar region so the lubrication theory approximation can be used for the Navier-Stokes equation. The cutoff frequency, f_c , is set by the fluidic resistance and capacitance [22] as follows:

$$f_c = \frac{1}{2\pi\tau_{fl}} = \frac{1}{2\pi RC} = \frac{1}{2\pi \left(\frac{12\mu\Delta l}{wh^3} \right) \left(\frac{\pi r^2}{E} \Delta H \right)} \quad (16)$$

To accommodate the human cornea with an approximately a diameter of 7.8 mm, the microfluidic sensing chambers and corresponding meandered sensing channels are designed on the peripheral of the contact lens at the sclera area. A realized microfluidic device for IoT appli-

cations is shown in Figure 9. For the prototyped contact lens, the sensing channel length is over 80 mm with a sensing channel width of 20 μm . This corresponds to a dynamic range of 130 mmHg—more than sufficient for measuring the IOP. The characterization results of the device can be found in [8].

4. Microfluidic sensor for smart skin applications

Ubiquitous sensing and smart skin applications that leverage flexible substrates for ultra-high sensitivity pressure sensing is of great interest to the IoT community. This is especially of interest when the sensor optical properties can be tuned to be optically transparent for a host of applications. Figure 10 shows a 3×3 array of optical transparent, microfluidic pressure sensors.

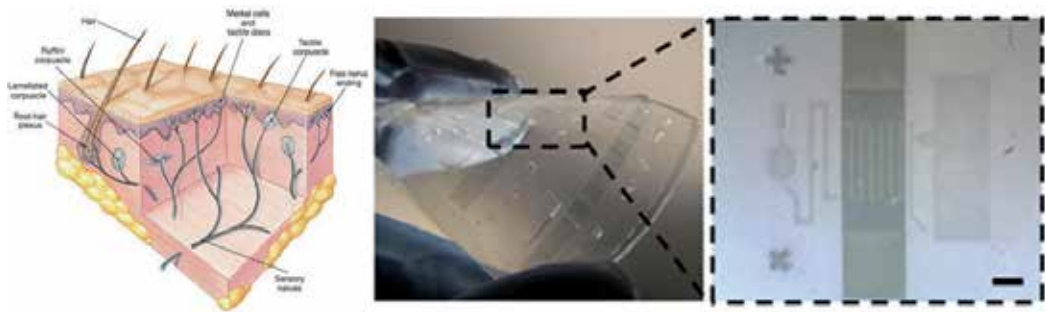


Figure 10. 3×3 array of optically transparent, microfluidic pressure sensor array (scale bar is 1 mm) for smart skin applications.

4.1. Device operation

The architecture of the microfluidic, capacitive pressure sensor is illustrated in Figure 11. It consists of a soft, micromachined elastomer to house fluid on a rigid plastic substrate. The highly deformable sensing chamber is designed to be tall and large to hold a volume of fluid much greater than the capacity of the sensing channel. Electrodes, in this case, transparent conductive oxide (TCO), are used to detect the degree of fluidic displacement as the sensing chamber deforms under applied pressures. Specifically, the large interfacial capacitance ($>20 \mu\text{F}/\text{cm}^2$) from the TCO and room temperature ionic liquid (RTIL) is employed [23]. To prevent air bubble generation, Laplace valves are placed at the exit and entrance of the sensing chambers. Optional mechanical concentrator(s) can be integrated to the sensor for additional sensitivity.

As pressure is applied at the sensing chamber, strain is induced on the elastomer housing the microfluidic network. In turn, an internal pressure gradient between the sensing chamber and sensing channel leads to an outward fluid displacement across the sensing channel. Due to the geometry difference between the sensing chamber and sensing channel, mechanical displace-

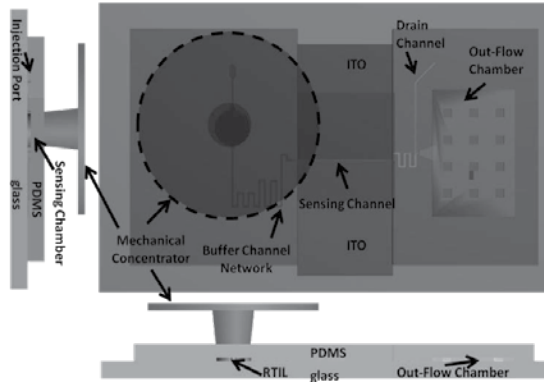


Figure 11. Microfluidic capacitive pressure sensor architecture.

ment amplification occurs as a result of the conservation of mass—a small compressive strain in the sensing chamber leads to a large displacement of fluidic across the sensing channel. Consequently, a change in the interfacial capacitance is detected across the coplanar electrodes. The causality of physics is illustrated in Figure 12, leading to a change in capacitance—where the strain on the elastomeric housing is exaggerated for illustrative purposes. When pressure is released from the sensing chamber, vacuum force is generated from the elastomer recovery, receding the fluid back to the sensing chamber and away from the coplanar electrodes. A mechanical concentrator, constructed out of rigid (~3 GPa) plastic, can subsequently be superimposed on top of the sensing chamber to further improve the sensitivity of the sensor. The concentrator serves to focus the mechanical pressure on the sensing chamber by using the area difference between the top disk area and the bottom disk that is in contact with the sensing chamber.

4.1.1. Interfacial capacitance

At the interface between RTIL and Indium Tin Oxide (ITO), there exists an electrochemical energy between Φ_m and π^* as shown in Figure 13a. In the inset, an example of an RTIL is shown. In this case 1-Butyl-3-Methylimidazolium Tetrafluoroborate (BMImBF₄) has attractive properties of low surface tension and is readily available, consisting of an anion and a cation. In order to maintain electrostatic neutrality between the two materials, a thin layer of ions are collected at the surface. As a result, an interfacial capacitance is formed. The associated electrical circuit model is shown in Figure 13b. The equivalent circuit model of the interfacial capacitance, C_I , can be described by the Gouy-Chapman Model [24]:

$$\frac{1}{C_I} = \frac{1}{C_H} + \frac{1}{C_G} = \frac{2}{(w-g)l} \left(\frac{d_{OHP}}{\epsilon_0 \epsilon_r} + \frac{L_D}{\epsilon_0 \epsilon_r \cosh\left(\frac{z\Phi_0}{2U_i}\right)} \right) \cong \frac{2}{(w-g)l} \frac{d_{OHP}}{\epsilon_0 \epsilon_r} \tag{17}$$

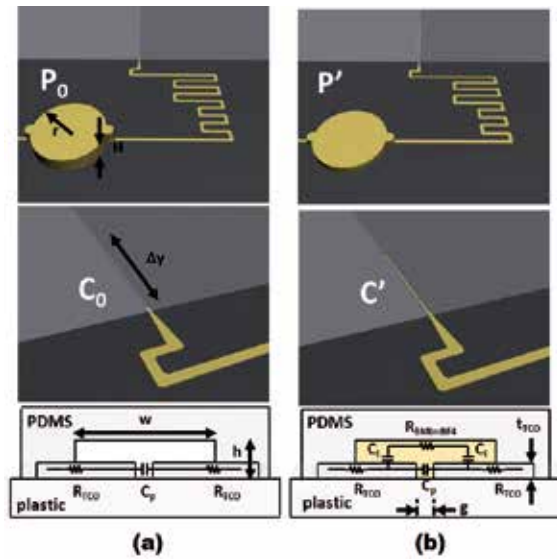


Figure 12. Illustration of device operation with equivalent circuit: (a) initial pressure and capacitance; (b) measured pressure and capacitance.

where w is the width of microfluidic channel, g is the gap between the electrodes, $\epsilon_0\epsilon_r/d_{\text{OHP}}$ is the capacitance per unit area, and l is the length of fluid overlap from the sensing channel mouth. The charge transfer resistance, R_{ct} , is a high-value resistance ($\sim\text{M}\Omega$) due to tunnel current leakage can be described as

$$R_{ct} = \frac{RT}{nFi_0} \quad (18)$$

where R is the universal gas constant, T is the temperature, F is the Faraday constant, n is the number of electrons in the unit reaction and i_0 is the current. R_{oxide} and R_{bulk} are the finite resistance of the electrolyte and metal.

The associated change in fringe capacitance, C_p can be described as [25]

$$C_p = \epsilon_0\epsilon_{\text{eff}} \frac{K(k'_0)}{K(k)} \quad (19)$$

where $K(k)$ is complete elliptic integrals of the first kind described as

$$k_0 = \frac{g}{s+g} \quad (20)$$

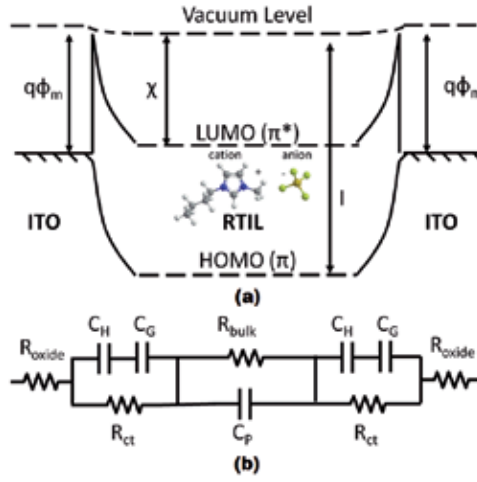


Figure 13. (a) Band diagram of the energy potential; (b) equivalent circuit model.

$$k'_0 = \sqrt{1 - k_0^2} \tag{21}$$

where g is the gap distance of the edge of the electrode from the symmetrical plane of the coplanar electrodes and s is the effective electrode distance as a result of the parasitic coplanar capacitance between the two electrodes whose value is typically much smaller than C_1 .

4.1.2. Electromechanical model

The equivalent electromechanical circuit model is shown in Figure 14. According to the strain-stress relationship, the change of the micro-chamber height (H) can be expressed as, $\Delta H/H = \sigma/E$, where E is Young’s Modulus of PDMS elastomer, and, σ is the loading pressure.

As normal pressure is applied at the sensing chamber, a resulting strain is induced on the elastomer housing the microfluidic network following the simple stress-strain relationship

$$\frac{\Delta P}{E} = \frac{\Delta H}{H} \tag{22}$$

As a result, an internal pressure gradient occurs between the sensing chamber and sensing channel in the microfluidic channel creating an outward fluid displacement across the sensing channel due to conservation of mass, as exhibited by the $\pi r^2 \Delta H = wh \Delta l$ relationship. By causalities in physics as previously described, a change in capacitance will be observed across the electrodes due to changes in pressure.

By inserting the stress-strain relationship and interfacial capacitance into the conservation of mass equation, the sensitivity of the device can be described by the following equation:

$$S = \frac{\partial C}{\partial P} = \frac{H}{E} \pi r^2 \frac{\epsilon_0 \epsilon_{r,fluid}}{d_{double\ layer}} \left(\frac{w-g}{2} \right) \frac{1}{wh} \frac{1}{2} \quad (23)$$

where H is the height of the sensing chamber, r is the radius of the sensing chamber, E is the Young's modulus of the membrane, w is the width of the sensing channel, g is the electrode gap, h is the height of the sensing channel and $\epsilon_0 \epsilon_{r,fluid} / d_{double\ layer}$ is the interfacial capacitance per unit area. This equation shows that the sensitivity of the sensor can be easily tuned by adjusting the geometries of the microfluidic network.

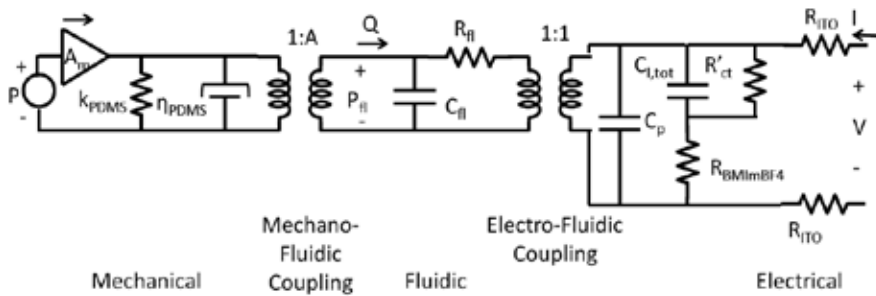


Figure 14. Equivalent electromechanical circuit model.

The fluidic resistance is assumed to operate by a pressure driven flow in the laminar region so the lubrication theory approximation can be used for the Navier-Stokes equation. The fluidic resistance, defined as ratio of hydrodynamic pressure over volume flow rate, of the sensing channel as

$$R = \frac{12\mu}{wh^3} \left[1 - \frac{h}{w} \left(\frac{192}{\pi^5} \sum_{n=1,3,5} \frac{1}{n^5} \tanh\left(\frac{n\pi w}{2h}\right) \right) \right]^{-1} \approx \frac{12\mu\Delta L}{wh^3} \quad (24)$$

when $h \ll w$. The fluidic capacitance is described as the ratio of chamber volume over applied hydrodynamic pressure. For the sensing chamber, this can be modeled as

$$C = \frac{\pi r^2}{E} \Delta H \quad (25)$$

when $h \ll w$. The microfluidic resistance and capacitance are believed to play an important role in the frequency response of the sensor. The fluidic capacitance is described as the ratio of chamber volume over applied hydrodynamic pressure.

Additionally, the amplification of mechanical concentrator is simply:

$$A_m = \left(\frac{D_{out}}{D_{in}} \right)^2 \quad (26)$$

where D_{out} is the upper diameter of the mechanical amplifier and D_{in} is the lower diameter of the mechanical amplifier [26].

4.2. Device fabrication

Techniques to fabricate microfluidics [27, 28] have been modified for these devices. A typical fabrication process is illustrated in Figure 15. The master mold, shown in Figure 16a, is fabricated by a two-step SU-8 process on a silicon substrate. The first step consists of forming the buffer channel, sensing channel, drain channel, and the associated microfluidic interconnects to a height of 15 μm . The second step consists of forming the sensing chamber, out-flow chambers and injection port to have a height of 200 μm . The thin film ITO electrodes are patterned with a hydrochloric acid wet etch process and traditional photolithography. Next, the PDMS elastomer is fabricated with a 10:1 (base: agent) mixture to create a thick replica mold of 1 mm. This replica mold is subsequently aligned to the ITO electrode pattern and bonded onto the glass substrate through oxygen plasma pretreatment as shown in Figure 16c.

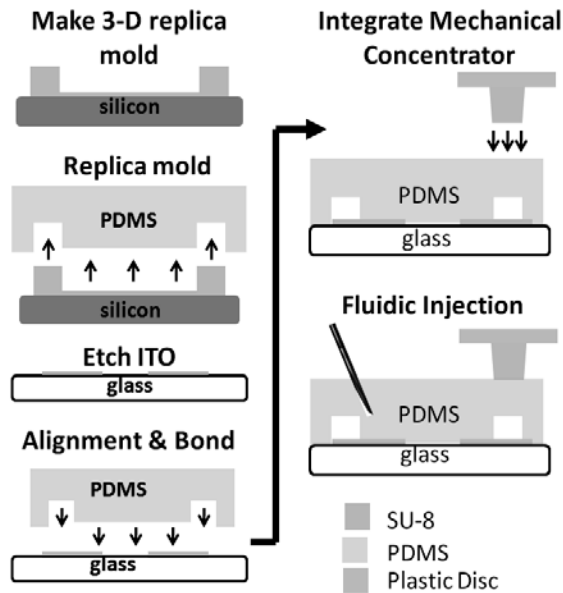


Figure 15. Microfabrication process.

A BD 30½ G needle is inserted into the injection port of the elastomer housing and a controlled volume of fluid is infused into the microfluidic network from a glass syringe using a syringe pump at a calibrated flow rate. Due to the small diameter of the gauge needle, the puncture

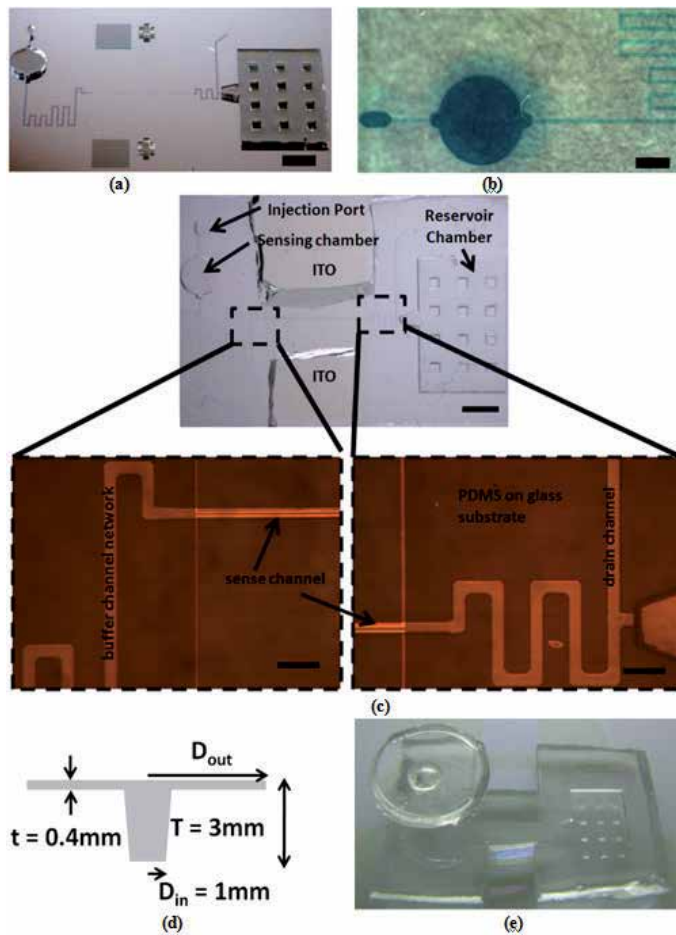


Figure 16. (a) 3-D replica mold. (b and c) Device. (d) Schematic of mechanical amplifier. (e) Mechanical amplifier integrated with microfluidic, capacitive pressure sensor.

hole is self-sealed after withdrawal due to the elastomeric properties of the PDMS. For illustrative purposes, dyed glycerol is injected as shown in Figure 16b. After the injection of RTIL, the patterned microchannels become invisible due to the close refractive index between BMImBF_4 (1.42) and the PDMS housing (1.4). The mechanical concentrator is constructed out of polystyrene, for its combination of mechanical rigidity (~ 3 GPa), optical transparency, low-cost and micromachinability with a programmable, CO_2 laser (universal laser systems), whose schematic is illustrated in Figure 16d. Furthermore, polystyrene and PDMS can form covalent bonding through oxygen plasma treatment leading to simple integration. This is a result of the plasma, creating hydrogen bondings of silanol groups with C-OH and COOH moieties on the oxidized-rich polystyrene surface [29]. Additionally, the PDMS molds can be transferred to a suite of other plastic substrates through simple plasma assisted bonding to form an array of flexible pressure sensors [30]. The finished device is illustrated in Figure 16e.

4.3. Characterization setup

The test setup to evaluate the sensor sensitivity is shown in Figure 17. It consists of a force gauge and a step motor mounted onto an optical table. As controlled normal pressure is applied to the sensing chamber, the fluidic displacement within the sensing channel is monitored with an optical microscope. The electrical impedance spectroscopy is monitored with a precision LCR meter and Labview software. The frequency dependent double layer capacitance response is plotted in Figure 18 where increments of 1 kPa are applied to the pressure sensor. The response double layer capacitance at the ITO/BMI₄ interface has a peak capacitance of approximately 25 $\mu\text{F}/\text{cm}^2$ at 30 Hz. This high capacitance per unit area indicates a successful surface engineering to roughen the electrode surface.

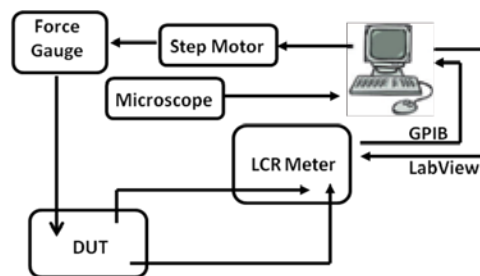


Figure 17. Measurement setup for sensitivity.

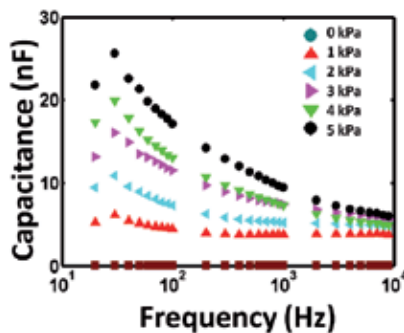


Figure 18. Frequency-dependent double layer capacitance versus frequency for applied pressure in increments of 1 kPa.

Images of the optically transparent, flexible pressure sensor array are shown in Figure 19 with device dimensions of $w = 100 \mu\text{m}$, $g = 20 \mu\text{m}$, $h = 15 \mu\text{m}$, $r = 500 \mu\text{m}$, $H = 150 \mu\text{m}$, $t_{\text{PDMS}} = 500 \mu\text{m}$, and $t_{\text{TCP}} = 1.5 \mu\text{m}$. A meandered fluidic sensing channel geometry with interdigitated sensing electrodes was chosen for a compact device with a larger dynamic range over the straight channel sensing channel topology. Linear capacitive pressure analog response is measured over the dynamic range of approximately 96 kPa. Beyond the dynamic range, the capacitive response saturates. The measured capacitance versus pressure sensitivity is

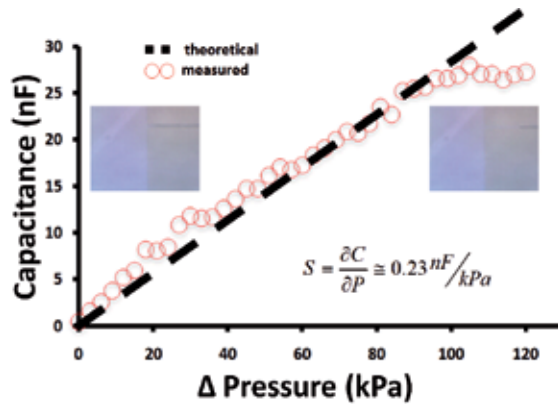


Figure 19. Measured capacitance versus applied pressure at 30 Hz of single pressure sensor within array (insets show images of fluidic displacement as a result of applied pressure with measured corresponding capacitance).

approximately 0.23 nF/kPa. The experimental sensitivity agrees well with the theoretically predicted sensitivity equation through carefully characterization of the interfacial capacitance and effective Young’s modulus of the sensing chamber structure.

To further improve the sensitivity of the device, mechanical amplification is investigated. With the mechanical amplification (A_m), the new sensitivity (S') increases by the following expression:

$$S' = A_m S \tag{27}$$

where A_m is set by D_{out} and D_{in} of the mechanical amplifier as previous described in the electromechanical model. The mechanical concentrator is constructed out of polystyrene, for its combination of mechanical rigidity (~3 GPa), optical transparency, low-cost and micromachinability with a programmable CO₂ laser.

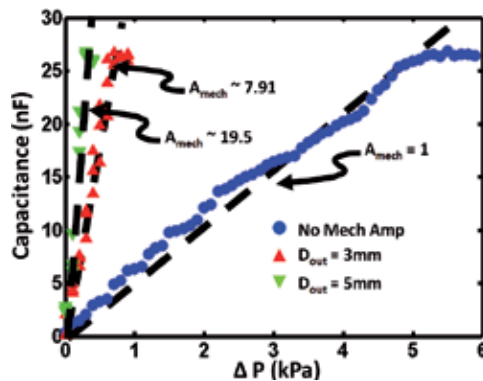


Figure 20. Measured capacitance versus pressure response at 30 Hz underlying the empirical computation model.

The measured capacitance versus pressure response are overlaid with theoretical sensitivity, at a fixed frequency of 30 Hz, is shown in Figure 20. The dynamic range of the device is set by the length of the sensing channel. Beyond the dynamic range, the capacitive response saturates, exhibited thorough measurement results. With the mechanical concentrators, a mechanical gain of approximately 19.5 is measured for $D_{out} = 5$ mm and $D_{in} = 1$ mm. A gain of 7.91 is measured when $D_{out} = 3$ mm. The disparity between the theoretical and measured mechanical concentrator amplification is believed to lie in the inability for the forces to sum across the surface of the applied pressure and focus onto the sensing chamber.

4.4. Time-resolved measurements

To shed light on the relaxation time constant of the pressure sensor, time-resolved measurements are conducted. A schematic of the test setup is shown in Figure 21. A 30 Hz sine wave with $500 \text{ mV}_{\text{pk-pk}}$ is applied from a signal generator applied to one electrode and a ceramic capacitor with a value of $7.4 \text{ } \mu\text{F}$ is connected to ground and parallel with the oscilloscope. The internal envelope detector function in the oscilloscope is used to smooth AC ripples. The data is saved on the oscilloscope and processed in Matlab[®]. The interface circuit does not amplify or compensate for the nonlinear characteristics of the sensor. The measured capacitance value follows the applied input pressure well indicating repeatability and negligible hysteresis.

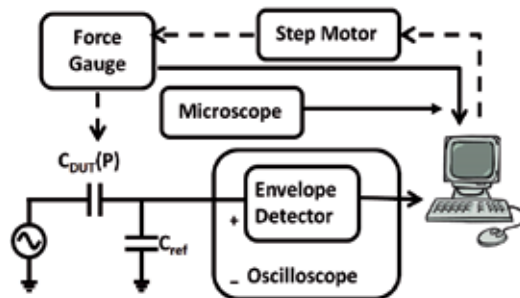


Figure 21. Time-resolved test setup.

A computer-controlled step motor and a force sensor are used to apply an external pressure of 1000 Pa and 500 Pa, respectively, at 1 Hz and 2 Hz, while measuring the electrical response. The fluid is displaced in the middle-length of the sensing channel with an offset pressure of approximately 2 kPa. The measured electrical response of the mechanical input is plotted in Figure 22, indicating repeatability and negligible hysteresis of the sensor. There is an observable phase lag (τ) between the applied input pressure and the measured voltage response. This is believed to be of three components: (1) elastomeric PDMS recovery response (τ_{PDMS}), (2) propagating velocity of the fluid (τ_{fl}), and (3) the steady-state charge buildup of the interfacial capacitance (τ_{RC}):

$$\tau = \tau_{\text{PDMS}} + \tau_{\text{fl}} + \tau_{\text{RC}} \quad (28)$$

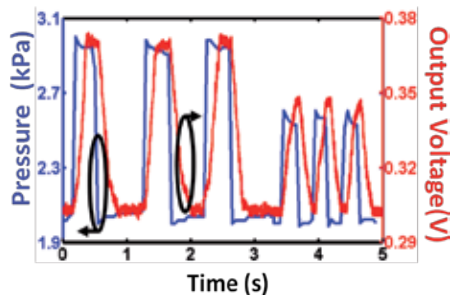


Figure 22. Time-resolved measurement results with applied input pressure on the left y -axis and corresponding output voltage on the right y -axis.

The frequency is not limited by the elastomer response, since PDMS has a frequency response in excess of 200 Hz [31]. The τ_{RC} is set by the electrical properties of the device that is on the order of μs . This also is not the limiting factor where R ranges from 30 to 100 Ω and C ranges from 0 to 27 nF. This arrives to the conclusion that the dominating factor that limits the frequency performance of the pressure sensor is the fluidic response set by the viscosity. To analyze the fluidic response, the flow is assumed to be dominated by a pressure driven flow in the laminar region. Thus, the lubrication theory approximation can be used for the Navier-Stokes equation. The resulting cutoff frequency, f_c is then approximately set by the fluidic resistance and capacitance from the following equation:

$$f_c = \frac{1}{2\pi\tau_{fl}} = \frac{1}{2\pi RC} = \frac{1}{2\pi \left(\frac{12\mu\Delta L}{wh^3} \right) \left(\frac{\pi r^2}{E} \Delta H \right)} = \frac{E^3 w^2 h^4}{24\mu\pi^3 r^4 H^2 \Delta P^2} \quad (29)$$

where E is the effective Young's modulus of the sensing chamber w and h are the width and height of the sensing channel, μ is the viscosity of the fluid (approximately 233 cP at room temperature[32]), r and H are the radius and height of the sensing chamber and ΔP is the pressure change over a period. A response and relaxation time is observed to be dependent on the fluidic RC time constant. This shows that the response time of the sensor can easily be tuned by adjusting the width and height of the sensing channel or the geometries of the sensing chamber. This also shows that the effective Young's modulus of the fluidic encasing will improve the frequency response, which can be tuned by adjusting different ratios of PDMS [33]. Furthermore, the magnitude of the input pressure and velocity of mechanical input also affects frequency response. The overshoot in the measured pressure indicates the viscoelastic nature of the elastomer. The underdamped measured output voltage suggests an RC time constant response corresponding with the large interfacial capacitance.

4.5. Summary of microfluidic sensor for smart skin applications

The development of ultra-high sensitivity, capacitive pressure sensors using ionic liquids is presented. These ultra-high sensitivities are achieved through three levels of amplification: (i)

fluidic displacement amplification through the geometric volume difference between the large sensing chamber and small sensing channel; (ii) ultra-high, capacitance formed at the interface between the electrode-liquid surface; and (iii) mechanical concentration of the pressure onto the sensing chamber through the construction of a rigid construct relatively to the elastomeric housing. The measured results demonstrate a 2000× improvement sensitivity over traditional capacitive pressure sensors. Repeatability and hysteresis are investigated through time-resolved measurements demonstrating excellent performance. In addition to ultra-high sensitivity, the pressure sensor is constructed out of optically transparent material; here it displays a linear response and has a low-cost, simple fabrication process. Without the mechanical amplifier, this sensor can be readily integrated with other lab-on-chip components constructed out of PDMS. With the addition of the mechanical amplifier, such sensors have potential applications in ultra-high sensitivity tactile sensing.

Author details

John Yan*

Address all correspondence to: john.yan@mail.npu.edu

Northwestern Polytechnic University, Fremont, CA, USA

References

- [1] J. Stankovic, "Research Directions for the Internet of Things," *IEEE Internet Things J.*, vol. 1, no. 1, pp. 3–9, March 2014.
- [2] C. Perera, A. Zaslavsky, C. Liu, M. Compton, P. Christen, Georgakopoulos, D., "Sensor search techniques for sensing as a service architecture for the Internet of Things," *IEEE Sensors J.*, vol. 14, no. 2, pp. 406–420, April 2014.
- [3] K. Lyytinen, Y. J. Yoo, "Issues and Challenges in Ubiquitous Computing," *Communications of the ACM*, vol. 45, no. 12, pp. 62–65, 2002.
- [4] G. M. Whitesides, "The Origins and the Future of Microfluidics," *Nature* 442, pp. 368–373, July 2006.
- [5] N. T. Nguyen, S. T. Wereley, *Fundamentals and Applications of Microfluidics*. Norwood, MA: Artech House, 2002.
- [6] T. Thorsen, S. J. Maerkl, S. R. Quake, "Microfluidic Large-scale Integration," *Science*, vol. 298, no. 5593, pp. 580–584, October 2002.
- [7] J. J. Yan, et al., "Vascular Impedance Assessment through Coupled Optomechanical Pressure and Flow Measurements," 11th Annual UC Systemwide Bioengineering Symposium, June 2010, Davis, CA.

- [8] J. J. Yan, "An Unpowered, Wireless Contact Lens Pressure Sensor for Point-Of-Care Glaucoma Diagnosis," Proceedings of 33rd IEEE EMB Conference, pp. 2522–2525, August 30th–September 3rd 2011, Boston, MA.
- [9] J. J. Yan, "Micromachined Optically Transparent, Flexible Pressure Sensor Array Exhibiting Ultra-High Sensitivity," J. Micro/Nanolithography, MEMS MOEMS, vol. 11, no. 1, pp. 013005-1–013005-5, February 2012.
- [10] D. Lloyd-Jones, et al., "Heart disease and stroke statistics – 2010 update: a report from the American Heart Association," Circulation. Vol. 121, pp. e46–e215, 2010.
- [11] F. Mattace-Raso, et. al., "Arterial stiffness and risk of coronary heart disease and stroke: The Rotterdam Study," Circulation vol. 113, pp. 657–663, 2006.
- [12] B. R. Munson, D. F. Young, T. H. Okiishi – 1990 – New York Fundamentals of Fluid Mechanics.
- [13] H. A. Quigley, A. T. Broman, "The Number of People with Glaucoma Worldwide in 2010 and 2020," Br. J. Ophthalmol., vol. 90, pp. 262–267, March 2006.
- [14] J. M. Tielsch, et al., "A Population-Based Evaluation of Glaucoma Screening – The Baltimore Eye Survey," Am. J. Epidemiol., vol. 134, pp. 1102–1110, 15 November 1991.
- [15] D. S. Friedman, et al., "Prevalence of Open-angle Glaucoma Among Adults in the United States," Arch. Ophthalmol., vol. 122, pp. 532–538, April 2004.
- [16] K. C. Katuri, et al., "Intraocular Pressure Monitoring Sensors," IEEE Sensors J., vol. 8, pp. 12–19, January–February 2008.
- [17] R. M. H. a. K. D. Wise, "An Intraocular Pressure Sensor Based On A glass Reflow Process," Workshop on Solid State Sensors and Actuators, Hilton Head, pp. 49–52, 6–10 June 2010.
- [18] M. Leonardi, et al., "First Steps Toward Noninvasive Intraocular Pressure Monitoring with a Sensing Contact Lens," Invest. Ophthalmol. Vis. Sci., vol. 45, pp. 3113–3117, September 2004.
- [19] P. J. Chen, et al., "Unpowered Spiral-tube Parylene Pressure Sensor for Intraocular Pressure Sensing," Sensors Actuators A-Phys., vol. 127, pp. 276–282, 13 March 2006.
- [20] Available: <http://www.nei.nih.gov/health/glaucoma/>.
- [21] J. C. Lotters, et al., "The Mechanical Properties of the Rubber Elastic Polymer Polydimethylsiloxane for Sensor Applications," J. Micromech. Microeng., vol. 7, pp. 145–147, September 1997.
- [22] D. Kim, et al., "A Method for Dynamic System Characterization using Hydraulic Series Resistance," Lab Chip, vol. 6, pp. 639–644, 2006.

- [23] T. Torimoto, et al., "New Frontiers in Materials Science Opened by Ionic Liquids," *Adv. Mater.*, vol. 22, pp. 1196–1221, 19 March 2010.
- [24] A. J. Bard, L. R. Faulkner, *Electrochemical Methods: Fundamentals and Applications*, 2nd ed. New York: Wiley, 2001.
- [25] H. A. Wheeler, "Transmission-Line Properties of Parallel Strips Separated by a Dielectric Sheet," *IEEE Trans. Microwave Theory Tech.*, vol. MTT-13, no. 2, 178–185, 1965.
- [26] Y.-M. L. I-Kuan Lin, Y. Liu, K.-S. Chen, X. Zhang, "Elastic and Viscoelastic Characterization of Polydimethylsiloxane (PDMS) for Cell-Mechanics Applications," *Mater. Res. Soc. Symp. Proc.*, vol. 1052, 2008.
- [27] S. R. Quake, A. Scherer, "From Micro- to Nanofabrication with Soft Materials," *Science*, vol. 290, pp. 1536–1540, 2000.
- [28] J. C. McDonald, D. C. Duffy, J. R. Anderson, D. T. Chiu, H. K. Wu, O. J. A. Schueller, G. M. Whitesides, "Fabrication of Microfluidic Systems in Poly(dimethylsiloxane)," *Electrophoresis*, vol. 21, no. 1, pp. 27–40, 2000.
- [29] A. Bubendorfer, et al., "Microfabrication of PDMS Microchannels using SU-8/PMMA Moldings and Their Sealing to Polystyrene Substrates," *Smart Mater. Struct.*, vol. 16, pp. 367–371, April 2007.
- [30] J. J. Yan, "Optically Transparent, Flexible Pressure Sensor Array Micromachined Utilizing Plasma Assisted Bonding," *Proc. SPIE MOEMS-MEMS*, vol. 8248, pp. 824803-1–824803-8, 21–26 January 2012, San Francisco, CA.
- [31] M. A. Unger, et al., "Monolithic Microfabricated Valves and Pumps by Multilayer Soft Lithography," *Science*, vol. 288, pp. 113–116, 7 April 2000.
- [32] P. G. Heiden, "Ionic Liquids in Chemical Analysis," *Choice: Curr. Rev. Acad. Librar.*, vol. 47, pp. 712–712, 2009.
- [33] K. Khanafer, et al., "Effects of Strain Rate, Mixing Ratio, and Stress-Strain Definition on the Mechanical Behavior of the Polydimethylsiloxane (PDMS) Material as Related to its Biological Applications," *Biomed. Microdevices*, vol. 11, pp. 503–508, April 2009.

Electroosmotic Flow Pump

Meng Gao and Lin Gui

Additional information is available at the end of the chapter

<http://dx.doi.org/10.5772/64601>

Abstract

Electroosmotic flow (EOF) pumping has been widely used to manipulate fluids such as liquid sample reagents in microfluidic systems. In this chapter, we will introduce the research progress on EOF pumps in the fields of microfluidic science and technology and briefly present their microfluidic applications in recent years. The chapter focuses on pump channel materials, electrodes, and their fabrication techniques in microfluidics.

Keywords: Electroosmotic flow pump, Channel material, Pump electrode, Fabrication, Microfluidic applications

1. Introduction

Micropumps are the essential active components of fluid transport systems in microfluidics. They can manipulate small volumetric fluids on spatial scales, from several to a hundred microns [1-3]. Nowadays, they have been widely used in many scientific and technical fields of microfluidics, such as biological/chemical analysis and assays [4-7], liquid drug reagent injection/delivery [8-9], and microelectronic chip cooling [10].

With the rapid development of microfluidic technologies, great attention has been paid recently to miniature micropumps with compact design for microfluidic analysis and assays. Miniature micropumps can be easily integrated into microfluidic systems and enable users to achieve low-cost portable pumping devices such as disposable insulin infusion pumps. Miniaturization of pumping systems can simplify the operation of sample introduction and transport in the microfluidic platform with less manual intervention. Meanwhile, miniaturization can greatly reduce the quantities of sample reagents and achieve microfluidic analysis or assays efficiently.

Recently, electroosmotic flow (EOF) pumps [11-12] have received extensive attention because of their ability to drive a wide range of liquid fluids and generate high pumping pressures or

flow rates with continuous pulse-free flows. Besides, the EOF pumps can exhibit precise control of small volumetric fluids in microfluidic systems under finely controlled electric fields. Compared with mechanical micropumps, EOF pumps do not require moving mechanical parts inside, which can be easily integrated into pumping platforms to achieve the miniaturization of microfluidic systems. Notably, by changing the strength and direction of the electric field through the pump channels, the EOF pumps can conveniently offer bidirectional fluid flows for microfluidic systems.

The pumping flows in EOF pumps are driven by the mechanism of electroosmotic flow phenomenon [13-15]. When in contact with an uncharged liquid fluid (e.g., deionized water, aqueous solution), channel wall surfaces of PDMS, glass, PMMA, or Si can carry electrostatic charges, forming an electrical double layer nearby. The electrical double layer has a compact layer (containing immobile ions) on the channel surface and a diffuse layer (containing mobile ions) in the liquid fluid. Once an electric field is applied through the pump channel, the mobile ions in the diffuse layer move under the electric field force. As a result of the viscous effect, the moving ions will drag their surrounding fluid molecules to the same speed, forming electroosmotic flow in the pump channel. In short, the electroosmotic pumping performance of EOF pumps is fundamentally dependent on the material property of the pump channel wall and electrical field applied to the pump electrodes. The fabrication of pump channels and electrode plays a vital role in cost control of the EOF pumps. The material and fabrication of the pump channel and electrode are also important considerations in the selection of EOF pumps for microfluidic applications.

Recently, the scientific and technical research of EOF pumping in microfluidics has often focused on the pump channel material, pump electrode, and their fabrication techniques. In this chapter, we will mainly present the research progress of EOF pumps in these aspects and briefly introduce new and recent applications of EOF pumps in microfluidics.

2. Channel material and fabrication

Generally, EOF pumps can roughly be divided into direct EOF pumps, porous membrane EOF pumps, and packed porous media EOF pumps, according to the type of EOF-generating pump channels.

2.1. Direct electroosmotic flow (EOF) pump

Direct electroosmotic flow (EOF) pumps utilize open pump channels to drive fluids inside. The pumping pressure or flow rate can be increased via enlarging the number of pump channels. Direct EOF pumps are extremely suitable for the introduction delivery of sample reagents containing cells, biomolecules, and larger particles.

Basically, the common direct EOF pumps are fabricated by capillaries (e.g., PMMA, fused silica capillaries), which are named open-capillary EOF pumps [16-20]. The open-capillary EOF pumps, compared with others, are simple, cheap, and easy to fabricate, because the capillaries

are popular on the market. However, the capillary cannot offer high pumping pressure or flow rate for microfluidic systems. In the open-capillary EOF pump, inert solid-metal-based thin wires are often used to fabricate the pump electrodes. Normally, the outer diameter of thin wires is much larger than the inner diameter of the capillary channel. To generate electric field through the capillary channel, the thin wire electrodes have to be inserted and fastened into two fluid reservoirs connected with both ends of the capillary. The open-capillary EOF pumps are widely used as sample introduction devices to drive liquid reagents into microfluidic chip platforms.

The direct EOF pumps can also be constructed by open channels. These pumps can be described as direct open-channel EOF pumps [20-24], which are usually used to perform on-chip integratable control of sample reagents in microfluidic chip systems. The open channels in these pumps are usually fabricated with photolithographic microfabrication technologies. Figure 1 shows a widely used direct EOF pump using a PDMS microchannel as an open pump channel. Two inert solid-metal wires (platinum or gold) are inserted into both inlet and outlet fluid reservoirs of the PDMS microchannel as the pump electrodes. The PDMS microchannel in this pump can be fabricated with the standard soft lithography technology, which will facilitate the integration of this EOF pump microfluidic systems. To obtain high pumping pressure or flow-rate fluid flows, the direct open-channel EOF pumps can be usually designed and fabricated with a large number of open pump channels in parallel.

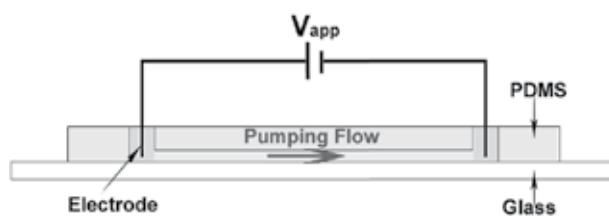


Figure 1. Open-channel EOF pump with metal wire electrodes.

2.2. Porous membrane electroosmotic flow (EOF) pump

Porous membrane EOF pumps [25-28] utilize a piece of porous membrane to construct sub-microscale or nanoscale pump channels within. They are miniaturized and highly integrated microfluidic pumping devices. Compared with the direct EOF pumps, the porous membrane EOF pumps under action of a large number of micro-/nanopump channels can offer high pumping pressure or flow-rate flows. The porous membranes are frequently made of glass, silica, alumina, or organic polymer (PC or PET) using the high-temperature sintering technique or etching technologies like chemical track etching, physical etching, and soft lithography. The drawback of the porous membrane EOF pump is that the sub-micro- or nanoscale pump channels in the pump cannot be used to transport cell, biochemical macromolecules, or large particle in aqueous suspensions.

Figure 2 shows a popular porous membrane EOF pump with mesh microelectrodes. In this EOF pump, the porous membrane is located between the inlet and outlet fluid reservoirs and vertically fastened to the macrofluid channel wall by both supporting frames. Two pieces of mesh microelectrodes are attached onto both sides of the membrane to reduce voltage drop and generate a high electric field through the pump channels. The pump channels embedded in the porous membrane are relatively short (from tens to several hundreds of μm). Hence, an electric field with high strength can be obtained when a low voltage is applied. In order to reduce fluid flow resistance, the micro-/nanopump channels embedded in membrane are often designed and fabricated straight from one side of the porous membrane to the other.

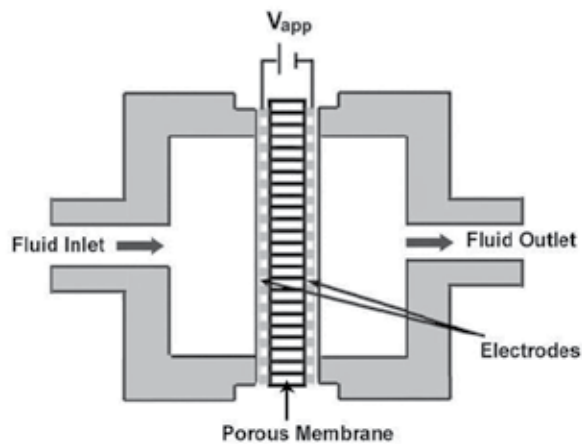


Figure 2. Porous membrane EOF pump with mesh microelectrodes.

2.3. Packed porous media electroosmotic flow (EOF) pump

Packed porous media EOF pumps [29-32], highly miniaturized and integrated microfluidic pumps, can drive high-pressure or flow-rate fluids. Similar to the porous membrane EOF pumps, the packed porous media EOF pumps have a large number of sub-micro- or nanopump channels inside. The sub-micro-/nanopump channels are usually prepared by packing sub-micro-/nanodielectric particles or columns into a mini-/microfluidic channel. These dielectric particles or columns can be made of fused silica, alumina, or organic polymer.

Figure 3 presents a typical example of packed porous media EOF pump with metal wire electrodes. In this EOF pump, a short mini-/microfluidic channel is used to build the pumping region with two pieces of porous membranes on both sides. The packed particles are held in place inside the fluid channel. Two metal wire electrodes are separately inserted into both inlet and outlet fluid reservoirs, paralleling to the fluid channel. Because the particles are randomly distributed inside the fluid channel, the fluid flow resistance in the pump will rise with pumping, thus leading to the reduction of pumping pressure or flow rate. To produce high flow rates or high pumping pressures, the EOF pump can be designed with a large number of

parallel sub-micro-/nanopump channels. Alternatively, sub-micro-/nanodielectric columns can be introduced and packed into this pump (shown in Figure 3) to construct parallel sub-micro-/nanopump channels. For convenient fabrication purpose, the packed columns should be short in length compared with the fluid channel.

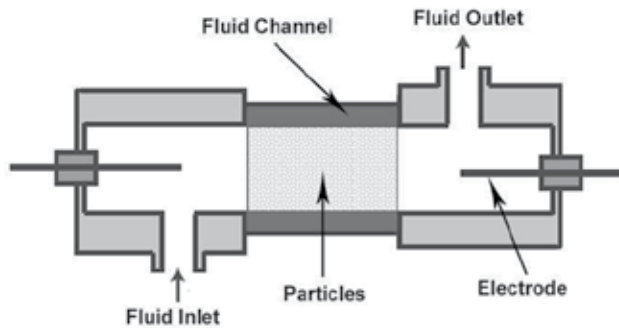


Figure 3. Packed porous media EOF pump with metal wire electrodes.

3. Electrode and fabrication

Electrodes, the key components of EOF pumps, can be used to induce the driving electric field through the pump channels with applied voltage. In EOF pumps, the material and fabrication of the electrodes are vital factors in pump performance and cost control. Basically, there are two electrode types. One is contact electrode exposed to the fluid and the other is noncontact electrode separated from the fluid. This section will show detailed description of them.

3.1. Contact electrode

Contact electrodes mainly made of solid metals are the most widely used electrodes in EOF pumps. The solid-metal-based contact electrodes are often divided into three groups, which are metal wire electrodes, membranous microelectrodes, and mesh microelectrodes.

Metal wire electrodes [33-36] are inserted into the inlet/outlet reservoirs of the pump channels in EOF pumps, as shown in Figure 13. These metal wire electrodes are the simplest type for EOF pumps, which can be bought easily. However, they are not suitable for the integration or miniaturization of the pumping devices in microfluidic systems. Due to the smaller size of metal wires as shown in Figure 3, the metal wire electrodes are not capable of generating a roughly uniform electric field throughout the whole pump channels with applied voltage. Therefore, the pump cannot offer steady flows with a uniform velocity field inside the channel.

Membranous microelectrodes [37-40] are often fabricated under the pump channel using sputtering or deposition techniques, as shown in Figure 4. They can be well miniaturized and

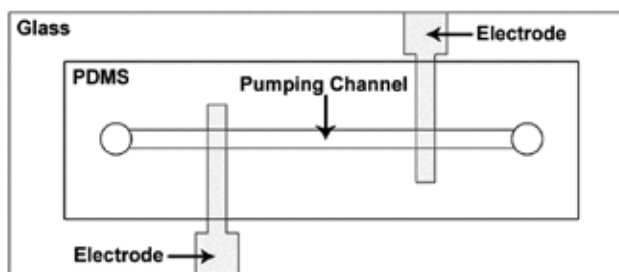


Figure 4. Membranous microelectrode used in open-channel EOF pump.

integrated into the on-chip pumping system. However, it is important to note that the membranous microelectrodes have to be fabricated separately with the pump microchannels, and they should be accurately aligned with the pump microchannels during bonding. The fabrication of these membranous microelectrodes is complex, expensive, and time-consuming.

Figure 5 presents the fabrication of the membranous microelectrodes together with the pump channels for the open-channel EOF pumps. The membranous microelectrodes are fabricated onto a glass substrate through techniques of sputtering and standard soft lithography (Figure 5 (a)), and the PDMS pump microchannel can be prepared by soft lithography technique (Figure 5 (b)). After fabrication, the PDMS pump microchannel is irreversibly bonded with the glass substrate. Since the membranous microelectrodes are located under the pump channel, the EOF pump cannot obtain a parallel electric field through the pump channel or drive uniform pumping flows. To achieve an almost uniformly distributed flow, the pump microchannel needs to be designed with a relatively low high-aspect-ratio section.

Similarly, mesh microelectrodes [41-43] are miniature and integratable ones for EOF pumps, as shown in Figure 2. They are very suitable for the porous media EOF pumps, which will strengthen the miniaturization and integration of the EOF pumps into microfluidic systems. In EOF pumps, the mesh microelectrodes are usually placed and fastened on both ends of the porous pump channels. During assembly, meshes of each electrode have to be aligned with the sub-micro-/nanopump channels. Different with the membranous microelectrodes, the mesh microelectrodes can induce a roughly uniform electric field in the pump channels. They can easily offer high flows at relatively low voltages. However, they do have the same characteristics that are extremely complex and expensive in fabrication.

The contact electrodes exposed to the fluid usually give rise to a serious problem of electrolysis during pumping. Bubbles or other electrolytic products can occur at the electrode surfaces, entering the pump channels and blocking the EOFs. What's more, the joule heat will be generated in the fluid. All bring a sharp decrease in electroosmotic mobility and flow rate. Even worse, the short circuit of high-voltage supply equipment happens sometimes. The use of inert solid-metal platinum (Pt) and gold (Au) electrodes can largely reduce the electrolysis in EOF pumps. The abovementioned problems can be eliminated if the solid-metal electrodes are separated from the aqueous reagents in the pump channels.

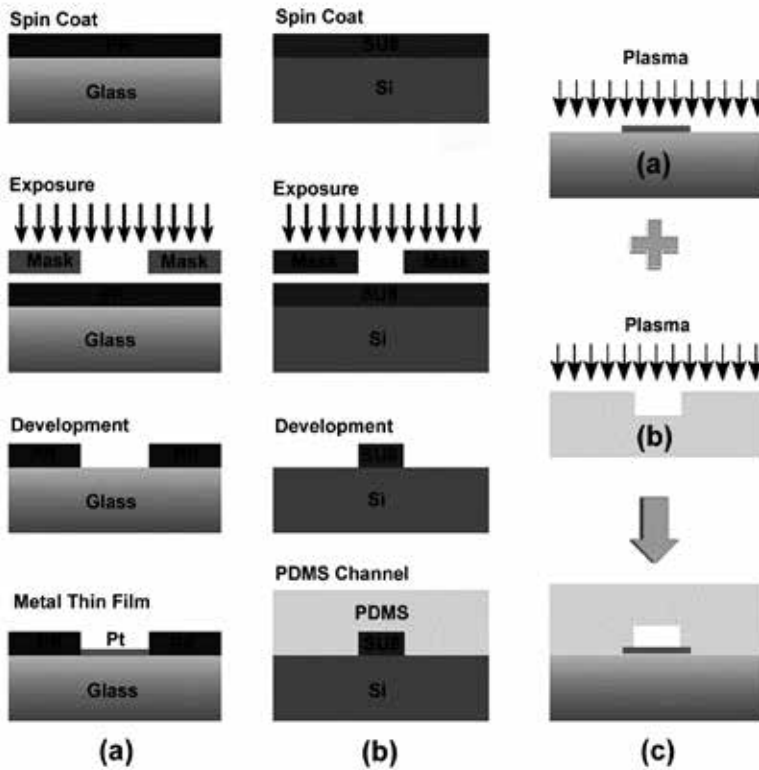


Figure 5. Fabrication of open-channel EOF pump with membranous microelectrodes and PDMS-based pumping microchannel.

3.2. Noncontact electrode

Noncontact electrodes have been developed to prevent the above problems. These noncontact electrodes often utilize nonmetal materials (e.g., polymer gel, silica, polyaniline, PDMS) as membrane layers to separate the solid-metal electrodes from the EOF pumping fluid. The membrane layers are capable of allowing ion charges to pass through but stopping water molecules, and thus bubbles and by-products from electrolysis at the electrode surfaces can be prevented from entering the EOF pump channels in these micropumps.

Gel-type salt-bridge electrode, a widely used noncontact electrode in the field of electrochemistry, has been successfully fabricated for EOF pumps with bubble-free formation [22, 33]. Figure 6 shows a typical bubble-free EOF pump with this gel-type salt-bridge electrode. As shown in Figure 6, this EOF pump employs a thin gel region to protect the solid-metal wire electrode from the fluid. The wire electrode is immersed in the electrode reservoir filled with a conductive aqueous solution. When a high voltage is applied to the pump, the electrolysis can still emerge inside the pump. But, bubbles can only be generated at the wire electrode

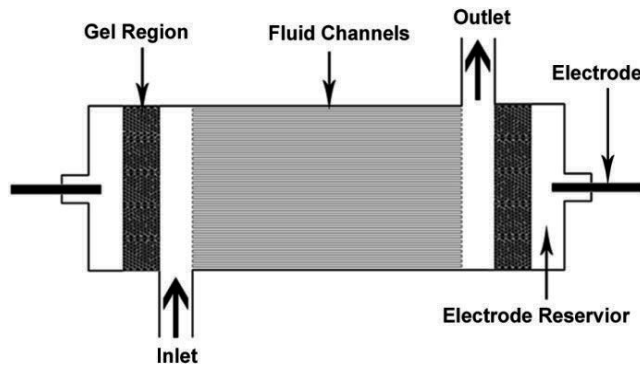


Figure 6. Gel-type salt-bridge microelectrode used in open-channel EOF pump.

surfaces in both electrode reservoirs, having no effect on the fluid flows in the pump channels. In this pump, both of the two gel regions are located in the electrode reservoirs between the metal wire electrodes and the parallel pump channels. The polymer gel, a sensitive polymer material, can be used for the microscale gel regions with the normal photolithography technique. During photolithographic fabrication, the mask for both two gel regions always has to be aligned costly and accurately. As a result, the fabrication of these gel-type salt-bridge electrodes requires a complex process. Another potential problem for this electrode is that the gel region can be easily collapsed due to the poor compatibility of gel material to the electrode reservoir wall. In the worst cases, electrolysis and bubbles will also be generated in the pump channels.

Other noncontact microelectrodes, such as fused silica capillary microelectrodes [31, 44], polyaniline-wrapped aminated graphene microelectrodes [45], and Ag/Ag₂O microelectrodes [46], have been successfully fabricated to work as noncontact electrodes for bubble-free EOF pumps. In fabrication, three noncontact microelectrodes can be made from the chemical synthesis or assembly method in the laboratory. Compared with the gel-type salt-bridge microelectrodes, the three microelectrodes are robust in long-time running. However, the fabrication of this kind of electrodes is also a very complex, time-consuming, and expensive process. Now, the first challenge is to develop a new noncontact electrode with a simpler and cheaper fabrication technique.

Injecting wettable liquid metal into microchannels to make noncontact electrodes should be a simpler and cheaper method for bubble-free EOF pumps. Figure 7 shows a handy liquid-metal (GaInSn)-based EOF pump fabricated in a PDMS microfluidic chip [47]. In this pump, the liquid metal is a kind of metal alloy (GaInSn), which can be easily injected into microchannels by a simple syringe. The melting point of this liquid metal is only 10.6 °C below room temperature. As shown in Figure 7, two pairs of liquid-metal electrodes are fabricated parallel to each other and vertical to the pump channel in the same horizontal plane of the microfluidic chip. These two pairs of electrodes are also designed symmetrically to both sides of the pump channel. To induce high electric field strength in the pump channel when a relatively low

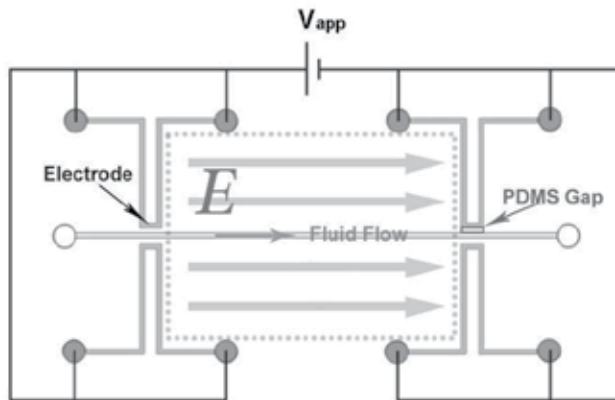


Figure 7. Handy liquid-metal microelectrode used in open-channel EOF pump.

voltage is applied, the electrodes are placed very close to but always not in contact with the pump channel. In this pump, the PDMS gaps are designed to be $\leq 40 \mu\text{m}$ between the liquid-metal electrode channels and the pump channel. For the convenience of liquid-metal injection, the liquid-metal electrode microchannels are all designed in the ohm shape.

Figure 8 depicts the typical fabrication of the liquid-metal noncontact electrodes for the open-channel EOF pump. Compared with membranous or mesh microelectrodes (shown in Figure 5), the liquid-metal electrode channels can be easily made just in one step together with the pump channel using the same fabrication technique. Furthermore, the liquid-metal electrodes can also be easily designed and fabricated in any shape and any location in the EOF pump. Using liquid-metal-filled microchannels as noncontact electrodes can provide an efficient approach to the miniaturization and integration of EOF pumps in microfluidic systems.

4. Applications

EOF pumps can offer a simple and cost-effective way to generate adequate pumping pressures and flow rates for microfluidic systems. They have been widely and successfully used in many areas of microfluidics. In this part, we will briefly introduce applications of EOF pumps in microfluidics. Based on the category of application areas, this section will be divided into 1) microfluidic delivery and actuation and 2) microelectronic thermal management.

4.1. Microfluidic delivery and actuation

Due to the simplicity of pumping components, EOF pumps have been widely used in microfluidic delivery of pure liquids or aqueous solutions. As a micrototal analysis pumping tool, the EOF pump is commonly fabricated to be disposable devices with a compact design. The online reduction of sample reagent quantities should be desirable. For microinjection delivery,

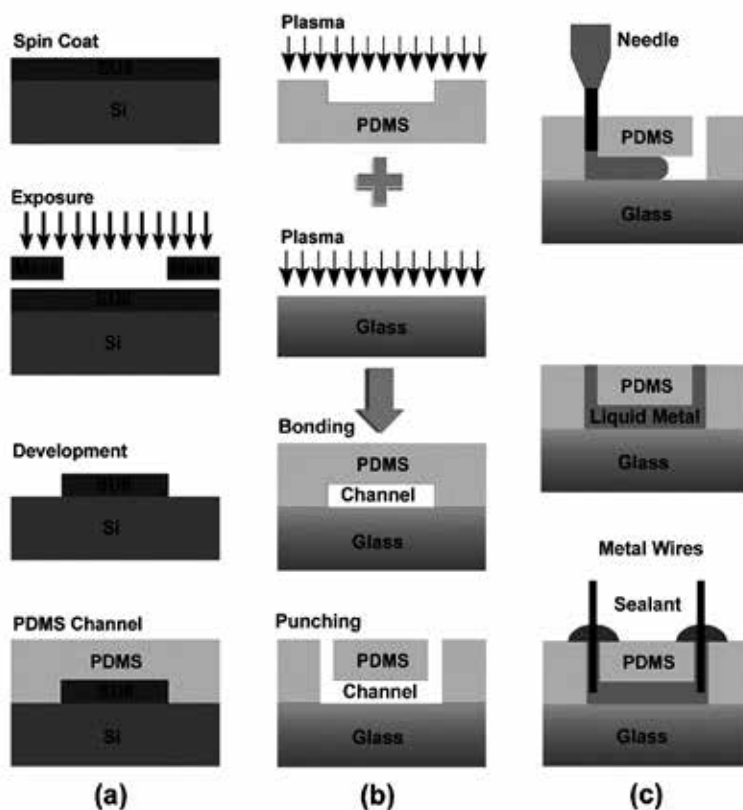


Figure 8. Fabrication of handy liquid-metal microelectrode for open-channel EOF pump.

in particular, the EOF pump is usually required to offer high flows. Preferentially, open-capillary EOF pumps [16-20] are used to perform the introduction of sample reagents into a microfluidic analysis or assay system. The open capillary has the ability to deliver a wide range of sample reagents such as pure liquid drug reagents and aqueous solutions containing cells, particles, or biochemical macromolecules. The porous media EOF pumps [25-32] can also be used to drive pure liquid sample reagents for the injection purpose. For on-chip microfluidic delivery, open-channel EOF pumps [20-24] are the most popular pumping devices. The reason is that the open pump channels and the pump electrodes can be easily and conveniently integrated into the microfluidic chip together with other functional components.

In most microfluidic systems, efficient mixing of sample reagents is extremely essential for improving the throughput of microfluidic assays and analysis. Many active mixing methods [48] using external actuation forces to perturb the sample reagents to enhance their diffusion have been recently developed to achieve a high mixing performance. Most of the external actuation forces are generated by mechanical moving, stirring, or vibrating. Owing to the fast electrical operation, the EOF pump has also been widely used to perform highly efficient active

mixing in microfluidics. The EOF-actuated mixing utilizes electroosmotic driving forces to induce oscillatory, turbulent, or chaotic flows in the sample reagents, while a periodic electric field is applied simultaneously [49]. Several typical open-channel configurations, such as T-shaped, Y-shaped, and multi-shaped configurations, have been developed for the EOF-actuated mixing [50-56]. The use of EOF pump does not require mechanical moving components and hence brings cheaper and more reliable microfluidic mixers. Besides, the EOF pump can also be used as a microactuator for focusing and separation of droplets, particles, or cells in microfluidic systems [57-58].

4.2. Microelectronic thermal management

With the rapid development of MEMS technologies, the design of a miniature electronic chip with more and more functional components has become an essential demand in recent years. Consequently, power consumption is increased to maintain operation which generates great heat flux. Air-forced cooling cannot remove such high heat flux from the hot chip. Micro-pumping that drives liquid fluids through microchannels is an efficient approach to perform heat dissipation of electronic components [10-12].

EOF pumps have been considered in microchannel-based liquid cooling for electronic chips owing to their low power consumption and high pumping pressure. EOF pumps can work without any noise during liquid coolant pumping. Recently, a porous media-based EOF pump [59] has been successfully utilized for liquid cooling of microelectronic chips. In this micro-channel liquid cooling system, the pump works as an external device to drive water coolant to force thermal dissipation of the hot region in the microelectronic chip. To reduce the thermal resistance, the microchannels filled with liquid coolant are tightly attached to the hot surface of electronic chip. Since the microchannels have high surface-volume ratio available for thermal dissipation, the EOF pump is capable of removing the heat generation efficiently.

5. Future and prospect

This chapter has briefly reported recent research progress of EOF pumps with emphasis on channel materials, electrodes, and their fabrication and summarized pump applications in microfluidics.

EOF pumping is commonly used in many microfluidic devices. Nowadays, it has become an increasingly popular tool to manipulate such liquid sample reagents with electric fields. The number of microfluidic applications is growing fast, and certain EOF pumping devices, like porous membrane EOF pumps (Osmotex), have been already commercially available. However, the popular use of EOF pumps in microfluidics may be limited due to the lack of high-performance pumps with cost-effective characteristics.

The EOF pump continues to be improved, which shows stable performance, rapid operation, and compact design. EOF pumps with noncontact electrodes have generated robust pumping flows without bubble formation, but there is still a lot of work to be done for improving these

pumps. Further research is required to understand the basic driving mechanism of gel, silica, or PDMS-based noncontact electrodes. Research on new material design and fabrication is also an urgent need for noncontact electrodes with low-cost and simple process. Another option of liquid metal, instead of solid metal and conductive aqueous solution in electrode reservoirs of noncontact electrodes, should be an alternative solution for the water electrolysis at the solid-metal electrode surfaces.

EOF pumps do not require mechanical moving components, and they can offer excellent miniaturization potential in integrated microfluidic applications. With applied electric fields, EOF pumps are capable of performing fine control of fluids fast. In the near future, the EOF pump should be an important element in promising implantable medical devices such as drug transport or infusion pumps.

Acknowledgements

This work is financially supported by the National Natural Science Foundation of China (Grant No. 51276189).

Author details

Meng Gao^{1,2*} and Lin Gui^{1,2}

*Address all correspondence to: mgao@mail.ipc.ac.cn

1 Key Laboratory of Cryogenics, Technical Institute of Physics and Chemistry, Beijing, China

2 Chinese Academy of Sciences, Haidian District, Beijing, China

References

- [1] D. J. Laser and J. G. Santiago. A review of micropumps. *Journal of Micromechanics and Microengineering*. 2004;14(6):R35–R64. DOI: 10.1088/0960-1317/14/6/R01
- [2] Peter Woias. Micropumps—past, progress and future prospects. *Sensors and Actuators B: Chemical*. 2005;105(1):28–38. DOI: 10.1016/j.snb.2004.02.033
- [3] Brian D. Iverson and Suresh V. Garimella. Recent advances in microscale pumping technologies: a review and evaluation. *Microfluidics and Nanofluidics*. 2008;5(2): 145-174. DOI: 10.1007/s10404-008-0266-8

- [4] Brian T. Good, Christopher N. Bowman and Robert H. Davis. An effervescent reaction micropump for portable microfluidic systems. *Lab on a Chip*. 2006;6(5):659-666. DOI: 10.1039/B601542E
- [5] Chang Kyu Byun, Kameel Abi-Samra, Yoon-Kyoung Cho and Shuichi Takayama. Pumps for microfluidic cell culture. *Electrophoresis*. 2013;35(2-3):245-257. DOI: 10.1002/elps.201300205
- [6] Chunsun Zhang, Da Xing and Yuyuan Li. Micropumps, microvalves, and micromixers within PCR microfluidic chips: Advances and trends. *Biotechnology Advances*. 2007;25(5):483-514. DOI: 10.1016/j.biotechadv.2007.05.003
- [7] Farid Amirouche, Yu Zhou and Tom Johnson. Current micropump technologies and their biomedical applications. *Microsystem Technologies*. 2009;15(5):647-666. DOI: 10.1007/s00542-009-0804-7
- [8] A. Nisar, Nitin Afzulpurkar, Banchong Mahaisavariya and Adisorn Tuantranont. MEMS-based micropumps in drug delivery and biomedical applications. *Sensors and Actuators B: Chemical*. 2008;130(2):917-942. DOI: 10.1016/j.snb.2007.10.064
- [9] Nan-Chyuan Tsai and Chung-Yang Sue. Review of MEMS-based drug delivery and dosing systems. *Sensors and Actuators A: Physical*. 2007;134(2):555-564. DOI: 10.1016/j.sna.2006.06.014
- [10] Vishal Singhal, Suresh V Garimella and Arvind Raman. Microscale pumping technologies for microchannel cooling systems. *Applied Mechanics Reviews*. 2004;57(3):191-221. DOI: 10.1115/1.1695401
- [11] Xiayan Wang, Chang Cheng, Shili Wang and Shaorong Liu. Electroosmotic pumps and their applications in microfluidic systems. *Microfluidics and Nanofluidics*. 2009;6(2):145-162. DOI: 1007/s10404-008-0399-9
- [12] Xiayan Wang, Shili Wang, Brina Gendhar, Chang Cheng, Chang Kyu Byun, Guanbin Li, Meiping Zhao and Shaorong Liu. Electroosmotic pumps for microflow analysis. *TrAC Trends in Analytical Chemistry*. 2009;28(1):64-74. DOI: 10.1016/j.trac.2008.09.014
- [13] Brian J. Kirby and Ernest F. Hasselbrink Jr.. Zeta potential of microfluidic substrates. *Electrophoresis*. 2004;25(00):187-202. DOI: 10.1002/elps.200305754
- [14] Vishal Tandon, Sharath K. Bhagavatula, Wyatt C. Nelson and Brian J. Kirby Dr.. Zeta potential and electroosmotic mobility in microfluidic devices fabricated from hydrophobic polymers. *Electrophoresis*. 2008;29(5):1092-1101. DOI: 10.1002/elps.200700734
- [15] Dongqing Li. *Electrokinetics in Microfluidics*. First ed. London, UK: Elsevier Academic Press; 2004. 652 p.
- [16] Shaorong Liu and Purnendu K. Dasgupta. Flow-injection analysis in the capillary format using electroosmotic pumping. *Analytica Chimica Acta*. 1992;268(1):1-6. DOI: 10.1016/0003-2670(92)85243-Y

- [17] Shaorong Liu and Purnendu K. Dasgupta. A simple means to increase absorbance detection sensitivity in capillary zone electrophoresis. *Analytica Chimica Acta*. 1993;283(2):747-753. DOI: 10.1016/0003-2670(93)85289-V
- [18] Shaorong Liu and Purnendu K. Dasgupta. Sequential injection analysis in capillary format with an electroosmotic pump. *Talanta*. 1994;41(11):1903-1910. DOI: 10.1016/0039-9140(94)00145-6
- [19] Shaorong Liu and Purnendu K. Dasgupta. Electroosmotically pumped capillary format sequential injection analysis with a membrane sampling interface for gaseous analytes. *Analytica Chimica Acta*. 1995;308(1-3):281-285. DOI: 10.1016/0003-2670(94)00478-5
- [20] Shaorong Liu, Qiaosheng Pu and Joann J. Lu. Electric field-decoupled electroosmotic pump for microfluidic devices. *Journal of Chromatography A*. 2003;1013(1-2):57-64. DOI: 10.1016/S0021-9673(03)00941-5
- [21] Amir Jahanshahi, Fabrice Axisa and Jan Vanfleteren. Fabrication of a biocompatible flexible electroosmosis micropump. *Microfluidics and Nanofluidics*. 2012;12(5):771-777. DOI: 10.1007/s10404-011-0905-3
- [22] Tomasz Glowdel and Carolyn L. Ren. Electro-osmotic flow control for living cell analysis in microfluidic PDMS chips. *Mechanics Research Communications*. 2009;36(1):75-81. DOI: 10.1016/j.mechrescom.2008.06.015
- [23] Iulia M. Lazar and Barry L. Karger. Multiple open-channel electroosmotic pumping system for microfluidic sample handling. *Analytical Chemistry*. 2002;74(24):6259-6268. DOI: 10.1021/ac0203950
- [24] John M. Edwards IV, Mark N. Hamblin, Hernan V. Fuentes, Bridget A. Peeni, Milton L. Lee, Adam T. Woolley and Aaron R. Hawkins. Thin film electro-osmotic pumps for biomicrofluidic applications. *Biomicrofluidics*. 2007;1(1):014101. DOI: 10.1063/1.2372215
- [25] Ceming Wang, Lin Wang, Xiaorui Zhu, Yugang Wang and Jianming Xue. Low-voltage electroosmotic pumps fabricated from track-etched polymer membranes. *Lab on a Chip*. 2012;12(9):1710-1716. DOI: 10.1039/C2LC40059F
- [26] Anders Brask, Jörg P. Kutter and Henrik Bruus. Long-term stable electroosmotic pump with ion exchange membranes. *Lab on a Chip*. 2005;5(7):730-738. DOI: 10.1039/B503626G
- [27] Yu-Feng Chen, Ming-Chia Li, Yi-Hsin Hu, Wen-Jeng Chang and Chi-Chuan Wang. Low-voltage electroosmotic pumping using porous anodic alumina membranes. *Microfluidics and Nanofluidics*. 2008;5(2):235-244. DOI: 10.1007/s10404-007-0242-8
- [28] Anders Brask, Detlef Snakenborg, Jörg P. Kutter and Henrik Bruus. AC electroosmotic pump with bubble-free palladium electrodes and rectifying polymer membrane valves. *Lab on a Chip*. 2006;6(2):280-288. DOI: 10.1039/B509997H

- [29] Ye Ai, Sinan E. Yalcin, Diefeng Gu, Oktay Baysal, Helmut Baumgart, Shizhi Qian and Ali Beskok. A low-voltage nano-porous electroosmotic pump. *Journal of Colloid and Interface Science*. 2010;350(2):465-470. DOI: 10.1016/j.jcis.2010.07.024
- [30] Zilin Chen, Ping Wang and Hsueh-Chia Chang. An electro-osmotic micro-pump based on monolithic silica for micro-flow analyses and electro-sprays. *Analytical and Bioanalytical Chemistry*. 2005;382(3):817-824. DOI: 10.1007/s00216-005-3130-7
- [31] Congying Gu, Zhijian Jia, Zaifang Zhu, Chiyang He, Wei Wang, Aaron Morgan, Joann J. Lu and Shaorong Liu. Miniaturized electroosmotic pump capable of generating pressures of more than 1200 bar. *Analytical Chemistry*. 2012;84(21):9609-9614. DOI: 10.1021/ac3025703
- [32] Shuhuai Yao, David E. Hertzog, Shulin Zeng, James C. Mikkelsen Jr. and Juan G. Santiago. Porous glass electroosmotic pumps: design and experiments. *Journal of Colloid and Interface Science*. 2003;268(1):143-153. DOI: 10.1016/S0021-9797(03)00730-6
- [33] Tomasz Glowdel, Caglar Elbuen, Lucy E. J. Lee and Carolyn L. Ren. Microfluidic system with integrated electroosmotic pumps, concentration gradient generator and fish cell line (RTgill-W1)—towards water toxicity testing. *Lab on a Chip*. 2009;9(22):3243-3250. DOI: 10.1039/B911412M
- [34] Fu-Qiang Nie, Mirek Macka and Brett Paull. Micro-flow injection analysis system: on-chip sample preconcentration, injection and delivery using coupled monolithic electroosmotic pumps. *Lab on a Chip*. 2007;7(11):1597-1599. DOI: 10.1039/B707773B
- [35] Shau-Chun Wang, Hsiao-Ping Chen and Hsueh-Chia Chang. Ac electroosmotic pumping induced by noncontact external electrodes. *Biomicrofluidics*. 2007;1(3):034106. DOI: 10.1063/1.2784137
- [36] Jessica L. Snyder, Jirachai Getpreecharsawas, David Z. Fang, Thomas R. Gaborskid, Christopher C. Striemer, Philippe M. Fauchet, David A. Borkholder, and James L. McGrathf. High-performance, low-voltage electroosmotic pumps with molecularly thin silicon nanomembranes. *PNAS*. 2013;110(46):18425–18430. DOI: 10.1073/pnas.1308109110
- [37] Timothy E. McKnight, Christopher T. Culbertson, Stephen C. Jacobson and J. Michael Ramsey. Electroosmotically induced hydraulic pumping with integrated electrodes on microfluidic devices. *Analytical Chemistry*. 2001;73(16):4045-4049. DOI: 10.1021/ac010048a
- [38] John Paul Urbanski, Todd Thorsen, Jeremy A. Levitan and Martin Z. Bazant. Fast ac electro-osmotic micropumps with nonplanar electrodes. *Applied Physics Letters*. 2006;89(14):143508. DOI: 10.1063/1.2358823
- [39] Chien-Chih Huang, Martin Z. Bazant and Todd Thorsen. Ultrafast high-pressure AC electro-osmotic pumps for portable biomedical microfluidics. *Lab on a Chip*. 2010;10(1):80-85. DOI: 10.1039/B915979G

- [40] Nazmul Islam and Davood Askari. Performance improvement of an AC electroosmotic micropump by hydrophobic surface modification. *Microfluidics and Nanofluidics*. 2013;14(3):627-635. DOI: 10.1007/s10404-012-1081-9
- [41] J.-Y. Miao, Z.-L. Xu, X.-Y. Zhang, N. Wang, Z.-Y. Yang and P. Sheng. Micropumps based on the enhanced electroosmotic effect of aluminum oxide membranes. *Advanced Materials*. 2007;19(23):4234-4237. DOI: 10.1002/adma.200700767
- [42] Z. Cao, L. Yuan, Y. F. Liu, S. Yao and L. Yobas. Microchannel plate electro-osmotic pump. *Microfluidics and Nanofluidics*. 2012;13(2):279-288. DOI: 10.1007/s10404-012-0959-x
- [43] Shawn Litster, Matthew E. Suss and Juan G. Santiago. A two-liquid electroosmotic pump using low applied voltage and power. *Sensors and Actuators A: Physical*. 2010;163(1):311-314. DOI: 10.1016/j.sna.2010.07.008
- [44] Wei Wang, Congying Gu, Kyle B. Lynch, Joann J. Lu, Zhengyu Zhang and Qiaosheng Pu. High-pressure open-channel on-chip electroosmotic pump for nanoflow high performance liquid chromatography. *Analytical Chemistry*. 2014;86(4):1958-1964. DOI: 10.1021/ac4040345
- [45] Rudra Kumar, Kousar Jahan, Rajaram K. Nagarale and Ashutosh Sharma. Nongassing long-lasting electro-osmotic pump with polyaniline wrapped aminated graphene electrodes. *ACS Applied Materials & Interfaces*. 2015;7(1):593-601. DOI: 10.1021/am506766e
- [46] Woonsup Shin, Jong Myung Lee, Rajaram Krishna Nagarale, Samuel Jaeho Shin and Adam Heller. A Miniature, nongassing electroosmotic pump operating at 0.5 V. *The Journal of the American Chemical Society*. 2011;133(8):2374-2377. DOI: 10.1021/ja110214f
- [47] Meng Gao and Lin Gui. A handy liquid metal based electroosmotic flow pump. *Lab on a Chip*. 2014;14(11):1866-1875. DOI: 10.1039/C4LC00111G
- [48] Chia-Yen Lee, Chin-Lung Chang, Yao-Nan Wang and Lung-Ming Fu. Microfluidic mixing: A review. *International Journal of Molecular Sciences*. 2011;12(5):3263-3287. DOI: 10.3390/ijms12053263
- [49] Chih-Chang Chang and Ruey-Jen Yang. Electrokinetic mixing in microfluidic systems. *Microfluidics and Nanofluidics*. 2007;3(5):501-525. DOI: 10.1007/s10404-007-0178-z
- [50] Chen-li Sun and Shin-Shian Shie. Optimization of a diverging micromixer driven by periodic electroosmotics. *Microsystem Technologies*. 2012;18(9):1237-1245. DOI: 10.1007/s00542-012-1475-3
- [51] Pin-Hsien Chiu, Chih-Chang Chang and Ruey-Jen Yang. Electrokinetic micromixing of charged and non-charged samples near nano-microchannel junction. *Microfluidics and Nanofluidics*. 2013;14(5):839-844. DOI: 10.1007/s10404-012-1116-2

- [52] Wee Yang Ng, Shireen Goh, Yee Cheong Lam, Chun Yang and Isabel Rodríguez. DC-biased AC-electroosmotic and AC-electrothermal flow mixing in microchannels. *Lab on a Chip*. 2009;9(6):802-809. DOI: 10.1039/B813639D
- [53] Naoki Sasaki, Takehiko Kitamori and Haeng-Boo Kim. AC electroosmotic micromixer for chemical processing in a microchannel. *lab on a Chip*. 2006;6(4):550-554. DOI: 10.1039/B515852D
- [54] Che-Hsin Lin, Lung-Ming Fu and Yu-Sheng Chien. Microfluidic T-form mixer utilizing switching electroosmotic flow. *Analytical Chemistry*. 2004;76(18):5265-5272. DOI: 10.1021/ac0494782
- [55] Ian Glasgow, John Batton and Nadine Aubry. Electroosmotic mixing in microchannels. *Lab on a Chip*. 2004;4(6):558-562. DOI: 10.1039/B408875A
- [56] Timothy J. Johnson, David Ross and Laurie E. Locascio. Rapid microfluidic mixing. *Analytical Chemistry*. 2002;74(1):45-51. DOI: 10.1021/ac010895d
- [57] Wei-Lun Hsu, Dalton J. E. Harvie, Malcolm R. Davidson, Helen Jeong, Ewa M. Goldys and David W. Inglis. Concentration gradient focusing and separation in a silica nanofluidic channel with a non-uniform electroosmotic flow. *Lab on a Chip*. 2014;14(18):3539-3549. DOI: 10.1039/C4LC00504J
- [58] Hai Jiang, Xuan Weng and Dongqing Li. A novel microfluidic flow focusing method. *Biomicrofluidics*. 2014;8(5):054120. DOI: 10.1063/1.4899807
- [59] Y. Berrouche, Y. Avenas, C. Schaeffer, Hsueh-Chia Chang and Wang Ping. Design of a porous electroosmotic pump used in power electronic cooling. *IEEE Transactions on Industry Applications*. 2009;45(6):2073-2079. DOI: 10.1109/TIA.2009.2031934

Fabrications and Applications in Energy Research

Laser-Based Fabrication for Microfluidics Devices on Glass for Medical Applications

Daniel Nieto García and Gerard O'Connor

Additional information is available at the end of the chapter

<http://dx.doi.org/10.5772/64324>

Abstract

We report a laser-based process for microstructuring glass materials for microfluidics applications. The hybrid technique is composed of a nanosecond Q-Switch Nd:YVO₄ laser for fabricating the initial microfluidic microstructures on soda-lime glass substrates and a thermal treatment for reshaping and improving its morphological and optical qualities. The proposed technique preserves the advantages of the laser direct-write technique in terms of design flexibility, simplicity, fast prototyping, low cost, and so on. The beam spot size, pulse overlapping, ablation threshold, debris deposition, heating temperature, and time are investigated and optimized for fabricating optimal microfluidics structures on glass. The manufactured chips for circulating tumor cells (CTCs) capture were tested with tumor cells (Hec 1A) after being functionalized with an EpCAM antibody coating. Cells were successfully arrested on the pillars after being flown through the device giving our technology a translational application in the field of cancer research.

Keywords: Laser microstructuring, microchannels, glass, microfluidics devices

1. Introduction

Microfluidics is a fast developing engineering science that controls the flow of minute amounts of liquids or gases in a miniaturized system in an increasing number of applications such as biomedical diagnostic, microfuel cells, and cooling in microelectronics [1–4]. The microfluidic devices are used in making rapid inroads in the modern analytical laboratory primarily because of their small physical footprint, speed and efficiency of chemical separations, and reduced reagent consumption. These applications demand transparent materials that permit high-resolution imaging, fluorescence microscopy, and also to analyze parameters such as laminar flow, mass transport driven by diffusion rather than turbulence, and constant removal of waste products [5–7].

Traditionally, lab-on-a-chip devices have been manufactured by silica due to its well-understood surface chemistry and favorable micromachining techniques that are ubiquitous in the microelectronics industry. Recently, researchers have begun to utilize devices fabricated from polymer substrates as an alternative to glass, although glass may still be the preferred materials in clinical medicine, biology, and chemistry. Microchannels fabricated on glass have a growing importance in the miniaturization of microfluidic devices for chemical and biological micro-total analysis system.

Glass materials are commonly used due to the beneficial optical properties, surface stability, and solvent compatibility, as well as due to the straightforward and well-understood fabrication techniques [8–10]. The mechanical rigidity, chemical resistance, and low-permeability properties of glass, combined with their optical transparency, make it a good choice for many demanding lab-on-a-chip applications. Glass materials overcome some limitations of polymers, they are reusable and have low autofluorescence and smooth surfaces. Nevertheless, the high cost of processing glass and of the material itself limit the use of glass as disposable devices. Two different approaches challenging demands to be solved on microfluidics, high-quality devices made of glass and disposable low-cost devices made of plastic.

There are large and well-developed micromachining methods for fabricating microfluidic devices on glass, the choice among them depends on the materials to be treated, and the size and shape of the required features. Embossing, injection molding, and other thermoforming techniques provide high throughput and cost, but are ineffective for glass [11]. Because lithography techniques require advanced facilities and numerous process steps, numerous researchers have explored the fabrication of channels in glass using other technologies, such as electron beam lithography, photolithography, and dry and wet etching [12–15].

Some of these techniques provide high-quality microfluidic systems, but require sophisticated equipment located in clean rooms and with the inconvenient of production toxic waste, which in terms of microfabrication means that there are significant challenges in fabricating low-cost and reliable microchannels in glass. For example, the surface roughness in a microchannel can be caused by an inaccurate and imprecise alignment of the mask used in the fabrication process.

Laser has become increasingly important in recent years for many fields, including microoptics, microelectronics, microbiology, and microchemistry. High micromachining quality with ns-pulse and fs-pulse lasers was demonstrated for direct ablation of dielectrics. Laser micromachining offers a single-step method for direct writing of microchannels in glass. Using this laser ablation technique, it is possible to fabricate geometries with variable depth and high aspect ratio that cannot be achieved through traditional microlithographic techniques. Laser ablation, because of its noncontact nature, allows the micromachining and surface patterning of glass materials with minimal mechanical and thermal deformation. Due to the low cost, the ease of implementation in industry, and the wide quantity of lasers available, this technique is extremely important for machining glass.

Fabrication of microchannels on glass by laser ablation techniques has been investigated and reported using CO₂, UV, and ultrashort pulse lasers [16–19]. For transparent materials, in the visible spectral range, laser ablation should ideally be performed with ultraviolet radiation because of the linear optical absorption in this wavelength range. Alternatively, nonlinear coupling of ultrahigh-intensity laser pulses in the near-infrared (IR) range with subpicosecond

duration may show advantages. The interaction between a laser beam and a material is determined by (1) laser characteristics (the wavelength, fluence or energy density, the pulse duration, repetition rate, and pulse energy); (2) the properties of the material (absorption characteristics and thermal relaxation) which is governed by the composition and structure of the material.

In this context, laser micromachining, because of its noncontact nature, offers several advantages for fabricating microchannels, including the capability to form complex shapes with minimal mechanical and thermal deformation. There are still significant challenges in fabricating low-cost and reliable microfluidic modules in transparent media. In particular, microfluidic devices for detection of circulating tumor cells have emerged as a promising minimally invasive diagnostic tool. Isolation of circulating tumor cells (CTCs) has become a central topic in cancer research where engineering and medical science converge with the common goal of capturing rare cell types in liquid biopsies as a starting point for early diagnosis and the development of point of care and single-cell analysis systems [20]. Several designs have explored in Polydimethylsiloxane (PDMS) and glass substrates leading to panoply of features and arrangements able to trap cells flowing through the device. In order to enhance the specificity and sensibility of such systems, a surface functionalization with EpCAM antibodies seemed to be the first choice for developing a micropillar coating, such antibodies are commonly employed for CTC isolation.

Micropillars were some of the first features developed for studying cell behavior such as cell spreading, motility, and mechanobiology, but they present an interesting feature to be developed as a potential substrate prone to coating and exhibiting exceptional optical conditions for microscopy applications [21]. Therefore, functionalizing micropillars with a steady topographical control will be an optimal platform for a point-of-care device or lab-on-a-chip technology [22].

In this chapter, we present a laser-based technology for fabricating microfluidic microchannels and chips for circulating tumor cells capture. In particular, we report a fast and simple method for the fabrication of the microchannels on glass using an Nd:YVO₄ nanosecond IR laser. The fabrication method combines two different laser routes: (1) a laser direct-write technique for fabricating the microchannels on glass and (2) a thermal treatment for reducing the damage created on the glass during the laser direct-write process. By combining these two laser process, it is possible to obtain high-quality microchannels with comparable characteristics as those obtained by other methods [23], preserving the advantages of the laser direct-write technique (flexibility in terms of design, fast prototyping, low-cost, noncontaminant, etc). In Section 2, the experimental procedure for fabricating the microchannels is presented. Section 3 analyzes the thermal treatment and morphological characterization of microchannels as a function of temperature. Section 4 presents some conclusions and remarks.

2. Materials and methods

In order to perform the microstructuring of the glass a Rofin model Nd:YVO₄ laser was used. This is a solid-state laser, operating at 1064 nm wavelength and using a Q-Switch regime, with

pulses of 20 ns and tunable repetition rate from single-shot to 200 kHz. For the thermal treatment, we used a Heraeus mufla furnace, equipped with a thermal ramp that allows us to control the heating speed of the glass.

For characterizing the microstructures and samples, we have used a PerkinElmer Lamb25 spectrometer (for measuring the transmission spectrum); a scanning electron microscope (SEM, Zeiss FESEM-ULTRA Plus) for determination of the chemical composition, a microscope Nikon MM-400 (visual inspection of the samples), and a confocal microscope SENSOFAR 2300 Plμ (topographic and surface roughness measurement). Cell culture and trapping were assessed by means of a Zeiss Microscope and Zen software.

The glass used as a substrate for fabricating the microchannels and microstructures was a commercial soda-lime glass, provided by a local supplier. The composition of this glass (O 50.25%, Na 9.08%, Mg 2.19%, Al 0.54%, Si 33.08%, Ca 4.87%) was determined by using a SEM EDX (Zeiss FESEM-ULTRA Plus).

3. Results

3.1. Laser microstructuring

The laser direct-write technique for fabricating microfluidics devices and microchannels is based on the ablation of a soda-lime glass substrate with a beam laser of circular Gaussian profile, followed of a thermal treatment in a Heraeus mufla furnace. The laser setup for fabricating the micropost system consists of a Q-Switch Nd:YVO₄ laser operating at 1064 nm combined with a galvanometer system for addressing the output laser beam. The beam is focused by a flat-field lens of effective focal length 100 mm that provides a uniform irradiance distribution over a working area of 80 × 80 mm² (Figure 1). In order to perform the thermal treatment that allows us to improve the quality of the originally generated microchannels, a furnace Heraeus mufla was employed.

For optimizing the fabrication process, we have done a previous study of the mark obtained by focusing one laser shot on the glass substrate [24]. This mark was then analyzed with a confocal microscope. This initial characterization step let us to determine the optimal laser parameters used in the laser direct-write process. The microchannels morphology was analyzed in terms of shape and roughness using a confocal microscope SENSOFAR 2300 Plμ.

For determining the size of the mark made by the laser beam in the glass substrate, a crater was made in the glass after firing one shot at a fluence of 112 J/cm². The applied fluence was calculated by using the expression $F_{th} = (2E_{th})/(\pi\omega_0^2)$, where E_{th} is the energy per pulse at the onset of ablation, ω_0 was determined by analyzing the mark obtained by the laser over the material.

Because the measured Gaussian spot size on the surface is not necessarily equal to the calculated spot size at the focal point of the lens, the ablation threshold was computed using the following equation $\phi_{th} = (2E_{th})/(\pi\omega_0)$, where E_{th} is the laser energy at the ablation threshold

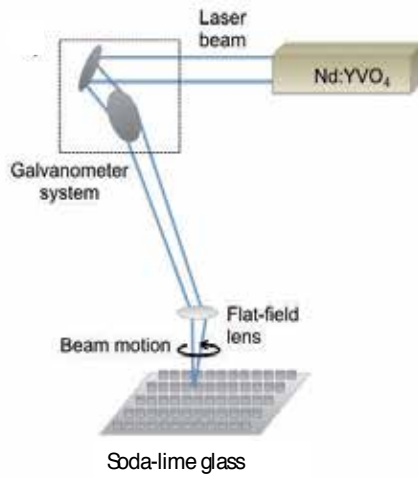


Figure 1. Laser setup for fabricating the microfluidic systems.

and ω_0 is the waist of the focal spot. Its value was obtained from the slope of the plot of $\ln(E_p/E_{th})$ against D^2 (diameter squared) ($D^2 = 2\omega_0^2 \ln\left(\frac{E_p}{E_{th}}\right)$ see [25] for details) where E_p is the energy per pulse (Figure 2).

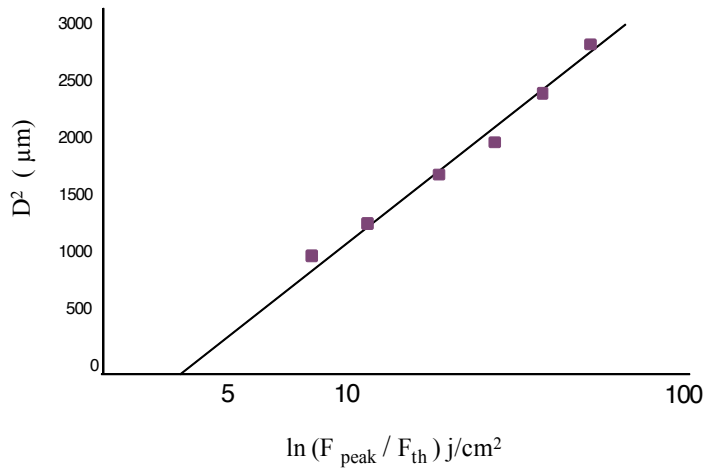


Figure 2. Linear relations between the squared diameter and the natural logarithm of the average laser fluences.

The main morphological parameters after laser ablation, such as depth and width for different number of pulses (fluence: 112 J/cm²), have been analyzed using a confocal microscope SENSOFAR 2300 P1μ and an optical microscope Nikon MM-400.

Figures 3 and 4 show the evolution of the damage (diameter and depth) at the substrate surface with the number of pulses (1–10,000 pulses). Measurements of the depth and diameter of the ablated holes can also provide important information about the material response to the nanosecond laser.

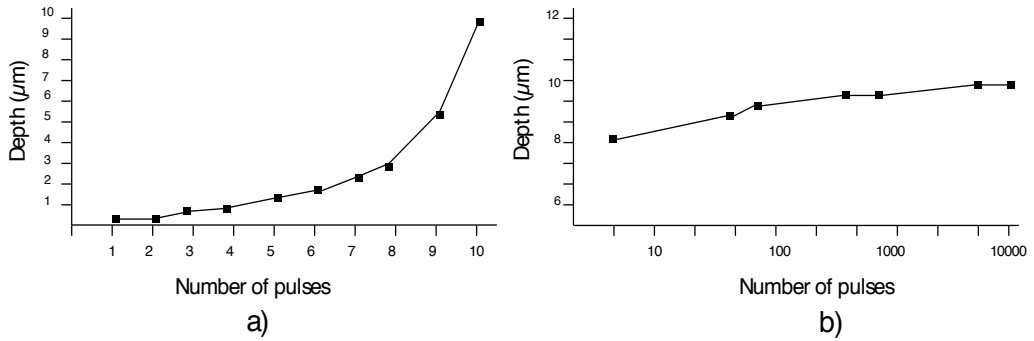


Figure 3. Evolution of depth versus number of pulses for (a) 1–10 pulses and (b) 10–10,000 pulses.

As shown in Figure 3a, the depth increases with the first pulses, reaching a depth value of 8 µm after 10 pulses, however after 10 pulses (Figure 3b), the depth increases slowly, varying only 2 µm after 500 pulses and maintain almost constant till 10,000 pulses. That behavior is due to the fact that the ablation plume does not have sufficient energy to take out the material detached on the ablation process.

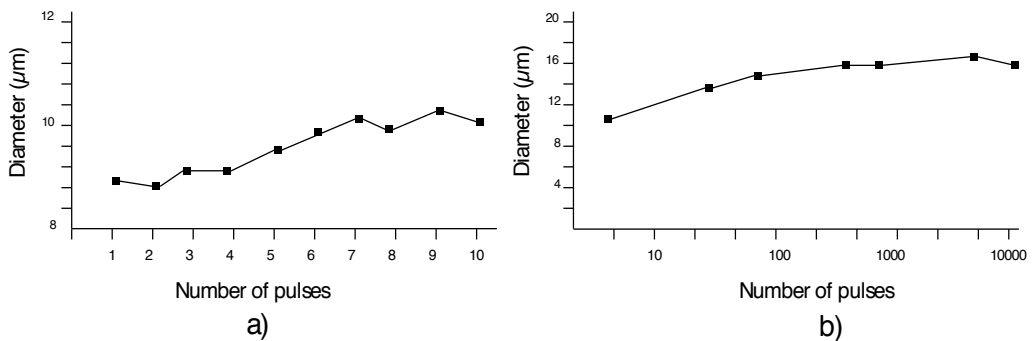


Figure 4. Evolution for diameter versus number of pulses: (a) 1–10 pulses and (b) 10–10,000 pulses.

From the slope obtained in Figure 4a, the evolution of diameter with the number of pulses can be deduced. The mark diameter increases slowly with the number of pulses, reaching a maximum value of depth 10 µm after 500 pulses, after this value (Figure 4b), increasing the number of pulses does not have a significant effect on the mark diameter.

For fabricating a homogeneous microchannel on glass, the optimization of the pulse overlaps, which determines the pulse per area is important to obtain quality microchannels. When the pulse overlap is high, there will be significant cracking in the microchannels edges because of the stress related with heat deposited in a small area. To obtain the optical pulse overlap, O_d , we use the following relation:

$$O_d = \left(1 - \frac{v}{2\omega_0 f} \right) \quad (1)$$

where v is the galvoscanner speed, $2\omega_0$ is the focused spot diameter, and f is the laser repetition rate.

The first experimental approach for obtaining uniform channels was checked at different scan speeds for getting the optimal pulses overlapping (Figure 5). The same laser parameters (10 kHz, 8 W) were used for fabricating all the lines varying only the scan speed.

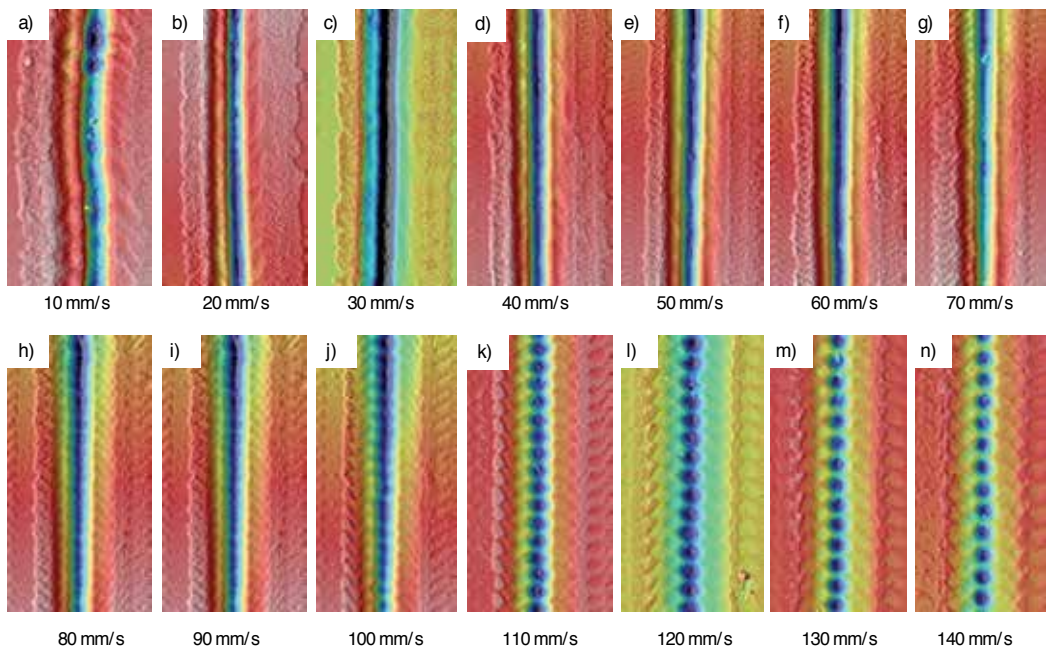


Figure 5. Confocal images of one microchannel obtained by laser ablation of glass at 10 kHz, 8 W for scan speeds values of (a) 10 mm/s, (b) 20 mm/s, (c) 30 mm/s, (d) 40 mm/s, (e) 50 mm/s, (f) 60 mm/s, (g) 70 mm/s, (h) 80 mm/s, (i) 90 mm/s, (j) 100 mm/s, (k) 110 mm/s, (l) 120 mm/s, (m) 130 mm/s, and (n) 140 mm/s.

As it can be appreciate in Figure 5, the best results were obtained for the channels fabricated between 40 and 80 mm/s (Figure 5d and h). At low scan speed, the high overlapping of the pulses delivers too much energy at the surface, which leads to an irregular channel. Low

overlapping creates a distortion on the microchannels (Figure 5j–n). For scan speeds higher than 80 mm/s, it can be appreciated the interaction of one pulse with the substrates (Figure 5a–c), which also increase the roughness average and does not allow the formation of the microchannels. Figure 6 shows the pulse overlap, obtained using Eq. (1), and the roughness average measured at different scan speeds. In terms of pulse overlap (Figure 6a), values in the range of 60–80% are needed for fabricating microchannels with good qualities. For scan speed values in the interval of 40–80 mm/s, roughness around 55 nm is obtained (Figure 6b).

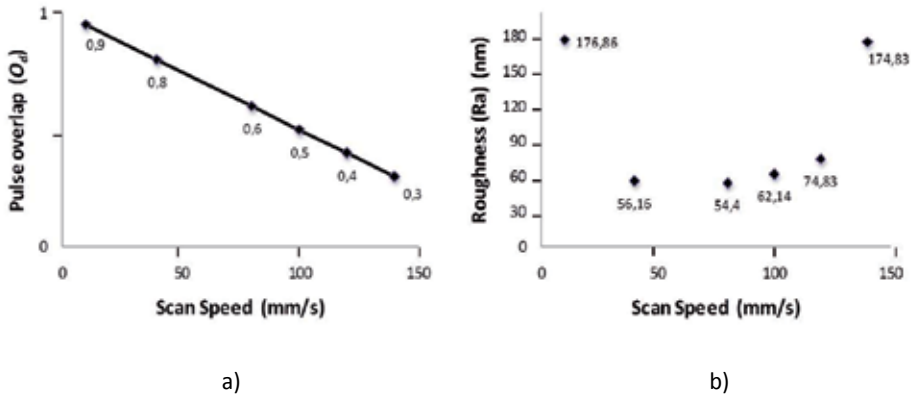


Figure 6. (a) Evolution of pulse overlap and (b) roughness versus scan speed in the range of 10–140 mm/s.

Figure 7 shows a microchannel fabricated using the optimal pulse overlap obtained from the study presented above, and laser parameters of 8 W, 10 kHz and scan speed of 50 mm/s. The resulting channel exhibits a surface roughness of 54 nm with a diameter of 8 μm and height of 3 μm .

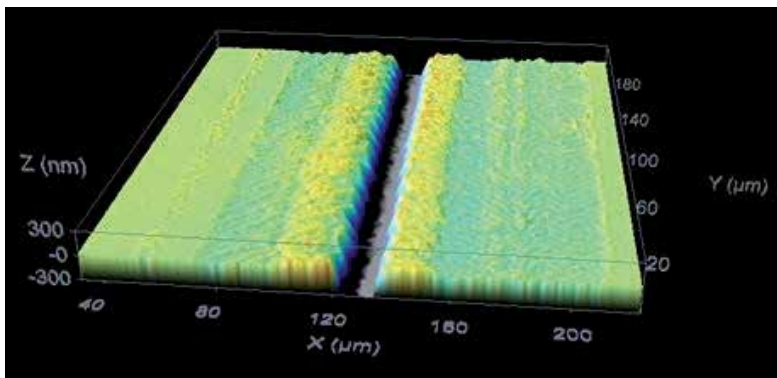


Figure 7. Initial microchannel fabricated by laser ablation.

In order to fabricate different microchannels configurations, a study of the evolution of depth and diameter with the number of laser passes over the same place was done (laser parameters:

8 W, 10 kHz and scan speed 50: mm/s). Figure 8 shows the evolution of depth and diameters varying the number of laser passes.

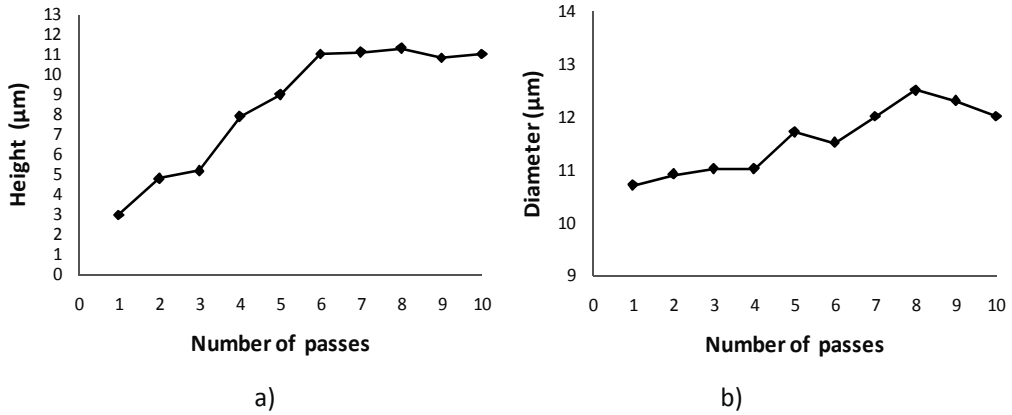


Figure 8. (a) Evolution of depth and (b) diameter with the number of laser passes.

It is evident from Figure 8 that the channel aspect ratio $\alpha = h/d$ varies with the number of passes. The diameter d reaches its saturation value after five laser passes, increasing just around 200 nm per laser pass and varying only 1 µm after five passes, above these values the diameter is maintained almost constant. In contrast, the ablation height h changes dramatically with the increase in number of pulses, after 6 passes this value remains constant. The height increases 1 µm per laser pass, up to a value of 12 µm. We can relate this behavior with the nonevacuation of the debris generated during laser ablation process that arise from the bottom of the microchannels and also because to the lack of focus as the depth of the microchannel increases. The diameter of the microchannel is maintained almost constant by increasing the number of laser passes, which can be related with the diameter of the laser beam used.

One of the important challenges to overcome using a laser direct-write process for fabricating microchannels in glass is to obtain good-quality junctions. The propelled material of the subsequent channels is deposited on the existing microchannel that turns into a bad quality of the microchannel. This debris changes the average roughness, and because it is crucial for obtaining high-quality elements, the microchannels were cleaned after laser exposure using chemical etching process of hydrofluoric acid (HF). The HF acid is an etchant that attacks glasses at significant high-etch rate [16]. Commercial soda-lime glass used in this work is composed of SiO₂ (73.8%), Na₂O (12.7%), CaO (8.6%), MgO (4.1%), Fe₂O₃ (0.14%), and Al₂O₃ (0.1%). Etching soda-lime glass in an HF solution forms insoluble products that are believed to be mainly CaF₂ and MgF₂.

The etching time, concentration of the acid, and the temperature of the process are important parameters to control the HF cleaning process. In terms of handle, HF is a strong corrosive and highly toxic at higher concentrations. The etching process was performed at 10% HF concentration, which in terms of security reduces considerably percentages of toxic vapor that

contaminates the work space. Figure 9 shows a SEM top view image of one microchannel before (Figure 9a) and after (Figure 9b) HF etching.

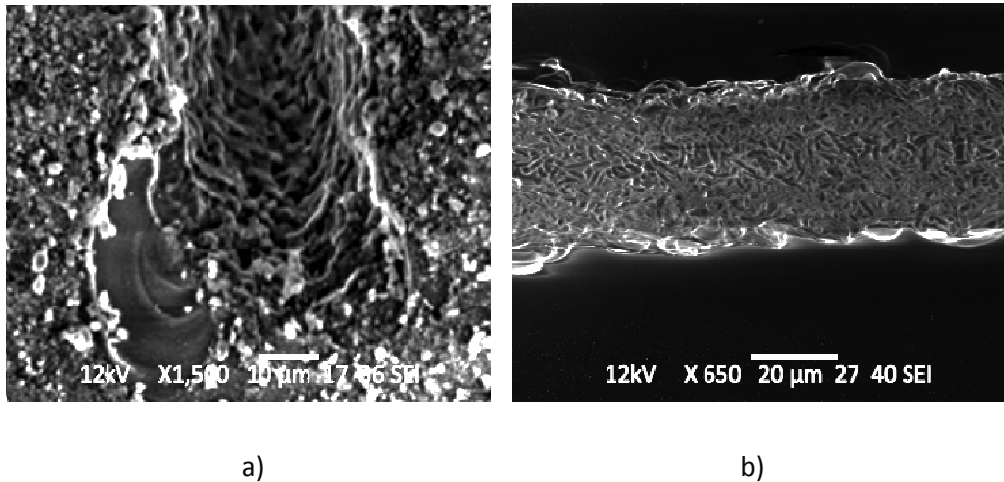


Figure 9. SEM image of the microchannel top surface (a) before chemical etching and (b) after 10 min in 10% HF aqueous solution.

In Figure 9a, debris deposited on the top of the microchannels during the laser ablation can be observed. In Figure 9b, after chemical etching, the debris was successfully eliminated.

3.2. Thermal treatment

A thermal treatment was applied into an oven to obtain the final elements and to improve the morphological properties. The samples were reflowed in a Heraeus mufla furnace for 2 h at temperatures between 620°C and 670°C (steps of 10°C). The working range has been chosen to be higher than the glass transition temperature of soda-lime glass ($T_g = 564^\circ\text{C}$). Figure 10 shows a 3D confocal image of microfluidic microchannels fabricated at different reflow temperatures.

As shown in Figure 10, at 620°C, there was not a significant modification in the surface shape, and at temperatures higher than 670°C, the initial shape surface profile becomes flat so that microchannels obtained by laser direct-write disappear.

This displacement of material due to the thermal treatment and the accumulation in the bottom turns into a reduction in height while the diameter is increased due to the material reflow from the top of the edges of the microchannels at the bottom of the crater. This effect allows both the thermal reflow and to fill the irregular structure of crater with material leading to an improvement on the morphological qualities.

The flow resistance for each microchannel depends on the geometry and roughness. The surface roughness on the wall of the microchannel increases when the flow rate decreases, so

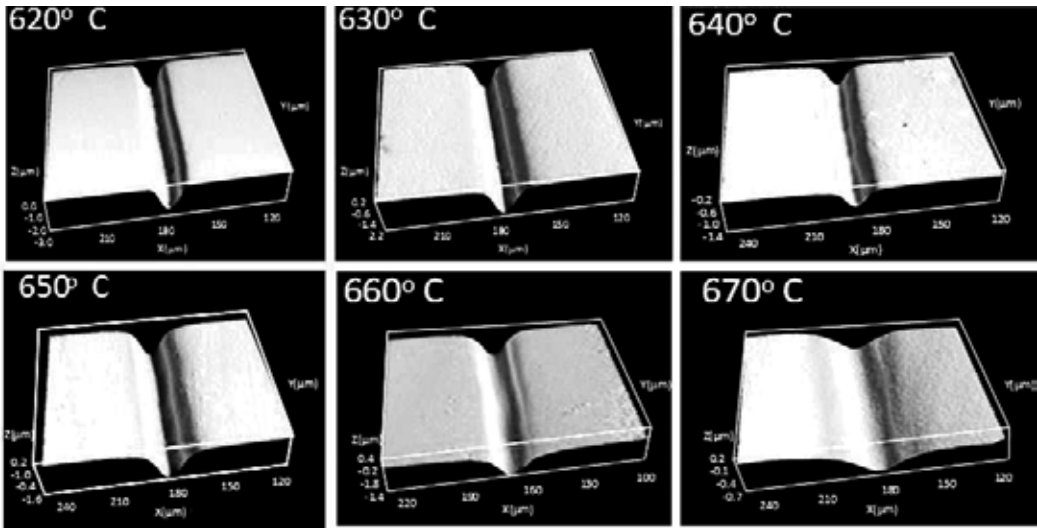


Figure 10. Confocal images of microchannels obtained after thermal treatment at different temperatures. Six different results at different reflow temperatures are shown: $T_1 = 620^\circ\text{C}$, $T_2 = 630^\circ\text{C}$, $T_3 = 640^\circ\text{C}$, $T_4 = 650^\circ\text{C}$, $T_5 = 660^\circ\text{C}$, and $T_6 = 670^\circ\text{C}$.

the change of hydraulic resistance is proportional to the change in the surface roughness. For determining the quality of the microchannels fabricated at different thermal reflow temperatures, it was determined the roughness at the bottom of the channels [26]. Table 1 shows the evolution of roughness for temperatures between 620 and 670°C, taken at steps of 10°C. The purpose of thermal treatment is to reduce the roughness generated during the laser direct-write process. It is important to find a compromise between shape modification and roughness. The shape should be maintained whereas the thermal reflow should reduce the surface roughness.

Temperature (°C)	Ra (nm)
Ra glass surface	3.68
Ra after laser ablation	640
620	125.14
630	57.14
640	39.45
650	29.40
660	16.43
670	7.35

Table 1. Comparative of roughness evolution with thermal reflow.

In order to study the microfluidics capabilities of our technique, after obtaining the best parameters for fabricating optimal microchannels, we focused on fabricating microchannels with different configurations trying to solve the main problems related with the laser ablation of glass, in particular for creating uniform and debris-free channels. Figure 11 shows some microchannels fabricated using the laser direct-write technique.

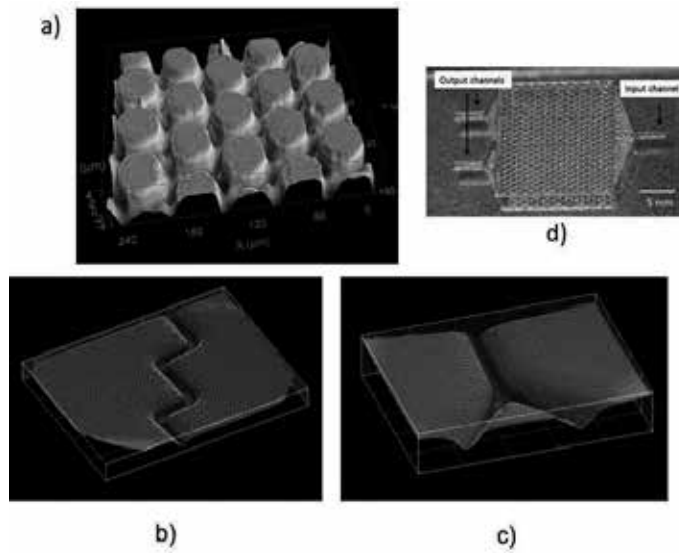


Figure 11. Microfluidics microchannels fabricated using the laser direct-write technique.

3.3. Biochip for capturing circulating tumor cells

In the previous work, we have demonstrated the suitability of the presented technique for fabricating a circulating tumor cell biochip [20]. The biochip is composed of a group of micropost (see Figure 11a), integrated in a microfluidics devices (see Figure 11d) for capturing circulating tumor cells. Using the aforementioned laser technique, we have fabricated an input channel for perfusing the media and two outputs channels for media removal (Figure 11d). The microfluidics devices were covered with a microscope cover slide (100 μm thickness). The manufactured chips were tested for detection of tumor cells (Hec 1A) after being functionalized with an EpCAM antibody coating. Cells were flown with media through the device allowing an interaction with the functionalized micropillars. After eluting the whole sample, chips were assessed for sensitivity and efficiency under a confocal microscope.

Fluorescently stained (DiO) CTCs were counted the cell trapping array region of the biochip using epifluorescent microscope (Zeiss Axio Vert A.1) was equipped with a 20 \times objective (Zeiss, numerical aperture = 0.4) and a low-light CCD camera.

Figure 12 shows the resulting cell isolation from cells flown in media. Pillars were able to trap circulating cells pumped in the device.

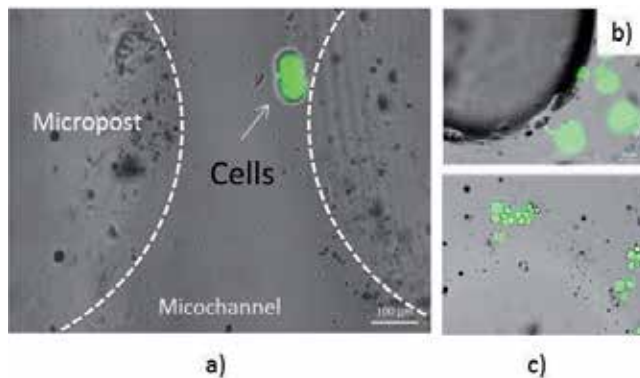


Figure 12. Cells attachment to the functionalized surface is observed in (a), (b), or (c). Cells are strongly bonded to the antibody surface and are not detached under flow conditions (white arrows show the location of the cells).

Pictures were taken along the device, there is a heterogeneous distribution for cell isolation along the posts while due to the chip dimensions few cells were found on the bottom (Figure 12c). In accordance to the surface functionalization protocol, the whole chip was coated with EpCAM antibodies, hence the bottom areas should be able to detain cells as well.

4. Conclusions

A hybrid method for fabricating microfluidic microchannels and a biochip for CTCs on soda-lime glass has been developed. The fabrication process consists of a combination of the laser direct-write technique for promoting glass structures and a thermal treatment for reshaping and or improving the morphological qualities of the generated microchannels. By applying the thermal treatment at 620°C (during 2 h), we are able to obtain high-quality microchannels maintaining the initial shape. This treatment allows us to reshape and improve the morphological, in terms of roughness, and optical qualities, in terms of transparency, of the generated microfluidics structures. This approach is a rapid and low-cost procedure to obtain glass microstructures where a chemical modification can take place, leading to the possibility of performing surface modifications with EpCAM antibodies to successfully stop circulating tumor cells. Therefore, the presented glass platform in this chapter can provide a good starting point to develop more complex systems aimed for single-cell analysis and isolation leading to a primary culture.

Acknowledgements

This work was supported by Xunta de Galicia, Spain, under Galician Programme for Research Innovation and Growth 2011–2015 (I2C Plan). We would also like to thank to Ramiro Couceiro for his assistance with the biological trials and confocal images.

Author details

Daniel Nieto García^{1,2*} and Gerard O'Connor²

*Address all correspondence to: daniel.nieto@usc.es

1 Microoptics and GRIN Optics Group, Applied Physics Department, Faculty of Physics, University of Santiago de Compostela, Santiago de Compostela, Spain

2 School of Physics, National Centre for Laser Applications, National University of Ireland, University Road, Galway, Ireland

References

- [1] D. Erickson and D. Li. Integrated microfluidic devices. *Analytica Chimica Acta*. 2004;507:11–26.
- [2] Y. Cheng, K. Sugioka and K. Midorikawa. Microfluidic laser embedded in glass by three-dimensional femtosecond laser microprocessing. *Optics Letters*. 2004;29(17): 2007–2009.
- [3] F. Cattaneo, K. Baldwin, S. Yang, T. Krupenkine, S. Ramachandran and J.A. Rogers. Digitally tunable microfluidic optical fiber devices. *Journal of Microelectromechanical Systems*, 2003;12(6):907–912.
- [4] G.M. Whitesides. The origins and the future of microfluidics. *Nature*. 2006;442:368–373.
- [5] T. Rajabi, V. Huck, R. Ahrens, M.C. Apfel, S.E. Kim, S.W. Schneider and A.E. Guber. Development of a novel two-channel microfluidic system for biomedical applications in cancer research. *Biomedical Engineering*. 2012; 57:921–922.
- [6] C.W. Huang and G.B. Lee. A microfluidic system for automatic cell culture. *Journal of Micromechanics and Microengineering*. 2007; 17(7):1266.
- [7] H. Andersson, A. Van Den Berg. Microfabrication and microfluidics for tissue engineering: state of the art and future opportunities. *Lab Chip*. 2004;4:98–103.
- [8] M.S. Giridhar, K. Seong, A. Schülzgen, P. Khulbe, N. Peyghambarian, and M. Man-suripur. Femtosecond pulsed laser micromachining of glass substrates with application to microfluidic devices", *Applied Optics*. 2004: 43(23):4584–4589.
- [9] Y. Li, S. Qu and Z. Guo. Fabrication of microfluidic devices in silica glass by water-assisted ablation with femtosecond laser pulses. *Journal of Micromechanics and Microengineering*. 2011;21:075008.

- [10] J.Y. Cheng, M.H. Yen, C.W. Wei, Y.C. Chuang and T.H. Young. Crack-free direct-writing on glass using a low-power UV laser in the manufacture of a microfluidic chip. *Journal of Micromechanics Microengineering*. 2005; 15:1147–1156.
- [11] H. Becker and U. Heim. Hot embossing as a method for the fabrication of polymer high aspect ratio structures. *Sensors and Actuators*. 2000; 83:130–135.
- [12] D. Martin Knotter. Etching mechanism of vitreous silicon dioxide in HF-based solutions. *Journal of American Chemical Society*, 2000;122(18):4345–4351.
- [13] P.A. Clerc, L. Dellmann, F. Gretillat, M.A. Gretillat, P.F. Inderm, S. Jeanneret, Ph. Luginbuhl, C. Marxer, T.L. Pfeffer, G.A. Racine, S. Roth, U. Staufner, C. Stebler, P. Thiebaud and N.F. de Rooij. Advanced deep reactive ion etching: a versatile tool for microelectromechanical systems. *Journal of Micromechanics and Microengineering*. 1998;8:272–278.
- [14] G. Kopitkovas, T. Lippert, J. Venturini, C. David and A. Wokaun. Laser induced backside wet etching: mechanisms and fabrication of micro-optical elements. *Journal of Physics: Conference Series*. 2007;59:526–553.
- [15] M. Wakaki, Y. Komachi, and G. Kanai. Microlenses and microlens arrays formed on a glass plate by use of a CO₂ laser. *Applied Optics*. 1998; 37:627–631.
- [16] I.K. Sohn, M.S. Lee, J.S. Woo, S.M. Lee and J.Y. Chung. Fabrication of photonic devices directly written within glass using a femtosecond laser. *Optics Express*. 2005;13(11):4224–4229.
- [17] M.T. Flores-Arias a, A. Castelo, C. Gomez-Reino and G.F. de la Fuente. Phase diffractive optical gratings on glass substrates by laser ablation. *Optics Communications* 2009; 282:1175–1178.
- [18] M. Stjernström and J. Roeraade. Method for fabrication of microfluidic systems in glass. *Journal of Micromechanics and Microengineering*. 1998; 8:33.
- [19] D. Nieto, M.T. Flores-Arias, G. O'Connor and C. Gomez-Reino. A Laser direct-write technique for fabricating microlens arrays on soda lime glass with a Nd:YVO₄ laser. *Applied Optics*. 2010; 49(26):4979–4983.
- [20] S.L. Stott, C.H. Chia-Hsien Hsu, D.I. Tsukrov, M. Yu and D.T. Miyamoto. Isolation of circulating tumor cells using a microvortex-generating herringbone-chip. *Proceedings of the National Academy of Sciences of the United States of America*. 2010;107:18392–18397.
- [21] Y. Dong, A.M. Skelley, K.D. Merdek, K.M. Sprott, C. Jiang. Microfluidics and circulating tumor cells. *The Journal of Molecular Diagnostics*. 2013;15:149–157.
- [22] B. Cheng, H. Song, S. Wang, C. Zhang, B. Wu, Y. Chen, F. Chen and B. Xiong. Quantification of rare cancer cells in patients with gastrointestinal cancer by nanostructured substrate. *Translational Oncology*. 2014;7(6):720–725.

- [23] D. Nieto, R. Couceiro, M. Aymerich, R. Lopez-Lopez, M. Abal and M.T. Flores-Arias. A laser-based technology for fabricating a soda-lime glass based microfluidic device for circulating tumour cell capture. *Colloids and Surfaces B: Biointerfaces*, 2015;134:363–369.
- [24] D. Nieto, M.T. Flores-Arias, G. O'Connor and C. Gomez-Reino. A Laser direct-write technique for fabricating microlens arrays on soda lime glass with a Nd:YVO₄ laser. *Applied Optics*. 2010;49(26):4979–4983.
- [25] A. Ben-Yakar and Robert L. Byer, Femtosecond laser ablation properties of borosilicate glass. *Journal of Applied Physics*. 2004;96:5316–5323.
- [26] D. Nieto, T. Delgado and M.T. Flores-Arias. Fabrication of microchannels on soda-lime glass substrates with a Nd:YVO₄ laser. *Optics and Lasers in Engineering*. 2014;63:11–18.

Microfluidics in Membraneless Fuel Cells

Jesus A. Diaz-Real, Minerva Guerra-Balcázar, Noe Arjona,
Francisco Cuevas-Muñiz, Luis Gerardo Arriaga and Janet Ledesma-García

Additional information is available at the end of the chapter

<http://dx.doi.org/10.5772/64448>

Abstract

In the 1990s, the idea of developing miniaturized devices that integrate functions other than what normally are carried out at the laboratory level was conceived, and the so-called “lab-on-a-chip” (LOC) devices emerged as one of the most important research areas. LOC devices exhibit advantages related to the use of microfluidic channels such as small sample and reagent consumption, portability, low-power consumption, laminar flow, and higher surface area/volume ratio that enhances both thermal dissipation and electrochemical kinetics. Fuel cells are electrochemical devices that convert chemical energy to electrical energy. These are considered as one of the greener ways to generate electricity because typical fuel cells produce water and heat as the main reaction byproducts. The technical challenges to develop systems at the microscale and the advantages of microfluidics exhibited an important impact on fuel cells for several reasons, mainly related to avoid inherent problems of gaseous-based fuel cells. As a result, the birth of a new type of fuel cells as microfluidic fuel cells (MFCs) took place. The first microfluidic fuel cell was reported in 2002. This MFC was operated with liquid fuel/oxidant and had the advantage of the low laminar flow generated using a “Y” microfluidic channel to separate the anodic and cathodic streams, resulting in an energy conversion device that did not require a physical barrier to separate both streams. This electrochemical system originated a specific type of MFCs categorized as membraneless also called colaminar microfluidic fuel cells. Since that year, numerous works focused on the nature of fuels, oxidants and anodic/cathodic electrocatalysts, and cell designs have been reported. The limiting parameters of this kind of devices toward their use in portable applications are related to their low cell performances, small mass activity, and partial selectivity/durability of electrocatalysts. On the other hand, it has been observed that the cell design has a high effect on the cell performance due to internal cell resistances and the crossover effect. Furthermore, current technology is growing faster than last centuries and new microfabrication technologies are always emerging, allowing the development of smaller and more powerful microfluidic energy devices. In this chapter, the application of microfluidics in membraneless fuel cells is addressed in terms of evolution of cell designs of miniaturized microfluidic fuel cells as a result of new discoveries in microfabrication technology and the use of several fuels and electrocatalysts for specific and selective applications.

Keywords: energy conversion systems, lab-on-a-chip, membraneless, microfluidic fuel cells

1. Introduction

1.1. Microfluidic fuel cells: concept, classification, and challenges

In 1989, R. Howe introduced the term “microelectromechanical systems” (MEMS) to describe a research field in which the machining was below the millimeter scale [1]. The rapid growth in the following years in this area generated several branches in electronics, including power sources technologies where fuel cells were comprised. However, hydrogen as the fuel for the supply of these miniaturized devices results very dangerously in the gas form and makes it complicated to store as liquid. Therefore, the use of hydrogen-containing liquid fuels such as alcohols became more attractive for portable applications due to their ease of storage and high-mass energy density (6.1 kWh/kg) [2]. The integration of these elements into the fuel cells introduced an important characteristic that well defines the operating principle of a microfluidic fuel cell (MFC).

Typically, an MFC is a fuel cell that operates with two liquids (one fuel and the other oxidant) that are introduced by a mechanical mean into a single microchannel at laminar flow (low Reynolds number) to establish an interface. The fuel and oxidant stream will be in contact with an anodic or a cathodic surface, respectively. Both parallel streams allow the continuous flow through the length of the channel without mixing and preventing possible fuel crossover. The low speed allows the diffusion of protons between the streams in order to perform the electrochemical processes, which replaces the proton-exchange membrane (PEM) [3]. From its first appearance in 2002 to the present day, several architectures regarding the shape of the channel, electrodes geometric arrangement, oxidant supply source, and fuels have been studied. It is also common to refer MFC as laminar flow fuel cells (LFFCs) in literature indistinctively.

1.2. Microfluidic fuel cell categories

With the recent development of MFCs, a subcategory has been created to include all these membraneless cells. Generally, fuel cells have been classified by the membrane used such as polymer electrolyte fuel cells (PEFCs), solid-oxide fuel cells (SOFCs), and others. In the case of the MFCs, two main aspects have been used to classify them and are based either on the physical phases in which fuel and oxidant streams are found [4] or the stream delivery mode onto the electrodic surface [5].

1.2.1. Liquid fuel/liquid oxidant

The first categorization distinguishes reactants in liquid phase. Several fuels have been studied, including alcohols (methanol and ethanol mainly) [6–9], formic acid [10–14], glycerol [15], glucose [16, 17], dissolved hydrogen [18], V^{+2} [19, 20], among others. It is common to see the use of dissolved oxygen as the oxidant phase [10, 12, 21, 22], while the same is not true in the case of H_2O_2 [23, 24], VO_2 [19, 25, 26], and $KMnO_4$ [25, 27, 28]. An important advantage is the wide range of pH supported by this type of MFCs since the membrane is not the limiting issue. This allows the choice of supporting electrolyte to tailor the optimal operating conditions for

the electrodic materials. However, a major issue in these systems is the sudden formation of bubbles due to the gas byproducts (namely, CO₂) that lead to the drop of ionic conductivity, perturbation of the colaminar interface, streams crossover, or even channel blockage [4].

1.2.2. *Liquid fuel/gas oxidant*

Oxygen is by far the most used, easily available, and low-cost oxidant for MFCs. It is well known that slow kinetics of oxygen reduction (cathodic side) greatly determine the efficiency of fuel cells and the same problem affects MFCs. To address this problematic issue, Jayashree et al. innovated an MFC by introducing the concept of an air-breathing cathode that enhanced the performance of this electrode since oxygen diffusion coefficient is four orders of magnitude higher in air than in an aqueous solution [29]. This opens the opportunity to hypothetically expand this idea to many other cells because the need of both streams is still necessary to form the colaminar interface. However, several considerations are needed to take into account during the implementation of air-breathing electrodes. Air access, atmospheric counterpressure, and drying rate in bigger electrode areas are some of the parameters that might affect the performance of these MFCs when they are scaled up.

1.2.3. *Flow-over stream*

One of the simplest models of MFCs involves the two distributions of the electrodes, as depicted in Figure 1: (a) a parallel arrangement (facing up or over the walls) with a vertical colaminar diffusion interface and (b) facing each (top-bottom) other with a horizontal interface. In the first case, reorientation of the interface induced by gravity is possible when there is an important difference in the densities of the streams, while for the configuration with a horizontal interface this issue is more evident, increasing the crossover stream rate [30]. Regardless of the crossover problem, the amount of electrolyte that is reacting and in intimate contact with the electrodic surface is limited to the geometry of the electrode and to the flow speed. This is due to the planar electrode configuration, and thus, only the adjacent fraction of the streams is available to react. Then, the local reactant concentration will decrease while the generated subproducts will increase. This situation, along with the low convective flow speed, will generate a depletion layer near the electrode surface and a gradient of reactant concentration. Therefore, the utilization of the electrolyte is minimal, which demands an improvement in the cell design to enhance the fuel utilization [5].

1.2.4. *Flow through stream*

Considering the issue on electrolyte utilization, three-dimensional porous structures for electrodes were proposed. This configuration makes use of the entry of the electrolyte through the electrode itself, forcing the intimate contact to maximize the reactant consumption by rapid convective transport, replenishing the species. Another name used to refer to this configuration is multiple inlets, and the term was first proposed by Kjeang et al. [31]. An MFC with carbon paper porous electrodes was reported by Salloum et al. that used formic acid as the fuel [27].

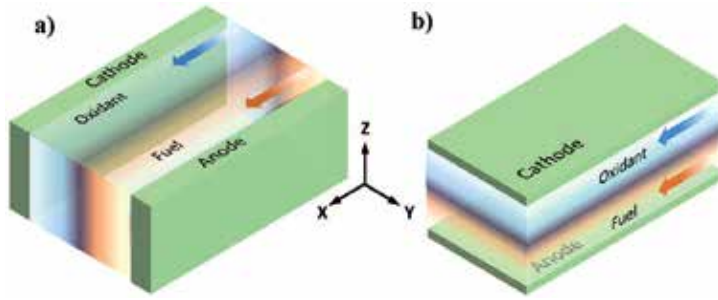


Figure 1. Schematic image of the overflow designs: (a) top-bottom electrode configuration and (b) side-by-side parallel configuration. The darker color shows the diffusion interface, while a transparent color shows the depletion layer near the electrode surface.

One important challenge that faces this type of electrodes is the electrocatalyst deposition. Since the porosities of the electrode are in a smaller scale, the classical paint-spray deposition technique cannot ensure a homogeneous dispersion in the inner electrode area. Hence, new techniques for electrode preparation needs to be further investigated.

2. Thermodynamic and kinetic of microfluidic fuel cells

Microfluidics is a research field in which the studied phenomena occurs in confined structures with a characteristic dimension within 1–1000 μm [32]. At this scale, low Reynolds numbers yielding laminar flows facilitate characterization of the fluid mechanics. Therefore, viscous and capillary forces, rather than volumetric or gravitational effects, govern these systems more importantly. The behavior of the fluids in the microchannels allows us to consider them as a continuum, and thus, we can follow the continuity equation for mass conservation for a fluid in Eq. (1)

$$\frac{\partial \rho}{\partial t} + \nabla(\rho \vec{u}) = 0 \quad (1)$$

If the density of the fluid remains constant, the equation is simplified by the condition of incompressible flow, $\nabla \cdot \vec{u} = 0$. Then, the Navier-Stokes equation is valid to describe the velocity field, \vec{u} :

$$\rho \left(\frac{\partial \vec{u}}{\partial t} + \vec{u} \nabla \vec{u} \right) = \rho \left(\frac{\partial \vec{u}}{\partial t} \right) = -\nabla p + \mu \nabla^2 \vec{u} + \vec{f} \quad (2)$$

with p being the pressure and \vec{f} a term summarizing all body forces per unit volume.

Since the main difference between PEMFC and MFC systems relies on the replacement a physical membrane with the liquid-liquid interface, their electrochemical operating principles remain almost identical. Due to the large amount of reports making use of organic molecules as fuel, it is convenient to remind the fundamentals of direct alcohols fuel cells (DAFC) [33]. For the sake of understanding the thermodynamics of their process, we will use CH₃OH electrooxidation on a Pt surface in acid media as an example. CH₃OH can be directly oxidized to carbon dioxide, although other subproducts (namely, formaldehyde, formic acid, etc.) can be produced depending on the reaction pathway.

In an assembled MFC, two reactions occur: (1) the fuel oxidation in the anode side and (2) the electroreduction of the oxidant (oxygen, for an example) at the cathode side. The general overall reaction is presented below:

Fuel/anode side	$\text{CH}_3\text{OH} + \text{H}_2\text{O} \rightarrow \text{CO}_2 + 6\text{H}^+ + 6\text{e}^-$	$E_{298}^\circ = 0.04 \text{ V/SHE}$	(Rxn. 1)
Oxidant/cathode side	$3/2\text{O}_2 + 4\text{H}^+ + 4\text{e}^- \rightarrow 3\text{H}_2\text{O}$	$E_{298}^\circ = 1.229 \text{ V/SHE}$	(Rxn. 2)
Overall	$\text{CH}_3\text{OH} + 3/2\text{O}_2 \rightarrow \text{CO}_2 + 2\text{H}_2\text{O}$		(Rxn. 3)

The overall reaction potential can be obtained by the subtraction of the anodic thermodynamic potential reaction to the cathodic value, $E_c - E_a = E_{\text{cell}} = 1.19 \text{ V}$. This process has an associated thermodynamic efficiency that can be calculated by obtaining the ratio of Gibbs free energy (the maximum electrical work of the system, ΔG°) between the enthalpy (the total available energy, ΔH°),

$$\varepsilon_{\text{eq}}^{\text{rev}} = -\Delta G^\circ / -\Delta H^\circ \quad (3)$$

Methanol has a theoretical enthalpy of combustion of -715 kJ/mol [34]. With the standard electromotive force equation, it is possible to calculate the ΔG° at equilibrium

$$\Delta G^\circ = -nF \times E_{\text{eq}}^\circ = -6 \times 96,485 \times 1.19 = -688.9 \text{ kJ / mol} \quad (4)$$

where F is the Faraday constant ($96,485 \text{ C/mol}$) and n is the number of exchanged electrons for the electrooxidation of CH₃OH. Then, the theoretical efficiency of the system is given by Eq. (5):

$$\varepsilon_{\text{eq}}^{\text{rev}} = -\Delta G^\circ / -\Delta H^\circ = 688.9 / 715 = 96.3\% \quad (5)$$

In a real experimentation, the formation of intermediates and subproducts determines in great measure the performance of the cell. These species depend on associated factors, but not limited to the reactive surface, catalyst composition, crystalline structure, and electrode

potential. Other conditions, such as pH, electrolyte temperature, fuel concentration, and reaction time/flow speed, also have to be considered [35].

The differences encountered between the theoretical and actual values for E_{cell} are usually addressed to three limiting factors: (1) charge transfer overpotentials (η_{act}) in either the anodic or cathodic catalyst due to slow kinetics, (2) the ohmic drop ($R_e j$, resulting from the product of the electrolyte resistance, R_e , and the recorded current density, j), and (3) mass transfer constrains [33]. Adding these new terms to the E_{cell} equation, the resulting expression is Eq. (6):

$$E_{\text{cell}} = E_{\text{eq}}^{\circ} - \eta_a - \eta_c - R_e j \quad (6)$$

With η_a being the anode overpotential and η_c the cathode overpotential, this equation considers both kinetic and mass transfer limitations. As previously mentioned, the specific reaction pathway might lead to incomplete fuel oxidation, and thus, the reaction will have a different number of exchanged electrons, n_{real} . If these considerations are included to the cell efficiency expression, we have Eq. (7):

$$\begin{aligned} \varepsilon_{\text{cell}}^{\text{CH}_3\text{OH}/\text{O}_2} &= -\frac{n F E_{\text{cell}}}{\Delta H^{\circ}} = -\left(\frac{n_{\text{real}} F}{\Delta H^{\circ}}\right) \left(\frac{n}{n}\right) \left(\frac{E_{\text{eq}}^{\circ}}{E_{\text{eq}}^{\circ}}\right) = \\ &= \left(\frac{n_{\text{real}}}{n}\right) \left(\frac{E_{\text{cell}}}{E_{\text{eq}}^{\circ}}\right) \left(\frac{\Delta G^{\circ}}{\Delta H^{\circ}}\right) = \varepsilon_F \varepsilon_E \varepsilon_{\text{eq}}^{\text{rev}} \end{aligned} \quad (7)$$

where ε_F is related to oxidation reaction efficiency and ε_E involves the kinetics and ohmic drop limitations. From this last expression, it is easy to understand that the only possible way to improve the cell efficiency is by decreasing the overpotentials and/or ohmic drop, and promoting the complete fuel oxidation [34].

For the ohmic loss, a factor that primarily contributes is the electrode separation (d) and the geometric exposed area (A). Thus, by increasing the ratio, A/d , ohmic losses are minimized. Nevertheless, ionic force in the electrolyte is significant to ohmic drop, and increasing the concentration of the supporting electrolyte reduces its negative impact. Mass transfer limitations are related to the availability of the species over the electrodic area. Then, the main issues are presented in the electrode vicinity due to the low concentrations as a consequence of the consumption of reactant species, which leads to the thickening of a depletion layer. This layer becomes a limiting mass transfer factor when fresh reactants are not efficiently replenished on the reactive surface, mainly due to slow flow rates [5]. The distributions of the species concentration are controlled by convective (stream flow) and diffusive (concentration gradient) transport, which are described by the mass conservation equation in Eq. (8):

$$\nabla(-D_i \nabla C_i + C_i \vec{\mu}) = S_i \quad (8)$$

with D_i the diffusion coefficient for the specie “ i ,” i being either the fuel or oxidant depending on the cell compartment, C_i the concentration of the specie “ i ,” and S_i the volumetric net rate of consumption for the specie “ i ” due to its corresponding electrochemical (oxidation or reduction) reaction. Then, S_i is estimated directly by the current density (i) obtained from the corresponding electrochemical reaction and given by the Butler-Volmer in Eq. (9):

$$S_i = \frac{i}{nF} = \frac{i_0}{nF} \left(\frac{C_i}{C_i^*} \right) \left[e^{\alpha_a f \eta} - e^{\alpha_c f \eta} \right] \quad (9)$$

where i_0 is the exchange current, C_i^* is the bulk concentration of specie i , α_a and α_c are the charge transfer coefficients for anodic and cathodic reactions, and η is the electrode overpotential. Since S_i depends on convective effects, the efficiency of the cell can be determined dividing by the flow rate:

$$\varepsilon_{fuel} = \frac{i}{nFv} \quad (10)$$

where ε_{fuel} is the fuel efficiency utilization and v is the fuel flow rate. Hence, higher flow speeds will supply the electrodes with electrolyte at the initial concentration preventing the increase of products in the depletion layer but decreasing ε_{fuel} .

3. Evolution of microfluidic fuel cell designs

The evolution of the microfluidic fuel cell is related to the pursuit of more power in less volume. Many factors have been considered including size, weight, physical resistance, and lifetime [14, 21]. Lightweight structural materials are preferred such as polymethyl methacrylate (PMMA) and poly-dimethylsiloxane (PDMS) [13, 14, 21, 36]. Moreover, UV-sensitive resists, such as SU-8, have demonstrated to be excellent candidates to build MFC pieces since they present some important advantages like the flexibility and capability to be sealed to each other by a hot-pressing technique [37].

3.1. Microfabrication techniques

In order to obtain more energy in the same volume, more sophisticated micromachining techniques have been employed. Some techniques even employ clean room facilities. The principal considerations for the choice of one or another micromachining technique are the selection of the structural material, the size of the microstructures, and the complexity of the structures. The polymers can be machined by Xerography, micromolding, hot embossing, and micromilling. In addition, assisted-laser techniques can be employed including photolithography, laser ablation, or stereolithography.

Micromilling is a very simple technique performed with a CNC micromilling cutter, useful for rigid polymers (i.e., PMMA). Micromilling is limited by the size of the cutter, it is uncommon to find below the 1/64 and often very fragile. Also, flexible polymers cannot be machined using this technique.

Xurography is a fast and low-cost process. It uses a plotter cutter to draw the channels in a protective mask placed over the substrate, later a conductive layer is placed over the substrate. Finally, the mask is removed leaving the conductive layer printed in the substrate. This technique is especially useful for electrodes and microchannels [38] (see Figure 2).

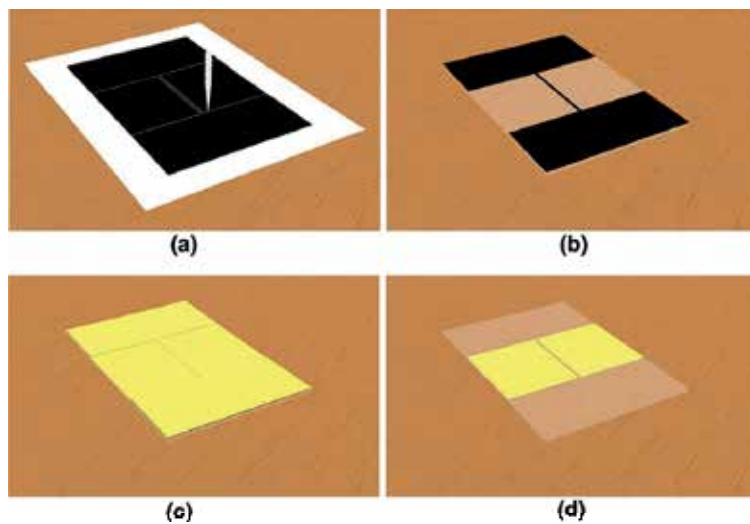


Figure 2. Schematics for electrodes on glass process flow based on xurography technique. (a) Patterning of vinyl film (xurography). (b) Removing of film and transfer on glass slide surface. (c) 30 nm Cr and 300 nm Au deposition. (d) Removing of film (dry liftoff) (taken from [39]).

Micromolding and hot embossing are similar techniques. A mold is used, however in micromolding a liquid resin is placed in a mold with the desired shape and is dried at room temperature by heat. In hot embossing, a solid polymer is heated to soften the material and then thermoformed by heat and pressure. Usually, these kinds of techniques are popular because of their simplicity. In both cases, the mold fabrication can be performed by micromilling or a laser technique.

Laser is a versatile tool for the construction of microstructures. Laser is used with a positive or a negative photoresin in order to obtain the desired pattern in the polymer. Laser techniques require the use of a clean room. In the photolithography, a UV laser beam is used to draw a pattern in a positive photoresin, generally a photoresist mask is used to protect the UV-sensitive material. Later, the sample is washed in order to remove the residues. Other alternative is the fabrication of a mold in negative photoresin, and later performed the casting of a polymer shell, as PDMS [13].

The technique of laser ablation allows drawing a microchannel from inside of a transparent polymer. A nanosecond or femtosecond pulsed laser is used to generate a three-dimensional pattern since the interior of material avoiding the need to paste several layers in the same piece (Figure 3) [39].

Stereolithography (SLA) is an additive technique (Figure 3). A negative photoresin (as SU-8) is placed over the support and cured with a laser beam, making a solid polymer with the desired structure. The main disadvantage of this procedure is the high cost of the machine (several hundred of dollars) [40].

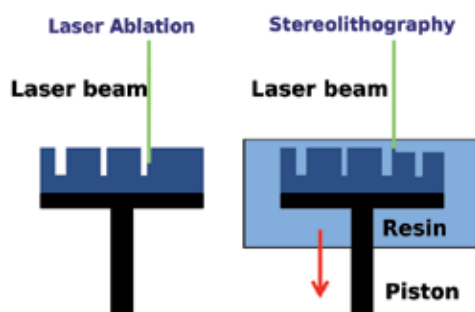


Figure 3. Destructive (laser ablation) and constructive (stereolithography): two different principles of microfabrication techniques. In ablation, the substrate is destroyed in order to obtain the pattern. In the stereolithography, the substrate is formed.

3.2. Microfluidic fuel cells two-dimensional electrode

We have seen a fuel cell evolution through the exhaustive analysis of literatures concerning membraneless MFCs. This evolution can be summarized at five principal stages:

- a. Close cells where both streams (anodic/cathodic) flow over electrodes.
- b. Open cells where both streams flow over electrodes.
- c. Open cells with an anodic stream flowing through the electrode.
- d. Close cells where both streams flow through electrodes.
- e. Open cells where both streams flow through electrodes.

The one and two stages correspond to microfluidic systems in which the anodic and cathodic streams are only in contact with the electrode surface (long and wide, Figure 4, delimited by blue arrows). The reason of this design is to consider membraneless MFCs with two-dimensional electrodes. In addition, because of fuel and oxidant flow laterally to electrodes, these are called as MFCs with flow-over electrodes. All devices that operate under this condition (lateral flow) and use small organic molecules (i.e., formic acid, methanol, ethanol, glycerol, etc.) as fuels and oxygen as oxidant have shown low-power densities, where an important limiting factor is the reduced geometrical area. With this in mind, plenty of investigations have

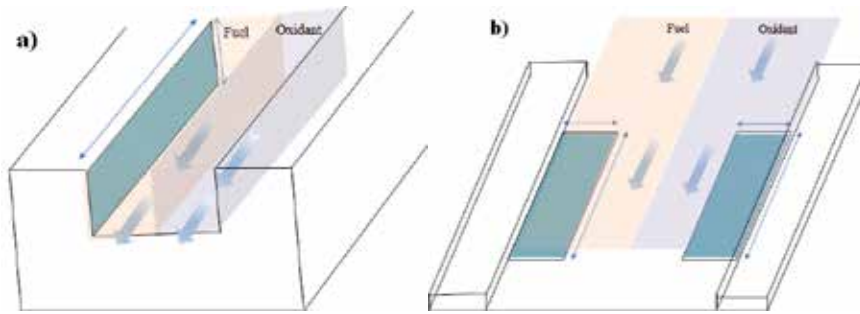


Figure 4. Contact area of fuel and oxidant streams in membraneless microfluidic fuel cells with two-dimensional electrodes: (a) “Y”-type with electrodes on channel walls [19] and (b) “Y” type with electrodes on channel floor [13].

been focused to increase the activity through enhancing the cell design, and others using supports with high surface area of different nature, such as carbon nanotubes [14, 15] and polyaniline [41]. These supports also enhance the reaction due to the improvement of electron transfer, modifying the metal-support interactions. The low concentration and diffusivity of oxygen in solution are another important parameter that limits the power density of membraneless MFCs [10]. For this reason, the two-dimensional electrode MFC has been slightly modified using porous air-breathing cathodes (Figure 5). Hence, it profits from the oxygen in air that has 10,000-fold higher diffusivity than in aqueous solution. Also, the oxygen concentration in air is higher (10 mM) than in solution (2–4 mM) [29].

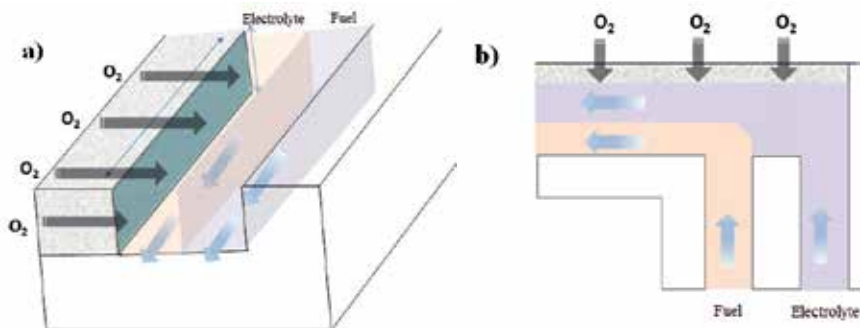


Figure 5. Membraneless microfluidic fuel cell with porous cathode as flow-over electrode: (a) typical “Y” and “T”-like configuration and (b) “F”-like channel configuration.

3.3. Microfluidic fuel cells three-dimensional electrode

Another strategy to enhance the power density is related to the increase of the contact area between the electrocatalyst and electrocatalytic solution. Carbon paper as porous electrode has been used as diffusor in proton exchange membrane (PEM) fuel for cells many years before the first membraneless MFC was reported [42–45]. Kjeang et al. have explored the use of these

porous carbon electrodes in MFC, where fuel and oxidant are circulating through them, emerging the term of “MFCs with flow through electrodes” or “three-dimensional electrode MFCs” (Figure 6) [31, 46]. These devices benefit from the high surface area of carbon paper ($230 \text{ m}^2 \text{ g}^{-1}$) and carbon nanofoam ($450 \text{ m}^2 \text{ g}^{-1}$) to enhance the cell performance.

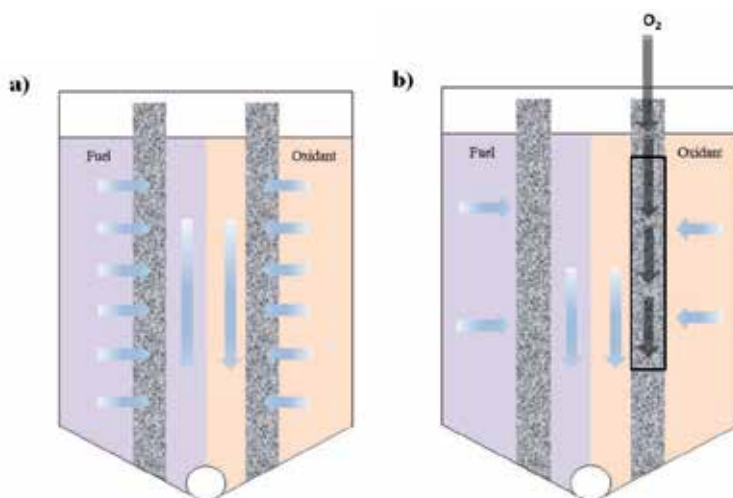


Figure 6. (a) Schematic representation of membraneless microfluidic fuel cell with flow through electrodes and (b) with air-breathing window [48, 49].

The modifications of membraneless microfluidic fuel cells between flow-over electrodes and flow through electrodes as well as the use of air as oxygen source have resulted in enhancement of the cell performance. Figure 7 illustrates the evolution of these devices by changes in contact areas as discussed earlier. Changes were observed in the current density as a function of the MFC stage. The range in the stage: (i) is in the order of $8\text{--}12 \text{ mA cm}^{-2}$ and (ii) it depends on the utilized fuel. The use of porous material as the oxygen source (stage ii) in an air breathing resulted in current densities from 15 to 130 mA cm^{-2} . The use of a flow through anode (stage (iii)) increases the current density up to 140 mA cm^{-2} . In the case of an MFC, which works with a flow through anode and cathode, formic acid as fuel and oxygen-saturated solution as oxidant, the reported current density was of 20 mA cm^{-2} (stage (iv)) [47].

When the MFC with flow-through electrodes combines oxygen from air and from an oxygenated solution, the current density increases to values up to 100 mA cm^{-2} as tested for different fuels [48]. In the case of formic acid, current density of almost 500 mA cm^{-2} has been reported [49]. As summary, the performance of membraneless MFCs has shown high dependence on the way that the fuel and oxidant streams flow in the anode and cathode as well as with strategies to increase/enhance the oxygen source. The use of electrodes with higher surface areas as flow-through electrodes can be considered as an important alternative to improve the cell performance of this kind of devices, which could allow them for use as power supplier for small devices such as cellphones, cameras, etc.

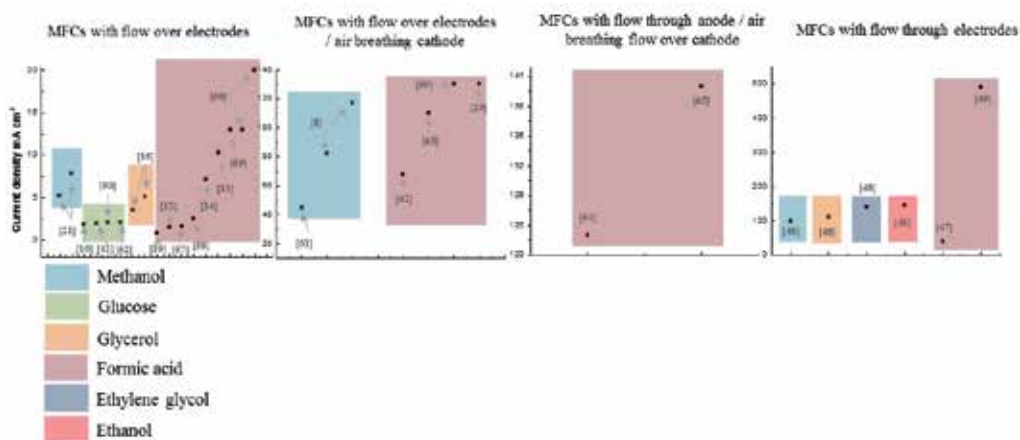


Figure 7. Current density evolution on single membraneless microfluidic fuel cells, which employ small organic molecules as fuel as function of contact form of fuel and oxidant streams to electrode surfaces (references used are listed from left to right) [21, 16, 51, 52, 12, 53, 54, 13, 55–57, 8, 58–61].

4. Fuels and performance evolution

Several research groups have worked on the development of such energy conversion devices that operate on various fuels such as glycerol, ethylene glycol, formic acid, glucose, ethanol, and methanol. Many designs have been optimized, as well as manufacturing techniques incorporating computational tools for modeling and construction photolithography equipment and numerical control systems, high-resolution components and electronic interconnect assembly, and development of electrocatalytic anodic and cathodic materials of inorganic and enzymatic nature.

In this context, we highlight the bimetallic core-shell materials (core-shell) used as anodes and cathodes for the oxidation of various fuels and the reduction of oxygen, respectively. For example, AuAg supported on nanoparticulated carbon was used for glucose electrooxidation in alkaline media [16, 50]. AuAg/C exhibited good stability, higher current density, and more negative anodic potential (ca. 150 mV) associated with this reaction than that achieved with bare Au supported on Vulcan. The performance of AuAg/C and Au/C was evaluated in a glucose laminar membraneless microfluidic fuel cell where the incorporation of Ag in the electrocatalyst contributed to increasing the AuAg/C activity using low Au loading.

With regard to recent development of cathodic electrocatalytic materials, stand-up PtAg/C alloys were employed for the oxygen reduction reaction (ORR). High selectivity for ORR was observed in the presence of glucose (100 mM) in basic media [51]. This result allowed the use of these bimetallic materials as cathode in an MFC that used glucose as fuel with an additional advantage arising from the use of less noble metal and less expensive material such as silver.

The combination of high selectivity of PtAg/C in the ORR and AuAg/C in the glucose oxidation reaction allowed the construction and evaluation of a glucose MFC with outstanding per-

formance at zero flow condition [52]. MFC was also evaluated with a simulated body fluid solution that contained salts commonly present in the human blood plasma, reaching a power of 240 mW cm^{-2} at zero flow. These results envisage the incorporation of this MFC as a portable power source in lab-on-a-chip devices without the need of external pumps.

Dector and coworkers developed a small air-breathing hybrid MFC using glucose from human serum and blood as a fuel with O_2 supplied from air [53]. This device showed an excellent performance (200 mW cm^{-2}) and good stability with potential applications as power source for use in building implantable and portable biomedical devices.

A new concept of membraneless air-breathing nanofluidic fuel cells with flow-through electrodes that can be powered by several fuels (individually or mixed) in alkaline media (i.e., methanol, ethanol, glycerol, and ethylene glycol) was recently reported [48]. A novel Cu@Pd core-shell electrocatalyst synthesized by chemical method revealed morphologies of nanorods particles of 10 nm in length and a typical semispherical particle with a diameter of 6 nm. The electrocatalytic properties of the rod/semispherical Cu@Pd nanoparticles supported on Vulcan carbon showed higher activity than commercial Pd/C in the electro-oxidation of each fuel and the mixture of them. The air-breathing nanofluidic fuel cells constructed with Cu@Pd/C anode exhibited individual power densities and current densities higher than 16 mW cm^{-2} and 100 mA cm^{-2} , respectively. A mixture of four fuels resulted in a voltage of 0.61 V with current and power densities of 108 mA cm^{-2} and 18 mW cm^{-2} , respectively. The reported devices displayed a better performance than current state-of-the-art systems and demonstrated the feasibility of developing multiuse nanodevices that provide constant power regardless of the fuel employed.

Finally, ethylene glycol has been used as fuel in PEM (polymer exchange membrane) fuel cells operating at temperatures ranging from 60 to 130°C [54, 55]. In microfluidic fuel cells, the use of ethylene glycol (EG) as well as glycerol has been sparse, and it could be related to the low performance by activity problems of electrocatalysts that are still found in PEM fuel cells. Arjona et al. [56] published, for the first time, the use of ethylene glycol in a membraneless MFC with lateral flow. In this work, a metal mixture of AuPd supported on polyaniline was used as anode. The performance device was tested as a function of EG concentration showing a maximum performance at 2 M EG and room temperature. A cell voltage of 0.53 V and a maximum current and power density of 14.2 mA cm^{-2} and 1.6 mW cm^{-2} , respectively, were achieved using oxygen from a saturated solution. The resulting cell voltage was comparable with those values reported for PEM fuel cells (0.4–0.65 V), which operate at higher temperatures ($60\text{--}90^\circ\text{C}$) [54, 55]. The finding was attributed to the enhancement in the electronic properties by the metal-metal AuPd interactions as well as the effect of polyaniline, which could enhance the metal/support interactions.

5. Conclusions and perspectives

Many reports published in the last decades have contributed to several findings in the MFC technological area. As discussed, numerous issues relevant to MFCs need further investigation and optimization.

The current trend is to develop devices that combine all three properties: power generation, energy storage, and electronic interface for a specific application. These three functions integrated in a single device with a dimension in the micro- or nanometrics have placed the technology in the category of lab-on-a-chip.

Some limiting conditions, such as potential drop and ohmic resistance, have been observed in the assembly of these MFCs. All electrical contacts and external circuit wiring are necessary to be optimized in order to reduce their impact on the MFC performance. The new machining technologies, such as three-dimensional printing, offer a precise and accurate option to develop the cell assembly parts.

In terms of electrochemistry, charge transfer is also a problem that affects many systems to date. These phenomena can be studied by properly implementing a reference electrode to provide a more detailed insight into the electrochemical processes occurring in each compartment. The sluggish kinetics is usually related to the electrocatalytic material and proper pH selection. However, temperature, fuel concentration, and other physicochemical parameters are factors to investigate with each new emerging cell design.

The development of these devices involves a multidisciplinary task in electrochemistry, nanotechnology, electronics, physics, mathematics, mechanical engineering, computer sciences, biotechnology, biomedical, and environmental engineering.

Acknowledgements

The authors thanks to Mexican Council of Science and Technology CONACYT for the financial support through the projects Laboratorio Nacional (Grant LN271649) and Fronteras de la Ciencia (Grant 611).

Author details

Jesus A. Diaz-Real¹, Minerva Guerra-Balcázar², Noe Arjona¹, Francisco Cuevas-Muñiz¹, Luis Gerardo Arriaga¹ and Janet Ledesma-García^{1*}

*Address all correspondence to: janet.ledesma@uaq.mx

1 Center Research and Technological Development in Electrochemistry, Parque Tecnológico Queretaro Sanfandila, Queretaro, Mexico

2 Division of Research and Postgraduate, Facultad de Ingeniería, Universidad Autónoma de Queretaro, Cerro de las Campanas, Queretaro, Mexico

References

- [1] Chih-Ming H, Yu-Chong T, Micro-electro-mechanical-systems (MEMS) and fluid flows. *Fluid Mechan.* 1998;30:579–612. doi:10.1146/annurev.fluid.30.1.579
- [2] Lamy C, Demarconnay L, Coutanceau C, Leger J, Development of electrocatalysts for the solid alkaline membrane fuel cell (SAMFC). In *ECS Trans* 3 (1); october 29–november 3, 2006; Cancun. Mexico; pp. 1351–1360.
- [3] Chohan ER, Markoski LJ, Stoltzfus J, Moore JS, Kenis PJA, Microfluidic Fuel Cells that Lack a PEM. *Power Sources Proc.* 2002;40:317–320.
- [4] Goulet MA, Kjeang E, Co-laminar flow cells for electrochemical energy conversion. *J. Power Sources* 2014; 260:186–196. doi:10.1016/j.jpowsour.2014.03.009
- [5] Mousavi Shaegh SA, Nguyen NT, Chan SH, A review on membraneless laminar flow-based fuel cells. *Int. J. Hydrogen Energ.* 2011;36:5675–5694. doi:10.1016/j.ijhydene.2011.01.063
- [6] Chohan ER, Waszczuk P, Kenis PJA, Characterization of Limiting Factors in Laminar Flow-Based Membraneless Microfuel Cells. *Electrochem. Solid-State Lett.* 2005;8:A348–A352. doi:10.1149/1.1921131
- [7] Hollinger AS, Kenis PJA, Manufacturing all-polymer laminar flow-based fuel cells. *J. Power Sources* 2013;240:486–493. doi:10.1016/j.jpowsour.2013.04.053
- [8] Jayashree RS, Egas D, Spendelow JS, Natarajan D, Markoski LJ, Kenis PJA, Air-Breathing Laminar Flow-Based Direct Methanol Fuel Cell with Alkaline Electrolyte. *Electrochem. Solid-State Lett.* 2006;9:A252–A256. doi:10.1149/1.2185836
- [9] Whipple DT, Jayashree RS, Egas D, Alonso-Vante N, Kenis PJA, Ruthenium cluster-like chalcogenide as a methanol tolerant cathode catalyst in air-breathing laminar flow fuel cells. *Electrochim. Acta* 2009;54:4384–4388. doi:10.1016/j.electacta.2009.03.013
- [10] Chohan ER, Markoski LJ, Wieckowski A, Kenis PJA, Microfluidic fuel cell based on laminar flow. *J. Power Sources* 2004;128:54–60. doi:10.1016/j.jpowsour.2003.11.052
- [11] Morales-Acosta D, Morales-Acosta MD, Godinez LA, Alvarez-Contreras L, Duron-Torres SM, Ledesma-García J, Arriaga LG, PdCo supported on multiwalled carbon nanotubes as an anode catalyst in a microfluidic formic acid fuel cell. *J. Power Sources* 2011;196:9270–9275. doi:10.1016/j.jpowsour.2011.07.064
- [12] Cohen JL, Westly DA, Pechenik A, Abruña HD, Fabrication and preliminary testing of a planar membraneless microchannel fuel cell. *J. Power Sources* 2005;139:96–105. doi:10.1016/j.jpowsour.2004.06.072
- [13] Dector A, Esquivel JP, González MJ, Guerra-Balcázar M, Ledesma-García J, Sabaté N, Arriaga LG, Formic acid microfluidic fuel cell evaluation in different oxidant conditions. *Electrochim. Acta* 2013;92:31–35. doi:10.1016/j.electacta.2012.12.134

- [14] Morales-Acosta D, Rodríguez GH, Godínez LA, Arriaga LG, Performance increase of microfluidic formic acid fuel cell using Pd/MWCNTs as catalyst. *J. Power Sources* 2010;195:1862–1865. doi:10.1016/j.jpowsour.2009.10.007
- [15] Dector A, Cuevas-Muñiz FM, Guerra-Balcázar M, Godínez LA, Ledesma-García J, Arriaga LG, Glycerol oxidation in a microfluidic fuel cell using Pd/C and Pd/MWCNT anodes electrodes. *Int. J. Hydrogen Energy* 2013;38:12617–12622. doi:10.1016/j.ijhydene.2012.12.030
- [16] Cuevas-Muñiz FM, Guerra-Balcázar M, Castaneda F, Ledesma-García J, Arriaga LG, Performance of Au and AuAg nanoparticles supported on Vulcan in a glucose laminar membraneless microfuel cell. *J. Power Sources* 2011;196: 5853–5857. doi:10.1016/j.jpowsour.2011.02.081
- [17] Galindo R, Dector A, Arriaga LG, Gutiérrez S, Herrasti P, Maghemite as a catalyst for glucose oxidation in a microfluidic fuel cell. *J. Electroanal. Chem.* 2012;671:38–43. doi:10.1016/j.jelechem.2012.02.020
- [18] Cohen JL, Volpe DJ, Westly DA, Pechenik A, Abruña HD, A Dual Electrolyte H₂/O₂ Planar Membraneless Microchannel Fuel Cell System with Open Circuit Potentials in Excess of 1.4 V. *Langmuir* 2005;21:3544–3550. doi: 10.1021/la0479307
- [19] Ferrigno R, Stroock AD, Clark TD, Mayer M, Whitesides GM. Membraneless Vanadium Redox Fuel Cell Using Laminar Flow. *J. Am. Chem. Soc.* 2002;124:12930–12931. doi: 10.1021/ja020812q
- [20] Lee JW, Kjeang E, Nanofluidic fuel cell. *J. Power Sources* 2013;242:472–477. doi:10.1016/j.jpowsour.2013.05.129
- [21] Chohan ER, Spendelow JS, Gancs L, Wieckowski A, Kenis PJA, Membraneless laminar flow-based micro fuel cells operating in alkaline, acidic, and acidic/alkaline media. *Electrochim. Acta* 2005;50:5390–5398
- [22] Gonzalez-Guerrero MJ, Esquivel JP, Sánchez-Molas, Godignon P, Muñoz FX, Del Campo FJ, Giroud F, Minter SD, Sabaté N, Membraneless glucose/O₂ microfluidic enzymatic biofuel cell using pyrolyzed photoresist film electrodes. *Lab Chip* 2013;13:2972–2979. doi: 10.1039/C3LC50319D
- [23] Hasegawa S, Shimotani K, Kishi K, Watanabe H, Electricity Generation from Decomposition of Hydrogen Peroxide. *Electrochem. Solid-State Lett.* 2005;8: A119–A121. doi:10.1149/1.1849112
- [24] Kjeang E, Brolo AG, Harrington DA, Djilali N, Sinton D, Hydrogen Peroxide as an Oxidant for Microfluidic Fuel Cells. *J. Electrochem. Soc.* 2007;154:B1220–B1226. doi:10.1149/1.2784185
- [25] Kjeang E, Proctor BT, Brolo AG, Harrington DA, Djilali N, Sinton D, High-performance microfluidic vanadium redox fuel cell. *Electrochim. Acta* 2007;52:4942–4946. doi:10.1016/j.electacta.2007.01.062

- [26] Moore S, Sinton D, Erickson D, A plate-frame flow-through microfluidic fuel cell stack. *J. Power Sources* 2011;196:9481–9487. doi:10.1016/j.jpowsour.2011.07.024
- [27] Salloum KS, Hayer JR, Friese CA, Posner JD, Sequential flow membraneless microfluidic fuel cell with porous electrodes. *J. Power Sources* 2008;180:243–252. doi: 10.1016/j.jpowsour.2007.12.116
- [28] Fuerth D, Bazylak A, Up-Scaled Microfluidic Fuel Cells With Porous Flow-Through Electrodes. *J. Fluids Eng.* 2013;135:021102–021102-7. doi: 10.1115/1.4023449
- [29] Jayashree RS, Gancs L, Choban ER, Primak A, Natarajan D, Markoski LJ, Kenis PJA, Air-Breathing Laminar Flow-Based Microfluidic Fuel Cell. *J. Am. Chem. Soc.* 2005;127:16758–16759. doi: 10.1021/ja054599k
- [30] Yoon SK, Mitchell M, Choban ER, Kenis PJA, Gravity-induced reorientation of the interface between two liquids of different densities flowing laminarly through a micro-channel. *Lab Chip* 2005;5:1259–1263. doi: 10.1039/B508680A
- [31] Kjeang E, Michel R, Harrington DA, Djilali N, Sinton D, A Microfluidic Fuel Cell with Flow-Through Porous Electrodes. *J. Am. Chem. Soc.* 2008;130:4000–4006 doi: 10.1021/ja078248c
- [32] Zhao T, editor. *Micro Fuel Cells: Principles and Applications*. Burlington MA USA: Elsevier Science; 2009. 300 pp. doi:10.1016/B978-0-12-374713-6.00009-3
- [33] Koper MTM, editor. *Fuel Cell Catalysis: A Surface Science Approach*, Wiley; 2008. 697 pp. doi:10.1002/9780470463772
- [34] Dean JA, Lange's Handbook of chemistry. 15th ed. New York: McGraw-Hill; 1973. ISBN 0-07-016384-7.
- [35] Zhang J, *PEM Fuel Cell Electrocatalysts and Catalyst Layers: Fundamentals and applications*. London UK: Springer London; 2008. 1094 pp. doi: 10.1007/978-1-84800-936-3
- [36] Ho B, Kjeang E, Microfluidic fuel cell systems, *Cen. Eur. J. Eng.* 2011;2:123–131. doi: 10.2478/s13531-011-0012-y
- [37] Weinmueller C, Tautschnig G, Hotz N, Poulikakos D, A flexible direct methanol micro-fuel cell based on a metalized, photosensitive polymer film, *J. Power Sources* 2010;195:3849–3857. doi:10.1016/j.jpowsour.2009.12.092
- [38] Renaud L, Selloum D, Tingry S, Xurography for 2D and multi-level glucose/O₂ microfluidic biofuel cell. *Microfluid Nanofluid* 2015;18:1407–1416. doi: 10.1007/s10404-014-1539-z
- [39] Suriano R, Kuznetov A, Eaton SM, Kiyan R, Cerullo G, Chichkov BN, Levi M, Turri S, Femtosecond laser ablation of polymeric substrates for the fabrication of microfluidic channels, *App. Surface Sci.* 2011;257:6243–6250. doi:10.1016/j.apsusc.2011.02.053

- [40] Wong KV, Hernandez A, A Review of Additive Manufacturing. *ISRN Mechanical Engineering* 2012;2012:208760–208770. <http://dx.doi.org/10.5402/2012/208760>
- [41] Guerra-Balcázar M, Morales-Acosta D, Castaneda F, Ledesma-García J, Arriaga LG, Synthesis of Au/C and Au/Pani for anode electrodes in glucose microfluidic fuel cell, *Electrochem. Commun.* 2010;12:864–867. doi:10.1016/j.elecom.2010.04.009
- [42] Miachon S, Aldebert P, Internal hydration H₂/O₂ 100 cm² polymer electrolyte membrane fuel cell, *J. Power Sources* 1995;56:31–36. doi:10.1016/0378-7753(95)80005-2
- [43] Prater KB, Polymer electrolyte fuel cells: a review of recent developments, *J. Power Sources* 1994;51:129–144. doi:10.1016/0378-7753(94)01934-7
- [44] Lee WK, Ho CH, Van Zee JW, Murthy M, The effects of compression and gas diffusion layers on the performance of a PEM fuel cell, *J. Power Sources* 1999;84: 45-51. doi:10.1016/S0378-7753(99)00298-0
- [45] Glora M, Wiener M, Petricevic R, Pröbstle H, Fricke J, Integration of carbon aerogels in PEM fuel cells, *J. Non-Cryst. Solids*, 2001;285:283–287. doi:10.1016/S0022-3093(01)00468-9
- [46] Kjeang E, McKechnie J, Sinton D, Djilali N, Planar and three-dimensional microfluidic fuel cell architectures based on graphite rod electrodes, *J. Power Sources* 2007;168:379–390. doi:10.1016/j.jpowsour.2007.02.087
- [47] Arjona N, Goulet MA, Guerra-Balcázar M, Ledesma-García J, Kjeang E, Arriaga LG, Direct formic acid Microfluidic fuel cell with Pd nanocubes supported on flow-through microporous electrodes, *ECS Electrochem. Lett.* 2015;4:F24–F28. doi:10.1149/2.0031504eel
- [48] Maya-Cornejo J, Ortiz-Ortega E, Álvarez-Contreras L, Arjona N, Guerra-Balcázar M, Ledesma-García J, Arriaga LG, Copper-palladium core-shell as an anode in a multi-fuel membraneless nanofluidic fuel cell: toward a new era of small energy conversion devices, *Chem. Commun.* 2015;51:2536–2539. doi: 10.1039/C4CC08529A
- [49] Ortiz-Ortega E, Goulet MA, Lee JW, Guerra-Balcázar M, Arjona N, Kjeang E, Ledesma-García J, Arriaga LG, A nanofluidic direct formic acid fuel cell with a combined flow-through and air-breathing electrode for high performance, *Lab Chip* 2014;14:4596–4598. doi:10.1039/C4LC01010H
- [50] Cuevas-Muñiz FM, Guerra-Balcázar M, Esquivel JP, Sabaté N, Arriaga LG, Ledesma-García J, Glucose microfluidic fuel cell based on silver bimetallic selective catalysts for on-chip applications, *J. Power Sources* 2012;216:297–303. doi:10.1016/j.jpowsour.2012.05.101
- [51] Guerra-Balcázar M, Cuevas-Muñiz FM, Álvarez-Contreras L, Ledesma-García J, Arriaga LG, Evaluation of bimetallic catalyst PtAg/C as a glucose-tolerant oxygen reduction cathode, *J. Power Sources* 2012;197:121–128. doi:10.1016/j.jpowsour.2011.09.051

- [52] Arjona N, Dector A, Guerra-Balcázar M, Álvarez-Contreras L, Sabaté N, Esquivel JP, Ledesma-García J, Arriaga LG, Effect of metal content on the electrocatalytic activity of AuxPd mixtures and their use in a glucose membraneless microfluidic fuel cell, *RSC Adv.* 2014;4:26158–26165. doi: 10.1039/C4RA03141E
- [53] Dector A, Escalona-Villalpando RA, Dector D, Vallejo-Becerra V, Chavez-Ramírez AU, Arriaga LG, Ledesma-García J, Perspective use of direct human blood as an energy source in air-breathing hybrid microfluidic fuel cells. *J. Power Sources* 2015;288:70–75. doi:10.1016/j.jpowsour.2015.04.089
- [54] Serov A, Kwak C, Recent achievements in direct ethylene glycol fuel cells (DEGFC), *Appl. Catal. B* 2010;97:1–12. doi:10.1016/j.apcatb.2010.04.011
- [55] Livshits V, Peled E, Progress in the development of a high-power, direct ethylene glycol fuel cell (DEGFC). *J. Power Sources* 2006;161:1187–1191. doi:10.1016/j.jpowsour.2006.04.141
- [56] Arjona N, Palacios A, Moreno-Zuria A, Guerra-Balcázar M, Ledesma-García J, Arriaga LG, AuPd/polyaniline as the anode in an ethylene glycol microfluidic fuel cell operated at room temperature, *Chem. Commun.* 2014;50:8151–8153. doi: 10.1039/c4cc03288h
- [57] Li A, Chan SH, Nguyen NT, A laser-micro machined polymeric membraneless fuel cell, *J. Micromech. Microeng.* 2007;17:1107–1113. <http://dx.doi.org/10.1088/0960-1317/17/6/002>
- [58] Sun MH, Casquillas GV, Guo SS, Shi J, Ji H, Ouyang Q, Chen Y, Characterization of microfluidic fuel cell based on multiple laminar flow, *Microelectron. Eng.* 2007;84:1182–1185. doi:10.1016/j.mee.2007.01.175
- [59] Jayashree RS, Yoon SK, Brushett FR, Lopez-Montesinos PO, Natarajan D, Markoski LJ, Kenis PJA, On the performance of membraneless laminar flow-based fuel cells, *J. Power Sources* 2010;195:3569–3578. doi:10.1016/j.jpowsour.2009.12.029
- [60] Moreno-Zuria A, Dector A, Arjona N, Guerra-Balcázar M, Ledesma-García J, Esquivel JP, Sabaté N, Arriaga LG, Chávez-Ramírez AU, Formic acid microfluidic fuel cell based on well-defined Pd nanocubes, *J. Phys. Conf. Series* 2013;476:012033. doi: 10.1088/1742-6596/476/1/012033
- [61] J. P. Esquivel, F. J. Del Campo, J. L. Gómez de la Fuente, S. Rojas, N. Sabaté, Microfluidic fuel cells on paper: meeting the power needs of next generation lateral flow devices, *Energy Environ. Sci.*, 2014;7:1744–1749.
- [62] Mousavi Shaegh SA, Nguyen NY, Chan SH, An air-breathing microfluidic formic acid fuel cell with a porous planar anode: experimental and numerical investigations, *J. Micromech. Microeng.* 2010;20:105008. <http://dx.doi.org/10.1088/0960-1317/20/10/105008>

- [63] Ma J, Gago AS, Alonso-Vante N, Performance study of platinum nanoparticles supported onto MWCNT in a formic acid microfluidic fuel cell system, *J. Electrochem. Soc.* 2013;160:F859–F866; doi:10.1149/2.101308jes
- [64] Mousavi Shaegh SA, Nguyen NT, Chan SH, Zhou W, Air-breathing membraneless laminar flow-based fuel cell with flow-through anode, *Int. J. Hydrogen Energy* 2012;37:3466-3476. doi:10.1016/j.ijhydene.2011.11.051
- [65] Mousavi Shaegh SA, Nguyen NT, Chan SH, Air-breathing microfluidic fuel cell with fuel reservoir, *J. Power Sources* 2012;209:312–317. doi:10.1016/j.jpowsour.2012.02.115

Microfluidics in CO₂ Capture, Sequestration, and Applications

Taotao Fu

Additional information is available at the end of the chapter

<http://dx.doi.org/10.5772/64284>

Abstract

The abnormal climate change has made the reduction of CO₂ emission that received worldwide attention. The integration of CO₂ capture-sequestration application for enhanced oil recovery (EOR) technology will be the new trend. Several scholars have applied microfluidics in CO₂ capture, oil and gas analysis, and CO₂ sequestration. The mass transfer process for CO₂ capture can be intensified owing to the large specific surface/volume ratio and high contact area in microchannels. The small amount of feeding volumes of oil and gas samples and the quick response for the analysis make the microfluidics a promising tool for the oil and gas analysis. Moreover, microfluidics can reveal the transport mechanism at microscale for multiphase interfacial phenomena in microchannels within porous media during the CO₂ flooding process in line with the pressure, temperature, and material properties of the rock within the oil reservoir. This chapter will elaborate the progress of the application of microfluidic technology in the utilization of CO₂, including the mechanism of mass transfer for CO₂ in microreactors, the advantages of microfluidics in oil and gas analysis, and the fundamentals of microfluidics in CO₂ flooding, oil recovery improvement, and CO₂ sequestration.

Keywords: CO₂, fluid dynamics, interfacial phenomena, mass transfer, microfluidics, multiphase flow

1. Introduction

1.1. Progress of the intensification and mechanism of mass transfer for CO₂ capture in microreactors

Microreactors consist of microchannels with dimensions of several hundreds of micrometers. The pressure gradient, temperature gradient, and concentration gradient augment rapidly with the decrease of the length scale in microreactors, leading to the increase of the driving forces in mass transfer and heat transfer. With the scale down to micrometers, the surface/volume ratio

is enhanced usually to 10,000–50,000 m²/m³ (100–1000 m²/m³ in conventional equipment in chemical engineering processes), which is beneficial for the intensification of mass/heat transfer. The volume of the microreactors is significantly reduced also with the decrease of the length scale. Furthermore, the numbering-up strategy for the scale-up of microreactors is beneficial for the reactions with heat and explosion. The product properties can also be improved: strengthening of the transfer process can effectively improve the conversion, selectivity, and conversion rate of the product in the microreaction system. In addition, the microreactor is beneficial for the preparation of polymer particles, microcapsule and microemulsions due to the well-controlled property of the formation, structure, and composition of the polymer and the multiphase systems by using microreactors [1, 2]. The mass transfer process for CO₂ capture in microreactors is associated with the interfacial surface area between the CO₂ and the flowing liquid, contact method, reactor type and geometry, and flowing conditions as well as the liquid and gas properties [3]. Slug flow is found to be the most widely used flow pattern for CO₂ in flowing liquids in microchannels among other flow patterns such as bubbly flow, annular flow, and parallel flow. This section will review the fluid dynamics for gas-liquid two-phase flow in microchannels and the mass transfer mechanism for CO₂ capture in microreactors.

1.2. Pressure drop for gas-liquid two-phase flow in microchannels

The characteristics for the pressure for gas-liquid two-phase flow in microchannels differ significantly from those in conventional large-scale pipes due to the predominated effects of surface tension forces and viscous forces at the microscale in microchannels. The prediction for the pressure drop for gas-liquid two-phase flow in microchannels includes physical model, Lockhart-Martinelli model, and homogeneous model.

The pressure drop in the liquid filled microchannels with slug bubbles ΔP includes ΔP_B along the slug bubble induced by the frictional loss in the liquid film between the bubble and the channel walls, ΔP_{Caps} induced by the Laplace pressure across the caps of slug bubbles, and ΔP_F in the liquid plug. The pressure drop induced by the frictional loss in the liquid film and gutters between the bubble and the channel walls is often neglected in comparison with the other two kinds of pressure drops, both for bubbles in surfactant-free liquids and for the liquid phase with surfactants whose concentration is high enough [4, 5]. However, for intermediate concentrations of surfactant in the liquid, the pressure decreases rapidly across the body of the bubble owing to the concentration gradient of surfactant along the interface, giving rise to tangential surface tension tractions to immobilize the interface. This would increase the pressure drop across the bubble. Thus, bubbles within the channel can induce additional resistance to the flow, and the pressure drop across a single bubble within the microchannel ΔP_B can be evaluated by using Bretherton expression [6] and Ratulowski and Chang [7] expression, by assuming that Bretherton's law is valid in square and circular cross-section:

$$\Delta P_B = \begin{cases} 3.58 \frac{\sigma}{r} \left(\frac{3\mu u}{\sigma} \right)^{2/3} & \text{Ca} \leq 10^{-2} \\ 3.58 \frac{\sigma}{r} \left(\frac{3\mu u}{\sigma} \right)^{2/3} - 9.07 \frac{\sigma}{r} \left(\frac{3\mu u}{\sigma} \right)^{0.95} & 10^{-2} \leq \text{Ca} \leq 10^{-1} \end{cases} \quad (1)$$

where μ is the liquid viscosity, u is the superficial velocity of the gas-liquid flow, σ is the surface tension between the liquid and gas phases, and r is the radius of the microchannel. Whereas the whole Laplace pressure across bubbles in microchannels is related to the number of bubbles, which is hard to obtain in industrial processes. Thus, the whole Laplace pressure is always estimated by modifying the frictional factor for the pressure drop for single liquid-filled microchannel.

The frictional pressure between the liquid plug and the channel wall can be estimated by using the Hagen-Poiseuille equation at low Reynolds numbers, in which case the fluid flow in the liquid slug is deemed as laminar flow [8]:

$$\Delta P_f = f \left(\frac{4}{d_H} \right) \left(\frac{1}{2} \rho u^2 \right) (L_s) \quad (2)$$

where d_H is the equivalent diameter of the microchannel, ρ is the liquid density, and L_s is the length of the liquid plug. It should be pointed out that the pressure drop for gas-liquid two-phase flow in the slug bubble flow in microchannels is therefore related to the size and number of bubbles, which can modify the occupation for each part of pressure in the whole pressure drop in microchannels. However, for bubbles flowing in fluids in nontransparent microchannels during the application, the prediction of pressure drop for gas-liquid two-phase flow becomes difficult by using the physical model, as the lengths of the bubbles and liquid plugs are hard to obtain directly. It should be noted that the volume of a bubble flowing through a microchannel can be varied with the reduction of pressure along the channel. This effect becomes more pronounced in long microchannels. Moreover, the pressure drop of bubbles flowing in fluid-filled microchannels is also affected by the cross-section of the channel. Ratulowski and Chang [7] established an empirical expression to relate the pressure drop across a bubble and the capillary number in a square cross-sectional microchannel as $\Delta P_B = 12.2Ca^{0.55}$, when $3 \times 10^{-3} < Ca < 0.1$ [7, 9]. Wong et al. [10] extended Bretherton's analysis [6] to rectangular microchannels: $\Delta P_B \sim \sigma / r \sim Ca^{2/3}$. However, the analysis by Wong et al. [10] does not provide an explicit function form for $\Delta P_B \sim \sigma Ca^{2/3} / r$. Ca ($Ca = \mu u / \sigma$) is the capillary number, representing the ratio of the relative viscous force to surface tension force.

Lockhart and Martinelli proposed the prediction for gas-liquid two-phase flow in microchannels related to the pressure for a single liquid-filled microchannel by using a friction multiplier of the liquid phase, which can be expressed by the gas and liquid viscosity and density, and the volumetric fraction of the gas phase. In the homogeneous model, the gas and liquid phases are deemed to be mixed uniformly in microchannels. This model is proposed to predict the pressure drop for gas-liquid two-phase flow in conventional channels, with the prerequisite that the gas and liquid phases are mixed uniformly, i.e., the gas phase is dispersed uniformly in the liquid in the form of very tiny bubbles. However, in microchannels, this regime can only be achieved at extreme conditions. That is to say, this model is not valid in most situations in microfluidics applications.

1.3. Mass transfer of gas-liquid two-phase flow in microchannels

1.3.1. Mass transfer of gas-liquid two-phase flow under various flow patterns

The mass transfer between gas and liquid phases in microchannels dominates the flow patterns, which usually contain bubbly flow, slug flow, churn flow, annular flow, and parallel flow.

1.3.1.1. Bubbly flow

In this flow pattern, the diameter of bubbles is less than the channel diameter, which usually occurs under low superficial velocity of the gas phase and high superficial velocity of the liquid phase. The diameter of bubbles is manipulated by the gas and liquid flow rates, physical property of the fluids, and how two phases contact. In general, the surface area between gas and liquid phases increases with the reduction of the bubble size, which is beneficial for the enhancement of the mass transfer process.

1.3.1.2. Churn flow

Churn flow happens at high superficial velocity of the gas phase, within which long gas slugs and short liquid plugs pass through the channel. It is found that the mass transfer coefficient is higher in the churn flow than that in the slug flow. Yue et al. [11] found that the mass transfer coefficient increases with the increase of the gas flow rates and liquid flow rates.

1.3.1.3. Annular flow and parallel flow

When the superficial velocity of the gas phase is relatively high and that of the liquid phase is quite low, annular flow and parallel flow occurs, depending on the geometry of the contactor for the two-phase flows. The former is likely to happen at flow-focusing junctions, while the latter for T- and Y-junctions usually. In both cases, the gas and liquid streams flow in parallel along the microchannel, and the mass transfer thereby occurs at the interface of the gas-liquid two-phase flow. The experimental results show that in falling film microreactors, the enhancement of the mass transfer rate in the CO₂-monoethanolamine-H₂O system can be obtained [12]. However, the Marangoni effect in the falling film microreactor seems to be weaker than that in macrosystems, signifying that the convection is partially prevented by the limited size of the microchannel [12].

1.3.1.4. Slug flow

The mass transfer for slug flow in the gas-liquid two-phase flow in microchannels depends on the flow conditions, physical property of the fluids, the hydrodynamics of the fluids, and the geometry of microchannels. As this flow regime is always achieved at most of microfluidic applications, the following section will mainly focus on this flow regime.

1.3.2. Mass transfer mechanism

The key issue for mass transfer mechanism for gas-liquid two-phase flow in microchannels is to reveal the mass transfer rule across the gas-liquid interface and the influence of the lengths

of the gas slug and liquid plug on the mass transfer coefficient. Bercic et al. [13] investigated the absorption of CH₄ by using water in capillaries with diameters ranging from 1.5 to 3.1 mm, and found that the volumetric mass transfer coefficient $k_L a$ is predominated by the length of plugs rather than the length of bubbles when the liquid plugs are sufficient long. In their experiments, the mass transfer around the caps of the slugs dominates the whole process, and the mass transfer coefficient is proposed as

$$k_L a = \frac{0.111\mu^{1.19}}{\left((1 - \varepsilon_G)(L_B + L_S)\right)^{0.57}} \quad (3)$$

where L_B, L_S are, respectively, the length of the bubble and liquid plug. Van Baten et al. [14, 15] divided the mass transfer coefficient $k_L a$ for mass transport process for slug bubbles to the liquid plugs in vertical capillaries into two parts: one between bubbles' caps and plugs $k_{L, \text{cap}} a_{\text{cap}}$ and the other one between cylindrical parts of slug bubbles and the liquid films between the bubble and walls $k_{L, \text{film}} a_{\text{film}}$:

$$k_L a = k_{L, \text{film}} a_{\text{film}} + k_{L, \text{cap}} a_{\text{cap}} \quad (4)$$

When $Fo < 0.1$, both parts for the mass transfer process are important. When $Fo > 0.1$, the liquid films are saturated and the mass transfer between the caps and liquid plugs predominates. The liquid side mass transfer coefficient in the film can be calculated as

$$k_{L, \text{film}} = 2 \sqrt{\frac{D}{\pi t_{\text{film}}}} \frac{\ln(1/\Delta)}{1 - \Delta}; (Fo < 0.1), \text{ and} \quad (5)$$

$$k_{L, \text{film}} = 3.14 \frac{D}{\delta_{\text{film}}}; (Fo > 0.1) \quad (6)$$

where $(Fo = \frac{D}{t_{\text{film}} \delta_{\text{film}}^2})$, D is the diffusivity coefficient, and δ_{film} is the film thickness

$t_{\text{film}} = \frac{L_{\text{film}}}{U_B} \approx \frac{L_B - d_h}{U_B}$. Vandu et al. [16] found deviation between the experimental results and the predictions by using the expression proposed by van Baten et al. [14] for the absorption process of O₂ in water. They deemed that the deviation was caused by the fact that the van Baten et al.'s expression validated for long mass transfer unit, in which situation the liquid film between the bubble and the channel walls is saturated; while in the experiments of Vandu et al. [16], the length of the liquid film is short and the velocity of the bubble is high to make the liquid film unsaturated. Vandu et al. [16] obtained the mass transfer coefficient for the bubble caps

by using the classical penetration theory for mass transfer process as: $k_{L,cap} a_{cap} = 2 \frac{\sqrt{2}}{\pi} \sqrt{\frac{DU_B}{d_h}}$. Mass transfer coefficient for the liquid film by using the unsteady diffusion model as

$$k_{L, film} a_{film} = 2 \sqrt{\frac{DU_B}{\pi t_{film}}}$$

$$k_L a = \frac{2}{\sqrt{\pi}} \sqrt{\frac{DU_B}{(L_B - d_h) dh (L_B + L_S)}} + 2 \frac{\sqrt{2}}{\pi} \sqrt{\frac{DU_B}{d_h}} \frac{4}{L_B + L_S} \tag{7}$$

This equation is available for the situation when the mass transfer in the liquid film is predominated and unsaturated at $(u / L_S)^{0.5} > 3s^{-0.5}$. Another experimental fitting proposed by Yue et al. [17] is illustrated as $k_L a = 2(DU_B / (L_B + L_S))^{0.5} (L_B / (L_B + L_S))^{0.3} \cdot d_H^{-1}$ by performing experiments for the absorption of O₂ in water in square microchannels. The experiments of Yue et al. [17] were operated under short film contact time so that the mixing between the liquid film and the liquid plug is poor. In this case, the predictions proposed by van Baten et al. [14] and Vandu et al. [16] are not applicable. It is noteworthy that these expressions are applicable for physical absorptions process with tiny mass transfer between gas and liquid phases, in which the characteristic parameters for bubble slugs and liquid plugs should be evaluated to obtain the mass transfer coefficient. This limits the applications of these predictions. Furthermore, Yue et al. [17] suggested that the quantitative information on the circulation in liquid plugs and the mixing between the liquid film and liquid plug needs to be revealed for constructing a universal model for mass transfer in bubble slug flow pattern for the gas-liquid two-phase flow in microchannels.

For practical application several predictions for the mass transfer coefficient were proposed by using either the nondimensional analysis or energy dissipative model. Yue et al. [11] correlated the mass transfer coefficient in the form of the Sherwood number Sh with the Schmidt number Sc (representing the physical property of the fluids) and the Reynolds number Re (representing the flow conditions) as $Sh_L \cdot a \cdot d_h = 0.084 Re_G^{0.213} Re_L^{0.937} Sc_L^{0.5}$ for slug flow for the physical absorption of CO₂ into water in rectangular microchannels. Sh_L is the liquid Sherwood number defined by $Sh_L = k_L d_h / D_{CO_2}$, representing the relative magnitude of the liquid side mass transfer coefficient k_L to the diffusivity of CO₂ in the liquid. Sc_L is the liquid Schmidt number defined by $Sc_L = \mu_L / \rho_L D_{CO_2}$, representing the relative magnitude of the momentum diffusivity to the mass diffusivity. Re_G and Re_L are respectively the Reynolds number of the gas and liquid phases, defined by $Re = \rho u d_h / \mu$, representing the relative magnitude of the inertial forces to the viscous forces. These methods provide experimentally and semitheoretically the mass transfer coefficient prediction with relatively high precision only if the applications are conducted within the range of the experimental conditions performed by Yue et al. [11]. However, this method needs a series of experiments in a wide range.

The energy dissipative model [18] correlates the mass transfer coefficient with the dissipative parameter ζ (defined as $\zeta = \left(\frac{\Delta p_F}{L} \right)_{TP} u$) as the pressure drop along the channel differs for the

gas-liquid two-phase flow with and without mass transfer [18]. Δp_F is the two-phase frictional pressure drop, L is the length of the microchannel, and u is the superficial velocity. The subscript TP represents the two-phase flow. Yue et al. [11] applied this function in mass transfer for the absorption of CO₂ in water in microchannels and proposed a similar expression as $k_L a = 0.0863 \left(\frac{\Delta P_F}{L} \right)_{TP}^{0.881}$ performs well for the relatively small mass transfer rates, in which situation the mass transfer process has little effect on the flow dynamics of the gas-liquid two-phase flow in microchannels. In addition, the frictional pressure drop needs to be obtained for predicting the mass transfer coefficient in this method, limiting its usage.

1.3.3. Effects on the mass transfer process

Several studies have been performed for the various effects on the mass transfer process in microchannels. Eskin et al. [19] did experiments to study the effects of the size and length of microchannels on the mass transfer process for gas-liquid two-phase flow in microchannels, and found that the mass transfer coefficient increases with the reduction of the cross-sectional radius of microchannels. They proposed a model to predict the mass transfer coefficient for the mass transfer process of slug bubbles with the liquid plugs in long microchannels by taking into account the dynamical flow hydrodynamics such as pressure drop, variation of bubble size, and the variation of the local velocities. Shao et al. [20] conducted experiments on mass transfer process of CO₂/N₂ in 0.2 M NaOH aqueous solutions and water, respectively, in 0.25–1 mm capillaries, and found that the volumetric mass transfer coefficient for the chemical absorption process is 3–12 times compared to the physical absorption process. They also studied the effects of the length of slug bubbles and liquid plugs, the velocity of bubbles, and the size of microchannels on the mass transfer process, and found that the volumetric mass transfer coefficient ranged between 0.3 and 0.5 s⁻¹. Sobieszuk et al. [21] measured the interfacial area in the slug flow in a microchannel by using the Danckwerts' method for the CO₂ absorption from CO₂/N₂ mixture into KHCO₃/K₂CO₃ buffer solutions, and provides, for the first time, the mass transfer coefficients separately for the liquid film and the liquid caps. Sobieszuk et al. [12] further found that the enhancement of the overall rate of the mass transfer depends on the gas concentrations. Ichiyanagi et al. [22] performed detailed three-dimensional measurements of the velocity and concentration distributions for CO₂ dissolution process through the gas-liquid interface in microchannels by using the advanced technique confocal micron-resolution particle image velocimetry (micro-PIV) combined with laser-induced fluorescence (LIF). The LIF measurement demonstrated that the dissolved gas in the spanwise direction decreases with the increase of the Reynolds number. The molar fluxes in the streamwise direction were at least 20 times compared to those in the spanwise and depthwise directions, signifying that the enhancement of the momentum transport in the spanwise and depthwise directions plays an important role in the enhancement of the mass transfer for gas-liquid slug flow in microchannels.

Several investigations have been carried out on the dynamical mass transfer process for slug bubbles for gas-liquid two-phase flow in microchannels by taking advantage of the real-time recording of the movement of bubbles in microchannels with the help of high-speed digital

camera [23-28]. Tan et al. [23] found that bubbles formed during the mass transfer process of a CO₂/N₂ mixture with contact with the NaOH aqueous solution at the microfluidic T-junction are smaller than those formed without mass transfer process. The typical time for bubble formation ranges between 0.2 and 0.4s, during which the amount of mass transfer contributes to around 30–40% of the total transferred solute. The overall mass transfer coefficient during bubble formation stage is in the range of 1.4×10^{-4} to 5.5×10^{-4} m/s, and it increases with the elevation of the gas and liquid flow rates. It is deemed that the resistance in the gas side during the mass transfer process predominates; and the circulation in the slug bubbles significantly intensifies the mass transfer with the enhancement factor in the range of 5–15. Furthermore, they studied the effects of the angle of the junction on the mass transfer coefficient and found that the mass transfer coefficient in the liquid size achieves its maximum at 90° junction, and reaches its minimum at 150° junction.

1.3.4. Intensification of the mass transfer process

In order to intensify the mass transfer of CO₂ in fluids in microreactors, several methods have been employed, such as inducing turbulence by using the third inert gas and obstacles or particles in channels, specific geometry (curved) of the channel, and active forces. Su et al. [29] found that the mass transfer process can be intensified by adding solid particles in microchannels. Su et al. [30] introduced the third phase-inert gas into the liquid-liquid two-phase flow in microchannels to enhance the mass transfer coefficient. Tan et al. [24] performed experiments to study the effects of the curvature of the curved geometry for microchannels on the absorption of CO₂ for a CO₂/N₂ mixture contacting with NaOH aqueous solution, and found that the mass transfer coefficient is greatly augmented with the decrease of the curvature radius. That is, k_L in curved channels with the curve radius of 3 cm is nearly two times compared to that in a straight channel. They also proposed an expression to predict the mass transfer coefficient as $k_{L,R}/k_{L,R-\infty} = 1 + 91d_H/R$, where $k_{L,R}$ and $k_{L,R-\infty}$ are respectively the overall mass transfer coefficient in the curved channel with curve radius of R and in a straight channel, and d_H is the hydrodynamic radius of the microchannel.

The mechanism for mass transfer during CO₂ bubbles flowing in microchannels needs to be explored to be manipulated according to various applications, especially more attention should be paid to the dynamics of the gas-liquid interface during the mass transfer process and provide solid foundations for the coupling of transport and reaction, scale-up, and optimization of microreactors.

2. Microfluidic technology in oil and gas analysis, and CO₂ applications

Recently, microfluidic technique is found to be a promising tool for the oil and gas analysis, for measurements of parameters such as Henry's coefficient, solubility of gas in the liquid phase, and the gas-liquid reaction coefficient [31]. Sell et al. [32] provided a microfluidics technique to measure the diffusion coefficient for CO₂ in water and brine, with the advantage of only microliters of sample and analysis within minutes (Figure 1). However, established

macroscale pressure-volume-temperature cell methods require large sample volumes, which is completed within hours or days. They also found that pressure had no significant effect on diffusion rates, supporting an assumption applied by many sequestration models. Namely, time scales for dissolution are independent of reservoir depth or *ex situ* carbonation pressures. Fadaei et al. [33] also provided a microfluidic method to rapidly measure the CO₂ diffusivity in Bitumen, with the range of pressures of 1–5 MPa and at a room temperature of 21°C. They obtained the diffusion coefficients in the order of 10⁻¹⁰ m²/s, agreeing well with the relevant published data using conventional methods. Compared to the traditional methods (with 0.5 L of sample within hours or days), this method requires only 10 minutes and 1 nL plug of sample.

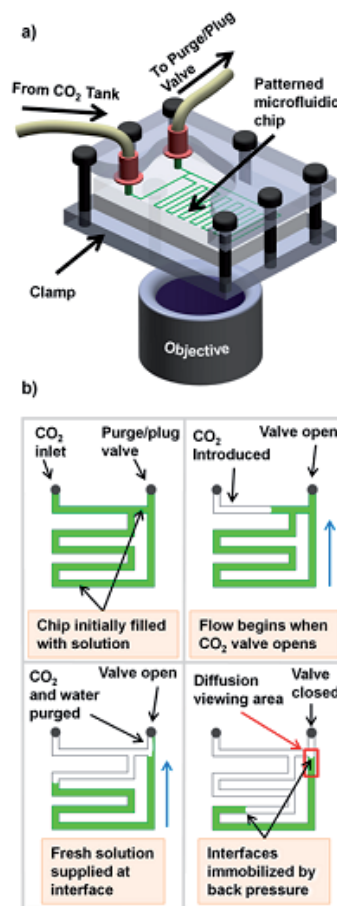


Figure 1. Microfluidic system used to measure the CO₂ diffusion coefficients in water. (a) Illustration of the experimental setup. (b) Schematic of the CO₂ diffusivity test initialization procedure. “Reprinted (adapted) with permission from Sell, A., Fadaei, H., Kim, M., Sinton, D., 2013. Measurement of CO₂ diffusivity for carbon sequestration: a microfluidic approach for reservoir-specific analysis. *Environmental Science & Technology* 47, 71–78. Copyright (2013) American Chemical Society.” (Sell et al. [32]) <http://dx.doi.org/10.1021/es303319q>

Lefortier et al. [34] presented a high-throughput method to rapidly measure the diffusion coefficients and solubility of CO_2 in pure solvents and mixtures in realtime by taking advantage of the visualization of the variation of CO_2 absorption fluids in microchannels. Sun and Cubaud [25] experimentally study the dissolution of CO_2 into water, ethanol, and methanol by using the microfluidic technique (Figure 2), and found that the bubble dissolution rate depends on the inlet gas pressure and fluid pair composition. For short period of time after the contact of fluids, the bubble length decreases linearly with time, displaying a fast diffusive behavior owing to the CO_2 concentration gradient localized in the thin gas-liquid interfacial region. The initial rate of the diminishing bubble size is proportional to the ratio of the diffusion coefficient to the Henry's law constant. This study shows that the gas saturation and sequestration processes can be achieved rapidly across quite short distances in microfluidic devices.

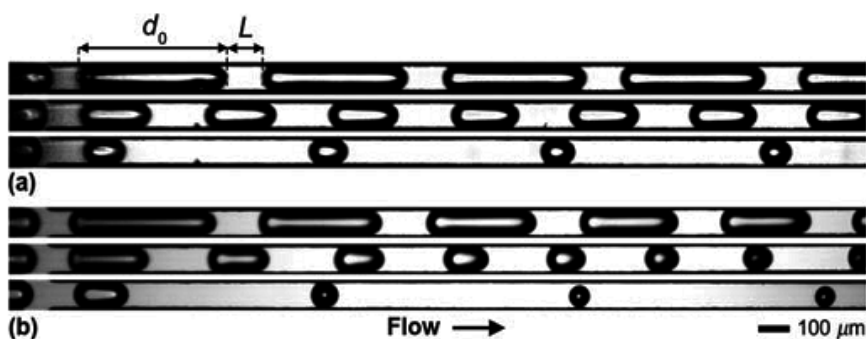


Figure 2. Examples of diffusive multiphase flows. (a) Weakly diffusive bubbles for CO_2 in water. The ratio of the liquid volumetric flow rates to the sum of the gas and liquid flow rates is 0.23, 0.47, and 0.80 from top to bottom. (b) Strong diffusive bubbles for CO_2 in methanol. The ratio of the liquid volumetric flow rates to the sum of the gas and liquid flow rates is 0.24, 0.51, and 0.68 from top to bottom. Reproduced from Sun and Cubaud [25] with permission of The Royal Society of Chemistry. <http://dx.doi.org/10.1039/C1LC20348G>

Abolhasani et al. [35] studied the automated microfluidic method for the rapid measurement of CO_2 mass transfer and solubility in physical solvents. The variation of slug bubbles flowing along the microchannel was dynamically recorded and analyzed to obtain the solubility of CO_2 in solvent. For CO_2 -dimethyl carbonate (DMC) system, the volumetric mass transfer coefficients ranged between 4 and 30 s^{-1} , and Henry's constants were within the range of 6–12 MPa. Li et al. [36] presented a microfluidic method to study rapid gas-liquid reactions for the rapid acquisition of the kinetic data for the reaction by also capturing the dynamical variation of slug bubbles flowing in microchannels (Figure 3). In this work, the application of microfluidic method was utilized for systems with relatively low concentrations of the reagents and products and for the low-viscosity media. This method is expected to apply for the CO_2 sequestration in the oil industry. Tumarkin et al. [37] conducted similar experiments to manipulate the solubility of CO_2 in water and a 0.7 M NaCl aqueous solution, by controlling the temperature of the fluids flowing in the microchannel. Bubbles experience shrinkage-expansion-shrinkage stage, termed as “bubble breathing,” when the cooling-heating-cooling system is applied to the bubble flowing system. Tumarkin et al. [38] controlled the size of

CO₂ bubbles by manipulating the temperature of the fluids, and functional particles were loaded at the gas-liquid interface to stabilize the bubble from coalescence. Park et al. [39] produced small CO₂ bubbles with a diameter less than 8 μm in microfluidic devices by manipulating the pH value of the liquid phase, and found that the bubble size depends on the flow rates of the liquid phase and the acid-base equilibrium established in the microchannels.

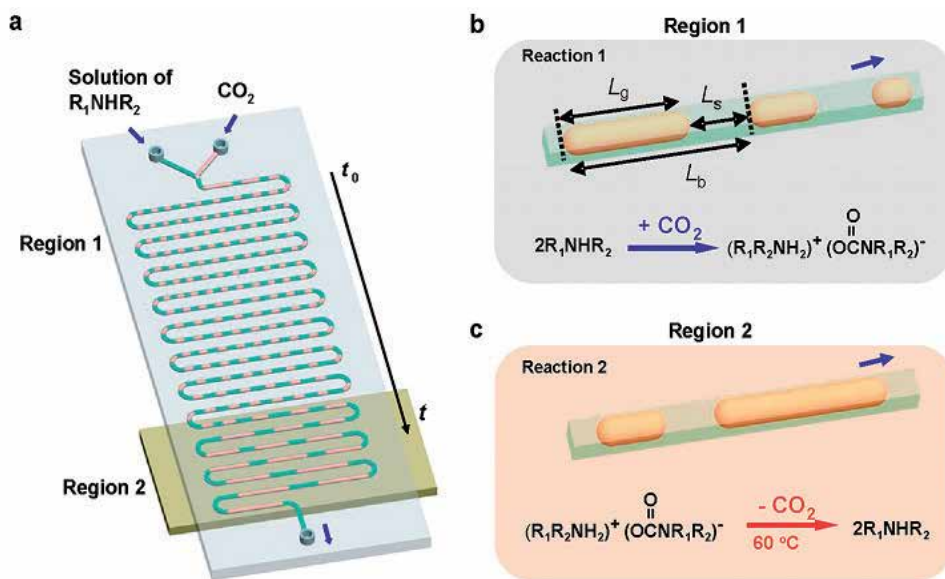


Figure 3. Reversible CO₂ binding to secondary amines performed in the microfluidic reactor. An ITO glass-based heater is placed underneath region 2, and an aluminum plate is placed underneath region 1 to maintain the temperature in this region at 23°C. (b) Reaction of CO₂ with a secondary amine in reaction 1, and the volume of CO₂ slugs decreases with CO₂ reacts with R₁NHR₂. (c) Release of CO₂ manipulated by the increase of the temperature in reaction 2. “Reprinted with permission from Li, W., Liu, K., Simms, R., Greener, J., Jagadeesan, D., Pinto, S., Gunther, A., Kumacheva, E., 2012. Microfluidic study of fast gas-liquid reactions. *Journal of the American Chemical Society* 134, 3127–3132. Copyright (2012) American Chemical Society.” (Li et al. [36]) <http://dx.doi.org/10.1021/ja2101278>

In summary, the microfluidic technique is a promising tool toward the measurement of the physical property of fluids involved during the CO₂ application, and gas and oil analysis, with the advantage of small sample size and short analysis time. However, the dynamics and mechanisms of the fluid flow and mass transfer in microchannels needs to be highlighted to meet these applications.

3. Microfluidic technology in CO₂ flooding, improving the oil recovery and CO₂ sequestration

With the increasing concern on environmental protection, the integration of CO₂ capture-sequestration-application for enhanced oil recovery technology will be the new trend in the

future. Microfluidics technology, with the unique advantages in realtime visualization and quantification, can reveal the transport mechanism in the microscale for multiphase interfacial phenomena in microchannels within porous media during the CO₂ capture-sequestration-application in line with the pressure, temperature, and material properties of the rock within the oil reservoir. These wells or salt sand underground aquifers comprise of porous media made of many tens of microchannels in a network structure, which are consistent with the conventional scale of microchannels used in the microfluidic technique [31].

3.1. Fluid dynamics

When CO₂ is injected into underneath wells, it becomes a supercritical fluid at the underground temperature and pressure. It is lighter than oil or brine and denser than CO₂ that is under normal conditions. Driven by the pressure, superficial CO₂ flows through the liquid-filled microchannel networks in the rock layer of porous media, and its flow paths are influenced by the heterogeneous structure of the porous media [40]. In microchannels, the tongue of CO₂ gaseous thread can breakup into bubbles driven by the capillary instability, and the generated bubbles can be captured or move through a straight microchannel or bifurcation junctions. Of course, these CO₂ bubbles will be absorbed slowly by the liquid phase [41]. In a CO₂ injection process, it usually takes three or four decades or even centuries of time for the complete absorption of CO₂. Although the microfluidic technology has been applied to study the CO₂ flooding in recent years, these studies on the dynamics and mechanics of multiphase flow in porous media consisting of microchannel networks have been carried out in the mid-20th century by the fluid mechanics community [42, 43]. For example, the famous viscous fingering phenomenon for miscible and immiscible two-phase flow in Hele-Shaw cells (rectilinear flow or radial source flow) has attracted attention for many years including the stability and nonstability mechanism of the interface, the bubble capture and release mechanism, the rupture of the interface, and the tip streaming of droplets and bubbles [44]. The interfacial phenomenon in the basic unit of the porous media network, or the loops of microchannels, has also been explored including the interfacial stability in symmetric and asymmetric loops and bubble capture in asymmetric loops [45-48]. For example, Oxaal et al. [45] studied the displacement of a high-viscosity fluid by a low-viscosity fluid that results in viscous fingering in homogeneous porous media. They found that the interfacial dynamics was dominated by the viscous forces at high flow rates and by capillary forces at low flow rates. Lenormand et al. [49] proposed a leaking mechanism to explain the dynamic phenomena in drainage for the displacement of one fluid by another in a network consisting of many ducts. They found that the wetting fluid motion at the edges was much slower than the nonwetting fluid, which was affected by the viscosity of the latter fluid. The local phenomenon was found to be linked with the drainage pressure and imbibition pressures at the microscale, and the macroscopic effect at the network scale was found to be related to the topology of the nonwetting fluid at the end of the drainage. The dynamics of trapped bubbles was influenced by their size and topology.

Recently, with the development of microfluidic techniques, detailed information on the two-phase interfacial phenomena in microfluidic loops has been explored. Al-Housseiny et al. [48]

provided a microfluidic tool to control the interfacial instability by changing the geometry of the device, and found that a gradient in the passage can lead to different displacement behaviors. This finding can be used to manipulate instabilities in fluid-fluid systems in microfluidic devices. The interesting and complex problem is that the fluid can penetrate evenly or not the two identical daughter channels in a network composed of two identical channels that are linearly vary in radius [46, 47]. When the surface tension predominates at low capillary numbers, this geometry can lead to the fluid to enter only one of the two branches, signifying that the uniform fluid penetration into the network is not always stable. At high capillary number Ca , the interface advances together and the fluid penetration is stable as viscous forces are dominant. The system can also exhibit an interplay between viscous and surface tension effects. In addition, the preferential flow penetration increases with the decrease of the viscosity ratio. This study suggested that the sweep efficiency could be enhanced if the channels in the network became narrower in the flow direction for flushing wetting oils by a low viscosity solvent. They also showed that the presence of an elastic boundary could lead to the suppression of the instability of the dynamics of the propagating gas-liquid interface for the Hele-Shaw displacement of a viscous liquid by a gas underneath an elastic membrane, governed by the surface tension at the gas-liquid interface due to the tapered flow geometry underneath the deflected membrane [50]. Controlling instability of fingers for fluid-fluid interface is fundamental to a wide range of applications such as flows in porous media in enhanced oil recovery processes and carbon sequestration [47]. Other examples of two-phase flows in spatially varying geometries are flows of bubbles and drops through junctions, constricted capillaries, flexible tubes, and tapered channels [4, 41, 51-53]. Bubbles and droplets can pass through, be captured, stay or leave, and even break up into small ones in spatially varying geometries. For example, bubbles can be trapped or released from a linear pore, governed by a capillary number [41]. The critical capillary number characteristic of the transition between trapping and releasing depends nonmonotonically on the bubble size. To better explore the dynamics of the gas-liquid interface in microchannels, the detailed flow-field distribution can be provided by advanced measurement methods, such as micro-PIV (Figure 4) [4].

3.2. Oil recovery

Haas et al. [54] presented a lab-on-a-chip method to inform oil recovery by injecting steam underground in a process known as steam-assisted gravity drainage to extract bitumen—a very viscous oil, taking advantage of the pore-scale quantification of fluid dynamics at relevant reservoir conditions and pore sizes. It is found that the characteristic size of oil-in-water emulsions generated is reduced from 150 to 6 μm and the corresponding recovery effectiveness is enhanced by 50% with the additive.

3.3. CO₂ sequestration

Four mechanisms have been proposed for CO₂ sequestration in saline aquifers: structural and hydrodynamic capture due to the density difference between the liquid and CO₂, residual capture during the formation of the porous spaces, the solubility capture owing to the

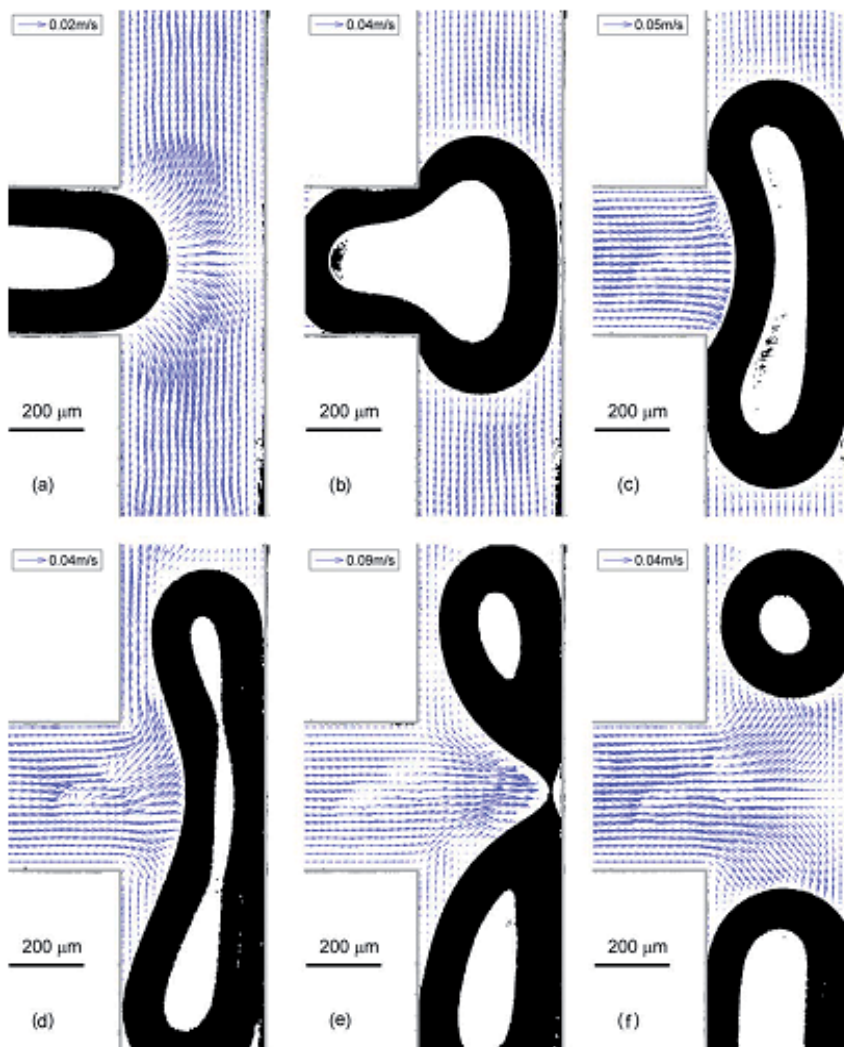


Figure 4. Velocity fields in the liquid phase around a breaking bubble at a T-junction with the help of micro-PIV. Reprinted from Fu et al. (2014). (Reproduced with permission. Copyright John Wiley and Sons, 2014) (Fu et al. [4]) <http://dx.doi.org/10.1002/aic.14377>.

dissolved CO_2 in the liquid phase, and mineral capture due to the stable carbonate formed by the reaction of CO_2 and rock minerals [40]. In general, low-pressure foam micromodel studies physically show the effect of foam within the porous media. To highlight chemical interactions with the oil phase requires all phases to be at reservoir pressure. Ma et al. [55] used a micromodel to investigate the sweep efficiency of the surfactant CO_2 foam in a heterogeneous network without oil at ambient conditions. Kumar Gunda et al. [56] designed a “reservoir-on-a-chip” to represent the pore structure of a naturally oil-bearing reservoir rock to perform conventional water-flooding experiments, and observed in real time the fluid-fluid interface

structure at the junctions of the porous media (Figure 5). The fluid-fluid interface is found to be trapped at some junctions by capillary trapping. Datta et al. [57] constructed velocity distributions in a fluid flow in a three-dimensional porous media by using the confocal microscopy, and they found that the velocity magnitudes and the velocity components both along and transverse to the imposed flow direction were distributed exponentially. They also observed that the pore-scale correlations in the flow were predominated by the geometry of the media, which suggested that the fluid flow through the pore space was not completely random despite the considerable complexity of it. Wu et al. [58] studied the effect of the wettability of the channel and the morphology of the network on the fluid flow for the displacement of oil by water in porous media with a microfluidic model. The former affects the structure of the water phase, while the latter determines the residual oil saturation. The networks used in this study were composed of about 600 grains separated by a highly connected network of channels with an overall porosity of 0.11–0.20. The findings suggested that the morphology of the complex network resulted in a complex flow behavior that was difficult to predict by solely on porosity, and they provided a versatile tool on the study of visualized multiphase flow behavior and displacement mechanism in porous media at the microscale, nanoscale, and pore scale.

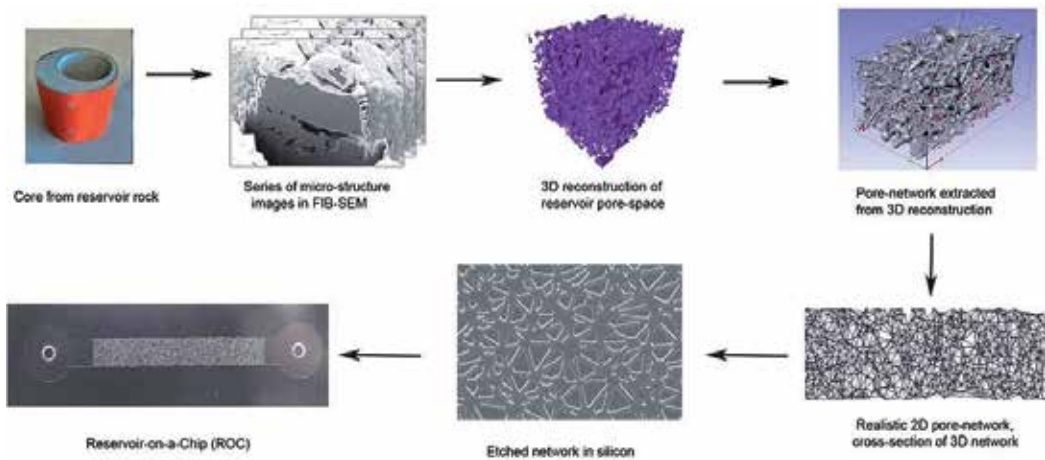


Figure 5. The conceptual map for “reservoir-on-a-chip.” Reproduced from Kumar Gunda et al. [56] with permission of The Royal Society of Chemistry. <http://dx.doi.org/10.1039/C1LC20556K>

Several studies show that the dynamics of the fluid-fluid interface at the microscale is influenced by the morphology and wettability of the microchannels in porous space. Berejnov et al. [59] constructed a lab-on-a-chip to study the effect of the wettability of microchannels on the selectivity and percolation patterns of multiphase flow in networks with 5000 channels at pore scale. Murison et al. [60] found that additional dissipation at small extension can be caused by the contact line pinning of gas beads for a dense packing. More attention should be paid to the effects of morphology of porous media and wettability on multiphase flow in porous spaces.

To overcome the difference between the material used for typical microfluidic devices (glass, silicone, and PDMS) and the real rock for CO₂ flooding and sequestration, Song et al. [61] presented a real-rock micromodel made in a naturally mineral substrate as shown in Figure 6, to directly study the multiphase flow behavior and multicomponent interactions in real time. They demonstrated the dissolution of carbonate rock with time resulted by hydrochloric acid flow relevant to acidizing processes for reservoir stimulations. Flow and crystal orientation-directed preferential dissolution was observed. This work paves the way for future applications of real-rock microfluidics, highlighting processes in the subsurface, to study the fundamental fluid-rock interactions and examine the effect of industrially relevant injection fluids on CO₂ storage in saline aquifers.

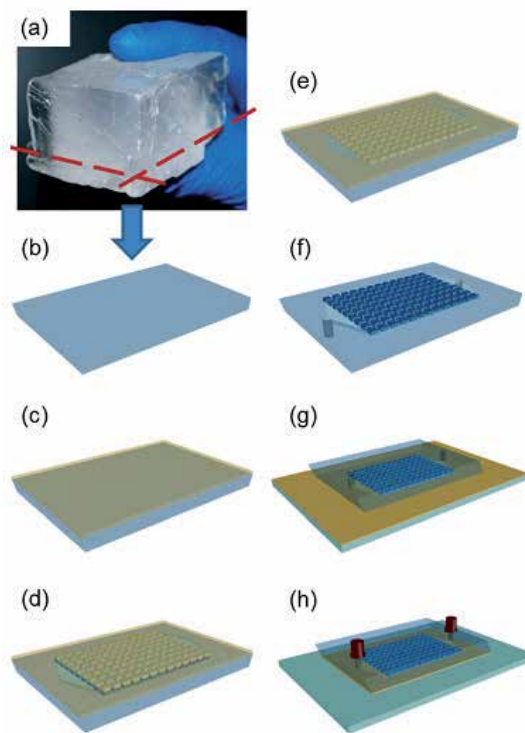


Figure 6. Fabrication of the microfluidic devices made in natural calcite material. Reproduced from Song et al. [61] with permission of The Royal Society of Chemistry. <http://dx.doi.org/10.1039/C4LC00608A>

In general, low-pressure foam micromodel studies demonstrate the effect of foam as a physical structure within the porous media. To include representative chemical interactions with the oil phase requires all phases to be at reservoir pressure. The microfluidic technique is also tested for high pressure CO₂ injection, supercritical CO₂ injection, CO₂-surfactant injection, and low-pressure air-surfactant injection [31]. Nguyen et al. [62] provided a microcore method to study the porosity and permeability changes for pore-scale analysis of superficial CO₂ reactive transport in saline aquifers at reservoir temperature and pressure conditions of 8.4 MPa and

40°C. Kim et al. [63] presented another lab-on-a-chip approach to understand the process of salt precipitation during CO₂ sequestration at pore scale. The dynamics of flow, evaporation, and salt formation within porous media could be observed in the complex networks consisting of microchannels with pore size distributions relevant to native porous media. Salt precipitation happens streamwise with a speed equivalent to 2% of the CO₂ velocity. The salt formation mechanism could also be identified at the pore scale using this method: large bulk crystals forming early in the trapped brine phases on the order of the pore size; and polycrystalline aggregated structures forming late in the evaporation process on a wide range of length scale. These findings can be used to explore the blockage phenomenon and well bore dry-out strategy. Nguyen et al. [64] evaluated nanoparticle CO₂ foam stability and EOR efficiency by using a micromodel approach, providing a quantitative measurement of bubble size and coalescence dynamics. In comparison to other similar cases with CO₂ gas, the nanoparticle-stabilized CO₂ foam showed a three-fold increase in oil recovery attributed to the role of the physical pore-scale bubble structures, which are rendered very stable in the presence of nanoparticles.

4. Conclusions and perspectives

In conclusion, microfluidic technique is a promising tool for CO₂ capture, sequestration, and application. To further take advantage of this new technique, several challenges, needs, and future directions should be highlighted. The detailed fluid dynamics for multiphase flow in single microchannels, single-stage microfluidic divergences and doublet microchannels, and multistage microfluidic divergences and network microchannels need to be explored. The fascinating fluid dynamics at fluid-fluid interface involving surface tension at microscale is still challenging. The stability and non-stability of the fluid-fluid interface at microchannels and networks need to be emphasized to gain insights into the mechanism for fluid flow in porous media for the CO₂ capture, sequestration, and applications. For example, the breakup and nonbreakup of the fluid-fluid interface and the trapping and releasing of bubbles in microchannels should be explored. Studies on the effects of the gas and liquid flow rate, pressure, temperature, the viscosity and surface tension of the liquid phase, the wettability of the channel wall, the geometry and size of microchannels, and the structural morphology of multistage microchannels on the dynamical evolution of the fluid-fluid interface should be explored.

It is urgent to conduct studies on CO₂ utilization in line with the pressure, temperature, and materials for porous media in practical application at the microreactor scale and pore scale. The most challenging problem is how to evaluate and manipulate the fluid-fluid interface for both immiscible and miscible systems at the microreactor scale and pore scale. Many of pore-scale phenomena need to be explored, including the behavior of the wetting films, the movement of contact lines and dynamic contact angles, the stability of capillary bridges, the dynamic instability of nonwetting fluid, the propagation of fluid-fluid interface, even the phase transitions during multiphase flowing, the heat and mass transfer across interfaces, and many others.

Acknowledgements

The financial supports for this project from the National Natural Science Foundation of China (21106093), the Research Fund for the Doctoral Program of Higher Education (20110032120010), and the Elite Scholar Program of Tianjin University are gratefully acknowledged.

Author details

Taotao Fu^{1,2*}

Address all correspondence to: ttfu@tju.edu.cn

1 State Key Laboratory of Chemical Engineering, Collaborative Innovation Center of Chemical Science and Engineering, Tianjin, China

2 School of Chemical Engineering and Technology, Tianjin University, Tianjin, China

References

- [1] K. S. Elvira, X. C. I. Solvas, R. C. R. Wootton, and A. J. deMello, *Nature Chemistry* 5, 905 (2013).
- [2] V. Hessel, I. Vural Gürsel, Q. Wang, T. Noël, and J. Lang, *Chemical Engineering & Technology* 35, 1184 (2012).
- [3] M. T. Kreutzer, F. Kapteijn, J. A. Moulijn, and J. J. Heiszwolf, *Chemical Engineering Science* 60, 5895 (2005).
- [4] T. Fu, Y. Ma, and H. Z. Li, *AIChE Journal* 60, 1920 (2014).
- [5] M. J. Fuerstman, A. Lai, M. E. Thurlow, S. S. Shevkoplyas, H. A. Stone, and G. M. Whitesides, *Lab on a Chip* 7, 1479 (2007).
- [6] F. P. Bretherton, *Journal of Fluid Mechanics* 10, 166 (1961).
- [7] J. Ratulowski and H.-C. Chang, *Physics of Fluids A: Fluid Dynamics* 1, 1642 (1989).
- [8] M. T. Kreutzer, F. Kapteijn, J. A. Moulijn, C. R. Kleijn, and J. J. Heiszwolf, *AIChE Journal* 51, 2428 (2005).
- [9] W. B. Kolb and R. L. Cerro, *Physics of Fluids A: Fluid Dynamics* 5, 1549 (1993).
- [10] H. Wong, C. J. Radke, and S. Morris, *Journal of Fluid Mechanics* 292, 95 (1995).

- [11] J. Yue, G. Chen, Q. Yuan, L. Luo, and Y. Gonthier, *Chemical Engineering Science* 62, 2096 (2007).
- [12] P. Sobieszuk, R. Pohorecki, P. Cyganski, M. Kraut, and F. Olschewski, *Chemical Engineering Journal* 164, 10 (2010).
- [13] G. Bercic and A. Pintar, *Chemical Engineering Science* 52, 3709 (1997).
- [14] J. M. van Baten and R. Krishna, *Chemical Engineering Science* 59, 2535 (2004).
- [15] J. M. van Baten and R. Krishna, *Chemical Engineering Science* 60, 1117 (2005).
- [16] C. O. Vandu, H. Liu, and R. Krishna, *Chemical Engineering Science* 60, 6430 (2005).
- [17] J. Yue, L. Luo, Y. Gonthier, G. Chen, and Q. Yuan, *Chemical Engineering Science* 64, 3697 (2009).
- [18] J. C. Jepsen, *AIChE Journal* 16, 705 (1970).
- [19] D. Eskin and F. Mostowfi, *International Journal of Heat and Fluid Flow* 33, 147 (2012).
- [20] N. Shao, A. Gavriilidis, and P. Angeli, *Chemical Engineering Journal* 160, 873 (2010).
- [21] P. Sobieszuk, R. Pohorecki, P. Cyganski, and J. Grzelka, *Chemical Engineering Science* 66, 6048 (2011).
- [22] M. Ichiyanagi, I. Tsutsui, Y. Kakinuma, Y. Sato, and K. Hishida, *International Journal of Heat and Mass Transfer* 55, 2872 (2012).
- [23] J. Tan, Y. C. Lu, J. H. Xu, and G. S. Luo, *Chemical Engineering Journal* 185-186, 314 (2012).
- [24] J. Tan, Y. C. Lu, J. H. Xu, and G. S. Luo, *Chemical Engineering Journal* 181-182, 229 (2012).
- [25] R. Sun and T. Cubaud, *Lab on a Chip* 11, 2924 (2011).
- [26] C. Zhu, C. Li, X. Gao, Y. Ma, and D. Liu, *International Journal of Heat and Mass Transfer* 73, 492 (2014).
- [27] C. Yao, Z. Dong, Y. Zhao, and G. Chen, *Chemical Engineering Science* 112, 15 (2014).
- [28] L. Yang, J. Tan, K. Wang, and G. Luo, *Chemical Engineering Science* 109, 306 (2014).
- [29] Y. Su, Y. Zhao, F. Jiao, G. Chen, and Q. Yuan, *AIChE Journal* 57, 1409 (2011).
- [30] Y. Su, G. Chen, Y. Zhao, and Q. Yuan, *AIChE Journal* 55, 1948 (2009).
- [31] D. Sinton, *Lab on a Chip* 14, 3127 (2014).
- [32] A. Sell, H. Fadaei, M. Kim, and D. Sinton, *Environmental Science & Technology* 47, 71 (2013).

- [33] H. Fadaei, B. Scarff, and D. Sinton, *Energy & Fuels* 25, 4829 (2011).
- [34] S. Lefortier, P. Hamersma, A. Bardow, and M. T. Kreutzer, *Lab on a Chip* 12, 3387 (2012).
- [35] M. Abolhasani, M. Singh, E. Kumacheva, and A. Gunther, *Lab on a Chip* 12, 1611 (2012).
- [36] W. Li, K. Liu, R. Simms, J. Greener, D. Jagadeesan, S. Pinto, A. Gunther, and E. Kumacheva, *Journal of the American Chemical Society* 134, 3127 (2012).
- [37] E. Tumarkin, Z. Nie, J. I. Park, M. Abolhasani, J. Greener, B. Sherwood-Lollar, A. Gunther, and E. Kumacheva, *Lab on a Chip* 11, 3545 (2011).
- [38] E. Tumarkin, J. I. Park, Z. Nie, and E. Kumacheva, *Chemical Communications* 47 (2011).
- [39] J. I. Park, Z. Nie, A. Kumachev, and E. Kumacheva, *Soft Matter* 6, 630 (2010).
- [40] D. P. Schrag, *Science* 315, 812 (2007).
- [41] G. Dawson, S. Lee, and A. Juel, *Journal of Fluid Mechanics* 722, 437 (2013).
- [42] G. I. Taylor, *Journal of Fluid Mechanics* 10, 161 (1961).
- [43] G. M. Homsy, *Annual Review of Fluid Mechanics* 19, 271 (1987).
- [44] H. E. Huppert and J. A. Neufeld, *Annual Review of Fluid Mechanics* 46, 255 (2014).
- [45] U. Oxaal, M. Murat, F. Boger, A. Aharony, J. Feder, and T. Jossang, *Nature* 329, 32 (1987).
- [46] T. T. Al-Housseiny, J. Hernandez, and H. A. Stone, *Physics of Fluids* 26, 042110 (2014).
- [47] T. T. Al-Housseiny and H. A. Stone, *Physics of Fluids* 25, 092102 (2013).
- [48] T. T. Al-Housseiny, P. A. Tsai, and H. A. Stone, *Nat Phys* 8, 747 (2012).
- [49] R. Lenormand, C. Zarcone, and A. Sarr, *Journal of Fluid Mechanics* 135, 337 (1983).
- [50] T. T. Al-Housseiny, I. C. Christov, and H. A. Stone, *Physical Review Letters* 111, 034502 (2013).
- [51] T. Fu, Y. Ma, D. Funfschilling, and H. Z. Li, *Chemical Engineering Science* 66, 4184 (2011).
- [52] X. Wang, C. Zhu, T. Fu, and Y. Ma, *AIChE Journal* 61, 1081 (2015).
- [53] X. Wang, C. Zhu, T. Fu, and Y. Ma, *Chemical Engineering Science* 111, 244 (2014).
- [54] T. W. de Haas, H. Fadaei, U. Guerrero, and D. Sinton, *Lab on a Chip* 13, 3832 (2013).

- [55] K. Ma, R. Liontas, C. A. Conn, G. J. Hirasaki, and S. L. Biswal, *Soft Matter* 8, 10669 (2012).
- [56] N. S. Kumar Gunda, B. Bera, N. K. Karadimitriou, S. K. Mitra, and S. M. Hassanizadeh, *Lab on a Chip* 11, 3785 (2011).
- [57] S. S. Datta, H. Chiang, T. S. Ramakrishnan, and D. A. Weitz, *Physical Review Letters* 111, 064501 (2013).
- [58] M. Wu, F. Xiao, R. M. Johnson-Paben, S. T. Retterer, X. Yin, and K. B. Neeves, *Lab on a Chip* 12, 253 (2012).
- [59] V. Berejnov, N. Djilali, and D. Sinton, *Lab on a Chip* 8, 689 (2008).
- [60] J. Murison, B. Semin, J.-C. Baret, S. Herminghaus, M. Schröter, and M. Brinkmann, *Physical Review Applied* 2, 034002 (2014).
- [61] W. Song, T. W. de Haas, H. Fadaei, and D. Sinton, *Lab on a Chip* 14, 4382 (2014).
- [62] P. Nguyen, H. Fadaei, and D. Sinton, *Journal of Fluids Engineering* 135, 021203 (2013).
- [63] M. Kim, A. Sell, and D. Sinton, *Lab on a Chip* 13, 2508 (2013).
- [64] P. Nguyen, H. Fadaei, and D. Sinton, *Energy & Fuels* 28, 6221 (2014).

Generation and Evaporation of Microsprays

Chin-Tai Chen

Additional information is available at the end of the chapter

<http://dx.doi.org/10.5772/64756>

Abstract

This chapter aims to comprehensively review the techniques and features of micro-sprays for various applications via micro-droplet generators over decades, especially focusing on the past and present microfluidics. It is organized briefly as below. The background of current research and development about the micro-spray techniques is first introduced, followed by the generation and evaporation of spray detailed with the concentrated respects of critical requirements for materials and facilities. Then, we address the critical design issues of micro-sprayers such as the actuators and nozzles required to be satisfactory for generating a number of droplets. Subsequently, we further describe characterization of droplets in form of spray concerning droplet size, speed, rates, and patterns in microfluidics. Moreover, the chapter presents the proof-of-concept and commercial applications of the micro-spraying processes, highlighting their current technical progresses and future challenges, which shall be intimately related to the droplet generation and evaporation including droplet evaporative cooling, direct printing, screen printing, nano-material coating, liquid nebulization, and miscellaneous employment. Finally, we draw a conclusion in the end of the chapter.

Keywords: Spray, droplet generation, droplet evaporation, micro-actuator, microfluidics

1. Introduction

Over the past 30 years, spray droplets have been investigated and engineered due to their frequent occurrence in nature such as sea water [1] and manual generation on hot surfaces such as liquid deposition [2]. This field of science and engineering has widely demonstrated their significance on thermal and fluidic dynamics, in particular related to cooling and evaporation of spray droplets. Those numerous droplets, as being mechanically pumped through small nozzles of a continuous fluid delivery system, have been used for different respects of the evaporative cooling since then. Compared to the conventional mechanical droplet generators, another type of the modern microfluidic generators can eject the micron-

sized droplets through micro-electro-mechanical actuators that typically feature light weight, small size, less noise, and high power conservation [3]. Furthermore, as bonding with an array of micro-nozzles (orifices), a number of femto- to pico-liter droplets can be simultaneously generated at high driving frequency (kilo- to mega-Hz), forming a highly directional spray away from the nozzle surface [4].

To acquire high quality sprays in many applications (e.g., evaporative cooling), generating the droplets efficiently from certain micro-nozzles to a targeted space or surface exhibits technical requirements for key parameters [1], including the velocity of the droplets, the number flux of droplets, and the Sauter mean diameter. In terms of hydrodynamic properties, a stream of micro-droplets typically experience in either case below: (1) impacting, wetting, and evaporating (and depositing) on a two-dimensional (2D) surface and (2) floating and evaporating within a three-dimensional (3D) space. In both cases, the intrinsic non-uniformity of a spray generated from a single nozzle is frequently encountered in the conventional liquid delivery system, leading to the poor performance in some applications such as evaporative cooling. For example, non-uniform temperature distribution on the wall surface may be resulted from the different droplet-size distributions (DSDs) [5]. Likewise, it is possible to encounter a complex problem of determining the efficiency of evaporative cooling occurred with non-uniform distributions of droplets [6]. Moreover, non-uniform droplets forming turbulent flows can be also caused by ambient air and pressure within the zone of the spray, thereby significantly influencing the evaporation of spray droplets [7].

On the other hand, in the recent years, many efforts of research and development in academics as well as industries have been made to facilitate the various components and devices fabricated by the spray printing (SP) techniques, including amperometric enzyme electrodes [8], organic transistor electrodes [9], metal silver films [10], counter electrodes for flexible dye-sensitized solar cells [11], carbon thin films on flexible substrates [12], organic field-effect transistors and complementary inverters [13], flexible polymer solar cell modules [14], etc. Compared to the current inkjet-printing (IJP) techniques [15], this SP process is generally characterized with one additional screen (mesh) for patterning a variety of materials coated on substrate surfaces. Moreover, the screen printing by spray further provides a capability of large-area patterning on substrates without requirement of precise positioning, and therefore becomes an alternative low-cost technology consuming little material and power. Accordingly, using the SP techniques as a simple manufacturing tool, several global manufacturers have developed the material-processing equipment and peripheral utilities from the laboratory to commercial grade, for example, Legend Star International Co., Ltd. (<http://www.lgs.com.tw>) and Diamond-MT, Inc. (<http://www.diamond-mt.com>), in order to offer the customizing design services for academic research and commercial production.

In addition, with the remarkable emergence of nano-science and technology, many functional and novel materials have consequently been exploited to generate specific thin films and nanostructures using this SP method. For instance, a variety of fabrication methods for deposition of thin-film oxides (e.g., yttria-stabilized zirconia, YSZ) such as chemical vapor deposition (CVD), physical vapor deposition (PVD), electrochemical vapor deposition (EVD), spray pyrolysis, slip casting, screen printing, and so forth were comprehensively presented

and discussed by Will et al. [16]. Compared to the other methods, spray pyrolysis (of a metal salt solution) can be reliably utilized to form amorphous to polycrystalline microstructures (metal oxide films) at economical cost, although post-thermal treatment is usually necessary. Using this kind of spray techniques, the continuing efforts were made for the film production of copper and hybrid nanoparticles [17], the generation of metal particles [18], and the generation of metal and metal oxide nanoparticles [19]. Furthermore, more extensive studies for spraying applications were also directed to other advanced materials including biomedical calcium phosphate [20], colloidal dispersion of alumina particles [21], and composite materials of silver nanoparticles [22]. Importantly, many of the fundamental principles (e.g., preparation of pure liquid and solution materials) and utilities (e.g., setup of a liquid delivery and spray system) were commonly adopted in another nebulization application, for example, the aerosol and pulmonary drug delivery [23–25]. Therefore, full understanding of fundamental spraying mechanism here is a substantial effort to realize the key performances for such practical applications of the droplet generation techniques.

This book chapter concisely reviews the recent development of spray techniques and applications in our daily life and industry using micro-droplet generation, particularly benefiting the public in many respects such as saving energy, cost and time. It is organized briefly as follows. First, the background of the past and present development associated with the spray techniques is introduced here in Section 1, followed by the elaboration of the spray generation and evaporation regarding various liquids and actuators in Section 2. Section 3 presents the important design issues of micro-actuators/nozzles and integration/control, basically considering the implementation of spray. Section 4 describes the general characteristics of droplets existing in spray such as their sizes, speeds, volumetric rates, and fluidic patterns. Section 5 demonstrates the up-to-date applications of the micro-spraying processes, expressing the potential development and challenges in the future, which include droplet evaporative cooling (DEC), direct printing (DP) and screen printing (SP), nanomaterial coating (NMC), liquid nebulization (LN), and miscellaneous utilities. Finally, we draw a conclusion in Section 6.

2. Fundamentals of microsyringing

Considering the common requirements of spray applications, a series of spraying processes should be comprehensively dealt with concerning the formation evolution of a spray: liquid supply and actuation, droplet generation, spraying, evaporating and deposition, as shown in Figure 1. Spraying droplets with different sizes (i.e., s_1 , s_2 , ..., and s_n) may impact and wet on surface (i.e., d_1 , d_2 , and d_m) through evaporating (and $m < n$). As a matter of fact, every step here may involve technically serious considerations and significantly influence the performances of a spray-based system in the various applications. Those consideration factors in the successful spraying of materials and components are briefly described, discussed, and analyzed as below.

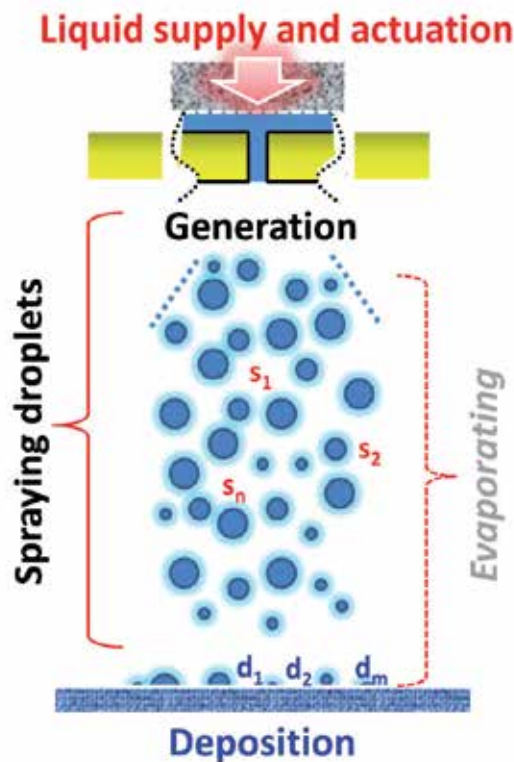


Figure 1. Schematic representation of spray generation and evaporation undergoing typically from one position of liquid supply and actuation (on the top) to another position of deposition on surface (at the bottom): those numerous droplets with various sizes are evaporating in air (s_1, s_2, \dots, s_n) and on surface (d_1, d_2, \dots, d_m).

2.1. Liquids and actuators

For many of applications, selecting suitable pure liquids or solutions is the most important factor in evaluating primary performances of spraying processes such as evaporative cooling efficiency and direct printing of materials. For pure liquids, their dynamic viscosities (e.g., pure water of 1.00 cp and ethanol of 1.09 cp at 20°C, where 1 cp = 1 mNs/m²) should be low enough for the liquid delivery (through a tubing system) and ejection (from a powered actuator). Also, their surface energies in air are typically ranging from 20 to 73 mN/m in order to (e.g., pure water of 72.86 mN/m and ethanol of 22.39 mN/m at 20°C). For liquid mixtures, the solid contents (e.g., silver and gold nanoparticles) have to be effectively dispersed in the solvent (i.e., aqueous or non-aqueous) by additional suitable surfactant (e.g., detergents), in which particle aggregation is avoided for the long-term operation [26]. The particle sizes, in general ranging from a few to hundreds of nanometers (nm), are also small to a certain extent depending on some limits of the fluid delivery pipes and exit nozzles [10].

Second, the means of actuation powerfully pumping (dispensing) the liquid out of the nozzles should be considered for different needs. For instance, some mechanically pneumatic pumps

connecting to metal nozzles are able to eject high-throughput sprays robustly but noisily; therefore, they are most often exploited for evaporative cooling in large buildings and facilities [27–29]. However, at smaller scales, many new types of micro actuators such as piezoelectric [3–4,30] and electrostatic [14,31] ones are used to take advantage of precise electrical control over spray. Compared to the former (pneumatic), these microfluidic actuators may be further explored for versatile circumstances of daily life using novel and versatile materials.

Using the fluidic actuators filled with suitable liquids, a number of droplets can be therefore pumped from the small nozzles as electrically powered. In theory, those droplets generally exhibit spherical shapes in air due to intrinsic surface tension of liquid as demonstrated in Figure 1. Thus, the individual volume (V) and surface area (A) of a formed droplet are geometrically estimated in Eqs. (1) and (2):

$$V = \frac{4}{3}\pi \times R^3 = \frac{4}{3}\pi \times \left(\frac{D}{2}\right)^3 = \frac{\pi}{6} \times D^3 \quad (1)$$

$$A = 4\pi \times R^2 = 4\pi \times \left(\frac{D}{2}\right)^2 = \pi \times D^2 \quad (2)$$

where R is the radius and D is the diameter for a single drop, respectively. In general, the droplet size, volume, and surface area here rely on the size of nozzle. The conventional metal nozzles have quite diverse diameters ranging from tens of micrometers (μm) to a few millimeters (mm). By contrast, the micron-sized nozzles used in micro-actuators are generally found with 10–100 μm in diameter. As a result, those droplets are generated to exhibit the corresponding volumes with tens to thousands of pico-liters ($\text{pl} = 10^{-12} \text{ l}$), primarily depending on the actuation means and devices. Obviously, the smaller droplets may be also yielded by simply reducing the nozzle diameter.

In fact, except for the called drop-on-demand (DOD) operation that is often used in IJP [32,33], the uniformity of size of individual droplets is one of the crucial factors considered for precise spraying in many applications [15]. For example, the thermal performances of a spray such as critical heat flux (CHF) can be significantly influenced by the deviation from the targeted value of the droplet size [34]. Hence, in many situations, it shall be substantially coped with the droplet size distribution as well as evaporation as follows.

2.2. Droplet size distribution and evaporation

The general droplet size distribution (DSD) in conventional sprays can be represented by classic Mugele-Evan (ME) relation as described in Eq. (3) [29,35], where $f_N(D)$ is the number (N) density distribution, and i and j are positive integers. Hence, the arithmetic mean diameter (AMD) (i.e., D_{10} , where $i = 1, j = 0$) is expressed in Eq. (4). Also, the well-known Sauter mean diameter (SMD) is defined for D_{32} (where $i = 3, j = 2$) as shown in Eq. (5) [36]:

$$D_{ij} = \left[\frac{\int_0^\infty D^i f_N(D) dD}{\int_0^\infty D^j f_N(D) dD} \right]^{\frac{1}{i-j}} \quad (3)$$

$$AMD = D_{10} = \int_0^1 D f_N(D) dD = \int_0^1 D dN \quad (4)$$

$$SMD = D_{32} = \frac{\int_0^\infty D^3 f_N(D) dD}{\int_0^\infty D^2 f_N(D) dD} = \frac{\int_0^\infty D^3 dN}{\int_0^\infty D^2 dN} \quad (5)$$

As the simplest case of a uniform spray, all of the droplets have the same diameter of D_s , thereby giving the $AMD = D_{10} = D_s$. Furthermore, in this special case, the SMD (i.e., D_{32}) can be clearly represented by the ratio of the single droplet volume (V)/surface area (A): $D_{32} = 6 \times (V/A)$, according to previous Eqs. (1) and (2). Based on this concept of the ratio of V/A , the SMD shows particular significance in some circumstances, where the surface area plays a critical role such as droplet evaporation time in air, as shown in Eq. (6) [1]:

$$\tau = \beta \times \frac{\pi \times D_s^2}{\alpha(T)} = \frac{\beta \times A}{\alpha(T)} \quad (6)$$

where β is the dimensionless coefficient, D_s is the single droplet diameter, α is the thermal diffusivity of the droplet, and T is the temperature, respectively. For example, supposed that the water with the $\beta = 3.23 \times 10^{-2}$ and $\alpha = 1.43 \times 10^{-7} \text{ m}^2/\text{s}$ at 25°C , a droplet of $D_s = 100 \text{ }\mu\text{m}$ is estimated with the evaporation time of $\tau = 7.10 \times 10^{-3} \text{ s}$ (i.e., 7.1 ms), while a shorter time of $\tau = 7.10 \times 10^{-5} \text{ s}$ (i.e., 71 μs) for a droplet with a 10-time smaller diameter (i.e., $D_s = 10 \text{ }\mu\text{m}$).

2.3. Spraying control

In regard to the spraying control, it is mostly concerned with the volumetric rate of a spray. As can be seen in Figure 1, some of the droplets ejected out of nozzles (i.e., s_1 , s_2 , and s_n) might reach, deposit, and grow on certain surfaces (i.e., d_1 , d_2 , and d_m), even though they fulfill the evaporation (in air) as mentioned above. Therefore, real-time control over the spraying is another crucial part of the microfluidic actuation. For a pneumatic pumping/dispensing system, switching the actuation of a spray on and off is frequently completed in a period of a few seconds, in order to get rid of excessive growth of deposit.

To achieve high-speed switching, however, digital control over micro actuation can be carried out precisely for the new types of microfluidic actuators, where they can operate electronically at driving frequencies more than tens of kHz [30]. Utilizing the present computer-assisted capability over one decade, those control systems have been developed and implemented with

graphical user interface (GUI) by using commercial software such as MATLAB, LabVIEW, C, C++, and Visual Basic languages.

Based on the fundamental knowledge of spray science and technology, two preliminary design issues of micro-sprayers for realizing precise droplet generation are further addressed and discussed below.

3. Design issues of microsprayers

3.1. Micro-actuators and nozzles

As illustrated previously in Figure 1, the liquid supply and actuation forming a spray have to be performed at the first stage. For the purpose of effective formation of a spray as exemplified in Figure 2, the fluidic systems with different complexity can be designed and built here. Figure 2(a) shows an infrared (IR) thermography picture (NEC G100, JP) of a conventional pneumatic system (red) mainly composed of liquid supply (through tubing) and a metal nozzle (exit diameter of 80 μm , GAU PU GP-A008, TW). As being pressurized (70 kg/cm^2) from an electric pump (at 110 V, 850 rpm), droplet jetting of a water spray with a rate of 22 ml/min was continuously formed in a conical shape (see S). Meanwhile, it generated a loud noise of 85 dB from 50 dB (due to large mechanical vibration) and high humidity of 80 RH% from 60 RH% (due to excessive growth of deposit) in the neighboring space, substantially posing a notable disadvantage in some applications of the public daily life.

To avoid the induced noise and humidity, the actuators and nozzles can be largely miniaturized and arrayed for generation of a spray at the micron scale, as demonstrated in Figure 2(b). Here, the commercial ink cartridge installed in a bubble-type inkjet printer (Canon PIXMA iP 2770, JP) is composed of a print-head with a resolution of $1,200 \times 4,200$ dpi (1,472 fine nozzles, droplet volume of 2 pl). After de-capping the printer and removing the original ink from the cartridge, then pure water was manually re-filled from the liquid supply of a tubing container. By virtue of a microelectronic controller of the printer, the print-head was successfully actuated in scanning motion, so that water droplet jetting of 1 ml/min from its array of nozzles was achieved (see S). Compared to the previous one, a lower noise of 60 dB as well as humidity of 60 RH% was obtained in the same environment, indicating a great improvement in the spraying performance (i.e., decrease by 25 dB and 20 RH%) because of more uniform and fine droplets.

3.2. Microsystem integration and control

As using micro-actuators and nozzles, another design issue on the implementation of a microsprayer includes the microsystem integration and control required for many situations [3]. For example, as exemplified in Figure 3(a), an electrical power supply and a signal generator were equipped and controlled here to adaptively vary the driving voltage (v_{drive} V) and frequency (f_{drive} kHz) for a micro-actuator (e.g., piezoelectric actuation). Consequently, droplet ejection of a spray is able to be finely tuned for optimal performance [4,30]. The droplet

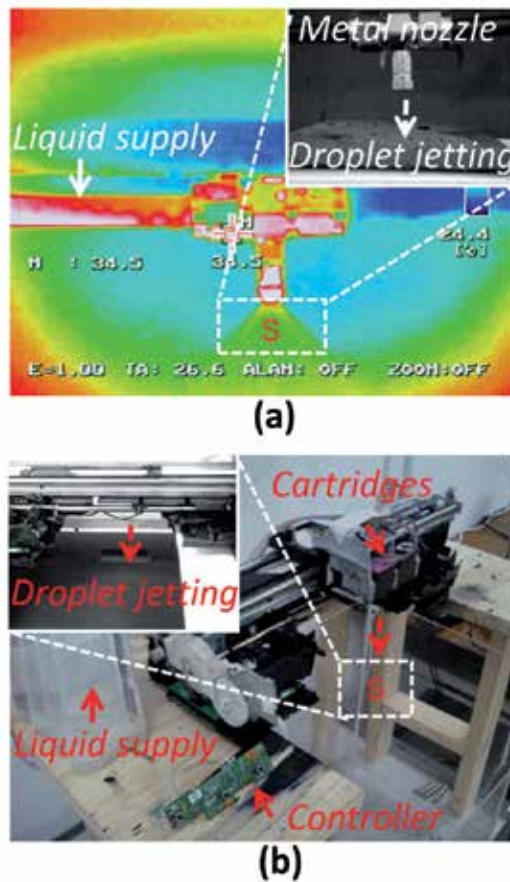


Figure 2. Demonstration and comparison with two types of spraying components and systems: (a) typical jetting process of water generated from liquid supply to a metal nozzle using a mechanical pump and (b) water droplets jetting from a liquid supply to a print-head cartridge with micro-actuators and nozzles using an inkjet printer.

velocity and volumetric rate for a spray may increase as raising the values of v_{drive} and f_{drive} . In addition, the compact liquid supply system comprising a tube and a container can be integrated and packaged with this microfluidic actuator (symbolized by A), as schematically depicted in Figure 3(b). Following the way, the fluid was expected to be slowly delivered (with an inner tubing diameter of 10 mm) from the bottom inlet to the top outlet (total vertical distance of 120 mm) as powered by microelectronic control and actuation (at v_{drive} and f_{drive}).

Such microsystem integration and control was realized by using a piezoelectric actuator under a suitable condition. As demonstrated in the IR thermography of Figure 3(c), one upward water spray was continuously generated in a period of 180 s from the fluidic outlet of the actuator (at v_{drive} of 60 V, f_{drive} of 90 kHz). However, their morphologic features changed apparently over time (i.e., 30, 90, and 180 s) implying the variation in physical properties (e.g., velocity and rate) and geometric pattern (e.g., turbulent flow). Hence, those characteristics of droplets within a spray are described and analyzed next in Section 4.

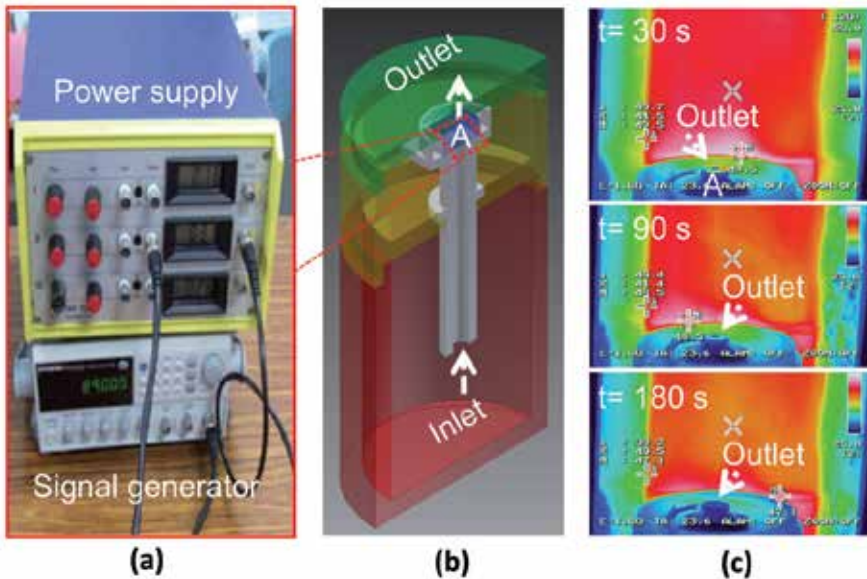


Figure 3. Integration, packaging, and test for a microsprayer: (a) electrical power supply and signal generator for controlling the micro-actuator during spraying, (b) liquid supply container integrated with the micro-actuator, and (c) thermography of droplet jetting with the electrical and liquid supply.

4. Characteristics of droplets in spray

From the view point of microfluidics, two significant respects can reflect the behaviour of a spray. One is the size and velocity of droplets, and the other is the rate and pattern of a spray. The former is primarily concerned with the kinematics of individual micro-droplets, while the latter is particularly emphasized to take into account the macrospraying phenomenon. Since either micro- or macro-behavior is important for a spray, one shall recognize their distinguishing characteristics entirely. Hence, the droplets in spray can be further elaborated and characterized as follows.

4.1. Size and velocity of a droplet

Conventionally, the size and velocity of a droplet can be visualized and calculated from particle image velocimetry (PIV), in which an expensive digital camera is used to perform the high-speed imaging capture (frame per second, *fps*, up to 10,000) for all droplets [29]. In this way, the droplet size distribution (DSD) and the others such as AMD and SMD can be calculated accordingly. From a practical view of convenience, while using a micro actuator mentioned previously, the initial velocity (v_0) of droplets on average can be simply evaluated as first-order approximation as proposed in Eq. (7), where η is the velocity coefficient, h_{nozzle} is the nozzle (via hole) thickness, and f_{drive} is the driving frequency, respectively. Moreover, assuming that the droplets travel a distance (s_a) under constant acceleration (a), this value (v_0) can be also correlated with the final average velocity (v_f) as expressed physically in Eq. (8):

$$v_0 = \eta \times (h_{\text{nozzle}} \times f_{\text{drive}}) \quad (7)$$

$$v_f^2 = v_0^2 + 2 \times a \times s_a \quad (8)$$

For instance, as demonstrated in Figure 4, a water spray was ejected from a piezoelectric micro-actuator at $f_{\text{drive}} = 90 \text{ kHz}$, in which micro-nozzles featured an average thickness (h_{nozzle}) of $40 \text{ }\mu\text{m}$ and an average diameter (d_{nozzle}) of $30 \text{ }\mu\text{m}$ [37]. Using Eq. (7), the value of (v_0/η) was approximated as $(30 \text{ }\mu\text{m}) \times (90 \times 10^3/\text{s}) = 3.60 \text{ m/s}$. Thus, under normal gravity (i.e., $a = 9.8 \text{ m/s}^2$) as demonstrated in Figure 4(a), this upward spray actually traveled a maximum distance $s_a = 0.12 \text{ m}$ to reach the final velocity $v_f = 0$. From Eq. (9) as ignoring the friction of air, the square of initial velocity was approximately calculated as $2 \times (9.8 \text{ m/s}^2) \times (0.12 \text{ m}) = 2.35 \text{ m}^2/\text{s}^2$, yielding $v_0 = 1.53 \text{ m/s}$ and $\eta = (1.53 \text{ m/s}) / (3.60 \text{ m/s}) = 0.425$ (i.e., 42.5%); therefore, this high velocity hindered those droplets from being clearly imaged by normal optical cameras ($f_{\text{ps}} = 30$) as illustrated in Figure 4(b).

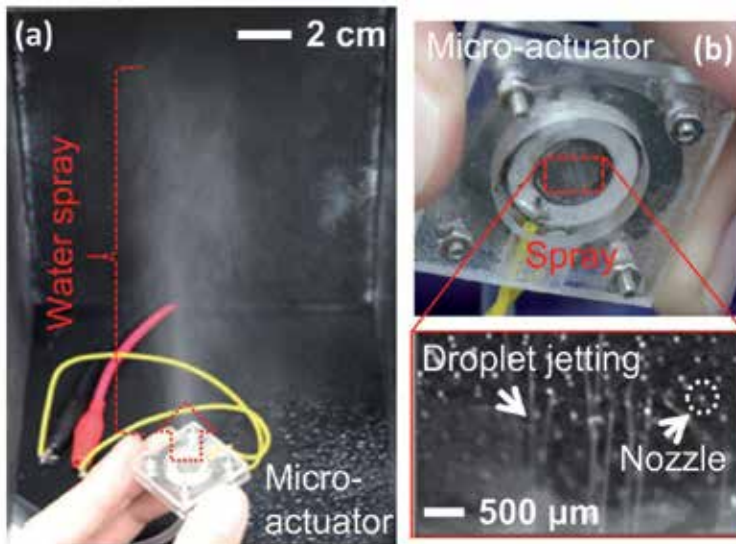


Figure 4. A group of droplets sprayed from a micro-actuator: (a) the upward formation of a water spray and (b) the downward droplet jetting from the micro-nozzles.

4.2. Rate and pattern of a spray

As a whole, the volumetric rate (ψ_v) of a microspray generated from the nozzles is straightforwardly determined by the droplet density (flux), driving frequency, and voltage. Again, using previous case as one example, the value of ψ_v for single droplet volume of 30 pl and firing nozzle number of 100 was estimated with a maximum of $(30 \text{ pl}) \times 100 \times (90 \times 10^3 / \text{s}) = 0.27$

ml/s = 16.20 ml/min. Nevertheless, this rate might drop dramatically due to failure of some nozzle during micro-actuation as shown in the inset of Figure 4(b). More importantly, the flow pattern of a spray was actually influenced by the flight velocity of droplets in air, typically leading to an appearance of turbulence [7,38]. In terms of fluid dynamics, this phenomenon pattern is associated particularly with a dimensionless Reynolds number (Re) as described in Eq. (9) [39]:

$$\text{Re} = \frac{\rho \times v \times l}{\mu} \quad (9)$$

where ρ is the density of liquid, v is the droplet velocity, l is the characteristic length, and μ is the dynamic viscosity of liquid, respectively. For instance, Figure 5 shows PIV imaging for patterns of sprays generated from micro-nozzles ($v = 3$ m/s), in which the liquid of pure water exhibited the $\rho = 10^3$ kg/m³ and $\mu = 10^{-3}$ Ns/m². Hence, the sparse spray ($l < 1$ mm) in Figure 5(a) was estimated with a low Re ($< 3,000$) such that it appeared like a laminar flow, while the turbulent flow with a large Re ($> 15,000$) was visualized for the dense spray ($l < 5$ mm) in Figure 5(b). Therefore, taking all of the characteristics of droplets into account, a variety of spray applications are described and illustrated in the next section.

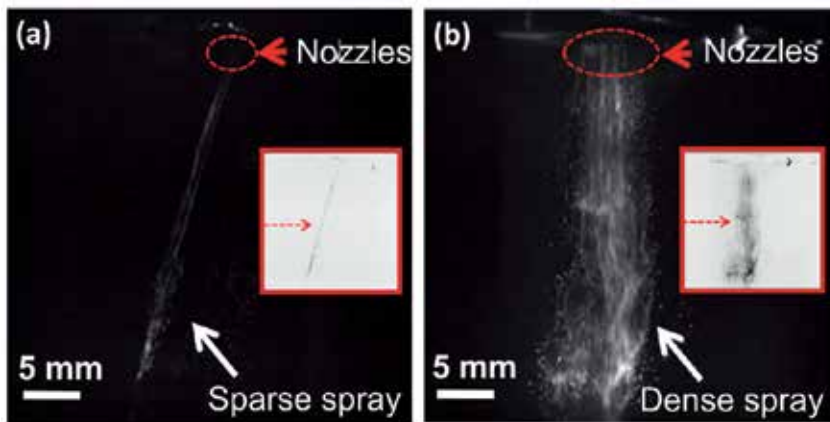


Figure 5. Various volume rates and microfluidic patterns of flow generated from the micro-nozzles of a micro-actuator: (a) a sparse spray and (b) a dense spray.

5. Applications

5.1. Droplet evaporative cooling

To date, droplet evaporative cooling (DEC) has been one of alternative means for reducing temperature of objects at low cost. It has been elaborated in decreasing the hot solid surfaces

with high values of CHF of 250–350 W/cm² [2,34]. Also, many other efforts have been made in the development of the spatial cooling systems, including the mechanical draft cooling tower and air-conditioning systems [28–29,40], in order to enhance the convective heat transfer in ambient environment. Figure 6(a) illustrates the photography pictures of such spray cooling circumstances, in which the conventional pumping liquid systems were operating indoors or outdoors. Also, using micro-actuators shown in Figure 6(b), the droplet ejection of water was periodically performed (between on and off) under ambient environment to demonstrate the temperature decrease of ~3°C visualized from the IR thermography [41].

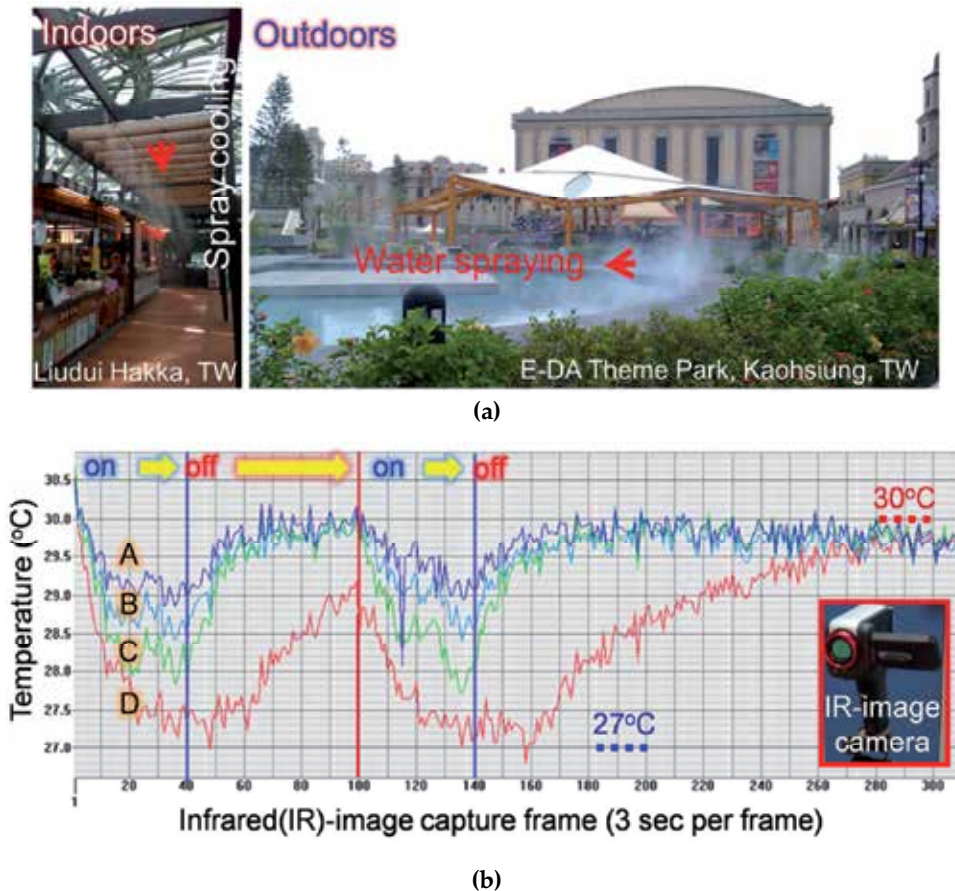


Figure 6. Evaporative cooling of droplets: (a) photography of water spray from traditional liquid supply outdoors and (b) temperature evolution of four positions (A, B, C, and D) over time within a spraying space, switching the micro-electronic actuator on (2 min) and off (3 min) alternatively during a period of 5 min.

In addition to the sprays of water, there are many colour liquids such as dye inks commercially available to be further adapted for industrial applications. Likewise, those inks have been used for direct and screen printing through generation of sprays as further discussed in the following.

5.2. Direct and screen printing

Instead of evaporating the liquid fully, ink deposition can be applied for printing as using diluted solutions with suitable solid content [42]. As a matter of fact, many printing methods have existed to date, mainly including the contact doctor-blade printing (DBP) method [43–46] and non-contact IJP method [8,33,47]. As compared to those DBP and IJP above, this kind of spray printing (SP) features the non-contact, high-speed, and large-area patterning capability [9,13]. With the assistance of one additional screen (mesh), the SP technique can be efficiently applied to perform the fine and complex patterning of micro-devices such as flexible dye-sensitized solar cells, polymer solar cell modules, and so forth [11,14].

For instance, Figure 7 demonstrates the spray printing of blue dye ink on a regular paper (A4 size) using a piezoelectric actuator and a mobile platform, in which direct printing of a spiral pattern (line width ~10 mm) and screen printing of a comb-type pattern (line width ~400 μm) were simply performed via a microelectronic controller (not shown here). Furthermore, fusing the novel materials from the emergence of nano-science and technology, those synthesized nanomaterials are suitable to be deposited and coated on substrates using the SP method for direct generation of thin functional films that is further described below.

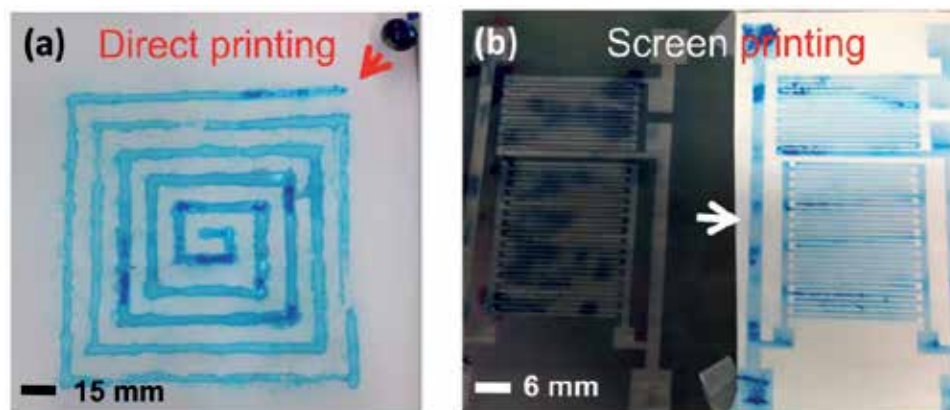


Figure 7. Spray printing of blue ink on a regular paper using a piezoelectric actuator: (a) direct printing of a square spiral pattern and (b) screen printing of a comb-type pattern.

5.3. Nanomaterial coating

The spray technique used as one of the deposition methods was thoroughly compared and analyzed with regard to solid oxide fuel cells (SOFC) applications by Will et al. [16], in which the formations of high-quality chemical composition films were emphasized. Besides those applications, a variety of nanomaterial coating with different chemical components were utilized in the study of spray printing (SP), which include nano-Cu particles and two-component Cu/Cu₂O [17], Cu and Ni particles [18], biomedical CaP ceramics [20], colloidal alumina particles [21], and silver (Ag) particles [22]. As shown in Figure 8, the silver ink diluted

with Ag nanoparticles was spray-printed on a flexible polyimide substrate, and then the dried film was formed after sintering. As can be seen clearly here in Figure 8(a), the grain-like boundaries were created due to insufficient adhesion of coating on substrate surface; the Ag particles typically less than 100 nm in size were also obtained as seen from the scanning electron microscope (SEM) picture in Figure 8(b). Poor electrical conductivity might be therefore expected in this case due to the non-uniformity of film morphology.

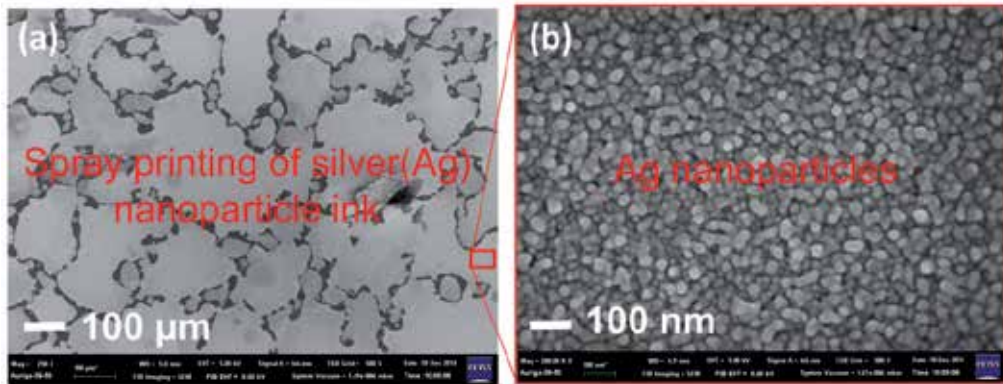


Figure 8. (a) Spray printing and sintering of silver (Ag) nanoparticle ink on polyimide surface and (b) magnified morphology of the printed Ag surface demonstrating the typical particle size less than 100 nm.

Obviously, it is noted here that the nanomaterial coating by spraying solutions may suffer from the weak interfacial strength between two layers of different materials. Nevertheless, compared to conventional deposition techniques such as PVD and CVD, this material coating application no doubt benefits low cost and time for processing, and therefore the interfacial problem deserves to be further improved in the future.

5.4. Liquid nebulization

For years, liquid nebulization has been generally used as an effective treatment for human airway disease such as panting. Mostly, with synthesis of different component concentrations and functions, aerosol delivery of pulmonary drug to human lungs is performed through spraying for medical therapy [48–49]. Because of the breathing need for patient therapy, those drug droplets of a spray generated from medical nebulizers typically feature an extremely small size ($< 5 \mu\text{m}$) to yield a high efficient absorption, in which the delivered amount of active drug could be as low as 20 mg for 4 h. Furthermore, micro actuators integrated with micron-sized nozzles are commonly applied in the nebulizers that have been commercialized and marketed over 10 years. As demonstrated in Figure 9, the portable and hand-held nebulizers with a compact size (e.g., $6.3 \text{ cm} \times 6.4 \text{ cm} \times 15 \text{ cm}$ for NH60) are available for quietly generating aerosol of different drugs such as albuterol, ipratropium, sulfate, etc. Aerosol performance on nebulization rate can be adjusted and controlled by users.



Figure 9. (a) Packet Air™ portable nebulizer by Microbase Inc. and (b) handheld tubeless nebulizer NH60 by Rossmax International Ltd.

5.5. Miscellaneous

In fact, all applications of the spray science and technology are quite versatile in many respects beyond those mentioned earlier [50–52]. The new development and progress in spray science and techniques can continue to be applied to more novel compound materials and micro-structured devices such as those demonstrated in the solar and fuel cells. Yet, the other multi-disciplines and creative ideas are being further blended into the field of sprays, perhaps yielding more fruitful applications in the future.

6. Concluding remarks

Over decades, many studies of science and technology have demonstrated the sprays to serve as an effective and efficient means for generation and evaporation of droplets. Many fundamental factors considered for pursuing the high-quality spraying involve appropriate selections of working liquids, operating actuators, droplet generation and evaporation, and spraying control. Preliminary design issues of microsprays concerning micro-actuators, nozzles, system integration, and control can be overcome by understanding and realizing fundamentals of working principles. Many applications in daily life and industry that include droplet evaporative cooling (DEC), direct and screen printing (SP), nanomaterial coating (NMC), and liquid nebulization (LN) have been demonstrated using spray techniques. In the future, this knowledge of science and technologies blended with the emergence of novel materials and devices may be promoted to the next generation of sprayers with higher performance than ever.

Acknowledgements

The author thanks research grant for this work partially by the Ministry of Science and Technology (MOST) under MOST 104-2221-E-151-036-MY2, Taiwan, ROC.

Author details

Chin-Tai Chen*

Address all correspondence to: chintai@kuas.edu.tw

Department of Mechanical Engineering, National Kaohsiung University of Applied Sciences, Kaohsiung, Taiwan, ROC

References

- [1] Andreas E. Time constants for the evolution of sea spray droplets. *Tellus*. 1990; 42B: 481-497.
- [2] Marcos A, Chow L, Du JH, Lei S. Spray cooling at low system pressure. In: *Proceedings of 18th IEEE SEMI-THERM Symposium*; 2002. p. 169-175.
- [3] Yang JC, Chien W, King M, Grosshandler WL. A simple piezoelectric droplet generator. *Exp. Fluids*. 1997; 23: 445-447.
- [4] Demirci U, Goksenin G, Yaralioglu G, Haggstrom E, Khuri-Yakub, BT. Femtoliter to picoliter droplet generation for organic polymer deposition using single reservoir ejector arrays. *IEEE Trans. Semicond. Manuf.* 2005;18: 709-714.
- [5] Sommerfeld M, Qiu, HH. Experimental studies of spray evaporation in turbulent flow. *Int. J. Heat. Fluid. Flow*. 1998; 19: 10-22.
- [6] Fisenko SP, Wang WN, Lenggono IW, Okyuama K. Evaporative cooling of micron-sized droplets in a low-pressure aerosol reactor. *Chem. Eng. Sci.* 2004; 61: 6029-6034.
- [7] Li T, Nishida K, Hiroyasu H. Droplet size distribution and evaporation characteristics of fuel spray by a swirl type atomizer. *Fuel*. 2011; 90: 2367-2376.
- [8] Hart AL, Turner APF, Hopcroft D. On the use of screen- and ink-jet printing to produce amperometric enzyme electrodes for lactate. *Biosens. Bioelectron.* 1996; 11: 263-270.

- [9] Jang Y, Park YD, Lim JA, Lee HS, Lee WH, Cho K. Patterning the organic electrodes of all-organic thin film transistors with a simple spray printing technique. *Appl. Phys. Lett.* 2006; 89: 183501.
- [10] Dong TY, Chen WT, Wang CW, Chen CP, Chen CN, Lin MC, Song JM, Chen IG, KaoTH. One-step synthesis of uniform silver nanoparticles capped by saturated decanoate: direct spray printing ink to form metallic silver films. *Phys. Chem. Chem. Phys.* 2009; 11: 6269-6275.
- [11] Peng Y, Zhong J, Wang K, Xue B, Cheng YB. A printable graphene enhanced composite counter electrode for flexible dye-sensitized solar cells. *Nano Energy.* 2013; 2: 235-240.
- [12] Abdelhalim A, Abdellah A, Scarpa G, Lugli P. Fabrication of carbon nanotube thin films on flexible substrates by spray deposition and transfer printing. *Carbon.* 2013; 61: 72-79.
- [13] Klim D, Baeg KJ, Yu BK, Kang SJ, Kang M, Chen Z, Facchetti A, Kim DY, Noh YY. Spray-printed organic field-effect transistors and complementary inverters. *J. Mater. Chem. C.* 2013; 1: 1500-1506.
- [14] Back H, Kong J, Kang H, Kim J, Kim JR, Lee K. Flexible polymer solar cell modules with patterned vanadium suboxide layers deposited by an electro-spray printing method. *Sol. Energy Mater. Sol. Cells.* 2014; 130: 555-560.
- [15] Chen CT. Inkjet printing of microcomponents: theory, design, characteristics and applications. In: Kamanina N. (editor). *Features of Liquid Crystal Display Materials and Processes*. Croatia: InTech; 2011. p.43-60. DOI: 10.5772/26225.
- [16] Will J, Mitterdorfer A, Kleinlogel D, Perednis D, Gauckler LJ. Fabrication of thin electrolytes for second-generation solid oxide fuel cells. *Solid State Ionics.* 2000; 131: 79-96.
- [17] Schulz DL, Curtis CJ, Ginley DS. Surface chemistry of copper nanoparticles and direct spray printing of hybrid particle/metallorganic inks. *Electrochem. Solid State Lett.* 2001; 4: C58-C61.
- [18] Kim JH, Babushok VI, Germer TA, Mulholland GW, Ehrman SH. Co-solvent assisted spray pyrolysis for the generation of metal particles. *J. Mater. Res.* 2003; 18: 1611-1622.
- [19] Makela JM, Keskinen H, Foesblom T, Keskinen J. Generation of metal and metal oxide nanoparticles by liquid flame spray process. *J. Mater. Sci.* 2004; 39: 2783-2788.
- [20] Leeuwenburgh SCG, Wolke JGC, Schoonman J, Jansen JA. Influence of deposition parameters on morphological properties of biomedical calcium phosphate coatings prepared using electrostatic spray deposition. *Thin Solid Films.* 2005; 472: 105-113.

- [21] Sen D, Mazumder S, Melo JS, Khan A, Bhattacharya S, D'Souza SF. Evaporation driven self-assembly of a colloidal dispersion during spray drying: volume fraction dependent morphological transition. *Langmuir*. 2009; 25: 6690-6695.
- [22] Park M, Im J, Shin M, Min Y, Park J, Cho H, Park S, Shim MB, Jeon S, Chung DY, Bae J, Park J, Jeong U, Kim K. Highly stretchable electric circuits from a composite material of silver nanoparticles and elastomeric fibres, *Nat. Nanotechnol.* 2012; 7: 803-809.
- [23] McPeck M, Tandon R, Hughes K, Smaldone GC. Aerosol delivery during continuous nebulization. *Chest*. 1997; 111: 1200-1205.
- [24] Wiedmann TS, DeCastro L, Wood RW. Nebulization of nanocrystals: production of a respirable solid-in-liquid-in-air colloidal dispersion. *Pharm. Res.* 1997; 14: 112-116.
- [25] Hertel SP, Winter G, Friess W. Protein stability in pulmonary drug delivery via nebulization. *Adv. Drug Deliv. Rev.* 2015; 93: 79-94.
- [26] Erbil HY. Evaporation of pure liquid sessile and spherical suspended drops: a review. *Adv. Colloid Interface Sci.* 2012; 170: 67-86.
- [27] Kang D, Strand RK. Modeling of simultaneous heat and mass transfer within passive down-draft evaporative cooling (PDEC) towers with spray in FLUENT. *Energy Build.* 2013; 62: 196-209.
- [28] Koseoglu MF. Investigation of water droplet carryover phenomena in industrial evaporative air-conditioning systems. *Int. Commun. Heat Mass Transf.* 2013; 47: 92-97.
- [29] Montazeri H, Blocken B, Hensen JLM. Evaporative cooling by water spray systems: CFD simulation, experimental validation and sensitivity analysis. *Build. Environ.* 2015; 83: 129-141.
- [30] Chen CT, Wang HY. Droplet generation and evaporative cooling using micro piezoelectric actuators with ring-surrounded circular nozzles. *Microsyst. Technol.* 2015; 21: 2067-2075.
- [31] Rahman K, Ko JB, Khan S, Kim DS, Choi KH. Simulation of droplet generation through electrostatic forces. *J. Mech. Sci. Technol.* 2010; 24: 307-310.
- [32] Li R, Ashgriz N, Chandra S. Droplet generation from pulsed micro-jets. *Exp. Therm. Fluid Sci.* 2008; 32: 1679-1686.
- [33] Hu BC, Weng RH, Chen CT. Silver conducting lines of dye-sensitized solar cells printed onto commercial building tiles. *Proc. Eng.* 2014; 79: 267-272.
- [34] Sawyer ML, Jeter SM, Abdel-Khalik SI. A critical heat flux correlation for droplet impact cooling. *Int. J. Heat Mass Transf.* 1997; 40: 2123-2131.
- [35] Mugele RA, Evans HD. Droplet size distribution in sprays. *Ind. Eng. Chem.* 1951; 43: 1317-1324.

- [36] Semiao V, Andrade P, da GracaCarvalho M. Spray characterization: numerical prediction of Sauter mean diameter and droplet size distribution. *Fuel*. 1996; 75: 1707-1714.
- [37] Huang JJ, Chen CT. Microelectroforming of a nickel nozzle plate featured with anti-stiction for a piezoelectric atomizer. In: *Proceedings of IEEE-NEMS*. 2013;p.490-493.
- [38] Kah D, Laurent F, Massot M, Jay S. A high order moment method simulating evaporation and advection of a polydisperse liquid spray. *J. Comput. Phys*. 2012; 231: 394-422.
- [39] Miyatake O, Koito Y, Tagawa K, MarutaY. Transient characteristics and performance of a novel desalination system based on heat storage and spray flashing. *Desalination*. 2001; 137: 157-166.
- [40] Fisenko SP, Brin AA, Petruichik AI. Evaporative cooling of water in a mechanical draft cooling tower. *Int. J. Heat Mass Transf*. 2004; 47: 165-177.
- [41] Wang HY, Huang C, Chen C. T. Specific design and implementation of a piezoelectric droplet actuator for evaporative cooling of free space. In: *Proceedings of IEEE-NEMS*. 2012;p.419-422.
- [42] Nagata R, Yokoyama K, Clark SA, Karube I. A glucose sensor fabricated by the screen printing technique. *Biosens. Bioelectron*. 1995; 10: 261-267.
- [43] Shaheen SE, Radspinner R, Peyghambarian N, Jabbour GE. Fabrication of bulk heterojunction plastic solar cells by screen printing. *Appl. Phys. Lett*. 2001; 79: 2996-2998.
- [44] Krebs FC, Alstrup J, Spanggaard H, Larsen K, Kold E. Production of large-area polymer solar cells by industrial silk screen printing, lifetime considerations and lamination with polyethyleneterephthalate. *Sol. Energy Mater. Sol. Cells*. 2004; 123: 749-756.
- [45] Krebs FC, Jorgensen M, Norrman K, Hagemann O, Alstrup J, Nielsen TD, Fyenbo J, Larsen K, Kristensen J. A complete process for production of flexible large area polymer solar cells entirely using screen printing. *Sol. Energy Mater. Sol. Cells*. 2009; 93: 422-441.
- [46] Krebs FC. Polymer solar cell modules prepared using roll-to-roll methods: knife-over-edge coating, slot-die coating and screen printing. *Sol. Energy Mater. Sol. Cells*. 2009; 93: 465-475.
- [47] Wang MW, Pang DC, Tseng YE, Tseng CC. The study of light guide plate fabricated by inkjet printing technique. *J. Taiwan Inst. Chem. Eng*. 2014; 45: 1049-1055.
- [48] McPeck M, Tandon R, Hughes K, Smaldone GC. Aerosol delivery during continuous nebulization. *Chest*. 1997; 111: 1200-1205.
- [49] Hertel SP, Winter G, FriessW. Protein stability in pulmonary drug delivery via nebulization. *Adv. Drug Deliv. Rev*. 2014; DOI: 10.1016/j.addr.2014.10.003.

- [50] Sazhin SS, Martynov SB, Kristyadi T, Crua C, Heikal MR. Diesel fuel spray penetration, heating, evaporation and ignition: modelling vs. experimentation. *Int. J. Eng. Syst. Model. Simul.* 2008;1: 1-19.
- [51] Li T, Nishida K, Hiroyasu H. Droplet size distribution and evaporation characteristics of fuel spray by a swirl type atomizer. *Fuel.* 2011; 90: 2367-2376.
- [52] Tveen-Jensen K, Gesellchen F, Wilson R, Spickett CM, Cooper JM, Pitt PR. Interfacing low-energy SAW nebulization with liquid chromatography-mass spectrometry for the analysis of biological samples. *Sci. Rep.* 2015; 5: 9736.

Overview of Materials for Microfluidic Applications

Emmanuel Roy, Antoine Pallandre, Bacem Zribi,
Marie-Charlotte Horny, François Damien Delapierre,
Andrea Cattoni, Jean Gamby and
Anne-Marie Haghiri-Gosnet

Additional information is available at the end of the chapter

<http://dx.doi.org/10.5772/65773>

Abstract

For each material dedicated to microfluidic applications, inherent microfabrication and specific physico-chemical properties are key concerns and play a dominating role in further microfluidic operability. From the first generation of inorganic glass, silicon and ceramics microfluidic devices materials, to diversely competitive polymers alternatives such as soft and rigid thermoset and thermoplastics materials, to finally various paper, biodegradable and hydrogel materials; this chapter will review their advantages and drawbacks regarding their microfabrication perspectives at both research and industrial scale. The chapter will also address, the evolution of the materials used for fabricating microfluidic chips, and will discuss the application-oriented pros and cons regarding especially their critical strategies and properties for devices assembly and biocompatibility, as well their potential for downstream biochemical surface modification are presented.

Keywords: microfabrication, prototyping, manufacturing, thermoplastics, thermoplastics elastomers, assembly, bonding

1. Introduction

Following Pasteur microbiology and Curie radiotherapy, the next coming and significant medical revolution is geared toward the foreseen convergence and integration of the following innovative science and technology components for the emergence of a new predictive, personalized, and preemptive medicine and practice. Bioengineering, microbiology, micro-

fluidics, optics, and electrochemistry are today the most significant key enabler disciplines. Their complementary features lead to complex systems and democratization and wide public access to personalized and new medical products that will promote both wealth and innovation at the same time, as the IT industry did in the last decades. This technological trend is of tremendous impacts in both sociological and economical applications. For example, the needs of *in situ* personal monitoring are crucial for the comfort and the health surveillance for our specific aging modern society, and it has become a major concern for the health care system. It offers additional opportunities to lower the hospital workloads and expense. It also promotes enhanced therapy efficiency through real-time and accurate monitoring for proper therapy delivery. The advent of rapid molecular diagnostic systems shortening pathogenic genomic identification down to 1–2 h in an integrated manner, beyond the standard cellular culture identification that may extend from several days up to few weeks is one of the most promising paths for decentralized and personalized medicine. In addition, it is also a powerful asset to address major problems in bacterial antibiotic resistance. Beyond human health, rapid molecular diagnostic approaches deserve multiple segments from water quality control to veterinary and agronomy fields for widely accessible, deployable, and low-cost analytical systems. The others aspects of the emergence of microfluidic polymer systems are to act as template for dedicated and addressable microenvironments, thus promoting the organogenesis of organs reconstruction and substitution and sustaining the development of novel drugs that are cost effective.

Moreover, the microfluidic science and applications are by essence multidisciplinary. For a targeted application, a seamless and holistic vision is of tremendous importance. In this chapter, we aim to provide an overview of materials used for microfluidic applications. Their selection, evaluation, and integration at both prototyping scale and toward mass production are discussed. Due to the fact that some materials and strategy might be suited for specific goals yet not fit for others, the specific drawbacks and advantages regarding their status and potentials toward a path to products are analyzed.

2. Materials for microfluidic applications

From research development to microfluidic platform applications and product transfer, a holistic and seamless strategy has to consider from the start point to the end. The right selection of the material interface, which might be suited for certain targeted applications, can be detrimental for another purpose. Therefore, navigating material sciences for microfluidic technology is somehow a nebulous nightmare. These difficulties are also enhanced according to the fact that these microfluidic techniques were developed by the physics and engineering landscapes involved in information technology (IT) research and development (R&D), and therefore they exploited silicon-based clean room technologies. The lack of an adequate material culture related to biomaterials and polymer-based microstructure induced obvious limitations, which is a significant inhibiting factor for further industrial transfers. Besides the complexity and the interdisciplines involved in microfluidic applications, where bioengineering, microbiology, microfluidics, optics, materials science, and electrochemistry are concerned,

proper and deep understanding and paradigms of each community are a must for any achievement of a significant system. Still at its early age, microfluidic science and technology have already made successful demonstrations addressing the issues; however, this knowledge is still mostly limited to chemistry, biology, and physics researchers; and unfortunately, it has not sufficiently penetrated yet the biomedical research and clinical environments. The goal of this chapter is thus to fill the gap and promote pertinent highlights on materials performance for microfluidic applications.

Legacies from microelectronics industry and the glassware history in biomedical and chemistry areas, both silicon and glass materials, constitute the initial materials for microfluidic device fabrication. Currently, materials dedicated to microfluidics can be categorized into three broad groups: inorganic, polymers, and paper. Beyond silicon and glass, inorganic materials extend over co-fired ceramics and vitroc ceramics. The second polymer-based category can be divided into two subcategories (i) thermoset materials, which are thermal or UV curable materials from a low viscosity precompound dispensed over a mold and (ii) thermoplastic materials, which are thermoformable materials amendable for rapid prototyping and manufacturing. Both polymer subcategories display rigid to elastomer mechanical properties, and through adaptable formulation and enriched chemical modification, offer a broad range of physicochemical surface properties. Finally, paper microfluidics is an emerging technology based on a patterning approach, where devices drive liquid through capillary actions via wicking in a cellulose matrix.

2.1. Inorganic materials: silicon, glass and ceramics

Silicon was the first material used for microfluidics [1]. Indeed, in the mid-80s, the microelectromechanical systems (MEMS), from which microfluidic technology is one of the branches that handle fluid, were developed by microelectronic technology. In MEMS, silicon material

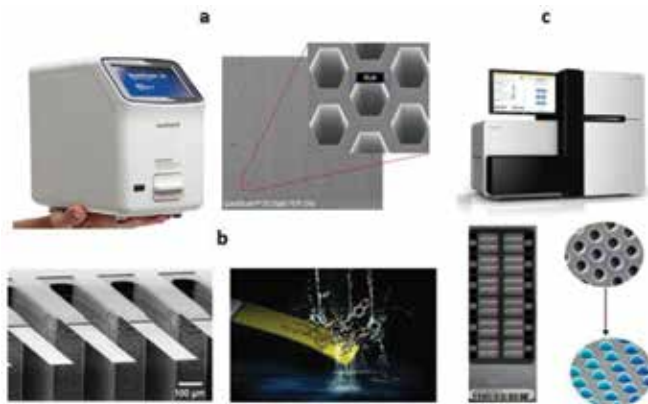


Figure 1. (a) QuantStudio 3D Digital PCR system from Life Sciences and its silicon chip, 60 μm hexagonal wells organized in a honeycomb structure. (b) Array of Si cantilevers for label-free biodetection of illicit drugs in water. (c) Next generation sequencing HiSeq 2000v3 system developed by Illumina and the silicon chip for microbeads immobilization.

was the standard material interface. Fabrication of silicon and glass devices involves either subtractive methods (e.g., wet and dry etching) or additive methods (such as metal/dielectric/insulate deposition). Silicon surface chemistry based on the silanol group (-Si-OH) is also well developed and large panels of surface biochemical modification accomplished via silanes chemistry are accessible. Silicon displays a high elastic modulus (~150 GPa) and so, in such a way, active pumping and valving integration, as well as Si brittle characteristics induced overall fragility. Therefore the narrow windows of mechanical properties are limiting factors. Transparent to IR light, but not in visible range, can cause serious issues and limitations that are obvious for biological fluorescence-based optical detection methods and for direct fluid imaging. Those issues can be partially solved via several hybrid system approaches, where Si channels can be sealed with transparent materials, such as glass or polymers, leading to a renaissance for Si-based detectors for microfluidic systems. However, Si microfluidic systems, where reagent storage and other embedded biochemical surface functionalization (e.g., DNA, proteins and cells patternings) are required, feature limitations when considering final assembly and package steps. Indeed, high pressure, temperature, and voltage constraints induced complex strategies for overall device integration concerns. Current approaches such as reactive ion etching (RIE) for plasma exposure in order to activate surface for sealing purposes or high temperature, high pressure parameters for anodic bonding methods are definitively not suitable when considering reagent integration, such as proteins, cells, and nucleic acids species. Even recent efforts developed by Ruchi et al. [2], who reported a low-temperature bonding strategy and Si-Si interface bonding at low-voltage direct current of about 80 V, the procedure was still performed at a processing temperature of 365°C. For the aforementioned strategy, where a hybrid system is implemented, the definite air-tight and water-tight sealing achievements, which are also of priority for biomedical applications considering contamination issues, suffer from the rather similar limitations. Indeed, hybrid approaches in most cases currently consist of realizing a pressure-free soft contact with the rigid silicon part that needs either oxygen plasma exposure or thermal treatment for sealing and device completion. However, at the research level, due to the high resolution of Si nanofabrication capabilities realized by either electronic beam or nanoimprint lithography among others, and its enriched surface chemistry means for biomolecular grafting, the following highly representative examples and significant achievements for the microfluidic community are highlighted. Applications related to the high-resolution capabilities of silicon extend over plasmonic, resonators, and microcantilevers systems. Indeed, high-quality nano-optomechanical resonators exhibiting mass sensitivity at the attogram level in the flow through operating environment have already been reported [3]. Si plasmonic microarrays have been interfaced for real-time and label-free monitoring of biomolecule interactions of A/G with immunoglobulin G (IgG) antibody [4]. Finally, as a tremendous achievement for the Si-based microfluidic approach, beyond the aforementioned limitations, we wish to underline the obvious advantages of the stationary Si-based system for complex digital qPCR platforms for genomic applications. Quantitative determination of pathogenic loads with such Si platforms definitely opens an area for medical research that benefits patients. In comparison to low-cost and single-use POC (Point-of-care) devices for decentralized purposes, where challenges involved with silicon materials imposed challenging technical needs, Si interface and glass are

strategic materials of interests for stationary and highly complex systems. **Figure 1(a)** presents the QuantStudio® 3D Digital PCR system and the related silicon chip developed by Life Sciences Technologies Inc. (St. Petersburg, FL, US). We also refer the readers to the silicon EWOD qPCR platform developed by Gidrol et al. [5] and for further interests to a recent review by V. Marx [6]. Finally, the silicon interface is the material of reference for the vast majority of nanomechanical biosensor [7] systems based on the cantilever approach as illustrated in **Figure 1(b)**. Recently, an array of Si cantilevers for label-free biodetection of illicit drugs in water has been reported [8]. For next generation sequencing (NGS) purposes, **Figure 1(c)** displays the HiSeq 2000v3 system developed by Illumina Inc. (San Diego, CA, US) and the silicon chip realized for microbeads immobilization.

Besides Si, glass, due to its wide applications in chemistry has been adopted as a key material for lab-on-a-chip fabrication. Optically transparent with excellent and low-fluorescence background, glass also displays highly suitable chemical resistance. Thus it has emerged as a material of choice. Its transfer to microfluidics has been facilitated due to the traditional “off-chip” chemistry developed over several decades. Glass microfabrication involves well-established processes such as UV photolithography and chemical etching; however, such technologies rank relatively low when considering further manufacturing perspectives, compared to rapid thermal molding technology for polymer-based microfluidic system. It is for this reason the glass is generally viewed as an application material. Conversely, it may be easier and potentially less cost effective to fabricate small number of microfluidic devices in glass than making molds for replication purposes using polymer-based systems. The chemical and thermal properties of glass enable a wide range of functions to be undertaken on the device, including the requiring aggressive and corrosive solvents, chemical agents, and others extreme temperature applications. Finally, assembly, conditioning, and on-chip reagent storage steps suffer similar limitations to the Si material. In particular, the glass fusion bonding is extremely slow and requires very high temperature. However, for high-pressure demanding applications associated with its strength, maintaining high level of channel integrity over operation, glass is definitively positioned at the preferred place. Compatible with electrophoretic-based separation techniques, microfluidic glass chips have been used for numerous demonstrators and coupled to either mass spectroscopy, electrochemical, or chemiluminescence detection means among others. From peptides to vascular biomarkers and DNA identification, we refer the reader to recent comprehensive reviews on advances for glass μ CE chips [9, 10]. Glass mostly used the microfabrication approach that involves standard UV photolithography in combination with either dried or wet etching protocols. Frequently used wet etching chemical solutions feature a significant isotropic etchant property, therefore, the achievement of microchannels with straight and high aspect ratio structures are challenging. Alternative etching profiles such as anisotropic or straight-walled patterns can be done with dried RIE processes. Micromilling of glass is the second-most used approach. It is a subtractive process, where a rotating cutting tool removes material from a workpiece. Compared to micromilling of polymers, more attention for glass is required. This is primarily due to its high hardness and low tensile strength. Most milling is done using computer numerical control system (CNC micromachining), which represents a great deal of opportunity and flexibility in terms of pattern generation. However during processing, overheating of the diamond-

coated drilling tool has to be considered, and cooling strategies therefore are implemented. Definitely, CNC micromachining offers a high level of interest for rapid prototyping of glass microchip, we refer the readers to the recently published micromilling tutorial review [11, 12].

Illustrating the high-performance capabilities of the glass interface for highly demanding applications, **Figure 2(a)** presents the microchip developed by Chan et al. [13] for the high-temperature synthesis of CdSe nanoparticles in nanoliter-volume droplets in a perfluorinated fluid carrier. **Figures 2(b)** and **(c)** highlight the recent efforts by Klearia (Marcoussis, France) and Dolomite (Royston, UK) companies for the development of low-temperature bonding protocols for embedded technologies. Finally, related to the development of NGS technologies, **Figures 2(d)** and **(e)** depict the glass chips made by Pacific Biosciences (Palo Alto, CA, USA) and Roche Diagnostics (Indianapolis, IN, USA) for their single molecule real-time sequencing technology (SMRT) and their 454 sequencing systems, respectively. Distributed by Weill Cornell Medical Researchers (Ithaca, NY, USA), each SMRT cell is provided at a cost of \$ 400.

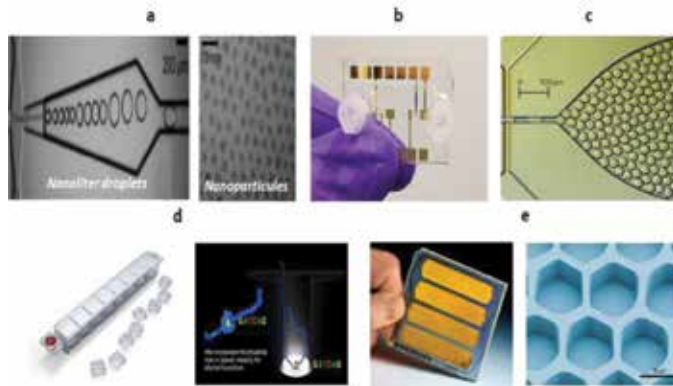


Figure 2. (a) Glass chip for high-temperature (300°C) synthesis of CdSe nanoparticles from nanoliter-volume droplets. (b) Array of Si cantilevers for label-free biodetection of illicit drugs in water. (c) High demanding (500°C and 300 bar) glass chip for droplet generation form dolomite. (d) Pacific Biosciences single molecule Real-Time Sequencing glass chip. (e) Glass PicoTiter plate for DNA sequencing systems from 454 DNA sequencing system.

Ceramic microfluidic platforms can be fabricated using low temperature co-fired ceramic (LTCC) technology for the achievement of hermetically sealed monolithic microfluidic platforms with homogeneous surface chemistry and physical properties through a pertinent cost-effective manner compared to Si and glass platforms. This is a well-established technology for low-cost and high-volume production of portable wireless electronic applications, but yet with limited involvement into the microfluidic landscape. However, its multilayer fabrication approach allows monolithic integration of complex structures. As a result, three-dimensional microfluidic channels and cavities have been already reported [14]. The compatibility with ink printing techniques has enabled the development of highly integrated devices that incorporate electrochemical detection as well as all the electronic components for signal and data processing [15]. However, the integration of optical detection means in such platforms still constitutes a serious issue due to the overall opacity of ceramic material. To mitigate this issue, two

strategies have been implemented: (1) the integration of optical fiber and (2) the implementation of transparent windows for localized optical analysis [16]. Recently, Microresist Technology Inc. (Berlin, Germany) developed a promising and organically modified ceramic Ormocer as an optically transparent and UV curable ceramic material to fix this issue.

2.2. Polymers: thermoset and thermoplastic materials

In the last 15 years, polymers have played the leading role from prototyping and manufacturing perspectives. This is because they offer a broad range of physical and surface chemical properties through adaptable formulation and enriched chemical modification. Based on their adhesiveness intrinsic properties, or activated bonding strategy, complex and 3D multilayered systems have been implemented. Considering both the cost of raw materials and manufacturing perspectives, several polymer interfaces, but none of all, are amendable to mass production processes (e.g., hot-embossing, injection-molding, and roll-to-roll). For the aforementioned thermoset subcategory, the most common materials are thermal and UV curable materials, Respectively, polydimethylsiloxane (PDMS) and the so-called SU-8 photoresist [17, 18]. On the thermoplastic side, the most popular materials are polycycloolefin (PCO), polycarbonate (PC), polytetrafluoroethylene (PTFE) and polystyrene (PS). Polycyclo-olefin offers high moldability and low water uptake [19, 20]. Polycarbonate [21] has excellent material toughness properties while polytetrafluoroethylene [22] and polyimide [23, 24] feature excellent chemical resistance, electrical, and thermal properties, respectively. Polystyrene has become more and more involved for cellular-based microfluidic systems, due to its wide applications in cell biology. Indeed, PS has provided decades of conclusions and sensitive protocol establishment, and numerous cell behaviors and functions have been determined [25]. Currently, PDMS and a dozen thermoplastic materials cover the vast majority of microfluidic research activities. The intensive use of PDMS is devoted to rapid prototyping and proof-of-concept demonstrations. However, despite its intrinsic drawbacks, mainly related to its cellular toxicity, molecular adsorption and absorption, gas permeability, and bonding issues, PDMS still appears as the preferred material in laboratories. Its industrial transfer is generally not overly recommended due to the cost concern. On the other hand, although thermoplastic interfaces offer the solution for product development, the entry cost in terms of required mold making as well as equipment setting limits its development. In addition, only well-established groups have significant infrastructures and facilities to afford it. To end this section, recently introduced soft thermoplastic elastomers (sTPE) are discussed. These materials bridge the gap between PDMS and classical rigid thermoplastic materials such as PC, PCO, and PS [48–52]. The sTPE materials are low-cost and commercially available polymers, offering transparency, biocompatibility, and flexibility compared to PDMS, and they can be rapidly thermoformed like currently used thermoplastics. Additionally, they display enhanced molding properties; indeed, low-pressure molding can be performed (e.g., <1–2 bar), lowering down the thermomechanical properties of the required molds. Due to their elastomeric properties, they can easily be peeled off from the mold. Assembling and bonding procedures are more convenient, and cohesive sealing can be done without thermal and/or plasma treatment. This material promotes a seamless integration, promoting therefore a realistic transfer path from prototyping to feasible and realistic industrialization. The sTPE

material could become a mainstream platform for microfluidic technology and POC applications.

2.2.1. Thermoset

Thermosets are liquid or solid materials at room temperature. Their molecular polymer chains cross-link through a process called curing, when the polymer is heated or exposed to light or to others radiations. The curing step involves an irreversible chemical reaction. Therefore once formed, the thermoset parts cannot be reshaped anymore. Typical examples of thermoset polymers used in microfabrication are PDMS and SU-8 materials.

2.2.2. PDMS

First introduced in the late 90s, PDMS [26] is the most common microfluidic substrate, a large portion (40–45%) of research papers published on microfluidic devices utilizes this material [27]. Devices' molds are formed via traditional micromachining and photolithography means and a mixture of two liquid polymer components are mixed together and then casted, cured, and finally peeled off from the master. Due to its elasticity, integration of microvalves or micropumps is possible, and complex 3D system and numerous point-of-care devices have been developed for research applications. PDMS displays excellent optical properties for convenient fluorescence detection and fluid imaging. Due to its gas permeability, PDMS appears as a material of choice for many but not all cellular studies.

On the other hand, four important properties of PDMS have negative impacts: (1) channel deformation due its high mechanical compliance, (2) evaporation and absorption, (3) leaching-out of uncrosslinked oligomers, and (4) hydrophobic recovery [25]. The compliance issue is particularly true considering cell culture experiments that require accurate control over shear force on the endothelial monolayer, the inability to account for mechanical deformation bias in data analysis and subsequent data interpretation [28]. Oxygen permeability in PDMS is three orders of magnitude higher as compared to PS, and may in fact produce a hyperoxic micro-environment leading to cellular stress [29, 30]. Water vapor resulting from the permeable PDMS also leads to problematic shifts on volumes, concentrations, and chemical balances [31]. PDMS is also largely prone to bulk absorption of hydrophobic compounds. Regehr et al. [32] have shown significant depleted estrogen levels in culture media, leading to inhibition of protein-1 activator. Similarly, important shifts were identified in response to fluoxetine over transfected human embryonic kidney (HEK) in between PDMS and polystyrene interfaces [33]. Finally, absorption not only affects fundamental cellular biology on chip, but also drug discovery and high-throughput screening applications. However, the PDMS abilities to provide rapid (1–4 h), easy, low-cost (50–200 \$/kg) and straightforward accessibility make it a major leading player for prototyping uses at academic level. However, its commercial applications are generally avoided. A noticeable exception emerges from this mainstream Eration, indeed around the multilayered PDMS pressure-actuated crossed-channel valve architecture initially developed by Quake et al. [34]; the Fluidigm company (San Francisco, CA, USA) has developed several impressive applications ranging from qPCR platforms to mass cytometer as depicted in **Figure 3(a)** and **(b)**. Such system can run 48 samples in 770 reaction chambers.

Each chip shown in **Figure 3(c)** ranges at a cost from \$ 400 to 800. This price highlights the intrinsic and overall PDMS difficulties and its lengthy processing steps to tackle for low-costs microfluidic system for single use perspective. We refer the readers to the following reviews for extended discussion related to microfluidic products development and the ambiguous positioning of PDMS material in the community for applications development [25, 35, 36].

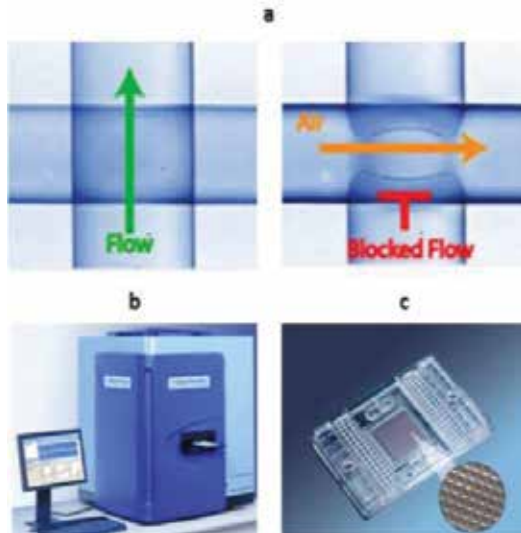


Figure 3. (a) Bilayer PDMS pneumatic valving microfluidic system, liquid flow inside the vertically oriented top channel and the bottom channel (air flow) is pressure-actuated for clogging/or liquid motion of the fluidic layer. (b) and (c) Biomark HD system for digital qPCR from Fluidigm, which run 48 samples in 770 reactions/sample chip.

2.2.3. SU-8: an epoxy-based material

Using classical means of photolithography or stereolithography, SU-8 microfluidic devices can be built in a complex 3D structure out of an initial liquid resist. SU-8 contains eight epoxy groups which undergo a very strong crosslinking upon exposure to UV light. Such composition and process lead to highly mechanically, thermally, and chemically stable materials. However, large internal stress exists due to the process, providing thus an overall brittle characteristic, and therefore making it difficult in handling and transferring part. SU-8 can be deposited and patterned in a range of thicknesses from nanometer to millimeter films, using lithography (either UV and e-beam), the lateral feature resolution extends from the macroscopic surface down to submicrometer. SU-8 can be structured also from the laser ablation approach. However, as for photolithography means, it appears that both methods have limited throughput [37]. Indeed, the cycle for resin preparation and others processes are lengthy. It seems that SU-8 is limited mainly to academic uses. For in-depth descriptions of the SU-8 interface for microfluidic applications, we refer the reader to a couple of comprehensive and exhaustive reviews [18, 38]. Beyond its use for direct microfluidic device fabrication, SU-8, due to its high mechanical strength and its capabilities to create high aspect ratio structures [39]

and complex 3D networks [40], is definitely a material of choice for mold master making. The SU-8 mold has been intensively used for hot-embossing of thermoplastic devices, or as an intermediate system for injection-molding [41].

2.2.4. *Alternative thermoset material*

Besides PDMS soft thermoset material, several attempts have been introduced in order to provide alternatives for soft thermoset materials and mainly the use of fluorinated-based polymers has been reported. The attractiveness of those solutions arises from the inertness of the perfluorinated compounds. De Simone et al. [42] have developed a photocurable soft perfluoropolyethers (PFPE). It exhibits low toxicity and low surface energy and displays enlarged chemical resistance. For multiphasic microfluidic environment, it might be a material of choice due to the fact that such Teflon-like structure is both oleophobic and hydrophobic. More recently, high aspect ratio (up to 6.5) PFPE microfluidic devices have been fabricated by a direct photolithographic process. Through a mask-assisted photopolymerization approach, the authors have successfully developed a rapid overall process of around 5 min and demonstrated important sealing capabilities, indeed the device can withstand a pressure up to 3.8 bar [43]. Finally, the devices have been tested with some model reactions employing organic solvents.

2.2.5. *Thermoplastic polymers*

2.2.5.1. *Rigid thermoplastics*

According to the aforementioned drawbacks of PDMS, intensive use of thermoplastic materials, such as polycarbonate and polystyrene, is increasing. These materials are amendable for rapid thermoforming manufacturing technology in the CD and biology industries. Those platforms have been clearly identified as materials of choice for microchip research and subsequent technology transfer. Complementary polymethylmethacrylate (PMMA) and polyimide, due their favorable position in the semiconductor industry, complete the set of foreseen thermoplastic candidate. More recently, polycyclo-olefin polymer has become another popular substrate for microfluidics. It displays high chemical resistance, low water absorption, and excellent optical transparency in the near UV range. The materials are moldable polymers when heated above their glass temperature, offering thus recyclable and reshaping perspectives. They also provide a subsequent bonding pathway. They are optically clear and commercially available, and they display slightly better solvent compatibility than PDMS. However, they are incompatible with most organic solvents, such as ketones and hydrocarbons. Currently used thermoplastic interfaces are rigid and stiff materials with Young modulus in the range of Giga Pascal. Consequently, they are not as convenient as PDMS to achieve conformal contact. Therefore, sealing strategies involve pressurized solvent-assisted and thermal approaches to melt surfaces. In addition, the following thermoplastics: perfluoroalkoxy (Teflon PFA) and fluorinated ethylenepropylene (Teflon FEP) can be used for extremely inert microfluidic devices. Ultimately, they feature nonstick and antifouling properties. PFA has been used for high-quality immobilization of *Escherichia coli*, *Pseudomonas*

putida, and *Bacillus subtilis* cells in highly dense microarray patterns [44, 45]. For more classically used interfaces, Zhang et al. [46] reported sealing and chemical surface modification of an integrated monolithic PMMA microdevice for DNA purification and amplification of *E. coli*. Also, a highly integrated polystyrene microfluidic chip coupled to electrospray ionization mass spectrometry for on-chip protein digestion and online analysis was developed [47]. One of the most important challenges faced when targeting for molding of thermoplastic parts is the realization of the master cavity featuring submicron resolution, high aspect ratio, and densely packed structure areas. Most of the materials are crystalline and/or semi-crystalline, and they display high coefficient of thermal expansion (CTE) and high shrinkage parameters compared to amorphous ones. Additionally, due to the fact that they are rigid and often brittle, they represent sensitive challenges from the manufacturing perspectives. The high shear force resulting from the pressurized environment generates asymmetric and/or random pull-off of plastic edges due to friction in demolding, which is downstream detrimental for sealing and bonding. The characteristics of the thermoplastic materials induce high specifications on the thermo-mechanical properties of the master molds. Currently, the impacts on the master mold making related to the realization of such thermoplastic parts are only metallic (stainless, nickel-cobalt alloy, and aluminum), and from prototyping perspectives, only few epoxy molds can be employed. Even if elegant CNC laser machining and electroplating processes are available for mold making, the implementation of such master are expensive and are limited in terms of resolution, pattern density, and aspect ratio. The work suggest an overall in-depth consideration when starting to envisage a microfluidic system development, undoubtedly a holistic approach should be taken. The overall chip constraints in terms of fabrication, sealing, packaging, thermomechanical loads, biological compatibility (both in terms of physicochemical surface properties and reagent integration), biomicrofluidic functions, microfluidic statistical, and robust properties have to be considered.

2.2.5.2. Soft thermoplastic elastomers: sTPE

The sTPE is a class of material in which elastomeric properties of elastomer rubber (e.g., PDMS) are embodied with the ease of processing of thermoplastic materials such as PMMA, PCO, and PC. The sTPE thus bridges the gap in between thermoplastics and elastomers, enhancing the advantages of each material. Moreover, the range of sTPE Young modulus extends continuously from 0.1 MPa to 1–5 GPa. The combination of elastomeric and thermoplastic properties makes these materials potential substitutes to PDMS and/or hard TP polymers that are commonly employed in microfluidics [48]. Unlike PDMS, sTPE can be used in the form of extruded sheets that provide off-the-shelf availability without the need of performing any precompounding step. Extruded films can be stored over a long period of time (e.g., several years) without any notable degradation, making it possible to use the material on demand at any time (**Figure 4(a)**) [49, 50]. The sTPE materials are available at low cost, and they display optical transparency and biocompatibility for proteins, nucleic acids, and cell and tissue engineering and diagnostics [49–53]. sTPEs are block copolymers comprising different monomer sequences that are distributed randomly or statistically in domains through diblock or triblock architectures [51]. For styrenics-based sTPE materials with low PS content (10–12%), thermodynamic incompatibility between blocks induces

nanophase separation and self-assembly of PS domains into nanometric clusters (typically 10–30 nm in diameter) that are distributed in a three-dimensional fashion within a hexagonal symmetry in the rubber matrix of ethylene-butylene (EB). This morphology provides the basis of the material performance: rigid PS domains act as junction points that stabilize the polymer matrix while the EB-dominant phase offers elastomeric properties. Moreover, size and cluster distributions promote the sTPE surface to be uniform and homogenous at the microfluidic device level [49–53]. As block copolymer materials, sTPE exhibits two glass transition temperatures corresponding to the EB soft block ($T_{g,EB} \sim -60$ to -75°C) and to the styrene rigid block ($T_{g,EB} \sim -90$ to 105°C), respectively. The negative value of $T_{g,EB}$ predicts liquid-like behavior of the materials.

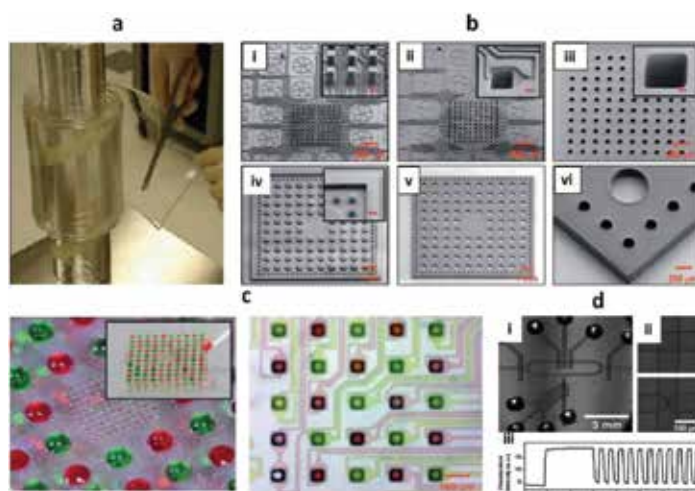


Figure 4. (a) Photograph of an extruded flexestene foil on a roll from which pieces can be cut conveniently before use. (b) Series of SEM images illustrating the fabrication of the microfluidic flexestene device. (i) SU-8 embossing mold used for the fabrication of the bottom flexestene membrane, (ii) Upper and (iii) lower side of the bottom sTPE membrane, (iv) SU-8 mold used for the fabrication of the top sTPE membrane, (v) overview, and (vi) close-up view of the top flexestene membrane. Scale bars in the insets of (i), (ii), (iii), and (iv) correspond to 50, 20, 10, and 200 μm , respectively. The images shown in (iv) and (v) were assembled from several SEM micrographs to achieve the desired field of view. (c) Photographs of an assembled 3D microfluidic immobilization after filling with solutions of a red and green dye (left), optical microscope image of the resulting red-green pattern obtained on the central region of the microfluidic device (right). (d) high-throughput fabrication method of sTPE multilayered microfluidic devices, (i) Optical micrograph of the whole micromixer made of two layers of sTPE material bonded on a poly(cyclo)olefin polymer substrate. The device size is smaller than a centimeter square, and each valve measures $200 \mu\text{m} \times 200 \mu\text{m}$, (ii) detailed view of a valve at both open and closed positions; and (iii) curve representing the valving cycle at 1.2 Hz, fluorescence intensity under the deflected membrane is registered, it is maximal when the valve is open and minimal when closed.

Indeed, like PDMS, which similarly displays a negative glass transition temperature, the selected sTPE forms a spontaneous and conformable close contact with flat substrates, generating tight air and water sealing [49–53]. Additionally, the soft blocks provide bonding capabilities above their glass transition, which implies that even at room temperature, the polymer chains can be reorganized according to the contact surface. The bonding strength is variable and dependent on time and temperature; and irreversible bonding was obtained at

room temperature [50, 52]. Depicting the enhanced molding capabilities of sTPE interface, Brassard et al. [51] have demonstrated the rapid and reliable patterning of open through-hole microstructures in sTPE material using a method based on hot-embossing (**Figure 4(b)**). The sTPE-based 3D microfluidic patterning device was then used for the immobilization of up to 96 different biological probes in a 10×10 array format of 50 μm×50 μm spots (**Figure 4(c)**).

Additionally, for novel tissue engineering biomaterial platform, high molding performances have been confirmed in a newly reported process. We reported a rapid microfabrication of a biocompatible sTPE sheet in an overall 3 min process operating within an ultralow applied pressure (1.6 bar) [52]. Smooth muscle cells contact guidance studies have been conducted over an array of 4-μm-patterned grooves [52]. For reader's information, contributing to the establishment of the biocompatibility, the bonding and the microfabrication performance of sTPE, which are highly dependent on block copolymers formulation (molecular weight of each block of each diblock (DB) and triblock (TB) and the DB/TB ratio) and also to the additives composition (tackifiers and processing agents); we underline the Flexstene sTPE materials performance (InfineFlex Inc., San Diego, US and Blackholelab Inc., Paris) for the fabrication of adjacent micropillar arrays with different heights for cellular studies [53]. We also demonstrated that sTPE can be used as a rapid technique for the fabrication and assembly of pneumatically driven valves in a multilayer microfluidic device using a simple SU-8 mold material for embossing purposes (**Figure 4(d)**) [54]. The quality of the obtained soft thermoplastic valve shows a robust behavior with an opening-closing frequency of 5 Hz. Finally, more recently [49], we demonstrated the implementation of a sTPE CD-like microfluidic system for genomic assay. This device integrates all required molecular assay steps, from cellular lysis to gDNA polymerase chain reaction amplification, amplicons digestion, and microarray hybridization on a plastic support. The low-temperature, pressure-free assembly and bonding of sTPE material on the flat polycyclo-olefin thin substrate offer a pertinent solution for simple and efficient loading and storage of the required on-CD board elements. This was demonstrated through the integration and the conditioning of microbeads, magnetic discs, and dried enzyme species. This work highlights a seamless strategy that promotes a feasible path to transfer from prototyping toward realistic industrialization. This work aims to establish the full and pertinent potential for sTPE centrifugal system as a mainstream microfluidic diagnostic platform for clinical molecular diagnostics, water and food safety, besides other applications.

2.3. Paper, biodegradable and hydrogel materials

2.3.1. Hydrogels

Hydrogels display a molecular architecture analog to extracellular matrix, with water uptake properties up to 80% of its total mass. Hydrogels are highly porous and thus an excellent matrix for cellular biology studies. However, direct tissue engineering from bulky hydrogels are challenging due to the restricted depth for nutrients diffusion of around hundreds micrometers [55]. Microfluidic technology, through both top-down and bottom-up approaches, has demonstrated its abilities to tackle this fundamental issue. From a top-down approach, microchannels are fabricated inside the hydrogel while for the bottom-up, hydrogels filled

microchannels cavities. Matrigel™ and collagen are the mostly used animal-derived hydrogels. They promote excellent cellular adhesion and proliferation [55]. Recently, Bang et al. [57] engineered a 3D neural circuit in a microfluidic Matrigel hydrogel system. They had grown, aligned, and organized 3D networks of axon bundles at an average speed of 250 $\mu\text{m} \cdot \text{d}^{-1}$ for a period of 6 *in vitro* days. Alternatively, alginate and agarose plant-derived hydrogels and synthetic ones, such as polyacrylamide or polyethylene glycol (PEG), can be used [58]. Even though synthetic hydrogels slightly lack cellular adhesion compared to animal-derived ones, they nevertheless promote higher flexibility and enriched formulation adaptability for fine tuning objectives. Hydrogel composition, structure, morphology, and rigidity have been used in a high-throughput manner in droplet-based microfluidics [59]. Recently, agarose hydrogels have been integrated in a microfluidic system for *E. coli* purification and concentration, and finally for fluorescence immune detection. Authors reported that 90% recovery efficiency could be achieved with a million-fold volume reduction from 400 μL to 400 pL . For concentration of 1×10^3 cells mL^{-1} bacteria, approximately ten million-fold enrichment in cell density was realized. Urine and blood clinical isolates were further tested and validated [60]. We refer the readers to follow the review for further reading [61].

2.3.2. Biodegradable materials

Biodegradable polymers for tissue engineering and drug delivery purposes display degradation time ranging from 24 h to several months. They offer, in a microfluidic format, a promising opportunity for microstructured tissue scaffolds. Commonly used biodegradable matrices are polycaprolactone, poly(lactide-co-glycolide), and polyglycolic acid (PGA). Their degradation and mechanical properties are tunable, and they display minimal changes in the systemic immune responses. Their degradation products such as glycolic acid for PGA are through metabolite response absorbed by the hosted living body. Curing of these materials takes place as their dimer version polymerizes via a ring-opening reaction under appropriated heating and catalytic steps. An excellent review related to biodegradable material properties and their microenvironment integration has been recently published [62]. Various technologies, such as printing, soft-lithography, stereolithography, hot-embossing, and injection-molding methods, have been used toward integration [63, 64].

2.3.3. Paper

Paper is the most recently introduced microfluidic material. Its cellulose matrix acts to wick liquids while specifically, hydrophobically, patterning areas to avoid liquid motion. The patterned barriers define the shape (i.e., width and length) while the thickness of the paper accounts for the height. Hydrophilic wicking regions thus serve as channel networks opened to air. Paper as chip material is one of the cheapest materials, and it can be easily stacked in 3D devices [65]. The fabrication approaches can be divided into two groups. Lithographic-based methods, where particular coated polymer areas are removed, thus are forming the channels. Second, the printing and the cutting approaches allow direct hydrophobic barrier definition without exposure of the effective channels to any reagents. Fundamentally, paper-based microfluidic systems are not suitable for large-volume samples and their applicable

detection perspectives are limited owing to the intrinsic cellulose matrix properties. Recently published by Mace et al. [66], paper-based diagnostic devices and their manufacturing perspectives are commented in detail. Wax printing approaches and assembly of 3D vertical flow assays are further discussed therein. Concerning printing and cutting approaches, the reported channel resolution is quite low and limited to 200 μm . Paper-based technology, displays undoubtedly tremendous limitations considering heterogenous component integration such as valves and other reagent storage issues. Recently, Thom et al. [67] have performed the integration of light-emitting diodes (LEDs) onto paper microfluidic device for the fluorescence detection of β -D-galactosidase. From medium to low complexity bioassay integrations, paper-based technology appears to be a promising pathway for portable and low-cost platform in the future, and thus a material of choice for optimized and multiplexed lateral flow assays in the health care segment. We refer the readers to follow recently published review for further reading on paper-based microfluidic system for bioanalytical applications [68, 69].

3. Conclusion

This chapter presents an overview of materials for microfluidic applications and their applications in recent research. The large range of materials dedicated to microfluidics is a key component for successful microfluidic applications. The optimal selection of an adequate material platform for a targeted application is of tremendous importance and represents significant technical challenges. In a concomitant manner, this decision has to be taken accordingly an exhaustive list of requirements essentially related to the biocompatibility, the overall thermomechanical properties, the latter inherent to bonding and reagent integration. Beyond the traditional proof-of-concept works developed at the academic research level, another higher level of concern exists when real applications and medical research are envisioned. Two important issues therefore need to be addressed. First, a reevaluation of the biocompatibility and the overall stability of the intrinsic microfluidic performance when handling real samples. The second aspect involves the scaling-up of each microfabrication, bonding, conditioning, and other packaging needs, and their interdependences and costs. The gap currently is wide in these aspects, and it is one of the most severe limitations for microfluidic applications. Therefore dedicated efforts are needed to tackle this issue. The introduction of sTPE highlights a seamless strategy that promotes a feasible path transfer from prototyping toward realistic industrialization, working from the earliest research steps to the end with a unique polymer interface. Beyond, the polymer materials presented in this chapter, there is tremendous space considering the introduction of other functional polymers in the microfluidic applications. We envision that new research activities focused on conductive, piezo, and magnetically doped polymers among other polymers not only provide a fantastic opportunity for further progress and advancement but also for a new field of research and IP development. The considerations extend surely over new blends of material development for specific goals and needs at large. The high level of multidisciplinary skills required in the field is challenging for the academic community; however, such multidisciplinary nature that extends from biology/medicine, microfabrication, microfluidic materials, and electronic and

optical through sensors also provide unique solutions. Definitively, the development of innovative materials will bring innovations, and our community has to act proactively in this direction for the success of microfluidic research and the real benefit for progress in health-related biomicrofluidic applications.

Author details

Emmanuel Roy*, Antoine Pallandre, Bacem Zribi, Marie-Charlotte Horny, François Damien Delapierre, Andrea Cattoni, Jean Gamby and Anne-Marie Haghiri-Gosnet

*Address all correspondence to: royemmanuel@live.com

Centre de Nanosciences et de Nanotechnologies, CNRS, Université Paris-Saclay, C2N Marcoussis, France

References

- [1] S. C. Terry, J. H. Jerman and J. B. Angell, A gas chromatographic air analyzer fabricated on a silicon wafer, *IEEE Trans. Electron. Dev.*, 26(12), 1880–1886, 1979.
- [2] R. Tiwari and S. Chandra, Low-temperature silicon-to-silicon anodic bonding using sodium-rich glass for MEMS applications, *J. Electr. Mater.*, 43(2), 555–566, 2014.
- [3] K. Y. Fong, M. Poot and H. X. Tang, Nano-optomechanical resonators in microfluidics, *Nano. Lett.*, 15(9), 6116–6120, 2015.
- [4] A. F. Coskun, A. E. Cetin, B. C. Galaterra, D. A. Alvarez, H. Altung and A. Ozcan, Lens free optofluidic plasmonic sensor for real-time and label-free monitoring of molecular binding events over a wide field-of-view, *Sci. Rep.*, 4(6789), 2014.
- [5] A. Rival, D. Jary, C. Delattre, Y. Fouillet, G. Castellan, A. Bellemin-Comte and X. Gidrol, An EWOD-based microfluidic chip for single-cell isolation, mRNA purification and subsequent multiplex qPCR, *Lab Chip*, 14, 3739–3749, 2014.
- [6] V. Marx, PCR: paths to sensitivity, *Nat. Methods*, 11, 241–245, 2014.
- [7] J. Tamayo, P. M. Kosaka, J. J. Ruz, Á. San Paulo and M. Calleja, Biosensors based on nanomechanical systems, *Chem. Soc. Rev.*, 42, 1287–1311, 2013.
- [8] E. Biavardi, S. Federici, C. Tudisco, D. Menozzi, C. Massera, A. Sottini, G. G. Condorelli, P. Bergese and E. Dalcanale, Cavitand-grafted silicon microcantilevers as a universal probe for illicit and designer drugs in water, *Angew. Chem. Int. Ed. Engl.*, 53(35), 9183–9188, 2014.
- [9] M. C. Breadmore, R. M. Tubaon, A. I. Shallah, S. C. Phung, A. S. Abdul Keyon, D. Gstoettenmayr, P. Prapatpong, A. Alhusban, L. Ranjbar, H. H. See, M. Dawod and J. P.

- Quirino, Recent advances in enhancing the sensitivity of electrophoresis and electrochromatography in capillaries and microchips (2012–2014), *Electrophoresis*, 34(1), 29–54, 2013.
- [10] R. A. Saylor and S. M. Lunte, A review of microdialysis coupled to microchip electrophoresis for monitoring biological events, *J. Chromatogr. A.*, 1382, 48–64, 2015.
- [11] D. J. Guckenberger, T. E. de Groot, A. M. D. Wan, D. J. Beebe and E. W. K. Young, Tutorial review micromilling: a method for ultra-rapid prototyping of plastic microfluidic devices, *Lab Chip*, 15, 2364–2378, 2015.
- [12] F. Z. Fang, X. D. Liu and L. C. Lee, Micro-machining of optical glasses—a review of diamond-cutting glasses, *Sadhana Acad. Proc. Eng. Sci.*, 28(5), 945–955, 2003.
- [13] E. M. Chan, A. P. Alivisatos and R. A. Mathies, High-temperature microfluidic synthesis of CdSe nanocrystals in nanoliter droplets, *J. Am. Chem. Soc.*, 127 (40), 13854–13861, 2005.
- [14] G. A. Grob, T. Thelemann, S. Schneider, D. Boskovic and J. M. Kohler, Fabrication and fluidic characterization of static micromixers made of low temperature cofired ceramic (LTCC), *Chem. Eng. Sci.*, 63, 2773–2784, 2008.
- [15] S. Gomez-de Pedro, M. Puyol, D. Izquierdo, I. Salinas, J. M. de la Fuente and J. Alonso-Chamarro, A ceramic microreactor for the synthesis of water soluble CdS and CdS/ZnS nanocrystals with on-line optical characterization, *Nanoscale*, 4(4), 1328–1313, 2012.
- [16] P. Couceiro, S. Gómez-de Pedro and J. Alonso-Chamarro, All-ceramic analytical microsystems with monolithically integrated optical detection cells, *Microfluid. Nanofluid.*, 18(4), 649–656, 2015.
- [17] S. K. Sia and G. M. Whitesides, Microfluidic devices fabricated in poly(dimethylsiloxane) for biological studies, *Electrophoresis*, 24(21), 3563–3576, 2003.
- [18] S. Arscott, SU-8 as a material for lab-on-a-chip-based mass spectrometry, *Lab Chip*, 14, 3668–3689, 2014.
- [19] A. B. Azouz, S. Murphy, S. Karazi, M. Vázquez and D. Brabazon, Fast fabrication process of microfluidic devices based on cyclic olefin copolymer, *Mater. Manuf. Process.*, 29, 93–99, 2014.
- [20] K. Tsougeni, K. Ellinas, H. Archontaki and E. Gogolides, A microfabricated cyclo-olefin polymer microcolumn used for reversed-phase chromatography, *J. Micromech. Microeng.*, 25, 015005, 2015.
- [21] D. Ogoczyk, J. Wegrzyn, P. Jankowski, B. Dabrowski and P. Garstecki, Bonding of microfluidic devices fabricated in polycarbonate, *Lab Chip*, 10, 1324–1327, 2010.
- [22] M. Salim, G. Mishr, G. J. S. Fowler, B. O'Sullivan, P. C. Wright and S. L. McArthur, Non-fouling microfluidic chip produced by radio frequency tetraglyme plasma deposition, *Lab Chip*, 7, 523–525, 2007.

- [23] H. Mogi, Y. Fukushi, S. Koide, R. Sano, T. Sasaki and Y. Nishioka, Ascorbic acid fuel cell with a microchannel fabricated on flexible polyimide substrate, *IEEJ Trans. Sens. Micromach.*, 134, 366–371, 2014.
- [24] A. Zulfiqar, A. Pfreundt, W. E. Svendsen and M. Dimak, Fabrication of polyimide based microfluidic channels for biosensor devices, *J. Micromech. Microeng.*, 25, 035022, 2015.
- [25] E. Berthier, E. W. K. Young and D. Beebe, Engineers are from PDMS-lad, biologists are from polystyrenia, *Lab Chip*, 12, 1224–1237, 2012.
- [26] E. Kim, Y. Xia and G. M. Whitesides, Polymer microstructures formed by moulding in capillaries, *Nature*, 376, 581, 1995.
- [27] H. Becker, Famous last words, *Lab Chip*, 11(13), 2133–2134, 2011.
- [28] J. W. Song and L. L. Munn, Fluid forces control endothelial sprouting, *Proc. Natl. Acad. Sci.*, 108, 15342–15347, 2011.
- [29] J. S. Gewandter, R. J. Staversky and M. A. O'Reilly, Hyperoxia augments ER-stress-induced cell death independent of BiP loss, *Free Radic. Biol. Med.*, 47, 1742–1752, 2009.
- [30] Y. Tang, E. A. Scheef, Z. Gurel, C. M. Sorensen, C. R. Jefcoate and N. Sheibani, CYP1B1 and endothelial nitric oxide synthase combine to sustain proangiogenic functions of endothelial cells under hyperoxic stress, *Am. J. Physiol.: Cell Physiol.*, 298, C665–C678, 2010.
- [31] E. Berthier, J. Warrick, H. Yu and D. Beebe, Managing evaporation for more robust microscale assays, Part 1, Volume loss in high throughput assays, *Lab Chip*, 8, 852–859, 2008.
- [32] K. J. Regehr, M. Domenech, J. T. Koepsel, K. C. Carver, S. J. Ellison-Zelski, W. L. Murphy, L. A. Schuler, E. T. Alarid and D. Beebe, Biological implications of polydimethylsiloxane-based microfluidic cell culture, *Lab Chip*, 9, 2131–2139, 2009.
- [33] X. Su, E. W. K. Young, H. A. S. Underkofler, T. J. Kamp, C. T. January and D. J. Beebe, Microfluidic cell culture and its application in high-throughput drug screening: cardiotoxicity assay for hERG channels, *J. Biomed. Screen.*, 16, 101–111, 2011.
- [34] M. A. Unger, H. P. Chou, T. Thorsen, A. Sherer and S. R. Quake, Monolithic microfabricated valves and pumps by multilayer soft lithography, *Science*, 288, 113–116, 2000.
- [35] M. I. Mohammed, S. Haswell and I. Gibson, Lab-on-a-chip or chip-in-a-lab: challenges of commercialization lost in translation, *Procedia Technol.*, 20, 54, 2015.
- [36] C. D. Chin, V. Linder and K. Sia, Commercialization of microfluidic point-of-care diagnostic devices, *Lab Chip*, 12, 2118–2134, 2012.
- [37] G. Chantal and M. Khan, Laser processing for bio-microfluidics applications (Part II), *Analyt. Bioanalyt. Chem.*, 385(8), 1362–1369, 2006.

- [38] A. Bertsch and P. Renaud, Special issue: 15 years of SU-8 as MEMS material, *Micromachines*, 6(6), 790–792; 2015.
- [39] R. Daunton, A. J. Gallant and D. Wood, Manipulation of exposure dose parameters to improve production of high aspect ratio structures using SU-8, *J. Micromech. Microeng.*, 22(7), 075016, 2012.
- [40] H. O. Moser and C. Rockstuhl, 3D THz metamaterials from micro/nanomanufacturing, *Laser Photon. Rev.*, 6, 219–244, 2012.
- [41] A. Shamsi, A. Amiri, P. Heydari, H. Hajghasem, M. Mohtashamifar and M. Esfandiari, Low cost method for hot embossing of microstructures on PMMA by SU-8 masters, *Microsys. Technol.*, 20(10), 1925–1931, 2014.
- [42] J. P. Rolland, R. M. Van Dam, D. A. Schorzman, S. R. Quake and J. M. DeSimone, Solvent-resistant photocurable liquid fluoropolymers for microfluidic device fabrication, *J. Am. Chem. Soc.*, 126, 2322–2323, 2004.
- [43] A. Vitale, M. Quaglio, S. L. Marasso, A. Chiodoni, M. Cocuzza and R. Bongiovanni, Direct photolithography of perfluoropolyethers for solvent-resistant microfluidics, *Langmuir*, 29(50), 15711–15718, 2013.
- [44] G. Stojkovića, M. Kriveca, A. Veselb, M. Marinšeka and P. Žnidaršič-Plazla, Surface cell immobilization within perfluoroalkoxy microchannels, *Appl. Surf. Sci.*, 320, 810–817, 2014.
- [45] W. H. Grover, M. G. von Muhlen and S. R. Manalis, Teflon films for chemically-inert microfluidic valves and pumps, *Lab Chip*, 8, 913–918, 2008.
- [46] Y. Zhang, K. T. L. Trinh, I. S. Yoo and N. Y. Lee, Integrated monolithic PMMA micro-device, for DNA purification and amplification of *Escherichia coli* pathogen, *Sensor. Actuat. B. Chem.*, 202, 1281–1289, 2014.
- [47] X. Hu, Y. Dong, Q. He, H. Chen and Z. Zhu, Fabrication of a polystyrene microfluidic chip coupled to electrospray ionization mass spectrometry for protein analysis, *J. Chromatogr. B.*, 990, 96–103, 2015.
- [48] G. Holden, N. R. Legge, R. Quirk and H. E. Schroeder, Thermoplastics elastomers, 2nd ed. Hanser/Gardner, Cincinnati, 1996.
- [49] E. Roy, M. Mounier, G. Steward, L. Malic, C. Liviu, M. Madou, M. Bergeron and T. Veres, From cellular lysis to gDNA micro-array detection, an integrated point of care thermoplastic CDlab, *Lab Chip*, 15, 406–416, 2015.
- [50] E. Roy, M. Geissler, J. C. Galas and T. Veres, Prototyping of microfluidic systems using a commercial thermoplastic elastomer, *Microfluid. Nanofluid.*, 11, 235–244, 2011.
- [51] D. Brassard, K. Li, M. Geissler, C. Miville-Godin, E. Roy and T. Veres, 3D thermoplastic elastomer microfluidic devices for biological probe immobilization, *Lab Chip*, 11, 4099, 2011.

- [52] M. Guillemette, E. Roy, F. Auger and T. Veres, Rapid isothermal substrate microfabrication of a biocompatible thermoplastic elastomer for cellular contact guidance, *Acta Biomater.*, 7, 2492–2498, 2011.
- [53] J. Wein, S. Jian, B. Wang, Y. Tan, X. Tu, E. Roy, B. Ladoux and Y. Chen, Fabrication of adjacent micropillars arrays with different heights for cell studies, *Microelectr. Eng.*, 158, 22–25, 2016
- [54] E. Roy, J. C. Galas and T. Veres, Thermoplastic elastomers for microfluidics: towards a high-throughput fabrication method of multilayered microfluidic devices, *Lab Chip*, 11, 3193–3196, 2011.
- [55] N. W. Choi, M. Cabodi, B. Held, J. P. Gelghorn, L. J. Bonassar and A. D. Stroock, Microfluidic scaffolds for tissue engineering, *Nat. Mater.*, 6, 908–915, 2007.
- [56] M. W. Tibbitt and K. S. Anseth, Hydrogels as extracellular matrix mimics for 3D cell culture, *Biotechnol. Bioeng.*, 103, 655–663, 2009.
- [57] S. Bang, S. Na, J. Kim and N. L. Jeon, Engineering-aligned 3D neural circuit in microfluidic device, *Adv. Healthc. Mater.*, 5, 159–166, 2016.
- [58] G. Y. Huang, L. H. Zhou, Q. C. Zhang, Y. M. Chen, W. Sun, F. Xu and T. J. Lu, Microfluidic hydrogels for tissue engineering, *Biofabrication*, 3(1), 012001, 2011.
- [59] M. Chau, H. Thérien-Aubin, Y. Li, Y. Wang, D. Velasco, E. Tumarkin, A. Ramachandran and E. Kumacheva, Microfluidic generation of composite biopolymer microgels with tunable compositions and mechanical properties, *Biomacromolecules*, 15, 2419–2425, 2014.
- [60] Y. Li, X. Yan, X. Feng, J. Wang, W. Du, Y. Wang, P. Chen, L. Xiong and B. F. Liu, Agarose-based microfluidic device for point-of-care concentration and detection of pathogen, *Anal. Chem.*, 86(21), 10653–10659, 2014.
- [61] V. van Duinen, S. J. Trietsch, J. Joore, P. Vulto and T. Hankemeier, Microfluidic 3D cell culture: from tools to tissue models, *Curr. Opin. Biotech.*, 35, 118–126, 2015.
- [62] D. I. Dan Cho and H. Jung Yoo, Microfabrication methods for biodegradable polymeric carriers for drug delivery system applications: a review microelectromechanical systems, *J. Microelectromech. Syst.*, 24(1), 10–18, 2015.
- [63] P. A. Gunatillake and R. Adhikari, Biodegradable synthetic polymers for tissue engineering, *Eur. Cell. Mater.*, 5, 1–16, 2003.
- [64] Y. Lu and S. C. Chen, Micro and nano-fabrication of biodegradable polymers for drug delivery, *Adv. Drug Deliv. Rev.* 56, 1621–1633, 2004.
- [65] H. Liu and R. M. Crooks, Three-dimensional paper microfluidic devices assembled using the principles of origami, *J. Am. Chem. Soc.*, 133(44), 17564–17566, 2011.

- [66] C. R. Mace and R. N. Deraney, Manufacturing prototypes for paper-based diagnostics devices, *Microfluid. Nanofluid.*, 16, 801–809, 2014.
- [67] N. K. Thom, K. Yeung, M. B. Pillion and S. T. Phillips, “Fluidic batteries” as low-cost sources of power in paper-based microfluidic devices, *Lab Chip*, 12, 1768–1770, 2012.
- [68] D. M. Cate, J. A. Adkins, J. Mettakoonpitak and C. S. Henry, Review, recent developments in paper-based microfluidic devices, *Anal. Chem.*, 87, 19–41, 2015
- [69] DY. Xia, J. Si and Z. Li, Fabrication techniques for microfluidic paper-based analytical devices and their applications for biological testing: a review, *Biosens. Bioelectron.*, 77, 774–89, 2016.

Microfluidics and Material Synthesis

Synthesis of Functional Materials by Non-Newtonian Microfluidic Multiphase System

Yong Ren, Kai Seng Koh and Yaping Zhang

Additional information is available at the end of the chapter

<http://dx.doi.org/10.5772/64521>

Abstract

With increasing level of polymer solution involvement in multiphase microdevice for formation of emulsion and fabrication of functional materials, it is of paramount importance to systematically understand the relevant physics of droplet formation in non-Newtonian fluids and how the material formation process may be affected due to the complex rheological effect. The chapter aims to review and discuss the recent advances in technologies that enable fabrication and application of functional materials formed from non-Newtonian microfluidic multiphase system. Rheological behavior of polymer solutions and the mathematical models are reviewed. The influence of microstructure on rheological behavior of polymer solutions and the fundamental physical phenomena driving non-Newtonian microfluidic multiphase system are discussed. Shear thinning and viscoelastic effect on breakup dynamics and droplet formation are presented. The microfabrication process of the device and synthesis of emulsion-templated materials with potential industrial and biochemical applications are elucidated.

Keywords: non-Newtonian fluid, microfluidic, multiphase system, functional material

1. Introduction

Emulsion is mixture of two immiscible liquids, where one liquid is dispersed as droplets in another liquid that forms a continuous phase [1]. The availability of a wide range of technologies for emulsion generation and manipulation by microfluidic multiphase system has enabled the applications of microfluidics in a plethora of fields, such as fabrication of core-shell microspheres and capsules using emulsion droplets as a template for drug encapsulation and release and generation of jets as precursors of microfibers for application in wound dressing and tissue engineering. Emulsion can be formed with aqueous/oil multiphase system or all aqueous multiphase system, both of which involves the use of Newtonian fluids or non-

Newtonian fluids. In Newtonian fluids such as simple organic liquids, solutions of low-molecular-weight inorganic salts, molten metals, or salts, the shear stress at steady condition in laminar flow is linearly proportional to the shear rate, i.e., the tensors that describe the viscous stress and the strain rate are related by a constant viscosity tensor which is independent of the stress state and velocity of the flow. In contrast, non-Newtonian fluids possess such properties that flow curve of shear stress versus shear rate is nonlinear or does not pass through the origin and the apparent viscosity as defined by shear stress divided by shear rate is not constant at a given temperature and pressure, as the apparent viscosity is also influenced by shear rate, the kinematic history of the fluid element, flow conditions, or microchannel configurations. The ever-expanding applications of microfluidic multiphase technologies increasingly require the use of non-Newtonian fluids, examples of which in daily life include cement paste, chocolate, coal slurries, greases and lubricating oils, molten polymer solutions, and cosmetics and personal care products such as shampoos, shaving foams, and toothpaste. Non-Newtonian multiphase microsystem has become a subject of intense research and is widely applied in biomedical engineering, food production, and energy applications. It is hence important to understand the associated physical phenomena, in particular the way how non-Newtonian rheological effect will alter breakup dynamics and, in turn, affect droplet formation, which can be characterized by droplet shape and size, as they are closely related with droplet stability as well as optical and mechanical properties [2]. For example, the shape and size of emulsion droplets have significant impacts on the drug release kinetics when they are used as template to synthesize microcapsules or microparticles for drug delivery [3, 4]. Monodisperse droplets with precisely controlled sizes can be used to deliver an accurate dosing of contained payload such as drug, flavoring, or chemical reactants [5]. Monodispersity and size tenability are highly desired to keep droplets exhibiting constant, controlled, and predictable properties. Nevertheless, the versatility in droplet size control is challenged by complex rheological properties of non-Newtonian fluids, such as formation of undesirable satellite droplets due to bead-on-string patterns, as a result of the stretching and thinning of non-Newtonian liquid filaments. Apart from that, a number of non-Newtonian fluids such as polymeric solutions, whole blood, or protein solutions with large polymeric molecules often exhibit elastic property with shear rate-dependent viscosity due to the stretching and coiling of the polymer chains [6, 7]. Novel applications may arise from non-Newtonian rheological behaviors [8]. For instance, three-dimensional (3D) focusing of microparticles can be achieved via an approach combining inertial and elastic forces in viscoelastic solutions [9]. The elasticity of the focusing fluid can facilitate formation of smaller droplets [10].

In this chapter, we aim to summarize the main technologies for non-Newtonian microfluidic multiphase system and discuss the recent advances in technologies that enable fabricating and characterizing functional materials formed from such systems. The chapter will start with review of rheological behavior of polymer solutions followed by discussion of the fundamental physical phenomena driving non-Newtonian microfluidic multiphase system where polymer solutions are involved; non-Newtonian viscosity effect on breakup dynamics and droplet formation; the techniques employed in device fabrication; and synthesis of emulsion-templated materials. Emphasis will be placed on synthesis of functional materials from single emulsion, double emulsion, or higher order emulsions. Finally we conclude with an outlook

to the future of the field. This chapter is meant to familiarize readers who may be new to the field of non-Newtonian microfluidics, as well as those readers who are new to the field of synthesis of functional materials, and eventually bridge the knowledge gap between the two disciplinary fields, leading to novel approaches for design of functional materials with tailored behaviors for specific applications.

2. Rheological characteristics of polymer solutions

Polymer solutions form a class of industrially significant materials exhibiting diversity of non-Newtonian rheological properties. The system with polymer solutions exhibits a rich spectrum of interesting and complex characteristics once the polymer molecules begin to interact, entangle, and knot up with each other. For example, a macromolecule responds to external force via straightening of chains, disentangling of loose networks, uncoiling and stretching, etc., in the presence of an imposed flow or force. Brownian effects tend to randomize the flow units present in such polymeric systems. The significant factors governing the rheological behavior of a polymeric system are the molecular weight, molecular weight distribution, the structure of the molecule, their possible configurations, and the chemical composition. The use of polymer solutions in microfluidic applications requires knowledge and understanding of their complex behaviors. First, we will review classification of non-Newtonian fluids and the mathematical models. Subsequently, the influence of microstructure on rheological behavior of polymer solutions will be discussed.

For an incompressible Newtonian fluid at steady condition in simple shear flow case where a thin layer of a fluid is contained between two parallel planes which have surface area of A and are parted by a distance dy , a shear by the application of a force F is exerted on the fluid, the shear rate may be expressed as the velocity gradient in the direction perpendicular to that of the shear force, and velocity vector has only one component along x direction with magnitude varying only in y direction, the shear will be balanced by an equal and opposite internal frictional force in the fluid:

$$\frac{F}{A} = \tau_{yx} = \eta \left(-\frac{dV_x}{dy} \right) = \eta \dot{\gamma}_{yx} \quad (1)$$

where τ represents shear stress, η the viscosity of fluid of interest, V the velocity, and $\dot{\gamma}$ the shear rate. The first subscript indicates the direction normal to that of shearing surface, while the second subscript refers to the direction of the force and the flow. The negative sign on the right hand side of Eq. (1) indicates that τ is a measure of the resistance to motion. Viscosity η only depends on material of interest, as well as temperature and pressure.

The shear stress for more general 3D case of an incompressible Newtonian fluid may be expressed for the x plane oriented normal to the x direction as follows [11]:

$$\tau_{xx} = -2\eta \frac{\partial V_x}{\partial x} + \frac{2}{3}\eta \left(\frac{\partial V_x}{\partial x} + \frac{\partial V_y}{\partial y} + \frac{\partial V_z}{\partial z} \right) \tag{2}$$

$$\tau_{xy} = -\eta \left(\frac{\partial V_x}{\partial y} + \frac{\partial V_y}{\partial x} \right) \tag{3}$$

$$\tau_{xz} = -\eta \left(\frac{\partial V_x}{\partial z} + \frac{\partial V_z}{\partial x} \right) \tag{4}$$

Similar sets of equations can be developed for the forces acting on the *y* and *z* planes. In each case, there are two shearing components and one normal component. The nine stress components of a fluid element are shown in Figure 1. $\tau_{xy} = \tau_{yx}$, and $\tau_{yz} = \tau_{zy}$, because of the equilibrium of a fluid element. Each component of normal stress consists of two components: isotropic pressure and a contribution from flow depending on fluid type:

$$\begin{aligned} P_{xx} &= -p + \tau_{xx} & \text{(a)} \\ P_{yy} &= -p + \tau_{yy} & \text{(b)} \\ P_{zz} &= -p + \tau_{zz} & \text{(c)} \end{aligned} \tag{5}$$

where *p* denotes the isotropic pressure and τ_{xx} , τ_{yy} , and τ_{zz} represent deviatoric normal stresses of Newtonian fluids or extra stresses of non-Newtonian fluids. For an incompressible Newtonian fluid, it is given by

$$p = -\frac{1}{3} (P_{xx} + P_{yy} + P_{zz}) \tag{6}$$

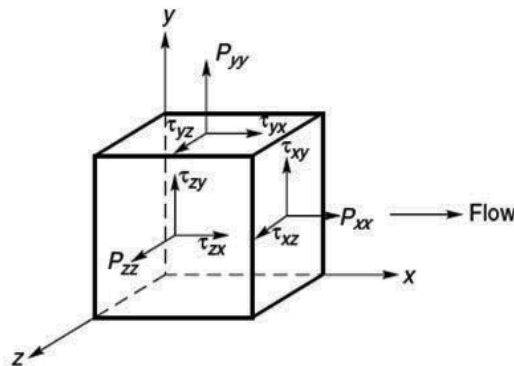


Figure 1. Stress components in 3D flow.

Based on Eqs. (5)–(6), it can be derived that

$$\tau_{xx} + \tau_{yy} + \tau_{zz} = 0 \quad (7)$$

For a Newtonian fluid in simple shear flow,

$$\tau_{xx} = \tau_{yy} = \tau_{zz} = 0 \quad (8)$$

Newtonian fluid thus not only possesses a constant viscosity but also satisfies the condition of Eq. (8). Boger fluids possess constant shear viscosity but do not conform to Eq. (8); thus they must be treated as non-Newtonian fluids. Three types of non-Newtonian fluids are ubiquitously applied and widely investigated [12–14]: (1) time-independent fluids (it can be further subdivided into three types including shear thinning, viscoplastic thickening, and shear thickening), (2) time-dependent fluids, and (3) viscoelastic fluids. Since most polymer solutions possess shear-thinning and viscoelastic behavior, only these rheological properties will be discussed in this chapter.

2.1. Shear thinning

Pseudoplasticity or shear-thinning behavior is characterized by an apparent viscosity which decreases with increasing shear rate. However, most shear-thinning polymer solutions and melts exhibit Newtonian behavior at very low and very high shear rates. The values of the apparent viscosity at very low and high shear rates are known as the zero shear viscosity, η_0 , and the infinite shear viscosity, η_{∞} , respectively. Thus, the apparent viscosity of a shear-thinning fluid decreases from η_0 to η_{∞} with increasing shear rate. As molecular weight of the polymer is smaller, or its molecular weight distribution becomes narrower, or as polymer concentration drops, it will extend the range of shear rate over which the apparent viscosity is constant. A selection of the more widely used viscosity models is summarized here.

i. *The power law or Ostwald de Waele model*

The relationship between shear stress and shear rate for a shear-thinning fluid can often be approximated by a straight line over a limited range of shear rate (or stress) plotted on double logarithmic coordinates. This part of the flow curve can be modeled by power law or Ostwald de Waele expression in the following form:

$$\tau = m\dot{\gamma}^n \quad (9)$$

so the apparent viscosity is thus given by

$$\eta = \frac{\tau}{\dot{\gamma}} = m\dot{\gamma}^{n-1} \quad (10)$$

In these equations, m and n are two empirical curve-fitting parameters and are known as the fluid consistency coefficient and the flow behavior index, respectively. The fluid exhibits shear-thinning properties, Newtonian behavior, and shear-thickening behavior when $n < 1$, $n = 1$, and $n > 1$, respectively. The smaller the value of n , the greater is the degree of shear thinning. This model applies for only a limited range of shear rates and therefore the fitted values of m and n will depend on the range of shear rates considered. The zero and infinite shear viscosities are not taken into account.

ii. *The Carreau viscosity equation*

The Carreau viscosity model incorporates both upper and lower limiting viscosities η_0 to η_∞ and is given by

$$\frac{\eta - \eta_\infty}{\eta_0 - \eta_\infty} = \left(1 + (\lambda \dot{\gamma})^2\right)^{(n-1)/2} \quad (11)$$

where n and λ are two curve-fitting parameters. This model can describe shear-thinning behavior over wide ranges of shear rates but only at the expense of the added complexity of four parameters.

iii. *The Cross viscosity equation*

This model has also gained wide acceptance and, in simple shear, is written as

$$\frac{\eta - \eta_\infty}{\eta_0 - \eta_\infty} = \frac{1}{1 + k \dot{\gamma}^n} \quad (12)$$

This model can be reduced to the Newtonian fluid behavior as k approaches 0 or the power law model as shown in Eq. (10) when $\eta \ll \eta_0$ and $\eta \gg \eta_\infty$.

2.2. Viscoelastic fluids

Such substances exhibit characteristics of both ideal fluids and elastic solids and show partial elastic recovery after deformation, as they have the ability to store and recover shear energy. Examples include polymer melts, polymer and soap solutions, and synovial fluid. The shearing motion of a viscoelastic fluid gives rise to the first and second normal stress differences N_1 and N_2 , expressed in terms of two coefficients, ψ_1 and ψ_2 , which for 1D flow are defined by

$$\begin{aligned} \psi_1 &= \frac{N_1}{\dot{\gamma}_{yx}^2} \quad (\text{a}) \\ \psi_2 &= \frac{N_2}{\dot{\gamma}_{yx}^2} \quad (\text{b}) \end{aligned} \quad (13)$$

At very low shear rates, the first normal stress difference, N_1 , is normally proportional to the square of shear rate, and N_1 is larger than the shear stress τ at the same value of shear rate. The ratio of N_1 to τ is often taken as a measure of how elastic a liquid is. When recoverable shear, $N_1/2\tau$, is greater than 0.5, it indicates a highly elastic behavior of the fluid. The two normal stress differences are used to categorize a fluid either as purely viscous ($N_1=0$) or as viscoelastic, and the magnitude of N_1 in comparison with τ_{yx} , is often used as a measure of viscoelasticity. N_2 is usually small, with maximum values not exceeding 20% of N_1 and with an opposite sign to N_1 . Measurement of N_2 is difficult and can be done using a special cone-plate apparatus [12]. N_1 is responsible for some spectacular phenomena, such as the Weissenberg effect [6]. The measurement of N_1 can be conducted by commercial rotational rheometers. For the flow of polymer solutions in porous media, extensional effects are often encountered and the fluid is stretched as the extent and shape of the flow passages change. Elongational viscosity η_E is defined as

$$\eta_E = \frac{P_{xx} - P_{yy}}{\dot{\epsilon}} = \frac{\tau_{xx} - \tau_{yy}}{\dot{\epsilon}} \quad (14)$$

where $\dot{\epsilon}$ is the elongational rate. Elongational viscosity can only be directly measured with devices like capillary breakup extensional rheometer [15]. The Trouton ratio, T_r , is defined as

..

$$T_r = \frac{\eta_E}{\eta} \quad (15)$$

For inelastic isotropic fluids, $T_r=3$ for all values of $\dot{\epsilon}$ and $\dot{\gamma}$, and any deviation from the value of 3 indicate the existence of viscoelasticity. The Maxwell model is one of widely used linear viscoelastic models; a mechanical analogue of this model is obtained by series combinations of a spring and a dashpot. Combining the Hooke's law of elasticity and Newton's law of viscosity, one can obtain

$$\tau + \lambda \dot{\tau} = \eta \dot{\gamma} \quad (16)$$

where $\dot{\tau}$ is the time derivative of τ , η is the viscosity of the dashpot fluid, and $\lambda (= \mu / G)$ is the relaxation time, which is a characteristic of the fluid. A more solid-like behavior is obtained by considering the so-called Voigt model which is represented by the parallel arrangement of a spring and a dashpot. The fluid total extra stress (τ_t) is given as the sum of an incompressible solvent contribution having a viscosity coefficient η_s and a polymer/additive stress contribution τ_p , as

$$\tau_t = 2\eta_s(II_D, III_D)D + \tau_p \quad (17)$$

The solvent viscosity coefficient in Eq. (18) has been made to depend on the second and third invariants (II_D, III_D) of the rate of deformation tensor D , which is defined as

$$D = \frac{1}{2}(\nabla V + \nabla V^T) \quad (18)$$

For viscoelastic fluids, η_s is set to zero for polymer melts or to a nonzero constant when dealing with a polymer solution based on a Newtonian solvent. Flows in viscoelastic solutions are governed by the Deborah number, De ; the Weissenberg number, Wi ; and the elasticity number, El . The Deborah number is defined as the ratio between the relaxation time of the fluid (λ) and the time of observation of the flow (t_f), such as the duration of the unsteady part of a flow:

$$De = \frac{\lambda}{t_f} \quad (19)$$

The Weissenberg number is defined as the product of the relaxation time and a characteristic rate of deformation of the flow (V/L) and quantifies the nonlinear response of the fluid

$$Wi = \lambda \frac{V}{L} \quad (20)$$

while El represents the ratio between elastic and inertial effects

$$El = \frac{Wi}{Re} = \frac{\lambda \eta}{\rho L^2} \quad (21)$$

where ρ is the density. High Wi may lead to onset of elastic instabilities of viscoelastic fluids, even under creeping flow conditions. For instance, fluids with large polymeric molecules often exhibit elastic behavior due to the stretching and coiling of the polymeric chains, which significantly enrich flow behavior [6].

2.3. Microstructure effect to rheology of polymers

The zero shear viscosity of most polymeric systems increases linearly with the molecular weight below a critical value of the molecular weight, which denotes the onset of entanglement. The zero shear viscosity scales with molecular weight more significantly with the molecular weight above this value. The rheology of polymers is also affected by the nature of chains

whether these are rod-like or coils and springs. For example, the charge-induced repulsive forces along the polymer chain will straighten the convoluted chain and impart some features of rod-like systems in the case of a polyelectrolyte in a weak electrolyte solution. Long molecules are normally randomly oriented at low shear rate, while the molecules become aligned along the direction of flow when increasing the shear rate progressively. The rheological properties are also extremely sensitive to chemical composition. In polymer industry, it is a common technique for producing new rheological properties by adding fillers. The extent of modifications of viscosity-shear rate curves for filled systems depends upon the size and shape of fillers as well as concentration [16]. Blending of polymers can also be used to improve rheological characteristics as compared to that of the constituents. Such a blend may exhibit viscosity larger than that of its constituents. Another way to obtain improved mechanical properties is to create a block copolymer. Such a molecule has long sequences of one type of polymer connected to long sequences of another polymer and exhibits elastic behavior at room temperature and ease of flow at high temperatures, leading to wide range of applications. Surfactant systems also constitute an important class of industrial materials which exhibit complex rheological behavior. The surfactant molecules have hydrophobic tails and hydrophilic heads. When a surfactant like soap or detergent is added to water with concentration beyond a critical value, micelles comprising several molecules begin to form. The formed structures have temporary and loose networks which are continuously broken down and reformed. The shape of micelles includes spherical, rod-like, lamellar sheets and lamellar droplets, which are subject to several parameters, including temperature, the shape of the surfactant molecule, and electrolytic nature of water.

3. Non-Newtonian viscosity effect on breakup dynamics and droplet formation

Emulsion droplets can be passively formed by fluid instabilities using four of the most prevalent microfluidic geometries found from literature: coaxial [17], flow focusing [18], T junction [19], and step emulsification [20]. The dynamics of the droplet formation in microsystem can be characterized by a transition from dripping to jetting regime, governed by the Weber number of the dispersed phase, We_{in} , defining the ratio of inertial force to surface tension and the capillary number of the continuous phase, Ca_{out} , defining the ratio of viscous force to surface tension:

$$We_{in} = \frac{\rho_{DP} L V_{DP}^2}{\sigma} \quad (22)$$

$$Ca_{out} = \frac{\eta_{CP,0} V_{CP}}{\sigma} \quad (23)$$

where L refers to the characteristic dimension of the microsystem and $\eta_{CP,0}$ is the apparent viscosity of the non-Newtonian fluid of continuous phase. The subscript "0" refers to zero

shear rate when a shear-dependent fluid is used, and DP refers to dispersed phase. Formation regime of droplets and its transition are also studied in glass capillary device, where dripping regime and jetting regime are dominant and their transition depends on both capillary number and Weber number [21]. Droplet formation occurs at small Ca_{out} and We_{in} when flows are dominated by surface tension, while jetting forms at large Ca_{out} or We_{in} when the viscous stress or the inertial force on the droplet is large enough to overcome surface tension. Droplets are generated after breakup of a jet at some distance downstream in this regime. Emulsification processes using T- or Y-shaped junctions in poly(dimethylsiloxane) (PDMS) microfluidic systems have been applied for bioassays or drug delivery. The scaling laws of droplet formation by cross flow in T-junction devices were investigated, leading to discovery of three droplet formation patterns: (1) at $Ca < 0.002$ (plug flow is dominant when squeezing regime occurs because cross-flow shear is low and cannot rupture the dispersed phase into drops), (2) at $0.01 < Ca < 0.3$ (droplets are formed with a size comparable to channel cross-sectional dimension in dripping regime because shear force is large enough to cause breakup at the T junction), and (3) transition regime between the two. Simple models for dimension prediction of droplets and plugs as functions of reciprocal Ca were suggested for the squeezing and dripping regimes, respectively [22]. The formation of plug-shaped droplets and mixing in the microchannel with a T junction were studied [23]. While the dynamics of droplet breakup has been systematically investigated in Newtonian fluids, the validity of the understanding has not been adequately confirmed in non-Newtonian fluid systems. With increasing level of polymer solution involvement, systematic understanding of the relevant physics of droplet formation in non-Newtonian fluids has become particularly important. The complex rheological properties of non-Newtonian fluids also affect breakup dynamics and furthermore challenge the versatility in droplet size control. For example, the stretching and/or thinning of non-Newtonian liquid filaments will lead to the formation of “bead-on-string” patterns, as the interface pinch-off is greatly hindered by the polymers’ tendency to recover their equilibrium state [24, 25]. These beads can subsequently become undesirable satellite droplets, increasing the polydispersity of the resultant droplet population. These examples attest to the need for a comprehensive understanding of the role of non-Newtonian viscosity effect in droplet formation using microfluidic systems. In this section, the non-Newtonian viscosity effect on the mechanism of droplet breakup, the characteristics of droplets such as final droplet size, and the frequency of droplet formation will be presented and discussed. We will focus on shear-thinning and viscoelastic fluids in different types of multiphase microsystems such as glass capillary device and planar PDMS device.

3.1. Shear-thinning effect

3.1.1. Glass microcapillary device

The dripping-to-jetting transition under various flow conditions in a Newtonian/shear-thinning multiphase microsystem was characterized [17]. A numerical model of the microcapillary co-flow device has been developed with a Newtonian fluid injected in a cylindrical capillary as the dispersed phase at a constant average velocity V_{DP} and a non-Newtonian outer phase injected through the coaxial square capillary as the continuous phase at a constant average

velocity V_{CP} (see Figure 2). The dispersed phase was silicon oil, while the continuous phase was 2% (w/v) aqueous solution of sodium rboxymethyl cellulose (CMC) ($M_w=250,000$ Da, $DS=1.2$), which is a pseudoplastic fluid and demonstrates shear-thinning behaviors with its apparent viscosity defined by Eq.(12) using Cross model. The breakup dynamics in a non-Newtonian fluid system was compared with a Newtonian fluid system at the same Weber number and capillary number using the same microdevice. For the Newtonian two-phase flow, silicone oil was also used as the dispersed phase, while 17% (w/v) aqueous solution of polyethylene glycol (PEG) ($M_w=8,000$ Da) was used as the continuous phase. The dispersed phase was purged out of the orifice (see Figure 3a) with a droplet growing in size and moving downstream while still connecting with the fluid neck through the orifice via a filament (see Figure 3b). The filament gradually became thinner (see Figure 3c) and finally broke up into a droplet (see Figure 3d). The process was repeated afterward. The interface between the two phases was tracked and compared with experimental measurements with reasonable agreement.

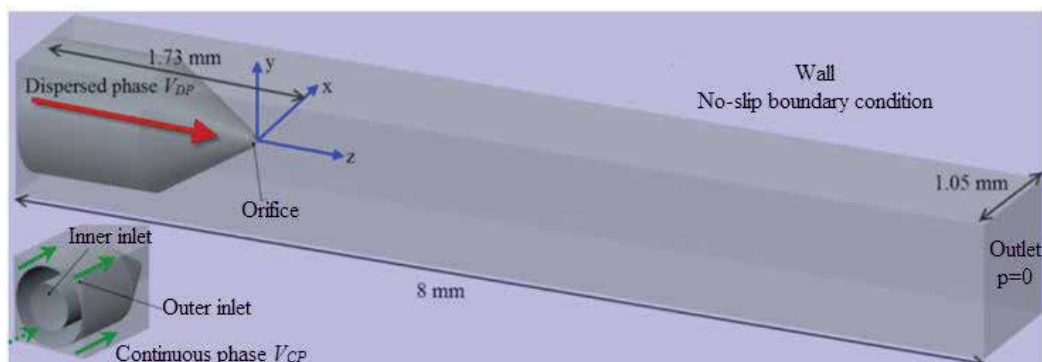


Figure 2. Schematic of the computational domain of multiphase microfluidic system. The closeup view of meshing of nozzle and inlets is shown in inset. Reproduced from Ref. [17] with permission from the Royal Society of Chemistry.

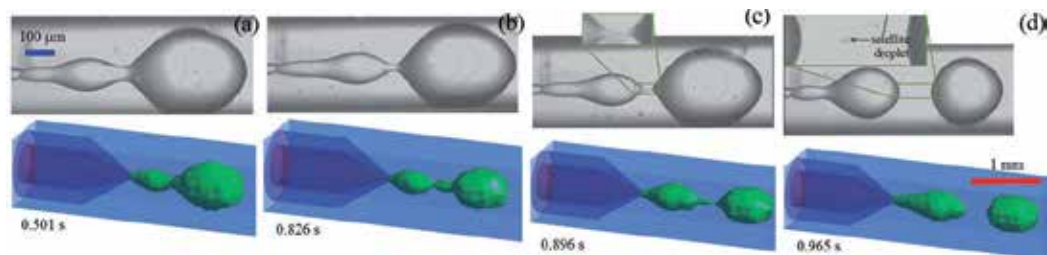


Figure 3. Time-lapse images of jet deformation and droplet formation from simulation (upper one in each sub-figure) and experiments (lower one in each sub-figure) using a Newtonian/shear-thinning two-phase co-flow system (silicone oil as dispersed phase and CMC solution as continuous phase). The blue and red scale bars are applicable for the experimental and simulation results, respectively. (a) The dispersed phase is purged out of the orifice; (b) the main droplet is connected with the fluid neck via a thin filament; (c) the filament becomes even much thinner; (d) satellite droplet occurs after breakup of the jet. Reproduced from Ref. [17] with permission from the Royal Society of Chemistry.

Droplet size scales inversely with the capillary number of the continuous phase in a monotonous fashion in the Newtonian/Newtonian two-phase system [26]. In contrast, the correlation between the droplet size and the capillary number in the Newtonian/shear-thinning two-phase system is different. As Ca_{out} and the shear rate of continuous phase increase, the viscosity of continuous phase is reduced for shear-thinning fluids such as CMC, leading to formation of larger droplets [27]. However, when Ca_{out} increases beyond a critical value, the viscous drag can overcome the surface tension effects that would otherwise minimize the stretching of the fluid neck by drawing the fluid interfaces closer to the orifice. The fluid neck becomes stretched and elongated at high Ca_{out} , fluid neck will subsequently become thinner, the shear rate of the continuous phase starts to decrease, the viscosity of continuous phase will increase for a shear-thinning fluid, and eventually the droplet undergoes size reduction beyond a critical Ca_{out} .

3.1.2. PDMS device

The effects of the generalized power law coefficient, the power law exponent and the yield stress on the mechanism of drop breakup, final drop size, and frequency of drop formation were studied using 3D volume of fluid (VOF) model in multiphase flows in T-shaped microchannel where the fluids are Newtonian/power law and Newtonian/Bingham [28]. The pressure implicit with splitting of operators (PISO) algorithm was used in the transient calculations for droplet generation and deformation. The technique of piecewise-linear interface construction (PLIC) [29] that satisfies the accuracy of the surface tension calculations was adopted in this numerical model. The droplet diameter decreased and frequency increased with $n \leq 0.9$ and $n \geq 0.92$. The products of η_{cp} and $\dot{\gamma}$ did not change much from $K = 0.0011$ to 0.0106 Pa s. For Bingham fluid, the droplet extension increased significantly as yield stress became larger. A plug-flow region was found in flows of Bingham fluids, and the width of the region was proportional to the yield stress. With a Bingham fluid as the continuous phase, an obvious transition period was found before the droplets can be formed steadily. During this transition period, droplets coalescence was observed. Microdroplet formation in different channel geometries has been studied. For instance, the formation of droplet from an aperture was investigated under the cross-flow conditions in microchannel emulsification process [30], where an oil phase was dispersed into shear-thinning continuous-phase fluid through a microchannel wall made of apertured substrate. The dispersed oil phase first grew to a jetlike deformed droplet, indicating that the net shear effect on the droplet surface in the flow direction of a non-Newtonian continuous phase is stronger than that in Newtonian flow. The detached droplet had a diameter less than half of the droplet size in the Newtonian flow case, showing a drastic reduction in the droplet size by the non-Newtonian effect in typical dripping regime, due to higher shear stress near the wall. Simulations of a droplet passing through an axisymmetric contraction were performed using VOF algorithm [31]. When the disperse phase was shear thinning, the local viscosity of the droplet decreased as it entered the contraction, remained low while within the contraction, and increased as it exited. When the continuous phase was shear thinning and the dispersed phase was Newtonian, the droplets tended to deform less than their shear-thinning counterpart when entering the contraction.

3.2. Viscoelastic effect

3.2.1. Glass microcapillary device

The flow patterns at different ratios of flow rate with viscoelastic continuous phase of 5% w/v PAA solution and dispersed phase of silicon oil were characterized [17]. The elastic forces from viscoelastic continuous phase help to overcome interfacial tension and thus facilitate transition to jetting at smaller magnitudes of the viscous forces. Droplets adopted a spherical or nearly spherical shape in Newtonian/Newtonian or Newtonian/shear-thinning multiphase microsystem, while the droplets experienced significant deformation in the viscoelastic non-Newtonian continuous phase, because elasticity of the suspending liquid can facilitate the deformation of the Newtonian droplets [32]. For instance, the droplets adopted an elliptical shape after breakup and relaxed into pointed shapes. Droplets became more pointed as the radius decreased and the flow rate ratio increased before it transitioned to the jetting regime. The degree of droplet deformation increased, leading to formation of droplets with more pointed shape, when elastic effect became more pronounced at higher Weissenberg number. This work helps to understand how the complex rheology behavior of viscoelastic fluid can influence the breakup dynamics and droplet formation in multiphase microfluidic system when glass capillary device is used.

3.2.2. PDMS device

Highly controlled shear in viscoelastic media can lead to droplet rupturing down to a unique size and the shear-thinning nature enhances the monodispersity [33]. The droplet formation and breakup dynamics of elastic and Newtonian fluids in T-shaped microchannels for continuous phase were investigated [34]. For both cases, reduction in droplet size was found when cross-flow shear force was increased via increase of viscosity ratio of continuous phase to dispersed phase. For non-Newtonian case, after the droplet grew to a large enough size and was pushed downstream by the cross-flow, dispersed-phase filament was formed between the junction and the connected droplet. The filaments were stretched at two different rates and broke up into secondary smaller droplets. A critical Ca number existed for the inception of monodisperse secondary drops. The obvious presence of the filament during the drop detachment process of these elastic fluids when compared to its Newtonian counterpart shows that fluid elasticity played an important role in resisting drop pinch-off, and the presence of elasticity created a significant difference in drop formation dynamics, while this contributed little to the final drop size and drop productivity. The morphology of droplets was determined by polymer molecular weight and viscosity ratio. A slight reduction in primary drop size is expected with increasing levels of elastic stress within the filament, as the mass of fluid within the filament between two primary drops is excluded from effectively draining into the primary drops at either end of the filament. Analysis of the filament dynamics during the drop detachment stage revealed that there are two distinct regions: a pre-stretch region and an exponential self-thinning region. The effect of viscoelasticity of drop and medium on drop deformation was investigated, and the strategy to control the drop shape was proposed [35]. When a Newtonian drop was suspended in a viscoelastic medium, in the narrow channel

region, ellipsoid-like droplet was found. In contrast, droplet normally adopted bullet-like shape in a Newtonian/Newtonian microsystem. When a viscoelastic drop was suspended in Newtonian medium, the drop swelling extent to the cross-stream direction was enhanced at the outlet of the channel, due to the normal stress difference developed in the viscoelastic fluid.

4. Synthesis of functional materials using microfluidics

4.1. Fabrication of microfluidic emulsification system

The most common microfabrication methods for creating microfluidic devices are photolithography and soft lithography. Studies in optimizing these techniques have been extensively reported [36–40]. Photolithography actually refers to the transfer of a pattern of chromium on a hard material such as glass or silica plate and is known as the most important step in the microfabrication process. The whole process of photolithography involves substrate cleaning, photolithography, metal deposition and wet/ dry etching [41]. Silicon wafer is initially heated to a temperature of 150 °C to remove any moisture that may be present on the surface. Contaminant on the surface of silicon wafer can be removed by cleaning procedure [42]. After the cleaning process, silicon wafer is spin coated with a thin and uniform layer of photoresist. The silicon wafer along with the photoresist is then placed into the ultraviolet (UV) exposure machine for alignment and exposure. The exposure of photoresist toward UV light triggers chemical reaction; thus the exposed photoresist can be removed by a solution aimed to remove unreacted photoresist. The geometric pattern can be defined onto the silicon wafer by either positive photoresist or negative photoresist. Positive photoresist becomes soluble upon exposure whereas the unexposed regions become soluble when negative photoresist is used [43]. Soft lithography is a low-cost technique to replicate the microchannel pattern using the master mould generated with photolithography technique. In most of the applications, PDMS is the preferred elastomeric materials to be used as the patterned replica which transfer the original pattern of a master by molding or printing. The flexibility of the PDMS replicas allows patterning on nonplanar structures through micro-contact printing or micro-molding. As compared to chromium mask, film masks with similar pattern not only cost 20–100 times cheaper but also with a shorter production time. The subsequent process is very similar to the photolithography process with the only difference in which the negative replica is generated by casting an uncured prepolymer of PDMS against the geometry design [36]. However, these techniques require sophisticated instrumentation and clean room that sometimes are not readily available. Consequently, rapid yet low-cost prototyping technology, as a result of impressive development of microfabrication process aimed at reducing the fabrication interval and cost needed in conventional microfabrication processes such as xurography, was proposed to construct the devices [44, 45]. In addition, most of these techniques do not require clean-room facilities as well as sophisticated steps to produce high-quality and long-lasting microfluidic devices [46]. Xurography utilized cutting plotter with a 10 µm resolution that can directly create microstructures without photolithographic process or chemicals [47]. The design pattern was cut onto an adhesive vinyl film. This was followed by removal of undesired portions of film using a pin/ blade. The remaining film with desired design was then transferred onto a substrate, i.e., transparent plastic with the aid of the application tape to prevent

deformation of the design. The transparent plastic along with the designated film was then used to create an epoxy master mould in order to produce replicas of PDMS device. Although xurography does not possess high resolution as compared to standard lithography techniques, the accuracy of this method was falling within 10 μm of drawn dimensions and the feature variability was less than 2 μm [47].

4.2. Synthesis of particles using single-emulsion template

The ability to form droplets with a microfluidic device allows one to structure fluids to disperse a continuous fluid into a series of equally sized liquid spheres. These spheres can then be solidified to produce particles of the same size and shape. Monodisperse microgels consisting of cross-linked network of poly(N-isopropylacrylamide) (PNIPAm) can be formed from single emulsion (see Figure 4) [48, 49]. Such PNIPAm microgels swell and shrank reversibly in response to changes in temperature. The size change occurred around 32°C, which is close to the human body temperature. Hence, these microgels have been extensively evaluated for controlled delivery of water-soluble drugs. Low polydispersity of PNIPAm microgels is desirable for drug delivery applications as it could lead to narrow distribution of drug loading levels and uniform release kinetics. Lipids or hydrocarbons are known as natural choice of the shell material as most of them are solid at room temperature, thus enabling the robust encapsulation under ambient conditions [50].

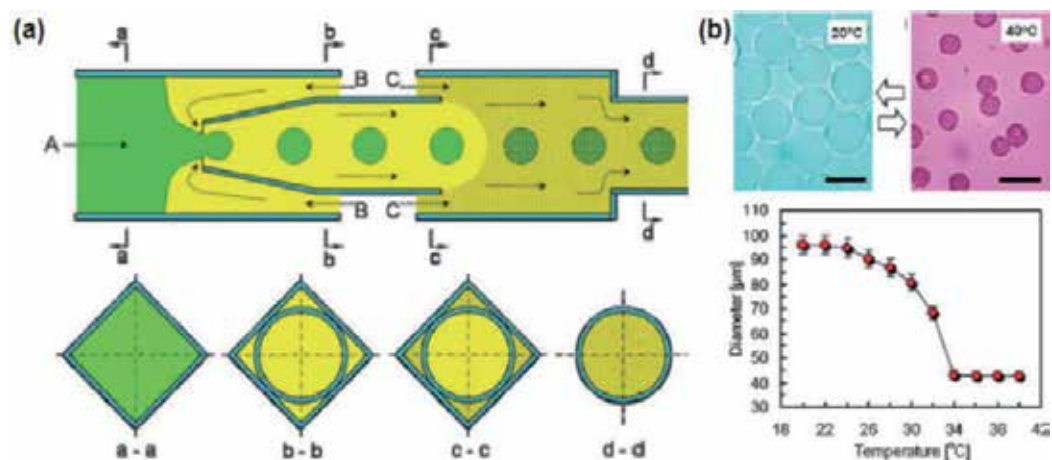


Figure 4. (a) Schematic illustration of a capillary-based microfluidic device for fabricating monodisperse PNIPAm microgels. Fluid A is an aqueous suspension containing the monomer, cross-linker, and initiator; fluid B is oil, and fluid C is the same oil as fluid B but contains a reaction accelerator that is both water and oil soluble. The accelerator diffuses into the drops and polymerizes the monomers to form monodisperse microgels. Cross-sectional views at different points along the device length are shown in the second row. Reproduced with permission from [48]. Copyright (2007) by Wiley-VCH Verlag GmbH & Co. KGaA. (b) Size change of PNIPAm microgels in water triggered by changing the temperature. The scale bar in Panel b denotes 100 μm . Reproduced with permission from [49]. Copyright (2008) by the Royal Society of Chemistry.

A demonstration of the fabrication of monodisperse colloidosomes, microcapsules with a shell composed of tightly packed colloidal particles, has been made using colloidal PNIPAm

microgels as building blocks [51]. An aqueous suspension of amine-functionalized sub-micrometer-sized PNIPAm microgels was emulsified in an oil capsule using a single-emulsion microfluidic device. Prior to emulsification, a small amount of glutaraldehyde was added to the aqueous mixture. The colloidal PNIPAm microgels assembled at the oil-water interface within the emulsion droplets due to the presence of hydrophobic isopropyl groups and hydrophilic acrylamide groups. Glutaraldehyde molecules, owing to their two reactive sites each, served as connecting links between the amine-functionalized microgels through an amine-aldehyde condensation reaction. Colloidosomes were formed via interlinking of the microgels at the oil-water interface, as shown in Figure 5a. The colloidosomes exhibited similar thermosensitive behavior with the constituent microgels. The diameter of the colloidosomes decreased by 42%, roughly equivalent to an 80% decrease in volume, when the temperature was higher than the phase-transition temperature of PNIPAm (see Figure 5b). Such material is thus very promising in applications that require targeted pulsed release of active materials.

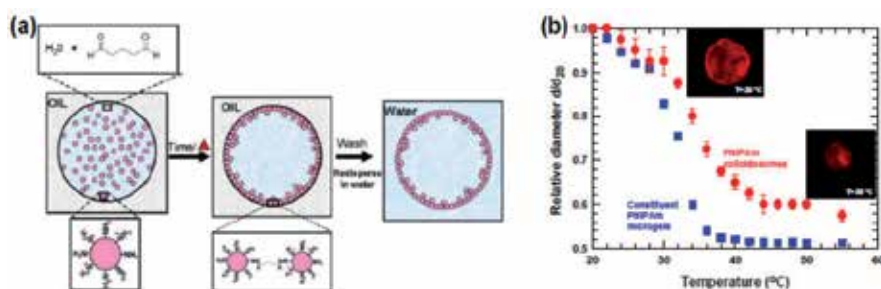


Figure 5. (a) Schematic representation of a technique used for fabricating colloidosomes using PNIPAm microgel particles as building blocks and emulsion droplets as templates. (b) Equilibrium size change of PNIPAm colloidosomes and the constituent PNIPAm microgels. Colloidosomes were dispersed in water and heated from 20 to 50 °C in fixed increments of 2 °C and then to 55 °C. Images were captured after allowing the sample to equilibrate for 30 min at each temperature. The sample was then cooled down to 20 °C using the same temperature steps. Size-change data of the constituent PNIPAm microgels over the same temperature range were collected using dynamic light scattering. Adapted and reproduced with permission from [51]. Copyright (2010) by American Chemical Society.

4.3. Synthesis of particles using double and higher order emulsion template

Double emulsion can also be used to template structures, but these structures have more elaborated shapes. To illustrate this templating process, thermoresponsive PNIPAm was chosen as the matrix polymer to obtain environmentally sensitive microgel particles with microshell structure [52]. To form the pre-microgel droplets, an aqueous microgel precursor solution was emulsified in a continuous oil phase. Pre-microgel droplets were loaded with inner droplets of another oil in the formation process, thereby creating a shell structure, as shown in Figure 6a. After droplet formation, the shell was gelled by thermal monomer polymerization by photochemical polymer-analogous gelation, yielding uniform PNIPAm microshells as shown in Figure 6b. Operating the device with different flow rates can produce shells with two cores, as shown in Figure 6c.

Colloidosomes of diblock copolymers have been fabricated by combining water-in-oil-in-water (W/O/W) droplet encapsulation and dewetting transition in a microcapillary device [53].

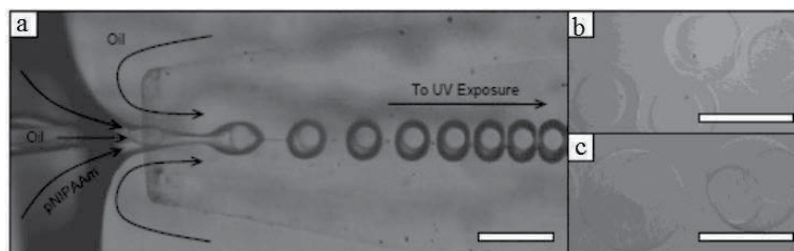


Figure 6. Microfluidic production of hollow microgel shells. (a) A glass microcapillary device is used to create an oil-water-oil double emulsion with a semidilute solution of cross-linkable pNIPAAm as aqueous phase. Subsequently, these droplets are cured by UV exposure as they flow through a delay capillary a few centimeters downstream (not shown). (b) pNIPAAm microshells obtained from the experiment in Panel A. (c) Double-core microshells obtained upon slight variation of the flow rates in the experiment. All scale bars denote 200 μm . Reproduced with permission from [52]. Copyright (2010) by the Royal Society of Chemistry.

The properties of the colloidosomes, for example, membrane thickness, mechanical response, permeability, and thermal stability, can be tuned by varying the block ratios of the block copolymers and the homopolymer [54]. Multicompartmental polymersomes can be generated based on encapsulation of a controlled number of single polymersomes through a reinjection method [55]. Besides using glass capillary devices, double emulsions can be formed in PDMS device. This can be achieved using two drop makers in series [56–58]. The first drop maker produced the inner drops, which were fed into the inlet of the second drop maker, which produced the outer drops. This type of double emulsification can be achieved using either cascading T junctions or flow-focus drop makers. Generally, serial flow-focus devices are used, because the symmetric injection of the middle and continuous phases helps prevent wetting of the drops on the channels, making the formation more robust. In addition to geometrical considerations like this, it is also necessary to control the wetting properties of the devices; however, in contrast to single-emulsion formation in which only uniform wetting is required, spatially patterned wettability is required in double or higher order multiple emulsification.

Wettability determines the type of emulsion formed in PDMS device channel: oil-in-water emulsions are formed in hydrophilic channels, while water-in-oil emulsions are formed in hydrophobic channels. The need to spatially control the wettability in PDMS devices has stimulated techniques to spatially modify device surface properties. With a photo-patterning approach, the devices were filled with a solution that only reacts with the channels under exposure to intense UV light [58]. Since the UV beam can be shaped using holes, slits, and lenses, this approach allows for the creation of complex wettability patterns. However, in the case of double-emulsion devices, only a very simple wettability pattern is needed, and the added complication of having to align the photo-pattern with the microchannels can make this approach unattractive in these instances. For the simple patterns needed for these devices, a different approach is available that trades versatility in the pattern shape for simplicity in the treatment process. This flow-patterning technique controls wettability by introducing a reactive solution into select portions of a device and preventing it from going using the flow of an inert blocker solution [59]. The reactive solution changes the wettability only in the treated

regions, while the untreated areas retain their default wettability. By controlling how the solutions are injected, wettability patterns for W/O/W or O/W/O double emulsions can be created.

One of the advantages of PDMS-based microfluidics is the ability to customize the devices to construct sophisticated channel networks. High-order multiple emulsions can be formed by scaling up device complexity. A high-order multiple emulsion is the logical continuation of a double emulsion to larger numbers of nested droplets: A triple emulsion is a double emulsion encapsulated within a droplet, while a quadruple emulsion is merely a triple emulsion inside yet another droplet. As shown in Figure 7a, double emulsions can be formed by addition of another droplet maker; together also pattern wettability, so that the inner drops were encapsulated within larger drops of an immiscible phase (see Figure 7b) [60]. The design can be further improved to make higher order emulsions such as triple, quadruple, and quintuple emulsions by addition of third, fourth, and fifth junctions, as shown in Figure 7c–e, respectively.

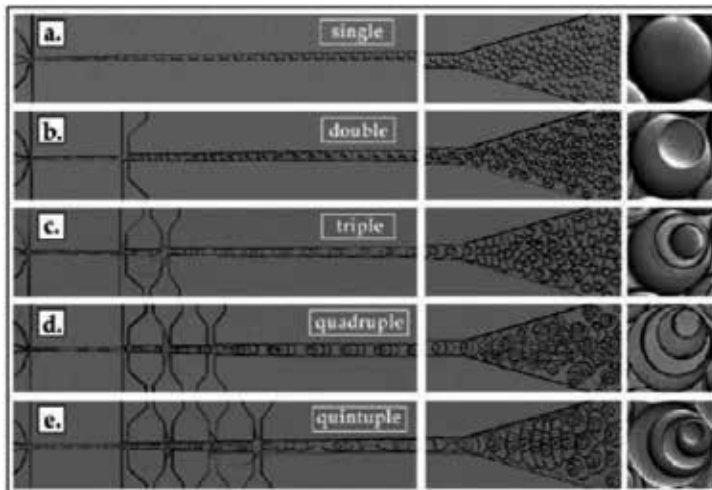


Figure 7. Serial drop maker arrays used to form multiple emulsions. A single-emulsion droplet takes one drop maker to create (a), whereas double, triple, quadruple, and quintuple emulsions take two, three, four, and five drop makers in series to create, (b), (c), (d), and (e), respectively. The wettability of the multiple emulsion devices has been patterned so that it inverts between hydrophilic and hydrophobic from one junction to the next. Reprinted with permission from [60]. Copyright (2009) by Wiley-VCH Verlag GmbH & Co. KGaA, Weinheim.

A number of polymer solutions cannot be used to synthesize particles in microfluidic devices, as challenged by their non-Newtonian properties. For instance, lipid melts such as coco glycerides tend to be viscous and stick to channel surfaces because of the amphiphilic properties of the constituent molecules; they also have low interfacial tension with oil or aqueous carrier phases. Polymer solutions of long-chain polymers such as PNIPAm or polyurethane-polybutadienediol (pU-pBDO) can form excellent particles, but appear to be viscous and have significant viscoelastic response at the shear rates required for controlled droplet formation, thus significantly limiting the applicability. One-step double emulsification enables formation

of monodisperse particles from fluids that cannot normally be used in droplet-based microfluidics, including viscous or viscoelastic polymer solutions or low interfacial tension polymer melts. For example, a robust droplet formation mechanism has been proposed and demonstrated with highly viscous inner jet surrounded by a Newtonian fluid in one-step double emulsification, leading to formation of equal-sized droplets (see Figure 8) [61]. It takes long time for the droplet to relax into a spherical shape because of high viscosity of the fluid. The shape of droplet can be fixed by rapid solidification such as photoinduced cross-linking. This provides alternate approach to synthesize new types of particles, such as those made from waxy lipids or semidilute entangled polymer solutions.

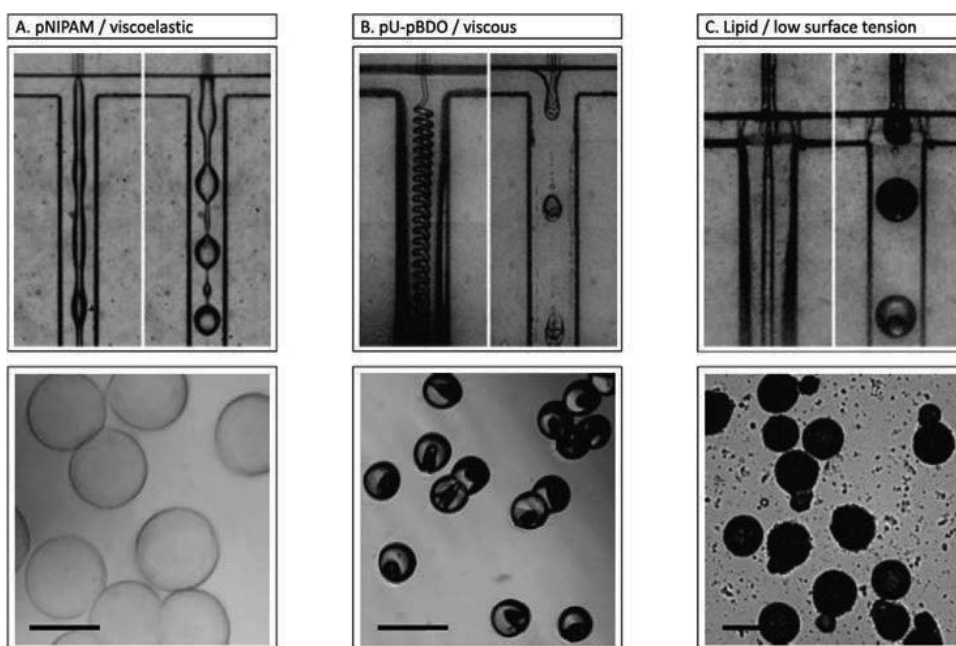


Figure 8. Demonstration of failing and succeeding emulsification using single- and one-step double emulsification, respectively. (a) Emulsification of a viscoelastic semidilute pNIPAM polymer solution and the resultant particles below. (b) Emulsification of a viscous and viscoelastic polymer solution composed of pU-pBDO and the resultant particles below. (c) Emulsification of a low interfacial tension and viscous lipid melt and the resultant particles below. All scale bars in the lower panels denote 100 μ m. Reprinted with permission from [61]. Copyright (2011) by Wiley-VCH Verlag GmbH & Co. KGaA, Weinheim.

5. Outlook

Functional materials such as microcapsules, microgels, colloidosomes, and microshells are ubiquitous in daily life and play crucial role in numerous industrial applications driven by microencapsulation. The materials can be obtained from the breakage of dispersed phase into droplets with controlled structure and monodispersed size in multiphase microsystem using emulsion as template. However, the practical applications of the technique are challenged as

the fluid precursors must be compatible with the formation of droplets in microfluidic devices. For instance, fluids with a low viscosity, negligible viscoelastic response, and moderate interfacial tension are required to facilitate formation of droplets. If even one of these constraints is not satisfied, polydisperse particles are formed or even jetting occurs. This may happen especially when one has to deal with biological fluids and polymeric solutions that contain molecules of high molecular weight. These complex fluids exhibit a non-Newtonian behavior which may considerably affect both the jetting/dripping transition and the growth of perturbations in the jetting regime. A number of novel approaches have been proposed in the last few years to fulfill research needs to achieve better control over drop size, degree of monodispersity, internal structure, and production rate. In this chapter, we have reviewed these novel microdroplet-based techniques when non-Newtonian fluids are involved. We focused on the synthesis of functional materials and how they can be linked with real industrial and biochemical demands. Despite of the rapid development, one of the major opened avenues for investigation is the material forming, through which one obtains a final solid phase, normally in the form of powders or suspensions made of microparticles, microcapsules, etc. More efforts should be given to the relevant research so that material forming can be carefully designed and well controlled to prevent unfavorable effects including coalescence, aggregation, or shell degradation and disintegration. Attention should also be paid to the development of advanced approach to inhibit the occurrence of satellite droplets and control polydispersity when non-Newtonian fluids are used in microfluidic system. This will eventually help to achieve applications such as advanced drug delivery.

Acknowledgements

This work was supported by Zhejiang Provincial Natural Science Foundation of China under Grant No. Q15E090001, Young Scientist Program from National Natural Science Foundation of China under Grant No. NSFC51506103/E0605, 2014 Zhejiang 1000-Talents Awards and Ningbo Natural Science Foundation under Grant No. 2015A610281.

Author details

Yong Ren^{1*}, Kai Seng Koh² and Yaping Zhang³

*Address all correspondence to: yong.ren@nottingham.edu.cn

1 Department of Mechanical, Materials and Manufacturing Engineering, The University of Nottingham Ningbo, China

2 Department of Chemical and Environmental Engineering, The University of Nottingham Ningbo, China

3 Department of Electrical and Electronic Engineering, The University of Nottingham Ningbo, China

References

- [1] Schramm, L.L. (2005). *Emulsions, Foams, and Suspensions: Fundamentals and Applications*. Wiley-VCH, Germany.
- [2] McClements, D.J. (2007). Critical review of techniques and methodologies for characterization of emulsion stability, *Crit. Rev. Food Sci. Nutr.* 47, 611–649.
- [3] Budhian, A., Siegel, S.J., Winey, K.I. (2007). Haloperidol-loaded PLGA nanoparticles: systematic study of particle size and drug content, *Int. J. Pharm.* 336, 367–375.
- [4] Berklund, C., King, M., Cox, A., Kim, K., Pack, D. (2002). Precise control of PLG microsphere size provides enhanced control of drug release rate, *J. Control. Release.* 82, 137–147.
- [5] Erb, R.M., Obrist, D., Chen, P.W., Studer, J., Studart, A.R. (2011). Predicting sizes of droplets made by microfluidic flow-induced dripping, *Soft. Matter.* 7, 8757–8761.
- [6] Bird, R.B., Armstrong, R.C., Hassager, O. (1987). *Dynamics of Polymeric Liquids. Volume 1: Fluid Mechanics*, Wiley, USA.
- [7] Larson, R.G. (1999). *The Structure and Rheology of Complex Fluids*. Oxford University Press, UK
- [8] Rao, M.A. (2007). *Rheology of Fluid and Semisolid Foods: Principles and Applications* (2nd ed.). Springer. p. 8. ISBN 978-0-387-70929-1.
- [9] Yang, S., Kim, J.Y., Lee, S.J., Lee, S.S., Kim, J.M. (2011). Sheathless elasto-inertial particle focusing and continuous separation in a straight rectangular microchannel, *Lab. Chip.* 11, 266–273.
- [10] Derzsi, L., Kasprzyk, M., Plog, J.P., Garstecki, P. (2013). Flow focusing with viscoelastic liquids, *Phys. Fluids*, 25, 092001.
- [11] Bird, R.B., Stewart, W.E., Lightfoot, E.N. (2002). *Transport Phenomena*, 2nd edition, Wiley, USA.
- [12] Barnes, H.A., Hutton, J.F. and Walters, K. (1989). *An Introduction to Rheology*, Elsevier, Netherlands.
- [13] Griskey, R.G., Nechrebecki, D.G., Notheis, P.J., Balmer, R.T. (1985). Rheological and pipeline flow behavior of corn starch dispersions, *J. Rheol.* 29, 349.
- [14] Mujumdar, A., Beris, A.N., Metzner, A.B. (2002). Transient phenomena in thixotropic systems, *J. Non-Newt. Fluid Mech.*, 102, 157–178.
- [15] Rodd, L.E., Scott, T.P., Cooper-White, J.J., McKinley, G.H. (2005). Capillary breakup rheometry for low viscosity elastic fluids, *Appl. Rheol.* 15, 12–27.
- [16] Shenoy, A.V. (1999). *Rheology of Filled Polymer Systems*, Springer, USA.

- [17] Ren, Y., Liu, Z., Shum, H.C. (2015) Breakup dynamics and dripping-to-jetting transition in a shear-thinning/Newtonian multiphase microsystem, *Lab. Chip.* 15, 121–134.
- [18] Roberts, C.C., Rao, R.R., Loewenberg, M., Brooks, C.F., Galambos, P., Grillet, A.M., Nemer, M.B. (2012). Comparison of monodisperse droplet generation in flow-focusing devices with hydrophilic and hydrophobic surfaces, *Lab. Chip.* 12, 1540–1547.
- [19] Wang, K., Lu, Y.C., Xu, J.H., Tan, J., Luo, G.S. (2011). Generation of micromonodispersed droplets and bubbles in the capillary embedded T-junction microfluidic devices, *J. AIChE.* 57, 299–306.
- [20] Couture, O., Faivre, M., Pannacci, N., Babataheri, A., Servois, V., Tabeling, P., Tanter, M. (2011). Ultrasound internal tattooing, *Med. Phys.* 38, 1116–1123.
- [21] Utada, A.S., Fernandez-Nieves, A., Stone, H.A., Weitz, D.A. (2007). Dripping to jetting transition in coflow liquid streams, *Phys. Rev. Lett.* 99, 094502.
- [22] Xu, J.H., Li, S.W., Tan, J., Luo, G.S. (2008). Correlations of droplet formation in T-junction microfluidic device: from squeezing to dripping, *Microfluid. Nanofluid.* 5, 711–717.
- [23] Tice, J.D., Lyon, A.D., Ismagilov, R.F. (2004). Effects of viscosity on droplet formation and mixing in microfluidic channels, *Anal. Chim. Acta.* 507, 73–77.
- [24] Oliveira, M.S.N., McKinley, G.H. (2005). Iterated stretching and multiple beads-on-a-string phenomena in dilute solutions of highly extensible flexible polymers, *Phys. Fluids.* 17, 071704.
- [25] Eggers, J., Villermaux, E. (2008). Physics of liquid jets, *Rep. Prog. Phys.*, 71, 036601.
- [26] Stan, C.A., Tang, S.K.Y., Whitesides, G.M. (2009). Independent control of drop size and velocity in microfluidic flow-focusing generators using variable temperature and flow rate, *Anal. Chem.* 81, 2399–2402.
- [27] Taylor, G.I. (1932). The viscosity of a fluid containing small drops of another fluid, *Proc. R. Soc. London. A.* 138, 41–48.
- [28] Hong, Y., Wang, F. (2007). Investigation of viscosity effect on droplet formation, *Microfluid. Nanofluid.* 3, 341–346.
- [29] Meier, M., Yadigaroglu, G., Smith, B.L. (2002). A novel technique for including surface tension in PLIC-VOF methods, *Eur. J. Mech. B Fluids.* 2, 61–73.
- [30] Qiu, D.M., Silva, L., Tonkovich, A.L., Arora, R. (2010). Micro-droplet formation in non-Newtonian fluid in a microchannel, *Microfluid. Nanofluid.* 8, 531–548.
- [31] Harvie, J.E., Davidson, M.R., Cooper-White, J.J., Rudman, M. (2007). A parametric study of droplet deformation through a microfluidic contraction: shear thinning liquids, *Int. J. Multiphas. Flow.* 33, 545–556.

- [32] Tretheway, D.C., Leal, L.G. (2001). Deformation and relaxation of Newtonian drops in planar extensional flows of a Boger Fluid, *J. Non-Newtonian Fluid Mech.* 99, 81–108.
- [33] Mason, T.G., Bibette, J. (1996). Emulsification in viscoelastic media. *Phys. Rev. Lett.* 77(16), 3481–3484.
- [34] Husny, J., Cooper-White, J.J. (2006). The effect of elasticity on drop creation in T-shaped microchannels, *J. Non-Newtonian Fluid Mech.* 137, 121–136.
- [35] Chung, C., Hulsen, M. A., Kim, J. M., Ahn, K. H., Lee, S.J. (2008). Numerical study on the effect of viscoelasticity on drop deformation in simple shear and 5:1:5 planar contraction/expansion microchannel, *J. Non-Newtonian Fluid Mech.* 155, 80–93.
- [36] Love, J.C., Anderson, J.R., Whitesides, G.M. (2001). Fabrication of three-dimensional microfluidic systems by soft lithography, *Mater. Res. Soc.* July, 523–528.
- [37] Chen, K.S., Ayon, A.A., Zhang, X., Spearing, S.M. (2002). Effect of process parameters on the surface morphology and mechanical performance of silicon structures after deep reactive ion etching (DRIE), *J. Microelectromech. S.* 11, 264–275.
- [38] Zhang, J., Tan, K.L., Hong, G.D., Yang, L.J., Gong, H.Q. (2001). Polymerization optimization of SU-8 photoresist and its applications in microfluidic systems and MEMS, *J. Micromech. Microeng.* 11, 20–26.
- [39] Reznikova, E.F., Mohr, J., Hein, H. (2005). Deep photo-lithography characterization of SU-8 resist layers, *Microsys. Technol.* 11, 282–291.
- [40] Becker, H., Gärtner, C. (2008). Polymer microfabrication technologies for microfluidic system, *Anal. Bioanal. Chem.* 390, 89–111.
- [41] Marty, F., Rousseau, L., Saadany, B., Mercier, B., Francois, O., Mita, Y., Bourouina, T. (2005). Advanced etching of silicon based on deep reactive ion etching for silicon high aspect ratio microstructures and three-dimensional micro- and nanostructures, *J. Microelectr.* 36, 673–677.
- [42] Kern, W., Puotinen, D.A. (1970). Cleaning solutions based on hydrogen peroxide for use in silicon semiconductor technology, *Rca Rev.* 31, 187–206.
- [43] Labeed, F.H., Fatoyinbo, H.O. (2014). *Microfluidics in detection science: lab-on-a-chip technologies*, Eds. Cambridge: Royal Society of Chemistry, UK.
- [44] Santana, P.P., Oliveira, I.M.F., Piccin, E. (2012). Evaluation of using Xurography as a new technique for the fabrication of disposable gold electrodes with high reproducible areas, *Electrochem. Commun.* 16, 96–99.
- [45] Fouchal, F., Dickens, P. (2007). Adaptive screen printing for rapid manufacturing, *Rapid Prototyping J.* 13, 284–290.

- [46] Cornelius, T.L. (2002). *Computer Aided and Integrated Manufacturing Systems*, Vol. 3: Optimization Methods, World Scientific, Singapore.
- [47] Bartholomeusz, D.A., Boulté, R.W., Andrade, D. (2005). Xurography: rapid prototyping of microstructures using a cutting plotter, *J. Microelectromechanical Syst.* 14, 1364–1374.
- [48] Chu, L.Y., Kim, J.W., Shah, R.K., Weitz, D.A. (2007). Monodisperse thermoresponsive microgels with tunable volume-phase transition kinetics, *Adv. Funct. Mater.* 17, 3499–3504.
- [49] Shah, R.K., Kim, J.-W., Agresti, J.J., Weitz, D.A., Chu, L.-Y. (2008). Fabrication of monodisperse thermosensitive microgels and gel capsules in microfluidic devices, *Soft Matter.* 4, 2303–2309.
- [50] Datta, S.S., Abbaspourrad, A., Amstad, E., Fan, J., Kim, S.H., Romanowsky, M., Shum, H.C., Sun, B., Utada, A.S., Windbergs, M., Zhou, S., Weitz, D.A. (2014). 25th anniversary article: double emulsion templated solid microcapsules: mechanics and controlled release, *Adv. Mater.* 26, 2205–2218.
- [51] Shah, R.K., Kim, J.-W., Weitz, D.A. (2010). Monodisperse stimuli-responsive colloids by self-assembly of microgels in droplets, *Langmuir.* 26, 1561–1565.
- [52] Seiffert, S., Weitz, D.A. (2010). Controlled fabrication of polymer microgels by polymer-analogous gelation in droplet microfluidics, *Soft Matter.* 6, 3184–3190.
- [53] Shum, H.C., Lee, D., Yoon, I., Kodger, T., Weitz, D.A. (2008). Double emulsion templated monodisperse phospholipid vesicles, *Langmuir.* 24, 7651–7653.
- [54] Shum, H.C., Kim, J.-W., Weitz, D.A. (2008). Microfluidic fabrication of monodisperse biocompatible and biodegradable polymersomes with controlled permeability, *J. Am. Chem. Soc.* 130, 9543–9549.
- [55] Kim, S.-H., Shum, H.C., Kim, J.W., Cho, J.-C., Weitz, D.A. (2011). Multiple polymersomes for programmed release of multiple components, *J. Am. Chem. Soc.* 133, 15165–15171.
- [56] Nisisako, T., Okushima, S., Torii, T. (2005). Controlled formulation of monodisperse double emulsions in a multiple-phase microfluidic system, *Soft Matter.* 1, 23–27.
- [57] Okushima, S., Nisisako, T., Torii, T., Higuchi, T. (2004). Controlled production of monodisperse double emulsions by two-step droplet breakup in microfluidic devices, *Langmuir.* 20, 9905–9908.
- [58] Abate, A.R., Krummel, A.T., Lee, D., Marquez, M., Holtze, C., Weitz, D.A. (2008). Photoreactive coating for high-contrast spatial patterning of microfluidic device wettability, *Lab Chip.* 8, 2157–2160.
- [59] Abate, A.R., Thiele, J., Weinhart, M., Weitz, D.A. (2010). Patterning microfluidic device wettability using flow confinement, *Lab Chip.* 10, 1774–1776.

- [60] Abate, A.R., Weitz, D.A. (2009). High-order multiple emulsions formed in poly(dimethylsiloxane) microfluidics, *Small*. 5, 2030–2032.
- [61] Abate, A.R., Kutsovsky, M., Seiffert, S., Windbergs, M., Pinto, L.F.V., Rotem, A., Utda A.S., Weitz, D.A. (2011). Synthesis of monodisperse microparticles from non-Newtonian polymer solutions with microfluidic devices, *Adv. Mater.* 23, 1757–1760.

High and Efficient Production of Nanomaterials by Microfluidic Reactor Approaches

Victor Sebastian Cabeza

Additional information is available at the end of the chapter

<http://dx.doi.org/10.5772/64347>

Abstract

This chapter overviews different approaches for the synthesis of nanostructured materials based on alternative methodologies to the most conventional and widespread colloidal wet chemical route and with a great potential applicability to large-scale and continuous production of nanomaterials. Their major outcomes, current progress in synthesis of micro and nanostructures by using microfluidics techniques and potential applications for the next future are reviewed throughout three different sections. Emphasis is placed on nanomaterials production basics, nanomaterials production techniques and microfluidic reactors (types, materials, designs). The integration of nanoparticle and microreactor technologies delivers enormous possibilities for the further development of novel materials and reactors. In this chapter, recent achievements in the synthesis of nanoparticles in microfluidic reactors are stated. A variety of strategies for synthesizing inorganic and polymeric nanoparticles are presented and compared, including continuous flow, gas-liquid segmented flow and droplet-based microreactors

Keywords: Microfluidics, inorganic nanomaterials, polymeric nanomaterials, microreactors, nanoengineering

1. Introduction

After more than twenty years of basic and applied research, nanotechnologies are gaining in commercial use due to their unprecedented potential. Nanomaterials are the heart of the nanotechnology, they are the key in the development of electronics, medical diagnostics and therapeutics, energy storage, cosmetics, catalysts, lubricants, pigments, healthcare. In fact, the latest update available from the inventory compiled by the Woodrow Wilson Center [1] indicates that the number of nanotechnology-based consumer products was above 1800 in 2014 and growing at a strong pace. These products are produced in more than 33 countries and can

be classified into different groups: Appliances, Automotive, Cross Cutting, Electronics and Computers, Food and Beverage, Goods for Children, Health and Fitness or Home and Garden. The composition of these products could contain up to more than 49 different types of nanomaterials, from gold to liposomes. Then, it is evident that during the past two or three decades there has been an explosive increase in our ability to nanoengineer and product nanostructures and nanosystems with an good degree of control. Therefore, given the expected economic and social impact of nanotechnology products and the fact that many areas of application are still scarcely explored, it seems reasonable to predict that industrial use of nanomaterials will continue to increase in the foreseeable future.

Nanomaterials can be defined as materials development at the atomic, molecular or macromolecular levels, in the length of scale of approximately 1- to 100-nm range in at least one dimension. Materials under these dimensions behave in a different mode that their bulk counterparts. The scale reduction provides special properties which are uniquely attributable to the nanoscale physical size. Consequently, it seems reasonable that the control in the synthesis procedure must be good enough to assure the properties of the nanomaterials produced. Otherwise, the quality of the products which contain those nanomaterials could be limited.

New materials properties are required as the Nanotechnology market is growing, which implies that highly sophisticated configurations at the nanoscale level need to be developed. These strict requirements on the characteristics of nanomaterials pose serious challenges to their mass production. In addition, many of the most sophisticated nanomaterials are nowadays prepared in lab scale by complex, multistep batch procedures that are not amenable to large-scale production [2]. This issue has been identified as one of the main barriers for the development of nanotechnology [3] and any potential technology able to overcome these drawbacks will enable the future development of Nanotechnology.

Microscale process engineering is the science of conducting chemical or physical processes inside small confined volumes, for instance inside channels with diameters of less than 1 mm (microchannels) or other structures with sub-millimeter dimensions [4]. These processes are usually carried out as continuous production with the potential to make microscale process a key for chemical production [4]. In fact, microscale process engineering enables an accurate control in the productivity of pharmaceutical and fine chemical industry. The small dimensions where the chemical reaction occurs lead to a relatively large surface area-to-volume ratios and promotes the heat and mass transport. In addition, the possibility of fast mixing of reactants and fast heating and cooling of reaction mixtures enables precise control of the reaction parameters. These advantages are well suited in the production of nanomaterials, where an exquisite control of synthesis conditions is required to assure an excellent quality.

This chapter overviews different approaches for the synthesis of nanostructured materials based on the application of microreactors derived from the microscale process engineering. The basics of nanomaterials production, the synthesis approaches to produce nanomaterials in continuous mode, present state-of-the-art and potential applications of microreactors for the next future are reviewed.

1.1. Overview of synthetic approaches to nanomaterials production

The fabrication of nanomaterials of tailored properties involves the control of size, shape, structure and composition. Fabrication techniques for nanostructures can be broadly divided into two categories: Top-down and Bottom-up approaches (Figure 1). Top-down approaches consist of the miniaturization or size reduction (for instance by etching or milling) of larger structures. On the other hand, bottom-up approaches are based on growth and self-assembly to build up nanostructures from atomic or molecular precursors. Lithographic patterning is usually the most common technique to structure bulk materials at the nanoscale. Optical lithography (also named Photolithography), has been the predominant patterning technique due to the fact that it enables the production of sub-100-nm patterns with the use of very short-wavelength light (currently 193 nm).

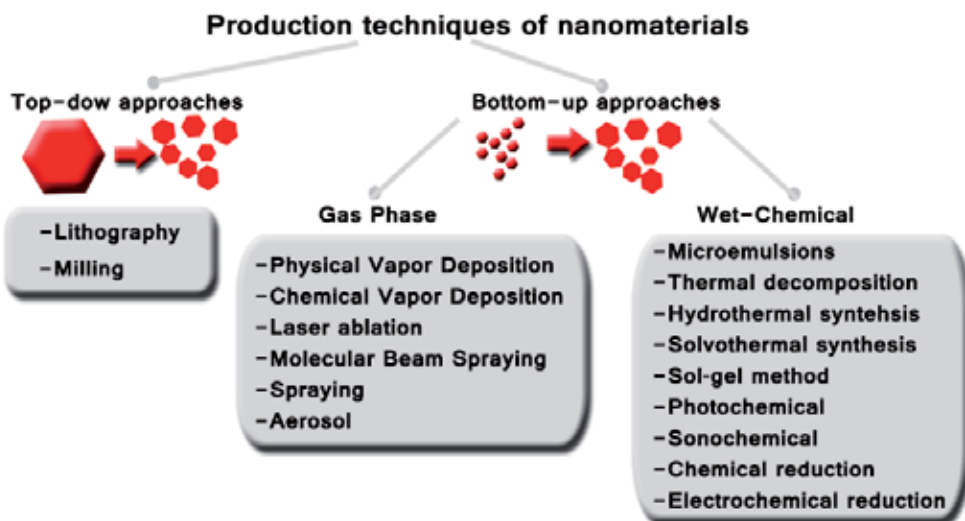


Figure 1. Scheme of the most relevant production techniques of nanomaterials

Regarding bottom-up approaches, they offers the most realistic solution toward the fabrication of complex and functional nanomaterials since the resolution and dimension control at the nanoscale level is better than in top-down approaches. Botton-up techniques can be classified into gas phase and wet-chemical methods, depending on the medium at which nanoparticles form (see Figure 1). The most important gas phase approaches comprise Physical Vapour Deposition, Chemical Vapour Deposition, Laser ablation, Molecular Beam Spraying, and Spraying-Aerosol. Physical vapor deposition (PVD) is a versatile method for preparing thin-film materials with structural control at the nanometer or even atomic scale by carefully monitoring the processing parameters. PVD involves the generation of vapour phase species via evaporation, sputtering, or laser ablation. Chemical vapor deposition (CVD) is a technique for thin film deposition which offers an excellent uniformity and it is amenable to large scale production. In CVD the substrate is exposed to one or more volatile precursor materials that

react and/or decompose on the substrate surface to produce the desired deposit. Molecular beam epitaxy (MBE) is a technique to produce ultrathin films as high quality epitaxial layers with very sharp interfaces and good control of thickness and chemical composition. To obtain epitaxial layers of high purity, the deposition takes place in very high vacuum. Spraying is a well-established method, which involves the atomization of chemical precursors into tiny droplets dispersed in a gas phase. Afterwards, the drops are combusted or evaporated to form nanoparticles or thin films. Pyrolysis is the chemical decomposition of organic materials by heating in the absence of oxygen or any other reagents. The use of a laser source induces a fast heating, in a solid target (ablation) either on the gas phase or in a liquid phase, which promotes the formation of nuclei and direct the growth of nanoparticles, for instance metal oxides.

Wet-Chemical techniques have been considered as one of the most important techniques for fabricating low-dimensional structures with an accurate control on the dimensions and composition. These techniques seem to be very attractive since they enable the production of a wide diversity of nanomaterials, at a low cost and with a high throughput to ease a high-volume production (see Figure 1). Nanomaterials can be tailored with sub-nanometer level accuracy by careful regulation of crystallization kinetics and thermodynamic parameters in liquid media under assistance of selected solvents, ligands and surfactants. Wet-Chemical techniques can be classified into: microemulsions, thermal decomposition, hydrothermal and solvothermal synthesis, sol-gel method, photochemical, sonochemical and electrochemical processes.

Microemulsions are ternary/quaternary systems of water, oil and amphiphilic surfactants forming micelles. Micelles form after the surfactant concentration is above the critical micellar concentration. Microemulsions can be generated after the solubilization of organic compounds in water (oil-in water, o/w), or hydrophilic compounds in the oil phase (water in oil, w/o). In addition, a high degree of complexity can be achieved producing multiple phase emulsions, such as w/o/w or o/w/o. Nanomaterials are usually produced by mixing two microemulsions, where each other contain a reactive chemical [5]. Once the microemulsions merge, new micelles are formed and the chemical reaction occurs. Then, micelles have the role of nano/micro reactor, confining the chemicals during the reaction. Consequently, microemulsions are a versatile preparation technique which enables an accurate control of nanoparticle properties such as size, geometry, morphology, homogeneity and surface area. Thermal decomposition is usually carried out with organometallic precursors compounds and metal complexes with the assistance of high boiling solvents. Hydrothermal and solvothermal synthesis are common methods to synthesize inorganic nanomaterials. These techniques take advantage of the high reactivity of metal precursors at elevated pressure and temperature. A good control on crystallization parameters such as pressure, temperature, time, pH and reactants concentration enable to tune the size and shape of nanomaterials. Sol-gel method it is generally used for the production of metal oxide nanomaterials and involves the hydrolysis, condensation and polymerization of metal precursors. A three-dimensional network is formed after the polymerization step, forming the gel, but a calcination treatment is usually required in order to drive off the structural water and transform the metal hydroxides into metal oxides. Photochemical techniques are based on the UV-irradiation of the chemical precursors to generate active

radicals which promote the NPs formation with a controlled kinetic rate. On the other hand, sonochemical approaches are associated with the absorption of ultrasound by water. Acoustic wavelengths range from 10 to 10^4 cm, which is far above the molecular or atomic range. Then, sonochemical reactions occur by the phenomena of acoustic cavitation, where the liquid is compressed or expanded according to the sound field. Hot spots are formed during the collapsing of bubbles generated during acoustic cavitation, achieving local temperatures of upto 4000K [6]. These conditions make water molecules dissociate into H and OH radicals and promote the reduction of metallic ions. Finally, chemical and electrochemical reduction approaches are one of the possible and powerful options for the fabrication of new types of nanomaterials. Chemical reduction relies in the presence of a substance, named reducing agent, with an oxidation potential high enough to easily donate electrons to an electron recipient compound, which is usually a metallic salt. If this electron transfer occur, metallic ions are reduced to atoms which form nuclei and later nanoparticles according to the nucleation-growth-ripening process [7]. However, this procedure is highly dependent from the presence of a proper reducing agent which enables the electron donation without potential interferences with the crystallization kinetics. On the other hand, electrochemical reduction processes, which involve electron transfer reactions at solid-liquid interfaces controlled by an externally applied voltage, are reliable tools for nanofabrication since the redox potential can be easily tuned according the redox potential required.

1.2. Nanomaterials production basics

Nanotechnology is a relatively new field; therefore applications of nanoparticles offer much promise to improve in future. However, most of applications based on nanoparticles are dealing only a few nanoparticle materials such as gold, silver, silica, alumina, carbon nanotubes, titanium oxide and zinc oxide. But, many other interesting nanomaterials that show unique and useful properties still remain on the laboratory bench due to slow progress in bridging laboratories with high-scale production factories [8]. The lack of development of large scale production is being considered as one of the main obstacles. For instance, carbon nanotubes (CNTs) was considered a remarkable nanomaterial due to their unique physical and chemical properties. However the number of applications of CNTs was limited at the Early 90's because the prize was too high (more than 1000\$/gram). Nowadays, Microreaction technology is expected to have a number of advantages for chemical production [2] as the high heat and mass transfer rates possible in microfluidic systems allow reactions to be performed under more aggressive conditions with higher yields that can be achieved with conventional reactors [10]. In addition, new reaction pathways considered too difficult to explore in conventional microscopic equipment could be pursued because if the microreactor fails, the small amount of chemicals released accidentally could be easily contained. Microreaction technology enables a continuous production, as well as allows the presence of integrated sensor and control units to follow the nanomaterials quality or even alert about any fails. A failed microreactor can be isolated and replaced while other parallel units continued production. Also these inherent safety characteristics could allow a production scale systems of multiple microreactors enabling a distributed point-of-use synthesis of chemicals with storage and shipping limitations, such as highly reactive and toxic intermediates [2,10]. Moreover, scale-

up to production by replication of microreactors units used in the laboratory would eliminate costly redesign and pilot plant experiments, thereby shortening the development time from laboratory to commercial-scale production.

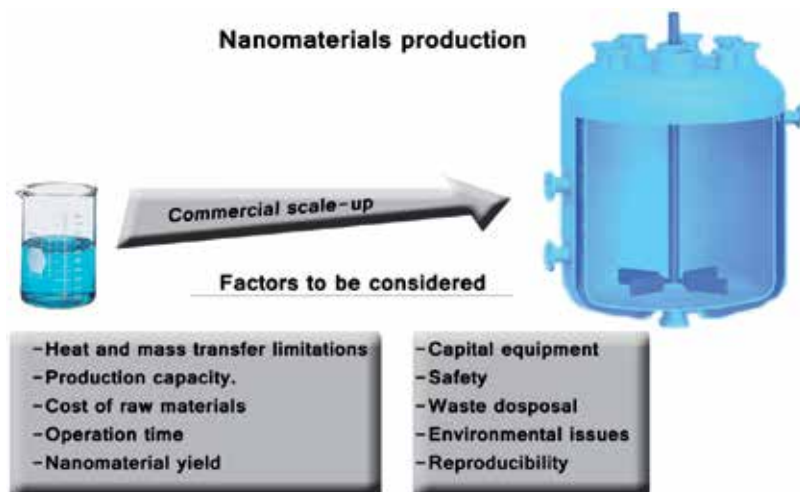


Figure 2. Factors to be considered in the commercial scale-up of nanomaterials production.

2. Microfluidic technology

Microreactors or Microfluidic reactors constitute perhaps the enabling technology of highest potential for liquid phase synthesis of nanomaterials since they have been proposed to overcome the inherent discontinuity and reproducibility of batch reactors, the inter and intra-batch dispersion regarding the physicochemical characteristics of the product nanomaterials and the difficulties regarding scale-up [2]. In addition to their well-known enhancement of heat and mass transfer, microfluidic reactors offer a flexible operation with modular design, with the possibility of increasing the number of modules to adapt to the specific process requirements. On the other hand, the scaling-up by arraying parallel microreactors allows capital investment and market growth to be coupled, reducing financial risk, which is especially important in emerging areas such as nanotechnology [2]. This section will deal with a summary of the most representative types of microreactors used in nanomaterials production, the synthesis approaches and few examples of nanomaterials production in continuous fashion.

2.1. Microreactors typology: From simple to complex

Considering that a microreactor is a micro vessel designed to contain chemical reactions, its design should maximize the reaction performance, which in nanomaterials typically means

achieving the highest yield to the desired particles shape, with a tunable size, as well as an homogenous size distribution. Considering the chemicals and the synthesis conditions, the function-relevant criteria, such as corrosion resistance, wettability, mechanical strength, and the temperature range in which the chemical reaction occurs and the material can be used, must be considered. In addition, some other aspects should be considered: price, availability, and workability. Nevertheless, no single material fulfils all these criteria to a completely ideal extent and it means that a compromise is usually required between the most important variables.

Microreactors have evolved from simple capillary tubing (Figure 3-a) to complex design integrating valves, control of operation parameters and in-situ characterization, appropriately named lab on a chip. Regarding capillary tubing microfluidic reactors, there are many choices in terms of materials (e.g., polytetrafluoroethylene (PTFE), glass, and fused silica) with an inner diameter of up to 25 μm . The most commonly used microfluidic reactors are made of polymers due to the fact that these microreactors are ease to fabricate at low cost and with an acceptable feature resolution (Figure 3). Polymer tubing made of transparent or semi-transparent material ease the optical access while the nanocrystallization reaction is carried out, which is convenient to follow the reaction advance (Figure 3-b). Among the polymer tubes, those made of PTFE are the most widely used since they can tolerate a broad range of chemicals and elevated temperatures up to 240 $^{\circ}\text{C}$. Considering the hydrophobic nature of PTFE, it naturally resists channel fouling and blockage when aqueous streams are injected in the reactor.

The straight tubing is a simple design that suffers from mixing limitations. Such mixing limitations (slow mixing) are undesirable for the synthesis of uniform nanocrystals, especially in the case when fast reduction or decomposition of a nanoparticle precursor is involved. Segmented flow is usually arranged to overcome this limitation (this flow approach will be discussed in section 2.2). Chaotic advection can effectively accelerate mixing in slug flow by using unsteady fluid flow to stretch and fold the slugs in a channel. Figure 3-c,d show that using a pinched tubing accelerate the mixing in comparison with a straight channel. However, it is not easy to create a homogenous distribution of pinched zones. Polymer tubing is usually used to fabricate coaxial flow microsystems (Figure 3-f)). These systems are used to produce microparticles by the drop-flow approach (this concept will be discussed in sections 2.2 and 2.4). For instance to produce o/w microparticles, an aqueous solution is pumped through the inner tubing. Oil stream is pumped through the outer tubing and it exerts shear on the aqueous phase at the annular junction, causing uniform microdroplets to break away and flow down the tubing.

An alternative to tubing microfluidic reactors is the use of microfluidic chips fabricated using the popular soft lithography technique. The most commonly fabricated microsystems are made of poly(dimethyl siloxane) (PDMS) and glass. The PDMS layer is peeled off and bonded to a glass slide to seal the channels (Figure 3 e, h, i, j). Figure 3-e depicts an elaborated PDMS-Glass microsystem, where an excellent control on fluid-dynamics is achieved. The channel dimensions (length and diameter) can be tuned according to the nano-crystallization reaction requirements, inserting meandering channels to improve the reagents mixing, as well as fabricating the proper micro-channels to control the pressure drop. However, these microsys-

tems have a limited operating temperature and pressures, as well as a poor chemical compatibility, since PDMS is swelled by most of the organic solvents. Some microreactors made of SU-8-PEEK have been reported to withstand temperatures and pressures up to 150°C and 2 MPa, respectively [11].

Sophisticated PDMS-glass microreactors can also be fabricated to produce microparticles by the before mentioned two-phase method using a co-flowing system. Differently from tubing co-flowing microsystems, lithography enables an accurate control on the nozzle zone where the non-miscible phases are put into contact, providing a superior control over fluid-dynamics. In addition, the microparticles production unit can be coupled to a polymerization unit by UV radiation, where a spiraling and gradually widening channel enables maximum absorption of radiated UV light for an inline photo-polymerization without coalescence and clogging issues (Figure 3-g) [16]. Figure 3-h depicts a PDMS glass microfluidic reactor also designed to receive a maximum absorption of LED radiation in order to promote a photochemical nucleation and shape selectivity towards certain Ag nanostructures. Figure 3-i shows another co-flowing system made in PDMS to produce PNIPAM polymeric nanoparticles with a tuneable size by the polymerization of NIPAM monomer. Monodisperse W/O/W double emulsions were prepared in glass microcapillary device, forming phospholipid vesicles using monodisperse double emulsions with a core-shell structure as templates (Figure 3-j). Finally, MPEG-PLGA nanoparticles can be produced with a high production speed by nanoprecipitation using a parallel flow focusing PDMS-Glass microfluidic reactor [19]. The microdevice contains 100 parallel outlets to improve the mixing of polymer-solvent-antisolvent system by diffusion and achieve a mixing time shorter than the nanoprecipitation time. An excellent mixing control was achieved and monodisperse nanoparticles was produced in a mixing time shorter than 60ms. The production speed can be further improved by several orders of magnitude just by increasing the number of outlet streams [19].

Metal based microreactors are especially advantageous for processes involving high heat load and toxic chemicals, except for strong acids, due to the good chemical compatibility and thermal resistance. Metal microreactors are usually fabricated using electrical discharge machining, laser ablation or etching techniques, which allow to achieve a precise shaping down to micrometer level. Highly precise microstructures can be also generated by the well-known lithographic structuring techniques (LIGA). Some of the difficulties in using metal microreactors arose from the leaks at the joints, but these days there are have been developed several welding, soldering and joining techniques that enable to create high-strength inter-metallic bonds. Metal microfluidic reactors withstand robust handling, which is quite convenient during cleaning operations. They have been also demonstrated in the synthesis of nanomaterials. Size-tunable methacrylic nanoparticles have been successfully produced by stainless-steel multilamination micromixer (Figure 4-a). The excellent mixing achieved in the micromixer promoted the nucleation step at a high extension and enabled to decrease the nanoparticle sizes under the ones obtained in batch reactors, saving also organic solvent. The same type of micromixer was also used to produce Au-SiO₂ nanoshells in a multi-step process (Figure 4-b). The micromixers enabled to improve the control over the optical properties of these nanoparticles, compared to the conventional batch process operation. A stainless steel

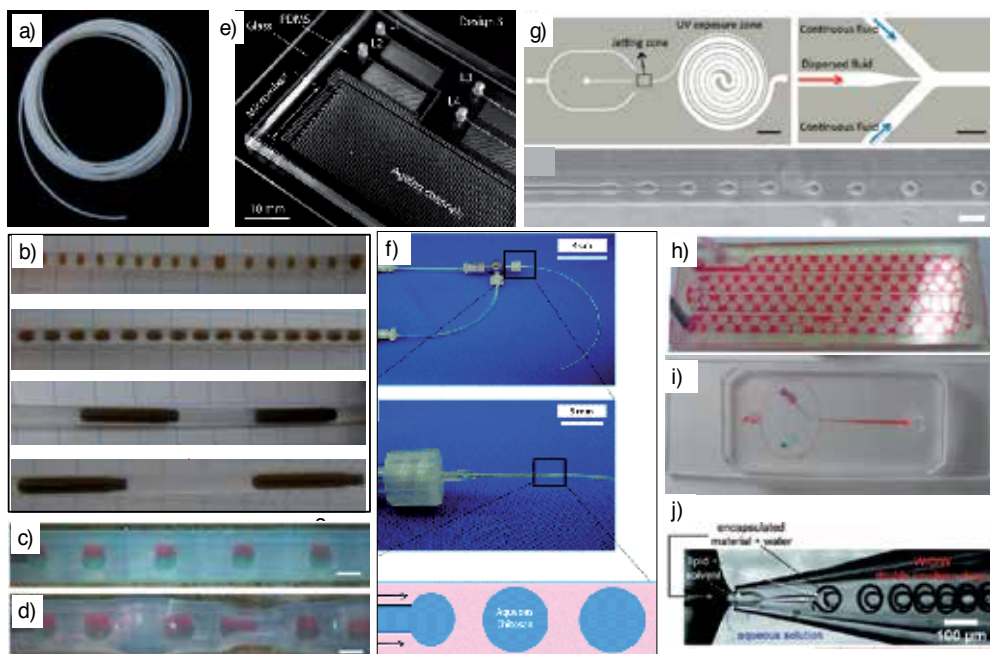


Figure 3. Examples of polymeric microreactors for nanomaterials synthesis. (a) PTFE tubing, (b) PTFE tubing microreactor, where the slug dimensions are modified to tune the crystallization kinetics of MOFs nanocrystals, (reprinted with permission from ref. [12], copyright 2013 American Chemical Society). (c-d) Straight and pinched PTFE microreactor to enhance the reactants mixing during the production of Au nanocrystals, (reprinted with permission from ref. [13], copyright 2014 John Wiley and Sons). (e) PDMS/Glass microreactor designed to produce SiO₂ nanocrystals (reprinted with permission from ref. [14], copyright 2004 American Chemical Society), (f) PTFE coaxial microreactor designed to produce chitosan microparticles (reprinted with permission from ref. [15], copyright 2013 The Royal Society of Chemistry) (g) PDMS-glass microsystem to produce uniform microbeads loaded with quantum dots. (reprinted with permission from ref. [16], copyright 2014 American Chemical Society). (h) PDMS-glass microsystem to produce Ag nanoparticles with a controlled size and shape by LED illumination. (reprinted with permission from ref. [17], copyright 2013 The Royal Society of Chemistry). (i) PDMS-glass microsystem to produce uniform PNIPAM nanoparticles by monomer polymerization. (reprinted with permission from ref. [18], copyright 2011 WILEY-VCH Verlag GmbH & Co.). (j) Glass parallel-flow focusing microsystem to produce uniform Phospholipid Vesicles. (reprinted with permission from ref. [26], copyright 2008 American Chemical Society).

spiral microreactor was used to control the production of Ag nanoparticles by gas and liquid segmented flow [22].

Silicon and glass-based microfluidic reactors are fabricated by the conventional lithographic techniques and have the advantage of high bond strengths which enable to work at high pressure. Differently from glass microreactors, silicon microreactors can be used in high temperature reactions because the high thermal conductivity of silicon. However, both materials are fragile, and these reactors do not withstand mechanical impacts. A spiral silicon- pyrex reactor was designed to have separated the mixing and reaction units and promote a homogeneous nucleation after a good mixing was achieved (Figure 4-c). This reactor could control the growth of Au nanoparticles, which is a pretty fast reaction and require from an excellent mixing control. The same design of spiral microreactor was applied in the synthesis of mesoporous nanomaterials (MCM-41), decreasing the synthesis time from days (batch reactor) to minutes

and improving the size and shape control [24]. Figure 4-d depicts a silicon-based microreactor where there are integrated two mixing units to control the growth and composition of Au/Ag hetero-structures. Glass microcapillary reactors can be fabricated with a higher resolution at micrometer scale than the polymer reactors ones, this fact enables to produce a better control in the production of emulsions and polymeric nanoparticles (Figure 3-j).

Finally, this section should highlight the existence of some other types of microreactors with a considered relevance in terms of functionality. Figure 4-e illustrates a continuous three-stage silicon-based microsystem consisting of mixing, aging and sequential growth stages, operating at 65 bar and temperatures as high as 340°C. This system is an example of complex fluid-dynamic control by the injection of different precursor flow-rates and pressure drop along the different microchannels. On the other hand, silicon and glass microreactors have the advantage of easy optical access, providing a mean for a wide range of in-situ characterization techniques. Figure 4-f depicts a microreactor where the size and shape of organic crystals can be determined by optical microscopy and the crystal phase determined by in-situ Raman spectroscopy. An advance microfluidic reactor for polymer particles production was designed using a sequence of microvalves which were digitally activated to control the composition of the polymer particles in a matter of seconds [29].

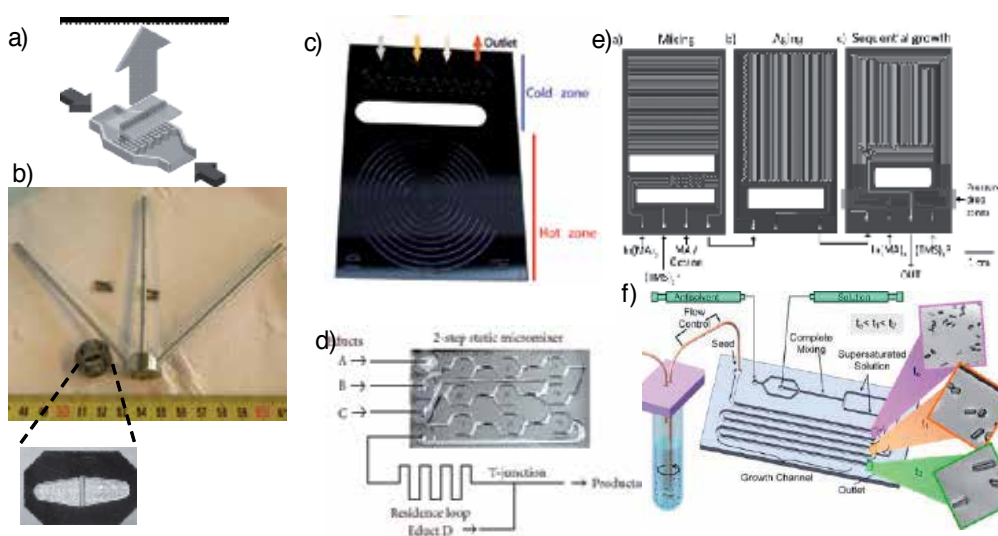


Figure 4. Examples of metal microreactors for nanomaterials synthesis. (a) Multilamination micromixer to produce polymer nanoparticles (ref. [20], reprinted with permission from ref. [21], copyright 2012 Royal Society of Chemistry). (b) Multi-step multilamination micromixer to produce Au-SiO₂ nanoshells (ref. [21], copyright 2012 Royal Society of Chemistry). (c) Spiral microreactor to produce Au NPs (ref. [23], copyright 2012 American Chemical Society). (d) Two-stage micromixer to produce Au/Ag NPs (ref. [25], copyright 2007 J. Michael Köhler et al.). (e) Three-stage microfluidic system to produce quantum dots (ref. [27], copyright 2011 WILEY-VCH Verlag GmbH & Co). (f) Microfluidic system with optical access for optical microscopy and Raman spectra coupling (ref. [28], copyright 2012 American Chemical Society).

2.2. Synthesis strategies in microfluidics

Regarding synthesis strategies, microfluidic reactors can be mainly grouped into two categories related with their flow pattern: single-phase and multi-phase flow. Continuous flow (or single-phase flow) microreactors allow facile change of experimental conditions within microseconds and usually improve the homogeneity of solution during the synthesis process in comparison with batch reactors. The operability and stability of this type of flow pattern is quite good. However, liquid flow within microchannels is strictly a laminar flow due to the small Reynolds numbers, then, the mixing is achieved predominately by molecular diffusion since the absence of turbulence. The small cross section in combination with the no-slip boundary condition at the channel walls lead to a parabolic velocity profile. This velocity profile depends on the position within the cross section and can promote a wide residence time distribution depending on the flow conditions. This fact can be a serious problem in the production of those nanomaterials whose crystallization kinetics is sensitive to the residence time distribution in the early stages of growth. If this occurs, growing nanoparticles flowing near the walls will spend significantly a long time inside the reactor, as compared to those flowing near the center (Figure 5). This performance implies that the ones flowing near the walls will be bigger in size than the ones flowing by the center. To overcome nanoparticles polydispersity, continuous flow microreactors can include a micromixing stage, where a good mixing is achieved by reducing the diffusion lengths. Micromixers can be classified in passive and active according to the existence of mechanical agitation or external forces. Passive mixing simply creates lamination of multiple fluid streams, increasing the interfacial area for diffusion (Figure 5). A passive micromixer is illustrated in Figure 4 b, where the multi-lamination is achieved by splitting the streams and then recombining them again. Although micromixing by multi-lamination is effective, the narrow microchannels can lead to high pressure drops. This fact is even more important in high viscous fluids, which limit the operability in microsystems. Active mixing is directed by applying external forces such as ultrasonic waves, electric and magnetic fields. However, the fabrication of these microsystems require special fabrication techniques [30].

Multi-phase flow facilitates the passive mixing and reduces the propensity to foul after extended operation. Multiphase flow can be also classified into gas-liquid and liquid-liquid flow regimes. In gas-liquid flow systems, it is distinguished the slug and the annular flow patterns depending on the gas and liquids superficial velocities. Annular flow occurs when a continuous gas core flow in the channel center and a liquid film at the walls. On the other hand, in slug flow, gas bubbles are located between two liquid segments (Figure 5). Viscous drag at the channel wall induces convective mixing (recirculation) within each slug. As a result, it ensures an excellent chemical homogeneity. In addition, the slug move at the same speed, this implies that the residence time distribution is narrower than with continuous flow operations. Consequently, slug or segmented flow has the potential to improve size distributions in nanocrystallization process. Then, an inert gas can be introduced in a liquid system to improve mixing and residence time characteristics.

In liquid-liquid segmented flow, the surface tension differences between immiscible streams enables to achieve a steady fluid segmentation (Figure 5). Considering the surface wettability

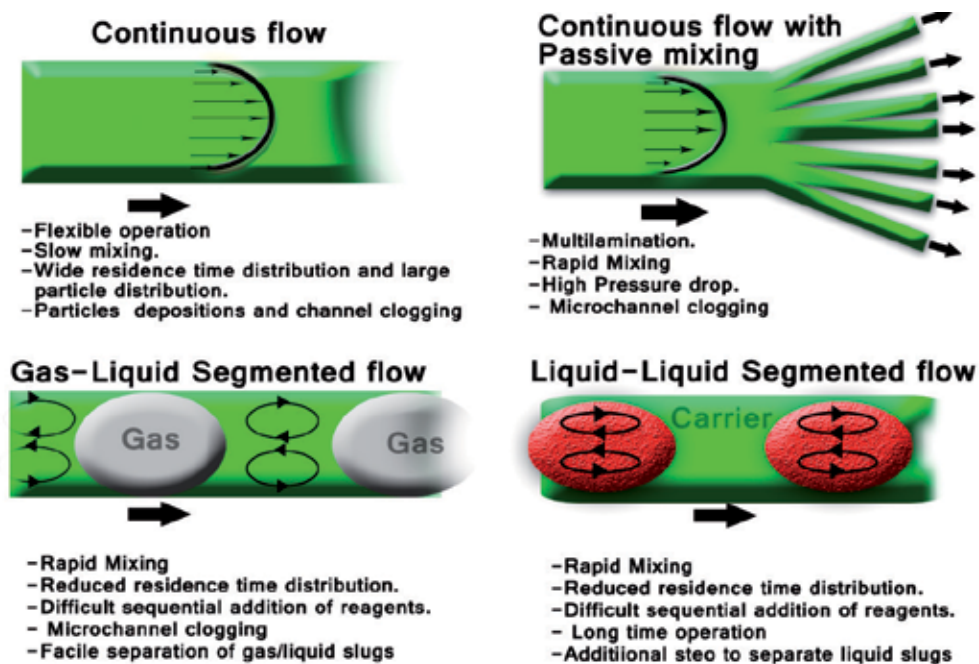


Figure 5. Comparison of the synthesis strategies in continuous microflows to produce nanomaterials: Continuous flow (with and without multilamination) and segmented flow (gas-liquid and liquid-liquid).

of the microchannel, the reactor clogging occurs usually with a high frequency in the gas-liquid slug flow since the liquid segments are flowing in contact with the microchannel wall. However, the liquid entities where the chemical reaction occurs are easier to separate in gas-liquid segmented flow. On the other hand the single-phase systems enable the subsequent addition of reagents in order to operate in a multi-stage system. A sequential addition of reagents in a multi-phase system is challenging because the formation of multiple liquid entities without connectivity. This issue can be addressed by the use of a merge drop flow, but, at the end, the segments merging could affect negatively to the residence time distribution.

2.3. Microfluidic synthesis of inorganic nanomaterials

Inorganic nanoparticles have been widely used in diverse areas such as electronics, energy, textiles, biotechnology and medicine, bio-imaging and bio-sensing. There have been tremendous interests in the development of microfluidic methods for producing inorganic nanoparticles because microfluidics provide an excellent control on the nanocrystallization process. There are numerous examples of synthesis of inorganic nanomaterials in microfluidic devices [31, 32], but some of them will be discussed in the present section due to their relevance and novelty.

Gold nanoparticles production has been extensively studied due to their wide variety of properties and the challenge in controlling the shape and size. Typical microfluidics recipes

involve the reduction of a gold precursor in the presence of different types of ligands and stabilizers. The presence of a strong reducing agent, such as sodium borohydride, promotes fast nucleation and the production of small nanoparticles. The reduction of Au ions occurs in a time scale of seconds, following a fast kinetic nanocrystallization. However, fast kinetic reactions should be carried out if the mixing time is shorter than the reaction time, otherwise a wide distribution of nanoparticles can be achieved. As it was considered in section 2.2, flow segmentation promotes a rapid mixing and an efficient heat/mass transfer by internal recirculation. But, it is required to operate with the proper segmented flow pattern and conditions in order to achieve the expected results. Consequently, the particle size distribution in fast kinetic reactions, such as Au nanoparticles production, is strongly dominated by the mixing conditions induced by internal recirculation and not only by the type of flow [33]. Figure 6 a-d illustrates the effect of the residence time on the Au nanoparticle size distribution. The length of the slugs is influenced by the residence time, obtaining small slugs at smaller residence times (Figure 6-c). The slug recirculation is higher in small slug than in the long ones, promoting a fast mass transfer. So the control of the slug length is a strict requirement to decrease the particle polydispersity (Figure 6-d). On the other hand, liquid-liquid and gas-liquid improve the micromixing but the grade of mixing achieved is not comparable, even if the residence time is the same. Figure 6 e-g shows that the particle size distribution of nanoparticles produced at the same residence time is sensitive to the fluid of segmentation. Air segmentation provides a better internal mixing than silicone oil (Figure 6-h) [33]. Silicone oil presents a higher viscosity than air, reducing both the slip velocity and the circulation rates.

Microfluidic reactors are able to produce complex hybrid nanostructures in a simple process that reduces the synthesis time and provide an additional level of reaction control that it is not attainable in bulk stirred reactors. Silica gold nanourchin particles with hyper-branched Au nanowires were produced in batch reactors after the sequential addition of reagents (at least 10 times) (Figure 6-m). Gold was anisotropically grown on the surface of silica nanoparticles decorated with Au seeds by maintaining a good control on the kinetics in a batch reactor (Figure 6-j). After several cycles of reagents addition, the length of the nanowires was long enough to use these hybrid nanostructures in SERS. However the exquisite control required during the sequential addition of reagents unable a reproducible production of these interesting nanostructures. The continuous production of gold nanourchin structures was achieved successfully in a PTFE microreactor using a single addition of reagents (Figure 6-i). The microreactor showed perfect performance for manipulating the reagent concentrations and promote a kinetic control of the reaction during the anisotropically growth of Au. Finally, those nanostructures showed a remarkable SERS performance, which evidences the quality of the produced nanostructures.

Gold nanorods have been widely used in biomedical application due to their interesting optical properties. The growth comprises a two-stage process: 1) Gold seeds formation and 2) Gold addition by the secondary growth of gold seeds. The optical properties of the resulted nanorods are sensitive to synthesis variables such as seed size, temperature, mixing, reagents concentration, reducing rate and so. In addition, the synthesis of Au nanorods is usually achieved in the presence of cetyltrimethyl ammonium bromide (CTABr), a high cytotoxic

ligand which requires several purification treatments after synthesis. Although there are several microfluidic approaches to produce Au nanorods and circumvent the limited reproducibility of Au nanorods production, they are based in the use of seeds and CTAB [36]. A new microfluidic approach enables the continuous production of Au nanorods in a single step (without seeds) and using a biocompatible ligand (Lysine) instead of CTAB [35]. Optical properties of the produced Au nanorods are tunable with the Lysine/Au precursor ration, obtaining nanorods with an aspect ratio of 5 and a Surface Plasmon Resonance Peak centered in 780nm. Moreover, microfluidics facilitate the manipulation of separate reagent streams, which enabled the fast screening and optimization of the synthesis conditions on demand. The Au nanorods produced by this approach were successfully applied as contrast agents in Photothermal Optical Coherence Tomography (OCT) of human breast tissue. The simplicity of this approach will made feasible that unskilled staff could in future produce this type of contrast agent on demand and out from the laboratory.

Magnetic nanoparticles (MNPs) are of significant interest due to their unique properties in terms of chemical stability, size-dependent magnetic response, biocompatibility, and low price, which make them ideal candidates in a wide-range of applications in biomedicine-related fields: drug delivery, hyperthermia, magnetic resonance imaging (MRI), tissue engineering and repair, biosensing, and biochemical separations [37]. High quality crystalline MNPs were obtained with a narrow size distribution of mean diameter 3.6 nm and standard deviation 0.8 nm in a passively-driven capillary-based droplet reactor [38]. Reagents were fully compartmentalised within the droplets, preventing the fouling of the channel walls. In contrast, when the reaction was allowed to proceed in a single-phase mode of operation, a dark brown deposit formed on the inner surface of the main channel within minutes. Then, as it was before mentioned, segmented flow is a useful tool to prevent microfluidic reactor from clogging and promote a narrow size distribution of nanoparticles during the growth process. However the flow segmentation can provide a new function, controlling the crystal phase. That is, by controlling the atmosphere in the gas segments, the crystalline phase and size of the resulting nanoparticles can be accurately tuned [37]. Pure magnetite nanocrystals with their characteristic octahedral shape were obtained when N_2 and H_2 were used to segmentate the liquid stream of reagents (Figure 7-a). In fact, the reducing properties of H_2 accelerates the production of high crystalline magnetite NPs in 1 minutes residence time at $100^\circ C$.; whereas flow segmentation with N_2 required 6 minutes. If O_2 was used instead of N_2 or H_2 , oxidant conditions direct the synthesis to the production of an orange colloid (Figure 7-a). The nanoparticles formed were nanoflakes with a mean size (along the longest axis) of about 30 ± 8 and 3 nm thickness which was identified as feroxyhyte (δ -FeOOH). Finally, carbon monoxide is generally considered as a poisoning agent in many catalytic studies but is also considered as a reducing agent or even a capping agent to direct the shape control in nanoparticle synthesis. When a CO-liquid segmented flow was created, it was observed that feroxyhyte was obtained at temperatures lower than $80^\circ C$ (see Figure 7-a). But these nanostructures were bigger in size than the ones produced with O_2 , (70 ± 12 nm and thickness of 3 nm). Then, at low temperatures CO does not act as a reducing agent, as H_2 does, and instead directs the oxidation of iron hydroxides to feroxyhyte. With a further increase of temperature to $100^\circ C$, crystalline and pure magnetite nanoparticles were obtained at 1 min of residence time,

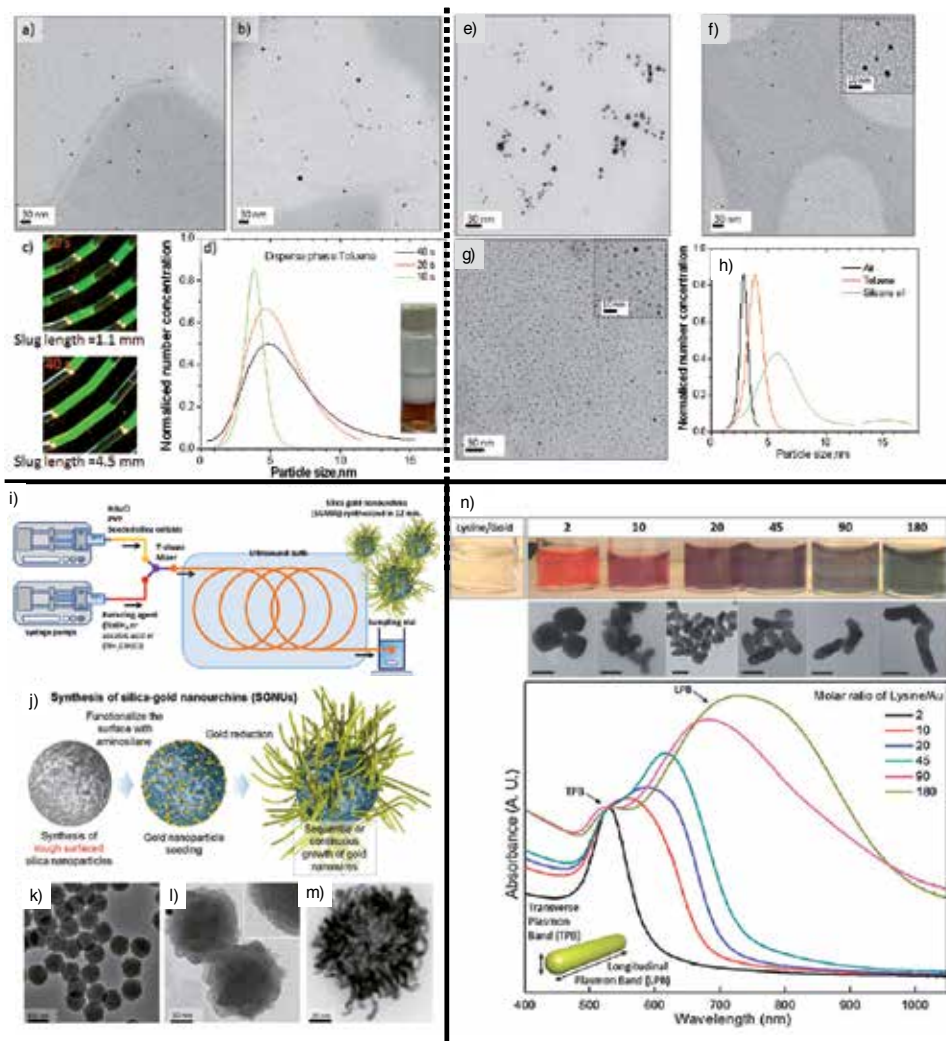


Figure 6. Gold nanoparticles produced in microfluidic reactors. TEM image of gold NPs synthesized in toluene-aqueous segmented flow: a) Residence time (Rt) = 10 s, b) Rt = 40 s, c) segmented slugs generated at Rt = 10 and 40 s d) Particle size distribution diagram from AuNPs obtained in toluene - aqueous segmented flow at Rt = 40, 20, and 10 s. TEM image of gold NPs synthesized at Rt = 10 s in a : (e) silicone oil-aqueous segmented flow, (f) toluene-aqueous segmented flow, (g) air - aqueous segmented flow. (h) Particle size distribution diagram from AuNPs obtained in silicone oil/toluene/air-aqueous segmented flow at Rt = 10 s.(reprinted with permission from ref. [33], copyright 2012 American Chemical Society).i) Microfluidic system to produce Au nanourchin particles ;j) Scheme for the synthesis of silica-gold nanourchins formation with representative images from: k) silica NP, l) silica decorated with Au NPs (m) Au nanourchin (reprinted with permission from ref. [34], copyright 2014 Royal Society of Chemistry). n) Absorption spectra and TEM images of the gold nanorods produced with microfluidic reactors. (reprinted with permission from ref. [35], copyright 2012 Royal Society of Chemistry).

confirming the reduction potential of CO at these conditions. Consequently the gas slug microfluidics provide a flexible, easy option to implement a process to produce customized iron oxide nanostructures.

Laboratory syntheses tend to be complex, based in multistep batch processes with yields that are typically well below the gram range. These batch processes often suffer from irreproducibility of the morphology, size, size distribution and quality. Then, implementing the continuous, or at least automated, production of nanomaterials is clearly desirable in terms of improving the product homogeneity and facilitating scale-up production. The continuous production of nanomaterials is challenging because of the difficulties involved in translating the complexity of nanomaterial synthesis into on-line operations. The production of hollow gold nanoparticles constitute a clear example of the strict requirements in the dimensional control, since their optical properties are sensitive to the nanoparticle dimensions and shell thickness. The synthesis of hollow Au nanoparticles comprises a multi-stage process: 1) Synthesis of a Co NP as a template, 2) Galvanic replacement of Co by Au^{+3} ions. The conventional lab scale production of hollow gold NPs deals with a reaction volume of 120 mL [39]. But if the production scale was increased 10 fold, the quality and consequently the optical properties, are not reproducible. The poor quality of the NPs in the scaled-up batch syntheses was probably caused by insufficient mixing as the reaction volume increased. This problem is even more serious if the nano-crystallization reaction is directed by a fast kinetic. A microfluidic system was proposed to overcome the production limitations of hollow gold nanoparticles, but incorporating two additional stages to yield nanostructures suitable for biomedical applications: 1) PEG functionalization to improve the biocompatibility and 2) Sterilization (see Figure 7-b). Considering the 4 implemented stages, high quality nanoparticles were produced in only 22 minutes, being the sterilization process the slowest stage (15 min). The galvanic replacement reaction is a fast process, and then it is required to get an excellent mixing of reagents to promote an even distribution of Au^{+3} ions over the Co templates. As can be observed in Figure 7-b, the galvanic replacement of Co by Au^{+3} ions was properly directed since there is no trace of Co in the NP volume, releasing the hollow structure. Consequently, the application of microfluidic systems on multi-stage reactions is highly convenient to preserve the quality of materials and reduce irreproducibility.

A continuous three-stage microfluidic system that separates the mixing, aging, and subsequent injection stages of InP nanocrystal synthesis was designed to optimize the synthesis conditions (Figure 4-d). The microfluidic system operates at high temperature and high pressure enabling the use of solvents such as octane operating in the supercritical regime for high diffusivity resulting in the production of high-quality InP nanocrystals in as little as 2 minutes (Figure 7-c). To control the size of InP nanocrystals, six sequential injections of chemical precursors were injected. This procedure ease the production protocol of these nanocrystals, since the sequential addition of reagents in a batch reactor requires at high temperature of an exquisite control and accuracy.

2.4. Microfluidic synthesis of polymeric nanomaterials

Microfluidic devices have emerged as promising tools for the synthesis of polymer particles. Over conventional processes, microfluidic-assisted processes allow the production of polymer particles with an improved control over their sizes, size distributions, morphologies, and compositions. This is particularly important since the synthesis of polymeric nanoparticles by

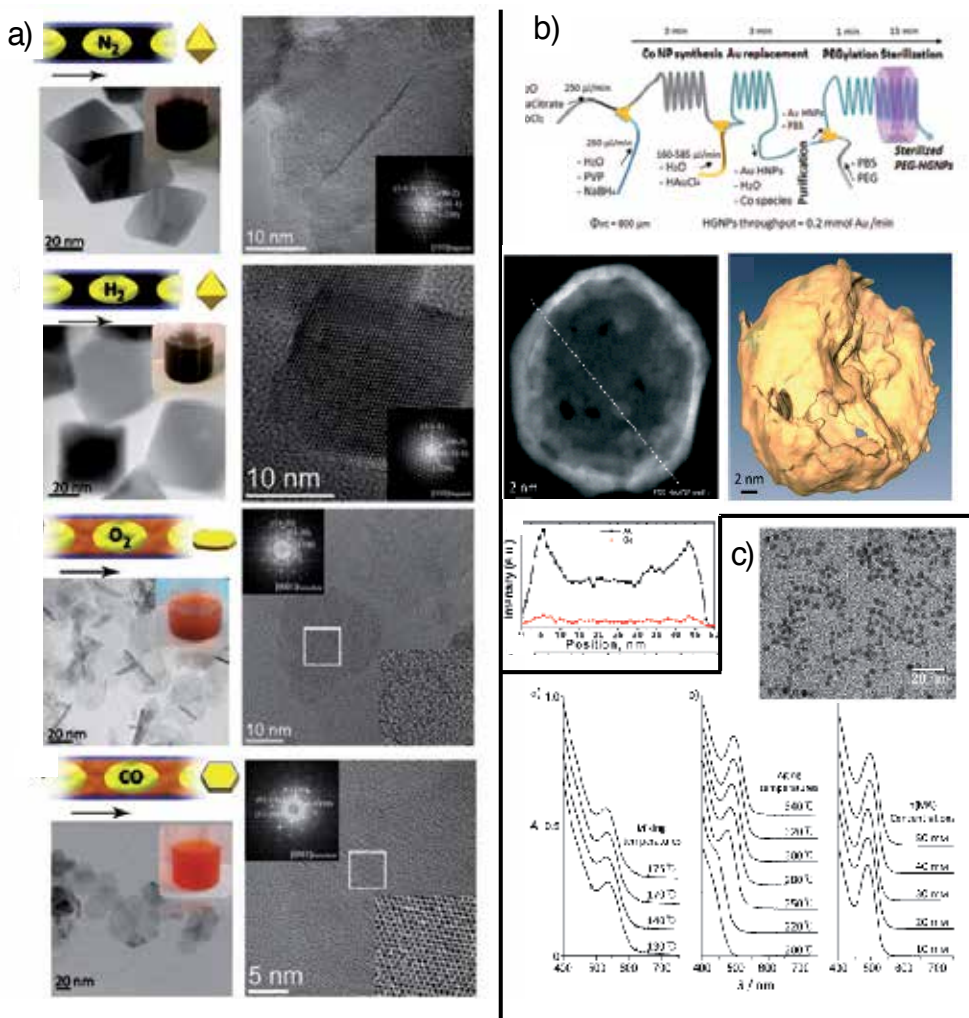


Figure 7. Synthesis of inorganic nanomaterials in microfluidic systems: a) Gas selective crystallization of iron oxides nanocrystals in segmented flow reactors(reprinted with permission from ref. [37], copyright 2015 American Chemical Society). b) Multi-stage production of hollow gold nanoparticles (reprinted with permission from ref. [39], copyright 2013 Royal Society of Chemistry). c) Production of InP nanocrystals in pressure and temperature condition (reprinted with permission from ref. [27], copyright 2010 WILEY-VCH Verlag GmbH & Co).

bulk methods typically lacks control over the mixing processes, which may compromise the properties of the resulting nanoparticles. Nanoparticles dimensions can be tuned by varying microfluidic parameters such as flow rates, precursor composition, and mixing time. The available techniques to produce polymer nanoparticles can be classified depending on the starting state of the polymers: From dispersion of preformed polymers and from polymerization of monomers. The most common techniques which use a preformed polymer can be stated as: solvent evaporation method, nanoprecipitation, emulsification, salting out, dialysis and supercritical fluids. On the other hand, the current techniques available for monomer poly-

merization can be divided into: emulsion, mini emulsion, micro emulsion, interfacial polymerization and radical polymerization.

This section will deal some of the most interesting examples of polymer nanoparticles production by the most relevant techniques for the production of polymer particles within microfluidic devices: (a) the direct polymerization through continuous flow projection photolithography [40], (b) nanoprecipitation and (c) the emulsification of liquid monomers, followed by the polymerization of the subsequent monomer droplets.

Polymerization through continuous flow projection photolithography consists in the UV irradiation, through the objective of an optical microscope, of a polymer solution flowing within a microchannel (See Figure 8-a). A mask placed in the field-stop plane of the microscope allows polymerizing and the desired particle shape to the flowing monomer solution. Then, the polymerized microparticles are formed when flow was stopped in the microfluidic device. Then, particles were pushed out of the polymerization area with flow of the monomer solutions. This approach is very powerful because it allows for nearly unlimited designs, including the production of barcodes and multifunctional particles [41].

Two-dimensional hydrodynamic focusing was commonly used to produce polymer nanoparticles (ca. PLGA) by nanoprecipitation. Three-dimensional flow-focusing prevent the formation of aggregates and microreactor fouling. While these approaches have provided significant advantages, there still remain challenges. First, these microfluidic approaches using slow diffusive mixing at a low flow rate, limiting the productivity. Second, diffusive mixing does not allow the development of particles that require the assembly of precursors dispersed in different phases, (e.g., lipid) in the aqueous phase with precursors (e.g., polymer) in the organic phase such as lipid-polymer hybrid nanoparticles [42]. To overcome those limitations and develop a high-throughput and reproducible nanoparticle synthesis technology, new advances have been performed in improving the mixing. The application of a microvortex considerable improves the mixing and enable a controlled nanoprecipitation [42]. The use of microvortices results in a rapid mixing between phases, enabling up to 1000 times higher productivity (3 g /hour) and better size control (30-170nm) than previous methods (See Figure 8-b).

A simple and versatile coaxial turbulent jet mixer consisting of coaxial cylindrical tubes where NP precursors and non-solvent are injected through the inner and outer tubes, respectively, was fabricated to produced PLGA-PEG, Lipid vesicles and polystyrene, obtaining production rates up to 3 kg/d (see Figure 8-c) [43]. This versatile mixer provides an inherently high NP production throughput due to operation in the turbulent regime (Re 500-3500) with device dimensions in the millimeter scale. The production rates achieved are suitable for in vivo studies, clinical trials, and industrial-scale production, while retaining the advantages of homogeneity, reproducibility, and control over NP properties (size and morphology). A strong point in using this type of microfluidic devices is the potential use in biomedical research laboratories, where it is not required specialized microfabrication facilities since this is a robust and simple device, as well as a microfluidic know-how to operate in the optimum conditions.

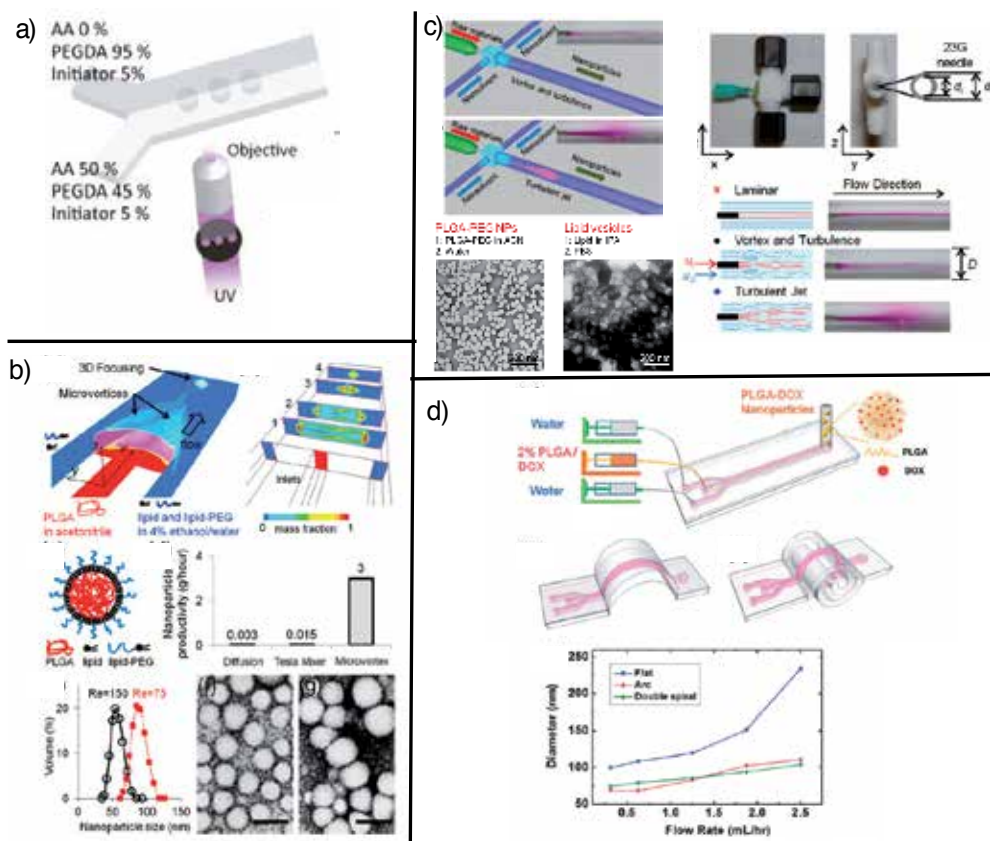


Figure 8. Synthesis of polymeric nanomaterials in microfluidic systems: a) Direct polymerization through continuous flow projection photolithography. Schematic diagram of dot-coded particle synthesis showing polymerization across two adjacent laminar (reprinted with permission from ref. [46], copyright 2012 American Chemical Society). b) Schematic and cross section views of a three-inlet microfluidic platform generating lipid-polymer hybrid nanoparticles through controlled microvortices by nanoprecipitation. Scale bars indicate 100 nm (reprinted with permission from ref. [42], copyright 2012 American Chemical Society). c) Schematic illustration of the coaxial turbulent jet mixer for high-throughput synthesis of NPs with turbulence induced by jetting. Photograph of coaxial turbulent jet mixer fabricated from PTFE tee union tube fittings and schematic illustrations and top views of fluid flow at laminar, vortex and turbulence and turbulent jet regimes (reprinted with permission from ref. [43], copyright 2014 American Chemical Society). d) Schematics of a microfluidic origami chip for synthesizing monodisperse DOX-loaded PLGA nanoparticles. Different 3D geometries (arc and double spiral) obtained by manually folding the origami chip. (reprinted with permission from ref. [44], copyright 2011 WILEY-VCH Verlag GmbH & Co).

A microfluidic origami chip with different geometries that enables the production of PLGA nanoparticles loaded with doxorubicin (DOX) by rapid mixing was designed to tune the nanoparticle size from 70 to 230 nm in a single nanoprecipitation step. The origami chip can be set in a two-dimensional flat geometry or can be folded in a three-dimensional geometry such as an arc or a double spiral. The combination of hydrodynamic focusing and 3D curved microchannels can significantly shorten the mixing distance and reduce the mixing time, which can reduce the mean nanoparticle size and size distribution (see Figure 8-d). The mixing time

in the 3D double spiral configuration was approximately 46% faster than the 2D flat configuration. This improvement was due to the formation of two counter-rotating vortices perpendicular to the flow direction that could efficiently increase the mixing after curved turns [44].

Multiple emulsion drops are useful in the production of complex microcapsules for encapsulation and sequential release of multi-component active materials while avoiding cross-contamination. Most approaches utilize sequential emulsification using a series of single drop microfluidics units, but the device fabrication requires complex procedures and a good control to synchronize the frequencies of drop generations in all drop units [45]. Figure 9-a shows a flow focusing microdevice to produce monodisperse multiple emulsion drops of high order using stable biphasic flows in confining channels. Four immiscible fluids are simultaneously introduced into the orifice in the form of a coaxial flow. This results in the formation of triple emulsion drops with the simplicity of a single emulsification process. The interesting novelty of this system is that the breakup of the interfaces is achieved in dripping or jetting modes, determined by the flow rates. The jetting breakup mode promotes the injection of different numbers of drops in the core of a multiple emulsion (see Figure 9-a). On the other hand, the dripping mode facilitates the production of monodisperse triple or quadruple emulsion drops with an onion-like configuration (Figure 9-b).

Loading inorganic nanomaterials in polymer particles entails the formation of multifunctional entities. Batch synthesis has been the method of choice for preparing inorganic-doped microparticles due to practical advantages in productivity and accessibility, despite limitations such as poor loading, low throughput, and material loss. In addition, a significant portion of loading materials is wasted during the multistep process of synthesis, purification, loading, and washing. These shortcomings are especially problematic when expensive inorganic nanomaterials are used [16]. Figure 3-g illustrates a microfluidic reactor designed to produce uniform emulsions loaded with quantum dots using high-throughput harmonic breakup of a jet in a high shear coflowing system with a well-designed nozzle. Uniform fluorescent microbeads containing about 10 wt % CdSe/ZnSe QD nanocrystals were produced with a tuned size ranging from 13 μm to 100 μm through in-line photopolymerization of biocompatible prepolymer resin. Unlike the batch synthesis, there are no additional washing steps required for the removal of unreacted residues causing dissipation of materials. Then, it is clear the advantages of microfluidics in producing complex nanostructures.

3. Conclusions and outlook

The characteristics of micro- and nanoparticle formulations produced by continuous flow microfluidic systems have remarkable advantages over traditional bulk methods that motivate their adoption. The exquisite control of flow and mixing conditions in microfluidics led to improved homogeneity of particle size distributions and the control of particle size in a reproducible and continuous fashion. Microfluidic systems often integrate real time analysis of the generated particles in order to tune the properties of the produced materials according to specifications. From the reported examples in this chapter, there is no doubt that microfluidic

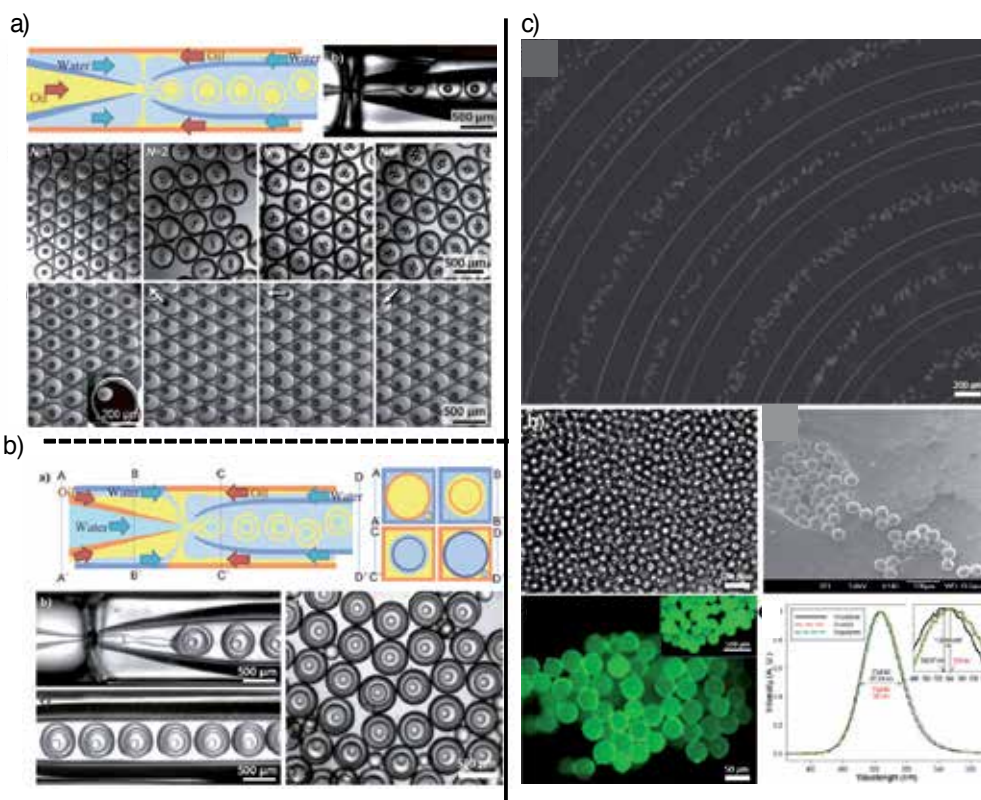


Figure 9. Synthesis of polymeric nanomaterials in microfluidic systems. a) Microfluidic capillary device for preparation of O/W/O/W triple emulsion drops. Microcapsules containing single-, two-, three, and four-core particles. Microcapsules containing a magneto-responsive core particle which align upon application of an external magnetic field. (reprinted with permission from ref. [45], copyright 2011 WILEY-VCH Verlag GmbH & Co.) b) Quadruple emulsion drops generation and downstream motion (reprinted with permission from ref. [45], copyright 2011 WILEY-VCH Verlag GmbH & Co.) c) Images and characteristics of the polymerized PEGDA microparticles produced by jet mode in a flow focusing microreactor and a spiral channel section for photo-polymerization. Pseudocolor fluorescent image of highly monodisperse PEGDA polymer beads with 9.9 wt % of highly loaded CdSe/ZnS core-shell nanocrystals. (reprinted with permission from ref. [16], copyright 2014 American Chemical Society)

devices will represent new promising tools for the production of size and shape-controlled inorganic, polymer and hybrid nanomaterials.

It is clear that microfluidics can reproduce the nanostructures synthesised in batch reactors, improving their properties and reducing the synthesis time. Furthermore, particles with new morphologies and multicomponent compositions, like janus or multicore emulsions colloid can be prepared only in such systems. However, microfluidics reactors will need to overcome some shortcomings such as fouling and low throughput production. Along with chemical stability, surface properties, and ease of fabrication, other important considerations should be taken in account. Although several nanomaterials have been produced in a high-throughput mode, the majority of the procedures reported suffer from this lack, which limits the implementation of this technology in companies and medical centres. Then, for future microfluidic

systems to become high-throughput platforms to produce high-value particulate materials beyond the lab bench, they will need to become robust, well-integrated, scalable, modular, computer controlled. Another avenue of future research will be the integration of a quality evaluation unit together with feedback control through a combination of microfluidics, robotics and automation. Consequently, continuous flow microfluidic systems will have the potential to become a standard technology to produce nano/micro-particle formulations with unprecedented homogeneity and fine control, which on the other hand are not feasible to achieve in bulk techniques

Meanwhile, the search for applications which require the use of relatively small amounts of high quality nanomaterials will be vital for the development of the field. Considering the good reproducibility and quality on nanomaterials produced using microfluidics, it is believed that microsystems will push forward new applications in promising fields such as nanomedicine, drug delivery, electronic displays, and photonics.

Acknowledgements

The People Program (CIG-Marie Curie Actions, REA grant agreement no. 321642) is gratefully acknowledged.

Author details

Victor Sebastian Cabeza^{1,2}

1 Institute of Nanoscience of Aragon (INA) and Department of Chemical Engineering and Environmental Technology, University of Zaragoza, Zaragoza, Spain

2 Networking Research Center on Bioengineering, Biomaterials and Nanomedicine (CIBER-BBN), Madrid, Spain

References

- [1] Wilson Center | Virginia Techstr. The project on Emerging Nanotechnologies [Internet]. Available from: HeaHPPT URL} <http://www.nanotechproject.org/cpi/search-products/> [Accessed: August-2015]
- [2] Victor Sebastian, Manuel Arruebo, and Jesus Santamaria. Reaction Engineering Strategies for the Production.. ;10:835-853. DOI: 10.1002/smll.201301641

- [3] Willems & van den Wildenberg (W&W). Roadmap Report on Nanoparticles [Internet]. November 2005. Available from: <http://nanoparticles.org/pdf/PerezBaxEscalano.pdf> [Accessed: August-2015]
- [4] Chih-Hung Chang, Brian K. Paul, Vincent T. Remcho, Sundar Atre and James E. Hutchison. Synthesis and post-processing of nanomaterials. *Journal of Nanoparticle Research*. 2008;10:965-980. DOI: 10.1007/s11051-007-9355-y
- [5] Christophe Petit, Patricia Lixon, Marie Paule Pileni. In situ synthesis of silver nanocluster in AOT reverse micelles. *The Journal of Physical Chemistry*. 1993;97:12974-12983. DOI: DOI: 10.1021/j100151a054
- [6] KS SUSLICK. THE CHEMICAL EFFECTS OF ULTRASOUND. SCI AMERICAN INC. 1989;;80. DOI: WOS:A1989R736400006
- [7] J. A. Marqusee and John Ross. Kinetics of phase transitions: Theory of Ostwald ripening. *The Journal of Chemical Physics*. 1983;79:373. DOI: 10.1063/1.445532
- [8] Takuya Tsuzuki. Commercial scale production of inorganic. *International Journal of Nanotechnology*. 2009;6:567-578. DOI: 10.1504/IJNT.2009.024647
- [9] Research And Markets. The Global Market for Carbon Nanotubes to 2024 [Internet].. Available from: <http://www.researchandmarkets.com/reports/2908187/the-global-market-for-carbon-nanotubes-to-2024> [Accessed: August 2015]
- [10] Jean-Claude Charpentier. Four main objectives for the future of chemical and process engineering mainly concerned by the science and technologies of new materials production. *Chemical Engineering Journal*. 2005;107:3-17. DOI: 10.1016/j.cej.2004.12.004
- [11] Yujun Song, Challa S S R Kumar and Josef Hormes. Fabrication of an SU-8 based microfluidic reactor on a PEEK substrate sealed by a 'flexible semi-solid transfer' (FST) process. *JOURNAL OF MICROMECHANICS AND MICROENGINEERING*. 2004;14:932-940. DOI: 10.1088/0960-1317/14/7/013
- [12] Lorena Paseta, Beatriz Seoane, Daniel Julve, Víctor Sebastián, Carlos Téllez, and Joaquín Coronas. Accelerating the Controlled Synthesis of Metal-Organic Frameworks by a Microfluidic Approach: A Nanoliter Continuous Reactor. *ACS Applied Materials & Interfaces*. 2013;5:9405-9410. DOI: 10.1021/am4029872
- [13] Lei Zhang and Younan Xia. Scaling up the Production of Colloidal Nanocrystals: Should We Increase or Decrease the Reaction Volume?. *Advanced materials*. ; 26:2600-2606. DOI: 10.1002/adma.201304897
- [14] Saif A. Khan, Axel Gu nther, Martin A. Schmidt, and Klavs F. Jensen. Microfluidic Synthesis of Colloidal Silica. *Langmuir*. 2004;;8604-8611. DOI: 10.1021/la0499012
- [15] Chandamany Arya, Jason G. Kralj, Kunqiang Jiang, Matthew S. Munson, Thomas P. Forbes, Don L. DeVoe, Srinivasa R. Raghavana and Samuel P. Forry. Capturing rare

- cells from blood using a packed bed of custom-synthesized chitosan microparticles. *Journal of Material Chemistry B*. 2013;1:4313-4319. DOI: 10.1039/c3tb20818d
- [16] Seung-Kon Lee, Jinyoung Baek, and Klavs F. Jensen High Throughput Synthesis of Uniform Biocompatible Polymer Beads with High Quantum Dot Loading Using Microfluidic Jet-Mode Breakup. *Langmuir*. ;30:2216-2222. DOI: 10.1021/la4041198
- [17] Simone Silvestrini, Tommaso Carofiglio and Michele Magg Shape-selective growth of silver nanoparticles under continuous flow photochemical conditions. *Chemical Communication*. 2012;49:84-86. DOI: 10.1039/c2cc35652j
- [18] Shuqiang Huang, Bingcheng Lin, Jianhua Qin Microfluidic synthesis of tunable poly-(N-isopropylacrylamide) microparticles via PEG adjustment. *Electrophoresis*. 2011;32:3364-3370. DOI: 10.1002/elps.201100340
- [19] Xianjie Kang, Chunxiong Luo, Qiong Wei, Chunyang Xiong, Qian Chen, Ying Chen, Qi Ouyang Mass production of highly monodisperse polymeric nanoparticles by parallel flow focusing system. *Microfluidics and Nanofluidics*. 2013;15:337-345. DOI: 10.1007/s10404-013-1152-6
- [20] Florence Bally, Dhiraj Kumar Garg, Christophe A. Serra, Yannick Hoarau, Nicolas Anton, Cyril Brochon, Dambarudhar Parida, Thierry Vandamme, Georges Hadziioannou Improved size-tunable preparation of polymeric nanoparticles by microfluidic nanoprecipitation. *Polymer*. 2012;53:5045-5051. DOI: 10.1016/j.polymer.2012.08.039
- [21] Leyre Gomez, Manuel Arruebo, Victor Sebastian, Laura Gutierrez and Jesus Santamaria Facile synthesis of SiO₂-Au nanoshells in a three-stage microfluidic system. *Journal of Materials Chemistry*. 2012;22:21420-21425. DOI: 10.1039/c2jm34206e
- [22] D.V. Ravi Kumar, B.L.V. Prasad, A.A. Kulkarni Segmented flow synthesis of Ag nanoparticles in spiral microreactor: Role of continuous and dispersed phase. *Chemical Engineering Journal*. 2012;192:357-368. DOI: 10.1016/j.cej.2012.02.084
- [23] Victor Sebastian Cabeza, Simon Kuhn, Amol A. Kulkarni, and Klavs F. Jensen Size-Controlled Flow Synthesis of Gold Nanoparticles Using a Segmented Flow Microfluidic Platform. *Langmuir*. 2012;28:7007-7013. DOI: 10.1021/la205131e
- [24] Xinqing Chen, Manuel Arruebo, King Lun Yeung Flow-synthesis of mesoporous silicas and their use in the preparation of magnetic catalysts for Knoevenagel condensation reactions. *Catalysis Today*. 2013;204:140-147. DOI: 10.1016/j.cattod.2012.07.017
- [25] J. Michael Kohler, H. Romanus, U. Hubner, and J. Wagner Formation of Star-Like and Core-Shell AuAg Nanoparticles during Two- and Three-Step Preparation in Batch and in Microfluidic Systems. *Journal of Nanomaterials*. 20017;:98134. DOI: 10.1155/2007/98134

- [26] Ho Cheung Shum, Daeyeon Lee, Insun Yoon, Tom Kodger, and David A. Weitz Double Emulsion Templated Monodisperse Phospholipid Vesicles. *Langmuir*. 2008;24:7651-7653. DOI: 10.1021/la801833a
- [27] Jinyoung Baek, Peter M. Allen, Mounqi G. Bawendi, and Klavs F. Jensen Investigation of Indium Phosphide Nanocrystal Synthesis Using a High-Temperature and High-Pressure Continuous Flow Microreactor. *Angewandte Chemie International Edition*. 2010;49:1-5. DOI: 10.1002/anie.201006412.
- [28] Mahmooda Sultana and Klavs F. Jensen Microfluidic Continuous Seeded Crystallization: Extraction of Growth. *Crystal Growth and Design*. 2012;12:6260-6266. DOI: 10.1021/cg301538y
- [29] Kan Liu, Hao Wang, Kuan-Ju Chen, Feng Guo, Wei-Yu Lin, Yi-Chun Chen, Duy Linh Phung, Hsian-Rong Tseng and Clifton K-F Shen A digital microfluidic droplet generator produces self-assembled supramolecular nanoparticles for targeted cell imaging. *Nanotechnology*. 2010;21:445603. DOI: 10.1088/0957-4484/21/44/445603
- [30] Ryan L. Hartman and Klavs F. Jensen Microchemical systems for continuous-flow synthesis. *Lab on a Chip*. 2009;9:2495-2507. DOI: 10.1039/b906343a
- [31] Samuel Marre and Klavs F. Jensen Synthesis of micro and nanostructures in microfluidic systems. *Chemical Society Reviews*. 2010;39:1183-1202. DOI: 10.1039/b821324k
- [32] Katla Sai Krishna, Yuehao Li, Shuning Li, Challa S.S.R. Kumar Lab-on-a-chip synthesis of inorganic nanomaterials and quantum dots for biomedical applications. *Advanced Drug Delivery Reviews*. 2013; DOI: /dx.doi.org/10.1016/j.addr.2013.05.006
- [33] Victor Sebastian Cabeza, Simon Kuhn, Amol A. Kulkarni and Klavs F. Jensen Size-Controlled Flow Synthesis of Gold Nanoparticles Using a Segmented Flow Microfluidic Platform. *Langmuir*. 2012; DOI: 10.1021/la205131e
- [34] Victor Sebastian, Seung-Kon Lee and Klavs F. Jensen Engineering the synthesis of silica-gold nano-urchin particles using continuous synthesis. *Nanoscale*. ; DOI: DOI: 10.1039/c4nr04021j
- [35] Victor Sebastian, Seung-Kon Lee, Chao Zhou, Martin F. Kraus, James G. Fujimoto and Klavs F. Jensen One-step continuous synthesis of biocompatible gold nanorods for optical coherence tomography. *Chemical Communications*. 2012;48:6654-6656. DOI: 10.1039/c2cc32969g
- [36] Suhanya Duraiswamy and Saif A. Khan Droplet-Based Microfluidic Synthesis of Anisotropic Metal Nanocrystals. 2009;24:2828-2834. DOI: 10.1002/smll.200901453
- [37] Ane Larrea, Victor Sebastian, Alfonso Ibarra, Manuel Arruebo and Jesus Santamaria-Gas Slug Microfluidics: A Unique Tool for Ultrafast, Highly Controlled Growth of Iron Oxide Nanostructures. *Chemistry of Materials*. 2015;27:4254-4260. DOI: 10.1021/acs.chemmater.5b00284

- [38] Kritika Kumar, Adrian M. Nightingale, Siva H. Krishnadasan, Nazila Kamaly, Marzena Wylenzinska, Arridge, Katharina Zeissler, Will R. Branford, Ecaterina Ware, Andrew J. deMello and John C. deMello Direct synthesis of dextran-coated superparamagnetic iron oxide nanoparticles in a capillary-based droplet reactor. *Journal of Material Chemistry*. 2012;22:4704-4708. DOI: 10.1039/c2jm30257h
- [39] Leyre Gomez, Victor Sebastian, Silvia Irusta, Alfonso Ibarra, Manuel Arruebo and Jesus Santamaria Scaled-up production of plasmonic nanoparticles using microfluidics: from metal precursors to functionalized and sterilized nanoparticles. *Lab on a Chip*. ; 14:325-332. DOI: 10.1039/c3lc50999k
- [40] Christophe A. Serra, Zhenqi Chang Microfluidic-Assisted Synthesis of Polymer. *Chem. Eng. Technol.*. 2008;31(8):1099-1115. DOI: 10.1002/ceat.200800219
- [41] Daniel C. Pregibon, Mehmet Toner, Patrick S. Doyle Multifunctional Encoded Particles for High-Throughput Biomolecule Analysis. *Science*. 2007;315:1393-1396. DOI: 10.1126/science.1134929
- [42] YongTae Kim, Bomy Lee Chung, Mingming Ma, Willem J. M. Mulder, Zahi A. Fayad, Omid C. Farokhzad, and Robert Langer, Mass Production and Size Control of Lipid-Polymer Hybrid Nanoparticles through Controlled Microvortices. *Nano Letters*. 2012;12:3587-3591. DOI: 10.1021/nl301253v
- [43] Jong-Min Lim, Archana Swami, Laura M. Gilson, Sunandini Chopra, Sungyoung Choi, Jun Wu, Robert Langer, Ultra-High Throughput Synthesis of Nanoparticles with Homogeneous Size Distribution Using a Coaxial, Turbulent Jet Mixer. *ACS nano*. ; 8:6056-6065. DOI: 10.1021/nn501371n
- [44] Jiashu Sun, Ya Yunlei Xianyu, Ya Mengmeng Li, Ya Wenwen Liu, a Lu Zhang, Dingbin Liu, a Chao Liu, b Guoqing Hub and Xingyu Jiang* A microfluidic origami chip for synthesis of functionalized polymeric nanoparticles. *Nanoscale*. 2013;(5):5262-5265. DOI: 10.1039/c3nr01289a
- [45] Shin-Hyun Kim and David A. Weitz One-Step Emulsification of Multiple Concentric Shells with Capillary Microfluidic Devices. *Angewandte Chemie International Edition*. 2011;50:8731-8734. DOI: 10.1002/anie.201102946.
- [46] Su Kyung Suh, Kai Yuet, Dae Kun Hwang, Ki Wan Bong, Patrick S. Doyle, and T. Alan Hatton Synthesis of Nonspherical Superparamagnetic Particles: In Situ Coprecipitation of Magnetic Nanoparticles in Microgels Prepared by Stop-Flow Lithography. *Journal of the American Chemical Society*. 2012;134:7337-7343. DOI: 10.1021/ja209245v

Edited by Xiao-Ying Yu

Increasing innovations and applications make microfluidics a versatile choice for researchers in many disciplines. This book consists of multiple review chapters that aim to cover recent advances and new applications of microfluidics in biology, electronics, energy, and materials sciences. It provides comprehensive views of various aspects of microfluidics ranging from fundamentals of fabrication, flow control, and droplet manipulation to the most recent exploration in emerging areas such as material synthesis, imaging and novel spectroscopy, and marriage with electronics. The chapters have many illustrations showcasing exciting results. This book should be useful for those who are eager to learn more about microfluidics as well as researchers who want to pick up new concepts and developments in this fast-growing field.

Photo by Ruliz / Can Stock

IntechOpen

